

MAY 13 1989

0830 - H-10
3.30

NAS 1.55:3032

NASA Conference Publication 3032

23rd Aerospace Mechanisms Symposium

*Proceedings of a symposium held at
NASA Marshall Space Flight Center
Huntsville, Alabama
May 3-5, 1989*



23rd Aerospace Mechanisms Symposium

Proceedings of a symposium sponsored by the
National Aeronautics and Space Administration,
Washington, D.C., the California Institute of
Technology, Pasadena, California, and the
Lockheed Missiles and Space Company, Inc.,
Sunnyvale, California, and held at
NASA Marshall Space Flight Center
Huntsville, Alabama
May 3-5, 1989



National Aeronautics and
Space Administration
Office of Management
Scientific and Technical
Information Division

1989

I

BLANK PAGE

H

PREFACE

The proceedings of the 23rd Aerospace Mechanisms Symposium, which was held at the NASA Marshall Space Flight Center, Huntsville, Alabama, on May 3 to 5, 1989, are reported in this NASA Conference Publication. The symposium was sponsored by the National Aeronautics and Space Administration, the California Institute of Technology, and Lockheed Missiles and Space Company, Inc.

The purpose of the symposium was to provide a forum for the interchange of information among those active in the field of mechanisms technology. To that end 22 papers were presented on aeronautics and space flight, with special emphasis on actuators, aerospace mechanism applications for ground support equipment, lubricants, latches, connectors, and other mechanisms for large space structures. The papers were prepared by authors from a broad aerospace background, including the U.S. aerospace industry, NASA, and European and Asian participants.

The efforts of the review committee, session chairmen, and speakers contributing to the technical excellence and professional character of the conference are especially appreciated.

The use of trade names or names of manufacturers in this publication does not constitute an official endorsement of such products or manufacturers, either expressed or implied, by the National Aeronautics and Space Administration.

BLANK PAGE

TABLE OF CONTENTS

	Page
<u>SESSION I</u>	
THE EVOLUTION OF SPACE MECHANISMS TECHNOLOGY IN THE EUROPEAN SPACE AGENCY R&D PROGRAM (D. Wyn-Roberts).....	1
A UNIDIRECTIONAL ROTARY SOLENOID AS APPLIED TO STRONGLINKS (E. W. Kenderdine).....	17
THE DESIGN AND ANALYSIS OF A DOUBLE SWIVEL TOGGLE RELEASE MECHANISM FOR THE ORBITER STABILIZED PAYLOAD DEPLOYMENT SYSTEM (Guy L. King and Ted Tsai).....	39
DESIGN, FABRICATION, AND TEST OF A 4750 NEWTON-METER-SECOND DOUBLE GIMBAL CONTROL MOMENT GYROCOPE (Lewis Cook, Paul Golley, Henning Krome, Joseph Blondin, Charles Gurrisi, and John Kolvek).....	59
<u>SESSION II</u>	
CAROUSEL DEPLOYMENT SYSTEM FOR COILABLE LATTICE TRUSS (Robert M. Warden and P. Alan Jones).....	77
DESIGN AND TESTING OF A DEPLOYABLE, RETRIEVABLE BOOM FOR SPACE APPLICATIONS (P. Becchi and S. Dell'Amico).....	101
DESIGN AND VERIFICATION OF MECHANISMS FOR A LARGE FOLDABLE ANTENNA (Hans Jurgen Luhmann, Carl Christian Etzler, and Rudolf Wagner).....	113
<u>SESSION III</u>	
EDDY-CURRENT DAMPER (R. C. Ellis, R. A. Fink, and R. W. Rich).....	127
DEVELOPMENT OF A PRECISION, WIDE-DYNAMIC-RANGE ACTUATOR FOR USE IN ACTIVE OPTICAL SYSTEMS (K. R. Lorell, J-N. Aubrun, D. F. Zacharie, and E. O. Perez).....	139
PYRO THRUSTER FOR PERFORMING ROCKET BOOSTER ATTACHMENT, DISCONNECT, AND JETTISON FUNCTIONS (Stephen Hornyak).....	157
DESIGN AND DEVELOPMENT OF A HIGH-STIFFNESS, HIGH RESOLUTION TORQUE SENSOR (Michael M. Socha and Boris J. Lurie).....	169

TABLE OF CONTENTS (Concluded)

	Page
<u>SESSION IV</u>	
ASTRONAUT TOOL DEVELOPMENT: AN ORBITAL REPLACEABLE UNIT - PORTABLE HANDHOLD (John W. Redmon, Jr.).....	181
DOUBLE LEAD SPIRAL PLATEN PARALLEL JAW END EFFECTOR (David C. Beals).....	195
TRACTION-DRIVE FORCE TRANSMISSION FOR TELEROBOTIC JOINTS (D. M. Williams and D. P. Kuban).....	207
FLIGHT TELEROBOT MECHANISM DESIGN: PROBLEMS AND CHALLENGES (John B. Dahlgren and Edwin P. Kan).....	223
<u>SESSION V</u>	
A FAMILY OF BAPTA'S FOR GEO AND LEO APPLICATIONS (W. Auer).....	241
SIGNAL AND POWER ROLL RING TESTING UPDATE (Dennis W. Smith).....	255
DESIGN OF A 60 GHz BEAM WAVEGUIDE ANTENNA POSITIONER (Kenneth S. Emerick).....	267
AGE DISTRIBUTION AMONG NASA SCIENTISTS AND ENGINEERS (Michael L. Ciancone).....	279
<u>SESSION VI</u>	
PANEL DISCUSSION	
<u>SESSION VII</u>	
PRACTICAL EXPERIENCES WITH WORM GEARING FOR SPACECRAFT POWER TRANSMISSION APPLICATIONS (William Purdy and William McCown).....	291
A TWO-AXIS LASER BORESIGHT SYSTEM FOR A SHUTTLE EXPERIMENT (Joseph F. DeLorme).....	309
THE IN-VACUO TORQUE PERFORMANCE OF DRY-LUBRICATED BALL BEARINGS AT CRYOGENIC TEMPERATURES (S. G. Gould and E. W. Roberts).....	319
APPENDIX - PANEL DISCUSSION SUMMARIES, 22ND AEROSPACE MECHANISMS SYMPOSIUM.....	335
ABBREVIATIONS AND ACRONYMS.....	343

THE EVOLUTION OF SPACE MECHANISMS IN THE ESA R&D PROGRAM

D. Wyn-Roberts*

INTRODUCTION

The evolution of space mechanisms is presently occurring very quickly in Europe, being driven by vigorous new programs in the area of Scientific Satellites, Columbus space station development, applications spacecraft for communications, Earth observation and meteorology, and the Ariane V and Hermes space transportation systems.

In this paper the status of recently completed and already ongoing technology developments will be discussed as well as some of the most important future developments. A selection will be made since the number of developments is rather large, but the aim will be to consider the applications or lessons learned from the technology programs and the application goals of the new areas.

SPACE MECHANISMS TECHNOLOGY IN THE ESA PROGRAM

The word mechanism tends to cover a wide range of items and disciplines, so Figure 1 has been evolved to give a classification of the disciplines involved. Based on this classification, the mechanism technology items included in the Agency's program for 1988 have been listed by category in Table 1.

A number of items which were already reported in 1985 [1] have been completed or are about to be finished and these will be considered first in order to determine the outcome of the technology work.

Finally, the new items will be described in order to determine the future direction of the mechanisms technology which is being developed.

EVOLUTION OF SPACE MECHANISMS TECHNOLOGY IN RECENT YEARS

Category 1 Electromechanical Components

There is continuous support of the development of electric motors for space use within the ESA technology program, since there is always a demand for special application devices. Of particular interest in this respect has been a superconducting motor for cryogenic use.

Support for this work commenced in 1981 and by the end of 1984 a superconducting motor, suitable for operation of scientific instruments in the

*ESTEC, Noordwijk, The Netherlands

focal plane of a cooled telescope for example, had been developed and tested by SEP and SAGEM in France. An already space-qualified size-stepper motor was used and the winding material changed to a niobium-titanium alloy. A heat dissipation of below 1 mW during operation was achieved. Testing included vibration and torque measurement at cryogenic temperature, together with an endurance test at liquid helium temperature [2].

This technology has been successfully transferred since the motor is being used as a component of the infra-red camera on the Infrared Space Observatory (ISO) project of ESA. A continuation technology study has recently been completed, the aim being to reduce the overall heat dissipation of such a motor including its lead wires.

A second example of recently completed motor technology is the so-called Digital Position Actuator (DPA). This has been less successful in terms of application, since no specific need has arisen. The development was based on a perceived need rather than an "external" interest or inquiry. The aim has been to develop a motor capable of indexing to a specific angular position on receipt of a digital command. Supposed application was in scientific instruments and/or robotics. An interesting feature was the strict packaging dimensions which were specified to house both motor and electronics. This was initially achieved by the contractor (Inland Motor Co., Ireland), but the electronics was rejected since not all were space approved. When space-approved devices were used, the dimensions could not be reached. The final dimensions achieved were 85-mm square cross-section by 190-cm long compared with a requirement of 70-mm diameter by 100-mm long. The motor developed was a dc brushless motor with trapezoidal motor flux distribution. It has the capability of indexing to a given angle (or series of angles) with an accuracy of 10 arcsec.

Category 2 Control Actuators

Category 2 considers Energy Storage Wheels (ESW) and reaction and momentum wheels.

In the case of ESWs, an increase in interest in these devices occurred in 1984, mainly because of the perceived possibility of using them in space station elements to replace batteries. A workshop to review the technology was held at NASA [3], and following this, in Europe new work was started on rotor development for an ESW suitable for space use.

The design and manufacture of such a rotor was completed at the end of 1986 under an ESA technology contract. The rotor consists of a hub made of high strength aluminum alloy with four spokes and an integral (thin) ring. The rim consists of carbon fiber cylinders mounted with interference fit to this ring. The carbon fiber rim concept enables a high energy density to be achieved, but still enabling the mass, volume, and diameter to be restricted. Both 2D and 3D stress analyses have been performed using the finite element approach. The octant model used for 3D analysis is shown in Figure 2; and the mechanical and functional characteristics are given in Table 2.

For the time being, interest in these devices has again lessened, and the first generation European Space Station (Columbus) will certainly use batteries. An extension contract to complete some testing of the rotor is planned for the near future, and then it seems that this technology will again become dormant until such time as project interest arises in it.

Category 3 Antenna and Instrument Mechanisms

This category covers a relatively wide range of items, which have no logical grouping characteristics in terms of mechanical function.

A particularly interesting device is the high-precision displacement mechanism. This has been under technology development for some time (since 1984) and is designed to actuate folding antenna panels on a sub-millimeter spaceborne radio telescope, with an accuracy approaching 1 micron. Two concepts for such a mechanism have been studied by Dornier (Germany) and Sener (Spain). The initial concept was a type of 3D leverage system with motion reduction via flexural members. A mock-up of this device was built and successfully tested under ambient conditions. A drawing of this device is shown in Figure 3A. Potential problems in the area of materials, thermal performance, and integration, however, led to the definition of a second device, shown in Figure 3B. Movement is caused by distortion of a flexural ring and this device has also been successfully tested under ambient conditions. Some further refinement of this design is necessary (e.g., in terms of reduction of high stresses) and it is intended to manufacture a space-approved version and perform thermal-vacuum testing in order to complete the technology development.

Another device of interest in this category is the so-called micro-gravity isolation mount (MGIM). This is a magnetically suspended, 6-degree-of-freedom platform on which experiments can be mounted. The suspension is activated by a positive feedback system causing the experiments to be isolated from external vibration disturbances in the frequency range of interest. The feasibility of this device has already been demonstrated under an ESA contract running from October 1985 to February 1987. The results of this work were presented at the 21st Aerospace Mechanisms Symposium at Houston. The interest in this work for space station application is continuing and a further contract was awarded in September 1988 in order to study the development of this device for mounting inside an experiment on the Columbus space station.

Category 4 Deployment Mechanisms

The only item presently included in this category is the coilable tube mast (CTM). A small diameter version has already been built by the SENER company in Spain and will fly on the Ulysses spacecraft. The latest version of the boom is shown in Figure 4, where the shape of the boom cross-section is also visible. The mechanism is capable of deploying and retracting the boom which has nominal length of 15 m. The initial development was completed in April 1988 with the achievement of the following:

1. Design and manufacture of a CTM with deployment/retraction capability
2. Manufacture of several tube samples in beryllium copper and carbon fiber reinforced plastic
3. Demonstration of continuous manufacturing methods for both tube materials
4. Functional life and vibration testing of the complete CTM. During life testing, 20 cycles of deployment and retraction were completed with full success, with no detectable damage occurring.

A new contract has been started on the CTM in order to obtain a qualified version with fully space-approved parts and components. Under this same contract, a qualification approach for a family of tube sizes, covering the diameter range of approximately 22 mm to 130 mm, will also be evolved.

It is also encouraging to note that this technology is being applied in another new area, namely to deploy an in-flight contamination experiment on the Shuttle under a cooperative U.S./European venture on the Technology Demonstration Program. The payload, which weighs 15 kg, is supplied by NASA, and ESA will supply the CTM. This will be a 15-m long retractable version with a cross-section diameter of approximately 63 mm, and will be ejectable for safety reasons.

The previous examples are of technology items already in a reasonably advanced, or even completed, stage of development. These examples illustrated that technology items must be continually reviewed and planned. Obviously certain items, such as the energy storage wheel and the digital positioning actuator seem to have been developed too early for direct application for project needs. The microgravity isolation mount technology, however, has been investigated largely without project support, but nevertheless subsequently raised interest especially among the scientific users community. It has also helped to raise the awareness and understanding of the microgravity phenomena and related engineering aspects.

Similarly, the CTM development has raised the interest of potential users and found application in an area which was not originally envisaged. Another deployment mechanism, the extendable and retractable mast (ERM) which was reported in Reference 7 has been successfully transferred to the Columbus project after completion of the technology work.

RECENT TECHNOLOGY

This section considers some of the newer items under investigation and indicates their expected applications.

The large momentum wheel work started at the end of 1984 with the Teldix company and its aim was to study momentum wheels suitable for eventual use on the Columbus Space Station. The momentum "ceiling" for the initial study was

1000 N-m-sec. In a continuation study completed at the end of 1988, a detailed design of a wheel of 1000 N-m-sec with a diameter of 60 cm (Columbus requirement) was completed, and an engineering model was built and tested. Prior to this work, no wheel above 70 N-m-sec had been built in Europe. The particular design challenges posed by this development can be summarized as follows:

- High centrifugal forces, 15 times higher than for previous wheels
- Increased vibrational loads
- Increased atmospheric loading on the housing
- Strength requirements approaching the limits of existing materials.

The final wheel design consisted of a steel rim held to a central ball bearing hub by five bolted spokes inclined by 8 deg. The nominal operating speed is 6000 rpm. A cross-sectional drawing of this wheel is shown in Figure 5.

At the present time the wheel momentum requirements for Columbus seem to be more in the region of 300 N-m-sec. The development of a 1000 N-m-sec wheel has been justified, however, from a technology point of view, since the higher requirements were a development driver. The problems overcome in developing a 1000 N-m-sec wheel enable the smaller (medium) wheel to be now developed much more easily.

Two technology studies have recently commenced in the mechanical systems category which are directly related to the Agency's Scientific Satellite Program.

The first one, Sample Acquisition Systems, is being undertaken to support the Comet Nucleus Sample Return mission (CNSR, now known as ROSETTA). In terms of mechanisms, this is an extremely challenging mission and the following are being studied in the technology work:

- Cometary soil properties
- Anchoring of the spacecraft to the comet surface
- Drilling of core samples
- Sampling of surface material
- "Harpooning" of the comet surface.

The initial study commenced in March 1988 with Tecnospazio and Tecnomare of Italy. A survey of possible cometary material properties was first carried out. Following this, a conceptual and trade-off phase on the mechanism design was completed. Baseline mechanisms have been chosen and will be designed in

detail in the final part of the study work. The baseline mechanisms chosen are shown in Figure 6. Of these, the most challenging is certainly the drill system. Core samples have to be extracted and then stored in sealed containers for return to Earth laboratories. The sampling requirements for this instrument are as follows:

Core sample

sample depth - 1 m required with goal of 3 m
sample diameter - 0.06 to 0.14 m

Volatile sample

depth - 0.2 m below core sample
volume - 15 dm³

Crust sample

depth - 0.05 m
volume - 4 dm³.

Following the completion of the design study, it is planned to initiate a new contract in order to manufacture and test prototype mechanisms.

The second technology study is for the Spin and Eject Mechanism to be used on the Cassini mission. This is a joint ESA/NASA mission. The "mother" spacecraft provided by NASA will orbit Saturn, whereas, ESA will provide a probe for landing on Titan, one of Saturn's moons. The cruise phase from Earth to Titan will have a duration of approximately 8 years and then the mechanism will eject the probe with a velocity of 0.3 m/sec relative to the Orbiter and with a spin rate of 10 rpm.

A contract to study this mechanism was started with the Piaggio company of Italy in May 1987. Design, dynamic analyses and finally a trade-off of several candidate mechanisms has been performed, leading to a choice of preferred mechanism. A detailed design and analysis of this will be made and then a mock-up of the device will be built and tested. The test will simulate the zero-g condition together with the probe inertia about the spin axis, which is 50 kg m². The expected probe mass for the Cassini mission is 192 kg. The chosen mechanism consists of a movable ring, used to eject the probe, which is pushed in a track of 30 deg inclination by four compression springs. The probe is released from the moveable ring by pyrotechnics for "launch." The Ring diameter is 0.5 m. A drawing of this mechanism is shown in Figure 7.

The remaining items in Table 1 will not be discussed in any detail since they are being negotiated and have not yet started. They are, however, of interest and the following short comments can be made.

The tether mechanism study will survey possible European tether missions and then lead to designs of various suitable tether mechanisms, followed by manufacture and testing of the most technologically challenging parts of these mechanisms.

In category 3, antenna deployment and pointing mechanisms will be studied for the next generation of European communication spacecraft, specifically the Data Relay Satellite, meant for communicating with the Columbus Space Station, and the experimental spacecraft known as SAT2. There is a high interest in Europe in antenna pointing mechanisms and the development of such a device for large angles has taken place under the ESA technology program. This is known as the Hemispherical Pointing Mechanism (HPM) and was mentioned in Reference 1. The design was based on an inclined wedge principle. An engineering model of a single axis drive unit has been developed and is planned to be thermal vacuum tested during 1989. There is presently project interest in this device for possible use in pointing a laser communication experiment.

Another category of interest is tribology, but this aspect needs a paper to itself and thus can only be touched upon here. At the time of writing, a new four-year contract for research into space tribology is being negotiated with the European Space Tribology Laboratory (ESTL). This contract will cover, in particular, the aspects listed below which are all aimed toward solving particular new project related problems.

1. High speed bearing lubrication
2. Slip ring lifetime improvement
3. Gearbox lubrication especially for robotics
4. Cryogenic tribology
5. High temperature tribology
6. Continuing fundamental investigations of space lubricants, especially MoS₂ and ceramics.

Further tribological studies listed in Table 1 are directed towards improvement in understanding the problems related to turbomachinery.

CONCLUSIONS

The evolution of space mechanisms in terms of increasing complexity and size is continuing. Spacecraft projects are finding increasingly more challenging roles for mechanisms and the technology work is being directed toward solving the problems raised.

In general, the high interest and support in the mechanisms technology development program could be said to be related to the relatively high success in both utilizing and directing the work for projects. Close liaison and careful planning therefore pays dividends in this respect. Nevertheless, it must be remembered that technology by its very nature explores relatively unknown areas, therefore not all lines of inquiry can be expected to lead to immediate applications. In this respect, it is important to retain

flexibility so that work can be re-directed or stopped if necessary. The lessons learned should then be utilized for further work.

REFERENCES

1. Wyn-Roberts, D.: Space Mechanism Development in the ESA Technological Research Programme. Proceedings of the Second European Space Mechanisms and Tribology Symposium (ESA SP-231), October 1985.
2. Bugeat, Petit, Valentian, Junca, and Verain: Electric Motor with Superconductivity Windings for Actuation Mechanism in the Focal Plane of a Space Cryostat. Proceedings of the Second European Space Mechanisms and Tribology Symposium (ESA SP-231), October 1985.
3. "An Assessment of Integrated Flywheel System Technology," NASA Conference Publication No. 2346, February 1984.
4. del Campo, F., del Torro, J., and Rivacoba, J.: Fine Adjustment Mechanism for FIRST. Proceedings of Third European Space Mechanisms and Tribology Symposium (ESA SP-279), October 1987.
5. Hostenkamp, R. G.: Design of a Linear Actuator and Breadboard Test Result. Proceedings of Third European Space Mechanisms and Tribology Symposium (ESA SP-279), October 1987.
6. Jones, D. I., et al.: A Microgravity Isolation Mount. 21st Aerospace Mechs. Symposium, Houston, May 1987 (NASA Conference Publication 2470).
7. Schmid, M. and Aguirre, M.: Extendable Retractable Telescopic Mast for Deployable Structures. 20th Aerospace Mechanisms Symposium, NASA Conference Publication 2423.

TABLE 1. MECHANISMS TECHNOLOGY BY CATEGORY

1. Electro-mechanical	<ul style="list-style-type: none"> ● Electric motors components ● Turbomachinery rotor dynamics
2. Control Actuators	<ul style="list-style-type: none"> ● Large momentum wheel ● Rotors for ESW's
3. Instrument and antenna mechanisms	<ul style="list-style-type: none"> ● High precision displacement mechanism ● Microgravity isolation mount ● Antenna deployment and pointing
4. Deployment mechanisms	<ul style="list-style-type: none"> ● Collapsible tube mast
5. Mechanical Systems	<ul style="list-style-type: none"> ● Sample acquisition systems ● Spin/eject devices for planetary mission ● Tether mechanism
6. Tribology	<ul style="list-style-type: none"> ● Tribology ● Seal material life test ● Advanced seal technology ● Advanced bearing technology

TABLE 2. ESW MECHANICAL AND FUNCTIONAL CHARACTERISTICS

● Outer diameter	600 mm
● Inner diameter (of composite rim)	510 mm
● Width	340 mm
● Outer diameter growth at maximum operating speed 24,000 rpm	2.8 mm
● Mass	60.5 kg
● Max-operating peripheral speed	770 m/sec (corresponding to 2566 r/sec angular velocity)
● Energy density at maximum operating speed	3.3 KWh

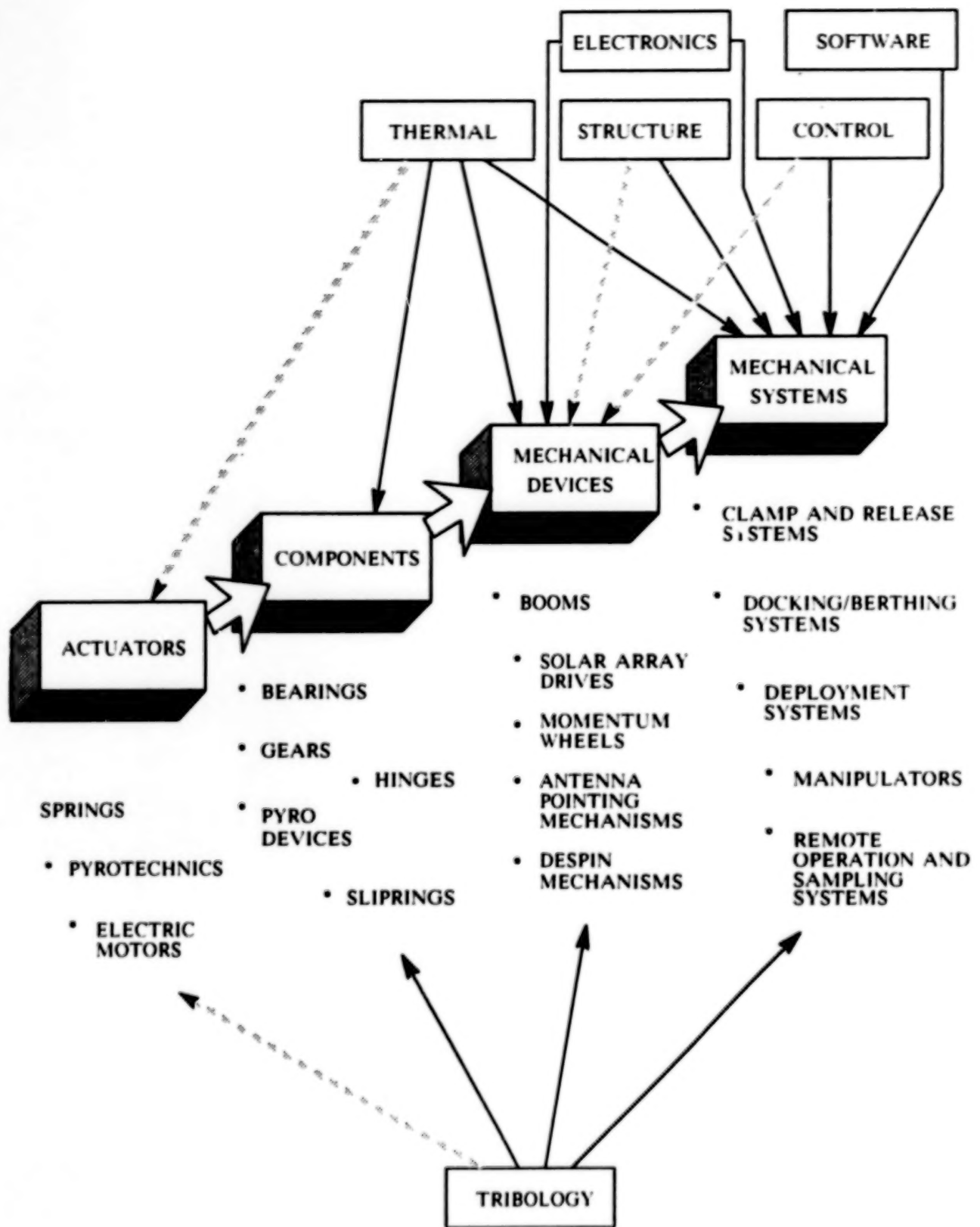
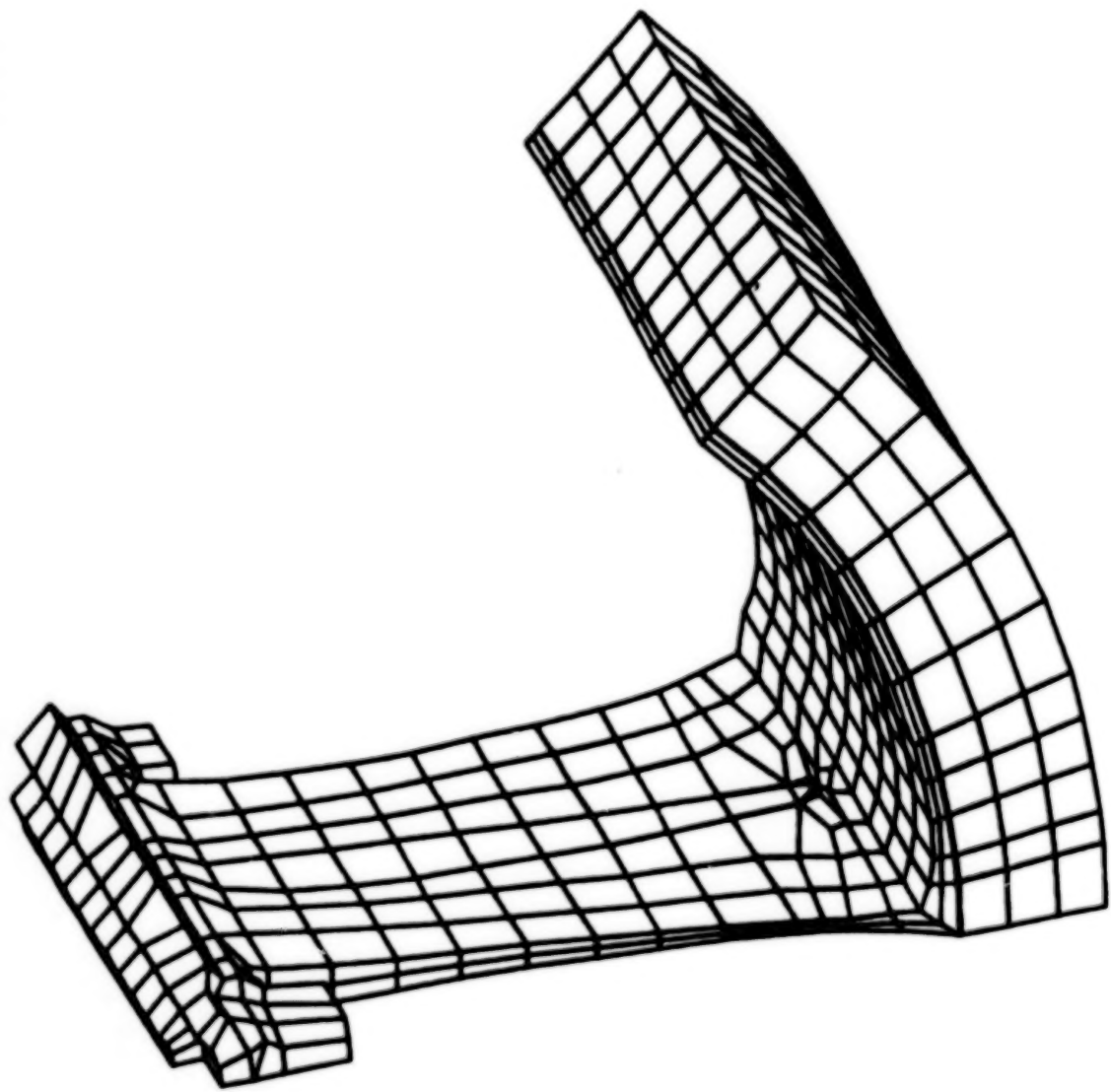


Figure 1. Mechanisms hierarchy.

PREP7 -INP-



1

Figure 2. Three-dimensional model of flywheel.

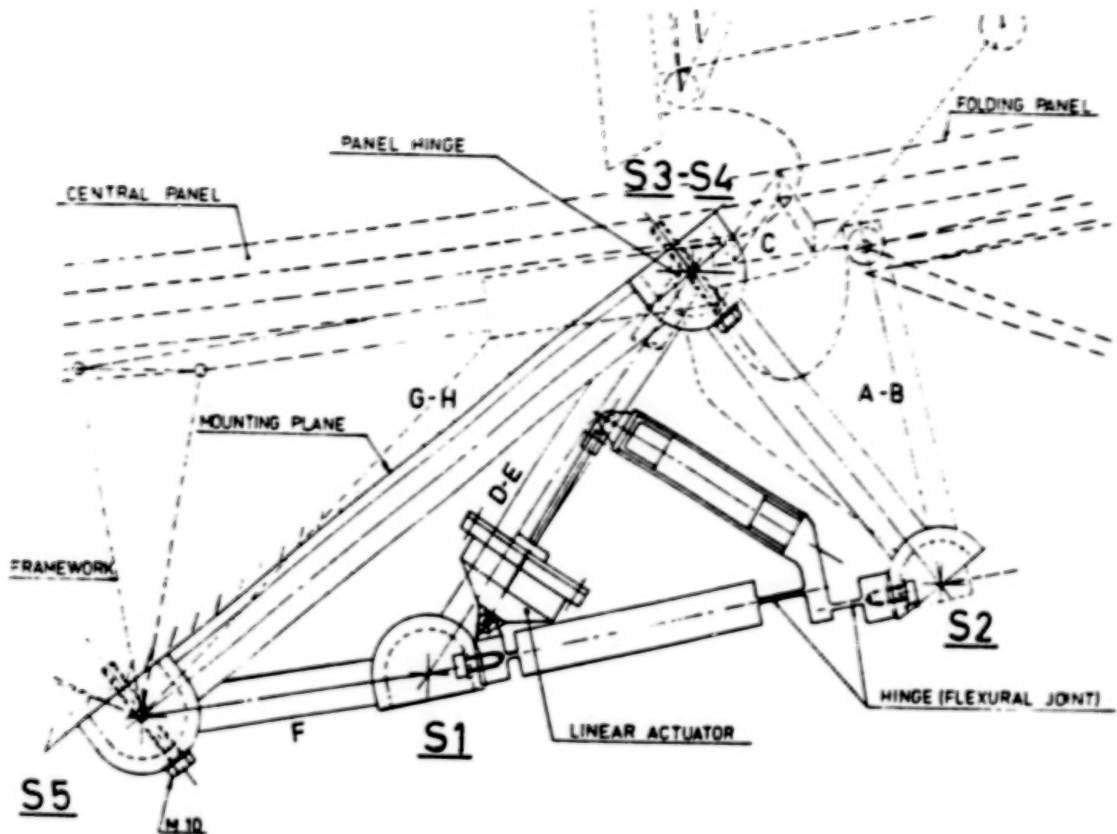


Figure 3A. Precision actuator type I.

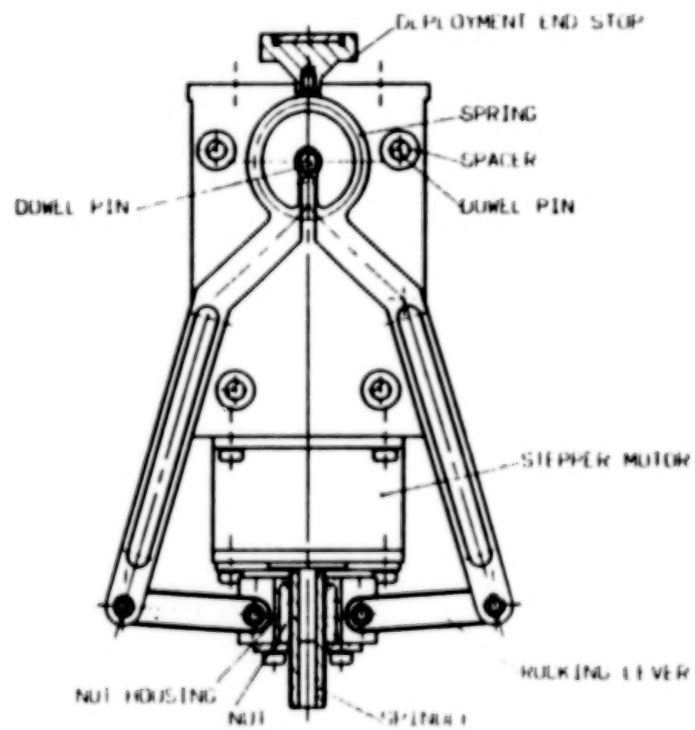
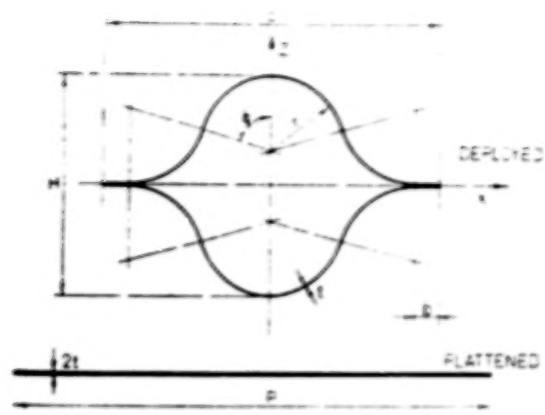


Figure 3B. Precision actuator type II.



Tube cross-section

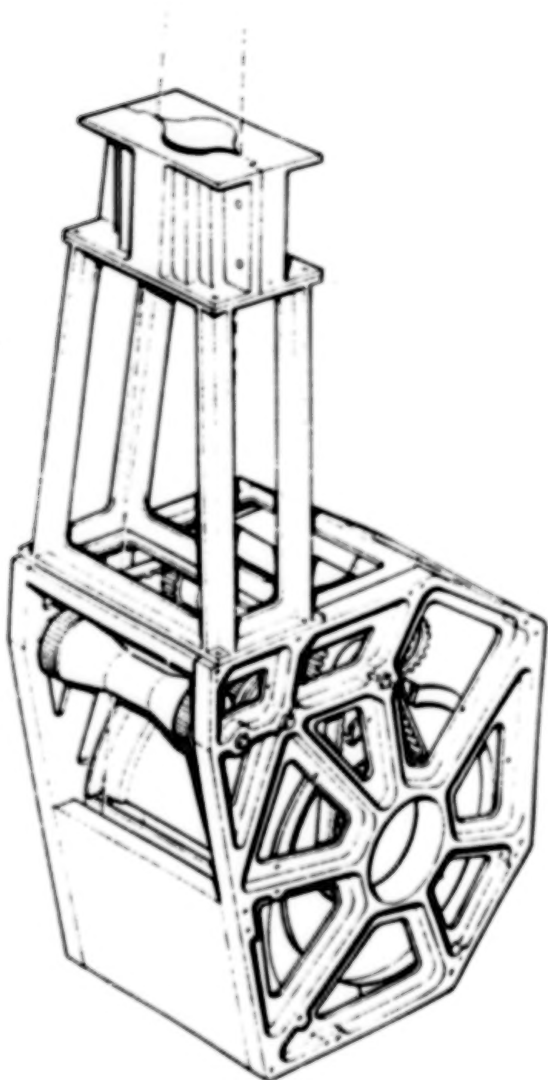


Figure 4. Coiled tubular mast.

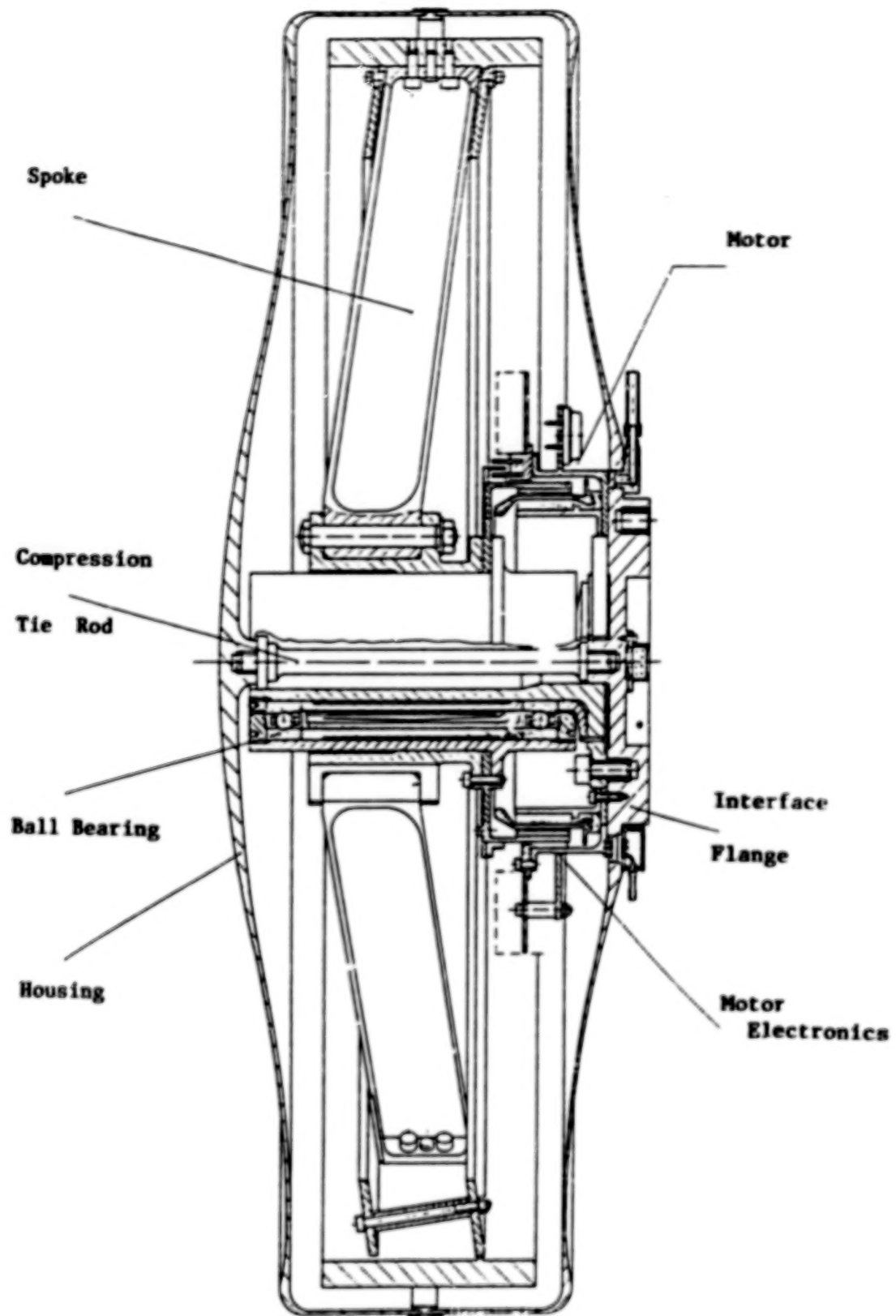


Figure 5. Large reaction wheel.

**BLANK
PAGE**

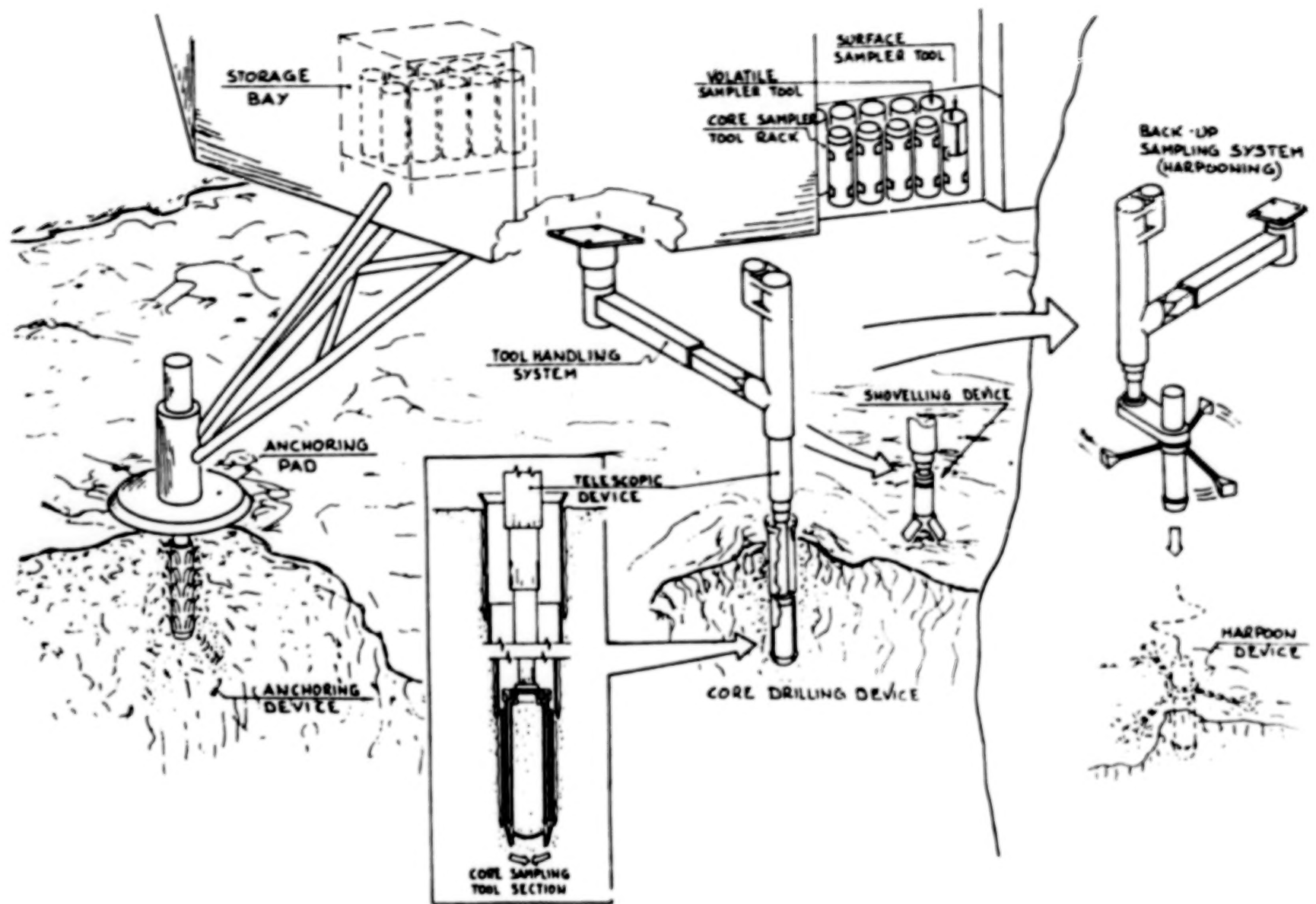


Figure 6. Comet surface sampling mechanisms.

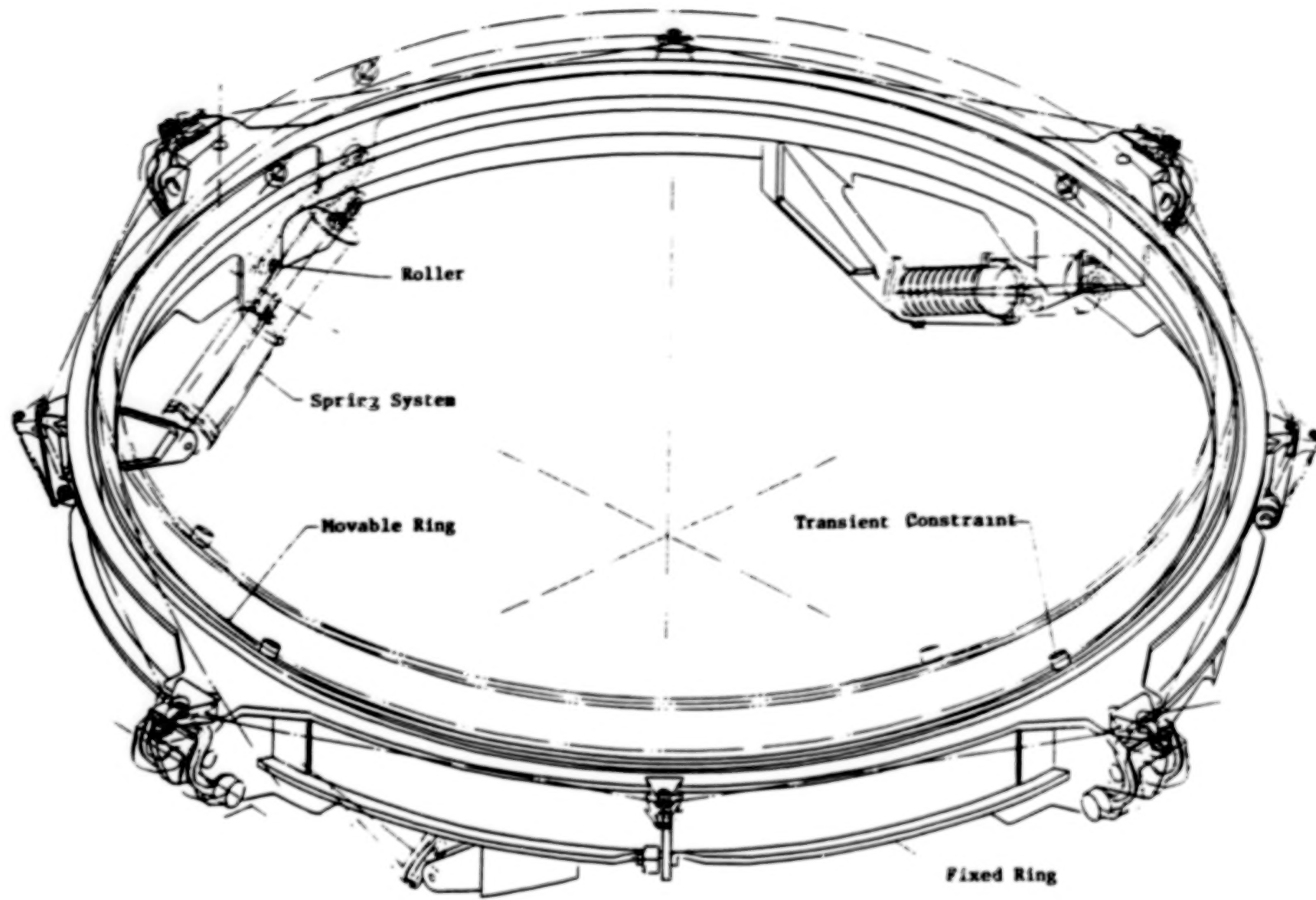


Figure 7. Spin/eject mechanism.

A UNIDIRECTIONAL ROTARY SOLENOID AS APPLIED TO STRONGLINKS

Eugene W. Kenderdine*

ABSTRACT

This paper describes the design goals and results of an advanced development stronglink project with special emphasis on a new rotary solenoid concept.

INTRODUCTION

During the handling, storage, transporting, and deployment of weapons, it is inevitable that accidents will occur. With nuclear weapons, it is mandatory that such accidents not result in nuclear detonation. Stronglinks are one of several interlocks on each weapon, designed to prevent accidental detonation in the event of abnormal environments (impact, fire, crush, etc.).

Stronglinks are electromechanical devices that prevent energy from being applied through a "barrier" to certain components in an "exclusion" region unless there is human intent that such energy be applied. The stronglink is an energy gating (or switching) mechanism with a built-in "combination lock." The only combination that will open this lock is an electrical unique signal (UQS) which allows the device to be driven from a "safed" state to an "enabled" state. Stronglinks are used strictly for safety purposes as differentiated from other devices used for security reasons.

The term "stronglink" comes from a concept of juxtapositioning this device with an environmentally "weak" device (weaklink). The weaklink is a component vital to the arming of the weapon (example: capacitors). Usually an attempt is made to "sandwich" the stronglink inside the weaklink so that any environmental "attack" on the stronglink will first irrevocably disable the weaklink before damaging the stronglink.

Stronglinks in the field are generally "one-shot," single-try devices. Each weapon system contains two stronglinks of different designs that respond to different UQS electrical pulse patterns. This is to prevent the possibility of a common mode of failure in the event of some unforeseen weakness in one device. Stronglinks consist of three major components:

1. Energy gating mechanism
2. Discriminator mechanism (combination lock)
3. Drive mechanism (usually two rotary solenoids).

*Sandia National Laboratories, Albuquerque, New Mexico.

Figure 1 shows the advanced development stronglink assembly with the major components indicated.

GOALS

The primary goals of this advanced development project were to achieve a smaller package (especially in the direction parallel to the solenoid axes) and to provide safety enhancement. Secondary goals were simplicity, reduced enabling time, and a more energy-efficient device.

UNIQUE SIGNAL (UQS)

The UQS is the only electrical pulse pattern that will allow the stronglink to advance to the enabled condition (see Fig. 2). The UQS is a predetermined pattern of groups of "A" and "B" events. Generally there is a mixture of 12 "A" events and 12 "B" events for a total of 24 events.

The 24 events give a gross total of 2^{24} possible combinations (16,777,216). The grouping of "A" and "B" events for a UQS format is rigorously analyzed to provide the highest possible odds against the signal being randomly generated in an abnormal environment. Grouping of events in a repetitive or "symmetrical" format is not allowed.

The "A" pulse event must clearly differ from the "B" pulse event with some characteristic such as amplitude, duration, polarity, point of application, etc. In one production stronglink, the two events are "short" (100 msec) and "long" (400 msec) pulses applied through a single circuit to a single solenoid. The solenoid releases a clock which in turn "shifts gears," depending on how long power is applied to the solenoid. In all other designs, two independent solenoids are used (with no clock). The solenoids are pulsed through two independent electrical circuits. It is the interplay of the two solenoids and the discriminator mechanism that either allows the stronglink to advance to the enabled condition, or irreversibly lock in a safe condition.

ENERGY GATING MECHANISM

Several different types of devices (with their related locking mechanisms) have been considered to control the passage of energy through the barrier into the exclusion region. Work continues on new concepts with the goal of further nuclear safety enhancement. The devices include locks on alternator shafts, gas valves, switch contact rotors, light shutters, magnetic flux shutters, and a device that moves a small portion of the physics package.

Current production stronglinks use switch contacts, magnetic flux shutters, and the physics package mechanism to perform the energy transfer function. This advanced development stronglink uses the magnetic flux shutter mechanism for energy gating.

With the magnetic flux device, an electrical transformer is split into its primary and secondary halves with an air gap between the primary and

secondary C-cores. A disk (safe/enable wheel) is placed in this air gap (see Fig. 3). The disk, except for localized magnetic "windows," blocks the passage of magnetic flux lines between the primary and secondary for all areas of the disk, except the windows. The discriminator mechanism locks the disk in the flux blocking mode unless the stronglink receives the UQS electrical pulse pattern. On receipt of the UQS, the disk is rotated from the "safe" position to the "enabled" position, allowing the primary to energize the secondary through the magnetic windows.

The primary lies outside the exclusion region; the secondary lies inside. The advantage of this type of energy transfer device is that wires are not required to cross the barrier into the exclusion region. This eliminates a path for electrical energy to cross the barrier (from lightning or any other source).

The disks are fabricated from a laminated material with ferrite windows. The laminates used to date are copper-steel-copper. Some work is also being done with a silver-nickel-silver laminate. The ferrite material is a solid solution of iron oxide and manganese oxide. The ferrite window is surrounded by a copper ring which provides magnetic isolation from the rest of the disk.

Physically the ferrite material is similar to a ceramic, which has created a fair amount of manufacturing problems. The windows are in the shape of a pair of half moons. The half moons are fabricated from a solid disk with a slitting (grinding) operation. Yields are not really satisfactory due to cracking of the ferrites. The ferrites also require a metalizing operation so they can be soldered into the copper rings.

Due to these processing problems, there have been continuing studies of alternate processes and alternate materials. An alternate design being considered uses an iron-nickel ribbon laminate construction similar to the transformer core construction. The laminates must stand on edge parallel to the disk axis of rotation to allow flux passage through the wheel.

DISCRIMINATOR MECHANISM (Combination Lock)

The discriminator mechanism is a type of mechanical "maze" representing the predetermined electrical UQS pulse pattern. If the solenoids receive the UQS, each pulse allows a correct step through the maze. An incorrect pulse pattern leads up a "blind alley" in the maze, causing stronglink lockup.

With the exception of the above mentioned stronglink containing the single solenoid and clock, all of our stronglinks are used in the field as one-shot, single-try devices. Lockup is electrically irreversible, and if it occurs, manual access is required to reset the device. The noted exception is a multiple-try device that is electrically resettable with an extra long (1200 msec) reset pulse. This device requires a much longer UQS (more events) to compensate for the multiple-try feature. For test purposes, all units are electrically resettable when correctly enabled with the UQS.

Past stronglinks have contained one of two general types of discriminator mechanisms. The first type features a gate (or two gates) working in conjunction with a discriminator wheel containing two rows of some type of teeth about the periphery of the wheel. One of the rows contains groups of teeth representing UQS "A" events; the other, "B" events. Where there is a group of teeth in one row, there are corresponding voids in the other row. When the "A" event gate is closed, the "B" event gate is opened and vice versa. The enabling logic thus requires the gate to be open for the row with advancing teeth, while the other gate is closed in the area of the voids. After a group of teeth in one row has passed through its gate, the gates must change states to allow for passage of teeth in the other row. If a tooth advances into a closed gate, it is blocked, and the gate can no longer be opened. Lockup has occurred.

The second type of discriminator mechanism uses a type of pawl/ratchet-wheel mechanism for signal discrimination. The ratchet wheel(s) contains "shallow" drive teeth and "deep" penalty teeth in groups representing the UQS. The enabling logic requires the pawl to drive the ratchet wheel only on the shallow teeth and to "skip" over the deeper penalty teeth. With an incorrect signal, the pawl becomes "entrapped" in a deep tooth, blocking the discriminator wheel from further advancement, and again requiring manual access to reset the device.

The subject stronglink features a new type of discriminator mechanism called a "spur gear discriminator" (see Figs. 4 and 5). The mechanism consists of two spur gear assemblies, one representing the UQS "A" events; the other representing the UQS "B" events. Each assembly has 16 tooth positions and advances one tooth position per UQS event. Each assembly consists of four levels of gear segments, with groups of teeth representing the UQS. One solenoid drives the "A" assembly; the other drives the "B" assembly.

In a "normal" pair of mating external spur gears, one gear rotates clockwise, the other counterclockwise. In this device, both gear assemblies rotate in the same direction (shown counterclockwise). Thus, at the interface "mesh," teeth of one assembly are advancing toward teeth of the other assembly. Each gear assembly will always have at least one tooth at one level in the mesh position for each of the 16 positions. Each gear assembly has a hold pawl (not shown) in its drive mechanism that prevents the assembly from backing up, i.e., each assembly can rotate only in the direction shown.

If the condition occurs where an "A" assembly tooth and a "B" assembly tooth of the same level are in the mesh position at the same time, the mechanism is locked. Neither assembly is able to advance or back up, which would be the response to an incorrect electrical pulse pattern. The enabling sequence thus requires sequentially pulsing the solenoids in such a manner as to prevent teeth from the two assemblies from ever coming into contact at the mesh position (the UQS pattern).

Consider the first two UQS pulse events (an "A" event followed by a "B" event). Looking at level "W," if in error, first pulse the "B" assembly,

tooth B2 advances to the mesh position opposing tooth A1, and lockup occurs. If the "A" assembly is correctly pulsed first with a single pulse, tooth A1 of level "W" moves out of the mesh position, allowing the passage of tooth B2. If, again in error, the "A" assembly receives two or more pulses instead of the correct single pulse, tooth A3 of level "Y" will advance to the mesh position opposing tooth B1 and lockup has again occurred. The mechanism operates similarly throughout the UQS pulse sequence. If, for any group of "A" or "B" events, the related solenoid receives more or fewer pulses than specified in the UQS, lockup will occur.

Safety is enhanced because this mechanism presents the same level of restraint throughout a pulse cycle (at least one tooth is always in the path of the opposing gear assembly). With existing devices the level of restraint can vary, depending on the exact gate position or the depth of pawl/ratchet-wheel engagement.

This device is simpler than the pawl/ratchet mechanism and should have fewer dynamic problems and frictional problems, as the two gear assemblies never come into contact during a normal operation. This device has the further advantage of having half the UQS events on one "wheel" and half on the other as opposed to existing devices having all UQS event positions about the periphery of a single wheel. This allows each wheel diameter to be reduced by half while maintaining the same tooth-to-tooth spacing (tooth size). This in turn reduces the inertia reflected to the solenoid to 1/16 of existing values. Since four levels (or rows) are required instead of two, the inertia ends up at 1/8 of existing values.

DRIVE MECHANISM

Oscillatory Rotary Solenoid

Each interrupted transformer type stronglink in production uses two 4-pole cylindrically shaped rotary solenoids (see Fig. 6) to receive incoming electrical pulse patterns and drive the discrimination mechanism. Rotary solenoids are used since they are more readily balanced against G forces than linear solenoids. The solenoid rotors operate between two stop pins, impacting one pin when energized, and the other when de-energized. The rotor stretches an extension spring or winds a torsion spring during the energized stroke. The spring returns the rotor in the opposite direction when the solenoid is de-energized. This oscillatory motion is converted to a rotary motion by the discriminator pawl/ratchet-wheel mechanism. The drive pawl picks up a new ratchet-wheel tooth on the energized stroke and advances the ratchet wheel one unique position on the de-energized spring return stroke (representing one UQS event).

Figure 7 shows the oscillatory rotary solenoid magnetic torque output (measured without the return spring), and it shows the return spring torque; both are plotted against rotor displacement. Without stops, the magnetic torque goes from a zero value, to some maximum value, and back to zero over 45-deg displacement. The first zero torque value occurs when the rotor poles

are midway between the stator poles. The second zero torque occurs after 45-deg rotor displacement when the rotor and stator poles are aligned. The area (12.8×10^{-3} J) under the magnetic torque curve between 0 and 45-deg represents the gross energy available to operate the mechanism for one on-off pulse cycle. Since the device cannot start with zero torque, the rotor is biased from the initial zero-torque position with one of the rotor stop pins. For the device illustrated, the second stop pin limits the rotor travel to 24 deg within the 45-deg total displacement shown.

The area (3.46×10^{-3} J) under the spring curve represents the actual energy stored in the spring. As can be seen, the maximum spring torque is determined by the minimum solenoid torque. While some margin is required between the magnetic torque and spring torque, most of the area between the two curves represents wasted energy. More than being wasted, the excess energy aggravates "bounce" conditions during impact between the rotor and its energized position stop pin. With past development units, this sometimes caused "double pulsing" of the ratchet mechanism, and required damping of the discriminator ratchet wheel to keep the bounce within acceptable limits.

While there have been some dynamic problems with the oscillatory solenoids, the real driving force for consideration of a new solenoid design related to packaging. The axial length of the solenoid cylindrical housing was too great for a "flatpack" stronglink geometry. Consideration was given to laying the solenoids on their sides and using a right angle drive, but the added complexity was undesirable.

Unidirectional Solenoid

The flatpack application led to consideration of a two-pole, horseshoe-shaped stator design, with a two-pole rotor. For approximately the same energy output, this configuration gives a larger package measured normal to the rotor axis, but its axial length is half the cylindrical package length. The overall volume of the horseshoe package is slightly less than the cylindrical package.

After a fair amount of "cogitation" over the two-pole design, the unidirectional solenoid concept occurred. Why not stretch a spring slightly beyond high center (toggle style) during the energized stroke, and have the spring continue the rotor travel in the same direction during the de-energized stroke.

The two-pole rotor and stator (horseshoe) were originally considered for the unidirectional solenoid concept, but eventually a two-pole horseshoe stator and a four-pole rotor were chosen (see Fig. 6). Viewed parallel to the rotor axis, the four-pole rotor profile is identical to the oscillatory solenoid rotor.

Since magnetic flux lines pass through all four poles on the oscillatory device, and only two poles with the unidirectional device, the axial pole thickness of the unidirectional rotor has been doubled. This provides the

same area rate of change during rotor and stator engagement for both devices. With the same flux density for both devices, torque-displacement characteristics are nearly the same. Some differences occur, apparently due to different geometry of the flux leakage paths.

The "over high center" spring action is achieved with a four-lobed cam (see Fig. 8) attached directly to the rotor, plus a cam follower, and an extension spring that loads the follower against the cam. The rotor-cam rotates 45 deg during the solenoid energized stroke, and an additional 45 deg in the same direction during the de-energized stroke, for a total rotor-cam rotation of 90 deg for each on-off electrical pulse. When energized, the rotor-cam drives the follower "uphill" on the cam (stretching the extension spring) for approximately 35-deg rotor cam rotation, at which time the follower crosses the cam high point (spring "high center"). The follower then goes slightly "downhill" to the 45-deg end of energized stroke position, where it stays magnetically detented as long as the solenoid is energized. When the solenoid power is turned off, the stored spring energy forces the follower "downhill" on the cam, driving the rotor-cam forward for the 45-deg de-energized stroke. The rotor cam stays at this position, mechanically detented by the spring loaded follower, until the solenoid is re-energized to repeat the on-off cycle on the next cam lobe. Note: except for flatpack considerations, this unidirectional cam mechanism could be applied to the original cylindrical solenoid, converting it from an oscillatory to a unidirectional device.

Advantages

The unidirectional device has significant advantages over the oscillatory device. Figure 9 compares the packaging of the two types of solenoids and their discriminator mechanisms and indicates the "flatpack" advantage of the unidirectional device.

Since it is no longer necessary to convert oscillatory to rotary motion, a simple direct gear drive can replace the pawl/ratchet-wheel mechanism. This eliminates the continual impacting and drag of the ratcheting operation, reducing wear, friction, and dynamic problems.

The unidirectional solenoid, with gear drive, advances the discriminator wheel one unique position on the energized stroke, and a second unique position on the de-energized stroke. The oscillatory solenoid stores spring energy on the energized stroke and advances the discriminator wheel a single position on the de-energized spring return stroke. The unidirectional solenoid can therefore go through an equal number of unique discriminator wheel positions (UQS events) with half the number of on-off solenoid pulses. All else being equal, this allows enabling in half the time, and halves the battery energy requirements. The number of possible UQS "A" and "B" event combinations is unchanged, so the "uniqueness" of the pattern is unaffected.

The unidirectional solenoid cam is contoured to "match" the magnetic torque-displacement curve, so the shape of this curve is immaterial. The only

critical feature of the curve is the area (energy) under the curve. With oscillatory devices it is very difficult to match solenoid output torques with spring torques.

The unidirectional solenoid also has advantages compared to a stepper motor. The stepper motor requires sequential energizing of multiple coils to achieve its action (versus the rotary solenoid single coil). For comparable housing volumes, the stepper motor individual coils and magnetic flux paths are necessarily smaller. They thus produce much less torque for a much smaller displacement. The stepper motor requires a more complex programmer to sequentially energize the coils than is required for the simple on-off pulses of the rotary solenoid. Finally, while the bi-directional capabilities of the stepper motor might have advantages for other applications, this capability is not an advantage for our existing discriminator mechanisms. Since the stronglinks are one-shot, single-trip devices, the ability to "back out" of a locked position cannot be allowed.

Energy

Figure 10 shows the torque-displacement curve for the unidirectional solenoid magnetic output (without a spring), and it shows the torque-displacement curve for the cam-spring mechanism. The lower portion of the figure is an X-Y schematic of one of the four cam lobes, relating follower positions to the various torque conditions. Similar to the oscillatory solenoid, the magnetic torque goes from a zero value, to some maximum value, and back to zero during 45 deg of rotor rotation. The initial zero torque value occurs when the rotor poles are symmetrically positioned about the stator poles; the second occurs when two of the rotor poles are aligned with the two stator poles. The area under the torque-displacement curve from 0 to 45 deg represents the total gross energy available to drive the rotor-cam assembly through one on-off 90-deg pulse cycle.

Again, the device is unable to start with zero magnetic torque, so the rotor is biased 7 deg in the direction of desired rotation. With the unidirectional device, the rotor must operate through multiple revolutions, so rotor stop pins are not used. The initial 7-deg bias is attained by the mechanical detenting action of the cam follower at the root position of the cam. The energy represented by the area under the magnetic curve from 0 to 7 deg is "lost" for driving purposes, since power is off while the cam follower passes through this portion of the cam.

To achieve 45-deg rotation during the energized stroke starting from the 7-deg biased position requires that the rotor pass through the second zero torque position (45 deg) and continue to the 52-deg position. Magnetically, the rotor and stator poles attempt to stay aligned at the 45-deg position. This means the spring must "overpower" the magnetic torque to advance the rotor from the 45-deg position to the 52-deg position. This represents additional lost energy. The magnetic torque curve from 45 deg to 52 deg is a negative mirror image of the positive portion of the curve from 38 to 45 deg. Thus, the net energy for driving the rotor-cam assembly for one on-off pulse

cycle (7 to 97 deg) is represented by the area (8.8×10^{-3} J) under the magnetic curve from 7 to 38 deg. Dividing this energy by 90 deg (in radians) gives a constant torque of 5.65 N-mm (0.80 in.-oz) throughout the 90-deg total on-off stroke.

Spring-Cam

The solenoid torque-displacement curve of Figure 10 is determined by actual Instron test data. Using this data, a spring torque-displacement curve is derived by calculating data points so that the algebraic sum of the magnetic and spring torques for all displacements is equal to the above constant torque of 5.65 N-mm. The area under the spring curve from the start position to the spring "high center" position (7 to 42.4 deg) is used to determine the spring energy storage requirement. A spring is selected to meet this requirement with a reasonable (packageable) displacement. The 42.4-deg high center position is the point at which the magnetic torque has dropped to the calculated constant value of 5.65 N-mm. Beyond this point, as the magnetic torque continues to drop, the spring can no longer be stretched. Its torque must now start to aid the solenoid magnetic torque to maintain the constant output.

After the spring is selected, the cam follower moment arms are determined to meet the spring displacement requirement at one end, and give a reasonable cam size at the other end. Returning to the derived spring torque-displacement curve, incremental steps are considered along the displacement coordinate axis from 7 to 97 deg. Each increment defines a cam (and rotor) displacement and defines an incremental area (energy) change. With this energy change, a change in spring length is determined, which in turn gives a follower position. This gives a new radial dimension for the cam. This radial dimension combined with the selected incremental angular displacement gives a polar coordinate point on the cam. Taking many increments along the displacement axis from 7 to 97 deg defines one lobe of the cam. This is repeated to give four lobes equally spaced at 90 deg.

Due to the solenoid and spring characteristics, the cam starts with a steep rise (high solenoid torque; low spring force) and levels off toward the high point of the cam (low solenoid torque; high spring force). On the "downhill" side of the cam (solenoid power off), the slope increases toward the end of the de-energized stroke to compensate for a weakening spring.

As noted earlier, the 52-deg rotor-cam orientation is a magnetic detent position at the end of the energized stroke. The "downhill" portion of the cam has an inflection point at this position, being steeper behind the inflection point than ahead of it. Behind 52 deg, the spring overpowers the rotor (which attempts to stay at the 45-deg pole-aligned position) and rotates it to the inflection point. Ahead of 52 deg, the spring torque is weaker than the reverse magnetic torque, so further "overpowering" (advancement) is not possible. Thus, the follower stays at the inflection position as long as the solenoid remains energized. When it is de-energized the follower continues downhill for the de-energized stroke (from 52 to 97 deg).

CONCLUSIONS

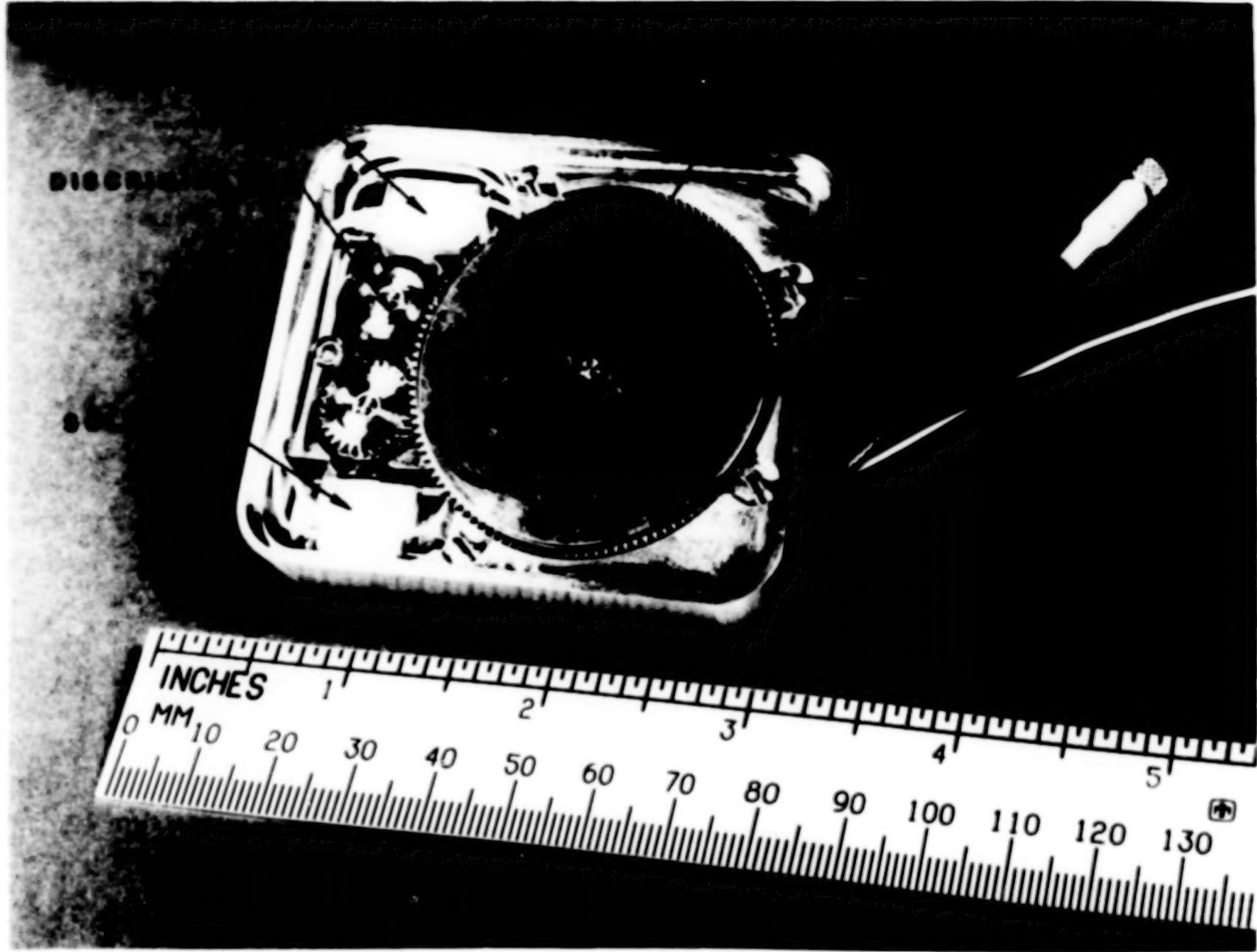
The unidirectional solenoid provides the following stronglink improvements:

1. Volume is reduced 47 percent.
2. Enabling time is reduced 50 percent (1200 msec to 600 msec).
3. Useable energy per on-off pulse is increased from 3.46×10^{-3} J to 8.83×10^{-3} J. Since this provides two unique discriminator positions instead of one, this results in a 510-percent increase in energy efficiency.

The spur gear discriminator provides a more constant restraint on the safe-enable wheel, thereby enhancing safety. The use of a direct gear drive in place of the pawl/ratchet-wheel mechanism should reduce wear, friction, and dynamic problems. Total piecepart quantities are reduced which should increase reliability and decrease costs.

Due to program budget cuts October 1, 1988, work on this project has been greatly curtailed. This has limited testing to bench runs of two prototypes plus Instron torque/displacement tests of two solenoids. A limited capability pulse generator has been fabricated to operate the prototypes. While this pulse generator cannot be adjusted to optimize the pulse format, it will allow additional data to be taken, and facilitate the use of a high speed camera to study the dynamics of the device.

While testing has been minimal, results are encouraging. These results, combined with development history of production components of similar complexity, indicate this stronglink could be developed and used as a replacement component for future applications. Overall, this advanced development program has met its initial goals.



27

Figure 1. Stronglink assembly.

27

UNIQUE SIGNAL (UQS)

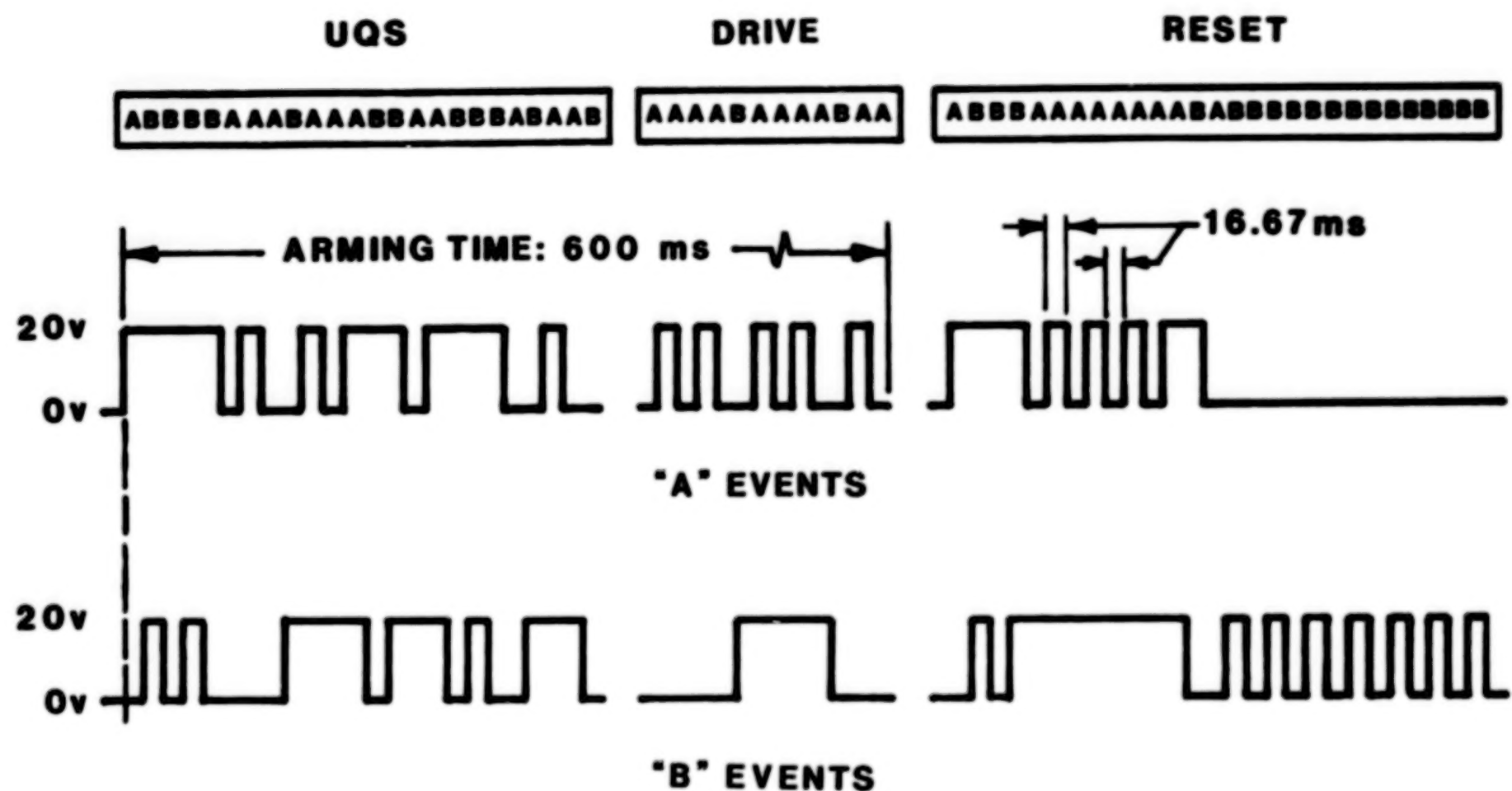


Figure 2. Electrical pulse format.

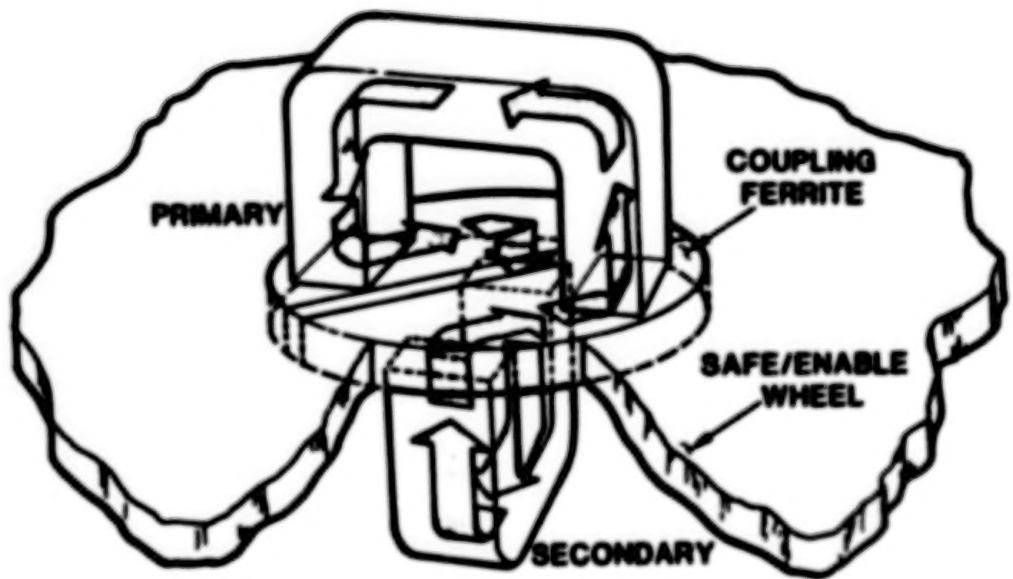


Figure 3. Interrupted transformer flux path (enabled).

**BLANK
PAGE**

30

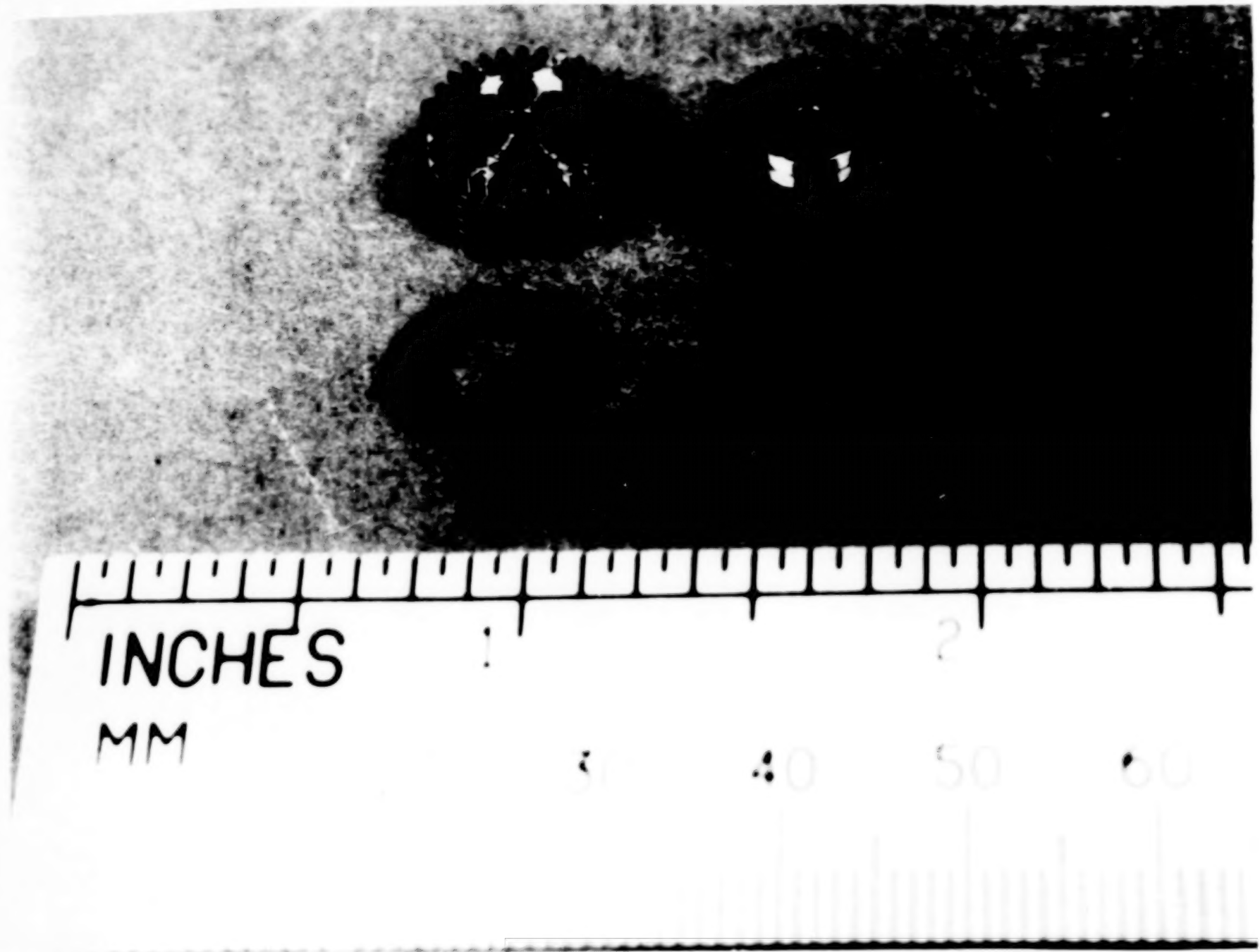
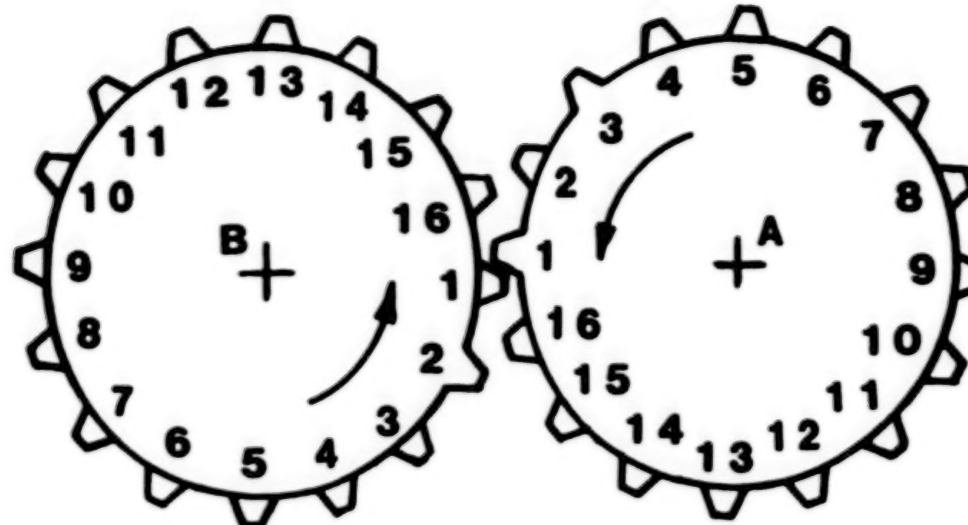


Figure 4. Spur gear discriminator.

30

"B" EVENTS



"A" EVENTS

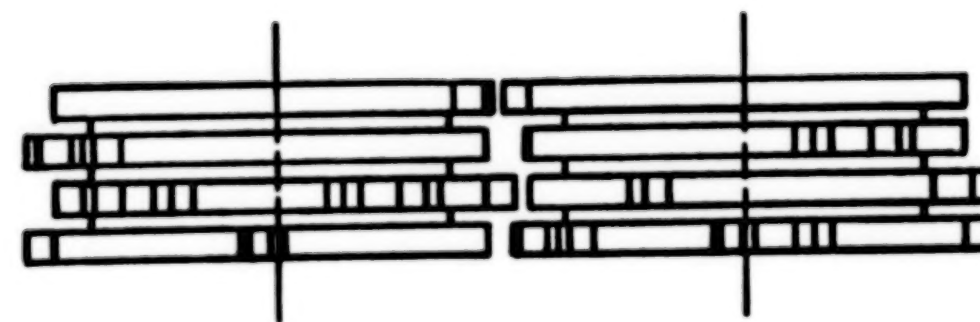
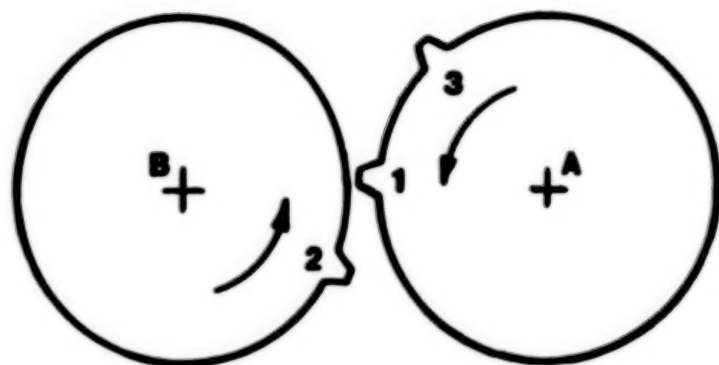


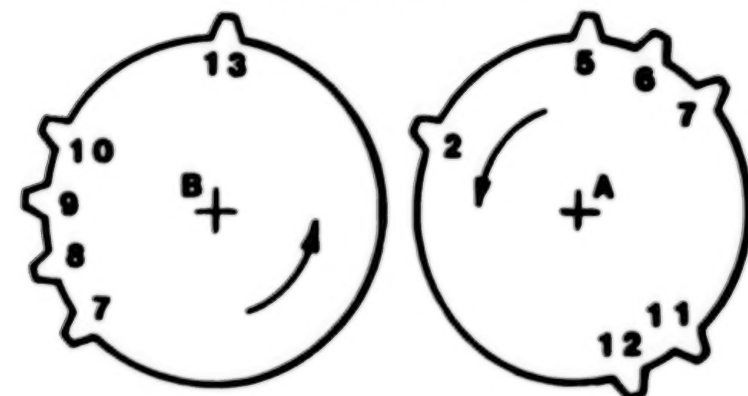
Figure 5A. Spur discriminator assembly.

UQS: ABBBBAAABAAABBAABBBABAAB

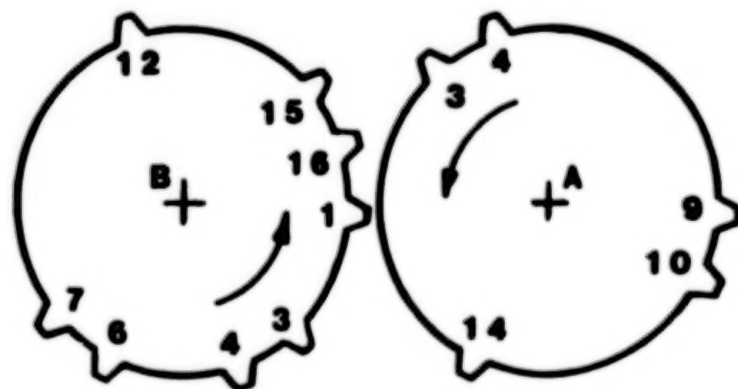
LEVEL "W"



LEVEL "X"



LEVEL "Y"



LEVEL "Z"

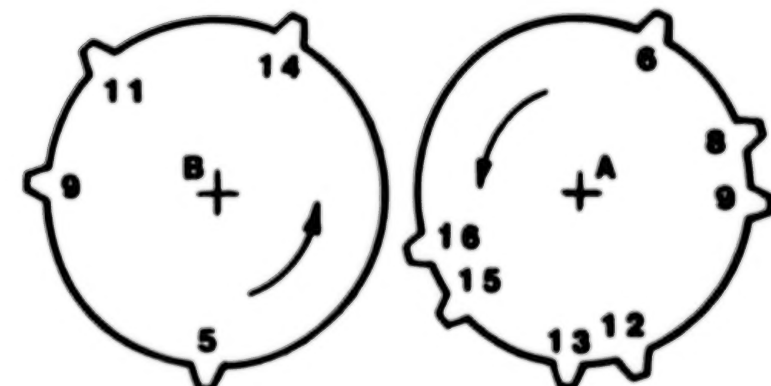


Figure 5B. Gear segments.

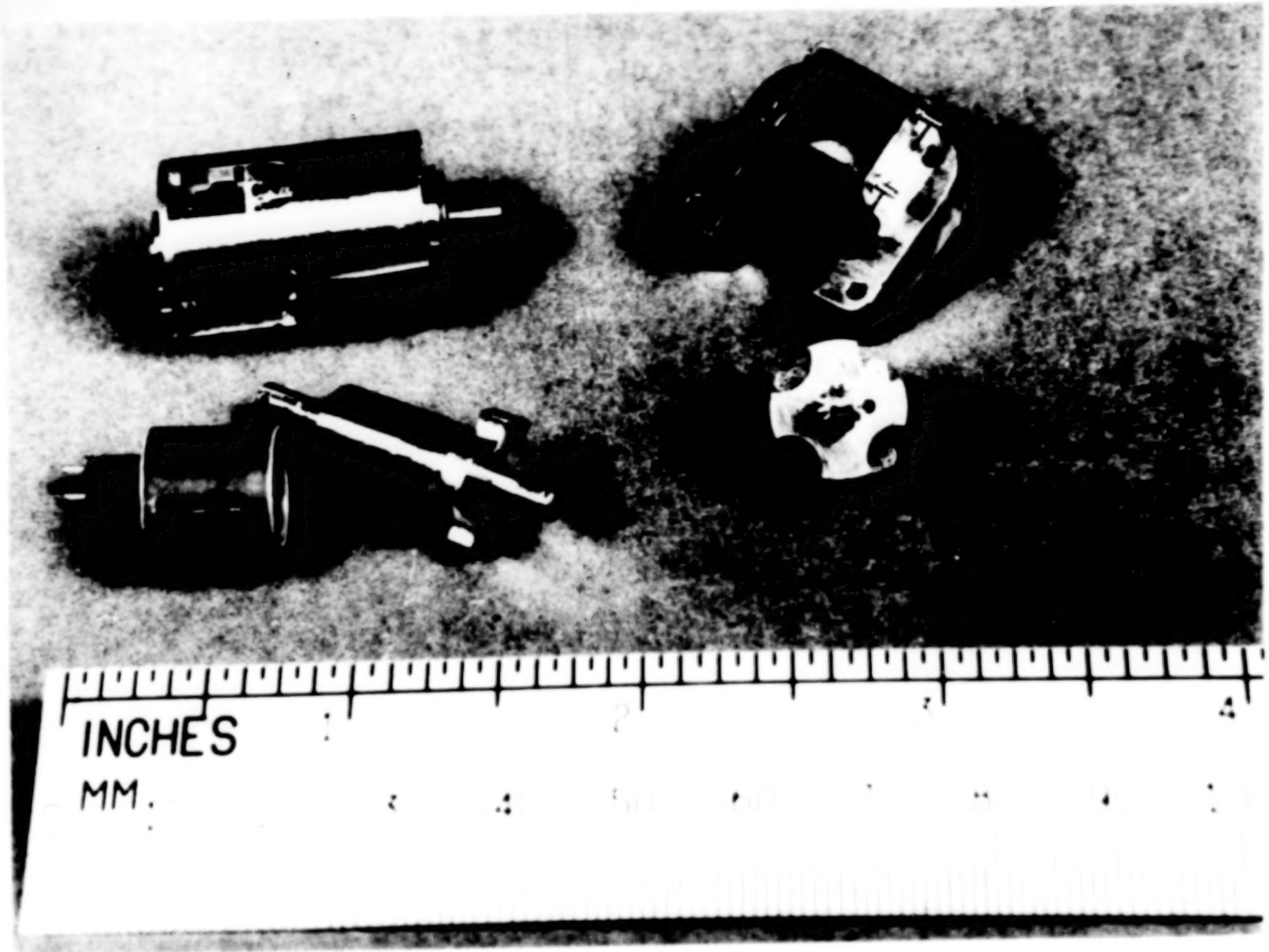
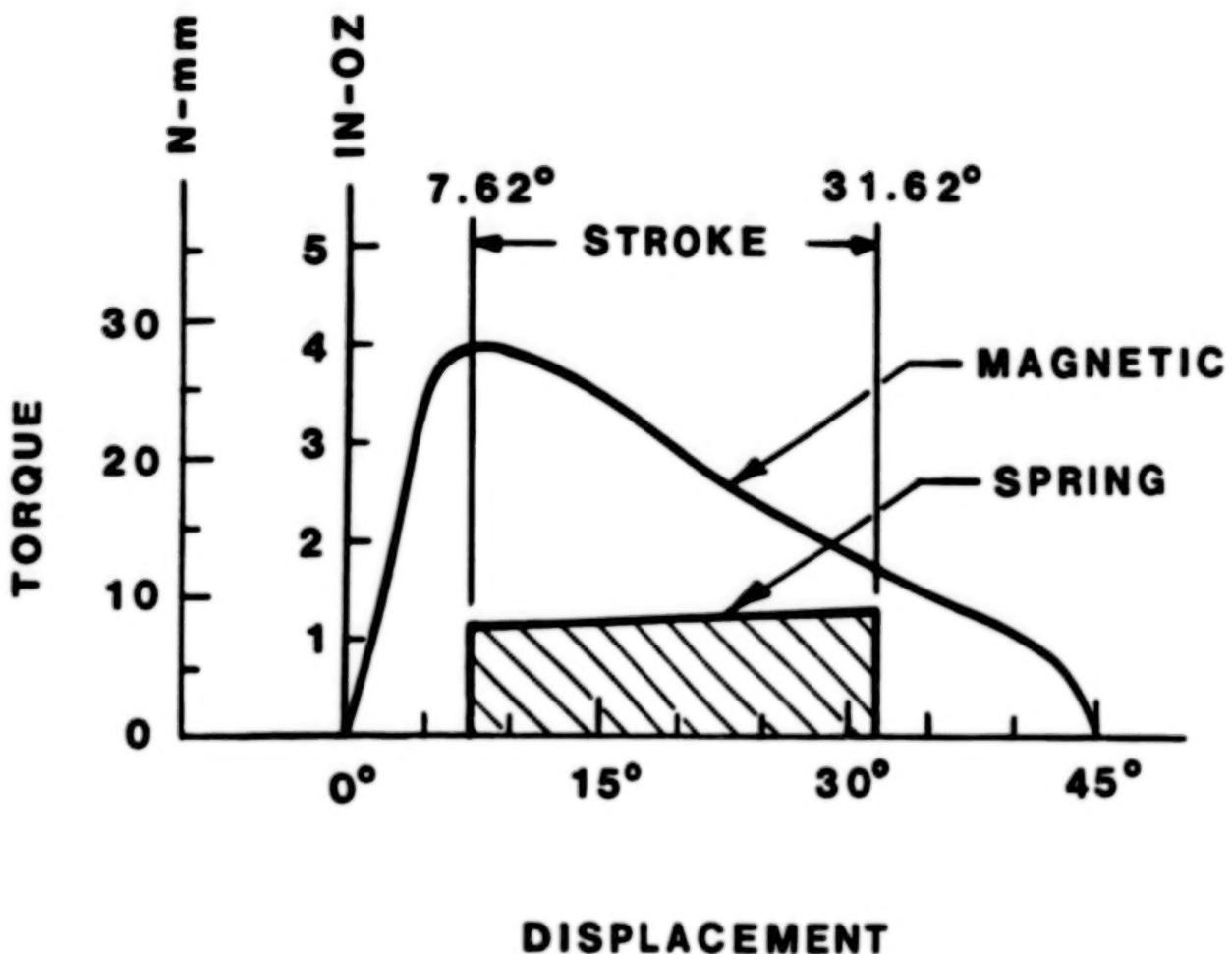


Figure 6. Solenoids, oscillatory (l), unidirectional (r).



USEABLE ENERGY (SHADED AREA):
 $3.46 \times 10^{-3} \text{ J} (0.49 \text{ IN-OZ})$

Figure 7. Oscillatory solenoid output.

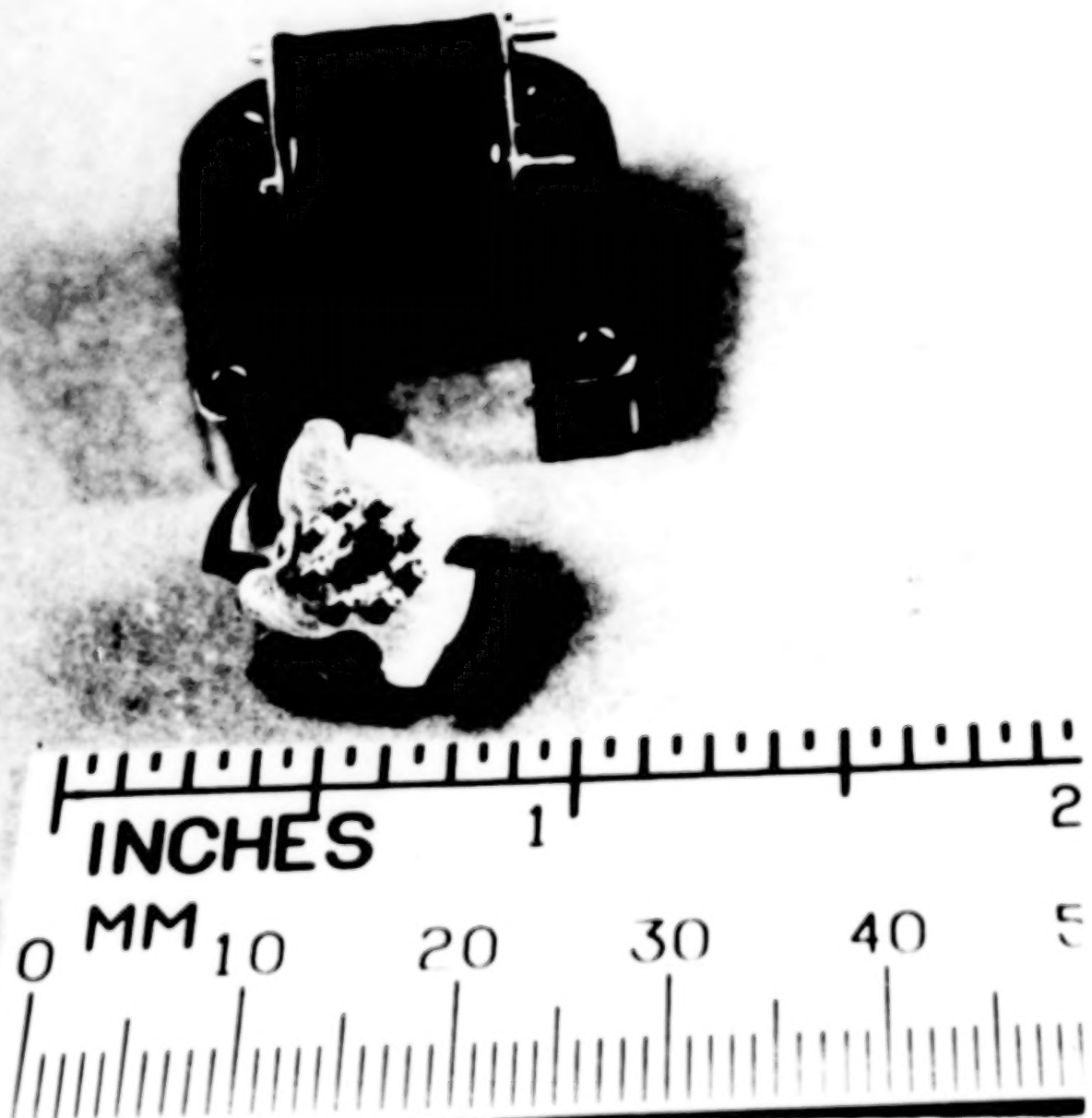


Figure 8. Unidirectional solenoid.

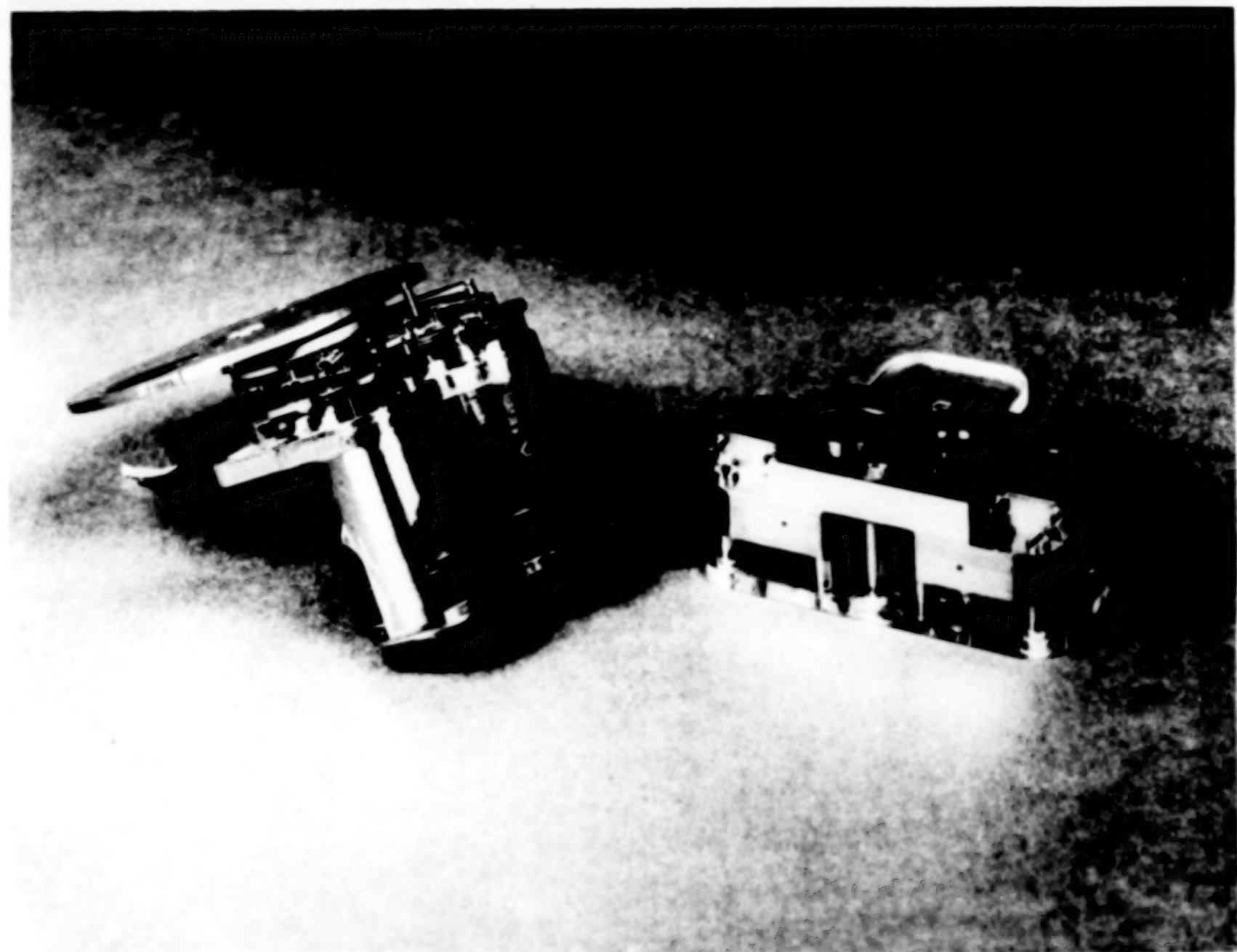
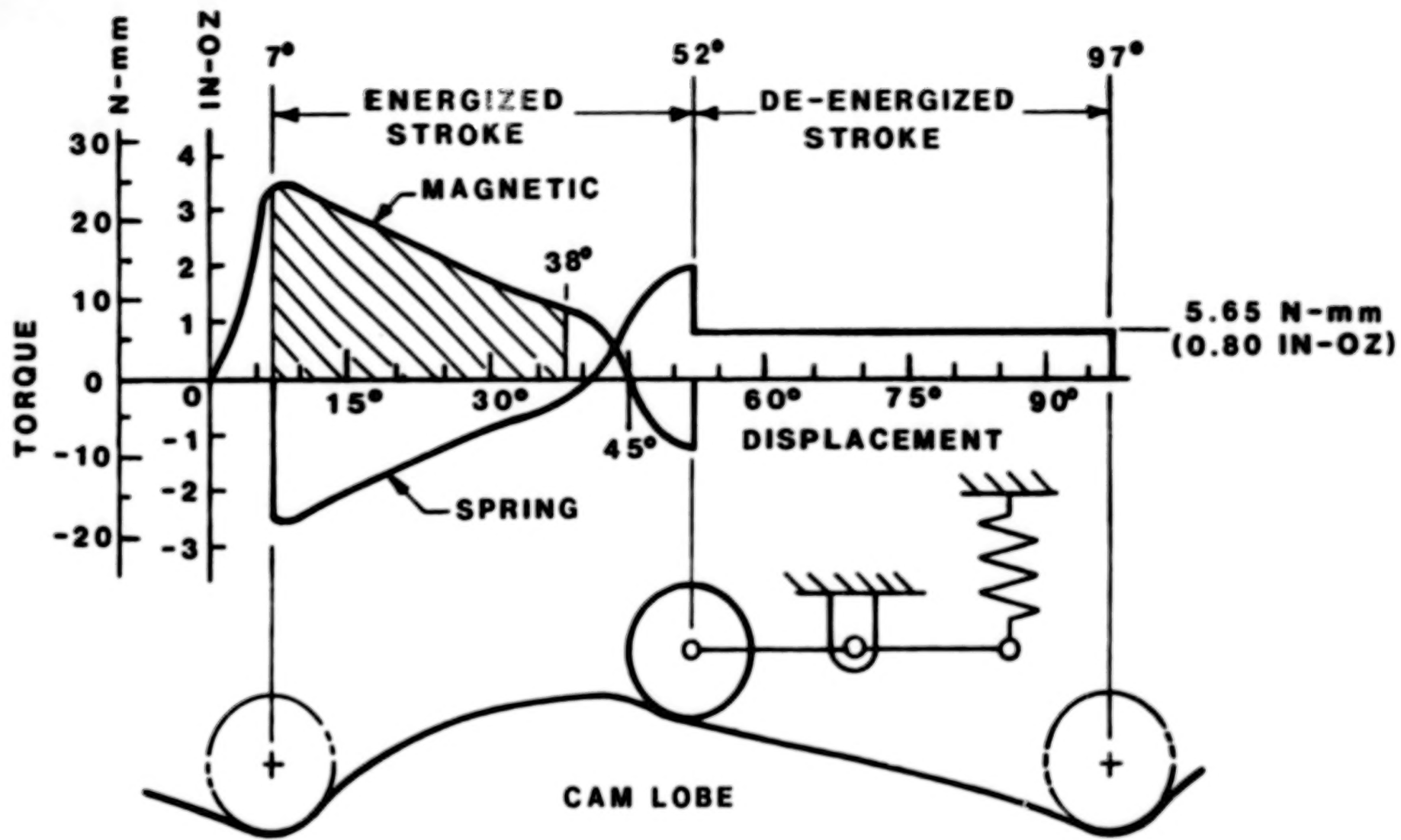


Figure 9. Stronglink modules. Production (l), advanced development (r).



USEABLE ENERGY (SHADED AREA): 8.83×10^3 J (1.25 IN-OZ)

BLANK PAGE

THE DESIGN AND ANALYSIS OF A DOUBLE SWIVEL TOGGLE RELEASE MECHANISM
FOR THE ORBITER STABILIZED PAYLOAD DEPLOYMENT SYSTEM

Guy L. King* and Ted Tsai*

ABSTRACT

A new NASA deployment system called the Stabilized Payload Deployment System (SPDS) will soon be operational. The lightweight and heavy-duty system rolls payloads over the orbiter's side rather than ejecting them upward. The system will enhance the orbiter capability of carrying larger and heavier payloads. This paper describes the design, function, and analysis of a new three-pin "double" swivel toggle release mechanism which is crucial to the successful development of the SPDS.

INTRODUCTION

The SPDS is being jointly developed by NASA/JSC and Rockwell International/Space Transportation Systems Division. SPDS will be used in the National Space Transportation System (NSTS) to permit on-orbit deployment of payloads independent of other payload handling equipment such as the Remote Manipulator System (RMS). The SPDS is a compact electromechanical system which attaches the payload to the orbiter through the payload retention structure (trunnions). The system is designed to rotate payloads out of the Orbiter payload bay at a predetermined angular position and effect a payload separation on command. This paper focuses on the two fault tolerant release mechanisms that play a key role in the critical payload separation. It describes in detail the design, function, and analysis performed on the two fault-tolerant double-swivel toggle mechanism that is held in place by a swivel ring and three pyro actuated retaining pins under a high elastic preload. Removal of one or more pins will instantly release the spring loading and subsequently cause the unstable swivel links to move away from the joint. Detailed design analogy of the mechanism is discussed along with the NASTRAN finite element and stress concentration analysis that was performed to investigate the hoop strength and the local yielding of the double swivel configuration. Structural stress contours (load paths) are presented and the overall description of SPDS is also included.

RELEASE MECHANISM DESIGN

The 82-kg (180-lb) SPDS (Fig. 1) is a bridge-mounted structure that can be positioned in any bay on the port or starboard longeron of the orbiter. The first application of SPDS is on the port side longeron replacing the RMS. The payload deployment and release sequence are shown in Figure 2. In the

*Mechanical Design and Analysis Branch, Structures and Mechanics Division,
Lyndon B. Johnson Space Center, Houston, Texas.

SPDS deployment sequence, the first two steps are to insure that there is sufficient clearance for payload deployment. The motions of SPDS pedestals are controlled by actuators and drive motors. Once the payload reaches the final angle, the payload oscillations are damped through the spring damper (Fig. 1). After the payload is stabilized, it is released through a double swivel toggle release mechanism (Fig. 3) located within the release head. The major components of the release head consist of the swivel, the housing, and the pyrotechnic retractors. A circular plate which is connected to the payload interface plate is held to the housing by the toggle. The other end of the toggle is held in place by three pyrotechnic pins. On command, the three pins will retract and release the toggle. The final design configuration of the mechanism assures free swiveling at both ends of the toggle. A cross section view of the swivel toggle mechanism is shown in Figure 4. The double swivel toggle is made of three main components: the swivel bolt (with the top swivel ball), the swivel socket (with the lower swivel ball), and the swivel ring as shown in the figure. The bolt is fastened into the lower swivel socket. The inner surface of the ring is spherically contoured and fits on top of the lower ball. The pyrotechnic pins are 120 deg apart and the flat side of the pin tip rests on top of the swivel ring. The mechanism is held in tension by tightening the swivel bolt into the socket. The assembly is strain gauged to obtain an accurate reading on the 8007 Newton (1800 lb) design preload. When the pyrotechnic pins are fired, the pins retract and the circular payload plate is separated by an expulsion spring within the main housing. The elastic preload of the toggle provides the additional spring load for payload separation. The three-pin toggle release sequence is illustrated in Figure 5. During a nominal deployment, payload interface components including the swivel toggle stay with the payload.

The illustration in Figure 5 constitutes the heart of the design concept of the release mechanism. During the earlier development of the SPDS, the design was simply inadequate in the release mechanism. A three-pin toggle release mechanism design was then brought into the system. The one piece toggle had a single swivel on the upper end (Fig. 6). To assure the free motion of the toggle after the pyro initiation, another swivel was developed on the other end (the swivel ring) of the toggle. When the swivel toggle is properly preloaded, any moment or lateral loading from the payload interface plate will be directly transmitted through the housing of SPDS. The toggle itself will experience very minimum load variations. Before the pyro initiation the tension loaded toggle mechanism restrained by equally spaced pins constitutes a well balanced and stable loading pattern. The retraction of all pins will immediately release the toggle. If any one or two pins were to malfunction, the double swivel toggle would still permit clean separation because the swivels would rotate clear of the failed pin/pins. The toggle mechanism had been through several preliminary design configurations until the final double swivel was fully developed and chosen as the baseline. The original design had a one piece toggle with a sloped toggle/pin contact surface (Fig. 6). The pendulum type movement of the single upper swivel should have provided enough rotation to move clear the un-retracted pin/pins. The clearance created by the toggle swing motion will be the length of the

toggle times the swing angle. The sloped toggle/pin contact surface was intended for easier toggle separation. However, when the mechanism was preloaded, the sloped surface of the pins brought on high local contact stresses. The sloped surface, which varied at times, also induced an undesirable axial pin reaction tending to retract the pins prematurely. To prevent the inadvertent retraction, a high shear retaining pin must be incorporated into each pyro pin. When tested, the configuration was locked up by the preload when only one pin was retracted. The lock-up was caused by high frictional forces in the single swivel ball and the tolerance-induced unequal pin load distribution. The design progressed to the double swivel but still keeping the sloped toggle/pin interface contact (Fig. 6). The configuration during the test did not hang-up but the force tending to retract the pins remained. Flat surfaces were finally incorporated into the toggle/pins interfaces (Fig. 6). The configuration eliminated the undesirable pin retraction forces and became the baseline. The new swivel at the lower end of the toggle was made possible by the creation of the swivel ring. The new design provides additional flexibility to the mechanism. The additional toggle movement with respect to the un-retracted pin/pins will be based on (1) the movement of the swivel ring about the swivel ball, (2) the geometrical outer contour of the ring, and (3) the relative pin/ring location. Most of all, the flexibility of the lower swivel will induce the swing motion of the toggle and eliminate the lock-up of the mechanism. Tests were performed with the absence of dry film lubricant to intentionally induce sticking surfaces around the swivels. No hang-up occurred. The mechanism with 8007 N (1800 lb) design swivel preload has also been successfully tested through the design thermal and vibration load environments. The 8007 N (1800 lb) preload proved to be adequate to keep the system joint intact with no premature joint separation. Design analysis was also performed to evaluate the strength of the new, small, and high performance mechanism. As a result, a minimum modification was applied to the bolt head. The modification was to assure that the toggle is elastically preloaded and no permanent local structure yielding would occur. The analysis in detail is discussed in the following section. The new two fault tolerant double swivel release mechanism became baseline for the deployment system and has been released for patent.

DESIGN ANALYSIS

A MSC/NASTRAN (The MacNeal-Schwendler Corporation/NASA Structural ANalysis) finite element analysis is performed to evaluate the strength of the toggle elements. Structure stress contours are plotted. Structure load paths and strength are evaluated. The analysis reconfirms that the design concept of the mechanism is sound. A stress concentration analysis is also performed and a simple design modification is applied to the fillet of the swivel bolt head. The modification significantly increases the preload/fatigue strength and the reliability of the mechanism.

Design Preload

The double swivel mechanism is designed for the reliable payload deployment. A proper amount of preload applied to the swivel bolt is

important. The abutment materials (housing and the attached plate) should always be in compression. In the meantime, the total bolt tension should not induce permanent deformations which would consequently release the elastic spring loading of the mechanism. For a normal operational environment, the load experienced by the toggle mechanism will mainly be the high preload. As long as the release head (preloaded joint) is in compression, the moment and lateral loads from the payload interface plate will be directly transmitted into the housing. There will be minimum tension loads applied to the release head. Based on the relative stiffness between the toggle and the abutment housing material, only a portion of the tension load will actually be transmitted into the preloaded toggle. Design analysis is performed to evaluate the load paths and the capability of the swivel mechanism based on the 8007 N (1800 lb) design preload.

Materials

The swivel bolt is made of MP35N (AMS 6884) bar. The swivel socket and the ring are Inconel 718 (AMS 5664) bar. In the range of the system operating temperature, which is from -73°C (-100°F) to 135°C (275°F), the high strength alloy have similar thermal expansion coefficients. At the highest 135°C (275°F) operating temperature, the MP35N will lose 10 percent of its room temperature strength and the Inconel 4 percent.

NASTRAN Finite Element Analysis

All three major components of the toggle mechanism (Fig. 4) are modeled (Fig. 7). All nominal dimensions are used. A cylindrical coordinate system (R , θ , and Z) was used for the model. The cylindrical geometry of the structure cannot be treated axisymmetrically because of the three localized pin reactions. However, with proper applications of mirror-imaged boundary conditions (constrained in the circumferential θ -direction at the RZ planes), only one-sixth (a 60-deg section) of the 360-deg circumference is needed to represent the entire swivel structure. The circular section is from the middle of a pin connection to half way to the next pin. NASTRAN three-dimensional solid elements (CHEXA/CPENTA) are used for the model. A simple inhouse preprocessor is developed to generate the math model. The model mesh size/density and element aspect ratios are arranged for proper model fidelity. The unconstrained model contains 7000 degrees-of-freedom (DOF). Boundary conditions are constrained in Z -direction at the lower pin/ring and upper bolt head/abutment interfaces (Fig. 7). The spherical surface contact between the ring and lower swivel ball are simulated with NASTRAN gap elements in the spherical radial direction. All gaps will be closed under the preload compression. It requires no iterative scheme to search for the load-induced gap contact or opening. A linear static analysis is performed. The results prove that all gap elements are in compression (closed). The bolt preload is simulated with fictitious thermal shrinkage of the material in the axial (Z) direction. The applied thermal load, which is a -111°C (-200°F) temperature differential, is randomly selected for the linear analysis. The computed total reactions at the boundary constraints will be the equivalent preload which produces the linear resultant stresses of the math model.

The computed results are processed to produce the structure deformed shape and stress contours (in forms of constant stress lines or color fringes) with the PDA Engineering/PATRAN (post-NASTRAN) processor. The exaggerated (dramatized) model deformed shape is shown in Figure 8. The total computed boundary reactions (equivalent swivel preload) is 7940 N (1785 lb) which is coincidentally very close to the actual design preload of 8007 N (1800 lb). For the linear static analysis, the displacements/stresses at the desired magnitude of applied loading are simply obtained by a linear ratio. The computed maximum tensile stress is $5.158 \times 10^8 \text{ N/m}^2$ (74,806 lb/in.²). The stress contours of the major principal stresses of the worst stressed (deformed) section are presented in Figure 9. High stresses and stress concentrations are clearly shown at the neck of the swivel bolt. The bolt neck has the minimum area for load paths with sharp change of the cross section from the bolt head. Stresses (mainly the hoop stresses) in the swivel ring are relatively low and uniformly distributed. The concern of the distortion and the separation of the swivel ring from the lower swivel is thus removed. Although the toggle is loaded at three localized pin/ring interfaces, the resultant loads (stresses) transmitted into the swivel, especially the bolt, are nearly axisymmetrical. The finite element analysis provides a good overall view of the structural load paths (stress patterns). The analysis reconfirms the overall design of the toggle mechanism. The critical link of the release mechanism is the swivel bolt which is subjected to the common stress concentration effect. The strength (preload allowable) of the mechanism will be based on the strength/shape of the bolt. A change to one or more of the geometrical/material parameters of the bolt (for instance, increasing the rounding radius at fillet or the radius of the neck) can rather easily increase the total strength of the entire mechanism. Analysis is now focused on the stress concentration of the swivel bolt.

Evaluation of Swivel Strength and Preload

To evaluate the highly localized and concentrated stresses, the finite element analysis will require additional local model refinement in a great detail at the fillet of the bolt. The complexity of the model will be further increased if the 20 node brick elements are to replace the current 8 node elements for better accuracy. The finite element solution is always considered an approximation to the usually unknown exact solution. Without the actual experimental data (say, photoelasticity), the accuracy level of detailed stress concentration analysis of the conventional h-version NASTRAN finite element method, which uses fixed low order polynomial element shape functions, will still be somewhat uncertain. No model refinement is performed. Experimental datum/formulations of stress concentration factors of available design configurations will be used to evaluate the bolt strength.

The diameter of the bolt shank is $5.03 \times 10^{-3} \text{ m}$ (0.198 in.). The cross section area A of the shank is $1.9864 \times 10^{-5} \text{ m}^2$ (0.03079 in.²). For a preload P of 7940 N (1785 lb), the average shank tensile stress σ_z (P/A) becomes $3.997 \times 10^8 \text{ N/m}^2$ (57,972 psi). The NASTRAN computed maximum tensile stress is $5.158 \times 10^8 \text{ N/m}^2$ (74,806 psi) which is at the neck of the bolt. If the maximum is divided by the average, the stress concentration factor K_t is estimated at

1.29. The term "stress concentration factor K_t " is loosely defined as the maximum local stress divided by the average stress in the bolt shank. The concentration factor of 1.29 is certainly unrealistic (and, in this case, low), because the math model does not include the necessary detailed refinement for the highly localized effect. Two configurations of the available textbook charts for stress concentration factors are selected for evaluation. The first is the "Round Shaft with Shoulder Fillet in Tension" and the second is the case of "T-head" as shown in Figure 10. The major difference between the two is the manner of loading. The loading of T-head will result in much higher concentrated stresses. As shown in Figure 10, the actual swivel bolt is compared to the two classical configurations. The configuration of the swivel bolt is less critical but closely resembles the T-head. The spherical contour of the bolt head will assist the line flows and reduce the local stress concentration. The stress concentration effect for the swivel bolt should be between the two configurations as the flow lines demonstrate in the figure. The existing NASTRAN swivel model is again utilized for the general comparison of three configurations. Because the load path into the bolt is nearly axisymmetrical, a simplified and axisymmetrical swivel model (a 10-deg section) is utilized (Fig. 11). First (as case 1), a uniform tension is applied to the top surface of the bolt head to simulate the round shaft with fillet in tension. Reactions at the pin-ring interfaces are computed. Next, for the case of the preloaded swivel, the spherical bolt head is constrained and the previously computed pin-ring interface reactions (from case 1) are re-applied at the same locations. Finally (case 3), the bolt head is constrained only at the flat shoulder surface of the bolt head as the worst case (proximity effect) of the T-head. The results (Fig. 11) clearly showed the highest stresses (stress concentration) for T-head and the lowest for the round shaft in tension. The design stress concentration factors for T-head will be conservatively used to evaluate the swivel strength. The design factors for T-head are available in R. E. Peterson's "Stress Concentration Design Factors." Although the T-head is of rectangular cross sections (with a constant thickness h), the design data is applicable to the head of a round bolt as discussed in the text. The major geometrical parameters for the T-head are the size (width D and depth m) of the head, the width of the shank (d), and the fillet radius (r). For a constant ratio of r/d , the stress concentration factors with respect to various D/d and m/d are provided. A total of four charts are available in the book for $r/d = 0.05, 0.075, 0.10,$ and 0.20 . Based on the geometry of the bolt head, the ratios of $D/d (= 2.2)$, $m/d (= 1.2)$, and $r/d (= 0.126)$ are defined (Fig. 12). By using the available datum of the four charts and the geometrical parameters of the bolt head ($D/d = 2.2$ and $m/d = 1.2$), a relation between the stress concentration factor (K_t) and the fillet rounding ratio (r/d) is developed in Figure 12. For the current swivel bolt configuration with the nominal ratio r/d of 0.126 , the corresponding stress concentration factor becomes a high 3.5 based on the T-head configuration. Accordingly, for the 8007 N (1800 lb) design preload, the maximum stress will exceed the yielding allowable and the bolt head design is modified.

The swivel bolt is MP35N (AMS 5884) bar. In the range of the system operating temperatures (-73°C to 135°C), the minimum F_{ty} is $1.427 \times 10^9\text{ N/m}^2$

(207,000 psi) at 135°C (275°F): To consistently maintain the linear spring loading of the toggle, any localized yielding (permanent release of the spring load) is considered unacceptable. A 1.4 factor of safety is applied to the yielding (not the ultimate) allowable.

$$F_{ty, \text{allowable}} = 1.427 \times 10^9 / 1.4 \text{ N/m}^2 \\ = 1.020 \times 10^9 \text{ N/m}^2 (= 147,857 \text{ psi})$$

For the design preload of 8007 N (1800 lb), the average bolt shank stress is

$$\sigma_z, \text{average} = P/A \\ = (8007 \text{ N}) / (1.9864 \times 10^{-5} \text{ m}^2) \\ = 4.033 \times 10^8 \text{ N/m}^2 (= 58,495 \text{ psi})$$

Based on the material yielding allowable with 1.4 factor of safety, the allowable stress concentration factor of the swivel bolt should not exceed

$$K_t = (F_{ty, \text{allowable}}) / (\sigma_z, \text{average}) \\ = (1.020 \times 10^9 \text{ N/m}^2) / (4.033 \times 10^8 \text{ N/m}^2) \\ = 2.53$$

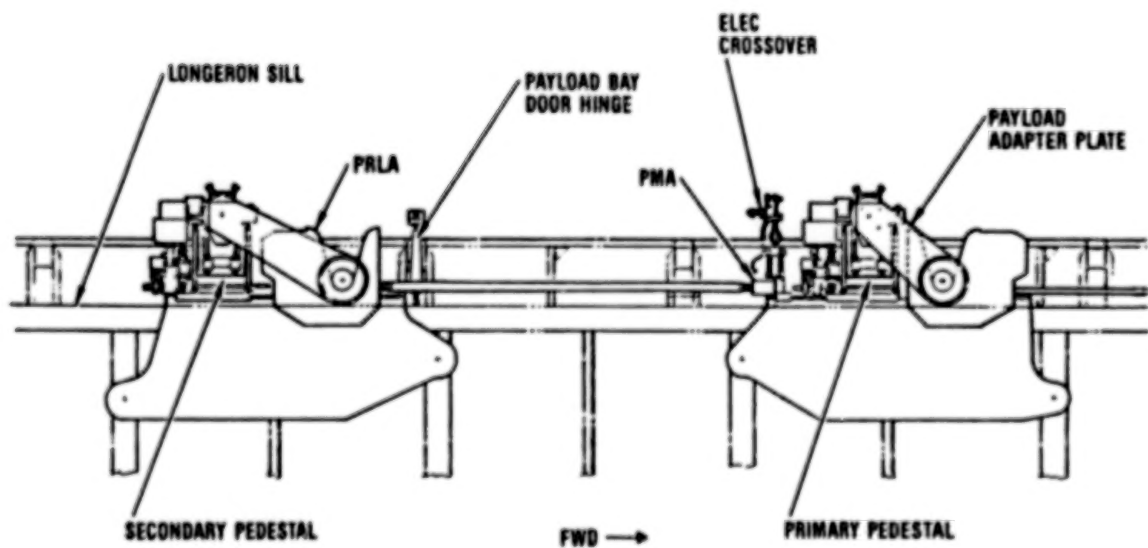
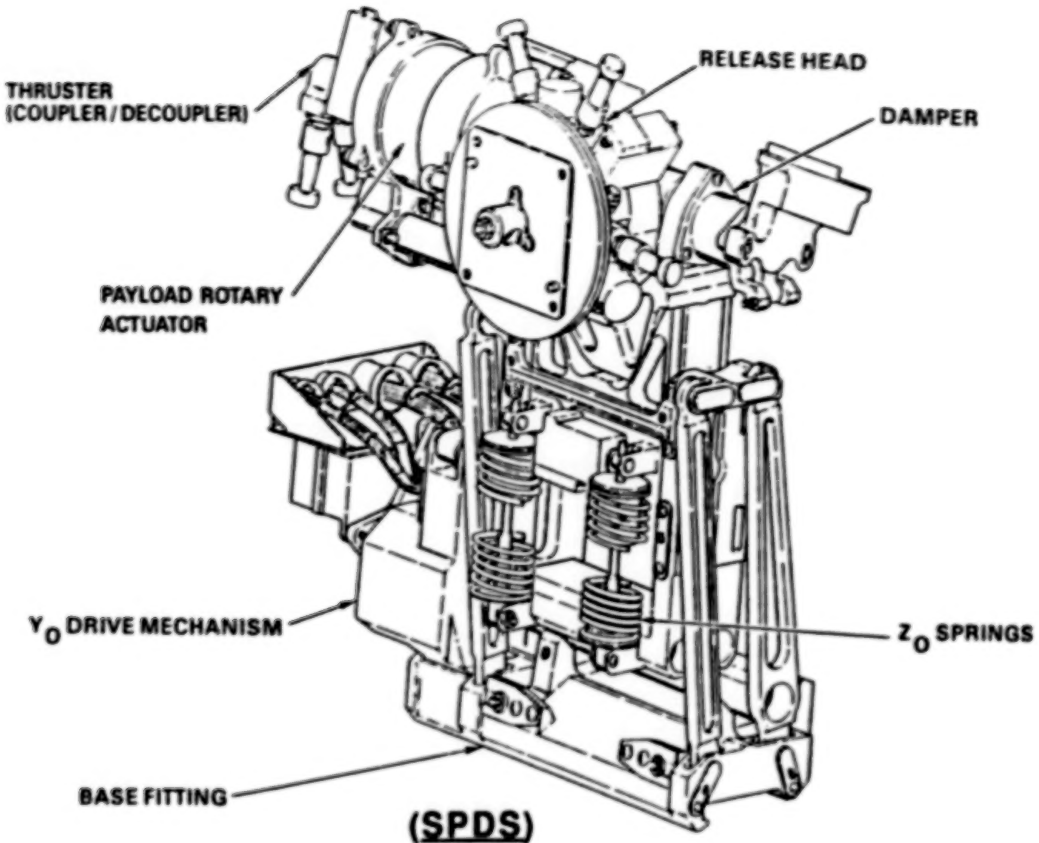
Going back to the K_t and r/d relationship in Figure 12, the corresponding r/d ratio for K_t equals to 2.53 is 0.26. In other words, if the shank radius d (5.0292×10^{-3} m) remains unchanged, the radius r (6.35×10^{-4} m) of the fillet rounding should be increased to avoid any local yielding of the bolt.

$$r = (d)(0.26) \\ = (5.0292 \times 10^{-3} \text{ m})(0.26) \\ = 1.31 \times 10^{-3} \text{ m} (= 0.051 \text{ in.}).$$

The 6.35×10^{-4} m (0.025 in.) fillet rounding radius of the original design was consequently changed to 1.31×10^{-3} m (0.051 in.). The minimum modification significantly increased the reliability and the static/fatigue strength of the mechanism.

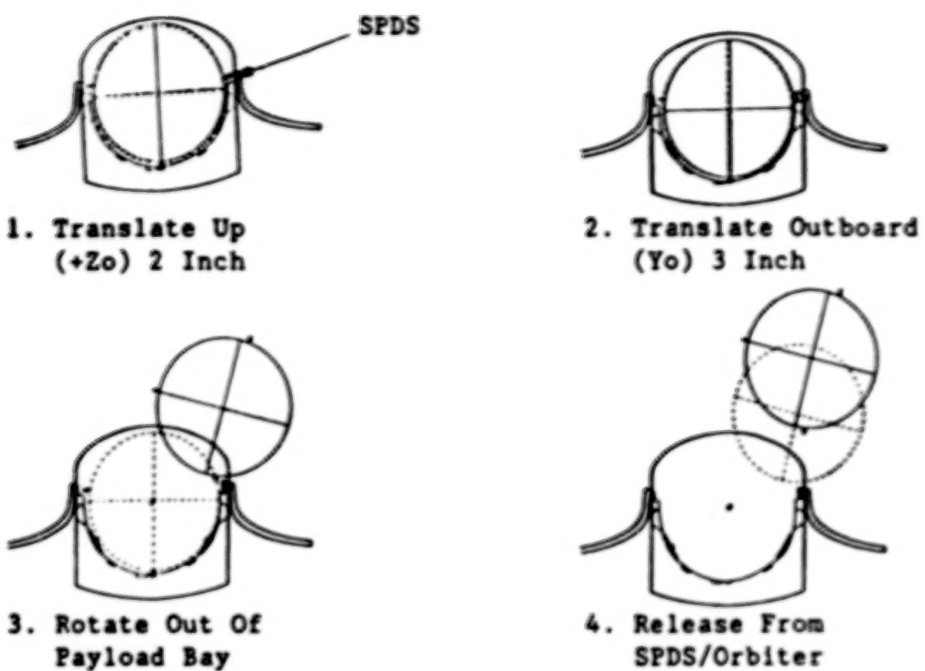
CONCLUSION

A three-pin double swivel toggle release mechanism has been developed for the new SPDS. The two fault tolerant mechanism is small, lightweight, heavy-duty, and easy to assemble. The mechanism is innovative of its "double" swivel design. The design concept was verified by tests and analyses. The mechanism is designed for the long duration in space prior to the payload deployment. It is essential that the design be fully reliable. With the aid of the finite element analysis, the stresses in the mechanism were visualized. By simply modifying a geometrical parameter (the fillet rounding) of the swivel bolt, the toggle became insensitive to local stress concentrations and the system strength and reliability was significantly increased.

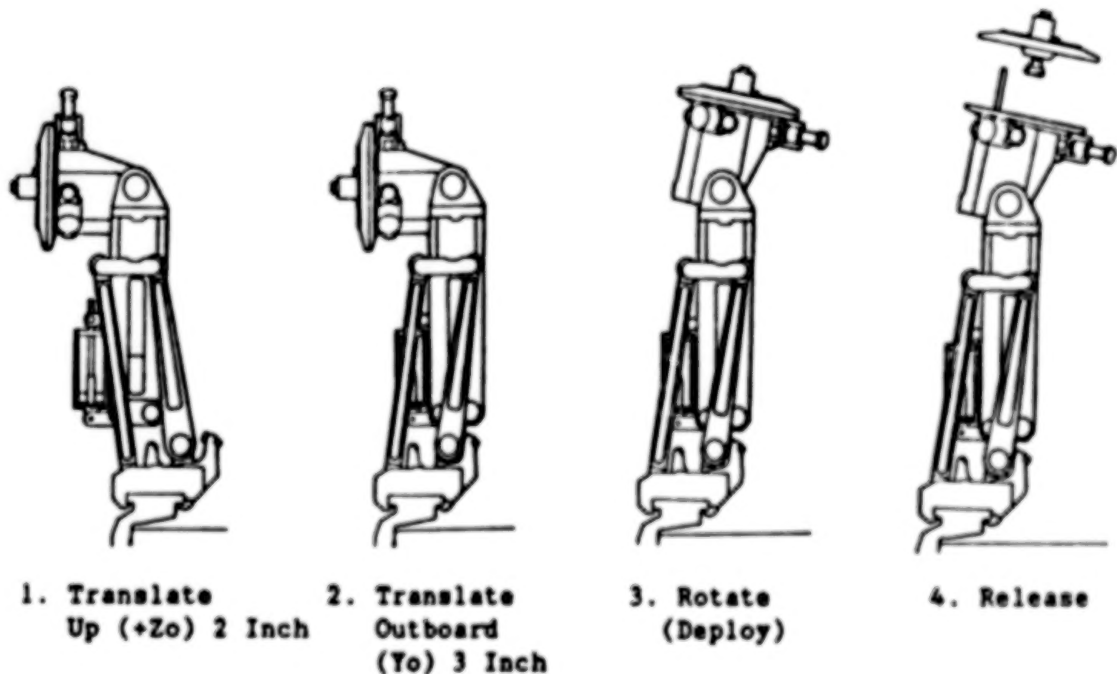


ORBITER SPDS APPLICATION
(PAYLOAD BAY VIEW LOOKING OUTBOARD PORTSIDE SHOWN)

Figure 1. Stabilized Payload Deployment System (SPDS).

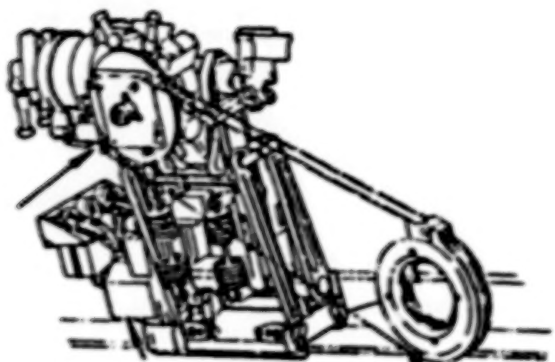


PAYOUT RELEASE SEQUENCE
(ORBITER PAYLOAD BAY LOOKING AFT)



SPDS PAYLOAD RELEASE MOTION
(SPDS SIDE VIEW)

Figure 2. SPDS payload deployment and release sequence.



SPDS RELEASE HEAD

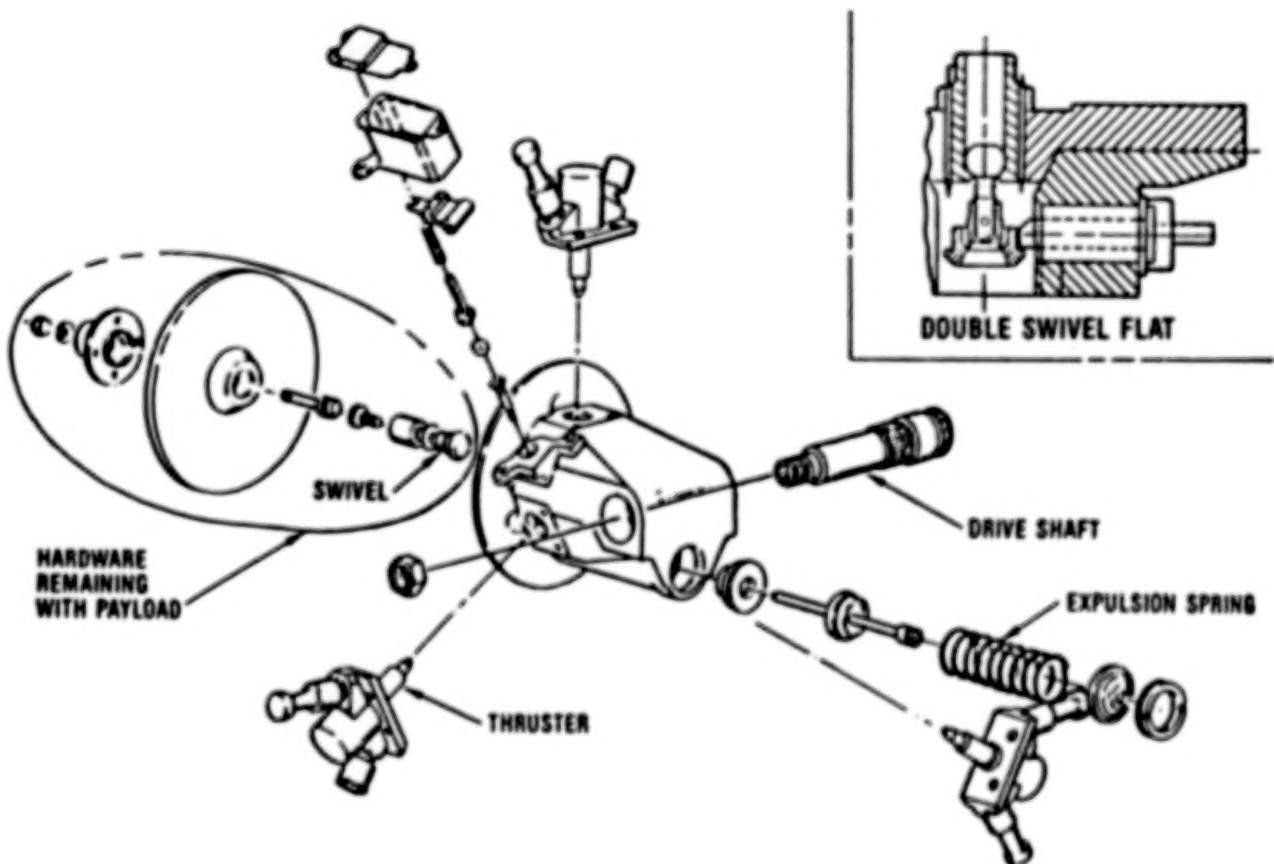
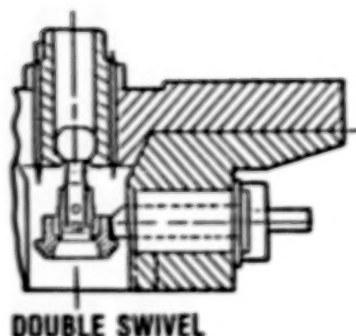
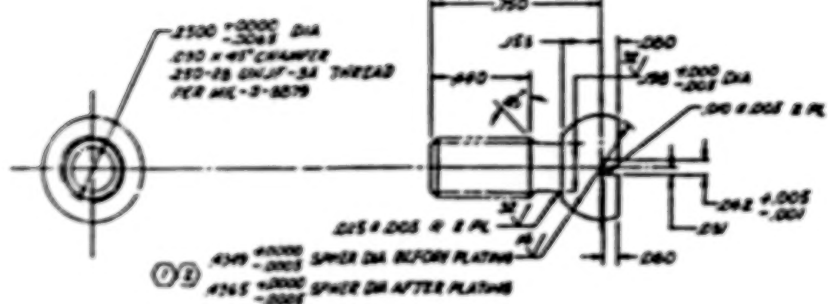


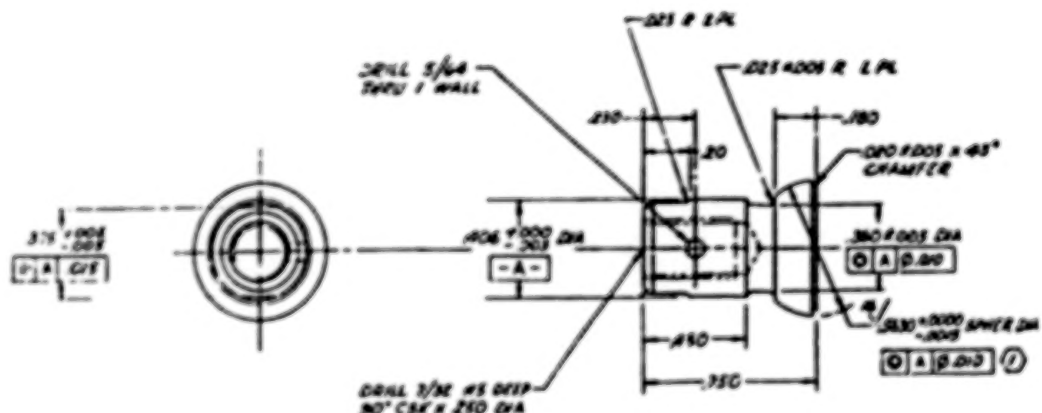
Figure 3. SPDS three-pin toggle payload release mechanism.



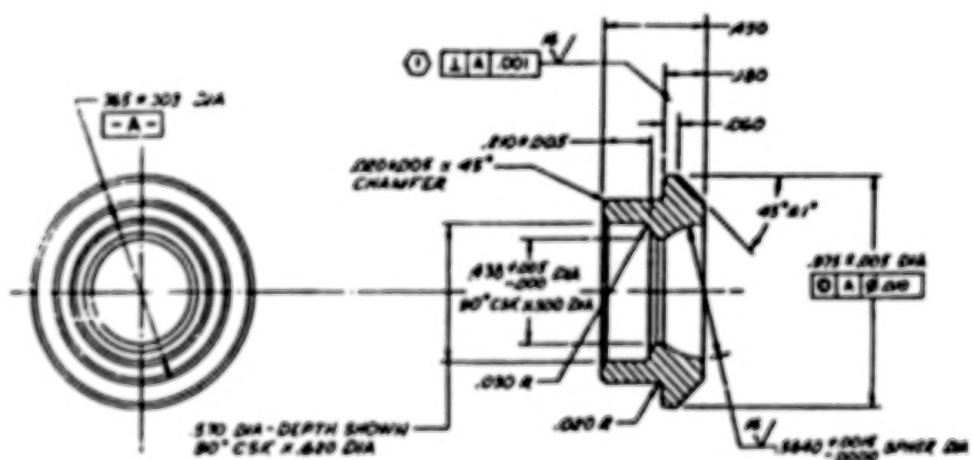
DOUBLE SWIVEL



SWIVEL BOLT

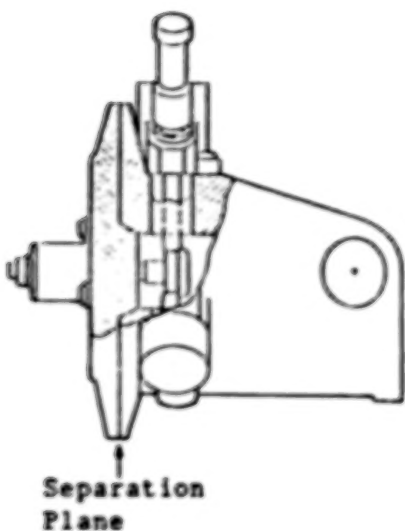


SWIVEL SOCKET

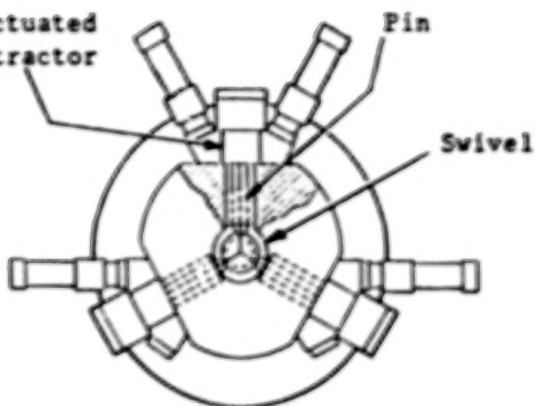


SWIVEL RING

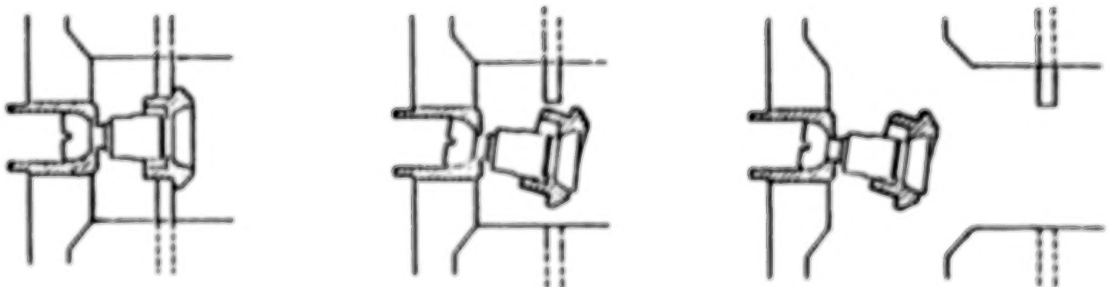
Figure 4. Double swivel toggle components.



Pyro Actuated Pin Retractor



3-PIN TOGGLE RELEASE MECHANISM



1. 3 pins lock swivel and payload in place
2. Removal of one or more pins causes the unstable swivel to move away from any remaining pins
3. Swivel and payload separation

RELEASE ANALOGY

Figure 5. Two fault tolerant three-pin toggle release sequence.

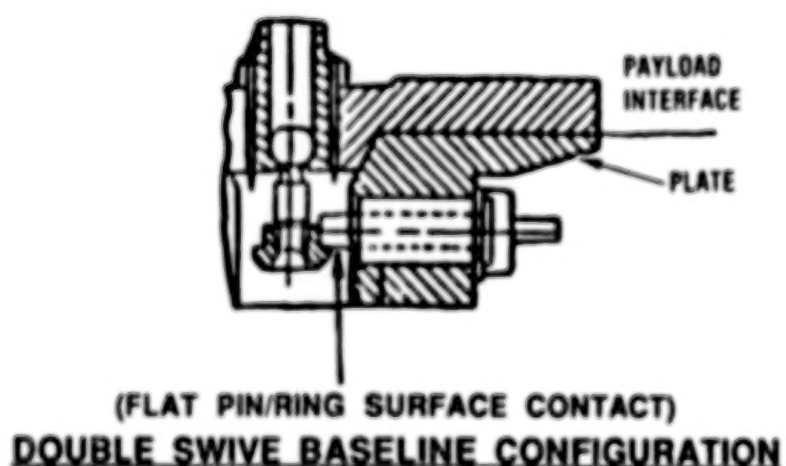
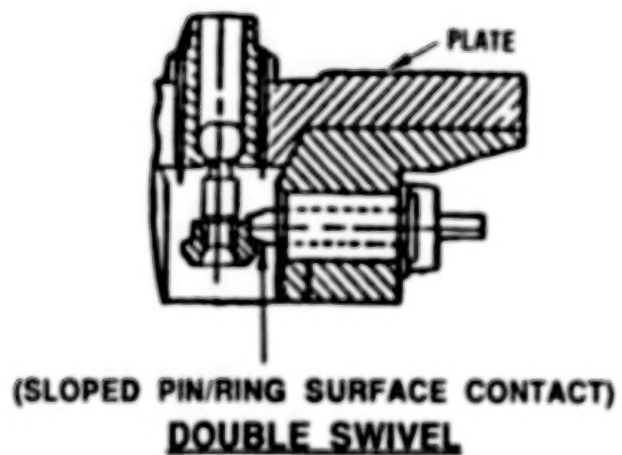
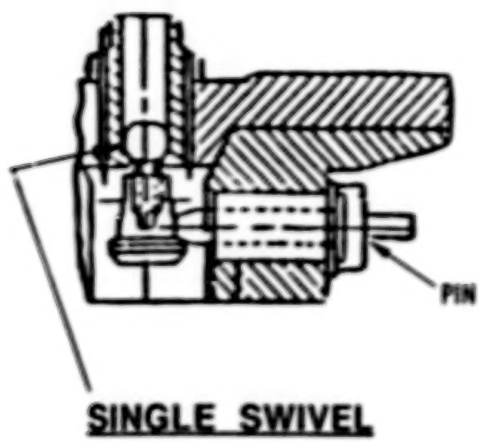


Figure 6. Three-pin toggle release concept development.

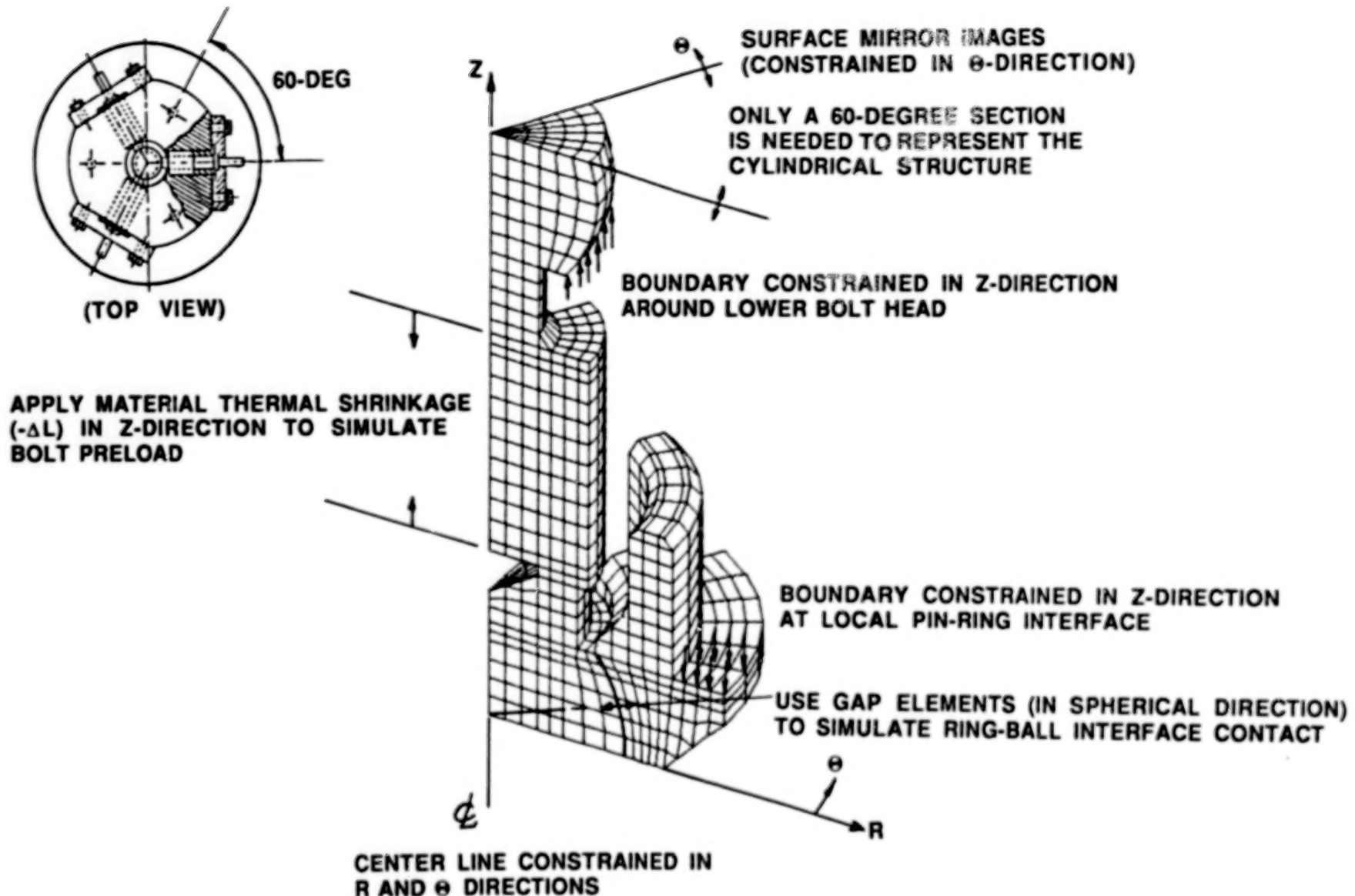


Figure 7. Double swivel toggle NASTRAN finite element idealization.

52

TOTAL PRE-LOAD = 1785 LB

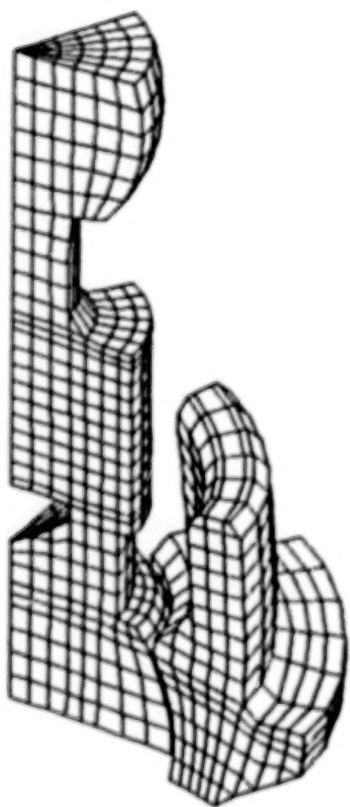
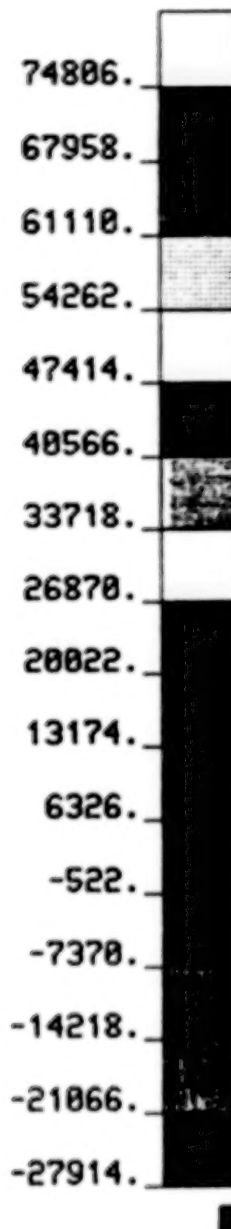
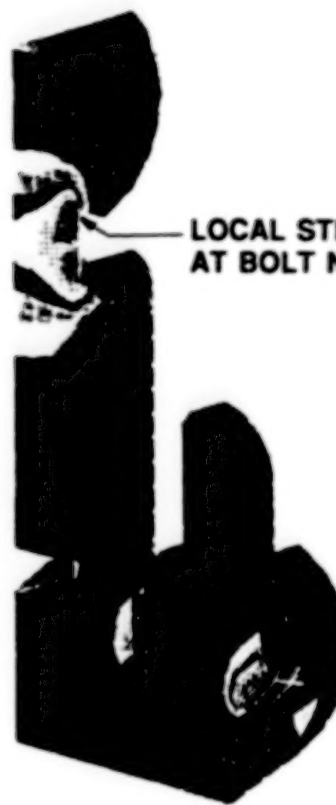


Figure 8. Exaggerated finite element model deformed shape.

**BLANK
PAGE**

TOTAL PRE-LOAD = 1785 LB

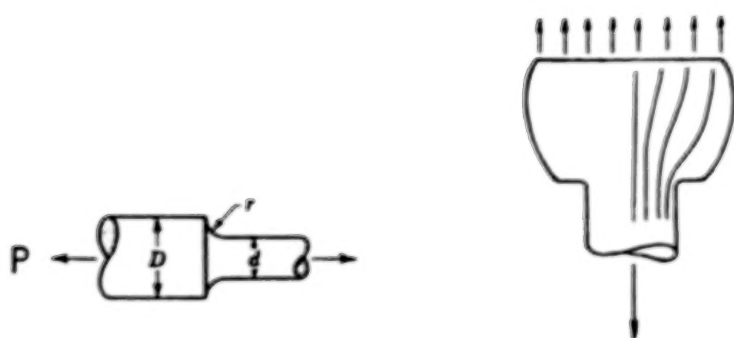
X
Y
Z



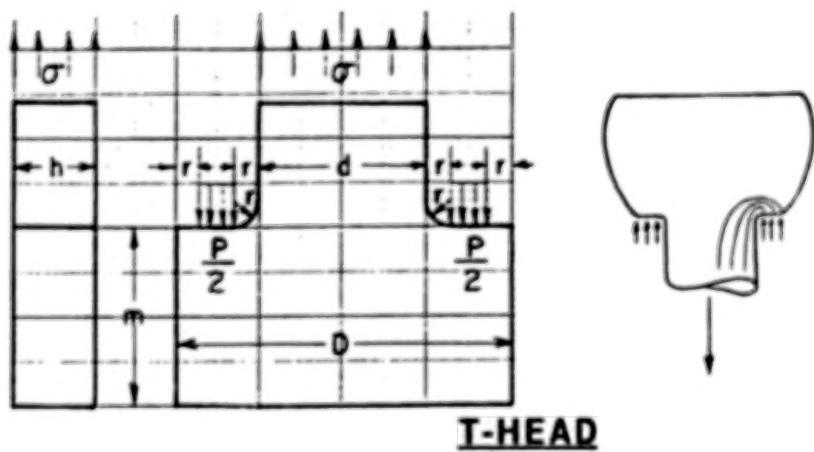
UNIT IN PSI
OR X (6.8948×10^3 N/m²)

Figure 9. First principal stresses, pre-loaded three-pin toggle release swivel.

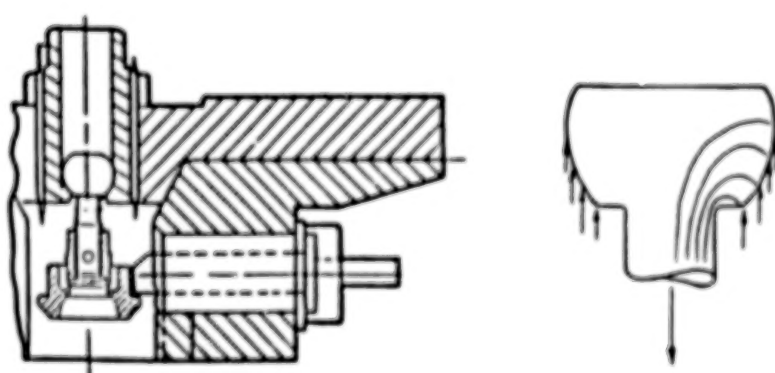
54



ROUND SHAFT WITH SHOULDER FILLET IN TENSION



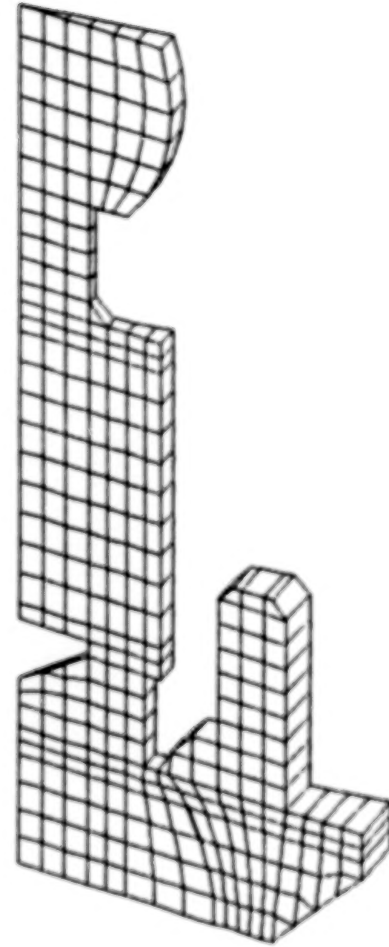
T-HEAD



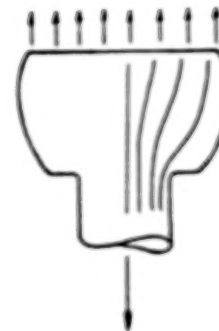
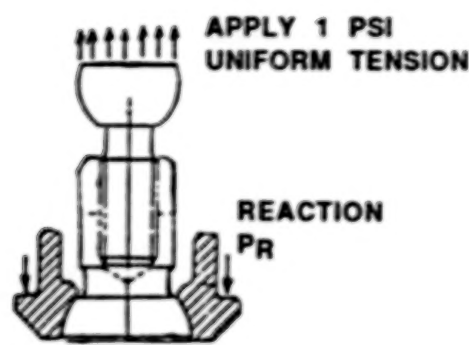
SWIVEL BOLT HEAD

Figure 10. Configurations of stress concentration effect.

**BLANK
PAGE**

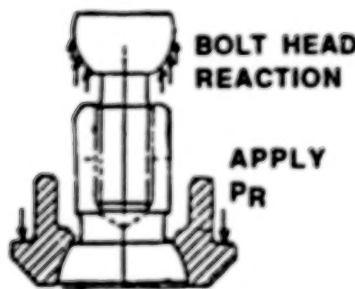


(1) ROUND SHAFT WITH SHOULDER FILLET IN TENSION



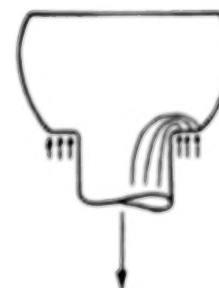
$\sigma_{1st-principal} = 5.18 \text{ PSI}$
 $\sigma_{z,max} = 5.10 \text{ PSI}$
 $\sigma_{zr,shear} = 1.05 \text{ PSI}$

(2) ACTUAL SWIVEL



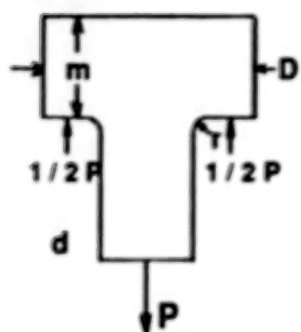
$\sigma_{1st-principal} = 5.36 \text{ PSI}$
 $\sigma_{z,max} = 5.24 \text{ PSI}$
 $\sigma_{zr,shear} = 1.27 \text{ PSI}$

(3) WORST T-HEAD



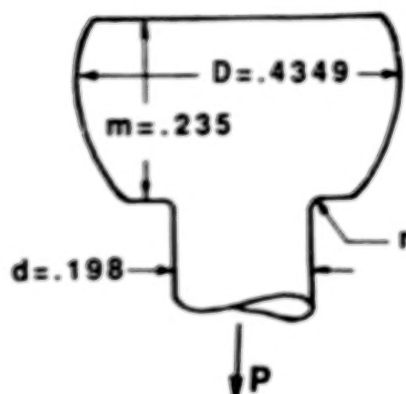
$\sigma_{1st-principal} = 5.52 \text{ PSI}$
 $\sigma_{z,max} = 5.40 \text{ PSI}$
 $\sigma_{zr,shear} = 1.68 \text{ PSI}$

Figure 11. Comparison of tension-loaded, preloaded, and T-head swivel using NASTRAN.



$m/d=1.2$ & $D/d=2.2$
for the swivel bolt

$K_t=5.6$ (for $r/d=.05$)
 $K_t=4.45$ (for $r/d=.075$)
 $K_t=3.8$ (for $r/d=.10$)
 $K_t=2.9$ (for $r/d=.20$)



$$m/d = (.235)/(.198) = 1.2$$

$$D/d = (.4349)/(.198) = 2.2$$

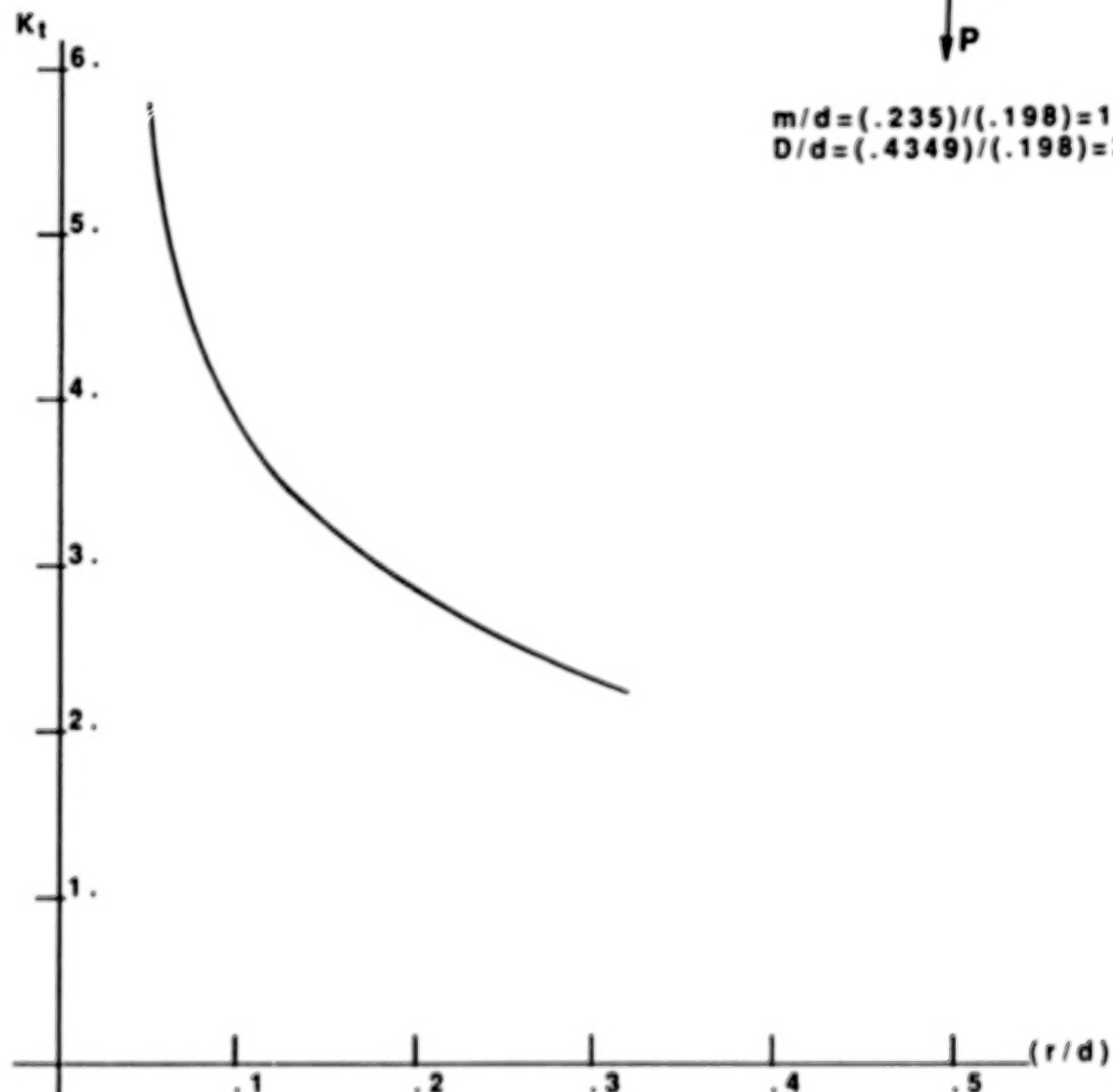


Figure 12. Stress concentration factors (K_t) for a T-head with variable fillet radius (r).

BLANK PAGE

DESIGN, FABRICATION AND TEST OF A 4750 NEWTON-METER-SECOND
DOUBLE GIMBAL CONTROL MOMENT GYROSCOPE

Lewis Cook*, Paul Golley*, Henning Krome*,
Joseph Blondin**, Charles Gurrisi**, and John Kolvek**

ABSTRACT

In recognizing the need to develop future technologies in support of the space station, NASA's Advanced Development Program (ADP) placed as its goal the design and fabrication of a prototype 4750 N-m-sec (3500 ft-lb-sec) Control Moment Gyroscope (CMG). The CMG uses the principle of momentum exchange to impart control torques to counteract vehicle disturbances. This paper examines the selection of the double gimbal over the single gimbal CMG and describes the major subassemblies of the selected device. Particular attention is given to how the man-rated mission requirement influenced the choice of the materials, fabrication, and design details employed.

Physical characteristics and the results of functional testing are presented to demonstrate the level of system performance obtained. Comparisons are made of the measured system responses against the predictions generated by computer simulation.

INTRODUCTION AND HISTORY

NASA initiated the ADP in parallel with the Phase B definition and preliminary design efforts for the space station. The purpose of this program was to focus on technologies applicable to the initial space station with the goal of accelerating these technologies to meet the proposed operational schedule for the station. Other objectives of the ADP were to enhance the performance of the space station, reduce life cycle cost during the operations phase, and reduce risks encountered during the development phase.

The Attitude Control Stabilization (ACS) team of the ADP proposed a number of technical activities, one of which was the design, fabrication, and test of a prototype CMG. Using a CMG for control of the Space Station Freedom seemed obvious since a CMG has a replenishable momentum capability, which is achieved through appropriate gravity gradient desaturation maneuvers and requires no consumables. NASA's experience with this type of control was amply demonstrated on the Skylab program in the mid-seventies. Skylab used three double-gimbal CMGs (DGCMGs) for attitude control, and employed gravity gradient maneuvers and a thruster system for momentum bias desaturation.

*NASA Marshall Space Flight Center, Huntsville, Alabama 35812.

**Allied-Signal Aerospace Company, Guidance Systems Division, Teterboro,
New Jersey 07608.

The first decision to be faced by the ACS team was whether to develop a DGCMG or a single gimbal CMG (SGCMG) for the space station prototype.

The advantages of DGCMGs include:

- Much simpler control laws without elaborate singularity avoidance
- No impact of unit failure on control laws
- No impact of failure on spherical momentum envelope shape
- Growth capability by adding individual DGCMGs without impacting control laws
- Simpler vehicle mounting geometry.

SGCMGs have an advantage in that they can provide greater torque capability for the same angular momentum. Since the Space Station Freedom has no rapid maneuvering requirements necessitating high torques, this did not prove to be an important consideration for this application.

System-level trade studies involving weight, size, power, and reliability produced no advantage to either type, since the SGCMGs require oversizing to produce the same angular momentum envelope as DGCMGs. The flexibility of the DGCMG to support a large variation in vehicle inertia, especially during station build-up, ultimately proved to be the main consideration for the selection. Since the ACS control laws are not affected by the number of units employed, the initial manifest need not contain the full complement of units. As the station assembly configuration changes, additional CMGs could be added at any time to support the ACS requirements.

The prototype CMG design parameters were extrapolated from the Skylab CMG experience, and improvements were made in a number of areas based primarily on the momentum storage capability and the long life required for the Space Station Freedom application. Marshall Space Flight Center (MSFC) was selected to lead the CMG development effort, since that center had been responsible for the Skylab CMG development and had the technical expertise and testing capability for continued CMG development. Subsequently, MSFC selected the Guidance Systems Division (GSD) of the Allied-Signal Aerospace Company (formerly The Bendix Corporation) to design, develop, and fabricate a prototype CMG under NASA contract NAS8-36628. The final concept is a double gimballed system with unlimited freedom for the outer gimbal and a 50-percent increase in angular momentum from the Skylab CMG. Mechanical features incorporated are an on-orbit servicing capability, power and signal transfer through rotary transformers and fiber optics respectively, and an active oil lubrication system for the spin bearings. The three-year development has resulted in a prototype CMG which will undergo verification and life testing at MSFC.

System Requirements

The CMG was designed to meet the following minimum system requirements:

- Angular momentum to be 4750 N-m-sec (3500 ft-lb-sec) at a speed of 6600 rpm
- Peak output torque applied to the space station shall be equal to or greater than 274 N-m (200 ft-lbs) for the maximum coupling condition with a maximum gimbal rate of 0.057 rad/sec (3.27 deg/sec)
- Outer gimbal to provide unlimited angular freedom
- Inner gimbal to provide ± 1.57 rad (90 deg) angular freedom
- Rotor design to have a safety factor of 4 on yield stress
- CMG design goal to insure reliability and a 10-year operational life.

CMG Configuration Trade Studies

A trade study was performed to optimize the selection of the rotor material. The study compared a wide range of candidate materials for the following mechanical properties:

- Material strength
- Fracture toughness
- Stress corrosion resistance (MSFC-SPEC-522B)
- Producibility.

In addition to the above parameters, the following constraints were also considered:

- Rotor diameter of 63 cm (25 in.)
- Rotor speed less than 9000 rpm
- No maraging steel
- Use of materials with published data base.

In order to make comparisons between various materials, three candidate systems were established and analyzed. Each of the designs was analyzed for weight, inertia, momentum, and yield stress. In addition, rotor stiffness and resonant frequencies were examined for each case. The conclusion of this study led to the selection of Custom 455 stainless steel as the optimum rotor material..

A second trade study was performed to determine the feasibility of replacing CMG rotor bearings during the mission. The long duration mission proposed for the space station program requires that the CMG rotor spin bearings must perform consistently for a minimum of 10 years. Even with a theoretical reliability of 0.999, the possibility of bearing deterioration or failure exists. Typically, degradation in bearing performance is characterized primarily by an increase in average friction torque with a corresponding increase in motor power consumption. In the case of serious bearing degradation, a bearing replacement would prevent loss of the CMG and its corresponding impact on the mission. As a result of the trade study, a bearing configuration has been incorporated into the CMG rotor bearing design which could support replacement of the bearings on-orbit if deterioration is detected.

Repairability and ORU Design Concept

The prototype CMG was designed using the orbital replaceable unit (ORU) concept to make repairs and component replacement in space as convenient as possible. For CMG removal, the mounting pads were designed for captive bolts, which prevent bolt loss after removal. Sufficient clearance exists between electrical connectors to allow insertion or removal by an astronaut wearing a space suit. The CMG is provided with handles to allow relative ease of on-orbit handling.

Electronic assemblies can be replaced without disturbing the mounting of the CMG. However, for safety considerations, it is recommended to remove power from the CMG prior to this replacement. Captive bolts and quick disconnects will facilitate the replacement of the ORUs.

Spin bearing replacement was designed to be achieved after placement of the CMG into a space station "shirt-sleeve" work area. The actual replacement procedure requires some mechanical acumen and extensive training to become familiar with the unit, tooling, and assembly sequence.

DESIGN DESCRIPTION

The design of the CMG is an evolution based on many CMG and momentum exchange devices built and flown since the Skylab program. Most of the major components of the system have a successful heritage and design base in keeping with the man-rated mission requirements of the Space Station Freedom. The system shown in Figure 1 consists of a rotor mounted within two sets of orthogonal gimbals so as to orient the spin axis of the rotor in any desired direction. All the drive and support electronics are mounted on the mounting ring and gimbal structures to minimize signal transfer across the gimbal pivots.

A simplified block diagram of the system is presented in Figure 2. The Outer Gimbal Electronics Assembly (OGEA) accepts the external electrical interface in the form of power and a MIL-STD-1553 serial communications link. In the OGEA a microprocessor channels the communication of command and

telemetry signals, and thus requires no analog signal processing of any type. Power is transferred across the outer gimbal pivot using redundant rotary power transformers. Communication between the OGEA and Inner Gimbal Electronics Assembly (IGEA) is performed via a Fiber Optic Rotary Joint (FORJ). In this manner no contacting signal transfer is employed where life limitations might be of concern.

The Rotor Electronics Assembly (REA) controls and monitors the speed of the rotor and is mounted on the inner gimbal. Signal transfer is accomplished from the IGEA to the REA by a limited-motion twist capsule, which is protected by gimbal stops that limit the inner gimbal motion to 90 deg. The major electrical functions are cross-strapped to improve overall system reliability and minimize the orbital replacement operation.

The major interface characteristics are described below:

- Size:
 - Length: 1.21 m (47.8 in.)
 - Width: 1.16 m (45.9 in.)
 - Height: 1.15 m (45.5 in.) - With outer cover in place
- Weight: 279 kg (615 lb)
- Mounting: 4 Point C.G. (Gimbal axes lie in the mounting plane)
- Power: (120 Vdc)
 - Quiescent: 95 W
 - Spin-Up (Peak): 240 W

The following sections will describe in further detail the major components of the system and what requirements influenced the design or fabrication activities.

Rotor Design and Safety Analysis

A cross-section of the rotor installed in the Inner Gimbal Assembly (IGA) is presented in Figure 3. The rotor is a single-web wheel forged from Custom 455 stainless steel. It is supported at each end by a single angular contact ball bearing. Outside diameter of the rim is 0.635 m (25.0 in.) and the overall shaft length is 35 cm (13.85 in.). Custom 455 is a precipitation hardenable steel and is considered highly resistant to stress corrosion cracking. Extensive testing was performed by GSD to properly qualify this material and verify the physical and mechanical properties.

A finite element model of the rotor was created and analyzed for stresses and deflections using NASTRAN. The centrifugal loading of the rotor at 6600 rpm produces the maximum steady operational forces. Gyroscopic stresses on the rotor are of much less concern due to the low level of output torque that is required of the system. A modified Goodman diagram presented in Figure 4

illustrates that the combined centrifugal (steady) and gyroscopic torquing (cyclic) stresses are well within the infinite life region of the graph.

A design requirement was placed on the rotor to provide a factor of safety of four on yield stress at 105 percent of the nominal wheel speed (6930 rpm). An analysis of the rotor stress results in a peak value in the web of 296 MPascals (43 kpsi). Comparing this to the 1.2 GPascals (175 kpsi) yield strength of the material produces a safety factor greater than required. During component test, the rotor was subjected to an overspeed of 1.33 times the nominal speed (8800 rpm), and survived.

Spin Bearings and Lubrication System

The spin bearings used in the design are angular contact type 107H size ball bearings with special retainers. This configuration has been used previously and dates back to the Skylab CMG. The bearing retainers have been modified to provide proper distribution of the lubricant to the ball and race contact zone. The material for the races and balls is VIM-VAR 52100 chrome steel, and the retainer is fabricated from a cotton-based phenolic impregnated with bearing lubricant.

When assembled, the bearings are preloaded by a constant force Belleville spring that ensures the bearings remain preloaded under all conditions. Low-level heaters are provided in the housing for low temperature operation if required.

To support the 10-year life requirement, an active lubrication system was chosen. This system will provide a flow of new KG-80 lubricant in a "one-time-through" manner to continually lubricate the bearing over the design life of the CMG. The reliability of the bearing is enhanced by this system and is far superior to grease lubrication for long mission durations.

Torque Motor and Transmission

To develop the required torque of 272 N-m (200 ft-lb), a torque motor and geared transmission are utilized. The motor is a brushless DC type design capable of developing 12 N-m (9 ft-lb) or torque. An ironless stator is employed which produces no hysteresis or eddy current losses, and thus eliminates magnetic cogging and drag torques for better system performance.

The gear train employed in the transmission is shown in Figure 5 and consists of a two-stage, parallel-path spur gear arrangement. Windup of one gear train path with respect to the other provides a preload that effectively eliminates backlash in the transmission. A gear ratio of 27.76 to 1 allows the motor to achieve the required torque level. This type of configuration has been employed on previous designs, including a unit that has accumulated six years of special life testing under severe duty cycle operations.

These components are housed in the Torquer Module Assembly (TMA), along with a multi-speed resolver used for rate feedback. Shown in cross-section in

Figure 6, this assembly is identical for both the inner and outer gimbal pivots.

Gimbal Drive Electronics

Both the inner and outer gimbals are rate controlled in a closed loop manner using a phase-locked-loop technique. This technique permits high input command resolution and precise rate control without the necessity for precision low-signal-level analog electronics. In operation, the 16-bit digital rate command is applied to a digital low-pass filter, the output of which is accepted by a Binary Rate Multiplier (BRM). The BRM acts as a digital number-to-frequency converter.

A 16-speed resolver acts as a rate sensor and produces an output whose frequency is proportional to the gimbal speed. The resolver and BRM outputs are applied to a phase detector which produces an output proportional to the phase difference between the two input frequencies. The phase detector output is then applied to a compensation network needed for loop stability, and a notch filter to attenuate phase detector carrier harmonics. This signal is then applied to a power amplifier which contains a multiplier unit to achieve commutation for the torque motor. A current feedback technique is utilized by the amplifiers to produce a current-source drive. In response, the motor accelerates to a speed which causes the resolved output frequency to come into exact correspondence with the command frequency.

Rotor Drive Electronics

The rotor drive is also controlled by a phase-locked-loop design. Nominal wheel speed is defined as 6600 rpm, but the system is capable of being commanded to operate at 5 percent above and below this value. A frequency is generated by a Hall resolver and compared to the commanded reference frequency. The difference in these two signals generates an error signal that is applied to a phase detector, amplified, and frequency shaped. It is then applied to the PWM current amplifier which is commutated by the output of the Hall resolver. A current feedback technique is utilized by the amplifiers to produce a current source-drive to the spin motor.

MATHEMATICAL MODELING

For design and analysis purposes, the behavior of the CMG can be characterized by a 6-mass model. This model represents both the inner and outer gimbal loops which are coupled as a function of the inner gimbal angle. In general, the loops are designed as high-gain wide-bandwidth rate loops to enhance small signal performance and damp the gear train resonance. A digital prefilter is used to provide the overall bandwidth characteristics as viewed by the vehicle control loops. When the proper stabilization networks are employed, the inner gimbal loop produces the frequency response characteristics shown in Figure 7.

From this linear model, a nonlinear representation was developed that permits a more accurate determination of CMG performance. A simulation was generated using the Boeing Computer Services EASY-5 Analysis Program, and incorporates nonlinear effects such as: torque motor saturation, gear train compliance, electronic limits, and pivot friction. The model can be exercised for any type of input command (i.e., sinusoidal, step, impulse, or impulse train).

TEST RESULTS

Support Equipment

The CMG system is supported during testing by an automated computer-controlled test station. Interface to each of the two channels of the CMG is via a single cable, which supplies power and provides a dual redundant serial data link. The station uses an IBM PC/AT computer equipped with a 30-Mbyte hard disk drive. All operator interface and monitoring of the CMG is provided by a MIL-STD-1553 serial communications bus which plugs directly into the computer. Power requirements to the system are provided by a 120-Vdc supply that is controlled and monitored by the test station computer.

The computer displays the command status and health of the system on a CRT monitor. Response data from the unit is processed and various flags, alarms, and shutdowns are automatically implemented by the station. Hard copy of the display may be obtained on command or at regular intervals. Test data can be stored or transferred to floppy disk for post processing.

Force and Moment Table

To measure output performance, a force and moment table was designed and built for the CMG system. This table uses four piezoelectric three-axis force sensors, whose outputs are summed according to their mounting geometry to produce the three forces and moments that completely describe the system mechanical output. Using a digital signal analyzer, these signals can be displayed in either the time or frequency domain to characterize the output performance levels as described in the following paragraphs.

Frequency and Step Response

Figure 8 shows the results obtained for the frequency response test of the inner gimbal loop. This is typical of results obtained for both loops and demonstrates the dependency on the inner gimbal angle. In general, the agreement is excellent when compared with the predicted results given earlier, although the test data has slightly more peaking. This effect was also noticed in the step response behavior of the system in both the overshoot and settling characteristics observed. This difference has been attributed to the gear train stiffness being lower than anticipated.

Gimbal Rate Linearity

Gimbal loop scale factor and linearity were measured for various commanded rates. The test consisted of commanding a constant rate for a known period of time and computing the actual rate from the change in gimbal angle. Figure 9 presents a plot of the difference between the measured rate and linear fit of the data. The results are typical for both loops and yield a linearity in the 0.1-percent range. Due to the manner in which the test was performed, these results represent errors in the test method employed rather than the system accuracy. This is consistent with the expected performance for the phase-locked-loop implementation as well as the commanded zero rate drift, which is below the threshold of what could be measured.

Torque Noise

Torque noise is defined as the undesirable component of torque produced by the actuator when a constant rate is commanded. Expressed in terms of the RMS components produced in the frequency domain, a measurement of this noise is given in Figure 10 for a 5.7 mrad/sec (0.327 deg/sec) commanded rate. Major contributors to this error source have been identified as the dc offset in the drive voltages and the transmission gearing. This plot is typical of both the inner and outer gimbal loops, and incorporates special balancing circuits to minimize the effect of the offset of the drive voltages. Total noise when viewed in the time domain produces a value of approximately 2-percent RMS for the case given.

Induced Vibration

Another performance parameter important to the operation of the space station is the induced vibration of the CMGs. Concerns exist for potential coupling to the inertial sensors, located on the same pallet, as well as the effect produced on the station micro-gravity environment. The dominant contributor to this performance is the balance of the rotor wheel as it rotates at the nominal speed of 6600 rpm. A full characterization of the system would consist of the three forces and moments that would be seen at the mounting interface for a host of gimbal positions. Typical values for these parameters have been measured, and result in forces that range from 0.45 to 2.2 N (0.1 to 0.5 lbs) and moments that range from 0.68 to 0.27 N-m (0.5 to 0.2 ft-lbs).

Gimbal Angle Readout

A readout of the gimbal positions is provided as a system output to provide necessary information to the momentum management and vehicle control laws. Measurements of the readout accuracies of both gimbals were below 1.7 mrad (0.1 deg) for all cases measured.

Wheel Speed Control

During all operations of the CMG, the wheel speed was monitored and the performance of the loop has exceeded the design goal of 0.1 percent. Actual speed never exceeds 2 rpm from the commanded value even during maximum rate conditions.

CONCLUSIONS

The development of the prototype DGCMG has provided NASA with a working design that meets or exceeds the goals of the Advanced Development Program. In addition to providing a safe design for man-rated missions, this device can contribute to the Attitude Control System definition and address concerns at a relatively early stage in the space station development. Major accomplishments of the program include the following:

- Successful demonstration of compliance to all the system requirements and design constraints imposed
- Concurrence of analytical models and simulation results to the measured performance
- Development of the necessary test station and the measurement equipment needed to characterize output performance.

PROPOSED FUTURE TESTS

The results obtained to date represent the current state of the system characterization. Future work is planned to improve the response and evaluate other performance parameters.

Cross-compensation

At present, cross-coupling between the inner and outer gimbal servo loops causes variations in the frequency response as a function of the inner gimbal angle. Although these bandwidth variations appear to be acceptable for the accuracy requirements of space station, a proposed improvement is to use a variable cross-feed compensation. The expected results would produce a frequency response characteristic nearly independent of inner gimbal angle.

Small Signal Characterization

Results for relatively large signal performance have previously been shown to agree with the linear model of the system. Small signal rate commands will be used to determine the effect of non-linearities such as dead-zone, if any exists, and gimbal friction. If required, these test results could then be used to modify both the model itself and the values assumed. The result would be a high-fidelity model that could be used to assist analyses and simulations of the ACS.

Life Tests

Current plans call for verification and life testing at MSFC. The support test equipment has been designed to simulate the duty cycle commands expected for Freedom, and thus provide a means to address the design life performance.

**BLANK
PAGE**

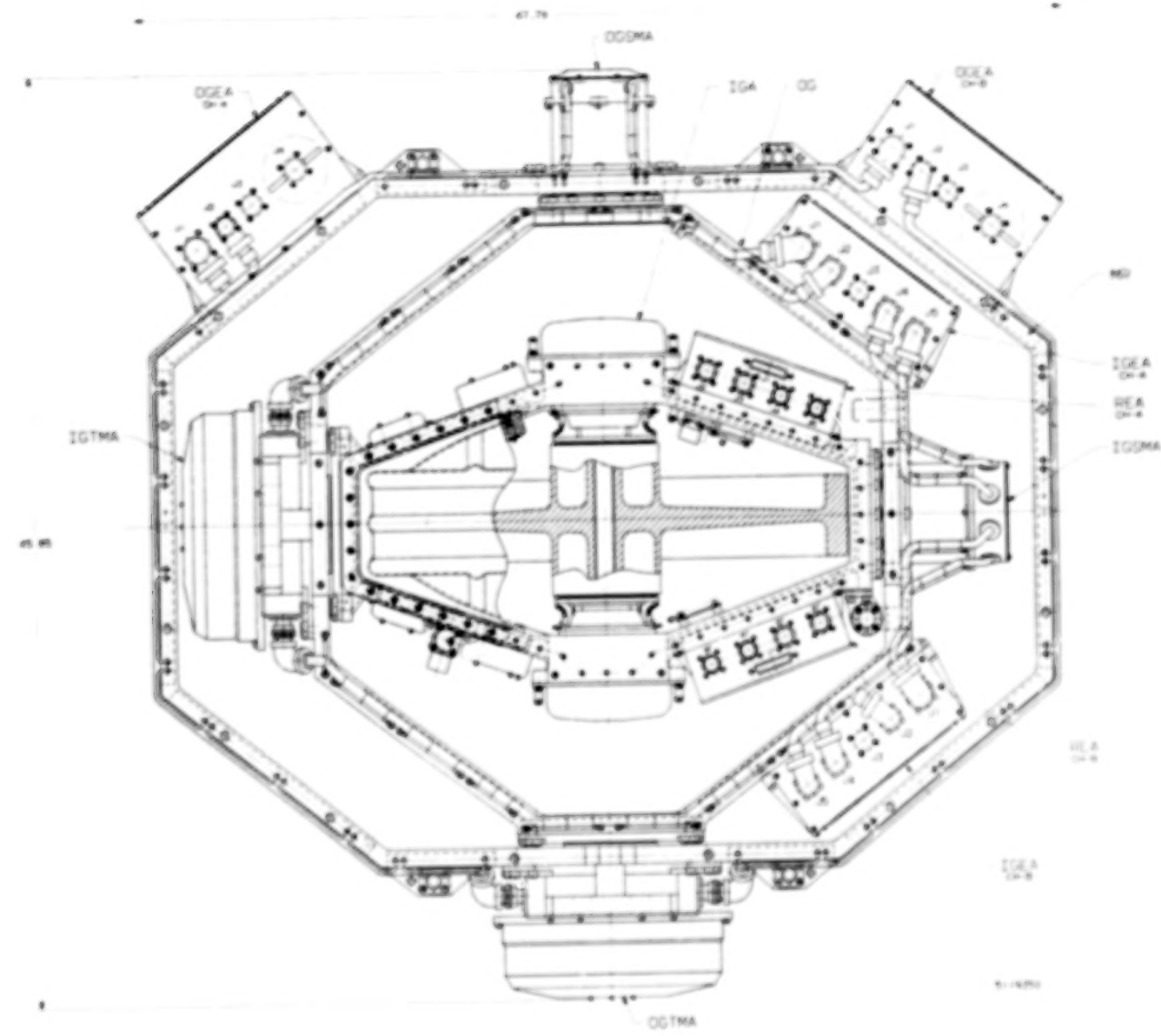


Figure 1. Layout of prototype DGCMG system.

**BLANK
PAGE**

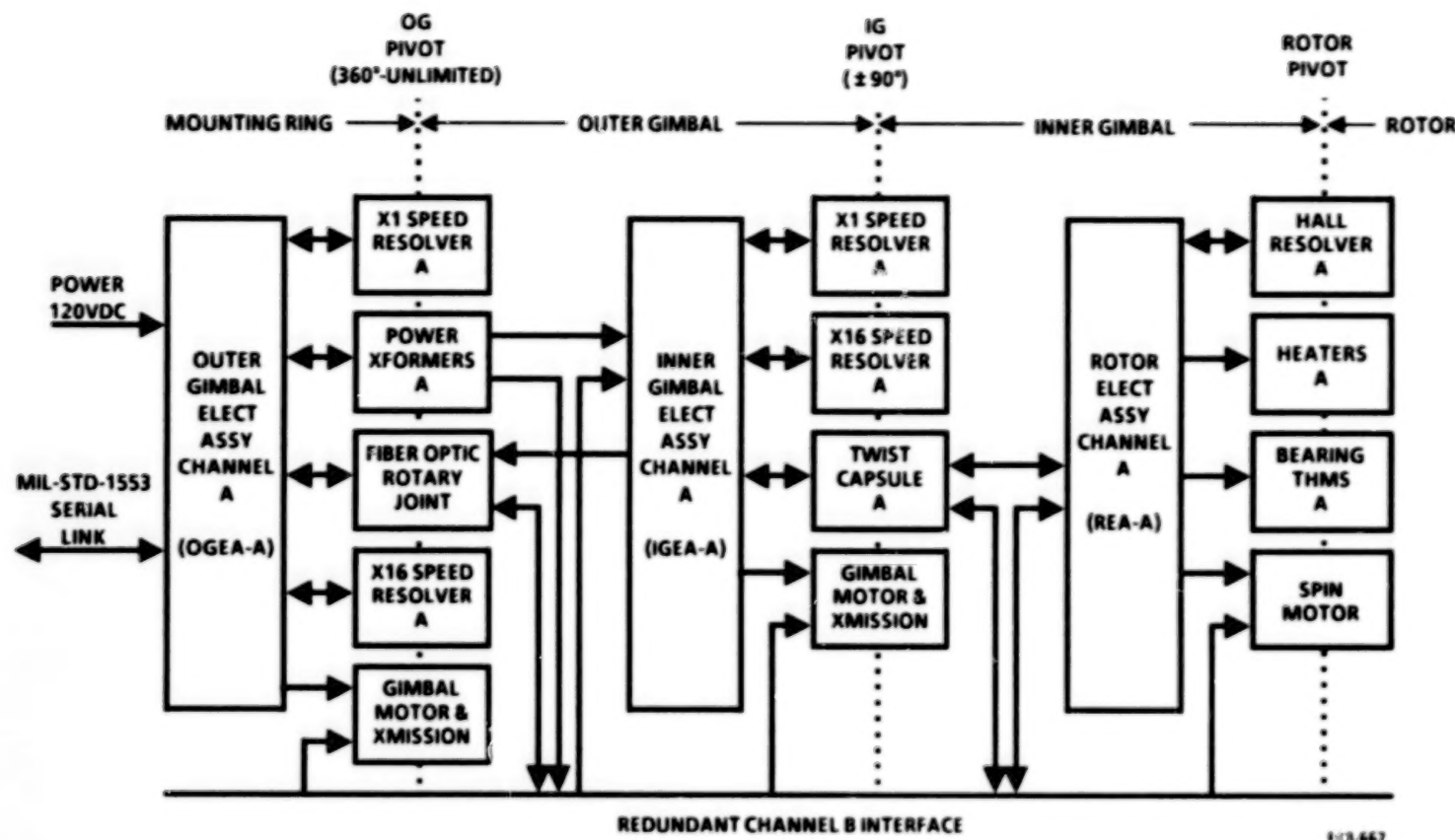


Figure 2. System block diagram.

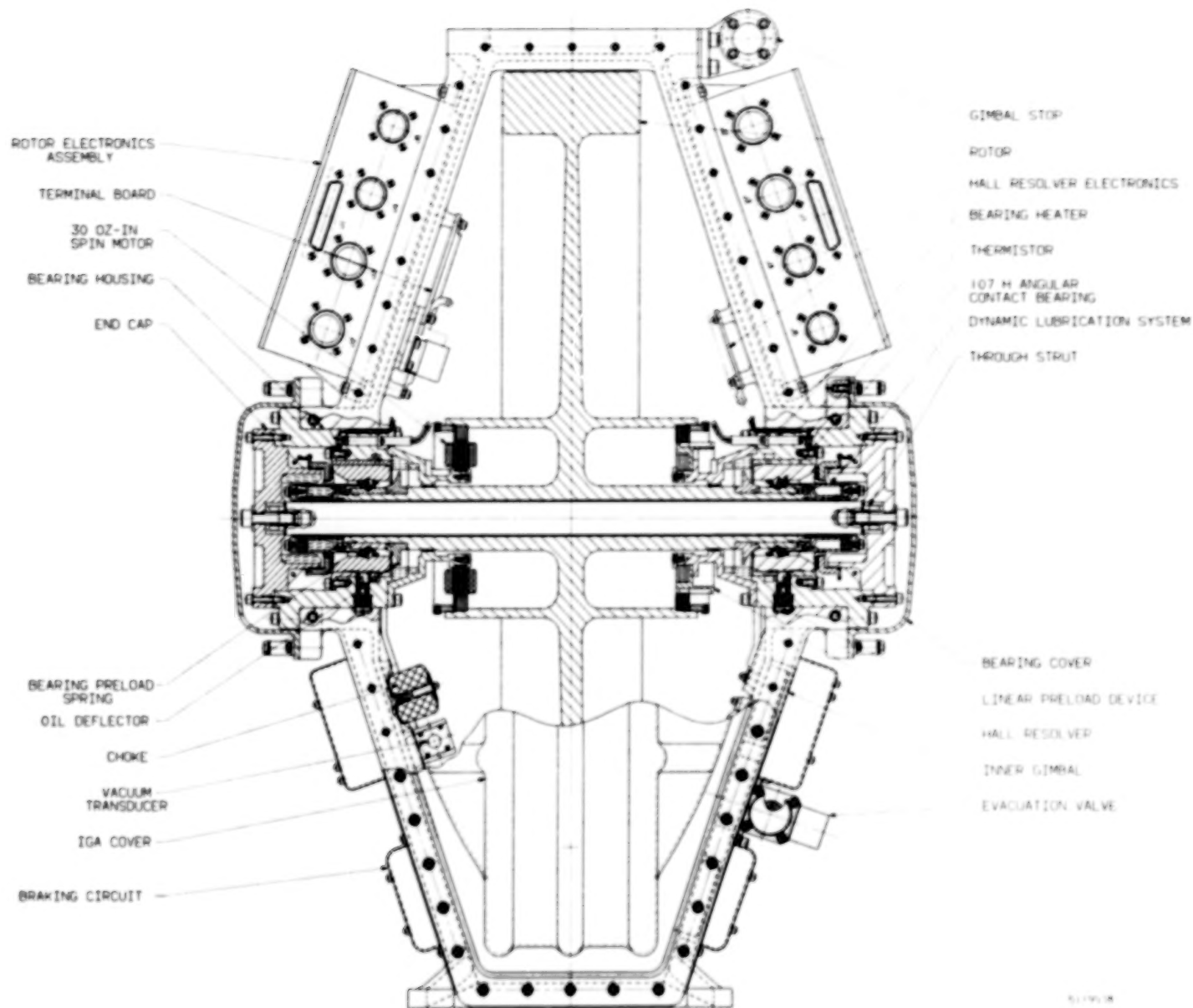


Figure 3. Inner gimbal assembly.

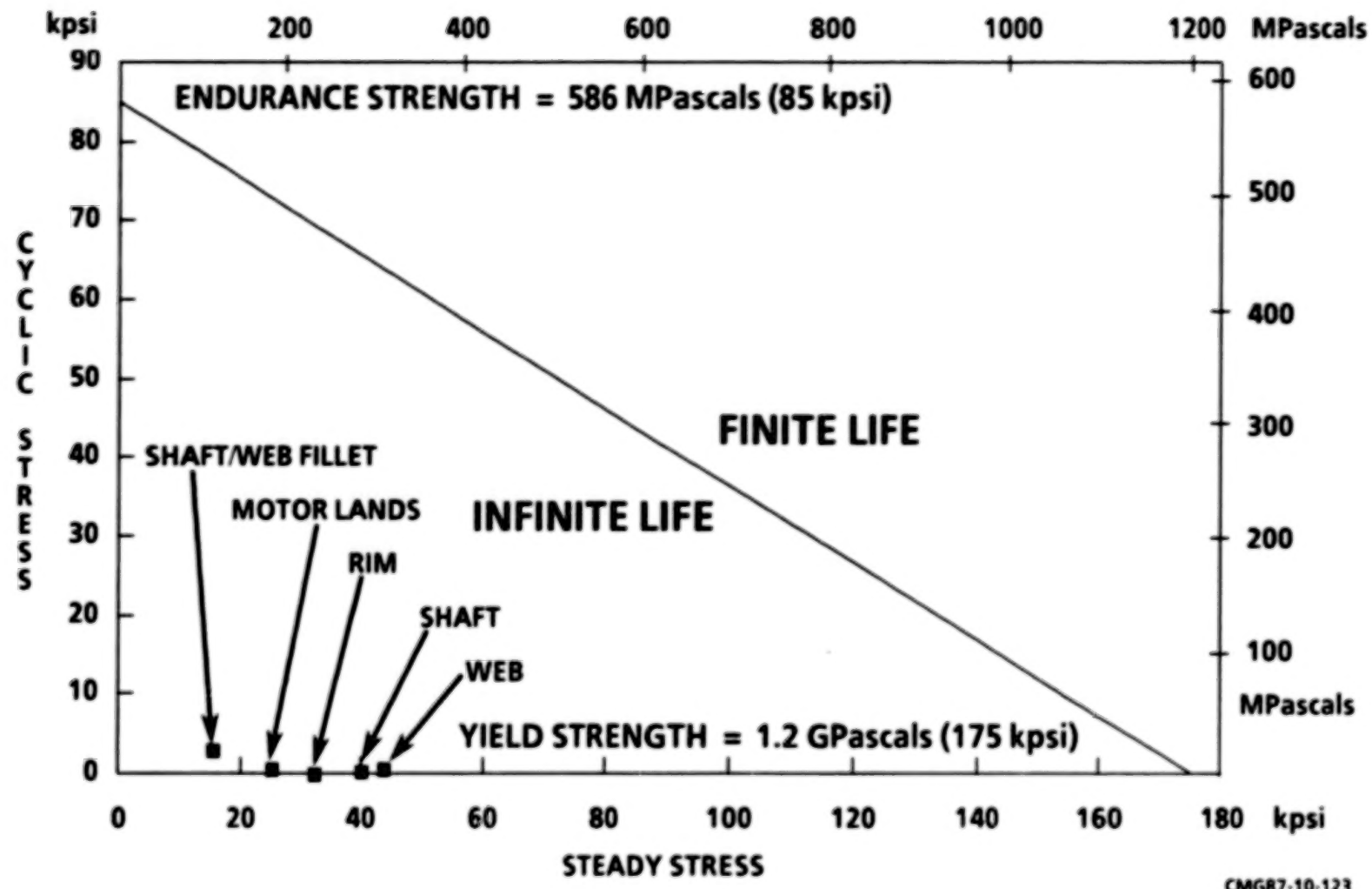


Figure 4. Modified Goodman diagram of rotor stresses.

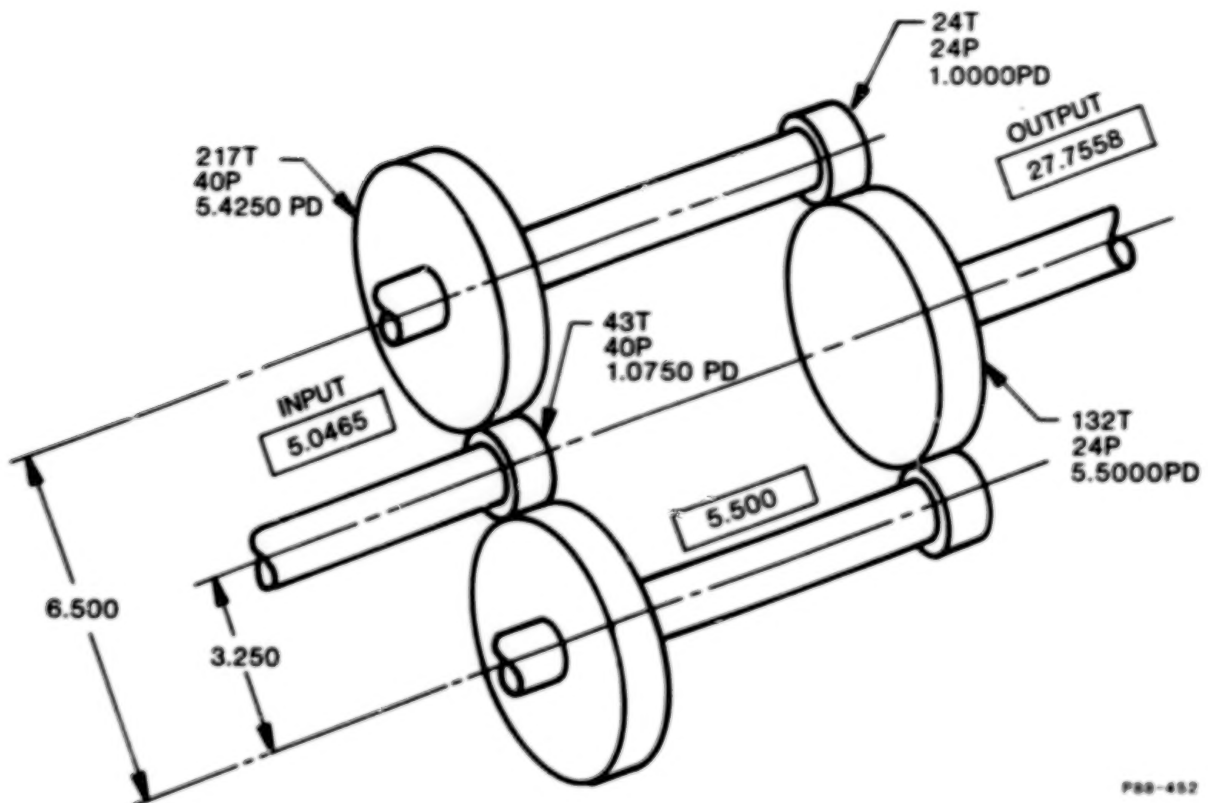
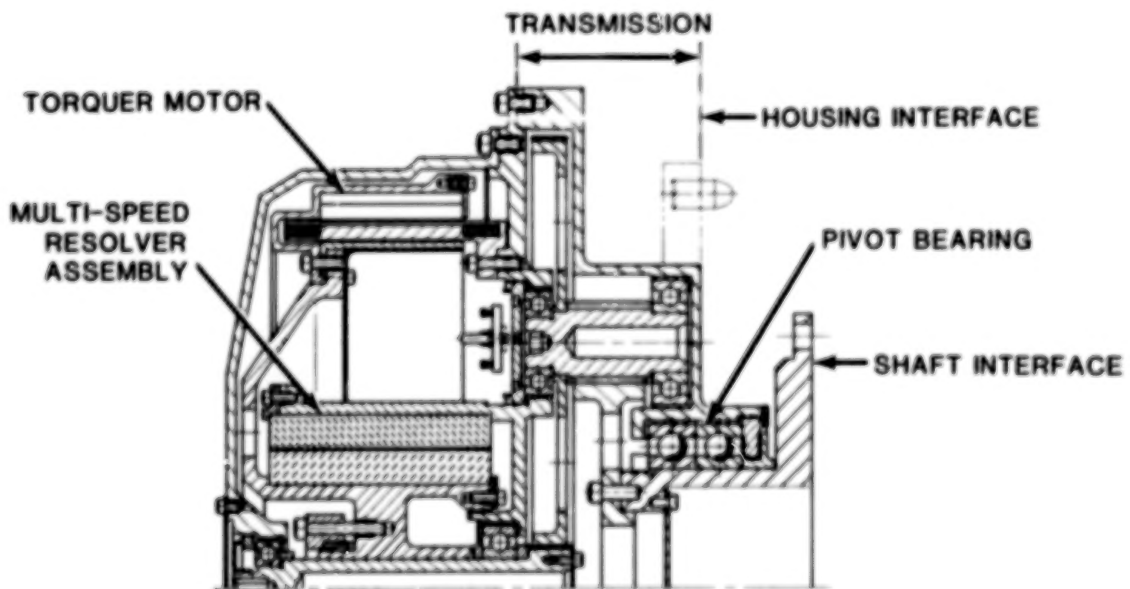


Figure 5. Parallel path gear train transmission.



5119559-4
PBB-512

Figure 6. Torquer module assembly cross-section.

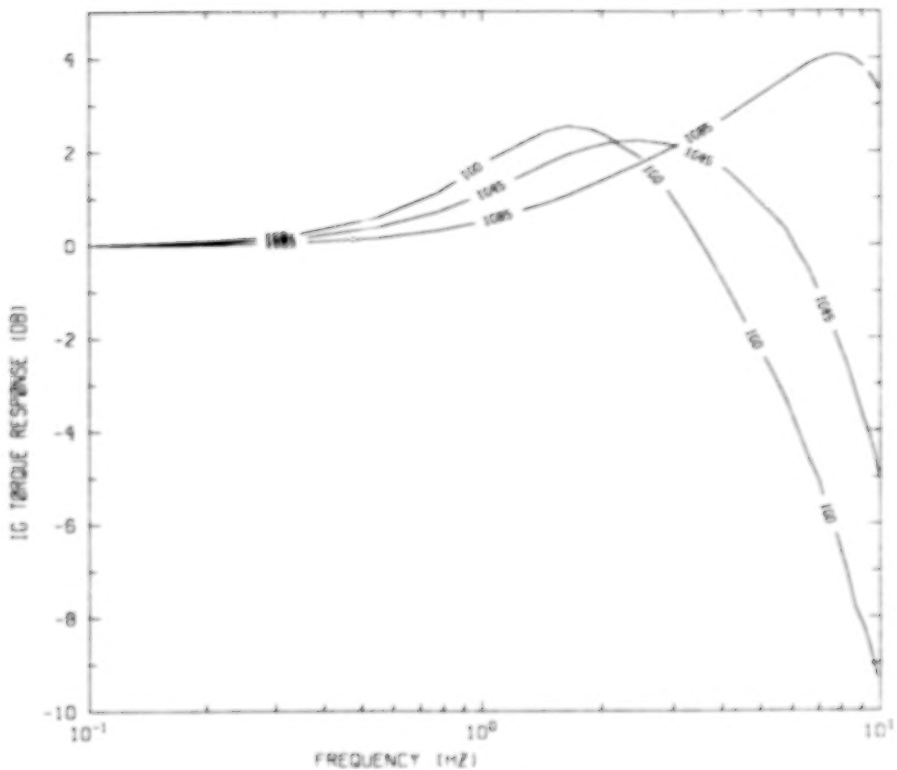


Figure 7. Math model prediction of IG loop frequency response.

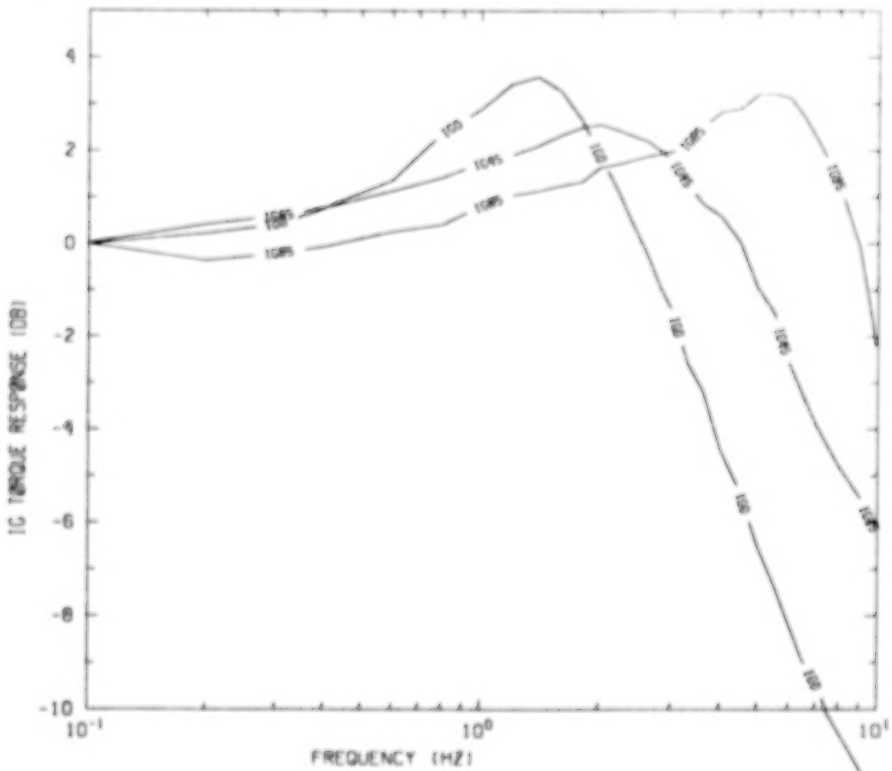


Figure 8. Measured IG loop frequency response.

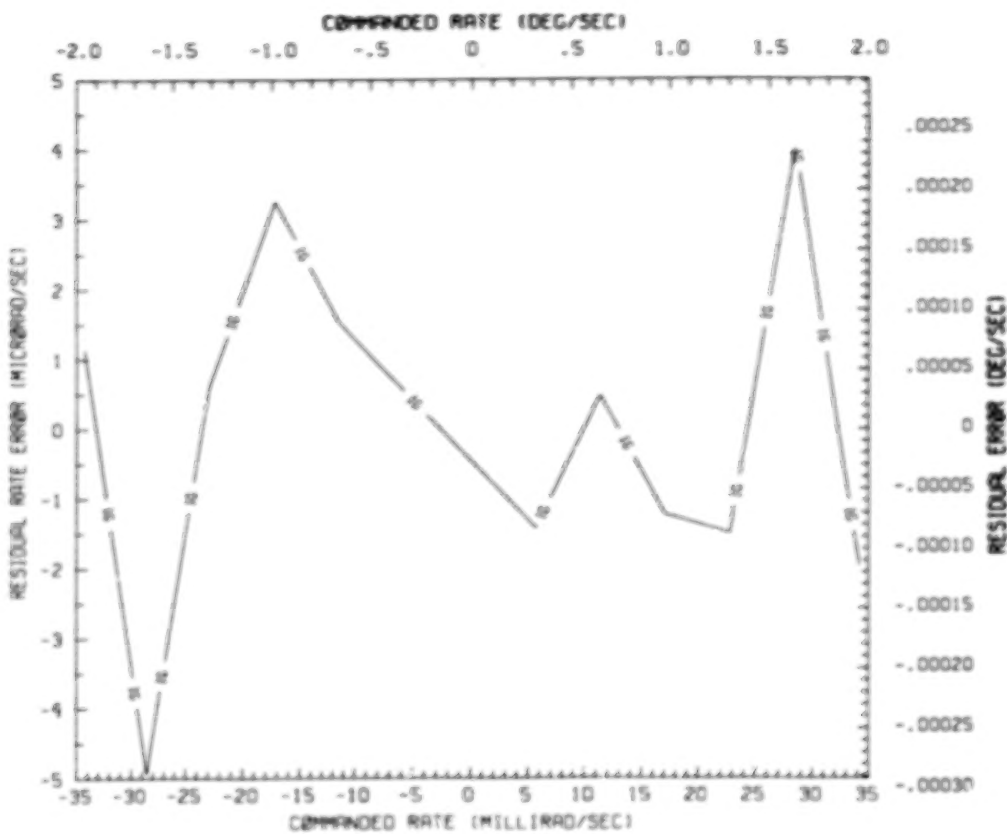


Figure 9. Inner gimbal loop linearity performance.

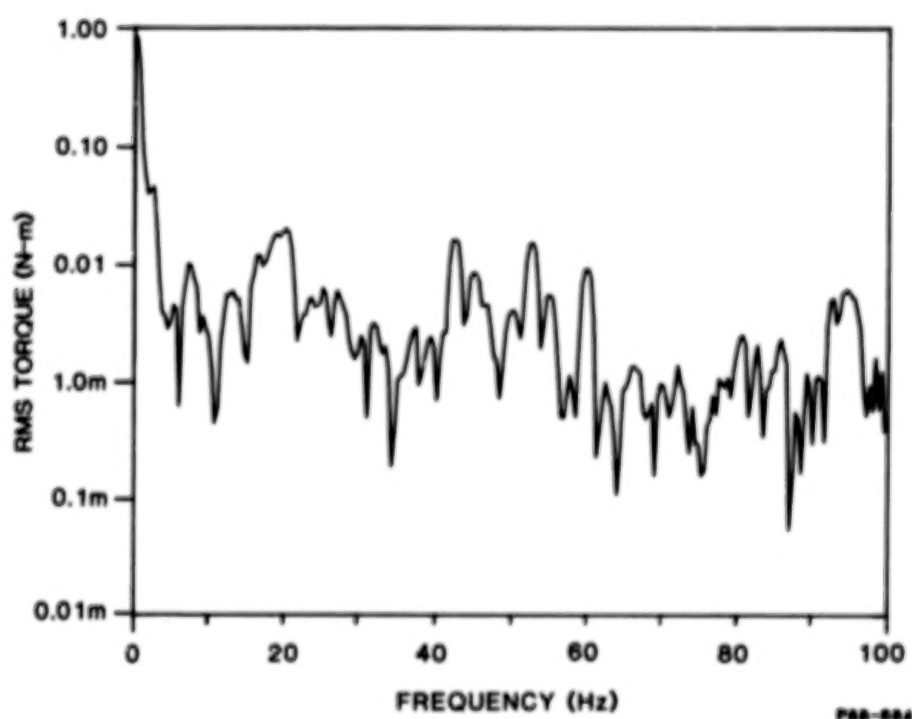


Figure 10. Torque noise performance.

CAROUSEL DEPLOYMENT MECHANISM FOR COILABLE LATTICE TRUSS

Robert M. Warden* and P. Alan Jones*

ABSTRACT

AEC-Able Engineering Company, Inc. (ABLE) has developed a unique mechanism for instrumentation and solar-array deployment by combining two technologies. The first technology (initiated by the Jet Propulsion Laboratory and later developed by Lockheed Missiles and Space Company [1]) is the "smart" motor which can operate in either an analog mode to provide high speed and torque, or in a stepper mode to provide accurate positioning. The second technology is a mechanism developed by ABLE, where a coilable lattice mast is deployed then rotated about its axis with a common drive system, thus eliminating the need for a second drive system. A prototype unit has been designed, built, and tested. A review of the design and function of this system is presented along with structural and thermal test data.

BACKGROUND

In the early 1960s, a triangular lattice truss made of unidirectional fiberglass rods was developed which was capable of retracting and extending. Retraction is accomplished by the coiling of the continuous longitudinal element, which then acts like a spring to deploy the mast. This type of mast has been used extensively for space application because it is lightweight, strong, and stiff, and stows to a small fraction of its (deployed) length (Fig. 1).

Lanyard Deployment

A key to using this structure is the deployment mechanism which controls the extension and retraction. The simplest and lightest way to control deployment is by running a cable or "lanyard" down the middle of the mast. This lanyard is attached to the top plate at one end and to a motor or rate limiter at the other (Fig. 2A). In this way, the lanyard is paid out gradually so that the mast deploys at a controlled rate. The mast is very strong and stiff when fully deployed, but it does have some disadvantages. This is because during deployment the mast has a relatively weak and flexible transition section which may be undesirable. Also, during deployment and retraction, the top of the mast rotates with respect to the base about the mast centerline. This rotation is unacceptable for some applications.

*AEC-Able Engineering Company, Inc., Goleta, California.

Elevating Nut Deployment

A second deployment method was developed where the mast is enclosed in a large, thin-walled tube or canister, and deployment is controlled by a large rotating nut at the top (Fig. 2B). The most important change to the mast is the addition of roller lugs which enable the mast to be constrained at a deployed section rather than at the flexible root. This greatly increases strength and stiffness during deployment. The motorized elevating nut continuously transports the rollers up or down to deploy or retract the mast. The mast is prevented from rotating as it deploys by guide rails inside the nut, and the stowed mast is allowed to rotate at the base.

The elevating nut method has several advantages. The mast has nearly full stiffness and strength throughout deployment, and the tip deploys without rotating. There are, however, some disadvantages to this system. The elevating nut is a relatively heavy, complex component supported by large bearings. Weight reduction can be accomplished only by more complex and costly machining or by using more exotic materials. The elevating nut also increases the envelope of the system and, at full deployment, the mast is subject to free-play due to the clearances required at the roller-lug-to-elevating-nut interface.

Carousel Deployment

The subject of this paper is an alternate method called "carousel," which has some of the advantages of the other methods and offers unique features of its own. The carousel method is similar to the elevating nut method, except that the nut has been removed and the motor drives a turntable at the base. During deployment, the mast tip does not rotate, and the mast has significant strength and stiffness. The system weighs less than the elevating nut-method but more than the lanyard method, and the packaging volume is slightly more than that of the lanyard method.

Unique to this system is the fact that once the mast is fully deployed, it changes smoothly from axial deployment to rotational movement (Fig. 3). The outstanding advantage of the carousel system is that when combined with the smart motor technology, the same drive mechanism used for deployment may also be used for tracking. The turntable/drive system is common to both functions, thus eliminating the need for a second drive system.

THE MOTOR

The Carousel Deployment System takes advantage of "smart" motor technology [1]. The basic elements of this technology are a brushless dc motor and a control circuit which operates the motor in either an analog or stepper mode. To deploy the mast, the motor operates in the analog mode to provide the speed and power required to deploy the mast and, if needed, to extend a solar array. Once the mast is fully deployed, the motor operates

either in the analog mode to rapidly slew the mast into position or, more importantly, in the stepper mode to accurately rotate the mast at a constant rate.

A "dual-drive" gear box is used to complete the drive system. The dual-drive was developed by JPL as a reliable, redundant drive system for aerospace applications. This system uses harmonic drives to provide independent load paths from two motors to a common output. (This technology was presented at the 16th Aerospace Mechanisms Symposium in 1982.)

CAROUSEL DEPLOYMENT SYSTEM DESCRIPTION

The carousel deployment system consists of a thin aluminum cylindrical shell which contains three principle functional areas: turntable, storage section, and transition section.

Turntable

The turntable at the base of the system is a rotating platform which is driven by the motor. The platform is supported by large-diameter duplexed bearings which are preloaded against each other to eliminate any free-play or dead band over the required temperature range (Fig. 4). The bearings are supported by thin-walled shells to accommodate thermally-induced distortion without greatly increasing bearing preload. The radial flexibility designed into the system allows thermal deflection without sacrificing overall system stiffness. The bearing supports are designed with radial interference at room temperature and are assembled by heating one bearing seat while cooling the other, then slipping the bearing in place. The base of the mast is mounted to the turntable platform, which is open in the center to provide space for a slip ring assembly if needed. A large-diameter internal gear is used so that room is available to add encoders or potentiometers, depending on the application's telemetry requirements.

Storage Section

Above the drive area is the storage section which contains the stowed mast when the system is retracted. There is enough clearance between the mast and the storage shell to allow mast rotation, but not enough to allow excessive excursions during vibration or launch.

Transition Section

Immediately above the storage section is the transition section, where the mast smoothly changes from the stowed to the deployed state. This operation is the key to carousel system success. Transition guides are curved rails which control the transition shape of the mast and thus control the deployment of the system. Rollers are attached to the mast at each batten frame and protrude into the rails to constrain and guide the mast during deployment.

The mast shrinks in diameter as it goes through the transition section. For the elevating nut method, this problem is solved by contouring the rails to match the mast (Fig. 5). For the carousel system, however, this is not feasible due to interference between the guides and the mast when the system is in the tracking mode. A slightly larger-diameter canister and longer rollers are used and the transition rails are of a constant thickness, so that there is clearance for the mast to rotate once the mast is fully deployed and no rollers are engaged.

Mast axial strength is increased by using guide rails on both sides of the roller lugs. The mast diameter is smaller when it goes through transition so that the transition section is of asymmetrical hour-glass shape. The roller lugs must be long enough to accommodate the change in mast radius and still adequately engage in the transition guide.

FUNCTIONAL DESCRIPTION

When power is applied to the motor the turntable rotates, uncoiling the mast by driving it up through the guide rails. Deployment continues until the mast is almost fully deployed and only the last roller lug is left in the guide rail (Fig. 6). The last amount of deployment extends the last roller lug out of the guide so that it is only constrained by a gate. By continued rotation of the turntable the last roller leaves the gate, and the mast begins to rotate on the turntable about its centerline. The gate must close for the mast to continue rotating. In this rotation mode, the motor is switched to the stepper mode to provide accurate rotational movement.

BASELINE DESIGN

To verify the carousel deployment concept, ABLE designed and built a full-size demonstration unit which incorporated an existing mast design with the following properties:

Mast Diameter	0.254 m	10 in.
Mast Length	5.5 m	18 ft
Longeron Diameter	3.8 mm	0.150 in.
Batten Diameter	2.3 mm	0.090 in.
Diagonal Diameter	0.8 mm	0.032 in.

The mast was constructed of unidirectional S2 glass/epoxy fiberglass elements, aluminum fittings (6061-T6), epoxy adhesive (EA 934), and stainless steel fasteners.

One of the design goals was to provide room for a payload within the volume defined by the transition guides. A mechanism at the top of the mast enables it to pass smoothly through the transition guides and to fully retract by allowing the top attachment points to move radially inward as well as to pivot.

STRUCTURAL TESTING

Various tests were run to characterize the system. The test program was divided into performance and deployer torque determination. Bending tests were performed to determine strength and low-load stiffness characteristics. Low-load stiffness was targeted because it normally defines a system's natural frequency. The general procedure used was to apply a lateral tip-shear load to the horizontally-mounted mast. Lateral tip deflections were then recorded for loading and unloading. The test loads, deflections, and set-up geometry were used to deduce equivalent system stiffnesses. The mast's shear and root deflections were included in this equivalent stiffness.

Bending strength and equivalent stiffness are given as:

$$M_{CR} = V_{MAX}L$$

$$EI = \Delta V / \Delta \delta \quad L^3/3$$

where

M_{CR} = maximum bending strength (in.-lb)

V_{MAX} = maximum applied lateral tip shear (lb)

L = boom deployed length (in.)

EI = bending stiffness (in.-lb²)

ΔV = change in lateral tip shear loading (lb)

$\Delta \delta$ = change in lateral tip deflection (in.) .

Various mast system configurations were tested and characterized. The test parameter variations were deployed length, mast axial compressive load, mast root condition, and transition guide extensions. A total of 108 system configurations were examined.

For most partially-deployed configurations of the carousel mast, the maximum bending moment the system can withstand is dictated by the loads at the roller-lug-to-transition-guide interface. Typically, the lateral tip load can be increased to the point where the local side load at the roller lug overcomes the internal preload provided by the mast. The lug then separates from the transition guide. The mast's maximum moment strength can be increased over the tested design by incorporating a captured roller lug design.

Table 1A gives maximum bending strengths for various configurations. The values shown are averaged from various tests to highlight trends. Transition guide extensions improved maximum bending strength during the deployment phase by a factor of 3.8. However, with transition-guide extensions installed,

bending strength during deployment is about 1/4 of fully-deployed bending strength. Maximum bending strength was not greatly influenced by the mast's end condition. Axial mast compression had only a slight effect on bending strength. As axial compressive load was increased, bending strength slightly decreased (by about 1 percent per pound of axial load). These data are presented in Figure 7.

Bending stiffness data are presented in Table 1B for various test trends. The average values indicate that there is negligible variation due to axial compressive load variation. Transition guide extensions improve bending stiffness performance during deployment by a factor of about three. But even this improved stiffness was only 3 percent of the fully-deployed value. This marked difference, shown graphically in Figure 7, is due to the difference in the mast longeron-end conditions. When the mast is fully deployed, the longerons terminate directly into the turntable with zero curvature. Loads are reacted axially, which is an inherently stiff load path. In the partially-deployed mast condition, the longerons have curvature which causes some of the load reaction to be in bending, a less stiff load path.

Torsional tests were performed to determine the carousel deployer's characteristics under torsional loading. The mast system was again mounted horizontally at both half and full deployment. The mast tip was supported with a pinned-end-bearing mechanism. In this way, end-shear deformation was minimized while allowing full torsional deflection. A torque was applied and angular deflections were measured and recorded at multiple load points.

Table 2 summarizes torsional performance as a function of both axial compressive load and transition-guide-extension configuration. An unexpected trend can be observed in Figure 8. For test set-ups where transition guide extensions were installed, increasing axial mast load increased torsional stiffness. Conversely, for cases without transition guide extensions, increasing axial load decreased torsional stiffness. Another expected trend that was observed was greater stiffness under counterclockwise loading than clockwise loading for the partially-deployed test configurations. This effect is due to longeron curvature in the mast transition zone. A clockwise torque twists the mast in the same direction as the transition shape. A counter-clockwise torque loads against this shape. This effect is accentuated by the addition of axial compressive loading.

To characterize the carousel drive actuator and control system design, mast axial load and ambient temperature were varied. An additional test was run which focused on drive torque variation during the terminal phase of deployment, when the deploying mast shape changes from its standard helix to a straight, stiff configuration.

The tests where mast axial compressive load was varied were done at room temperature with the system mounted horizontally. The mast tip was supported by a bridle mounted to an overhead track. In this way variations in mast bending load were kept to a minimum. A weight pan, cable, and load cell

arrangement maintained a constant axial compression load as the mast deployed. Axial loads were varied between 0 and 26.7 N (0 and 6 lb).

Figure 9 presents the test results in a graphic format. Results are nearly linear for all three test conditions. As indicated in Figure 9, with no compressive load the system requires a 0.35 N-m (3.1 in.-lb) torque to restrain the system against its inherent self-deploying force. However, with a 71.2 N (16 lb) axial preload, the system requires 0.51 N-m (4.5 in-lb) of torque to drive the system out.

The system was placed in a thermal chamber and mounted to deploy vertically upward, causing a gravity load which varied with the length of boom deployed. This load proved manageable. Since it would not affect the qualitative results, a variable counterweight system was not installed.

The system was tested at room temperature [approximately 21°C (70°F)] at -51°C (-60°F), and at 68°C (140°F). System motor-drive torque was indicated by an in-line torque transducer. Tests were conducted after the mechanism reached the prescribed test temperature and had soaked for a minimum of one hour.

In order to isolate the drive torque characteristics from those due to the mast's self-deploy force, the carousel was run at test temperatures and voltages with the mast fully extended. In this way the mast rotated as a rigid body, and its strain energy did not affect the indicated torque values. Any variations observed were due only to turntable-torque-requirement changes.

Table 3 gives a summary of the results. Figure 10 presents the data graphically. Torque required to deploy the system varied from a 0.41 N-m (3.65 in.-lb) driving torque at -51°C (-60°F) to a 0.22 N-m (1.95 in.-lb) restraining torque at 140°F. At low temperatures the mast's self-deploy force is not enough to overcome the internal bearing drag. At high temperature the bearing drag drops to near zero and the self-deploy force dominates the system requiring a restraining torque. Retraction must be motor driven as both bearing drag and mast self-deploy force inhibit retraction at all temperatures. The variation in retraction torque is from 1.21 N-m (10.75 in.-lb) at -51°C (-60°F) to 0.69 N-m (6.10 in.-lb) at 140°F. The variation is almost entirely due to changes in bearing drag, as the self-deploy force is almost independent of temperature. Since observed torque variations were small, the bearing-support-skirt design performed satisfactorily. The radial compliance built into the system satisfactorily isolated the bearings from the thermal loads in the stiff mounting rings over a wide temperature range. It is estimated that the torque variations are in the range associated with changes in bearing lubrication viscosity.

CONCLUSION

The test program has shown that the carousel deployer concept is a viable technique with sufficient maturity to consider for flight development and certification. The components exhibited mechanical stability and minimal

torque variations during deployment under various thermal and mechanical loading conditions. The tests showed that, as in nut-deployment technique, the transition guide shape and size are the critical factors contributing to smooth deployment. Their successful design is a critical undertaking for proper operation.

The thermally-compliant, dual-bearing support concept proved to be successful over a wide temperature range. No binding or low-load deadband was observed at either hot or cold temperatures. This design concept is generic enough to apply to various thermal/mechanical conditions.

The existence of moderate bending and torsional structural stiffness and strength during deployment was verified by the test program. The carousel-deployed mast may be used to deploy, pretension, and track payloads such as solar arrays or antennae. Structural performance is improved during deployment by the use of transition guide extensions.

It is recommended that if additional structural stiffness and strength are required during deployment, future carousel development programs implement the transition-guide extension design option and captivated rollers. To maintain the smallest package volume, the transition guide extensions can be designed to articulate into position or to be part of a payload support structure. This test program has provided a database from which system designers can make application-specific structural design choices.

REFERENCE

1. 18th Aerospace Mechanisms Symposium, NASA Conference Publication 2311.

TABLE 1A. BENDING STRENGTH TEST RESULTS

			Transition Guide Extension			
Deployed	Load		Installed		Removed	
Position	(N)	(lb)	(N)	(in.-lb)	(N)	(in.-lb)
Last Roller Disengaged						
1/4	0	0	24.9	220.3	6.2	54.9
	22.2	5	25.7	227.3	9.1	80.4
	44.5	10	27.4	242.8	--	--
1/2		0	22.8	201.9	6.6	58.7
	22.2	5	20.3	180.1	7.2	63.8
	44.5	10	19.6	173.6	--	--
1/1	0	0	74.1	655.7	68.0	602.2
	22.2	5	74.1	656.3	63.5	562.1
	44.5	10	66.6	589.2	62.0	548.5
Last Roller Engaged						
1/4	0	0	27.8	245.8	5.7	50.3
	22.2	5	26.5	234.6	5.9	51.9
	44.5	10	25.0	220.9	--	--
1/2		0	29.5	260.9	7.9	70.3
	22.2	5	26.2	232.1	7.4	65.8
	44.5	10	25.7	227.5	6.5	57.7
1/1	0	0	--	--	--	--
	22.2	5	--	--	--	--
	44.5	10	--	--	--	--

TABLE 1B. BENDING STIFFNESS TEST RESULTS

		Transition Guide Extension					
		Load		Installed		Removed	
Position	(N)	(lb)	(N-m ²)	(lb-in. ²)	(N-m ²)	(lb-in. ²)	
Last Roller Disengaged							
1/4 Depl.	0	0	165.9	5.78 x 10 ⁴	69.4	2.42 x 10 ⁴	
	22.2	5	148.4	5.17 x 10 ⁴	29.8	1.07 x 10 ⁴	
	44.5	10	147.2	5.13 x 10 ⁴	--	--	
1/2 Depl.	0	0	522.3	1.82 x 10 ⁵	147.2	5.13 x 10 ⁴	
	22.2	5	487.9	1.70 x 10 ⁵	--	--	
	44.5	10	476.4	1.66 x 10 ⁵	--	--	
1/1 Depl.	0	0	1.52 x 10 ⁴	5.29 x 10 ⁶	1.43 x 10 ⁴	4.98 x 10 ⁶	
	22.2	5	1.27 x 10 ⁴	4.41 x 10 ⁶	1.43 x 10 ⁴	4.97 x 10 ⁶	
	44.5	10	1.32 x 10 ⁴	4.60 x 10 ⁶	1.37 x 10 ⁴	4.79 x 10 ⁶	
Last Roller Engaged							
1/4 Depl.	0	0	324.3	1.13 x 10 ⁵	76.9	2.68 x 10 ⁴	
	22.2	5	324.3	1.13 x 10 ⁵	68.3	2.38 x 10 ⁴	
	44.5	10	238.2	8.30 x 10 ⁴	--	--	
1/2 Depl.	0	0	485.0	1.69 x 10 ⁵	205.2	7.15 x 10 ⁴	
	22.2	5	450.6	1.57 x 10 ⁵	212.7	7.41 x 10 ⁴	
	44.5	10	516.6	1.80 x 10 ⁵	--	--	
1/1 Depl.	0	0	1.43 x 10 ⁴	4.98 x 10 ⁶	--	--	
	22.2	5	1.43 x 10 ⁴	4.97 x 10 ⁶	--	--	
	44.5	10	1.37 x 10 ⁴	4.79 x 10 ⁶	--	--	

TABLE 2. TORSIONAL TEST RESULTS: STIFFNESS, GJ

		Loading Direction				
		Load		Clockwise		Counter-Clockwise
Test Set-Up	(N)	(lb)	(N-m ²)	(lb-in. ²)	(N-m ²)	(lb-in. ²)
During Deployment						
Transition Guides Installed	0	0	215.8	7.52×10^4	301.3	1.05×10^5
	22.2	5	255.1	8.89×10^4	367.3	1.28×10^5
	44.5	10	244.8	8.53×10^4	344.6	1.20×10^5
	0	0	37.6	1.31×10^4	29.3	1.02×10^4
	22.2	5	17.2	5.99×10^3	23.8	8.31×10^3
	44.5	10	12.7	4.44×10^3	22.1	7.70×10^3
Fully Deployed						
Transition Guides Installed	0	0	272.9	9.51×10^4	321.4	1.12×10^5
	22.2	5	283.8	9.89×10^4	364.5	1.27×10^5
	44.5	10	262.9	9.16×10^4	373.1	1.30×10^5
	0	0	244.5	8.52×10^4	228.7	7.97×10^4
	22.2	5	221.8	7.73×10^4	228.7	7.97×10^4
	44.5	10	210.1	7.32×10^4	242.5	8.45×10^4

TABLE 3. TORQUE VERSUS TEMPERATURE RESULTS

		Turntable (N-m)		System (N-m)	
Temp. (°C)	Volts	Mean	Band	Mean	Band
<u>Deployment</u>					
-51	28	-0.47	0.08	-0.41	0.28
21	28	-0.11	0.06	0.19	0.25
60	28	-0.07	0.05	0.22	0.21
<u>Retraction</u>					
-51	28	0.41	0.09	1.21	0.45
21	28	0.13	0.06	0.78	0.26
60	28	0.10	0.06	0.69	0.25

		Turntable (in.-lb)		System (in.-lb)	
Temp. (°F)	Volts	Mean	Band	Mean	Band
<u>Deployment</u>					
-60	28	-4.18	0.75	-3.65	2.5
70	28	-.99	0.54	+1.70	2.2
140	28	-.65	0.44	1.95	1.9
<u>Retraction</u>					
-60	28	3.60	0.80	10.75	4.0
70	28	1.16	0.56	6.90	2.3
140	28	0.89	0.50	6.10	2.2

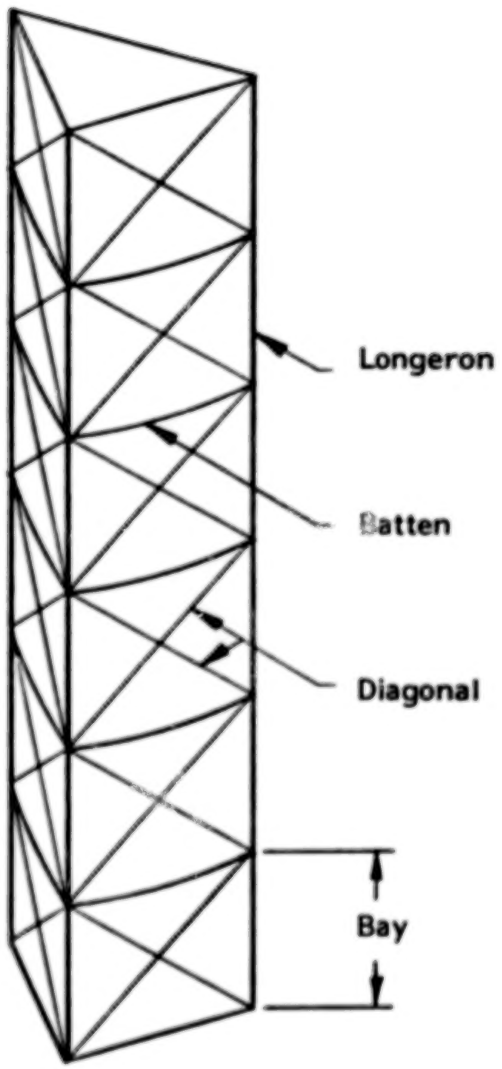
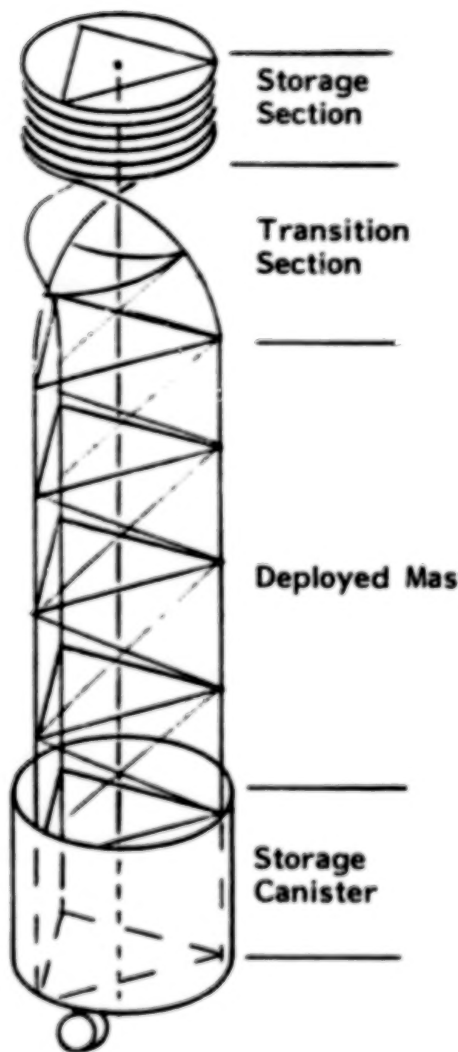
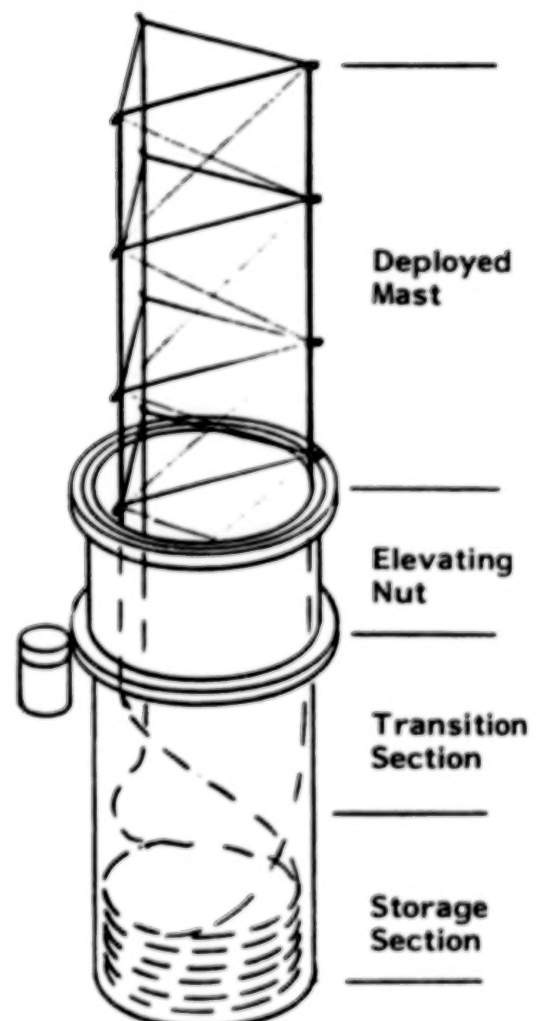


Figure 1. Triangular lattice structure.



A: Lanyard



B: Elevating Nut

Figure 2. Lanyard and elevating nut deployment schematics.

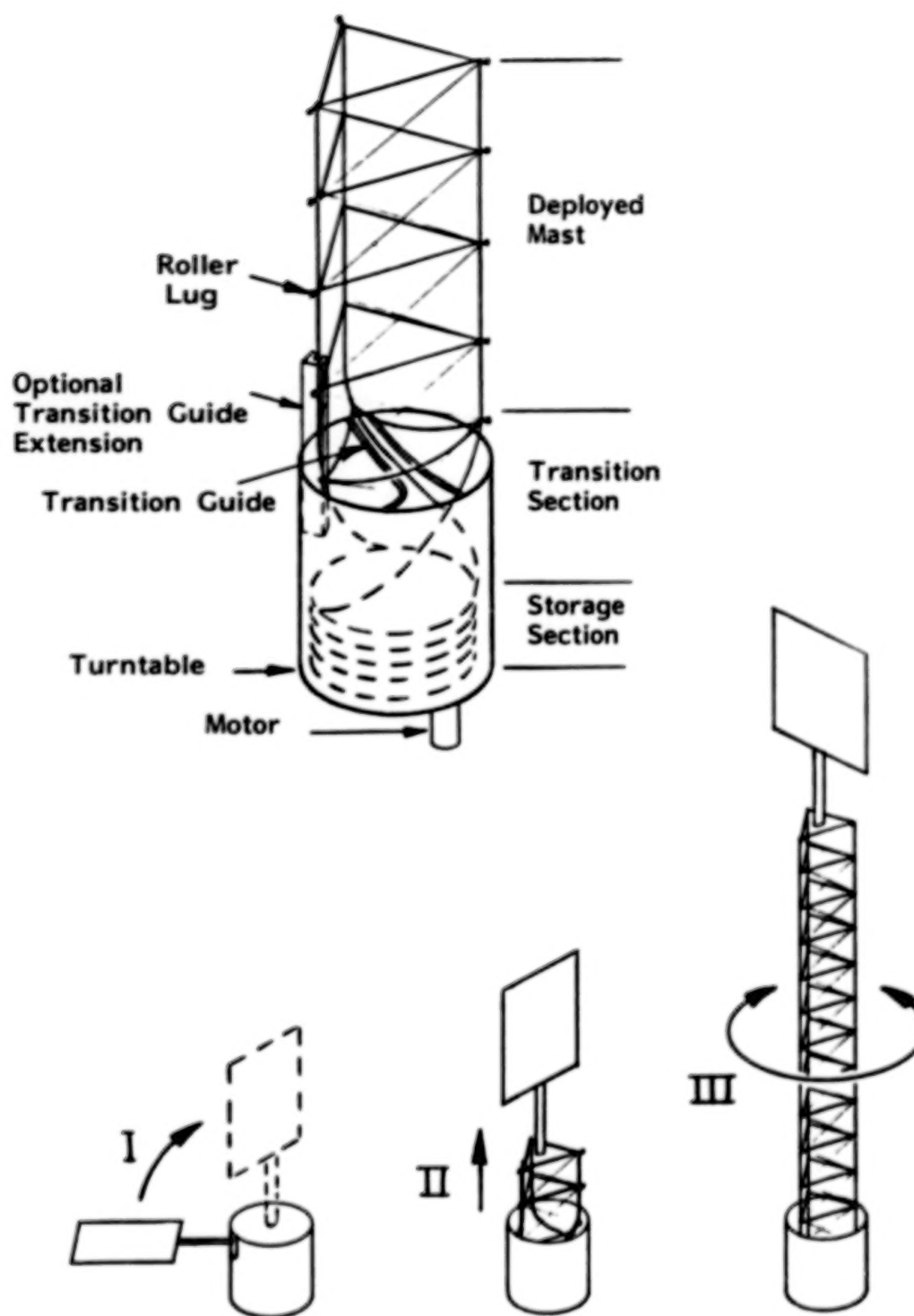


Figure 3. Carousel deployment schematic.

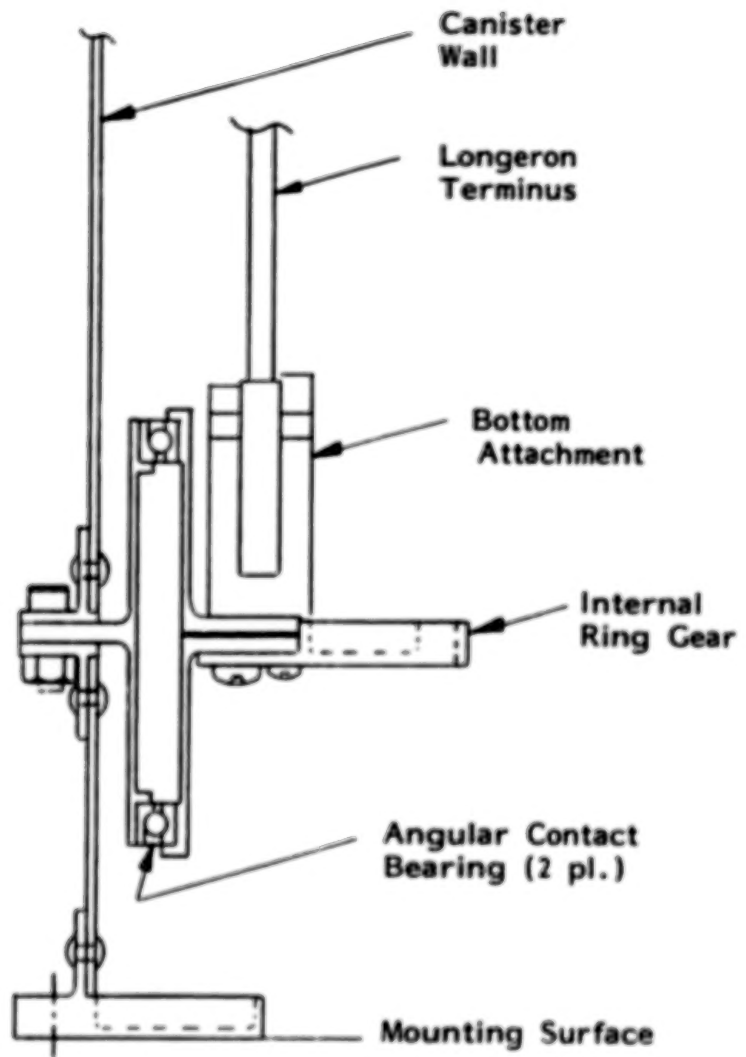


Figure 4. Turntable bearing detail.

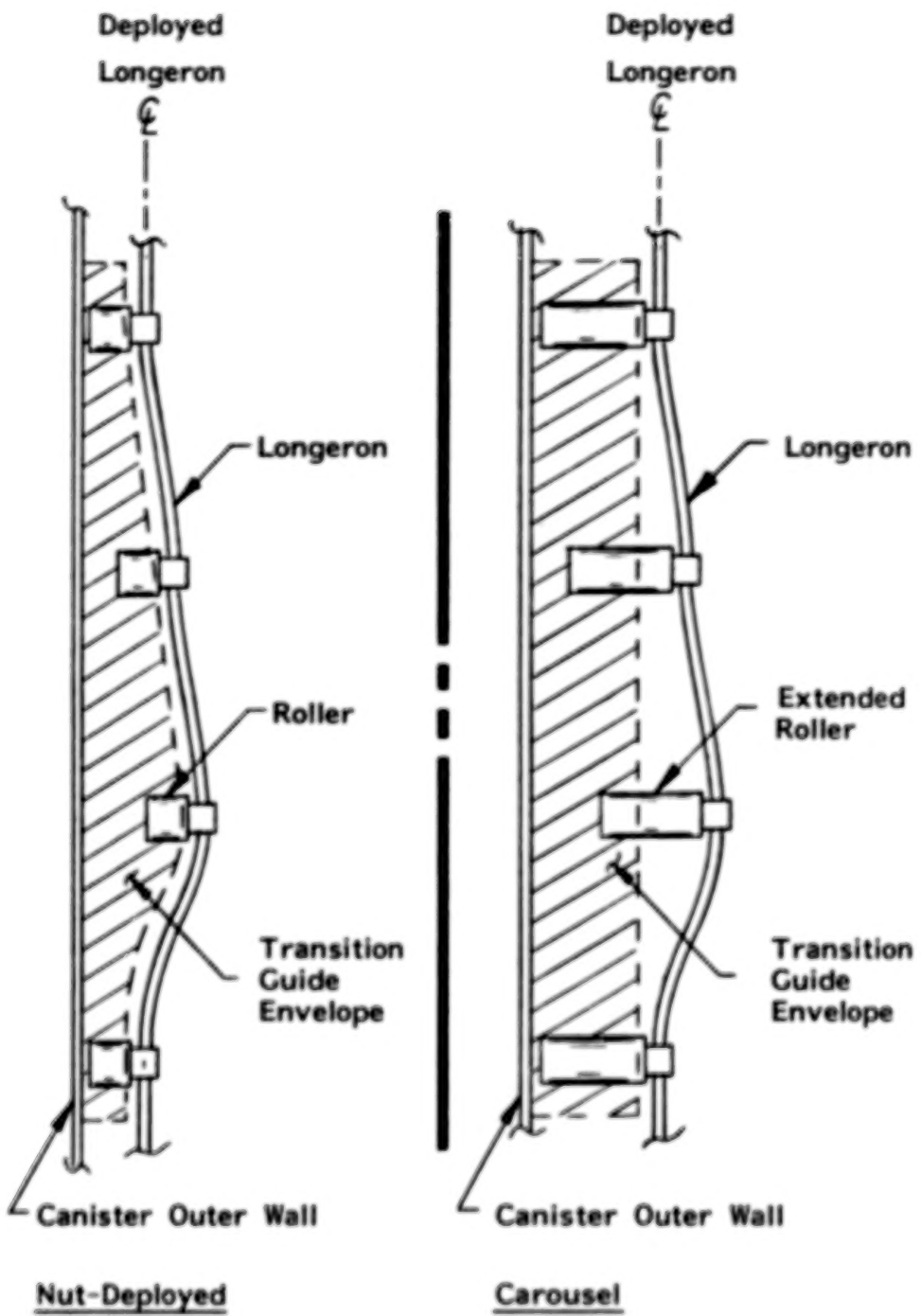


Figure 5. Transition section guides.

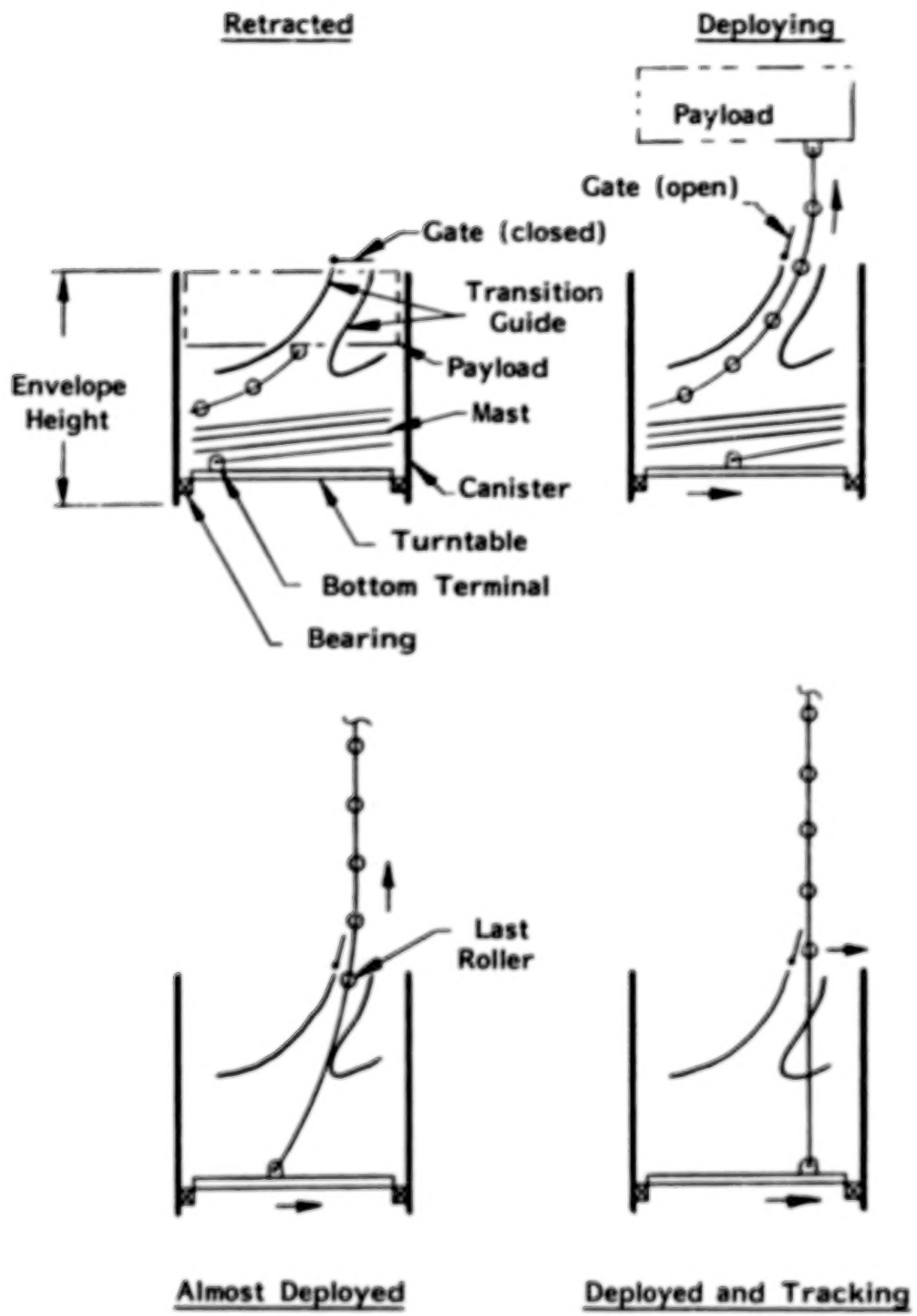


Figure 6. Functional sequence.

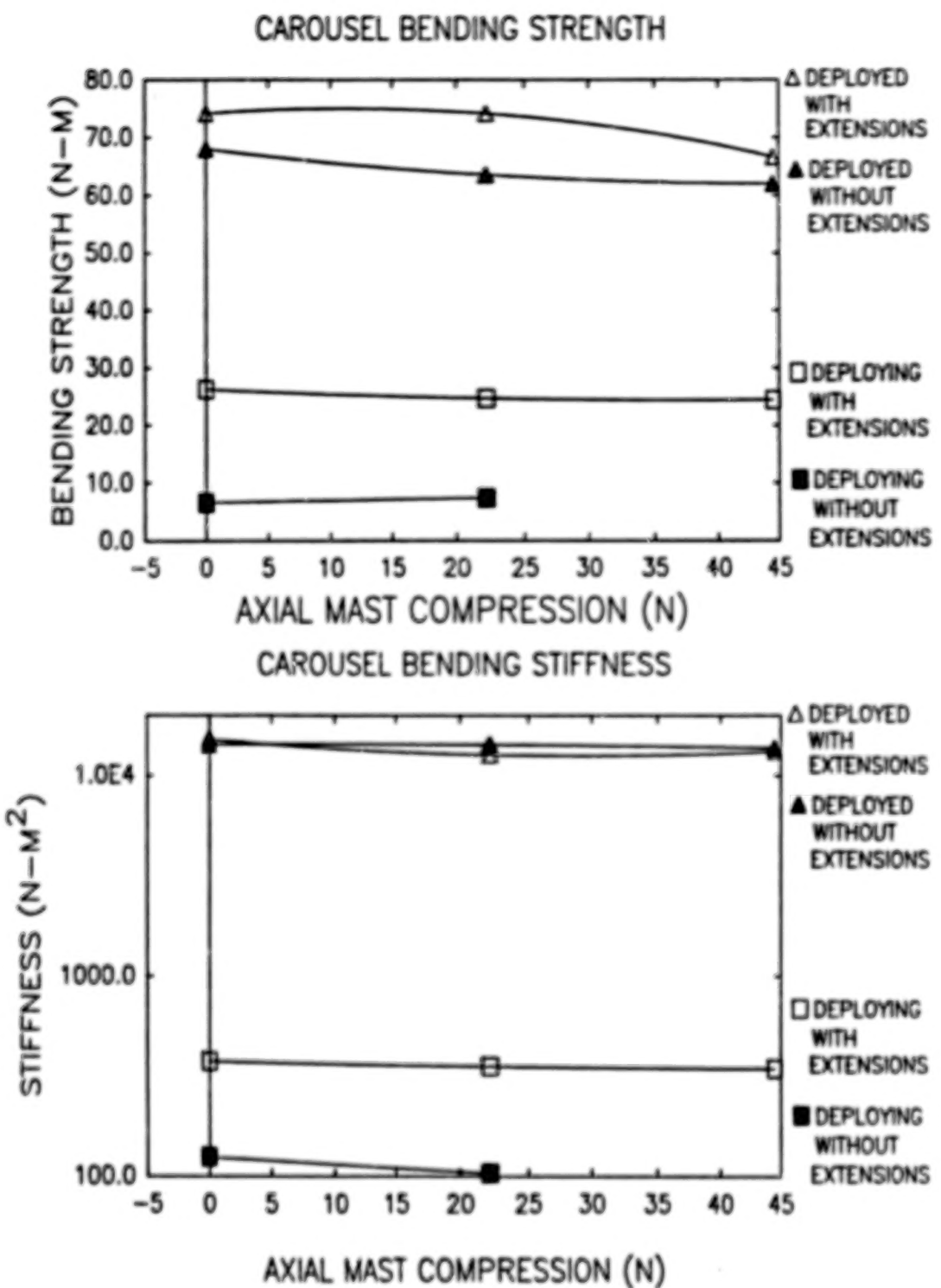


Figure 7. Bending test results.

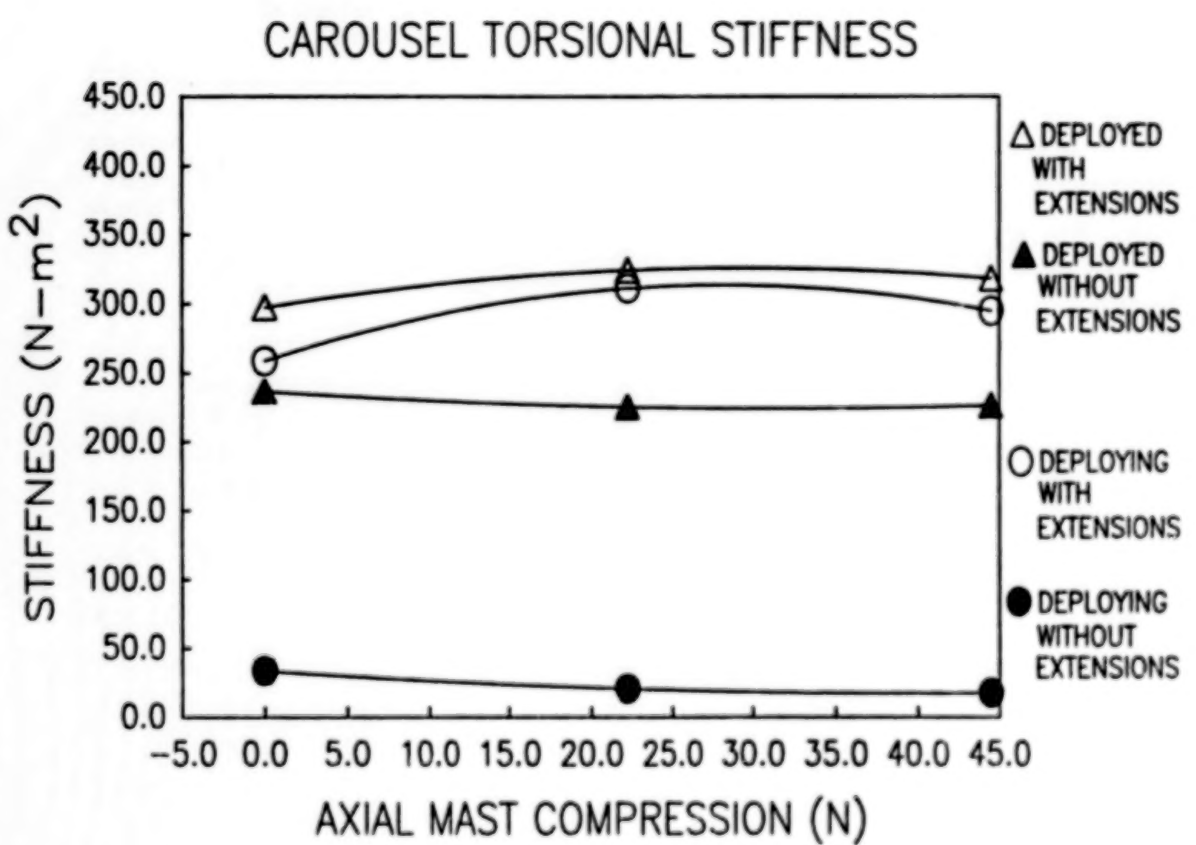


Figure 8. Torsional test results.

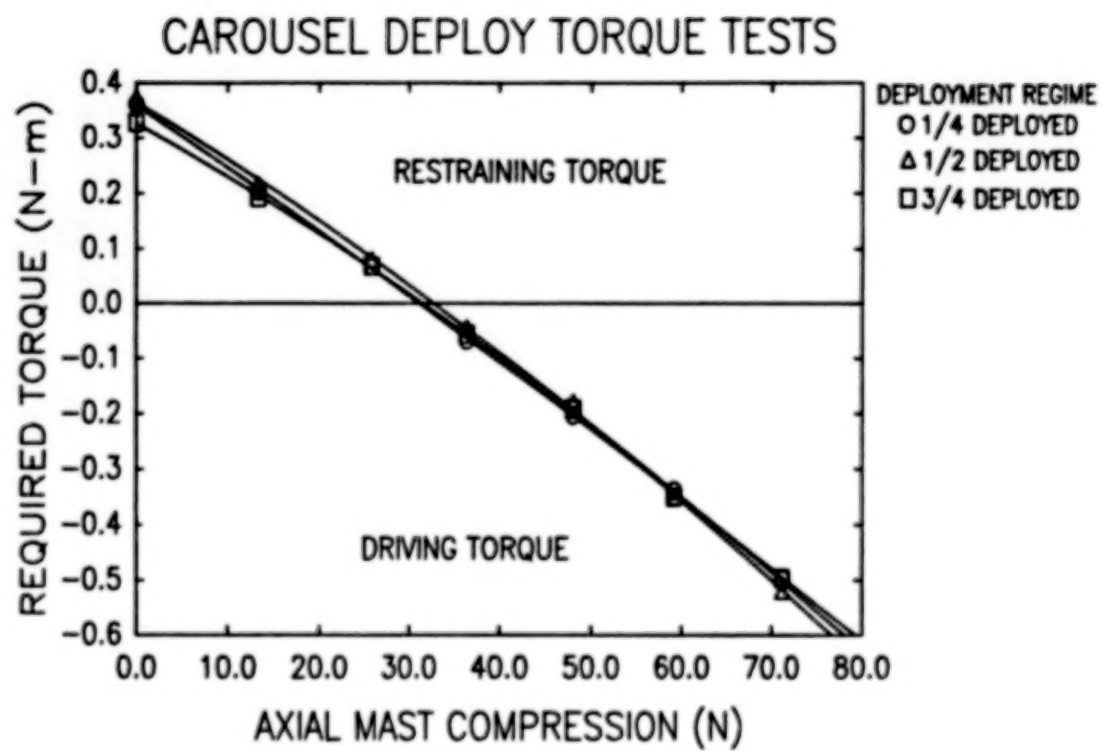


Figure 9. Deployment torque-versus-axial-compression test results.

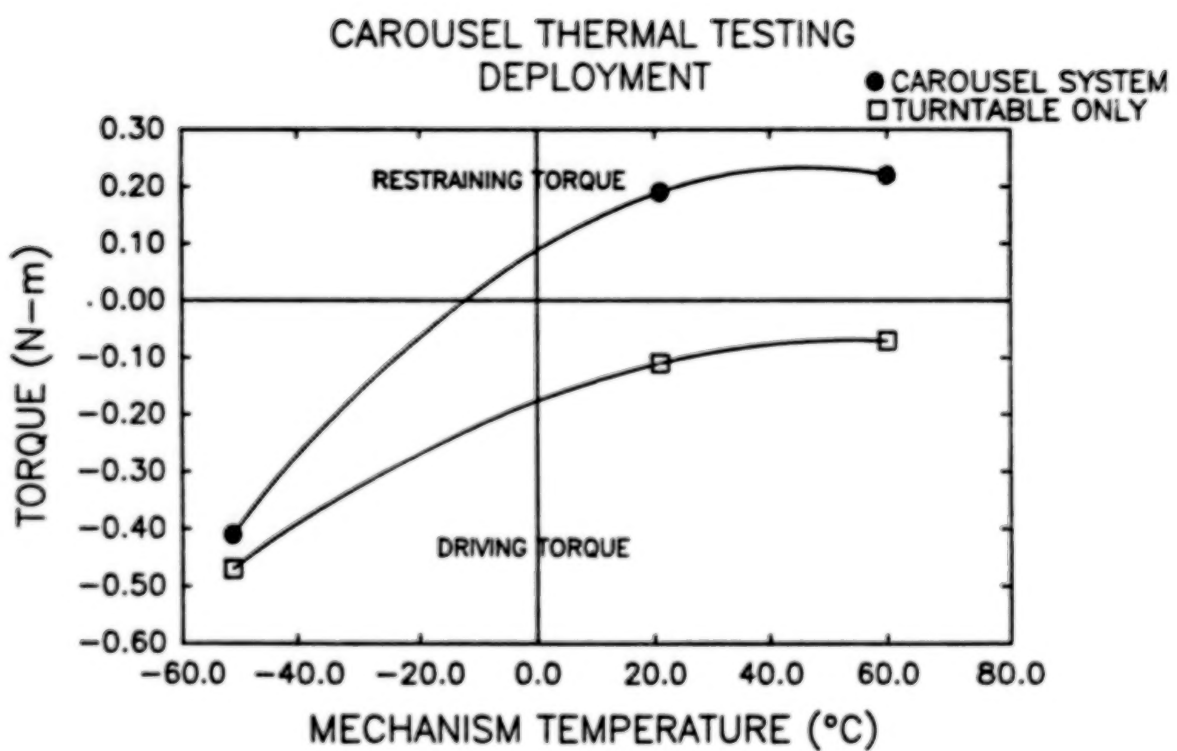


Figure 10. Carousel deployment torque versus temperature.

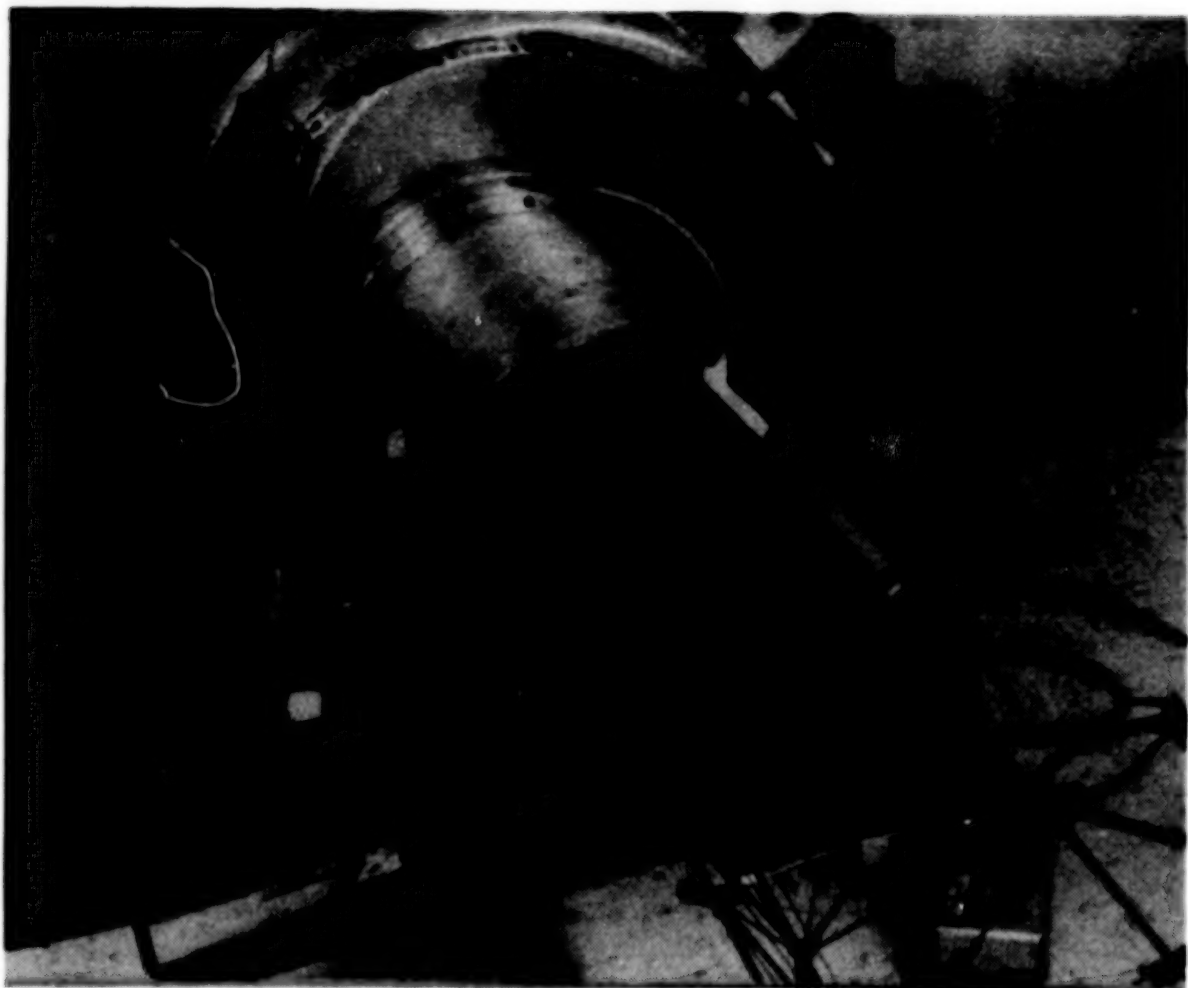


Figure 11. Structural test photo.



Figure 12. Thermal test photo.

DESIGN AND TESTING OF A DEPLOYABLE, RETRIEVABLE BOOM
FOR SPACE APPLICATIONS

P. Becchi* and S. Dell'Amico*

ABSTRACT

The Deployable Retrievable Boom (DRB) was developed by Piaggio under contract to the Italian Space Agency (PSN/CNR) as part of the joint U.S.-Italian program Tethered Satellite System (TSS).

The design mission of the boom, two of which will be carried by the TSS satellite during its first mission (scheduled for launch in January 1991), is to support, deploy, and retrieve an experiment package for the study of the electromagnetic field surrounding the satellite. The mechanism includes a jettisoning provision and deployable harness for the supported payloads connection.

The design was conceived for missions requiring launch and re-entry with the NASA Space Transportation System (STS).

This boom is based on a tubular telescopic concept as are other existing European boom designs. Particular emphasis has been given to payload harness connection capability and safety provision in order to meet STS requirements.

In this paper, the design and development of the boom will be presented and discussed, with particular emphasis on trade-offs and on techniques developed to overcome specific design or manufacturing problems. Major results of qualification testing will be presented and compared to the original requirements of the TSS mission. Finally, development potential of the design concept and its limitations will be discussed.

INTRODUCTION

PSN has requested R. Piaggio to design two booms for the TSS1 mission scheduled in January 1991. Piaggio is undertaking design, manufacturing, and qualification of a DRB for the TSS1 mission which will support the RETE experiment.

The project was begun in January 1987. Initial development tests were performed in ESTEC IN April 1987. Qualification is now almost completed and delivery is planned for March 1989.

*I.A.M. Rinaldo Piaggio S.p.A. Finale Ligure, Italy.

The reason for developing a new boom design for an important application came from a number of peculiar requirements that became the design goals of the contract:

- Be capable of deployment and restowage in agreement with STS safety rules
- Provide an inherent jettison capability to be used to improve mission success
- Provide support and deployment of high voltage harness for payload probes
- Be capable of partial deployments necessary for payload measurements
- Reduce as much as possible the number of electromagnetic drive motors necessary for deployment, retrieval, and off-load
- Use a simple and reliable mechanical design.

The following sections will show how the above criteria have been met, creating a new and unique multi-purpose mechanism. Qualification test results will be presented with emphasis on safety and performances, in particular, in comparison with predicted analytical results.

DESCRIPTION OF R. PIAGGIO CONCEPT

The DRB qualification unit is shown in Figure 1. The figure shows an assembly drawing of the complete unit with a section showing the tubular elements in stowed position and the drive motor. It also shows the folded payload harness, the pyro cutters, and the Marman clamps.

The design performs five basic mechanical functions that will be discussed separately in order to simplify the description. These are:

- A tubular telescopic boom with its deployment mechanism
- Latch mechanism to support launch and re-entry loads
- Deployment and support for high voltage harness
- Jettisoning mechanism capable of disconnecting payload harness
- Jettison prevention latch to avoid jettison of a stowed boom.

BOOM AND DEPLOYMENT MECHANISM

The boom structure consists of seven tubular elements nested inside each other, with a length of 400 mm and diameters ranging from 50 to 120 mm. When deployed, each tube overlaps the nearest one by a length of 1 diameter to

provide sufficient stiffness at the joints. The length and number of tubes have been adjusted to the mission requirements, in particular for the reduced stowage envelope available due to the position on the upper satellite floor. The material used for the tubes is a 2024 aluminum alloy mechanically milled down to a thickness of 0.4 mm. The tolerance in thickness can be 0.02 mm with a maximum roundness error of 0.05 mm. Quality and tight tolerances are fundamental requirements for the achievements of required performances. The tubes slide one against the other over vespel pads. Consequently, tight tolerances mean low friction and high stiffness.

Flanges at both ends of each tube support the pulleys and distribute the concentrated loads for deployment and retrieval operations. These flanges also support the sliding pads. The stiffness and strength of the boom depend primarily on tube overlap and, consequently, on the deployed length so that a minimum frequency of 40 Hz can be met in stowed condition without the need for an off-load device. When fully deployed, the frequency will be around 2 Hz.

The deployment mechanism concept is shown in Figure 2.

The system provides a parallel and simultaneous deployment of all tubes.

The first tube (n.1) is pushed directly by a worm-screw nut mechanism connected to the drive motor that provides the power during the whole deployment phase.

The second tube (n.2) is connected by two steel wires to the fixed tube (n.0) passing through two pulleys mounted at each end of the tube (n.1).

The motion of the first tube relative to the fixed one (n.0) determines the motion of the second tube (n.2).

All the other tubes are connected sequentially in a similar manner as shown below:

- Tube n.2 connected to tube n.0 pulley on tube n.1
- Tube n.3 connected to tube n.1 pulley on tube n.2
- Tube n.4 connected to tube n.2 pulley on tube n.3
- Tube n.5 connected to tube n.3 pulley on tube n.4
- Tube n.6 connected to tube n.4 pulley on tube n.5
- Tube n.7 connected to tube n.5 pulley on tube n.6.

The first tube is driven by the spindle where the stepper motor is mounted. The stepper motor gives a 0.36 Nm torque transformed to deployment

thrust by the spindle-nut. Low detente torque and high efficiency of nut-spindle due to use of a recirculating satellite nut made necessary the conception of a retention device for resisting launch accelerations.

LATCH MECHANISM

To prevent deployment during accelerations and vibration, an additional latch mechanism was required. This mechanism was not present on initial design but was added when a recirculating nut was selected in place of a conventional nut. To reduce the complexity of adding a new independent mechanism, we have elected that latching be performed by the same actuator utilized for the deployment. This has been possible utilizing the sequential position characteristics of our mechanism. In this way the first revolution of the spindle is utilized to release the two hooks that latch the last tube.

During restowage when the last tube reaches its completely stowed condition, the hooks latch by action of a spring, preventing deployment in re-entry. The motion of each hook is connected to two microswitches that monitor and control completion of restowage (Fig. 3). In this way there is a completely redundant monitor of this safety device. If the boom does not retrieve enough or the hooks fail to engage properly, the booms will be jettisoned, saving the satellite and the remaining scientific missions.

To add additional safety to the mechanism, a retention device was added to the latch system so that in case of successful restowage the boom cannot be jettisoned. This retention consists of two hooks that become engaged at the same time as the latches, preventing the jettison of the booms when they are completely stowed. This reduces greatly the risk of unwanted jettison near the orbiter or in the cargo bay. All those mechanical interconnections should increase the reliability and safety of the mechanism.

JETTISONING MECHANISM

According to safety requirements of the STS, a jettisoning mechanism has been studied for the ejection of the boom in case of failure to retrieve.

The fixed part of the boom structure (tube n.0) is connected to the external shroud through a Marman clamp mounted at the outer end. In addition, rollers support the other end of the tube (n.0) and are connected with three tension springs to the external shroud.

As shown in Figure 4, release of the Marman clamp by pyro-cutters allows deployment of the mechanism and disconnection of the harness by two separable connectors. The rollers guide the initial phase of the ejection, providing a well-defined trajectory and preventing possible contacts with other spacecraft subsystems.

This mechanism is designed with simple and already tested components and with enough elastic potential energy to ensure a safe ejection. All the single point failure elements have been doubled to provide complete

redundancy. Jamming or cold-bonding risk is minimized using special coating and dry lubrication materials. Pyro and their control units comply with NASA Safety Requirements.

HARNESS DEPLOYMENT AND SUPPORT MECHANISM

The harness of the payload is stored in two symmetric fanfold configurations as shown in Figure 5. The conductors are divided into two cables containing coaxial and twisted conductors. The two cables are held by brackets pivoting on the tube tip flanges. In the stowed configuration, the harness is packed by holding the supports perpendicular to the boom axis. The mechanism concept is simple and does not require high torque drawn by the drive motor.

QUALIFICATION TEST RESULTS

In January 1987, we started the so-called first phase of the contract, and successfully tested one prototype of the DRB in the ESTEC vacuum chamber HBF3 in April 1987.

The design of the proto unit was simplified (only five tubes and 1.5 m deployment length) but it was representative of some critical design features:

- Tube dimensions and thicknesses
- Pads materials
- Thermal finishing
- Deployment mechanism design and materials.

A photograph of the proto-DRB is shown in Figure 6.

The test, organized and set-up with the cooperation of ESTEC personnel, was performed with the following scope:

- Performing a thermal balance test with temperature measurement along the boom
- Showing the capability of deployment and retraction in the worst thermal condition obtained during the orbital simulation of the thermal balance test.

In October 1988 we started qualification tests using the experience gained in proto testing. A photo of the qualification model is shown in Figure 7. The test sequence was of course a complete set of environmental tests followed by a performance and life test in the solar simulation chamber HBF3. The qualification thermal vacuum test was very similar to the jettison mechanism. The improvement over the prototype manufacturing tolerances is so good that obtained performances are well beyond the prototype ones.

After this we performed a jettison test to show performance of the jettison mechanism. The improvement over the prototype manufacturing tolerances is so important that obtained performances are well beyond the prototype ones. In particular, we have shown a very good correlation between finite elements with calculated fundamental frequencies, and the one measured during vibration test. This meant that at each joint, backlash and free play are eliminated to the extremely good manufacturing results.

During thermal vacuum testing we have shown the capability to deploy, restow, and latch in all thermal conditions, including the qualification temperature margins. Temperatures observed on the boom vary from a maximum of 60°C at the satellite interface in the orbital hot case to a -85°C at the payload interface in the deployed cold case.

We have, nonetheless, experienced some problems in performing the requested number of 50 orbital-complete deployment and retractions. This is due to the lubrication system selected for the spindle, where the molybdenum disulfide was very easily worn out by the nut. We will repeat this test after spindle refurbishment for a verification of the allowable number of deployments.

PERFORMANCES AND RESULTS FOR FUTURE UTILIZATION

The DRB design is based on the use of tubular elements built using commercial aluminum alloy tubing. We have defined a manufacturing procedure that can produce tubes with minimum thickness as low as 0.3 mm, keeping the external and internal surface tolerances below 0.05 mm. We are also investigating the possible use of a high performance material like CFRP, but we feel that the achievable tolerances will not be significant over aluminum with minimum thickness.

We have evaluated the possible performance of aluminum DRB in a range that we consider optimum for its characteristics:

- Length - 5 to 25 m
- Stiffness - 1000 to 100000 (N*m)².

Those studies are contained in Reference 4.

Some of the possible applications reviewed there are summarized here:

- Support antennas of up to 40 kg to a distance of 10 m from spacecraft
- Support an experiment of 10 to 20 kg at 15 m from spacecraft.

CONCLUSIONS

The R. Piaggio DRB shows good performance, with reasonable design complexity and cost. The Italian space authority, PSN, has given R. Piaggio

the opportunity of applying this concept and showing its capability in a complex configuration and complete design.

Although the requested sizes were not the optimum for the best performance of a tubular telescopic boom, the results of the tests performed up to now are very promising. R. Piaggio is looking forward to the opportunity of showing the capability of the DRB in an application where the required dimensions are more consistent with boom optimal performance, as shown in the above examples.

REFERENCES

1. Becchi, P.: Tubular Telescopic Mast. Estec Working Paper No. 1288.
2. EASTP for LHSA, "Mechanism Phase 2 Report," Esa Contract 3787/78/NL/HP.
3. FASTP for LHSA, "Tube Study Phase 2 Report," Esa Contract 3787/78/NL/HP.
4. Becchi, P., and Miranda, D.: Deployable/Retrievable Boom; One Application to Tethered Satellite. Proceedings of 3rd European Space Mechanism Technology Symposium.

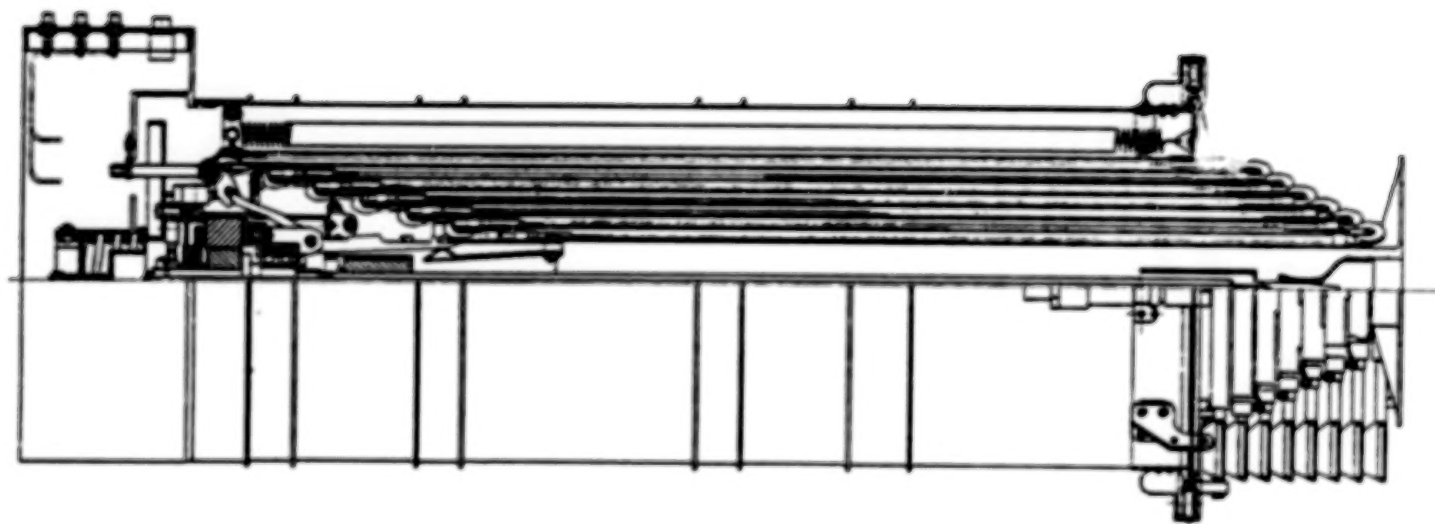


Figure 1. Assembly drawing of DRB.

108

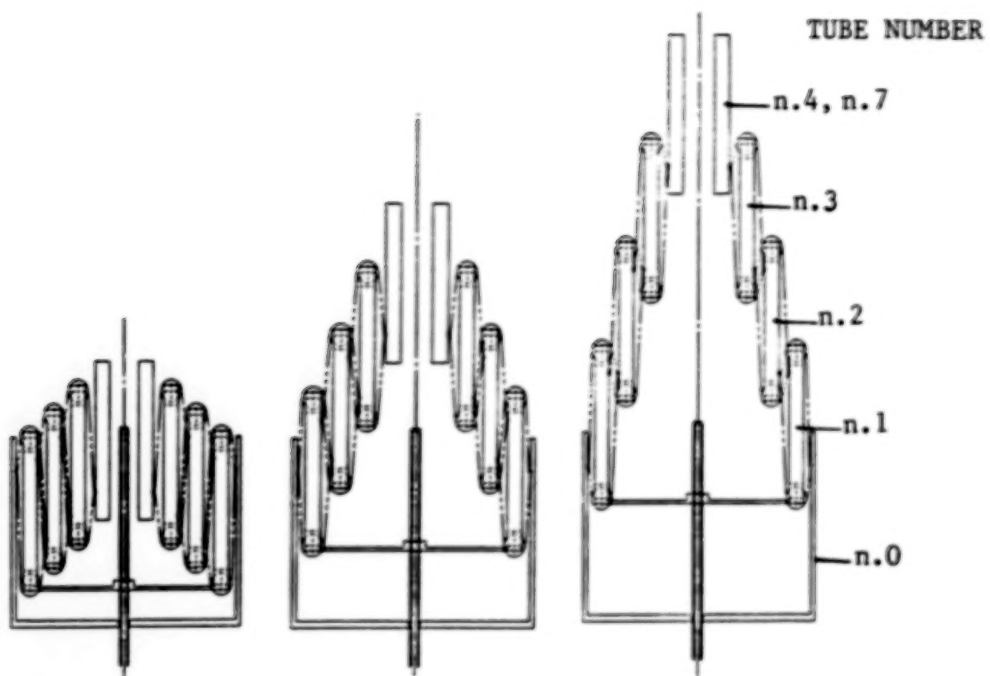


Figure 2. Deployment mechanism concept.

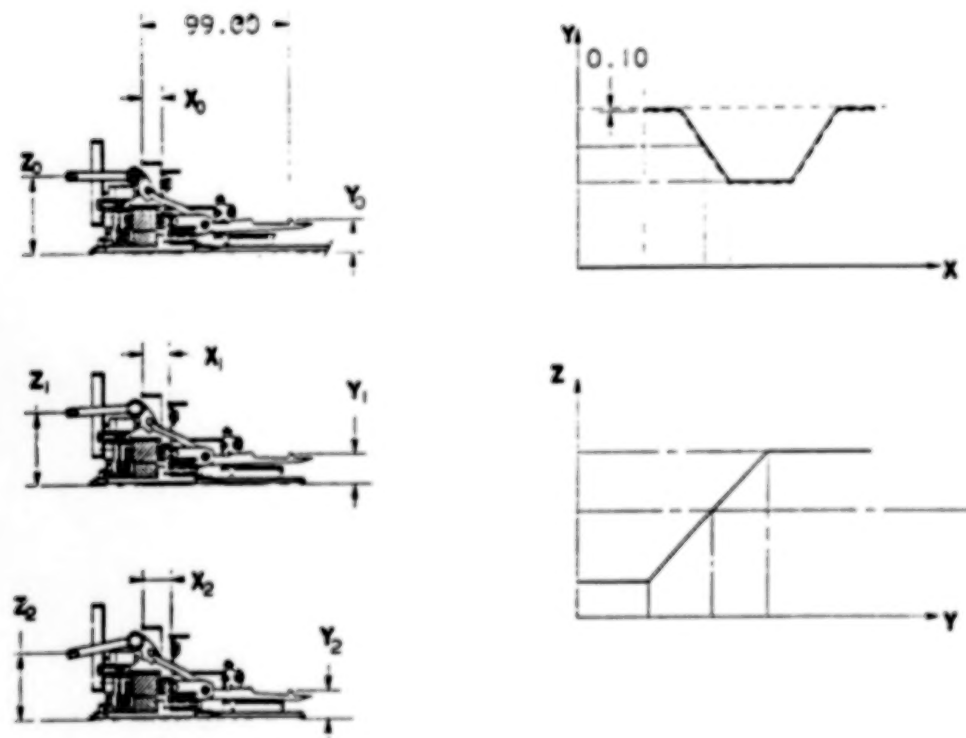


Figure 3. Latch mechanism concept.

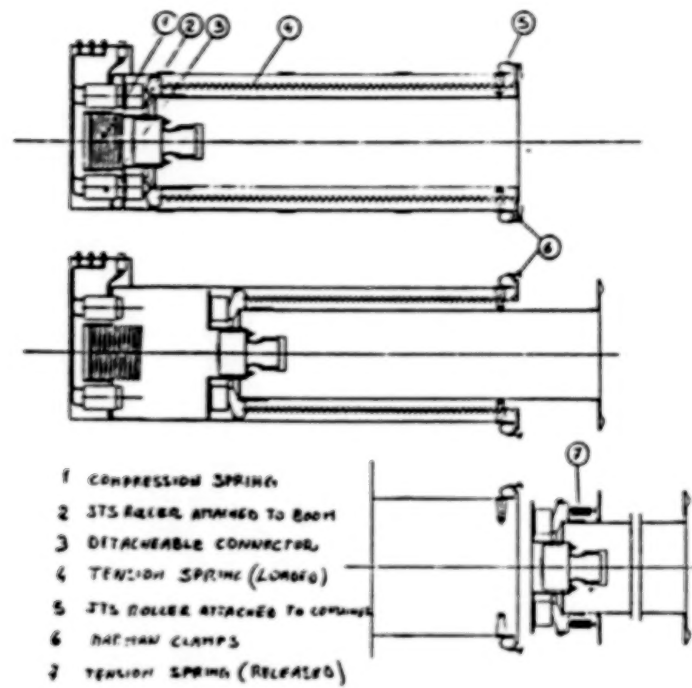


Figure 4. Jettison release system.

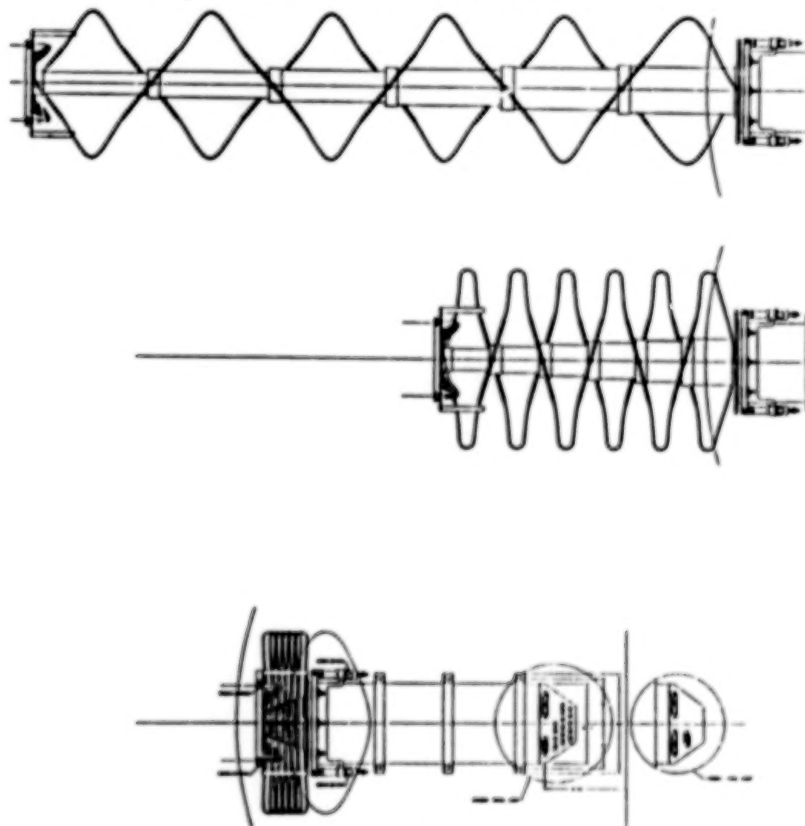


Figure 5. Payload harness system.

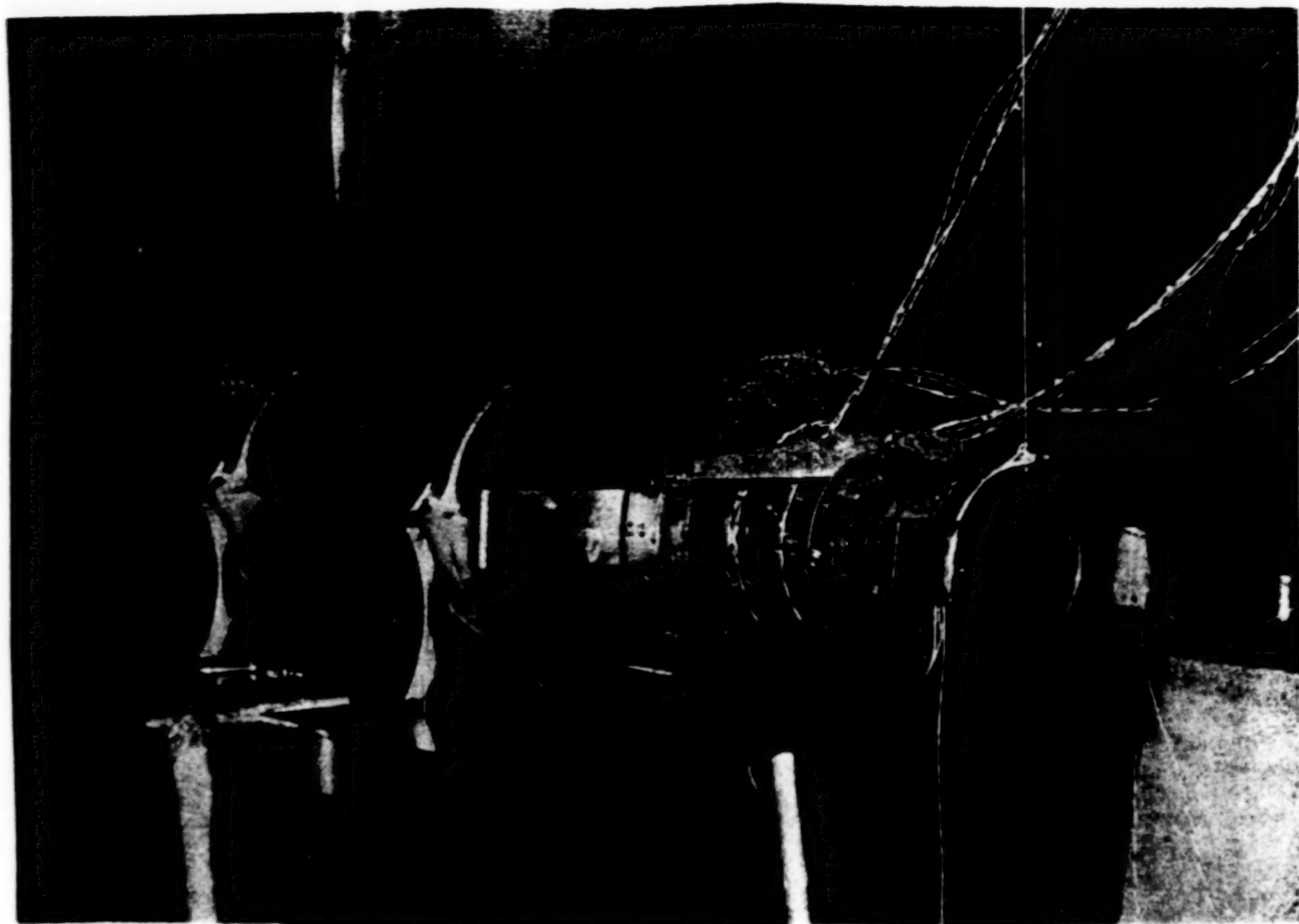


Figure 6. Prototype during testing.

111

111

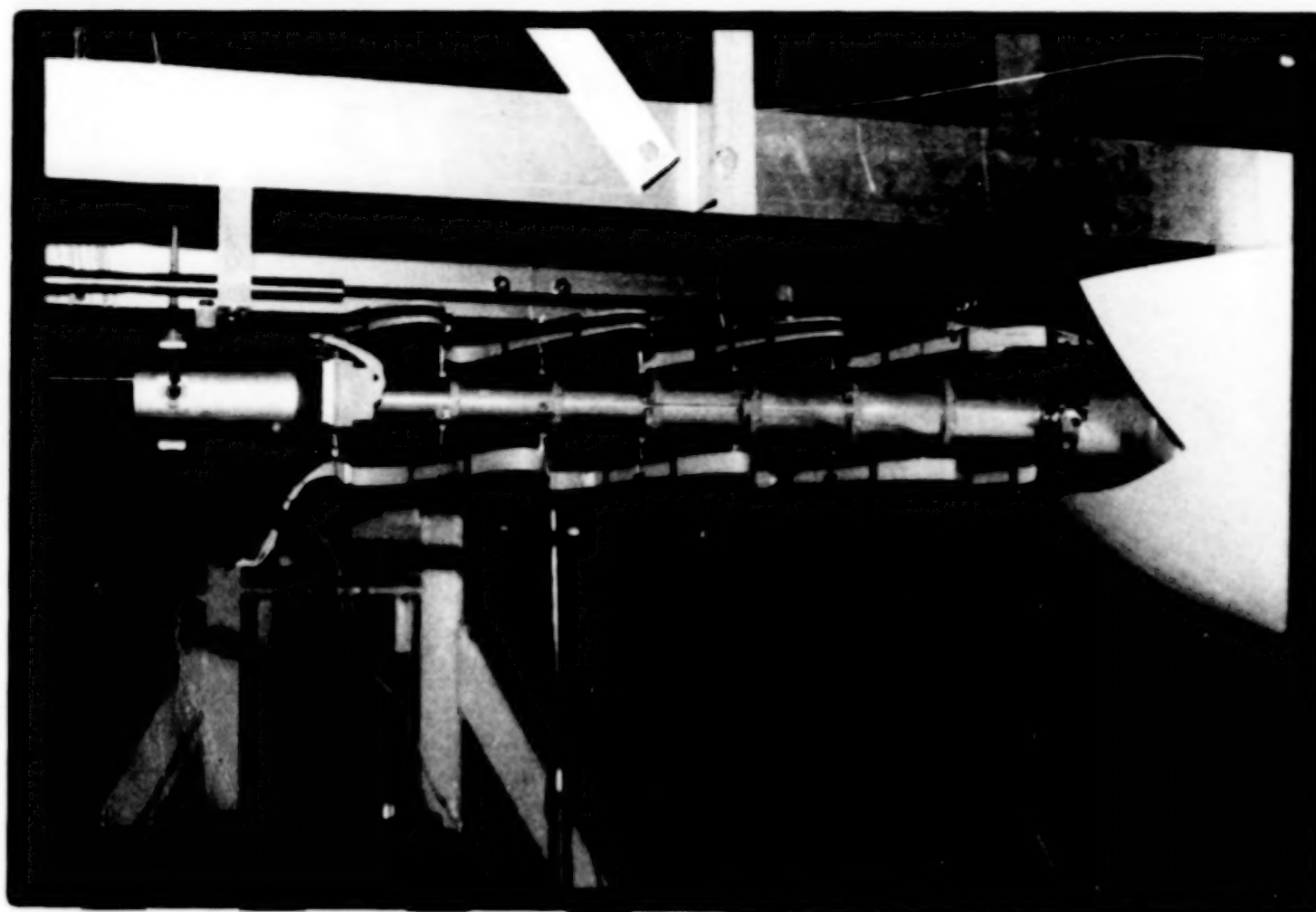


Figure 7. DRB qualification model.

DESIGN AND VERIFICATION OF MECHANISMS FOR A LARGE FOLDABLE ANTENNA

Hans Jurgen Luhmann*, Carl Christian Etzler*, and Rudolf Wagner*

ABSTRACT

The Synthetic Aperture Radar (SAR) Antenna onboard the ESA Remote Sensing Satellite (ERS-1) is a 10-m x 1-m planar array. It is folded into a dense package for launch and deployed in orbit. The resulting three antenna conditions, i.e., stowed, deploying, and deployed, pose different and in some cases conflicting requirements. Numerous mechanisms were developed to meet these requirements. This paper presents the most characteristic design requirements and constraints, their impact on the design, and the resulting features of the mechanisms.

INTRODUCTION

The SAR Antenna (see Fig. 1) consists of five panels of 2 m x 1 m each. Flat rectangular slotted waveguides form the radiating surface. They are made from Carbon Fiber Reinforced Plastics (CFRP) for reasons of thermal stability and low mass. Very few CFRP sandwich beams, as mechanical stiffeners, provide integrity and stiffness for the waveguide array. The resulting maximum panel thickness is 0.060 m.

The panels are connected in four axes by four pairs of Panel Hinge Assemblies (PHA). Each assembly includes a pair of ball bearings in titanium brackets and allows mutual panel rotation by at least 180 deg.

A Deployable Truss Structure (DTS) made from CFRP tubes provides structural depth as a basis for high surface accuracy and high mechanical stiffness at minimum antenna mass. The DTS incorporates the locking devices for the deployed stage and also transfers drive forces to the panels during the deployment (see Fig. 2).

Deployment is driven, in several phases, by a number of drive mechanisms. These include, for each of the two antenna wings: a leaf spring in the long foldable bar of the DTS; a leg spring assembly in the outer panel axis; a speed controlled dc motor near the inner panel axis, and attached to the rigidly mounted center panel.

In stowed configuration the panels are folded to a stack of 0.3-m thickness. The DTS folds completely between the panels with no extra space. A Hold-down and Release Mechanism (HRM) keeps the panels fastened during launch and releases upon telecommand. The HRM includes six pretensioned

* Daimler-Benz AG, Friedrichshafen, Germany.

clamping levers on the longitudinal sides of the panel stack and a spring driven cable release system with pyrotechnic cutter.

The deployment sequence as depicted in Figure 2 is characterized by four events:

1. Release of antenna package by the HRM
2. Deployment phase 1 (spring driven) of first antenna wing and latching
3. Deployment phase 2 (motor driven) of first antenna wing and simultaneous deployment phase 1' of second wing and corresponding latchings
4. Deployment phase 2' of second wing and latching.

The driving requirements for the antenna structural and mechanisms design are summarized as follows:

- Dimensions of aperture 10 m x 1 m
- Stowed volume to be minimized
-> 2.05 m x 1.1 m x 0.65 m including rigid mounting frame
- Mass to be minimized
-> 85 kg including mechanisms, rigid mounting frame, thermal hardware
- Stiffness
lowest eigenfrequency > 50 Hz stowed, > 4 Hz deployed
- Drive force margin
release/deployment driving forces > 3 x resisting forces
- Release and latching shocks severely constrained
- Surface accuracy < ± 3 mm maximum including manufacturing, deployment, thermal, and other effects.

The following sections address the technical problems and solutions in detail.

MECHANISMS FOR LAUNCH

Mechanism-structure interaction is the characteristic feature of the antenna in launch configuration driving the design of the HRM. Based on the requirements indicated above, the HRM has to provide secure locking for launch and allow unconstrained reliable release in orbit.

The large panel surface area, and their limited thickness, and thus low structural depth, made it difficult to meet the eigenfrequency requirement

without excessive mass penalty. Simple locking devices, say at the four panel corners, would put the stiffness requirement entirely to the panel structure and make heavy panels due to the thickness limits. Such heavy panels would pose a severe eigenfrequency problem and further penalties in terms of mass and complexity in the deployed configuration.

Yet another efficient fixation of the panel package was prohibited by electrical requirements: a locking device at the center point of the panel area, though most efficient structurally, would have imposed unacceptable disturbance on the electrical antenna characteristics, resulting from necessarily large brackets in the electrically most sensitive aperture area.

The HRM concept, as implemented, does the following:

- o Leaves the electrical aperture surface unaffected
- o Provides clamping at optimum stiffness, thus allowing minimum panel mass for favorable deployed properties
- o Presents the most mass-efficient design overall
- o Allocates all significant mechanism masses to locations on the fixed mounting frame, with no impact on the sensitive deployed frequency.

The central feature of the HRM system is six clamps, located at the four corners of the panel stack and in the center of the longitudinal edges (see Fig. 3). A "release system" of cables and pulleys connects the clamps to the "drive system" of two redundant spring drives. All details of the system are designed to meet the release force margin (drive factor >3) under worst case conditions, w.r.t. temperature and various uncertainties. In case one of the two drive springs should fail, the margin is still >1.5.

The design of the clamps is shown in Figure 4. The clamps are hinged to the fixed center panel and their hinged release heads act upon brackets in the outermost panel in the stack. The three panels in between are provided with solid brackets at the required locations so that the pretension force of 3000 N per clamp is transferred on a stiff path.

In the clamps' locking head, the locking function could be separated from the release function. Locking is provided by a four bar linkage system where a toggle lever is employed in overcenter position as the locking element. In order to ensure safe locking in the presence of loads and vibrations during launch, the toggle lever is blocked by an additional pawl. A feature of the release system is a multifunctional release lever. It serves as a balancing element during launch so that rotary oscillation induced through the ropes is limited to small oscillations and, thus, do not affect the position of the toggle lever. This is achieved by preloading the release lever by two springs. The release lever also serves as the unlocking element. After initiation of HRM release by ignition of the pyrotechnics and activation of the spring drives, the release lever is rotated to its endstop. During that

rotation the additional pawl is lifted off the endstop and the toggle lever is thus stretched and released.

To minimize shock loads, the rotating clamp is caught in a honeycomb absorber. It is then held in position by an arresting pin. The release system is designed such that three pairs of clamps are released in a sequence. Excessive release-force peaks are thus avoided, enabling a mass-efficient design of the spring drives.

A special development effort was required for the contact surfaces between the panels in the lines of action of the clamping forces. In order to achieve the stowed frequency requirement, those contact surfaces need to constrain all degrees of freedom between the panels, i.e., three displacements and three rotations. Upon release, they must in no way constrain the panel separation for reliable deployment. Detailed mechanical design and surface treatment of suitably-sized interface plates was the subject of a trade-off.

The selected surface design is shown in Figure 5. The plate, toothed in two orthogonal directions, constrains lateral displacements and normal rotation. Normal displacement and out-of-plane rotations are constrained by the preload force. The shaping as shown was selected for two reasons: the oblique surfaces of the teeth allow play-free contact between the two mating plates without posing exaggerated manufacturing tolerances for a perfect fit. One alternative considered employed two sets of in-plane shear pins, arranged in two orthogonal directions, in holes slightly eccentric from the otherwise flat contact surface. Vibration tests on a development model showed unacceptable degradations resulting from manufacturing imperfections which could be avoided by an unacceptable effort only. The other advantage of the toothed shape is the distribution of the contact forces to a large number of smaller surfaces.

A concentration of pressure in a small area and possible welding or other surface damage is thus avoided. A flat surface design, with clamping along the edges of the rectangle only, was discarded since damage in the center of the pressure area was observed after vibration testing.

The area size of the interface plate and the amount of the preload force was determined by a dynamic response finite element analysis from the launch loads. The assumption of perfect clamping, which was needed for eigenfrequency analysis, requires that stresses between the plates remain of the pressure type, when superimposing the effects of pre-load and dynamic forces and moments. That assumption was confirmed valid for all interface planes between panels, except for the one nearest the fixed panels. The highest dynamic loads are encountered here. Since neither the pre-load, nor the interface plate size could be suitably increased, the "clamping" assumption was dropped for the six contact points in that plane and the analysis was re-run with "hinged" connections. Acceptable performance was thus found. The interface plate design at those locations was adapted to the hinge solution and satisfactory performance was confirmed in the antenna vibration and deployment testing.

MECHANISMS FOR DEPLOYMENT

Several deployment configurations for the planar antenna have been investigated prior to development. Due mainly to the limited space at launch, all configurations are based on a five-panel solution. In stowed position, all panels are folded to a stack including all supporting elements in the space between.

One candidate was an antenna structure deployed and supported with a pantograph truss. Because of the complex design and the large number of bars and hinged joints for the pantograph, which would result in alignment problems, this design was dropped. Another solution was characterized by a planar structure without a supporting truss. Detailed investigations of that configuration showed that the required in-orbit stiffness would be difficult to meet. During these studies the necessity of the supporting structure has been perceived in order to provide structural depth and thus to provide stiffness in the deployed configuration. On this basis, the selected configuration was developed: an antenna structure system with deployable truss structure and rigid mounted center panel. This solution was preferred because of the following:

- Moderate number of bars and hinged joints
- High stiffness for light-weight design
- Maximum base for alignment determined by rigid-mounted central panel.

A disadvantage of this design is the two wing deployment which required separate drive and locking mechanisms for each wing. The actual deployment sequence is shown in Figure 2. Each wing deployment is performed in two independent steps:

- Deployment and latching of the outermost panel (Phase 1)
- Deployment and latching of the two panel wing (Phase 2).

For the drive mechanisms, a combination of spring drives (Phase 1) and motor drives (Phase 2) was developed in consideration of the primary requirements given above.

Deployment Mechanisms Phase 1

For the deployment of the upper panel from the panel package (panel 1), a low-weight drive is required. The application of a motor drive would be problematical because of the comparatively high mass. This would require higher panel stiffness for launch, and especially when deployed. In consequence of this, the panel mass would increase and space problems would arise due to the thicker stiffeners.

A principle demand to the design was to balance the conflicting requirements of drive torque margin at all deployment configurations versus low shock loads at the end of deployment. It was a further design goal to develop a spring drive with approximately constant drive torque, corresponding to the nearly constant resistive torques versus deployment angle. A combination of two spring drives - leaf spring plus leg spring - was chosen. The leaf spring drive consists of two parallel C-shaped leaf springs and forms a part of the foldable bar of the DTS (see Fig. 2). Beside the low weight, the triple function of this unit is a remarkable feature. It combines the function of the following:

- A hinge (enables folding of the deployable truss structure for launch configuration)
- A drive (deployment drive during phase 1)
- A latching mechanism (performs arresting of panel 1 due to the high stiffness in stretched position).

The drive characteristic of the leaf spring is included in Figure 6. Due to the decreasing drive torque near the end of deployment, the torque margin requirement is not met. This deficiency could have been improved by thicker leaf springs, but could not be accomplished here, due to the limited yield point, and space between the panels. Therefore an additional spring drive was introduced, called a leg spring drive. This lightweight drive is located at the outer axis of the antenna (see Fig. 2). The spring elements are placed eccentrically to the panel axis of rotation. Based on this arrangement, it was possible to provide a special spring characteristic, like a sinus half-wave, with its maximum at the middle deployment position, balancing the insufficient behavior of the leaf spring drive. The superimposed spring characteristic is shown in Figure 6. The superposition led to an approximately constant drive torque during deployment. Increased levels still exist at the start of deployment, caused by compressive loads in the stowed configuration, and at the end of deployment, due to the stretching of the leaf springs.

Deployment Mechanisms Phase 2

The deployment of the 2-panel wings is performed by motor drives as depicted in Figure 2. Spring drives were also taken into consideration, but their features of low mass and simplicity are more than counterbalanced by a number of reasons. One problem was initialization of this deployment step at the required time within the overall deployment sequence. Another problem arose from high resistive torque which is caused by the simultaneous rotation of all PHA bearings and nearly all DTS bearings. Further, the resistive torque of the cable harness between the intermediate panel (e.g., panel 2) and the center panel (panel 3) had to be considered. Thus, a strong drive was required in order to overcome the superimposed resistive torques in consideration of the drive torque margin requirement. The high energy excess arising from this requirement under normal operating conditions would lead to

a shock problem during latching. This could have been solved only by a complex and expensive viscous damping mechanism. The application of a simple stroke-dependent damper was not possible because latching of the antenna in a defined end position was required.

Those potential problems resulting from a spring drive led to the selection of a motor drive unit. The direct features are:

- Separation of the deployment steps (wing fixation during the deployment of the outer panel)
- Low deployment velocity and the possibility of a velocity-controlled deployment (providing low shock loads)
- Possibility of reverse operation in failure case
- Supply of high drive torque without any consequence to the shock load requirement
- High reduction gear (consequently the motor is less sensitive to the resistive torques of the antenna).

Selection of the motor type was guided by these considerations: Qualified drive units were available with or without brushes. Preference was initially given to a dc-brush motor without control equipment. The main disadvantage of a brush-less motor (stepper-motor) was seen in the need for control electronics which cause high costs and mass or space problems. However, after the first deployment tests at an advanced point of time, the deployment speed was found too high to meet the shock requirement. The deployment speed was then reduced and controlled by a small addition to the existing circuit hardware in the satellite system. But only one constant speed could be installed without any further reduction of speed at the end of deployment.

The dc-gearmotor is equipped with a redundant winding, a gearhead (reduction ratio 6000:1), and a torque limiter. The torque limiter consists of two friction discs with axial toothed. This slipping clutch was provided in order to protect the gearbox from high loads and to enable an overrunning capability of the motor in latched position.

The latching of the wing is performed by a two-bar system and a foldable element (see Fig. 7). During the deployment, the two-bar system is moved in the direction of its dead center configuration. In the end position, the two-bar system is locked by the stretched foldable element. The function of the foldable element is similar to the foldable bar of deployment Phase 1. Because of the known latching peak (see Fig. 6), the antenna will be accelerated at the end of deployment which causes higher shock loads. In order to balance the energy input from the foldable element, an additional damper was implemented. The design contained a small copper leaf (clamped

cantilever) which will be plastically deformed during the latching event of the antenna. Based on this improvement, the shock load requirement is met.

IN-ORBIT FUNCTION

The compliance with the stiffness requirement and the required accuracy of the deployed antenna is prerequisite for the in-orbit function.

The stiffness requirement was essentially met by provision of the DTS and its stiff locking mechanisms. In order to meet the accuracy requirement, several design features were introduced:

- Minimization of thermal deformations by selection of the CFRP-structural material
- Reduction of misalignment effects by
 - High quality demands to ball bearings and bearing fits
 - Application of titanium brackets at all hinge components (shafts and housings) in order to reduce thermal effects
 - Reproducible latching in defined end position (free of slipping).

Further improvements were gained from a shim procedure, in order to compensate actual misalignments due to manufacturing and integration tolerances. The antenna was aligned in a gravity compensation jig and the coordinates of 250 points on the deployed antenna were measured. A fine tuning of the panels' alignment was possible by shimming the interface points between panels and DTS, and by shimming the length of the foldable bars. The optimum shim corrections (location and thickness) were obtained from a computer program, based upon a finite element model of the antenna structure, plus optimization algorithm. This procedure was found very efficient, as no hardware iterations were needed, and the accuracy requirement was met after just one correction. The actual minimum/maximum deviations vertical to the frontside of the EM-antenna appeared in the range of ± 0.8 mm at ground conditions.

CONCLUSIONS

Numerous mechanisms were needed for the hold-down, release, deployment, and locking of the SAR antenna. Due to its complexity, and the various sometimes conflicting requirements, straightforward designs had to be corrected, or improved, during the course of the development. Several component tests, and several analyses had to be performed to cover all essential details. Particular emphasis had to be given to the reliable performance of all those mechanisms as a failure could result in a complete loss of the satellite mission, rather than just a performance degradation.

Acceptable performance of all mechanisms was eventually verified at the first full antenna model.

ACKNOWLEDGMENTS

The critical technologies for the antenna were developed in a pre-development program, sponsored by the German Federal Ministry of Research and Technology (BMFT). Actual and complete antenna development was performed within the ERS-1 program of the European Space Agency (ESA). Full qualification of the first antenna model has been completed and the flight model is in final acceptance testing.

The authors wish to thank the Agency for the support during the course of the program and for permission to publish this paper.

REFERENCES

1. Hardy, W. E.: ERS-1 AMI Antennas: The Design and Development Experience. Proc. IGARSS '88 Symp., Edinburgh, 13-16 September 1988 (ESA SP-284), p. 873-876.
2. Wagner, R.: Planar Array Antenna for ERS-1 Synthetic Aperture Radar. Proc. IGARSS '86 Symp., Zurich, 8-11 September 1986, (ESA SP-254), pp. 1181-1186.
3. Wagner, R.: Carbon Fibre Slotted Waveguide Arrays. Proc. Military Microwaves '86, Brighton, 24-26 June 1986, pp. 231-236.
4. Wagner, R., Luhmann, H.-J., Sippel, R., and Westphal, M.: Development Status of the ERS-1 SAR-Antenna. Proc. 2nd ESA Workshop on Mech. Techn. for Antennas, Noordwijk, 20-22 May 1986 (ESA SP-261), pp. 131-137.

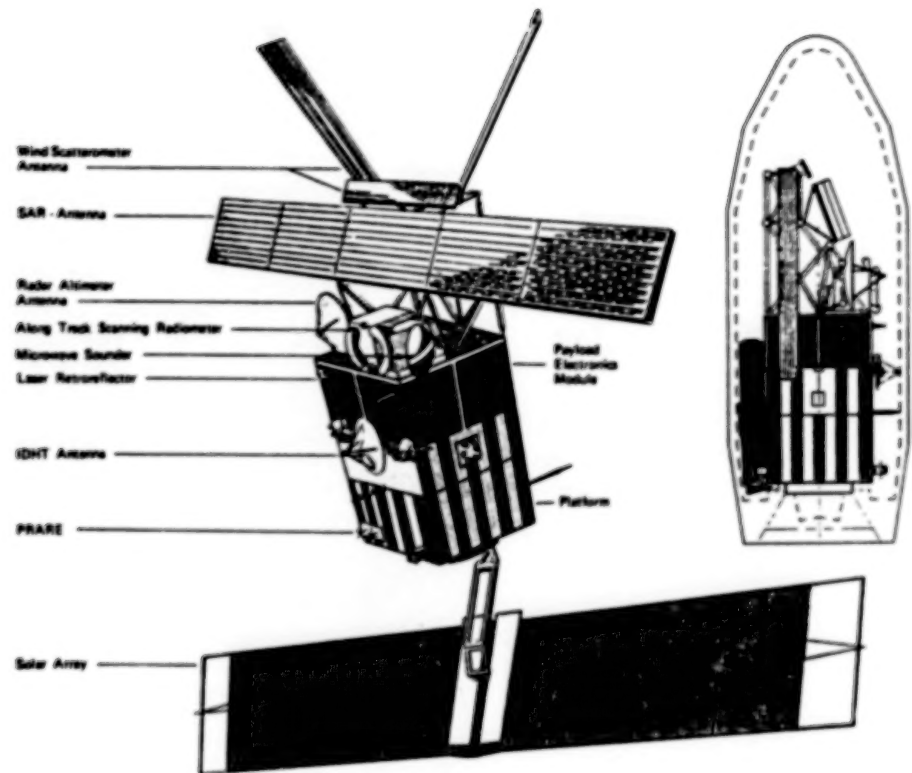


Figure 1. ERS-1 satellite in launch- and fully-deployed configuration.

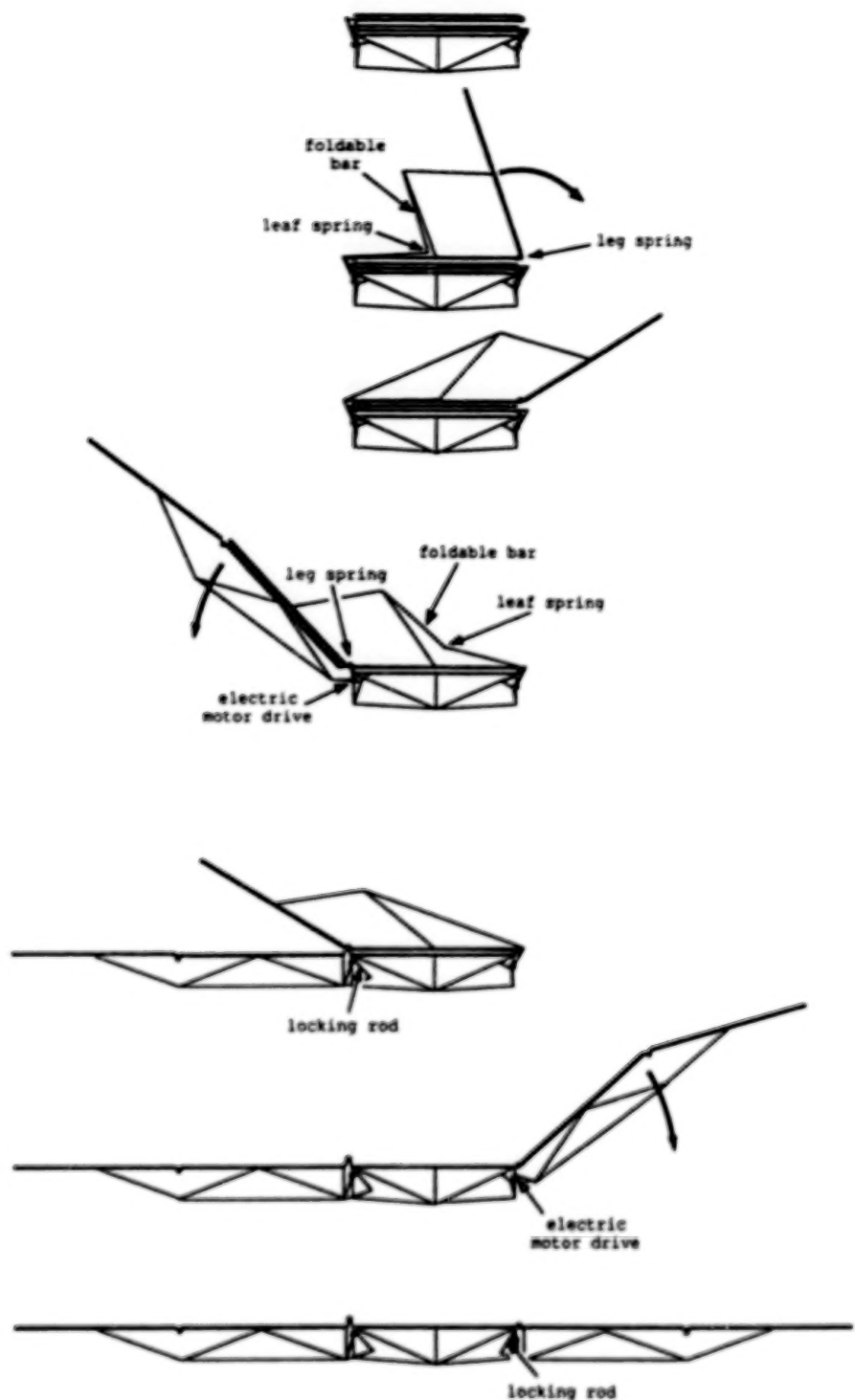


Figure 2. SAR-antenna deployment sequence.

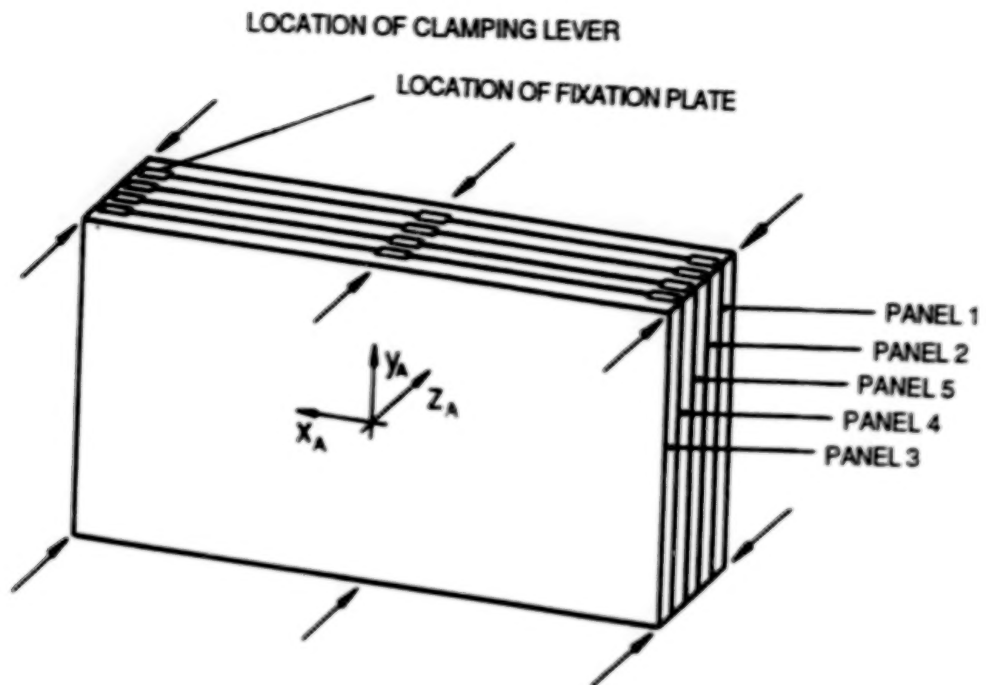


Figure 3. SAR-antenna launch configuration.

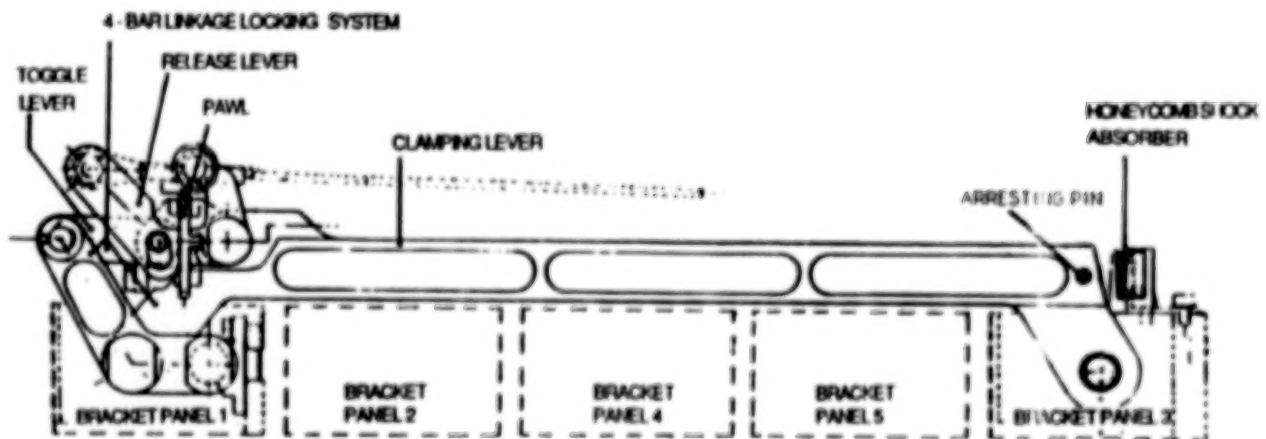
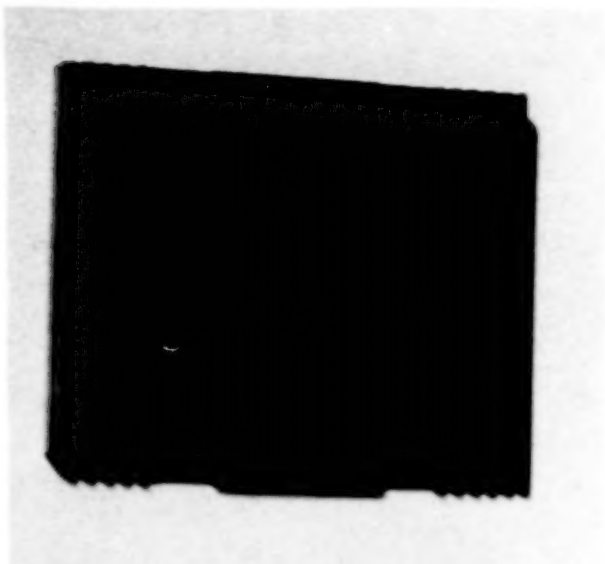


Figure 4. HRM clamping lever.



SINGLE FIXATION PLATE



FIXATION PLATES IN CONTACT

Figure 5. Panel fixation plate.

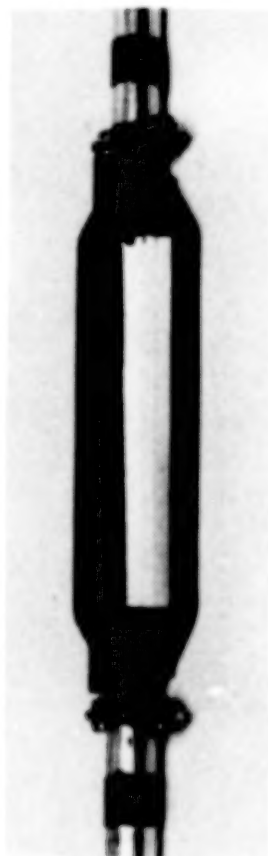
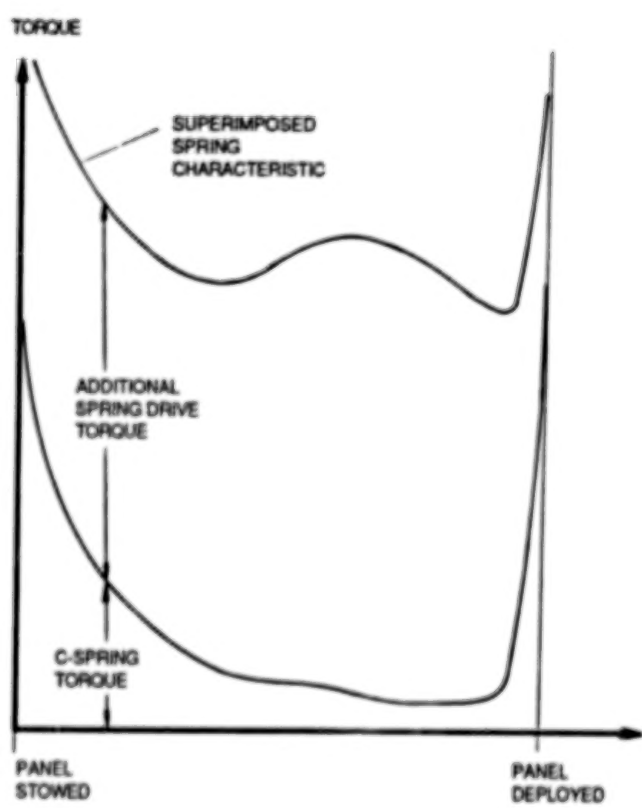
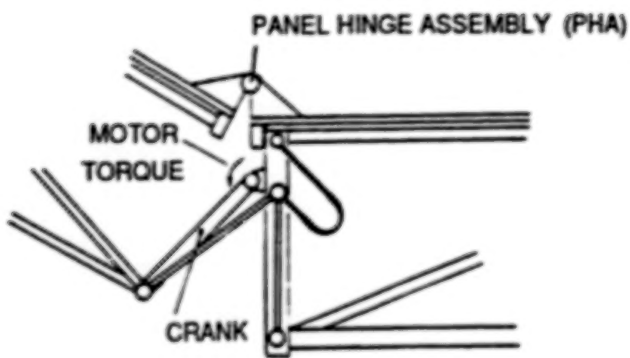


Figure 6. Torque characteristic of phase 1 deployment (photo of stretched leaf spring drive added).

INTERMEDIATE CONFIGURATION



DEPLOYED CONFIGURATION

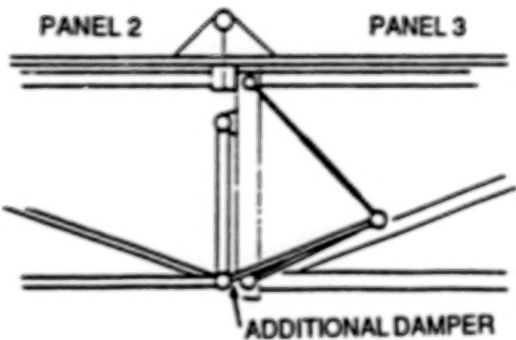


Figure 7. Details of phase 2 latching.

EDDY CURRENT DAMPER

R. C. Ellis*, R. A. Fink*, and R. W. Rich*

ABSTRACT

A high torque capacity eddy current damper has been successfully developed as a rate limiting device for a large solar array deployment mechanism. The eddy current damper eliminates the problems associated with the outgassing or leaking of damping fluids. It also provides other performance advantages, such as damping torque rates, which are truly linear with respect to input speed, continuous 360-deg operation in both directions of rotation, wide operating temperature range, and the capability of convenient adjustment of unit damping rates by the user without disassembly or special tooling.

INTRODUCTION

The eddy current damper shown in Figure 1 consists of a copper alloy disk which rotates between opposed samarium cobalt magnets. Rotation of the disk in the magnetic field generates circulating eddy currents within the disk which create a damping torque proportional to rotation speed. The damping output can be dramatically increased by coupling the eddy current disk to a gearhead speed increaser (Fig. 2). The overall damping rate is magnified by the square of the gear ratio since the gearhead acts to simultaneously increase disk speed while reducing the transmitted torque from the mechanical input of the unit. The damper design presented in this paper uses a four-stage planetary gearhead to boost the unit damping rate to 2260 N-m-sec/rad (20,000 in.-lb/rad/sec). Damping rates can be easily adjusted in the field by rotating the unit end bell, thereby misaligning magnets on either side of the eddy current disk.

The damper design also incorporates other special design features intended to minimize the size and weight of the unit and improve reliability.

EDDY CURRENT CONCEPT

Eddy current dampers have been utilized for many years in aircraft applications, but have not been fully developed for the special requirements of spacecraft application. The operating concept is relatively simple and can be compared to a generator with a shorted output. Referring to Figure 3, eight samarium cobalt permanent magnets are equally spaced on both sides of a copper alloy disk to provide a constant and uniform magnetic field. The rotation of the disk in the field produces a generated voltage in the disk. This voltage develops circulating currents within the disk which results in a

*Honeywell Space and Aviation Systems, Durham, North Carolina.

restraining torque proportional to velocity. The drag torque created is a very linear function of the rotational speed of the copper alloy disk. As the shaft rotational speed increases, the damping torque increases.

DISK MATERIAL INVESTIGATION

An important design tradeoff in eddy current dampers is encountered in the selection of materials for the eddy current disk. Minimum damper size and weight can be achieved by using materials with low electrical resistivity. Unfortunately, those alloys which have the lowest resistivity are highly susceptible to the influences of temperature changes on damping rates.

A study of available alloys and their properties was conducted. Figure 4 summarizes the temperature versus resistivity characteristics of relevant materials. Figure 5 lists selected materials for comparison.

The initial baseline magnetic design utilized a pure copper disk. A disk thickness of 0.2 cm was necessary to meet performance requirements. This thickness dictated the minimum magnetic air gap and consequently determined the magnet size along the direction of magnetization. Within the overall envelope constraints, the use of samarium cobalt magnets allowed a larger gap and thicker disk. Total unit length and weight increased, but not in direct proportion.

Figure 4 could also be considered as a plot of temperature coefficient versus disk thickness and/or magnet length.

The material chosen was Drive Harris 30 Alloy. It offered the best combination of performance versus temperature within the size and weight constraints. Other applications may result in the selection of a different alloy depending on system requirements and mechanical size limitations. From Figure 5, the disk thickness must be 2.9 times thicker than copper (ratio of resistivity). The thickness selected for the final design was increased to allow for magnetic fringing and leakage. Magnet length was selected to operate at the maximum energy product.

The temperature sensitivity using 30 alloy was lower than copper by a factor of 2.6. This resulted in a damping rate increase of 11 percent at -51°C and a decrease of 12 percent at 104°C.

A less obvious advantage with using the 30 alloy was the greater thermal capacity of the thicker alloy disk. During the required duty cycle, energy absorption in the disk resulted in a temperature rise of only 5°C. This temperature rise was reflected in a performance change due to the temperature coefficient. With a thinner copper disk, the thermal capacity was proportionally less, with a correspondingly higher temperature rise and adverse effect on performance.

MECHANICAL

Figure 2 depicts the overall damper configuration. Easily recognized in the figure are the input shaft, four planet stages, disk assembly between opposed magnets, and structural housing parts.

Disk Region

The damping torque is effected upon the solid copper alloy eddy-current disk. The disk (the final stage of the rotary damper drive train) is mounted to a stainless steel shaft which rotates in a pair of stainless steel bearings. The inboard end of the disk shaft is machined as a pinion which serves as the sun gear to the fourth planetary stage.

One member of each magnet pair is mounted to the housing and the other member is mounted to the end bell. These samarium cobalt magnets are bonded into indentations in their respective mounting surfaces and further secured by a lightweight stainless steel cover. This method provides positive positioning and ensures that the magnets are protected from any potential sources of abrasion or chipping.

Adjustment of the unit's damping rate is achieved by purposely misaligning opposing magnets through rotation of the end bell with respect to the disk housing. Locking screws and lock wiring positively position the end bell at any of nine damping rate settings from 1130 to 2260 N-m-sec/rad. (10,000 to 20,000 in.-lb sec/rad). Lower damping rates could be easily incorporated into the design by changing the gear ratio, the disk size, or the number of magnets.

Gear Train

The design has four planetary stages which combine for a 1600:1 gear ratio. Since the damping rate of the disk is increased by the square of the gear ratio, it constitutes a damping rate multiplier of 2.56×10^6 . All gears are made of 15-5 PH stainless steel heat treated to H1025 and are machined to AGMA Class 10.

The planet gears rotate on sintered bronze bearings impregnated with Bray Oil Company Type 815Z oil. To provide bearing redundancy, each planet gear rotates on the outer diameter of a sleeve bearing, and each sleeve bearing rotates on the outer diameter of a planet carrier post. In addition to the 815Z oil impregnation, the gears and bearings are lubricated with Bray 601 Micronic grease.

Ring gear teeth are machined into the stainless steel housing bore. The ring gears for stages one and two are identical in pitch diameter and diametral pitch and are machined in a single operation. Similarly, the ring gears for stages three and four are identical in pitch diameter and diametral pitch and are machined in a single operation. Machining the gear teeth

directly into the housing bore precludes the potential problems of shrink fitting a ring gear into the bore of a thermally dissimilar housing.

All sun gears have at least 18 teeth so that gear tooth stresses are kept within a reasonable range. The sun gears of stages one through three (starting at the mounting end) are integral to the planet carrier of the subsequent stage. The sun gear of stage four is a pinion machined onto the end of the eddy-current disk shaft.

The input shaft transmits applied rotational motion to the first stage of planetary gearing. It is positioned and supported by a pair of stainless steel ball bearings which are located within the input housing. The input shaft is machined from 15-5 PH stainless steel.

Structural Housings

The three structural housing parts are evident in Figure 2. From left to right, the disk housing, the gear housing, and the input housing.

Since the disk housing constitutes a part of the magnetic flux path, it is machined from a 416 stainless steel. Structurally it supports one set of samarium cobalt magnets and the inboard end of the disk/shaft assembly.

The gear housing serves both as a primary structural part and as two integral ring gears. The input housing supports the input shaft ball bearings (ABEC Class 7P) and is made from 6061 aluminum for weight reduction. By controlling bearing fits and machining tolerances, the differential expansion of the input housing and the input shaft bearings is held to an acceptable level. Locking inserts in the input housing are provided for mounting.

TESTING PROBLEM

Initial tests on the first unit were erratic and produced misleading results. Variations in unit speed were noted when a constant input torque was applied. These variations had a once-per-revolution component as well as multiple cycles per revolution. Each gear stage was producing cyclic load behavior at a frequency consistent with the gear ratio. Breakaway torque was also above specification limits.

Testing to characterize the problem was conducted. As these tests progressed, it was noted that the anomalies were becoming less pronounced. This indicated a need for unit run-in prior to substantive testing. Due to the slow operating speed (0.035 rad/sec), run-in time required to stabilize unit performance was established at 8 hr. The unit was driven with an input torque of 40 N-m for 4 hr in each direction. This resulted in 167 revolutions of the input shaft.

After completion of the run-in, speed variation was negligible. Equally significant was the breakaway torque which reduced to 1.1 N-m or less. Not only were the once-per-revolution variations decreasing, gear train smoothness

and friction torque was also improving. It was concluded that run-in primarily benefited the sliding contact surfaces on the planet bearings. Experience with gear trains using ball bearings and high quality gears indicates that run-in has a minor effect. The sleeve bearings, being porous, cannot be lapped or honed since the debris generated could be trapped in the pores, but run-in polishes the machined surfaces and smooths unit operation.

PERFORMANCE

The damper has the following performance and mechanical characteristics:

Continuous operation	40 N-m (350 in.lb)
Maximum torque level	80 N-m (700 in.lb)
Damping rate range (adjustable)	1130 to 2260 N-m-sec/rad (10,000 to 20,000 in.-lb-sec/rad)
Breakaway torque	1.1 N-m (10 in.-lb)
Angular range	Continuous rotation
Backlash	<0.50 deg
Weight	0.35 N (1.54 lb)

The damper provides a smooth resisting torque proportional to input speed. It will perform for more than 1000 cycles over a continuous rotational range with a maximum failure rate of 0.042×10^{-6} failures/cycle (per classical reliability analysis) under 40 N-m of applied load. It will also perform for shorter periods of time at 80 N-m. In fact, an early test unit continued to operate after 50 cycles while loaded to 120 N-m.

Breakaway torque is kept low by using lightly loaded ball bearings at the damper disk shaft. The 1.1 N-m breakaway torque value is low in view of the unit's high damping rate and input torque range. Backlash is minimized by tightly controlling bearing fits and gear dimensions, especially at the stage nearest the input shaft. Machining tolerances for these dimensions are typically held to ± 0.0025 to 0.0050 mm.

The damper can be field adjusted, without special tools, to any of nine settings from 1130 to 2260 N-m-sec/rad.

QUALIFICATION

The unit successfully completed qualification testing consisting of pyrotechnic shock, random vibration, and thermal-vacuum environments. Functional tests at maximum rated torque were conducted after each environment. Test levels and conditions are listed below.

1. Pyroshock with flat plate shock simulator:
4 shocks, 2 in each of 2 axes.
Ramp from 170 G at 100 Hz to 4700 G at 850 Hz.
Then constant 4700 G to 10,000 Hz.

2. Random Vibration

Frequency (Hz)	Power Spectral Density (G ² /Hz)	(dB/Oct.)
20		
20-50	0.1	+6 to 0.64 G ² /Hz
50-200	0.64	
200-400		-6 to 0.16 G ² /Hz
400-500	0.16	
500-1000	0.16	
1000-2000		-6 to 0.04 G ² /Hz
<u>Overall</u>	<u>18.6 GRMS</u>	

3. Thermal Vacuum Cycling

Pressure 1×10^{-5} Torr

Temperature Cycling -51°C to 104°C for 8 cycles.

CONCLUSION

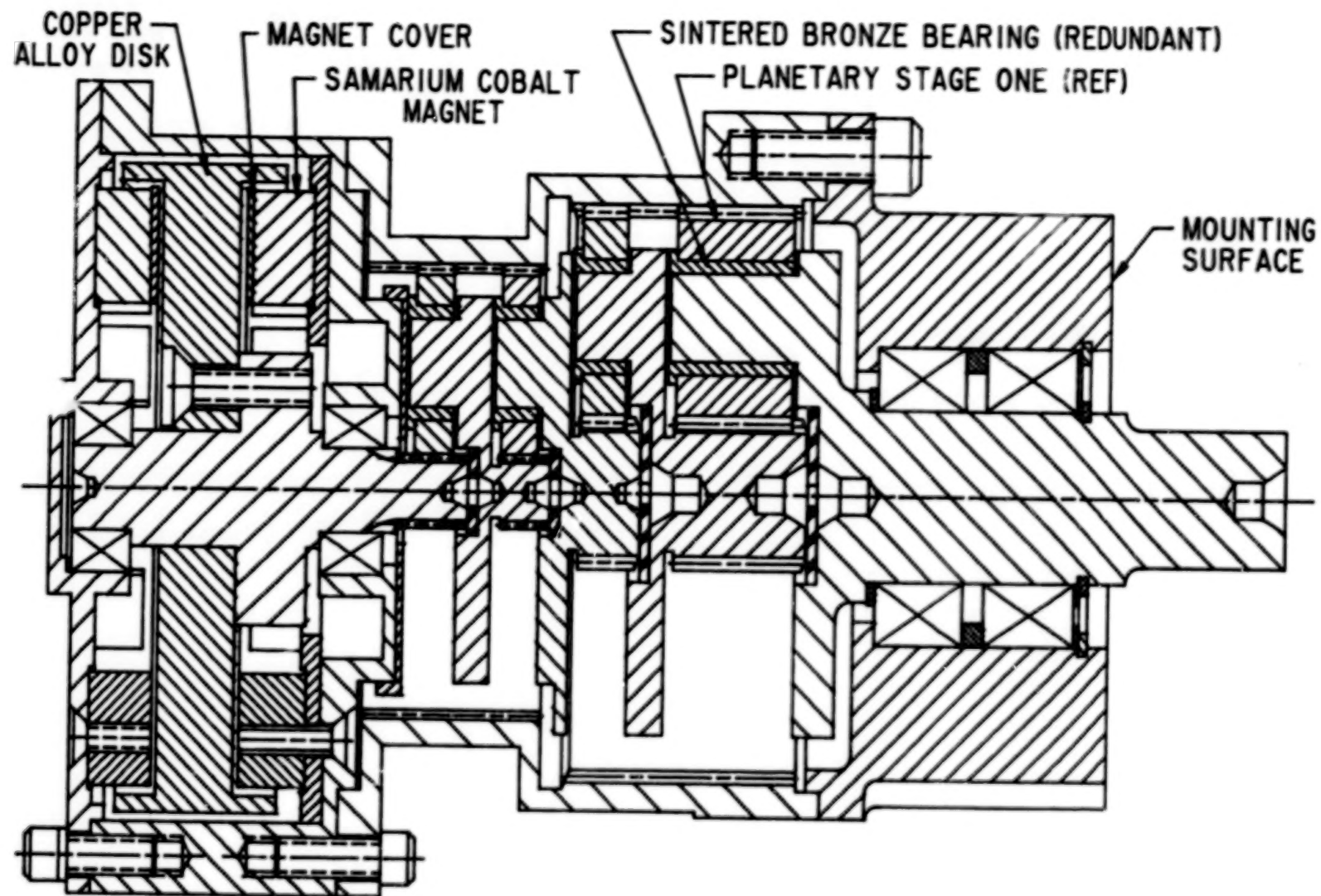
The Rotary Damper is a desirable alternative to a fluid damper, avoiding problems of contamination and limited rotation characteristics. Thermal effects are also minimized by material optimization. The unit described has successfully completed qualification.



Figure 1

133

133



MAGNETIC DAMPER

Figure 2

134

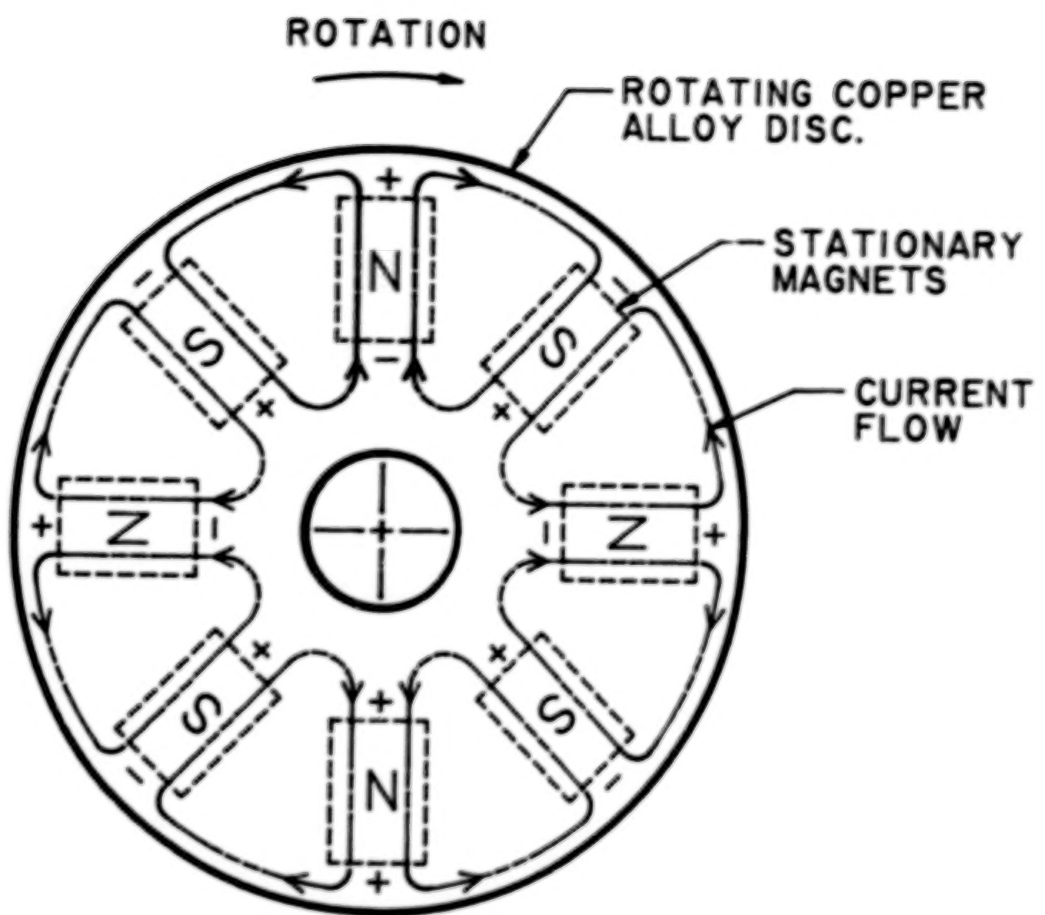


Figure 3

TEMPERATURE COEFFICIENT OF RESISTIVITY
VS.
RESISTIVITY FOR COPPER AND COPPER ALLOYS

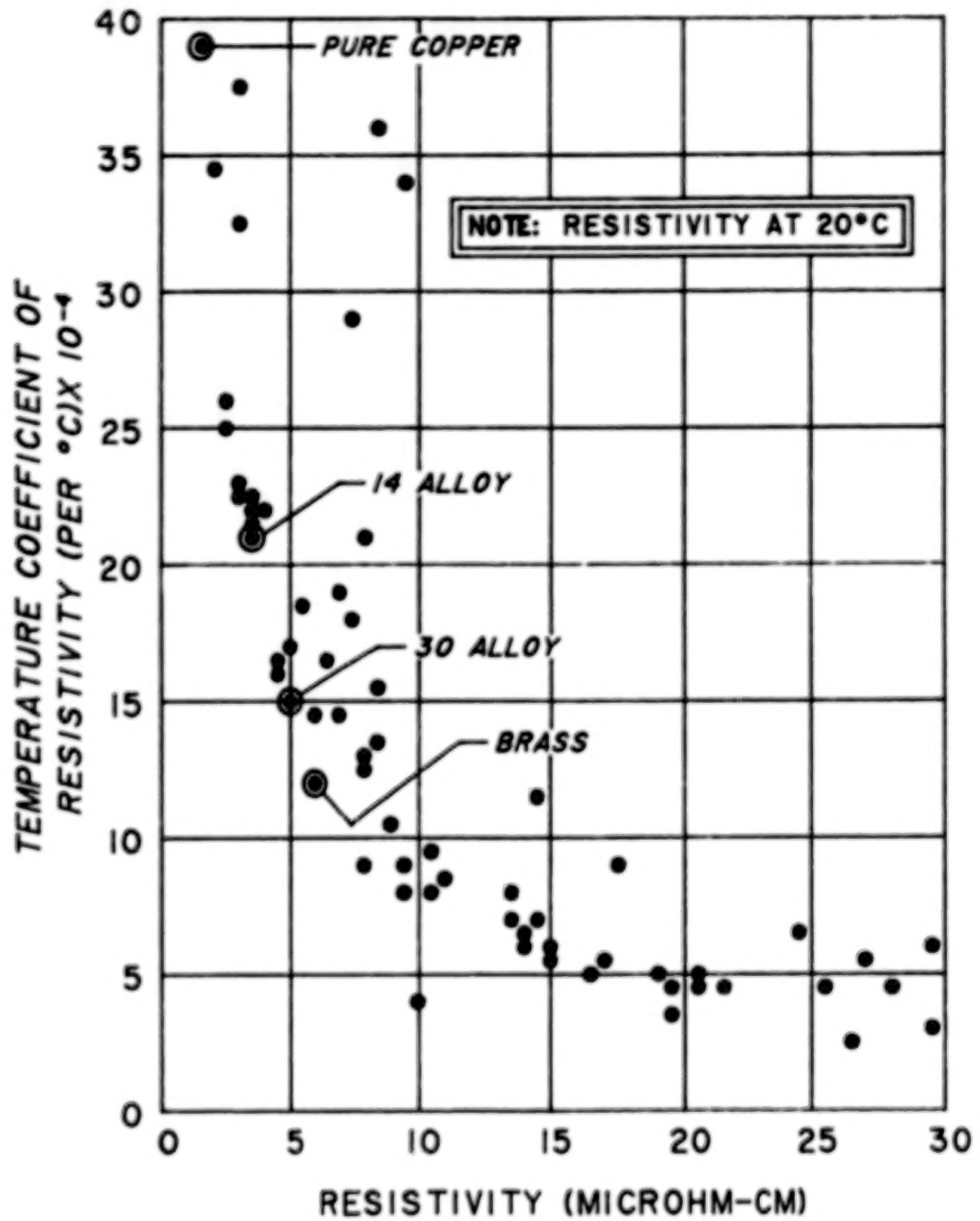


Figure 4

RESISTIVITY VS. TEMPERATURE COEFFICIENT
FOR SELECTED ALLOYS

<u>MATERIAL</u>	<u>RESISTIVITY (MICROHM-CM)</u>	<u>TEMP. COEFF. OF RESISTANCE (PER °C)</u>
SILVER	1.628	0.0038
COPPER (DRAWN)	1.724	0.0039
GOLD	2.44	0.0034
111 ALLOY (DRIVER-HARRIS)	2.9	0.0025
CD 1.07, SN 0.59, FE 0.02, SI 0.02	3.05	0.00224
MN 0.43, FE 0.01, MG 0.01	3.38	0.0019
BRONZE (COMMERCIAL)	4.2	0.0020
30 ALLOY (DRIVER-HARRIS)	5	0.0015
ZINC	5.97	0.0037
PD 10	6.05	0.00091
BRASS	6.21	0.0015

Figure 5

BLANK PAGE

DEVELOPMENT OF A PRECISION, WIDE-DYNAMIC-RANGE ACTUATOR FOR USE IN ACTIVE OPTICAL SYSTEMS

K. R. Lorell, J-N. Aubrun, D. F. Zacharie, and E. O. Perez*

ABSTRACT

This paper describes the design, operation, and performance of a wide-dynamic-range optical-quality actuator developed at the Lockheed Palo Alto Research Laboratory. The actuator uses a closed-loop control system to maintain accurate positioning and has an rms noise performance of 20 nm. A unique force offloading mechanism allows the actuator coil to dissipate less than 3 mW under quiescent conditions. The total available mechanical range is 2 mm. In addition to describing the actuator and its performance, this paper describes the operation of an experimental segmented optical system that uses 18 of these actuators to show how the actuator is integrated into an actual system.

INTRODUCTION

As requirements for ground- and space-based directed-energy, communication, and astronomical optical systems become more demanding, the size of the primary reflectors for these systems is steadily increasing. Large reflectors provide more efficient energy concentration at distant targets, or, in the case of astronomical instruments, their increased collecting area substantially improves the fundamental sensitivity and resolution of the instrument. For nearly 40 years, the largest available astronomical-quality reflector was the 5-m mirror of the Hale telescope. It is now commonplace to consider building optical systems with apertures in the 10- to 30-m range. The W. M. Keck Telescope, presently under construction in Hawaii, will have a 10-m-diameter primary mirror [1]. When completed, it will be the largest astronomical telescope ever built. NASA's currently planned Large Deployable Reflector (LDR), an orbiting infrared telescope, will have a 17- to 20-m primary mirror [2].

Three approaches are being developed for producing large optics. The simplest is to fabricate lightweight monolithic optical blanks as large as 8 m using a unique spin-casting technique [3]. The second approach is to make a thin monolithic meniscus mirror with up to several hundred actuators attached to the back surface [4]. These actuators can bend the glass to control the mirror figure and achieve a high-quality optical surface [5]. The third approach uses segmented mirrors, a physical necessity for larger systems and

*Lockheed Palo Alto Research Laboratory, 3251 Hanover Street,
Palo Alto, California 94304.

the only realistic solution for space applications for which size, weight, and in-orbit deployment are critical.

In the latter two approaches, unacceptable deformations result from the inherent flexibility and thermal sensitivity of either the mirror itself or the structure supporting the mirror; thus, active-control systems must be used to maintain the geometric integrity of the reflecting surface. Actuators that can deform a monolithic mirror, or align mirror segments with respect to each other, are essential to this new technology. In the Keck telescope, for example, the primary mirror is composed of 36 actively-controlled hexagonal segments that require a total of 108 actuators [6].

The design of segment-positioning actuators is a major technological challenge in the development of segmented optical systems. These actuators are required to have extremely low noise levels, be able to generate substantial forces over a wide mechanical range, and be able to support the segment (depending upon the application) in a 1-g field. They must also have a bandwidth sufficient to accommodate the spectra of the disturbances. In addition, because of thermal and power considerations, given that a typical large system may have several hundred actuators, energy dissipation must be minimized.

This paper describes the design, operation, and performance of a wide-dynamic-range optical-quality actuator developed at the Lockheed Palo Alto Research Laboratory. The actuator uses a closed-loop control system to maintain accurate positioning and has an rms noise performance of 20 nm. A unique force offloading mechanism allows the actuator coil to dissipate less than 3 mW under quiescent conditions. The total available mechanical range is 2 mm. The operation of an experimental segmented optical system that uses 18 of these actuators is also described, to show how the actuator is integrated into an actual system.

ACTUATOR DESIGN REQUIREMENTS

This section describes the main requirements and design considerations for segment alignment-control actuators. These requirements are also generally applicable to figure control actuators.

Dynamic Range and Sensitivity

In order to install and align a set of several hundred actuators in a segmented system that uses standard mechanical fabrication tolerances, each actuator must have a total range of motion on the order of millimeters. Irregularities and dimensional changes in the backup structure can then be compensated for without exceeding the displacement capability of the actuation system. Since each segment must be positioned to an accuracy on the order of 100 nm or better, the resultant dynamic range of the actuators must be on the order of 100,000:1.

In closed-loop operation, in which the control system drives the actuator in such a way as to zero out error signals derived from external sensors (e.g., edge sensors), the primary limiting factors are the actuator noise and its resolution. The larger of these two defines the actuator sensitivity and thus the low end of the dynamic range. As long as open-loop operations or feed-forward techniques are not required, the absolute accuracy of the actuator is not critical and does not impact the definition of its dynamic range.

Actuator Roughness

Unlike rigidly-mounted optical systems, large space systems, with their inherent flexibility, are very sensitive to uneven motions occurring in any part of the structure. Stepper motors for example, when used to move relatively massive segments, can induce unwanted modal excitations. Bearings, gears, roller screws, and other sliding mechanisms typically operate with friction and stiction characteristics that may seriously affect the performance of the system. These nonlinear effects often result in limit-cycle behavior that is unacceptable for an optical-quality actuator.

Power Dissipation

One of the major difficulties associated with more conventional actuator designs is the inability to maintain position in the face of a constant load without continuous power input. This power requirement has three disadvantages. First, it places an unnecessary burden on the system power supply; especially considering a large system which may have a hundred or more actuators. Second, the heat generated can deform the mirror or the support structure, thus requiring even more power from the actuators to compensate, which eventually leads to thermal runaway. Third, excessive heat from the actuators causes thermal pollution of sensitive infrared detection systems.

Power dissipation can be very severe for direct-drive actuators when they must, for any significant period of time, support a segment in a 1-g field or deform the surface of a mirror to correct for aberrations or wavefront errors. Thus, power efficiency becomes an important driver of the actuator design.

Bandwidth

Truly "static" alignment is an abstract notion. In a real system, the question always arises as to how often this alignment must be performed. Thus, because time is involved, the process is no longer "static" and the notion of bandwidth must be introduced, whether it be 0.1 Hz or 100 Hz. The problem is that the control system, and thus the actuators, must be able to respond at least as quickly as the disturbances that they are trying to correct. Structural deformations may take as long as several seconds (e.g., thermal effects, gravity vector changes), to just fractions of a second (e.g., distortion during slews, structural vibrations). For space applications in which a rapid response is often critical, a wide bandwidth is essential to optimize the operating duty cycle of the system.

Reliability

The reliability of the actuators is a critical issue for space applications, since failure of even a single actuator may degrade the performance of the entire system. Many systems remain dormant, either on the ground prior to launch or in space for some indeterminate length of time, and then must be ready to operate instantaneously on command. Thus, the reliability of the actuators is an important design consideration.

ACTUATOR DESIGN

Review of Existing Technology

The problem of accurate position control has been approached in different ways depending upon the application. The oldest and most commonly used approach is through a combination of motor (stepper or dc) and gear or screw mechanisms. The stroke can be very large, but accuracy and resolution are limited by several factors such as friction, stiction, backlash, bearing and gear train compliance, etc. Increasing the gear ratio may increase resolution, but will decrease the bandwidth proportionally; thus the combination of gear ratio and rotor inertia usually results in relatively low bandwidths.

The Keck telescope uses a hybrid actuator in which part of the gear ratio is provided hydraulically, thereby improving accuracy and resolution. However, the total equivalent gear ratio results in a bandwidth of less than 2 Hz. The original design for these actuators was purely mechanical, with a high-precision roller screw. The design could only achieve the desired 50-nm resolution by modeling friction effects in a dedicated control microprocessor that was required for each actuator.

Piezoelectric devices have been developed to specifically address active-optics problems. These direct-drive, analog actuators have essentially infinite resolution but a very small stroke; typically a few tenths of micrometers. They can also be very high bandwidth. However, because of creep, hysteresis and thermal sensitivity, they are not very accurate. More advanced designs improve the accuracy using feedback techniques. Finally, the high voltage required to drive piezoelectric actuators is usually undesirable for space applications.

Piezoelectric materials are used in quite a different way in the inch-worm actuator. Here they move a rod by a calibrated quantity. When the process is repeated, the rod advances by another step, and so on. In between moves, the rod is held firmly in place, thus no power is needed and the whole process is much less sensitive to the characteristics of the piezoelectric material. However, the resolution is now limited to that of the gripping procedure, and the actuator is very slow and still requires high voltages.

Another very commonly used actuator is the voice-coil type. In the classical design, the force-generating coil moves inside a field created by a

permanent magnet. In more recent designs, a permanent magnet moves inside a coil, or electromagnets interact with each other. All these designs are capable of large stroke and infinite resolution when driven by analog electronics. These actuators are basically force actuators, thus the position of the moving element is not related to the commanded current in a direct and precise manner. Another more severe drawback is that they require a constant supply of power in order to maintain a given force level. However, they can have high bandwidth and are very simple and reliable.

New Actuator Concept

The previous discussion indicates that conventional actuator designs are limited in at least one of five major characteristics and are thus unsuitable for active segment alignment or figure control. These five characteristics are dynamic range, bandwidth, friction/stiction, static force handling, and power consumption.

The approach taken for the Lockheed actuator addresses these five problems in a systematic manner, as summarized in Table 1.

First, dynamic range and bandwidth considerations mandate the use of a voice-coil-type actuator as the basic drive motor. To overcome the lack of accuracy and repeatability of the device, a local analog servo loop controls the coil current using a highly accurate position sensor.

The friction/stiction problem is solved by eliminating all bearings and bushings and relying solely on flexural elements. In this way, the need for lubrication is eliminated and the mechanism is extremely smooth. Also the device may stay inoperative for an indefinite amount of time without incurring the risk of locking its moving parts because of lubricant dry-up, vacuum welding, etc.

To obtain the correct output force level, constrain the degrees of freedom of the output shaft, and minimize power consumption, a four-bar linkage that acts as a lever is used.

One of the major difficulties associated with more conventional actuator designs, the inability to maintain position in the face of a constant load without continuous power input, is solved through the use of a force offloading system. This separately controlled automatic system uses a special control loop with a very long time constant that uses a small, separate actuator to move a spring attached to the main linkage mechanism of the actuator. When steady state is reached, the spring supplies a force to the output shaft which almost exactly balances the constant load seen by the main actuator.

Table 2 summarizes the characteristics of conventional actuators and compares them to the Lockheed design. The highlighted ratings indicate characteristics unacceptable in a segment alignment-control actuator.

SYSTEM DESCRIPTION

Figure 1 is a schematic diagram of the actuator and the electronic control system that drives it. The main force-producing actuator is shown attached to the output shaft by a special four-bar linkage. The linkage is arranged so that it provides a five-to-one reduction in linear travel and a corresponding five-to-one increase in force output. The moving components in the four-bar linkage are connected with flexures so that there are no backlash or friction-producing components in the drive train. The four-bar linkage with reduction ratio is shown in detail in Figure 2.

The actuator operates under closed-loop control by measuring the location of the output shaft with an inductive position sensor and comparing the commanded position with the measured position. The position error is then processed by the analog control electronics and a power amplifier provides the drive current to the moving-magnet actuator.

A separately-controlled automatic system to provide force offloading is shown in Figure 1. This system uses a special control loop with a very long time constant to measure the current in the main force-producing actuator. When the absolute value of this current exceeds approximately 60 mA, a small servomotor, the force compensation actuator in Figure 1, is commanded to move a leaf spring attached to the linkage mechanism of the main actuator. The leaf spring applies a force to the actuator which the primary control system senses and causes the main actuator to counteract. Because the primary control loop has a much faster response time (by four orders of magnitude) than the offload controller, the net disturbance to the position of the output shaft is essentially zero. As the leaf spring continues to slowly apply more force, the current required by the main actuator is constantly reduced. When the current in the main actuator drops below 20 mA, the offloading system shuts off and holds its last commanded position until the current again exceeds 60 mA. Of course, if the load on the actuator is truly constant, the current will remain between 20 and 60 mA indefinitely and the offload system will not be enabled again. The offload sequence is illustrated in detail in Figure 3.

The mechanical operating range of the Lockheed actuator is 2 mm. Because the actuator control system is entirely analog, it has essentially infinite resolution. However, practical limitations such as noise from the sensor and electronics mean that the limit of resolution is approximately 20 nm. Thus, the dynamic range of mechanical motion is 100,000:1. The key to this extremely wide dynamic range is the closed-loop control system which constantly monitors and corrects the position of the output shaft of the actuator. In order to obtain this performance, the control system relies on the precise measurement of the position of the output shaft. This is accomplished through the use of an inductive position sensor attached to the bottom of the actuator case.

One of the primary benefits of the use of closed-loop control is that the actuator position is no longer affected by disturbances or the magnitude of

the external load. In particular, because the flexures which allow the four-bar linkage to operate do have a finite transverse stiffness, they will deflect slightly under load. Thus, the use of closed-loop control to compensate for these minute transverse deflections is essential if the actuator is to have optical-quality performance.

The exploded view of the Lockheed actuator in Figure 4 shows the location of the various components. An operational prototype of the actuator is shown in Figure 5, with a portion of its case removed so that the internal components can be seen more easily. A schematic block diagram of the electronic control system is shown in Figure 6 and the actual electronic hardware required to drive the actuator is shown in Figure 7.

ACTUATOR PERFORMANCE

The performance of the Lockheed actuator has been characterized by measurements of time and frequency responses, the noise-equivalent position, and the effectiveness of the force offloading system.

The Bode plot of Figure 8 shows the actuator bandwidth set at 43 Hz. The resonance associated with the transverse compliance of the flexures in the four-bar linkage can be seen in the response dip at 115 Hz. The actuator has been tested to a bandwidth of 140 Hz driving a 1-kg load. However, because of the particular application (described in a later section), the bandwidth has been intentionally reduced.

One of the most important performance parameters for a closed-loop positioning system is the noise-equivalent position, i.e., the limit on the resolution of the actuator based on the noise in the sensor and electronics. Two measures of position noise with a 100-Hz cutoff frequency are shown in Figure 9; one for the actuator operating open loop and one for closed-loop. The two traces have rms values of 17 and 20 nm, respectively. The implication of nearly identical values of open- and closed-loop rms noise-equivalent position is that the actuator control system is operating at essentially the limit of sensor noise and environmentally-induced disturbances.

The ability of the actuator and the force-offloading system to respond to very rapid changes in applied load is illustrated in Figures 10 and 12. In Figure 10, the time scale has been expanded to show the well-damped nature of the response and the insensitivity of the actuator position to the applied load. Figure 11 shows the response of the high-bandwidth-position control loop and the low-bandwidth force-offload control loop. The current in the coil of the force-generating actuator is shown decreasing with a very long time constant (on the order of 20 sec, or a bandwidth of 0.008 Hz) to a steady-state value of 30 mA.

The angle of the control arm which moves the force-bias leaf spring is shown in Figure 12 along with the coil current. The change in angle of the control arm as it bends the leaf spring is exactly in opposition to the coil current. It is interesting to note how small an angular motion is required to

compensate for the 5-N load. The right hand abscissa indicates that the arm has rotated a total of only 6.5 deg.

The performance characteristics of the Lockheed actuator are summarized in Table 3.

APPLICATION

The primary motivation for developing the Lockheed actuator was to provide control capability for an experimental segmented optical system called the Advanced Structures/Controls Integrated Experiment (ASCIE). The ASCIE consists of a 2-m, seven-segment, actively controlled primary mirror supported by a lightweight truss structure. The actuator described in this paper is used to control the six peripheral segments of the primary mirror which surround the central fixed segment. Each segment can be positioned in three degrees of freedom: piston and two axes of tilt. An array processor connected to a digital computer is used to compute the commands to the 18-segment actuators. Measurements of how well each of the segments is aligned are provided by edge sensors which determine the relative position of a segment with respect to its neighbors.

The ASCIE laboratory hardware is shown in the photographs of Figures 13 and 14. The back structure of the ASCIE reflector and the actuators can be seen clearly in Figure 14. The performance of the ASCIE system when the segment actuators are being driven by the segment alignment control system is shown in Figures 15 and 16. Figure 15 shows the positions of the three actuators controlling the position of one of the segments. Note that the actuators move several hundred nanometers over a period of 5-sec in response to commands from the control system. Figure 16 shows the motion of the segment itself. Even though each of the three control actuators is moving in different directions, the segment maintains extremely accurate alignment in all three degrees of freedom.

CONCLUSIONS

This paper has described the design, development, and performance characteristics of a special actuator whose wide dynamic range, precise positioning capability, high bandwidth, and low static power consumption make it directly applicable for use in actively controlled optical systems. One of the main applications for this type of actuator is for segment position control in large segmented reflectors. A specific example is discussed in which 18 of these actuators are used to control the segment positions of a 7-segment segmented-optics testbed called ASCIE. Laboratory tests of actuator performance as part of the ASCIE system indicate that segment position can be held to piston rms values of less than 100 nm and tilt rms values of less than 200 nrad. This performance meets the requirements for an astronomical-quality optical surface and indicates that the actuator design described in this paper has successfully met its original design objectives.

REFERENCES

1. Nelson, J. E., Mast, T. S., and Faber, S. M.: The Design of the Keck Observatory Telescope (Ten Meter Telescope). Keck Observatory Report Number 90, Berkeley, CA, January 1985.
2. Swanson, P. N., Gulkis, S., Kuiper, T. B., and Kiya, M.: Large Deployable Reflector (LDR): A Concept for an Orbiting Submillimeter-Infrared Telescope for the 1990's. Optical Engineering, Vol. 22, March 1983, pp. 725-731.
3. Angel, J. R. P., and Hill, J. M.: Steps Toward 8-m Honeycomb Mirror Blanks-III: 1.8-m Honeycomb Sandwich Blanks Cast from Borosilicate Glass. Proceedings of the SPIE Conference on Advanced Technology Optical Telescopes II, Vol. 444, 1983, p. 194.
4. Woltjer, L., et al.: Proposal for the Construction of the 16-m Very Large Telescope. European Southern Observatory, Garching, FRG, March 1987.
5. Bushnell, D.: Aiming an Electromagnetic Beam by Bending Segments of a Large Reflecting Surface. AIAA Journal, Vol. 17, No. 4, April 1979.
6. Mast, T. S., and Nelson, J. E.: Figure Control for a Fully Segmented Telescope Mirror. Applied Optics, Vol. 21, 1982, pp. 2631-2641.

TABLE 1. LOCKHEED SOLUTION TO LIMITATIONS OF CONVENTIONAL DESIGNS

Problem	Solution
Dynamic Range	Use of electromagnetic actuator in an analog closed loop using special low-noise sensor electronics
Bandwidth	Use of electromagnetic actuator and moderate equivalent gear ratio
Stiction/friction	No bearings or lubricants Exclusively flex pivots
High power consumption	Four-bar linkage (lever) and force unload system
Inability to cancel static forces	Force unload system

TABLE 2. COMPARISON OF ACTUATOR CHARACTERISTICS

Actuator Type	Dynamic Range	Accu-racy	Resolu-tion	Smooth-ness	Band-width	Idle Power	Relia-bility
Stepper- or DC-motor-driven gear/screw	Large	Medium	Medium	Poor	Low	Low	Poor to Medium
Hydromechanical (Keck Telescope)	Medium	Good	Good	Good	Low	Low	Medium
Piezoelectric (open-loop)	Small	Poor	Good	Good	High	Low	Medium
Piezoelectric (with feedback)	Small	Good	Good	Good	High	Low	Medium
Inch-worm	Large	Good	Medium	Medium	Low	Low	Medium
Voice-coil (open-loop)	Medium	Poor	Good	Good	Medium	High	Good
Lockheed Design	Large	Good	Good	Good	Medium	Low	Good
Ideal Actuator	Large	Good	Good	Good	High	Low	Good

TABLE 3. PERFORMANCE CHARACTERISTICS OF THE LOCKHEED ACTUATOR

Dynamic Range	100,000:1
Total Mechanical Range	± 1 mm
Noise-Equivalent Position	20 nm (rms, measured using a 100-Hz filter)
Friction/Stiction	None
Typical Static Power Required	10 mW
Maximum Available Bandwidth	140 Hz
Maximum Available Force	± 45 N
Weight	700 g
Operational Features	<ul style="list-style-type: none"> ● soft startup and shutdown ● automatic force unloading ● all-analog electronics

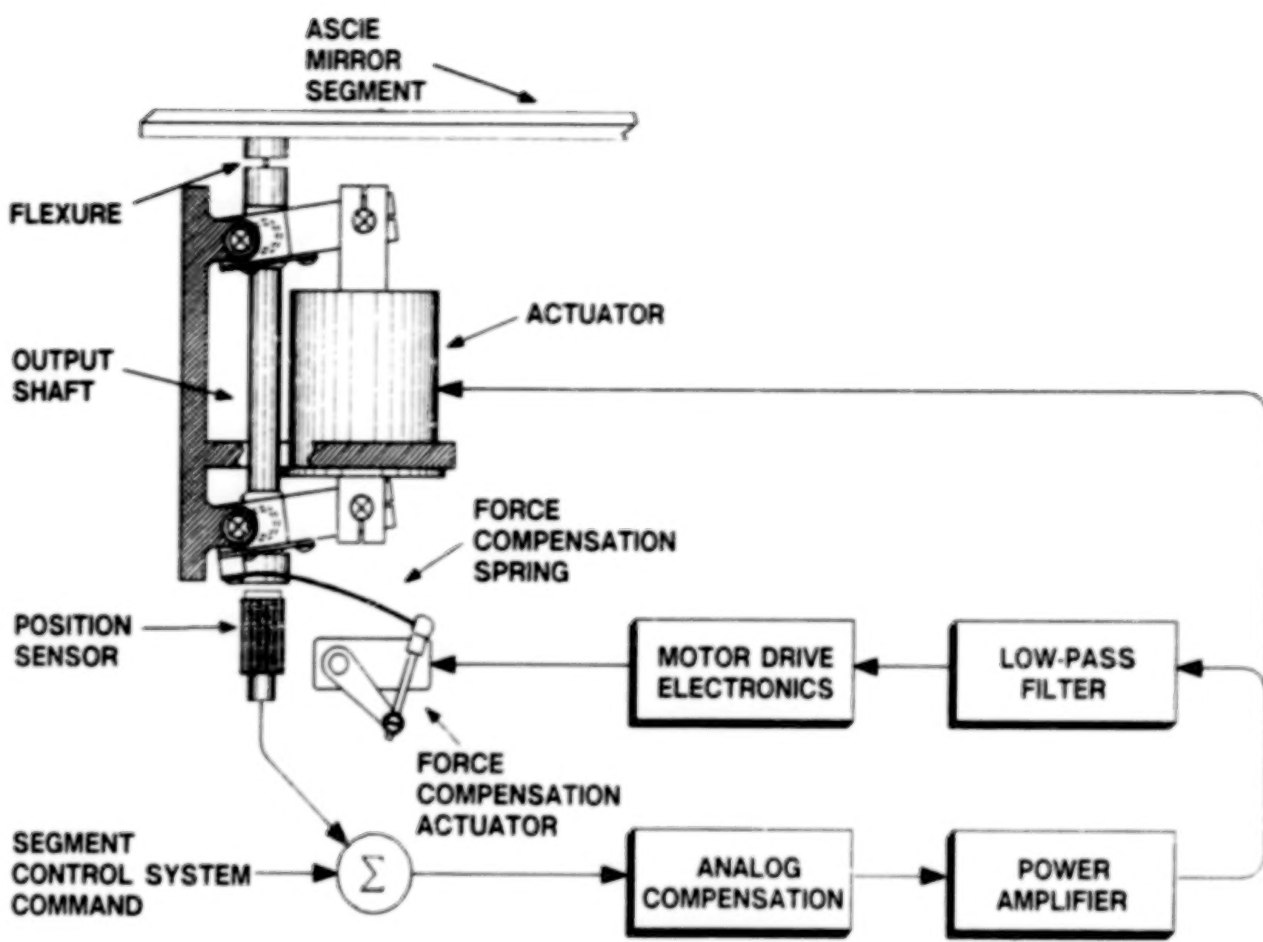


Figure 1. Schematic diagram of Lockheed actuator and closed-loop control system.

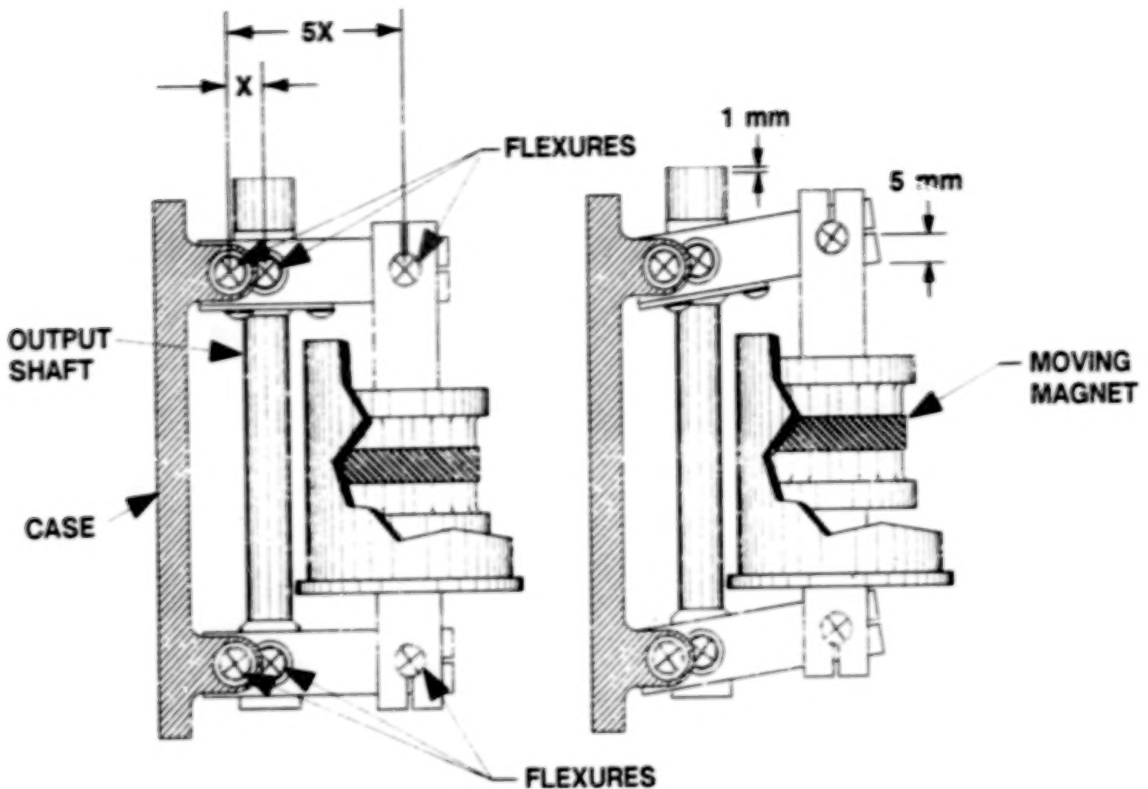


Figure 2. Four-bar linkage with 5:1 reduction ratio.

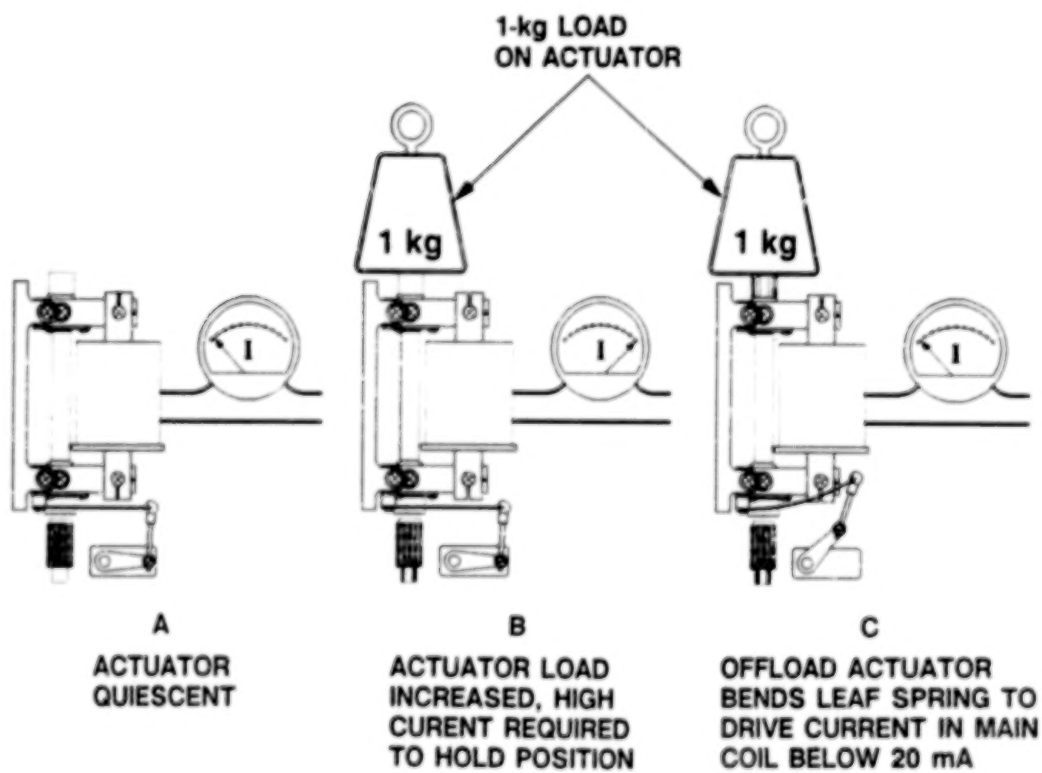


Figure 3. Operation of force-offloading system.

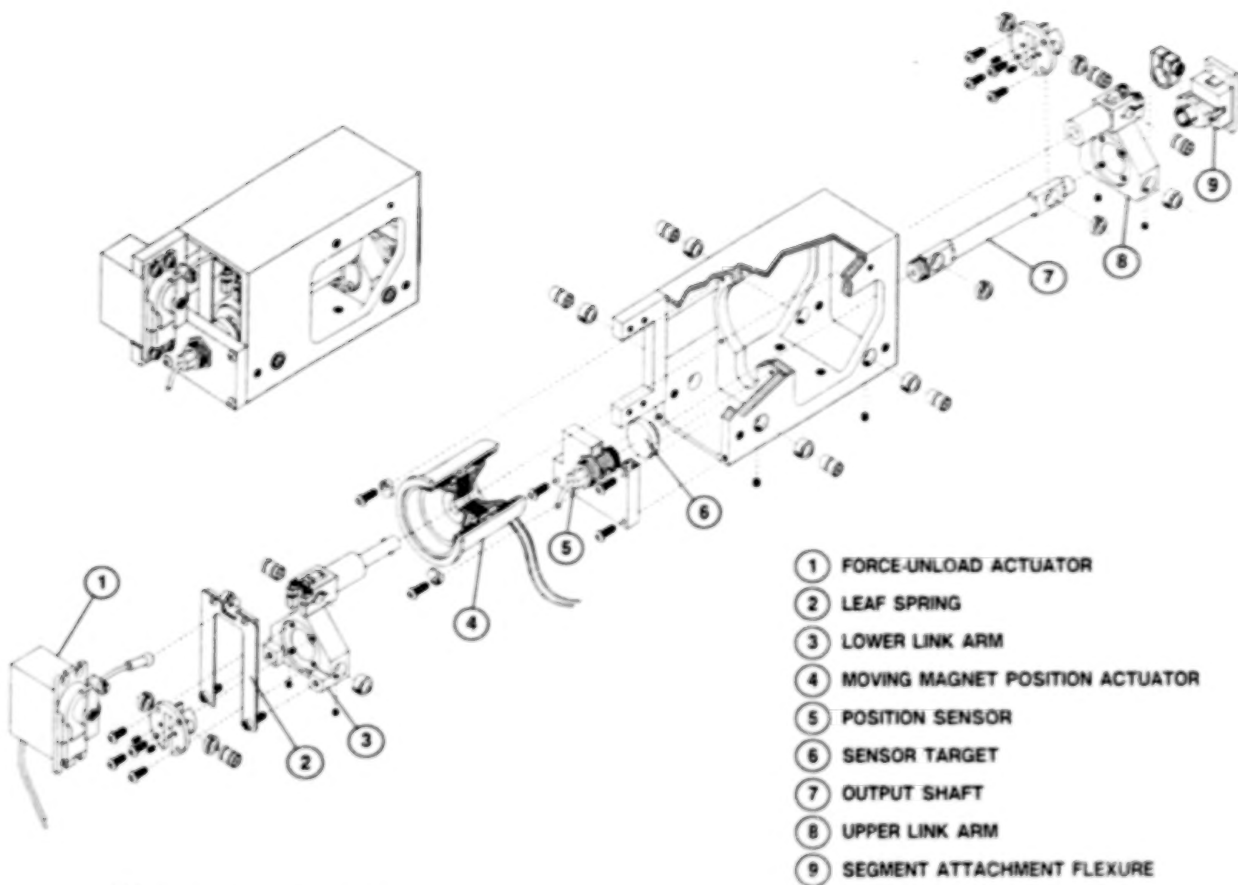


Figure 4. Exploded view of actuator mechanical components.

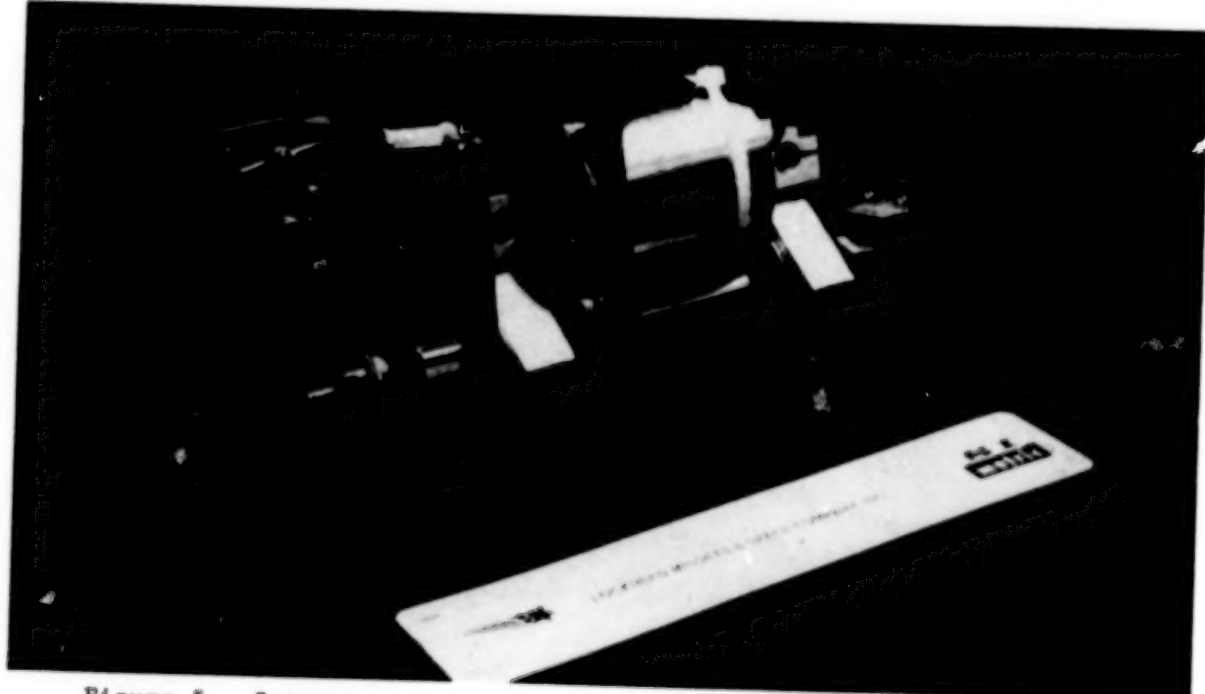


Figure 5. Cutaway version of actuator showing internal assembly.

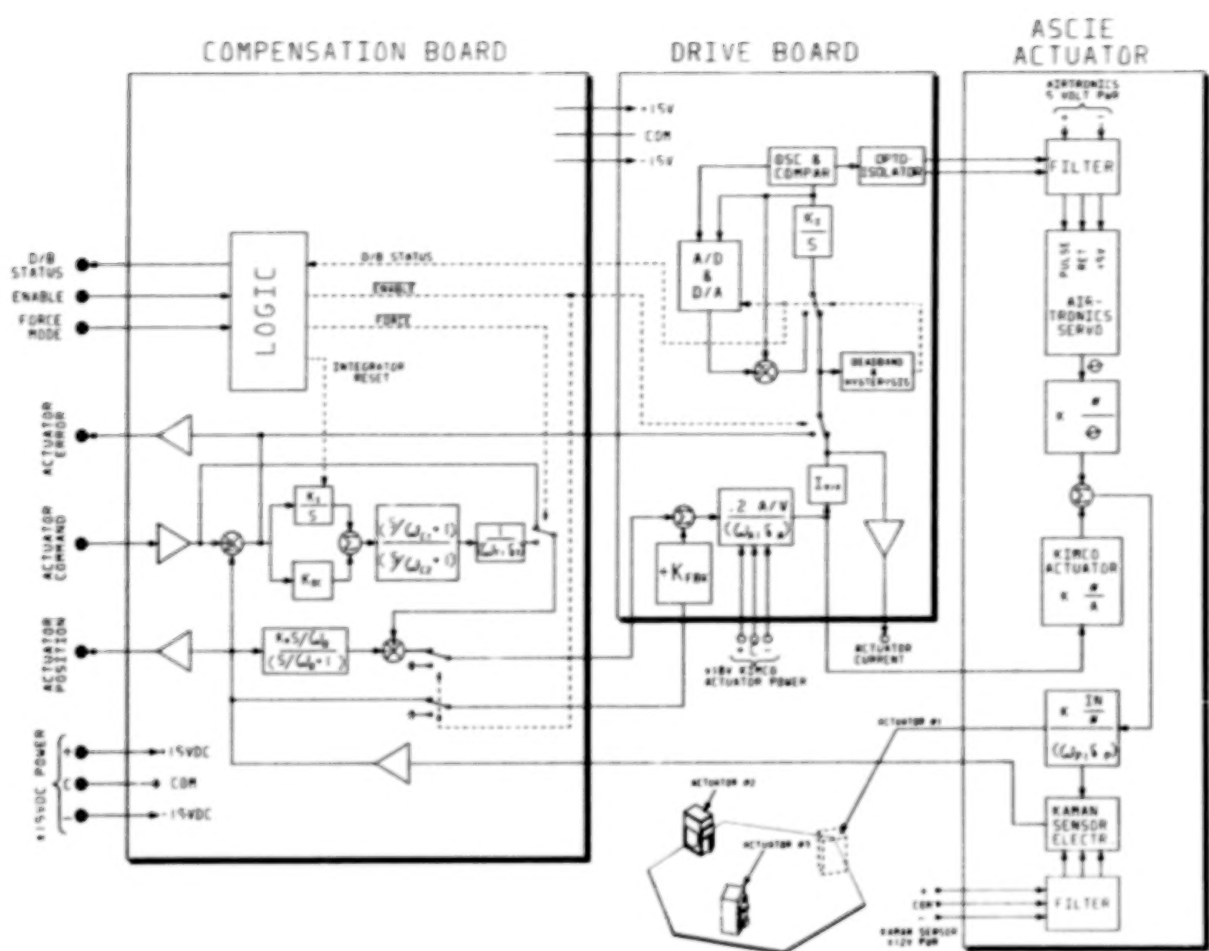


Figure 6. Schematic block diagram of actuator electronic control system.

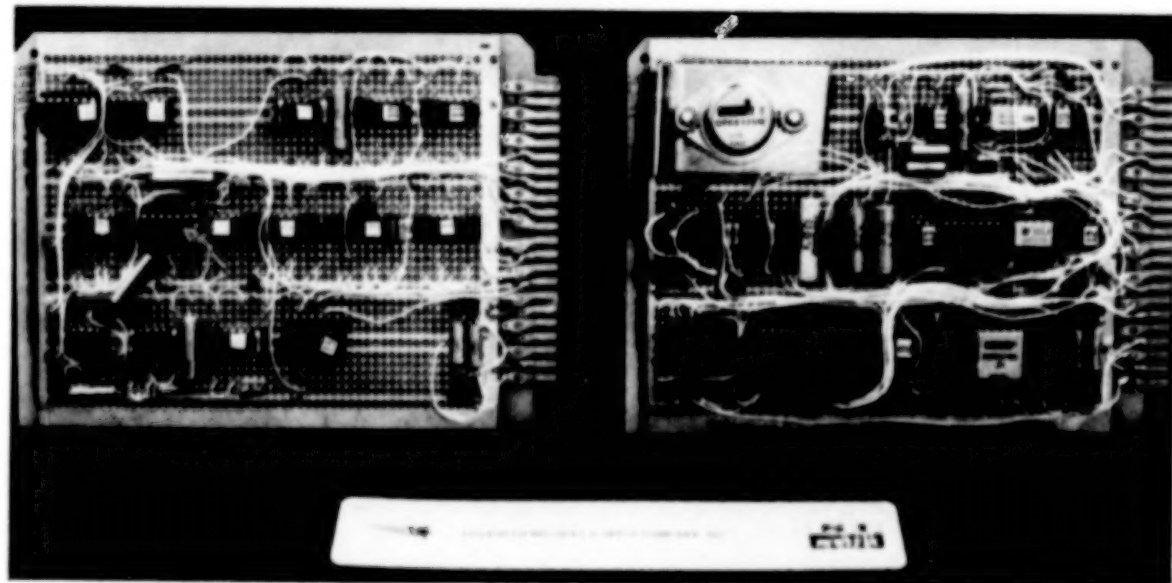


Figure 7. Electronics required for actuator drive and control.

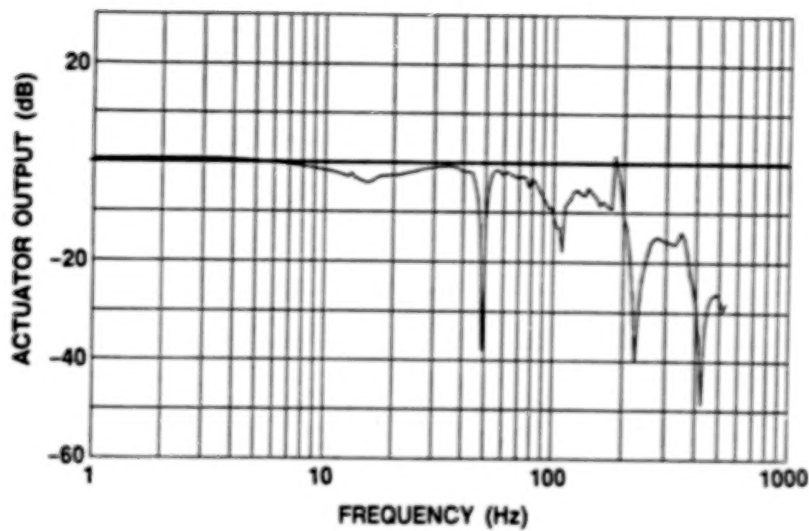


Figure 8. Bode plot of actuator response.

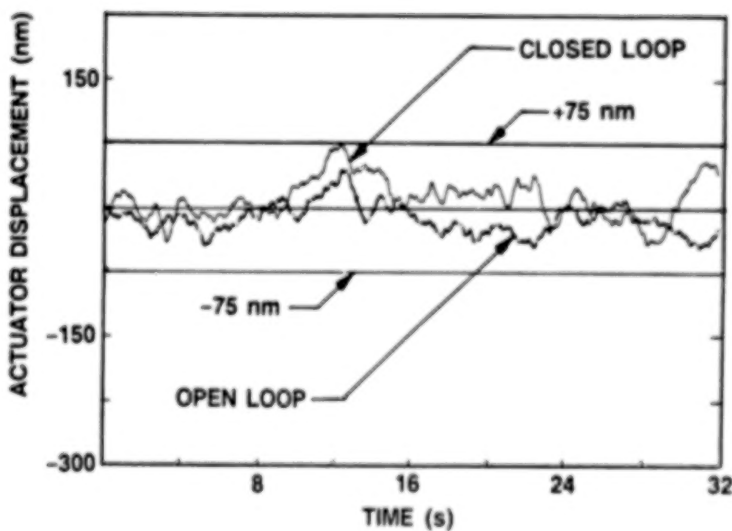


Figure 9. Actuator position noise under open- and closed-loop conditions.

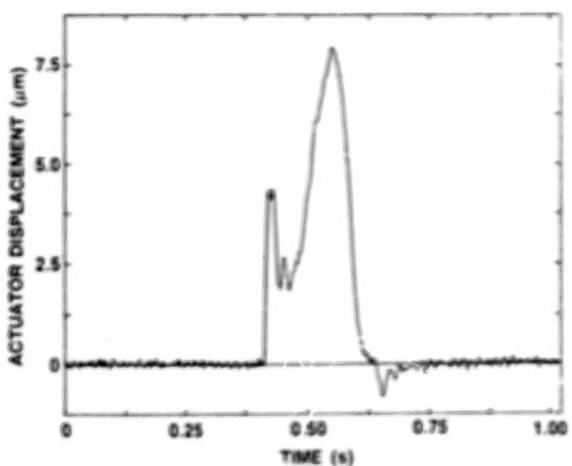


Figure 10. Actuator position response to a step increase in applied load.

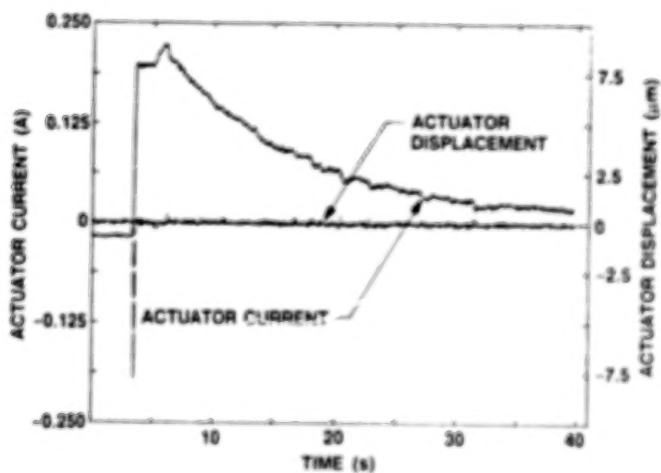


Figure 11. Actuator position response and current required after a step increase in applied load.

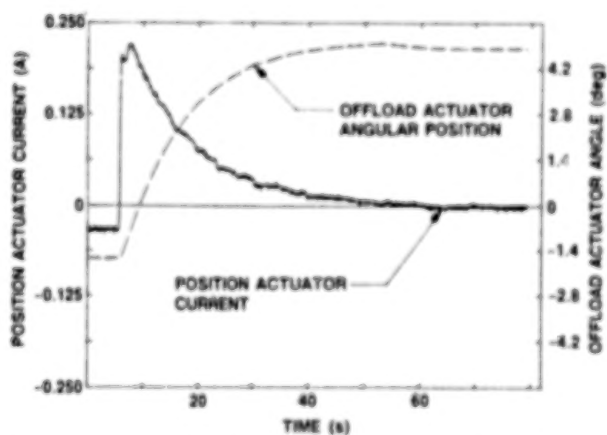


Figure 12. Actuator position response and motion of offloading actuator control arm after a step increase in applied load.

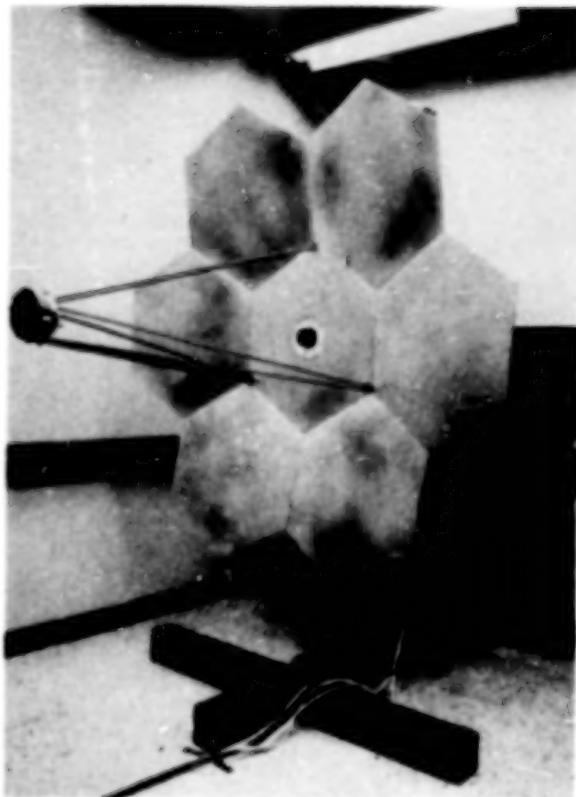


Figure 13. Front view of the Advanced Structures/Control Integrated Experiment (ASCIE).

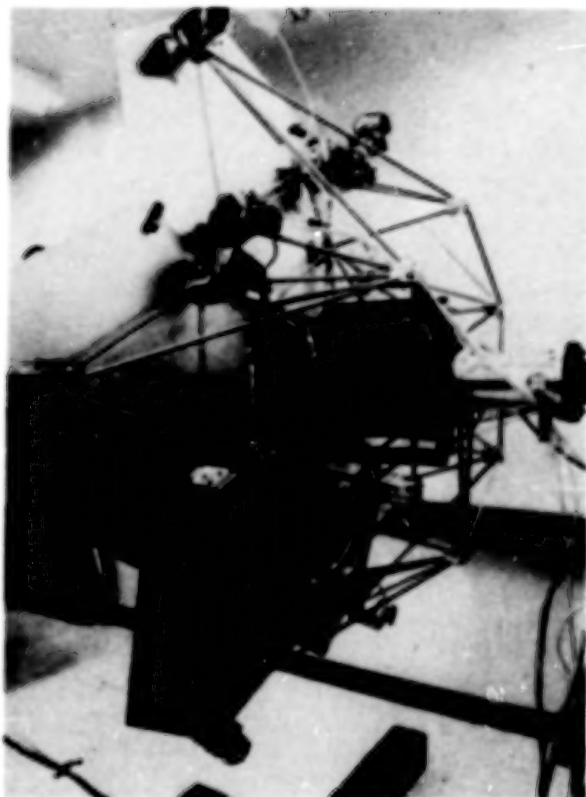


Figure 14. Rear view of ASCIE showing locations of segment-control actuators.

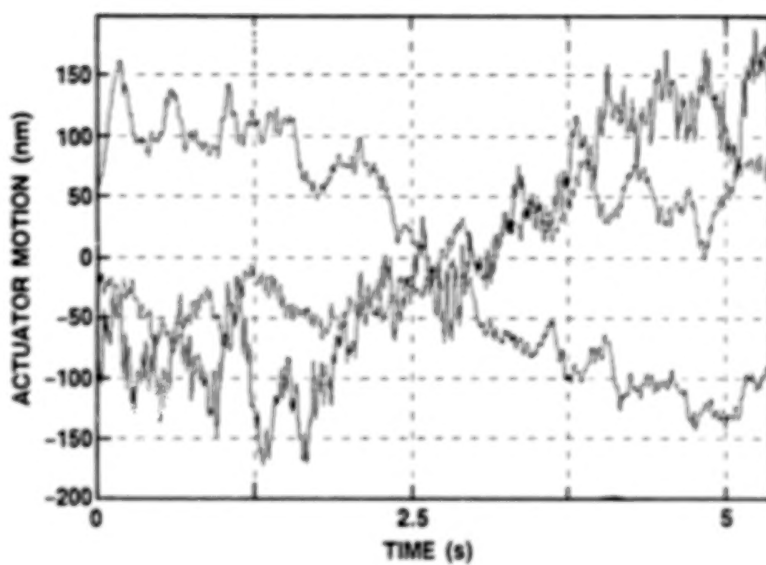


Figure 15. Actuator motion during 5-sec period while controlling the tilt and piston of an ASCI segment.

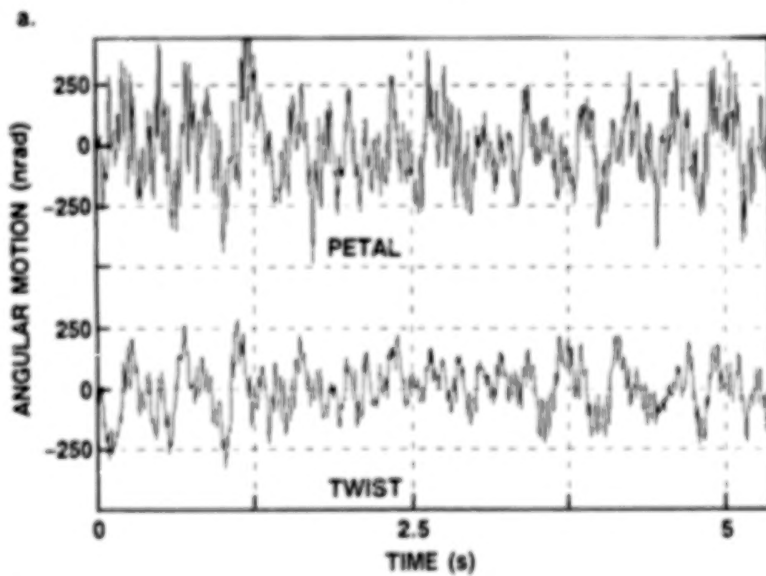
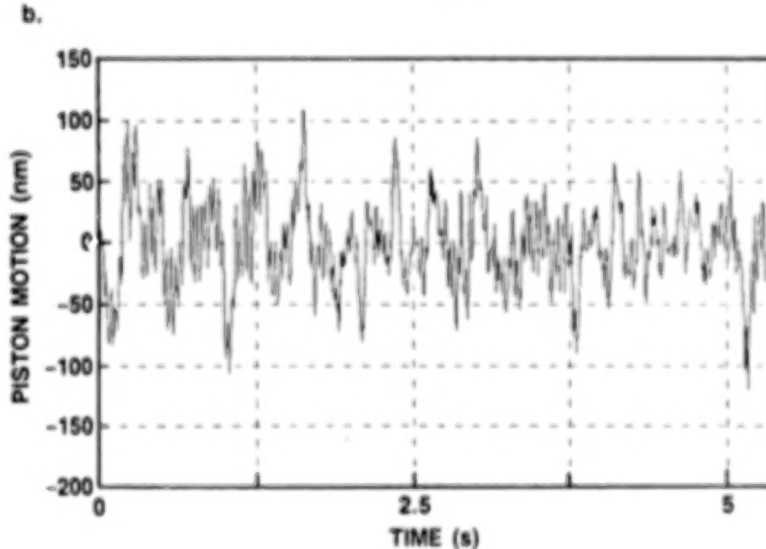


Figure 16. Segment tilt and piston errors corresponding to the same 5-sec period as actuator motion seen in Figure 15.



PYRO THRUSTER FOR PERFORMING ROCKET BOOSTER ATTACHMENT,
DISCONNECT, AND JETTISON FUNCTIONS

Stephen Hornyak*

ABSTRACT

The concept of a pyro thruster, combining an automatic structural attachment with quick disconnect and thrusting capability, is described herein. The purpose of this invention is to simplify booster installation, disengagement, and jettison functions for the U.S. Air Force's Advanced Launch Systems (ALS) program. A principal objective of the ALS program is to significantly reduce space transportation costs from those incurred with present launch vehicle systems.

INTRODUCTION

This pyro thruster study was made in support of the ALS program's charter, to create an economical and affordable "next-generation" space transportation system. ALS will provide routine access to space for large payloads in less than three weeks launch processing time, and will have higher reliability and safety standards than current expendables.

The payload delivery cost per pound to orbit will be reduced 90 percent compared to Titan IV recurring costs. Titan IV represents the benchmark for the ALS cost-reduction goal. This goal, as mandated by Congress, is defined as the average cost per pound of payload delivered to the ALS mission model, scheduled in the beginning of the 21st century.

This tenfold reduction of recurring costs in the area of manufacturing and launching the ALS will be achieved by using increased launch vehicle size, simplified vehicle configuration, higher production rates, larger production quantities, and improved business, competitive, and management practices. Significant technical contributors to the cost reduction include incorporation of appropriate new technologies and producibility improvements; emphasis on robustness built into a simple design to obtain higher reliability; cost-effective application of reusability techniques; and a practical, high-level automation of the vehicle integration and launch processes.

This cost reduction goal must also be reachable in terms of nonrecurring costs, up-front investments, and automation such as robotics and artificial intelligence.

*General Dynamics Space Systems Division, San Diego, California.

TECHNICAL DESCRIPTION

A typical arrangement for the booster aft and forward attachments to the core is shown in Figures 1 and 2, respectively. Each booster is attached to the core by two ball joints aft and one ball joint at the front of the booster. Each ball joint is attached to the housing of a pyro thruster by a collet chuck that has four collet grips, as illustrated in Figure 3. The four collet grips are seated in a slotted and grooved nut and are held in the locked position by a plug threaded to the piston rod. The ball race block has the shape of a stepped cylinder. It is lowered into the mating groove of the core's retainer block and latched in place automatically, as shown in Figures 3 and 4.

One of the two aft thruster housings branches out into three struts, forming a tripod. The ends of the tripod are pinned to the booster through monoballs, as shown in Figure 1. The tripod provides stability for the booster.

The other aft thruster housing branches out into two struts, forming a bipod. The bipod ends are pinned to the booster through monoballs (see Fig. 1). The bipod serves as a sway arm, allowing for relative motions between booster and core diameters.

Figure 2 depicts the forward attachment. The forward ball joint at the core interface is similar to the aft interface. The forward thruster housing branches out into a pivoting fork. These fork ends are pinned to the booster through monoballs. The pivoting fork, in combination with the thruster's ball joint, allows for large relative motions between booster and core along the longitudinal axes.

The pyro thruster has dual cartridges (see Fig. 3) to assure single-failure-tolerant jettison function. Booster disengagement and jettison are initiated by a guidance and control staging command to the laser fiber-optic controller. Disengagement occurs after cartridge ignition develops gas pressure, which forces the piston rod to unlock the collet plug. This causes the collet grips to collapse into the plug recess, unlocking the load-carrying ball. Increasing piston pressure rams the rod against an energy-absorbing stop, causing the thruster housing to move away from the interface. Thrusting characteristics are tailored to minimize shock (see Fig. 5).

The separation system is single-failure-tolerant for the separation function and dual-failure-tolerant against inadvertent pyro firing. High reliability is achieved through a simple, robust design, maximizing the use of proven technology and hardware.

All interfaces, including electrical umbilicals, are simple and accessible to facilitate installation, maintainability, and replaceability. No alignment or adjustment is required during installation; interfaces of all mating components are prealigned at factory level.

OPTIONS AND TRADE STUDIES

The following separation methods and combinations thereof have been investigated, and corresponding trade studies have been performed:

- Separation motors such as solid propellant staging rockets are costly, heavy, and inefficient.
- Of existing technologies, pneumatic pistons come closest to pyro thrusters, but have more parts and therefore less reliability.
- Coil or disk springs are large, heavy, and difficult to install.
- Kinematic methods (hinged booster aft attachment) require a large pivoting envelope.
- Mechanisms such as power-driven ganged latches, collets, or ball locks operated by ganged power hinges are complicated and heavy, with low reliability.
- All of the above-mentioned methods require additional explosive bolts or nuts, which increases complexity and cost while lowering reliability.

In commonly accepted practice, the booster disengagement and jettison functions are powered by separate energy sources. The structural joints are severed by pyrotechnic means, and then the booster is jettisoned using suitable thrusters. In most cases, the booster-to-core vehicle installation is difficult and requires time-consuming alignment operations.

The pyro thruster affords many advantages over other separation methods. The pyro thruster:

- Eliminates pyro fasteners at the three interface joints (such as explosive nuts or bolts)
- Is an integral part of the attachment structure
- Disengages the interface joint and performs the separation and jettison functions in one continuous stroke
- Requires minimum installation time (no alignment during installation)
- Reduces weight and cost
- Increases reliability
- Offers trouble-free producibility.

A novel feature of the pyro thruster is the incorporation of a unique and simple collet chuck, which is ideal to take the high interface loads while serving as a quick disconnect. The thruster is incorporated into the attachment structure, a new and outstanding feature of the separation system.

The pyro thruster concept shows these distinct advantages and is scheduled for further development. During the next four years, in Phase II of the ALS program, pyro thruster requirements will be finalized, preliminary design will be completed, and a prototype will be built and tested.

BOOSTER INSTALLATION

The booster is attached to the core in the vertical position. Booster installation is accomplished by using a handling yoke and an automated overhead crane, as shown in Figure 6. Attached to the yoke, the crane rotates and moves the booster out of the transporter using CAD-assisted computer control, verified by modern laser alignment technology for multi-axis automatic positioning. Continuous crane operation moves the booster into the mating position and aligns the ball races with their retainers at the three booster-core interfaces. After the races are lowered and seated, the retainer latches are activated and the ball races are captured (see Fig. 4). The retainers have tapered guiding surfaces for the races, to facilitate mating and to help relax the accuracy of the position control system.

The joints at the booster-core interfaces are designed to have liberal tolerances. Widening the manufacturing and alignment tolerances lowers cost and installation time, but causes a greater degree of booster-core misalignment, which in turn has an effect on flight control. This problem, however, can be solved by adding more power to the engines and widening their gimbal angles. This is a good example of the fundamental tendency in the ALS design philosophy of trading high performance for robustness.

High launch rate requires minimum installation time. Core-booster attachment hardware and positioning equipment must be robust, simple, and efficient. The core-booster integration operation must be automated to the highest practical and affordable degree.

During ALS Phase II, the requirements for booster handling, positioning, and installation will be finalized.

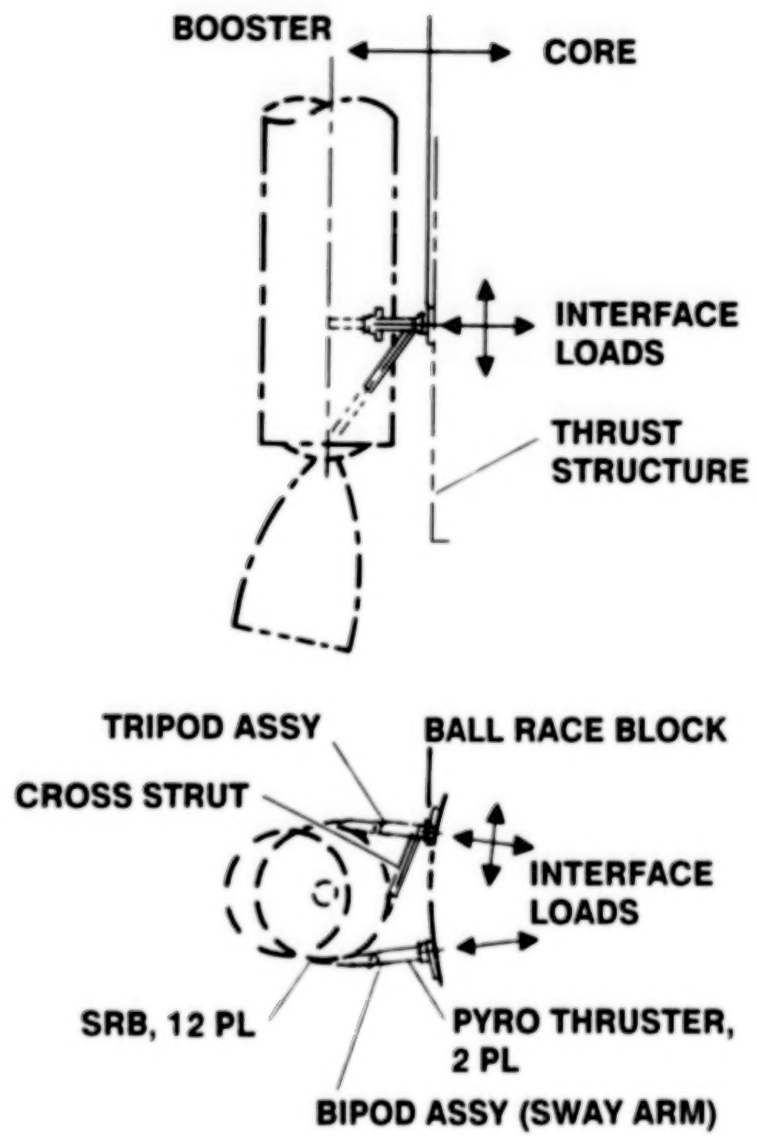
CONCLUDING REMARKS

Special attention and understanding are required to correctly interpret the relationship of robustness and redundancy in terms of reliability and safety, as applied to the ALS program. Explicit definitions, illustrated by examples that describe the meaning of this relatively new and difficult relationship, are needed to enrich and update the dictionary of technical terms. These definitions must then be tailored to ALS structural, mechanical, fluid, and electrical engineering applications. The definitions would be instrumental in guiding the design and failure mode analyses efforts.

Replacing high performance with robustness is a relatively new phenomenon in the modern aerospace business. To eliminate doubt and differing opinions during the design phase, mutual agreement on the interpretation of definitions is mandatory. In recent years, misdirection due to lack of unanimous interpretation of redundancy versus equivalent redundancy has led to disagreements. This resulted in design changes, impacting schedule and cost [1]. The technical term "equivalent redundancy" is being replaced by the more attractive word "robustness."

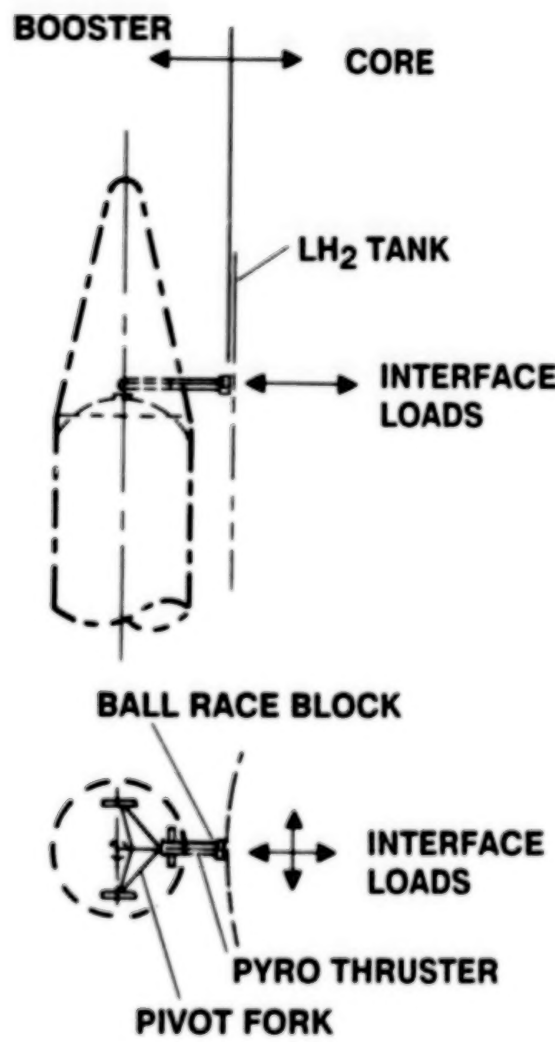
REFERENCES

1. Hornyak, Stephen: Inherent Problems in Designing Two-Failure-Tolerant Electromechanical Actuators. Proceedings of the 18th Aerospace Mechanism Symposium, May 1984, NASA Conference Publication 2311.



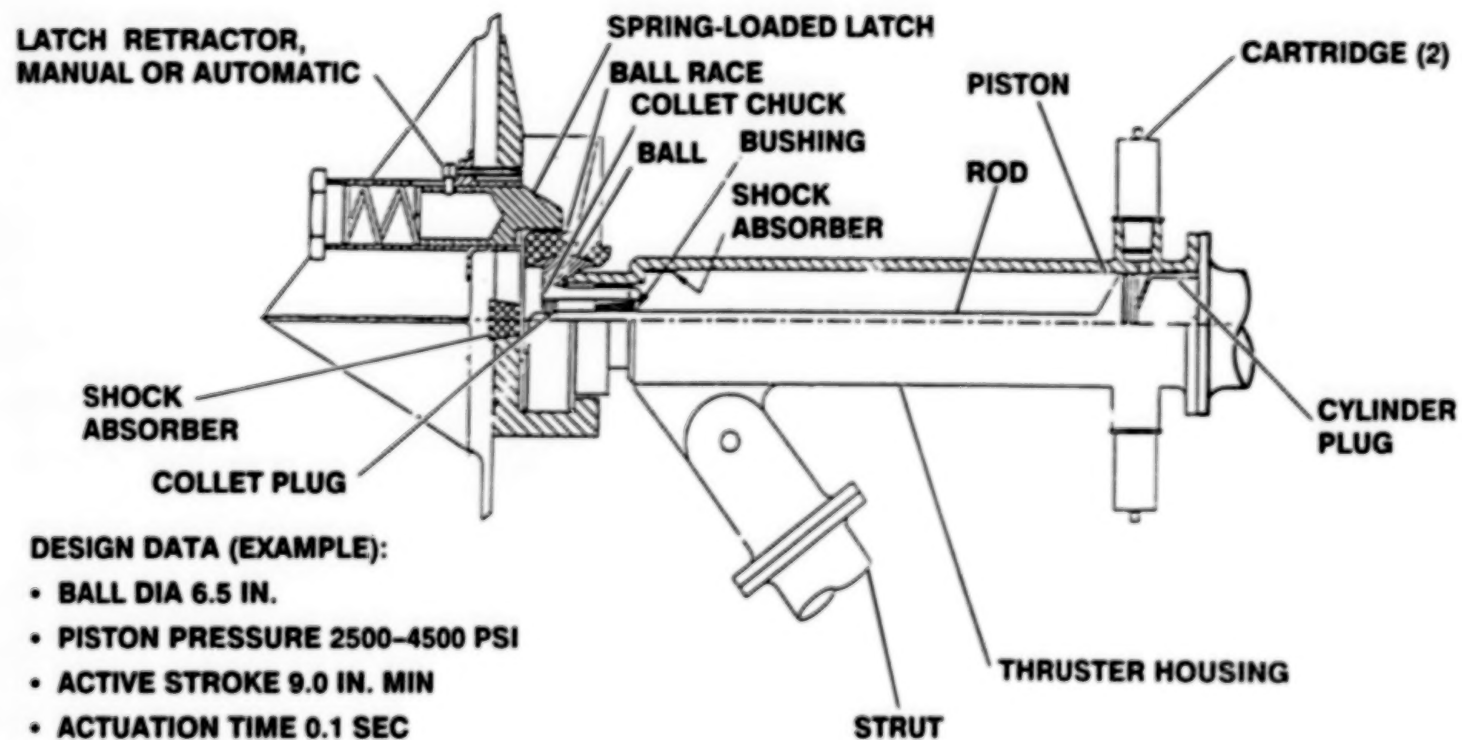
GST9228-1

Figure 1. Aft attachment.



GST9228-2

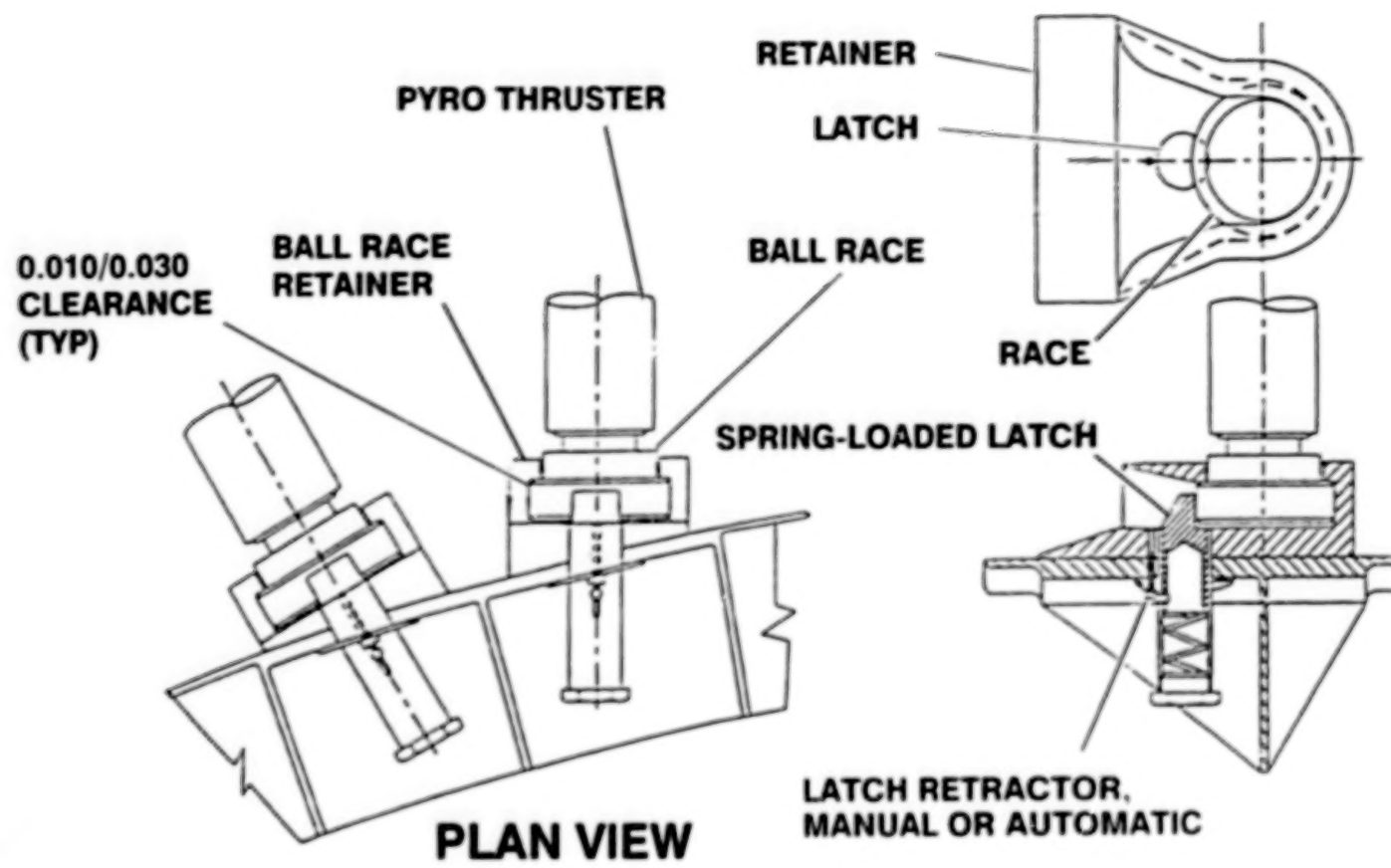
Figure 2. Forward attachment.



GST9228-3

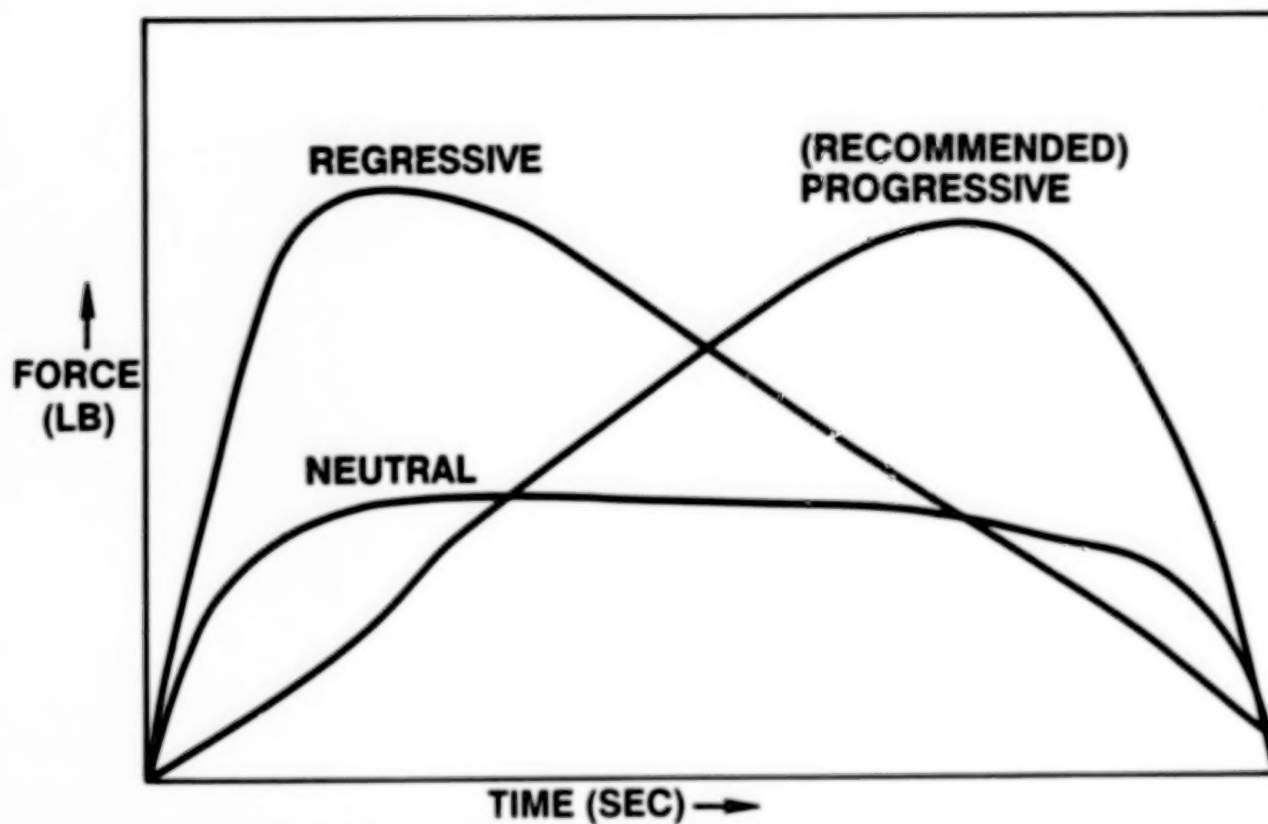
Figure 3. Pyro thruster quick disconnect (side view).

164



GST922B-4

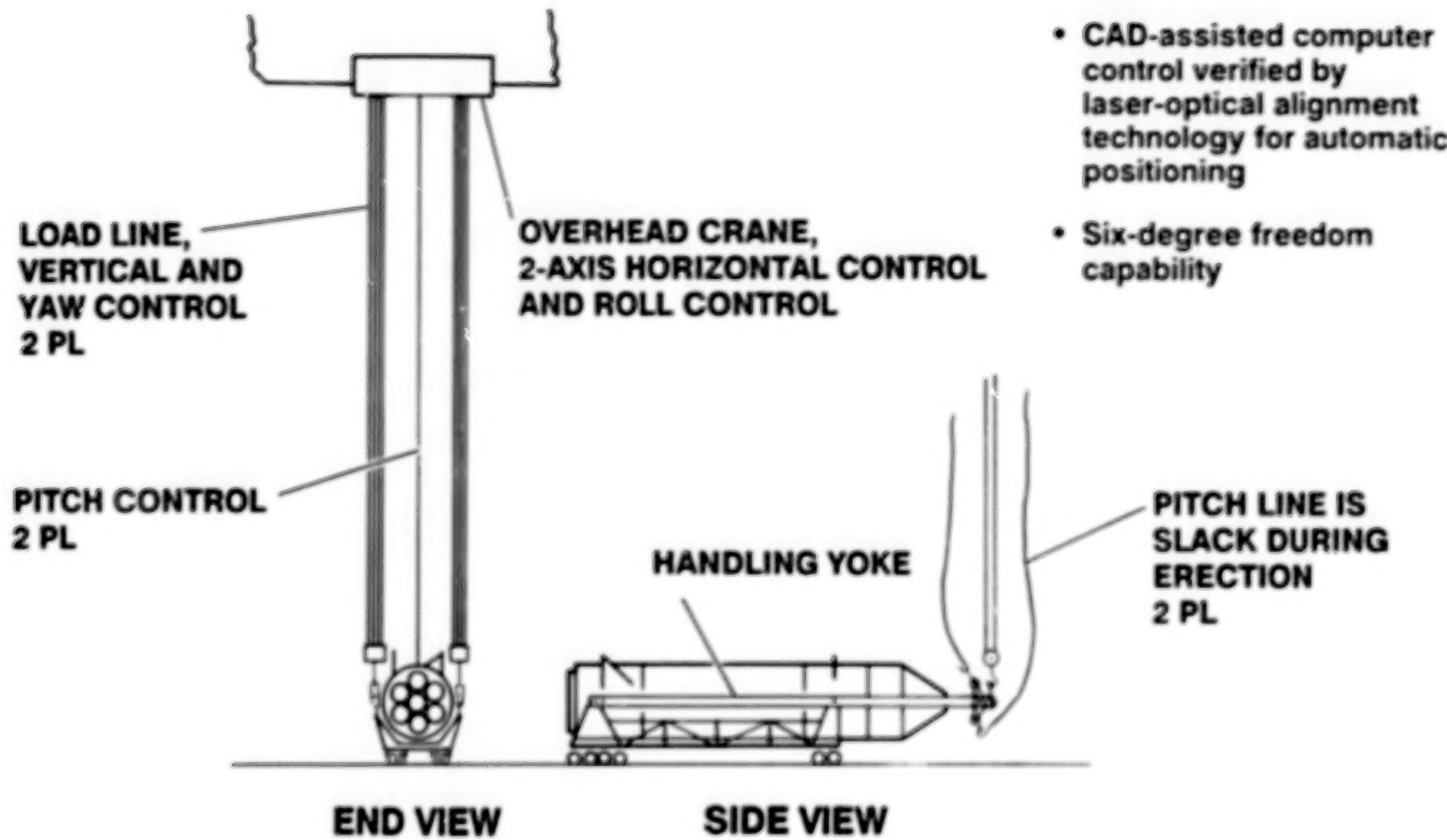
Figure 4. Automatic pyro thruster attachment.



PRESSURE AND FORCE VERSUS TIME ARE DEPENDENT UPON PROPELLANT GEOMETRY AND ARE THEREFORE TAILORABLE TO A CERTAIN EXTENT.

GST9228-5

Figure 5. Cartridge thrusting characteristics.



GST92266

Figure 6. Automated handling and positioning concept for core, booster, or shroud.

BLANK PAGE

DESIGN AND DEVELOPMENT OF A HIGH-STIFFNESS, HIGH-RESOLUTION TORQUE SENSOR

Michael M. Socha* and Boris J. Lurie*

ABSTRACT

The accuracy of precision pointing systems is often diminished by the inevitable presence of nonlinear drag torques resulting from rolling bearing friction and power/signal transfer cabling across rotary joints. These torques are difficult to characterize and impossible to predict analytically. However, the sensor described here provides torque knowledge that can be utilized by the controls designer to compensate for these nonlinearities. A prototype torque sensor has been built and tested, demonstrating that such a device is feasible for space-based precision pointing systems.

INTRODUCTION

Precision pointing applications require adequate knowledge of the system variables. Sensing torque directly in the precision motion control of spacecraft science platforms is recognized as a sound approach to significantly improving pointing performance. However, mechanical implementation and optimal control design remain challenges.

Previous torque-sensor designs are unacceptable for spacecraft science-platform articulation control. The problem is that the resulting devices are too flexible and of low resolution and low bandwidth. Existing designs today utilize displacement sensors configured on a flexible structure or shaft. Most designs use strain gauges as the sensing element, requiring rather flexible structures to obtain usable output signals. Other sensing elements suffer from the same flexibility and dynamic range limitations, or would require equipment too large or too complex to be incorporated practically.

A unique sensor has been designed and tested with encouraging results. The device uses a novel approach to sensing extremely small rotary motion, yet remains immune to cross-axis forces.

This paper presents a description of the hardware and design characteristics of the newly developed torque sensor, along with preliminary test data, a brief description of an integrated control methodology, and future applications.

*Member Technical Staff, Guidance and Control Section, Jet Propulsion Laboratory, California Institute of Technology, Pasadena, California.

GENERAL DESIGN REQUIREMENTS

The following summarizes the requirements and the assumptions considered in designing the torque sensor. The primary design objective was to maximize stiffness in all nonrotational axes. In terms of dynamics, the device is required to provide extremely fine resolution over a wide torque range, to possess wide sensor bandwidth, to have high signal/noise electrical characteristics, and to have minimum hysteresis. Also it must be reliable in a space environment, i. e., designed to withstand launch loads, survive radiation exposure, and satisfy electronics qualification requirements. Finally, as in all space applications, devices must have low mass and low power consumption, and be inexpensive to manufacture.

The prototype torque sensor discussed in this paper was sized to fit existing hardware and designed to meet the following specifications, which reflect equivalent requirements for a representative science pointing application:

Torque Range	0.01 N-m - 10.0 N-m
Torque Resolution	0.001 N-m
Signal/Noise	10:1
Structural stiffness	>50Hz
Hysteresis	Minimum (10% Goal)

HARDWARE DESCRIPTION

The torque sensor consists of the sensing element, a flat-spoke support structure, interface plates, and associated signal conditioning and amplifier electronics.

Element

The heart of the torque sensor is the sensing element. Many types of load cells could be configured in the sensor, but to produce usable output signals, they must be mounted on a flexible structure or configured with a lever system to gain a mechanical advantage.

To obtain the highest displacement sensitivity, piezoelectric ceramic material was selected. The inherent characteristics of this material result in extremely high sensitivity, and the property of this material applied here is the electric polarization on its surface produced by mechanical strain. Conversely, when a field is applied to piezoelectric material, it changes dimensions in all three axes. The degree to which these dimensions change relative to the applied field is expressed as the d constant. This constant is the stress-free ratio of developed strain to applied field. The

piezoelectric material selected for the torque sensor is from the lead-zirconate-titanate (PZT) family and has a d constant of approximately 110 C/N. A usable output signal must be obtained to resolve torque to the 0.001 N-m resolution specified as a design goal. Based on calculations using the assumed d constant, Young's modulus of 7.3×10^{-10} N/m², and a 2-mm thick, 5.07×10^{-4} m² area element, an output of 3.4 V would be achieved for 0.001 N-m of torque.

The required sensitivity relates to the extent to which the effects of coulomb friction from bearings, cables, and motor cogging must be reduced. This sensitivity is well within the capabilities of a torque sensor using a piezoelectric element. The torque sensor also has a large dynamic range that covers the maximum motor torque to the minimal error that must be corrected.

When purchased, the element was mounted to a brass baseplate to facilitate electrical connection, and the surfaces of the element were silvered for the same reason. One lead of a coaxial cable was soldered to the baseplate and the other to the element directly. Figure 1 shows the element placed between a mica insulator and a copper disk. Since the electric field is exposed at the surface of the element, the mica insulator isolates it from the mounting bracket. On the other side, the copper disk can pick off the electrical signal and distribute the preload force over a larger area of the element. The assembly is preloaded to remove compliance in the stack and creep in the assembly.

Flat Spoke Member

This member is a circular ring with thin, flat spokes machined radially along the circumference (see Fig. 2). It supports the sensor element along with its mounting brackets and provides structural stiffness. The flat spoke design provides a large aspect ratio to minimize deflection across the axis of rotation, and yet allows deflection about the rotation axis. The plate was machined from a single piece of 1.9-cm thick, 6061 T aluminum plate. A 15-cm hole is located at the center to lighten the component and, if necessary, allow passage of power and signal transfer cables through the device. The spokes measure 2-mm thick and approximately 2.5 cm in height. The goal was to make the spoke as thin as possible to maximize deflection in rotation and yet wide enough to resist moments across the axis of rotation. Maximum flexibility in rotation is needed to sense extremely small forces. This was accomplished by analyzing the spokes as simple cantilever beams with a very high aspect ratio to determine the optimum dimensions.

The end of each spoke has, parallel to the axis of rotation, a bolt hole for mounting to the interface plates. The diameter of the mounting pattern is 30 cm. Mounting consists of attaching alternating spokes to one plate, and the remaining spokes to the other plate. The equal mounting diameter maintains through-connection stiffness.

The use of multiple sensors positioned symmetrically around the device increases system stiffness and mechanical symmetry, and provides redundancy.

Only one element is needed to provide torque knowledge, so, in the event of a failure, any of the other elements could be activated.

Interface Plates (Fig. 3)

The interface plates serve two purposes. The first is to adapt the mechanical interfaces of the mounting structure to the spoke member described above. The second is to allow connection to alternating spokes. If the spoke member were mounted to a flat surface, rubbing would occur, restricting motion of the flat spokes. Protection against this is accomplished by machining standoffs on one side of each plate.

Launch Protection Assembly

The torque sensor must be rugged, reliable, and capable of withstanding launch vibration. The most sensitive component is the ceramic sensing element. Ceramic materials must be protected from shear and bending loads.

Due to the brittle nature of the ceramic material, a reliable method of protecting the device needs to be developed. A design concept for a launch protection assembly is presented. This device was not built during development of the prototype sensor. These materials are used most advantageously in a compressive loading condition.

The design shown in Figure 4 is believed to satisfy these requirements. The design shows an assembly that houses the brittle piezoelectric element so that shear and bending loads are eliminated and the element is subjected only to compressive loads. The drawing shows the fixed/floated combination for containing the element. The fixed side maintains the axial position of the element and carries part of the load. The other side is allowed to move axially in the other direction by means of a spring-loaded support. The spring's primary purpose is to relieve axial loads. It also relieves axial strains, such as those due to differentials in temperature or thermal expansion coefficients. The steel ball is used to alleviate loads and motion from the other degrees of freedom by allowing the element to roll when subjected to rotation or translation.

Electronics

A standard FET amplifier was used in this design and located as close to the sensor as possible. Sensor packaging must protect against thermal effects and interference from electromagnetic (EMI) sources such as the actuator motor.

PROTOTYPE TESTING

Testing of the prototype device was done to examine some of the fundamental design characteristics and to evaluate preliminary performance. The torque sensor was tested to determine the following:

- Cross-axis coupling
- Hysteresis
- Rotational stiffness
- Motor cogging.

Prototype testing of the torque sensor utilized existing hardware wherever possible to minimize development time and costs. The prototype sensor was sized to fit existing actuator hardware. However, the sensor could be made in any size to fit the application. A pointing control test-bed, located in JPL's inertial lab, was utilized to evaluate design characteristics and preliminary performance. The test-bed was designed for single-axis testing of precision actuators and pointing control algorithms. The test-bed adapts to different types of actuators and varying payload inertias. The actuator and payload are mounted on an air bearing to provide isolation and a frictionless rotary joint. The air bearing is configured with a calibrated spring connection between the levitated portion of the air bearing and ground, to simulate spacecraft boom rotational stiffness. The entire assembly is isolated from ambient noise by a concrete seismic pier. Test equipment includes dedicated microprocessor control electronics, a two-degree-of-freedom (DOF) rate gyro to measure platform motion, and data-acquisition equipment.

First calibration, sensor noise levels, and scale factor tests were performed to verify the sensor's operation and characterize its output signal.

Cross-axis coupling was determined by mounting the torque sensor on a horizontal test bench with the rotation axis parallel to the bench. Coupling from other axes would mean that forces not along the torque axis were detected by the sensor. This would corrupt the true torque knowledge to the controller and result in an incorrect torque command from the actuator. A rigid torque arm was bolted to one interface plate and the other plate secured to ground. A force was applied to the torque arm in different directions and the sensor output signal observed. It was found that cross-axis coupling significantly decreased with the steel-ball mounting arrangement, reducing the cross-axis signal to 10 percent of the rotation axis. The 10 percent cross coupling is felt by control analysts to be an acceptable value for three-dimensional pointing control to work properly.

Appraisal of hysteresis is important in all precision motion control systems. All mechanical systems exhibit hysteresis to some degree. Hysteresis represents lost motion that cannot be accounted for and therefore must be sensed and corrected. This is accomplished at the expense of additional hardware and control complexities. Every effort to minimize this lost motion should be taken. To determine hysteresis in the assembled device, the torque sensor was again mounted on the horizontal test bench with the rotation axis parallel to the bench. The rigid torque arm was mounted to one interface plate and the other plate secured to ground. Rotational motion

was sensed by an electronic gauge. An incrementally increasing load was placed on the torque arm and the corresponding rotational motion recorded. Then the load was removed in the same increments and the resulting motion recorded. Results of this test indicate a maximum hysteresis of 4.9 percent over a torque range of 0 to 18 N-m.

Rotational stiffness of the torque sensor was tested next. The test configuration is shown in Figure 5, which represents the payload inertia oscillating at its natural frequency on the science-platform boom. The torque sensor must not noticeably increase the flexibility in the support structure. The sensor assembly stiffness should be at least an order of magnitude larger than the stiffness of the boom. A requirement of 50 Hz for the assembly's natural frequency was selected. One sensor element was installed between two spokes and preloaded by the mounting brackets. Tests were performed with jumper bars attached to the remaining open spokes to vary the overall stiffness and determine the minimum output signal from the sensor. Once firmly tightened, an impulse input was commanded to the actuator. Payload motion was sensed by the gyro located on top of the structure along the axis of rotation and recorded. Minimum stiffness about the rotation axis was found to be 63 Hz.

Finally, the motor cogging test was performed. Cogging is defined as the variation in torque due to the interaction of the armature magnets with the iron lamination. It is position-related and independent of excitation. For this test, the torque sensor was mounted between the base of a direct drive actuator and ground. The actuator motor was a two-phase, 24-pole-pair, permanent-magnet, brushless, dc type. The motor was designed to generate a sinusoidal back-EMF signal with minimum harmonic distortion for low ripple characteristics. Low cogging torque is achieved by the use of nickel-iron lamination material and skewing of the lamination to cover as much of the space between the permanent magnets as possible. The test was performed with the air bearing turned off, using quartz, a natural piezoelectric material, as the sensing element. A constant rate input of 0.39 rad/sec was commanded to the actuator. Figure 6 shows a plot of the torque sensor output. The variations in the output can be seen to correspond to the motor pole frequency at the input rate.

INTEGRATED CONTROL METHODOLOGY

Bridge-type feedback control is used extensively in electrical communication engineering with great success. Specifically, it greatly reduces the loop transfer function variations caused by uncertain conservative resonant loads, and thereby allows much higher feedback and better accuracy of control. Use of a similar control scheme in mechanical actuation systems, driving flexible structures, also provides enhanced control capability, but it necessitates using two sensors at the junction of the actuator and load simultaneously. One provides angular velocity and the other provides torque.

Recently, the balanced bridge control theory (BBT) was developed at JPL to take advantage of several nested bridge-type feedback loops. The BBT

allows for large, wideband feedback around the actuator, greatly reducing the effects of imperfections caused by friction and cogging. In this way, a nearly ideal actuator can be implemented and used as a building block for precision pointing control.

OTHER APPLICATIONS

Sensor applications include spacecraft precision pointing and articulation control, distributed decoupling control of multilink systems (artificial limbs, manipulators, etc.), and large flexible structures.

SUMMARY

It has been demonstrated through design, development, and testing that the suggested torque sensor is feasible. The main design feature of the torque sensor that makes it unique is the novel configuration of the sensor support structure, which provides rotational compliance for the detection of small forces and cross-axis stiffness for isolation.

A prototype sensor has been built and tested to characterize its fundamental operating properties and has been used to measure motor cogging torques in a precision actuator.

This device provides increased control feedback knowledge for the precision science-platform pointing controls engineer without introducing "in-the-loop" flexibility. There are numerous applications for this technology in complex control systems and in precision motion control.

ACKNOWLEDGMENTS

The research described in this paper was performed by the Jet Propulsion Laboratory, California Institute of Technology, under contract with the National Aeronautics and Space Administration.

REFERENCES

1. Smoak, Richard H.: Materials Used in Devices for Active Control of Large, Flexible Space Structures. IOM 335/DS.0002.RD, June 21, 1988 (JPL internal memo).
2. Kynar Piezo Film Technical Manual, Pennwalt Corporation, Kynar Piezo Film Department, Valley Forge, PA (includes many further references).
3. Lurie, Boris J.: SRE Boom Torquer Control, and Torque Sensor Design. IOM 343-1074, October 8, 1987 (JPL internal memo).
4. Socha, Michael M., Lurie, Boris J.: Torque Sensor Development Program. IOM 343-88-1134, February 9, 1988 (JPL internal memo).

5. Lurie, Boris J.: Three Loop Balanced Bridge Feedback Motor Control. IOM 343-1058, April 15, 1987 (JPL internal memo).
6. Lurie, Boris J.: Three Loop Balanced Bridge Feedback Pointing Control. Proceedings of the American Control Conference, Atlanta, GA, 1988.

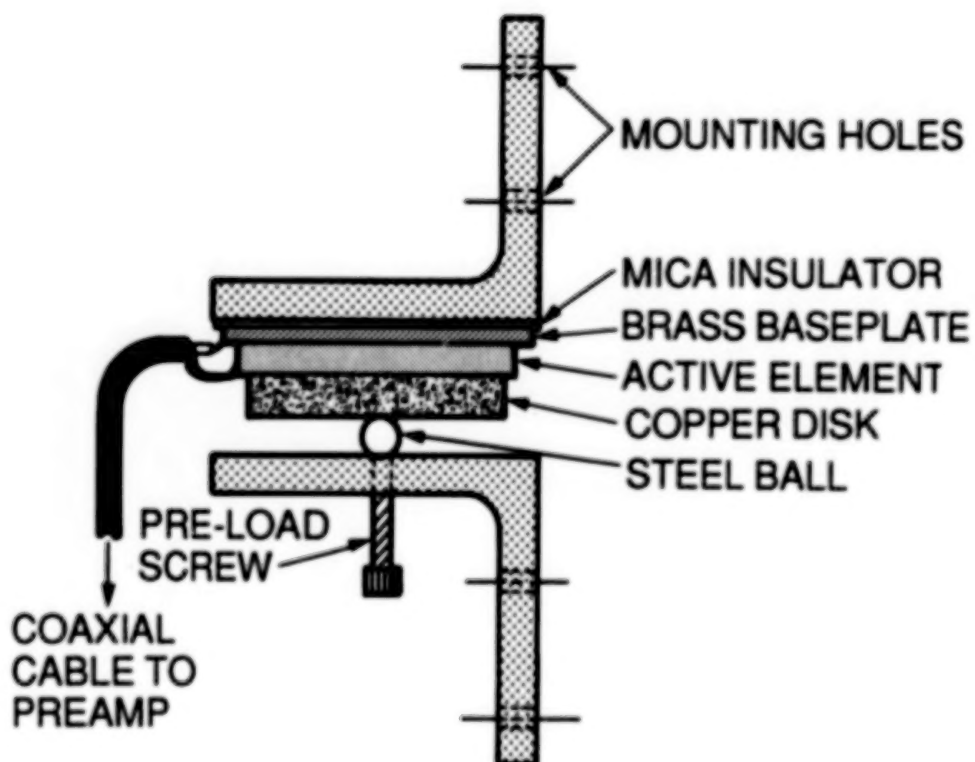


Figure 1. Piezo-ceramic sensor assembly.

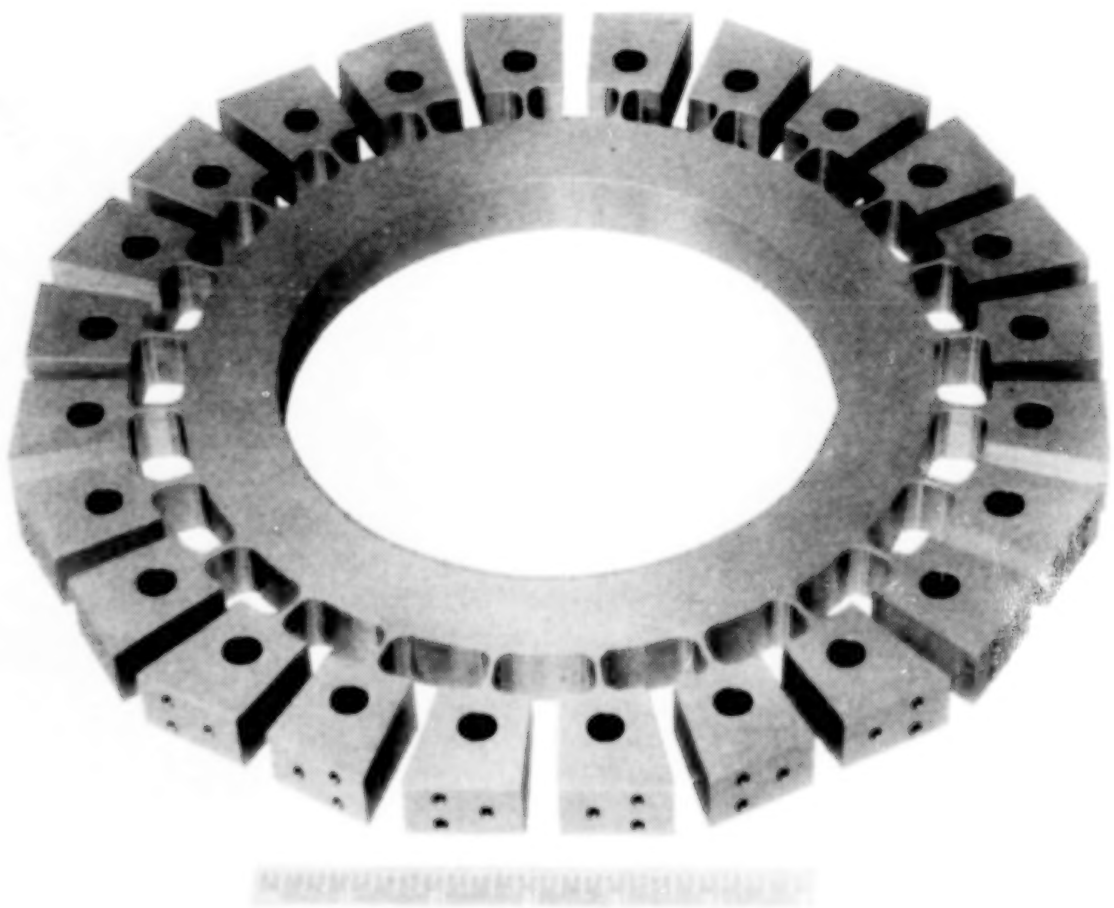


Figure 2. Flat Spoke Member

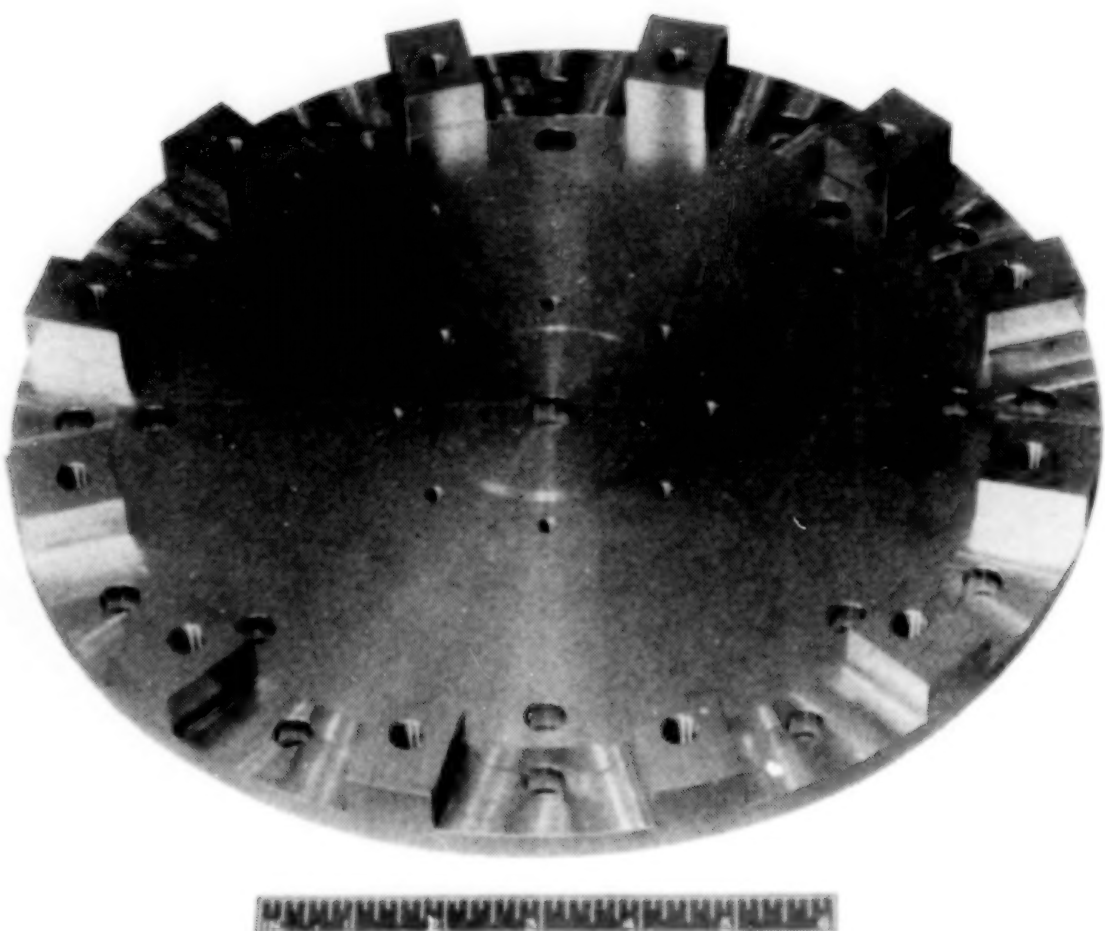


Figure 3. Interface Plate

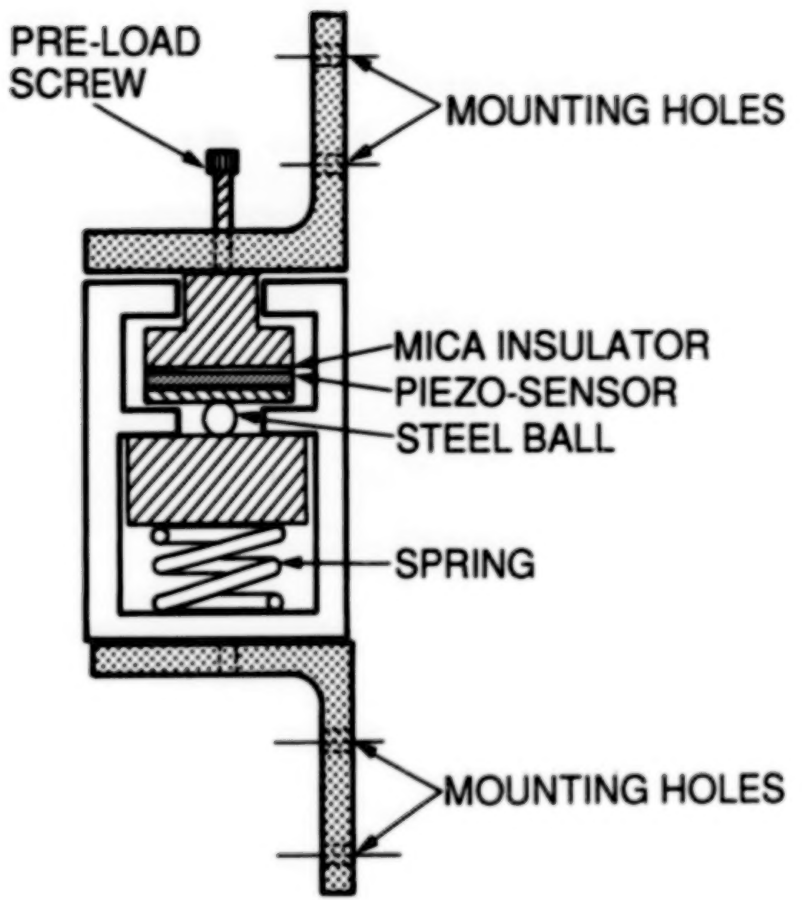


Figure 4. Launch Protection Assembly

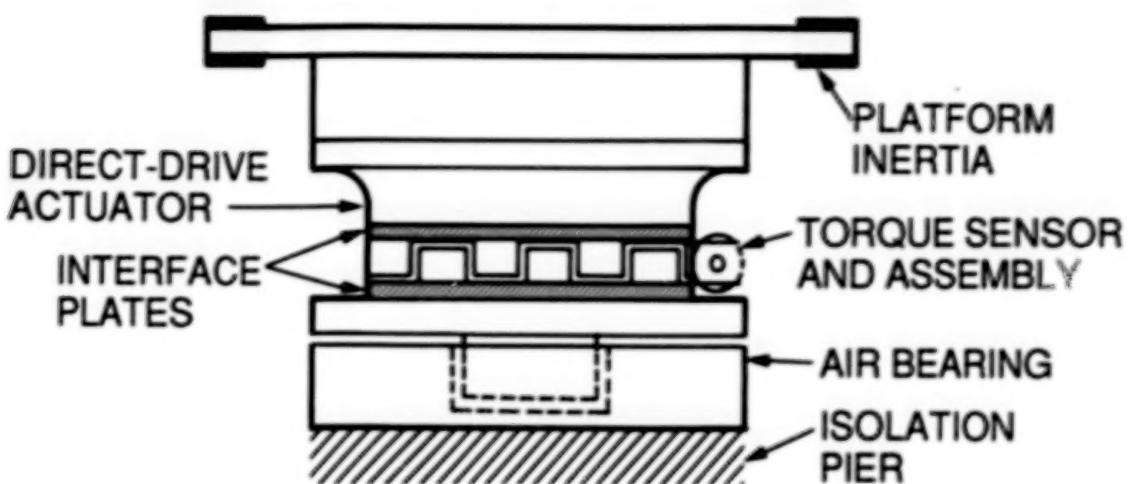


Figure 5. Torque Sensor Configured in Single-Axis Test Bed

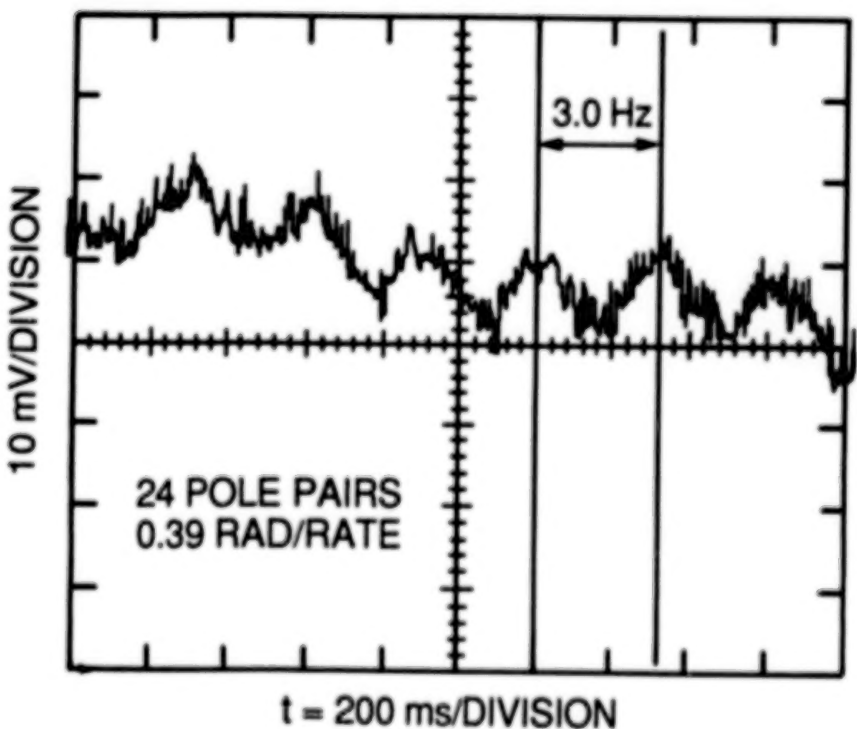


Figure 6. Motor Cogging

ASTRONAUT TOOL DEVELOPMENT:
AN ORBITAL REPLACEABLE UNIT-PORTABLE HANDHOLD

John W. Redmon, Jr.
Marshall Space Flight Center

ABSTRACT

This paper describes the design and development of a tool to be used during astronaut Extra-Vehicular Activity (EVA) replacement of spent or defective electrical/electronic component boxes (herein referred to as Orbital Replaceable Units or ORUs). The generation of requirements and design philosophies are detailed, as well as specifics relating to mechanical development, interface verifications, testing, and astronaut feedback. Findings are presented in the form of: (1) a design which is universally applicable to spacecraft component replacement and (2) guidelines that the vehicle-side designer of ORUs might incorporate to enhance spacecraft on-orbit maintainability and EVA mission safety.

INTRODUCTION

Earth-orbiting spacecraft destined for long-term use must frequently be designed for "orbital maintenance." Examples of such are the Hubble Space Telescope (HST), Space Station, AXAF, etc. On such a vehicle, the replacement of various "black boxes" such as data units, recorders, and batteries is due long before the useful life of the core vehicle is expended. Knowing this, the vehicle design groups can incorporate features which will facilitate on-orbit maintenance, e.g., quick-acting fasteners, dowels/guides, special fluid/electrical connections, handles, etc. Sometimes, however, these niceties cannot be successfully integrated. These instances include:

- Existing Spacecraft (HST)
- Unforecast Replacement (HST)
- Volume/Weight Constraints.

When these, or other, circumstances prevail, alternative schemes surface and are analyzed in regard to astronaut safety, EVA performance timelines, component downtime, etc. In the category of "handling," a convenient means must be provided for the astronaut to transport and articulate the "boxes" into and out of position, typically at an arms length, in tight quarters, combating the effects of fatigue and discomfort, and under poor lighting conditions. As a result, the need for a portable, universally applicable, latch-on type handle, or handhold, was precipitated. Requirements for such a device, as it pertains to the HST, are as follows:

- Box size 5 to 30 in.
- Box Design/Interface.....Flange Top/Smooth Top/Ribbed
(20 various designs/shapes)

Due to the quantity of boxes, the variety of sizes/designs, and the likelihood that more boxes could be added to the list at a later date, several design philosophies were incorporated early on:

- "Infinitely" adjustable clamp
- High degree of modularity/design flexibility
- Telescoping - No extensions to assemble while on-orbit
- Soft latch-elastomeric latch pads.

The design that followed may be described as a hand-actuated, double-telescoping, linear-clamping device with a ratcheted rack/pinion locking drive (see Figures 1 through 5). High linear resolution would be provided by a 120-tooth sawtooth ratchet which translates to 0.017 in. of spur gear pitch line movement; variability between ratchet teeth would be provided by compliance of the rubber pads.

DESIGN-ASTRONAUT INTERFACE

During the course of design, much contemplation was given to the amount of hand-cranked torque to be applied and the resulting linear clamping force exerted on the ORU. As a general guide, 40 to 50 in.-lbs was used as the input torque provided by an astronaut's gloved hand using "wrist action" motions. The required linear clamping load to effect a good latch, however, depends on the box surface area exposed to the latch pads, and temperature (due to the compliance of rubber and its frictional properties). Obviously, not enough load would result in a poor grip while, on the other hand, too much load could possibly damage the ORU. Due to this relatively wide variation in required load, torque limiting, or "clutching," was discounted as a means to assure grip integrity. Instead, it was decided to design the device with a high degree of "feel" or tactile behavior. This is accomplished by selecting a gear ratio, handle length, and compliance value commensurate with adequate linear loads, reasonable astronaut input torque values, and a rapidly increasing resistance to input torque, as the target clamp load is approached (i.e., feel).

DESIGN-MECHANICAL CONSIDERATIONS

The need for operational simplicity, tactile behavior, compactness, extremely fine linear adjustability, and ruggedness precipitated some rather interesting concerns in the mechanical packaging. With the small size, loads on the intricate gears and tiny shafts, as well as gear fastening problems, soon became apparent. Similarly, the need for smooth, frictionless operation under load and in the absence of lubrication surfaced. The challenge soon became how to package the drive gearing, ratchet gearing, crank handle, ratchet release, and pawl, locating each of the three shafts on miniature deep groove ball bearings. To accomplish this, several unconventional means were utilized.

Examples of these are: The use of large ball bearing/ small bearings on a common stepped shaft in order to facilitate assembly and provide a large

shaft diameter where more material was needed for strength and/or fastening interface; secondly, utilization of gear mesh interference to provide rotational constraint of the telescoping rods; and lastly, the use of an "overhung" or cantilevered rack gear in order to provide more extension length. All of these methods worked out very well and proved not to contribute to friction, play, or excessive deflections, despite the fact that these methods seemed somewhat "unorthodox."

Fastening concerns were found in two areas: (1) attachment of the gears, pawl, and cam to their respective shafts, and (2) attachment of the elastomeric latch pads to their aluminum backing plates. The fastening of gears to shafts was critical because of the very small moment arms (0.063 in.) and shear areas on the gear/shaft interface. Integral shaft/gear arrangements were discounted because of expense, tooling complexity, and loss of modularity. It was therefore decided to interference fit the gears on the shaft and fusion weld the assembly using the highly weldable, nickel-based "super alloy" Inconel 718 on the gears and shaft. Because of the interference fit, a high degree of fusion occurred thus resulting in superb strength; no warpage problems occurred.

In fastening the elastomeric latch pads, several means were considered: adhesive bonding, through molding, and mechanical fastening. Bonding and through molding were discounted because of poor strength and complexity. As a consequence, a rather effective rubber/metal fastening technique was developed. The method consists of riveting the rubber to the aluminum with special load distributing washers and standoffs so that the rivet does not squeeze the rubber, no more than 10 percent. The technique provides a tenacious hold on the rubber while proving to be simple to implement, and easily removed.

Some consideration was given as to what type of linear bearing should be employed on the telescoping rods. Since the rods are exposed to the astronauts' touch, no lubrication could be used. Several engineering polymers were considered but were discounted due to flow properties and the potential for excessive deflection to cause adverse gear loading (lack of engagement). A ball bushing would suit the need for low friction under load, however, these types of linear bearings have a large envelope. As a result, it was decided to utilize a "hard" bushing and design a "materials couple" which would foster low friction and abrasive wear resistance. For this, a Nitronic 60/CRES 304 couple was selected along with honed/polished surfaces to 16 RMS, generous entry blending and a 0.001/0.002 in. diametrical clearance. The arrangement has worked very well; there have been no indications of wear, scratching, galling, etc., and the surfaces appear new even after months of testing in "unclean" environments.

TESTING/VERIFICATION

Testing of the device occurred, in one way or the other, every day after the first prototypes were build. Formal testing included: (1) fit verifications on vehicle, (2) instrumented ORU box deflection tests, (3) manned

thermal/vacuum tests for environmental suitability, (4) overload tests, and (5) underwater neutral buoyancy tests. During the course of these tests, much valuable information regarding the usage of the device was generated, and feedback from the astronauts proved enlightening as to the mental and physical aspects of EVA spacecraft repair. In general, formal testing went exceptionally well; minor "tailoring" modifications were made to the rubber latch pads for enhanced grip, the crank handle swivel joint was beefed up due to its propensity to bend and gall, directional arrows and instructional nomenclature was added to the housing, and teflon friction washers were added to reduce swivel handle "floppiness." In no cases were there any failures which prevented operation of the device. Further, overloads ten times that anticipated produced only minor deflections in the rods; no sheared fasteners or welds occurred and none of the tiny 32-pitch gear teeth were deformed.

Informal testing, although not as well documented, was probably as useful as any formal testing. This kind of testing includes the numerous cycles and operational permutations that the device undergoes between formal tests, typically by individuals unaccustomed to the device. Three types of data are available from this: (1) acclimation data, the adaptation of an individual to the operational characteristics; (2) improper operation data, i.e., can the device be misused?; and (3) the numerous cycles the device undergoes under the above mentioned conditions. To conduct these tests it is only necessary to leave the tool on your desk for a few months and observe a wide variety of people attempt to use it without instructions. No failures occurred during this "phase" of testing and it was observed that the device is very "user friendly." Directional arrows and instructional information engraved on the housing proved helpful for communication references, quicker adaptation, and possible "panic" situations.

Destructive tests are planned but have not been accomplished at the time of this writing due to Neutral Buoyancy test schedules. Figures 6 through 8 depict tests and verification activity.

SUMMARY

Thus far, development has gone exceptionally well and mission confidence surrounding use of the device is growing as more test time and neutral buoyancy usage is accumulated. I would, however, like to bring out several considerations that EVA tool designers and/or vehicle designers might consider for future work as it pertains to orbital maintenance, and specifically, component replacement.

- If weight or volume constraints prevent incorporation of "built-on" handles and tethers, vehicle designers should consider a suitable interface for handling means. A flanged box, as shown in Figure 5, is one of the more suitable configurations. The flange should be sufficiently rigid to withstand clamping loads. Notches, recesses, and/or clamp position placards, indicating a preferred clamp orientation, would also be desirable.

- EVA tools/mechanisms should be designed for 1-g underwater operation. Frequently viscous drag prevents delicate spring-loaded mechanisms from functioning properly underwater.
- Provide "fit-check" models early on. Frequently drawing data does not accurately reflect conditions on the vehicle, due to cabling, insulation, etc.
- Slots, guides, dowels, and visual aids should be incorporated for ease of installation.
- Winged connectors, captive fasteners, and large backshells suitable for gloved-hand operation are desirable.
- Good line-of-sight and accessibility are important. ORU designers might consider "canted" connectors or use of oblique surfaces to enhance visibility/accessibility.
- Parking and stowage should also be considered. Considerable EVA time can be saved by incorporating "snap-action" latches, ball-lock pins, etc., to circumvent attachment of threaded fasteners on stowage pallets.
- Further EVA information can be attained from: NASA-STD-3000, MSFC-STD-512A, and JSC-20466.

ACKNOWLEDGMENTS

The author wishes to express gratitude to the following people for their invaluable assistance in the development of this device: Gene Simms, David Petty, Sam Wofford, and John Reaves.

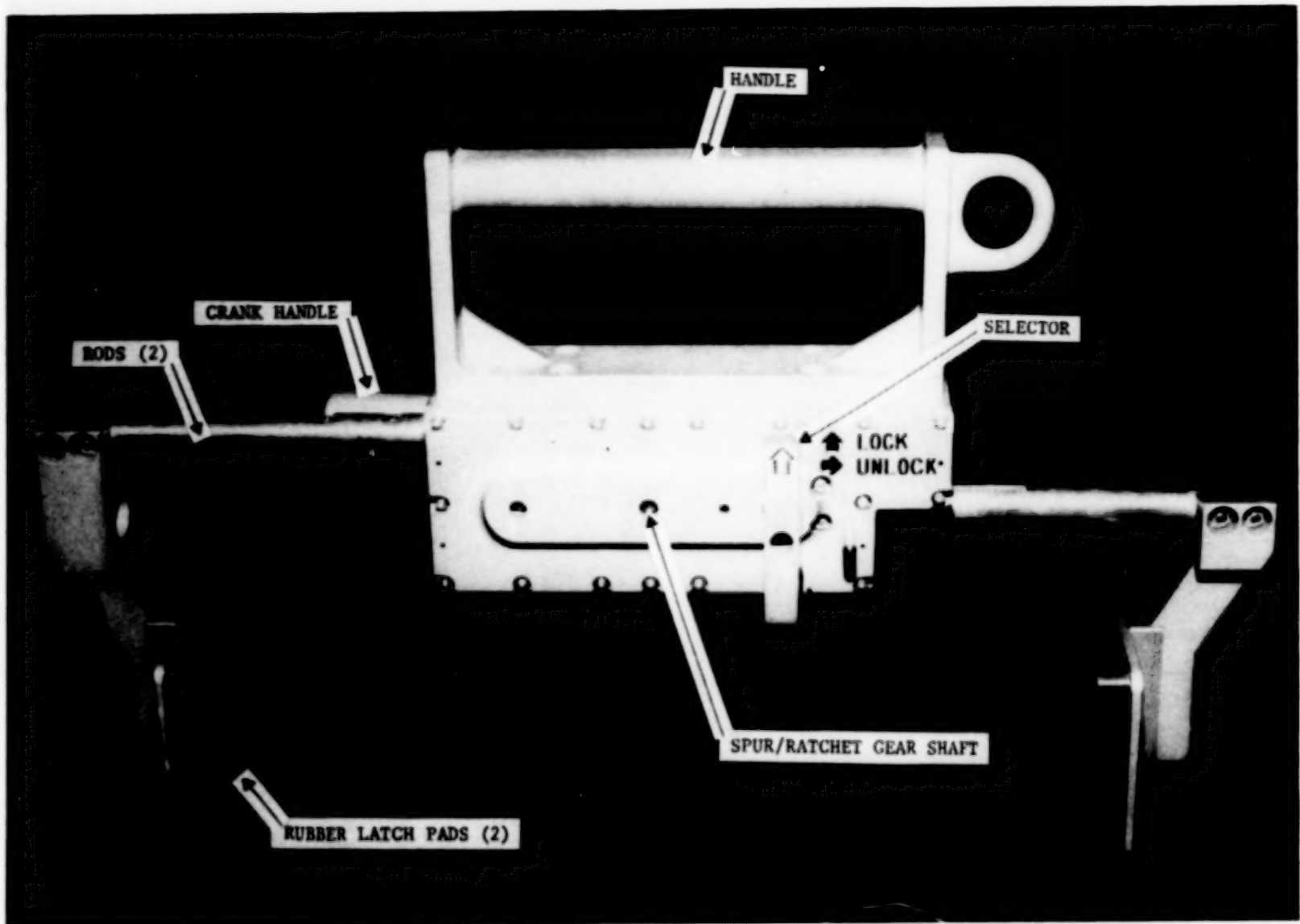


Figure 1. Portable Handhold (extended)

186

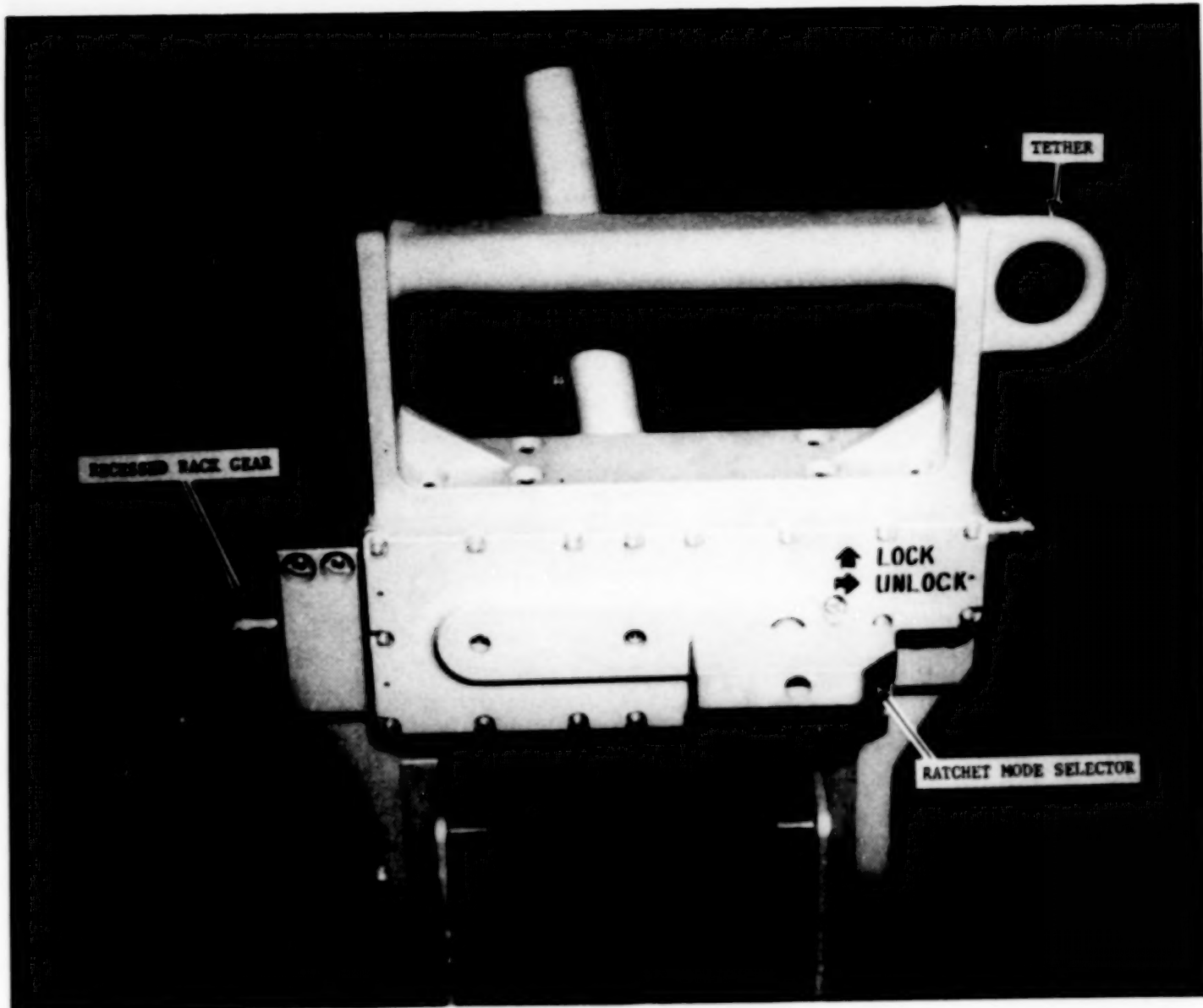


Figure 2. Portable Handhold (retracted)

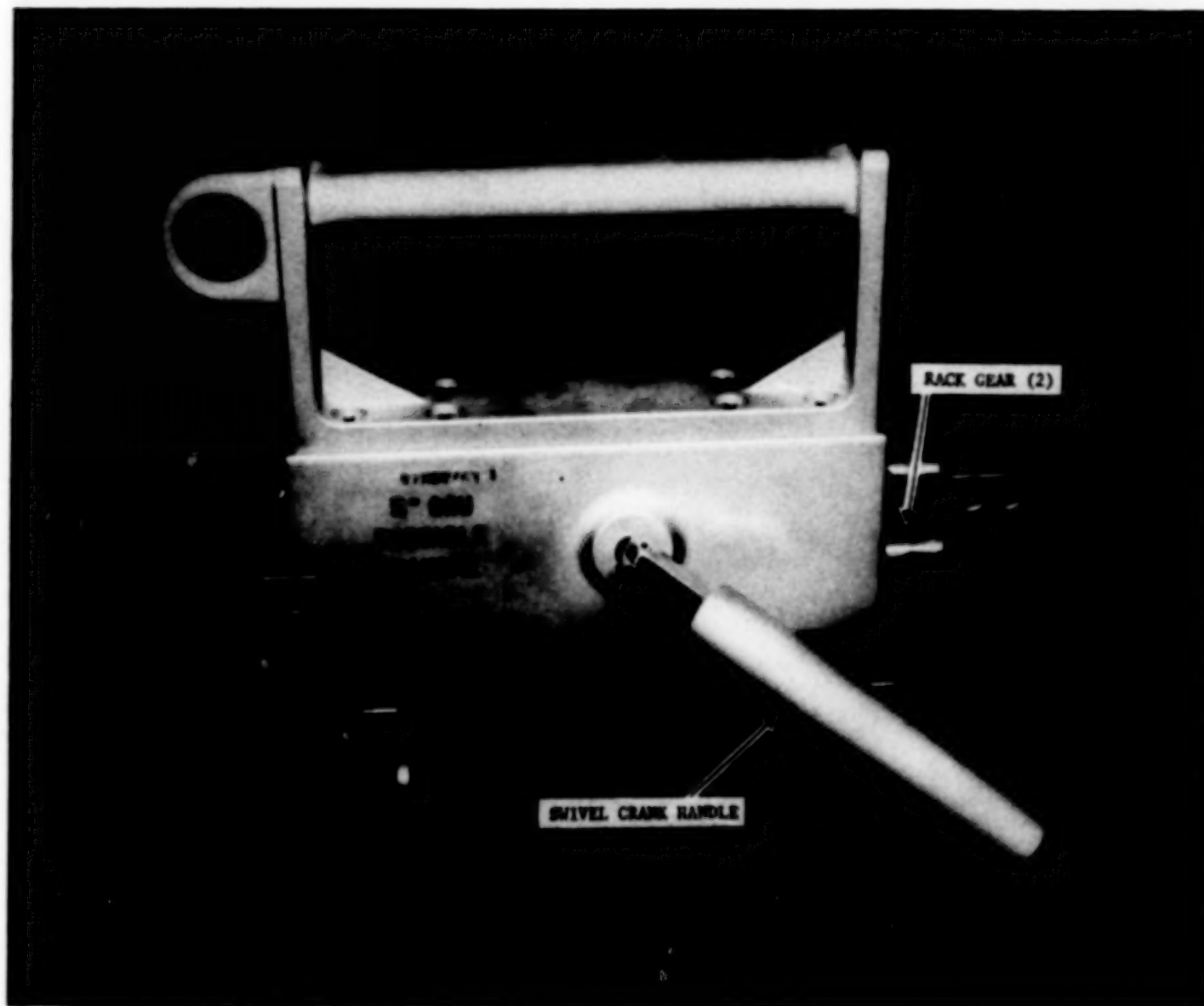


Figure 3. Portable Handhold

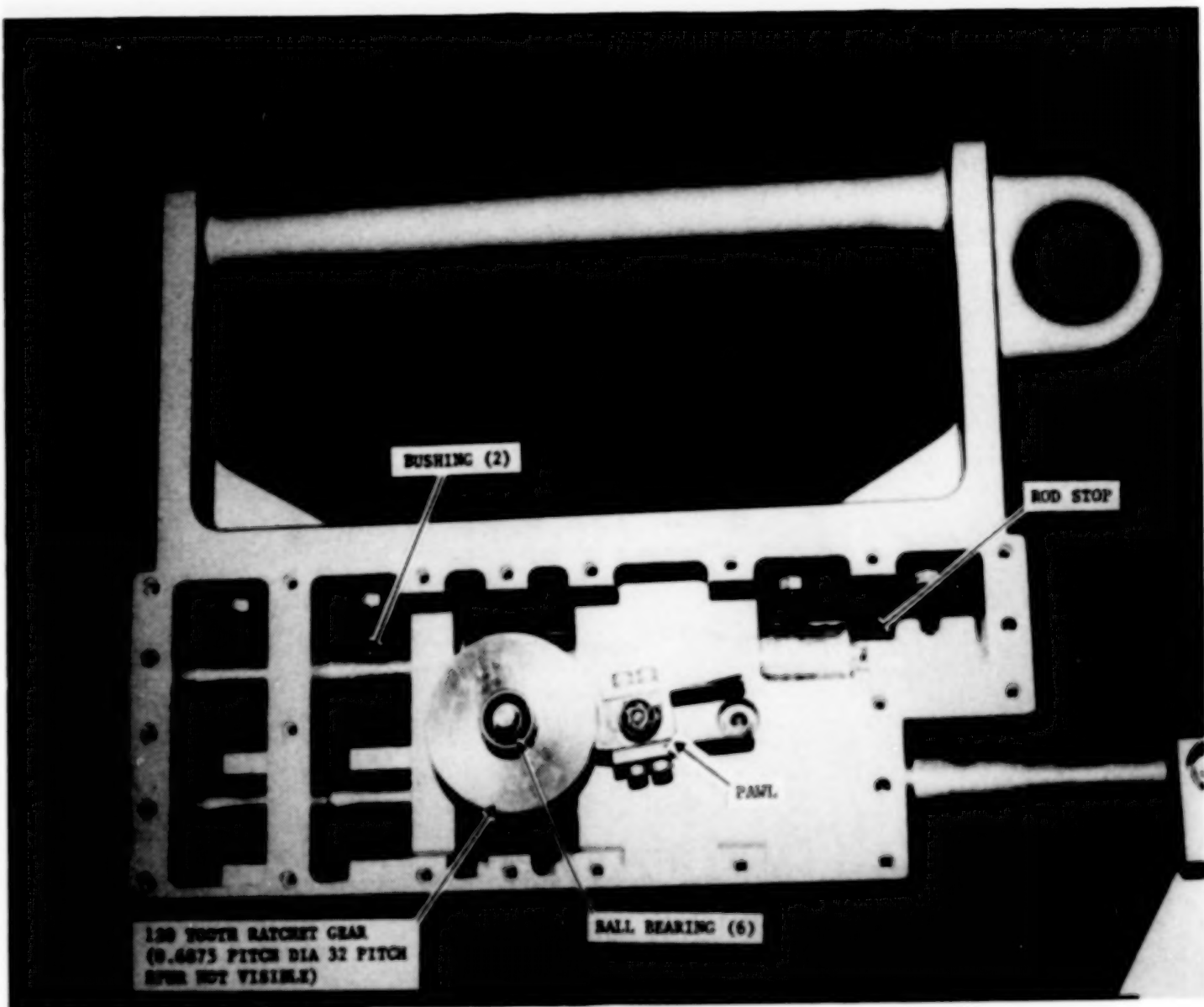


Figure 4. Cover Removed

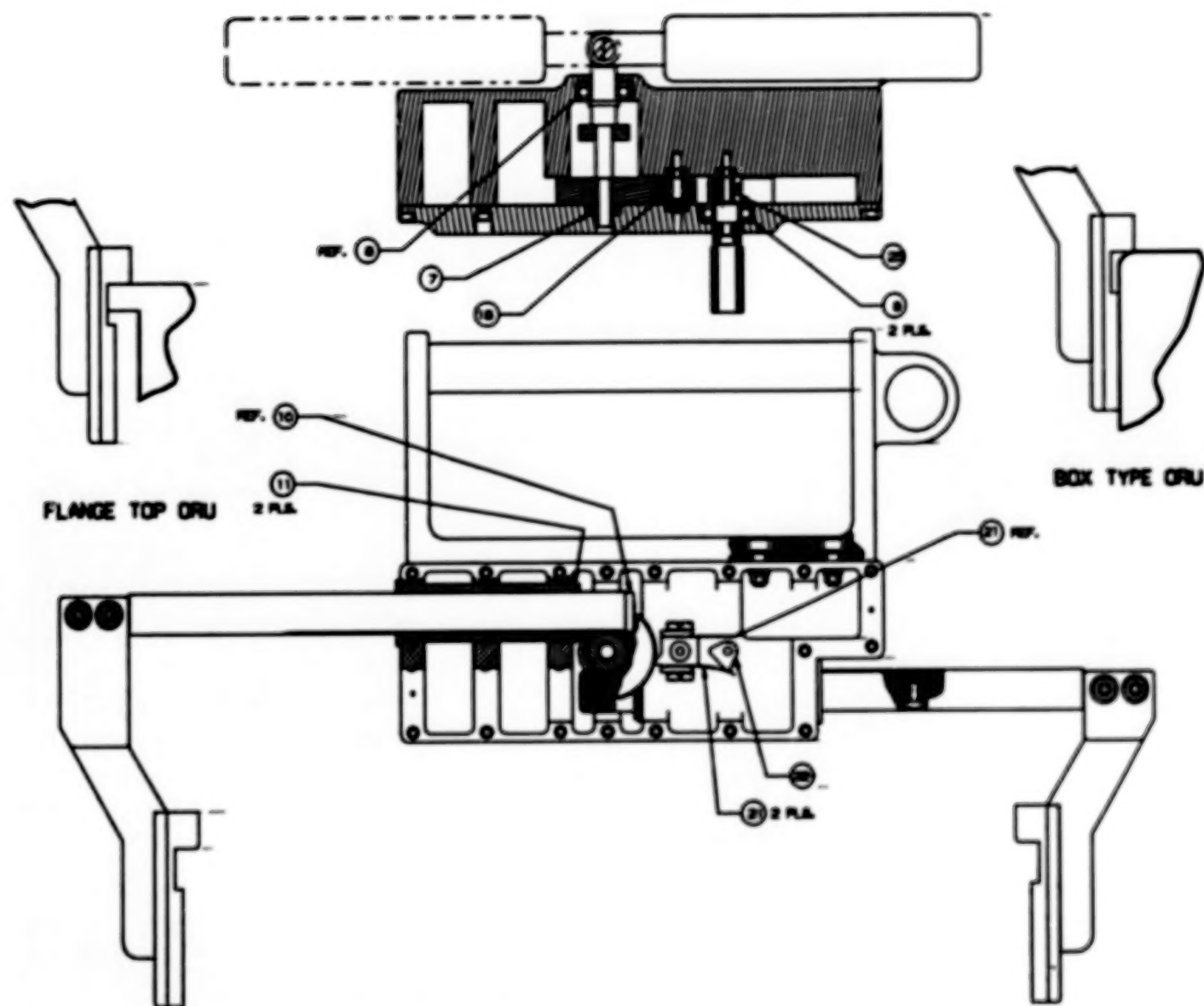


Figure 5. Internal Configuration



Figure 6. Fit checks with early prototype handheld verified acceptability of envelope and mission suitability.
Astronaut Bruce McCandless performs the test.



Figure 7. Later fit checks with flight fidelity unit verified latch and was useful in generating procedures and usage requirements.

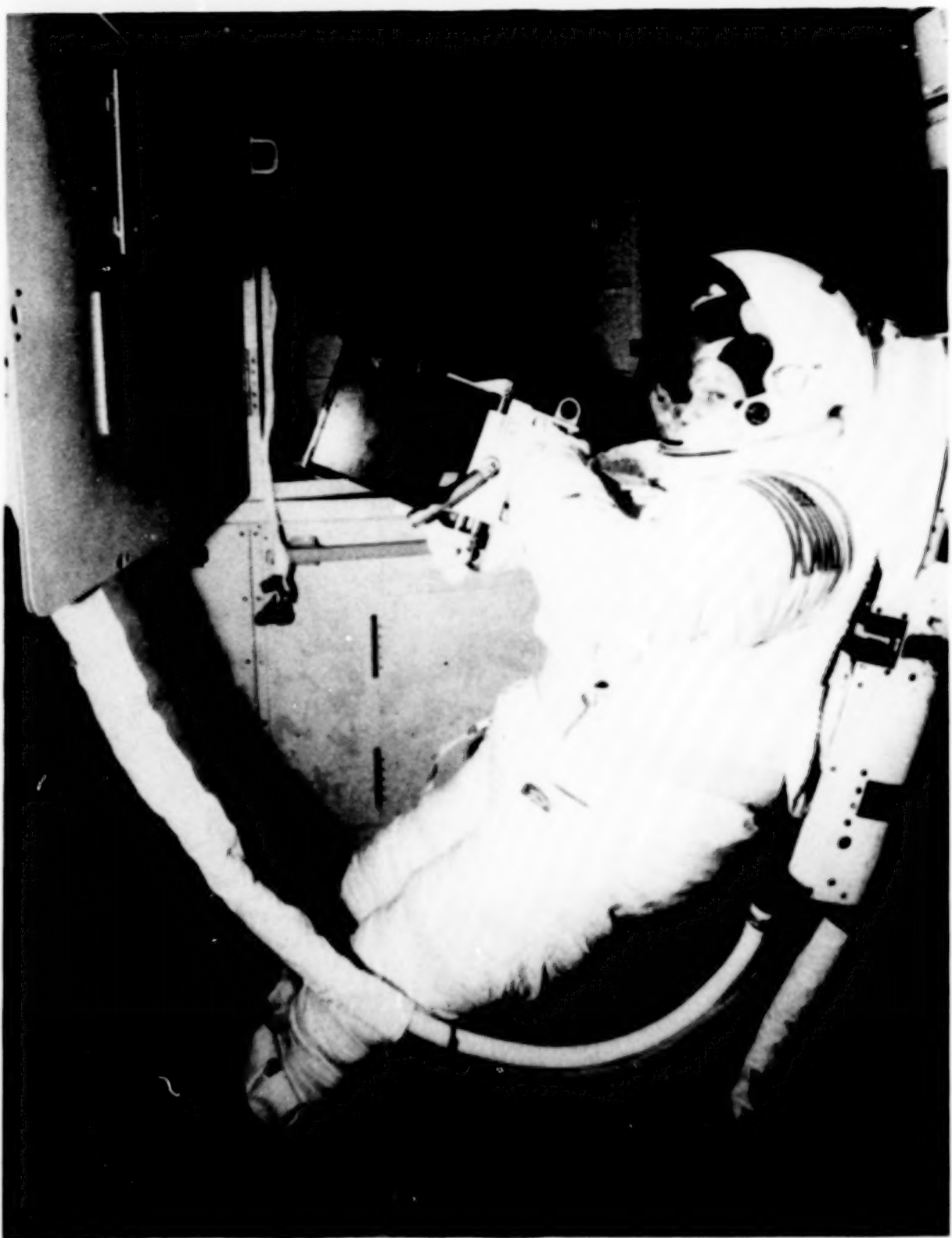


Figure 8. Neutral Buoyancy tests demonstrated usefulness
of device for positioning ORU boxes.

BLANK PAGE

DOUBLE LEAD SPIRAL PLATEN PARALLEL JAW END EFFECTOR

David C. Beals*

INTRODUCTION

Space Station Freedom currently is planned to be constructed by astronauts and highly sophisticated robots. The S.S. Freedom will require a large number of complicated Extra Vehicular Activity (EVA) tasks such as assembly of the structural truss, connection of fluid, gas, and electrical lines, and manipulation of large payloads in the hostile environment of space. NASA Langley Research Center's Automation and Technology Branch is conducting research in the development and use of robots in performing these EVA tasks. Since many EVA tasks require the dexterous hand manipulation which currently only an astronaut can provide, a robotic "hand" or "end effector" must be developed to meet these requirements. An end effector, the Double Lead Spiral Platen Parallel Jaw End Effector (Spiral), was developed as a response to problems in the design of the current LaRC Puma (LP) end effector, and to meet the needs of S.S. Freedom assembly tasks (see Fig. 1). It is highly controllable and compact, and has a very high gripping force for its size and weight.

This paper will discuss the design problems associated with the LP end effector and how the Spiral end effector addresses these problems, and will give results of test data for three end effectors: the Spiral end effector, the LP end effector, and the TRI (Telerobotics Model #EP75/30) end effector (see Fig. 2). The Spiral and LP end effectors use the same electric motor to power the jaws so direct comparisons can be made between the two designs. The TRI end effector was included in this series of tests as a benchmark of commercially available lightweight end effectors.

There are a number of general design guidelines used in the development of end effectors. Gripping strength and the knowledge of the absolute position of the end effector's jaws (fingers) are two of the most important design criteria. In addition, finger speed should neither be so slow as to be laborious nor so fast as to be uncontrollable. Also, it is desirable that the gripping force not diminish after the power to the end effector has been turned off. Parallel jaw motion, where the fingers are constrained to move transversely in one plane, is preferred over the four-bar mechanism motion which moves the fingers in two planes (see Fig. 3). The LP and TRI end effectors use four-bar mechanisms to keep the fingers parallel. This motion creates difficulties in grasping an object by a remote operator who must compensate for the fingers moving in two orthogonal axes. This motion is a problem in both the teleoperated (man-in-the-loop) mode and the robotic mode.

*NASA Langley Research Center, Hampton, Virginia.

If the fingers could be made to move in-plane while remaining parallel, considerable programming difficulty would be avoided. The most significant design problem involves converting the rotary motion of the motor shaft into linear motion of the fingers, while utilizing the motor torque in an efficient way to maximize the gripping strength and maintain a high degree of controllability. There are no firm requirements associated with these guidelines. Therefore, end effectors must either be designed for a specific task or designed for versatility, which will include compromises.

LaRC PUMA END EFFECTOR

The LP end effector was developed for research in the manipulation and assembly of S.S. Freedom hardware. The assembly evaluations involve struts with metal fittings on the ends which attach to the space station's truss nodes. The end effector must be capable of being accurately positioned over the fittings. Then the end effector must grip and turn the fittings in order to simulate the construction of the S.S. Freedom truss. The researchers were able to position the end effector over the fittings, and grasp and manipulate them. But when it came time to release the fitting, the end effector would seize and not release.

The problem is in the LP end effector drive system. An electric motor (rated for 13 W, 60 oz-in. peak torque) is used to turn a worm gear which reacts against a bevel gear. This bevel gear is secured to a four-bar mechanism which allows the fingers to remain parallel while moving in an arc (see Fig. 3). In order to gain enough mechanical advantage to firmly grip an object, the worm gear has a very low lead angle. This low lead angle makes the end effector self-locking. Once the worm has stopped, it cannot be reversed to release an object. The worm/bevel gear arrangement is subject to wear, which makes the fingers loose and adds to the positional uncertainty of the fingers.

DOUBLE LEAD SPIRAL PLATEN PARALLEL JAW END EFFECTOR

The Spiral was developed as a solution to the problems of the LP end effector. The result is an end effector which is more efficient, has a greater gripping strength, and is highly controllable.

The problem of keeping the fingers parallel while moving in plane was solved by using a rail system to hold the fingers. Linear bearings mounted on hardened steel rails react the loads without excessive deformation.

To efficiently use the small torques of the compact motor, a very efficient means of doing work is needed. One of the more efficient and basic ways of lifting objects is to utilize a roller on an inclined plane (see Fig. 4). The roller reduces friction, and a low angle inclined plane makes it possible for small amounts of "pushing" force to raise large weights. The penalty one pays is that a long incline may be needed to lift an object up a short distance.

The principle of the inclined plane was used in the Spiral end effector design. By wrapping the inclined plane in a spiral, a considerable length can be incorporated in a small disk. A roller, placed in a spiral channel and constrained to move in one plane by rails, would be able to move back and forth and take advantage of the inclined plane's work efficiency. A spiral has the further advantage that each complete rotation is a constant lead pitch. This means that once the angle of the spiral is known, the position of a constrained roller is also accurately known. Two spirals, one the mirror image of the other and with a common center point, allow two constrained rollers to move in a back-and-forth motion. The distance between the rollers is a linear function of the spiral's rotation angle.

The Spiral end effector's design is based on two mirrored spirals machined into a rotating platen. The platen is attached to a gear reduction unit which increases the motor's output torque while reducing the angular velocity. The angular velocity of the platen determines the fingers' speed. The fingers, constrained by the rails, are attached to rolling pins which ride in the spiral channels. As the platen rotates, the pins roll in the channel moving the fingers either forward or backward, depending on the platen's direction of rotation. The gripping force of the fingers is a function of the spiral's inclined plane efficiency and the torque increase through the gear reducer. The platen makes only three-and-a-half revolutions to move the fingers their full travel distance. Therefore, a decrease in the motor's output speed, along with the concomitant increase in torque, is advantageous (see Fig. 5).

TEST RESULTS

The Spiral, LP, and TRI end effectors were tested for gripping strength, positioning accuracy, finger speed, and gripping force relaxation. The Spiral and LP end effectors use the same electric motor for their input power, so a comparison of the performance between the two will show directly the advantages or disadvantages of each design.

GRIPPING STRENGTH

In order to measure the gripping strength, a force sensor was placed between the jaws of the end effectors, and the stalling force at a number of different input power levels was recorded (see Fig. 6). A second degree least-squares curve fit was generated for each data range. The Spiral end effector was the most powerful end effector of the group, showing a maximum gripping force of nearly 80 lb. Using the same motor for input power, the Spiral end effector has a 250 percent increase in gripping strength over the LP unit.

POSITIONING ACCURACY

The three end effectors were fitted with digital shaft encoders which were used to record the number of encoder counts per unit length of jaw movement (see Fig. 7). A least-squares fit line was developed for the data to

determine the degree of linearity in the positioning system. The Spiral end effector showed the greatest degree of linearity. The data points on both the opening and closing sides of the chart fall on the line. The LP and TRI end effectors are fairly linear. However, both showed a degree of hysteresis when the jaw movements changed directions. These hysteresis effects could build at every movement reversal, and eventually cause confusion as to the absolute jaw position.

FINGER SPEED

The opening and closing finger speed of the three end effectors was measured for a high and low range of no load power levels (see Fig. 8). The LP end effector was the fastest, the TRI was moderate, and the Spiral was the slowest of the group. The Spiral's speed is not a disadvantage for most applications, and can be an advantage in a teleoperated mode where there are reaction control time considerations and the slower speed allows time for fine corrections.

GRIPPING FORCE RELAXATION

A force sensor was placed between the jaws of the end effectors which were loaded at 36.5 lb (the maximum for the LP). The input power was then turned off, and the relaxation force was monitored over a period of an hour and a half (see Fig. 9). All of the end effectors performed well in this test, with the TRI showing less relaxation than the other two.

CONCLUSIONS

The Double Lead Spiral Platen Parallel Jaw End Effector is an extremely powerful, compact, and highly controllable end effector that represents a significant improvement in gripping force and efficiency over the LP end effector. The Spiral end effector is very simple in its design and has relatively few parts. The jaw openings are highly predictable and linear, making it an ideal candidate for remote control. The finger speed is within acceptable working limits and can be modified to meet the user's needs; for instance, greater finger speed could be obtained by increasing the spiral's pitch. The force relaxation is comparable to the other tested units. Optimization of the end effector design would involve a compromise of force and speed for a given application.

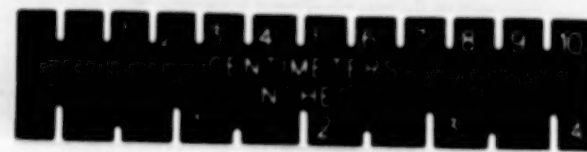
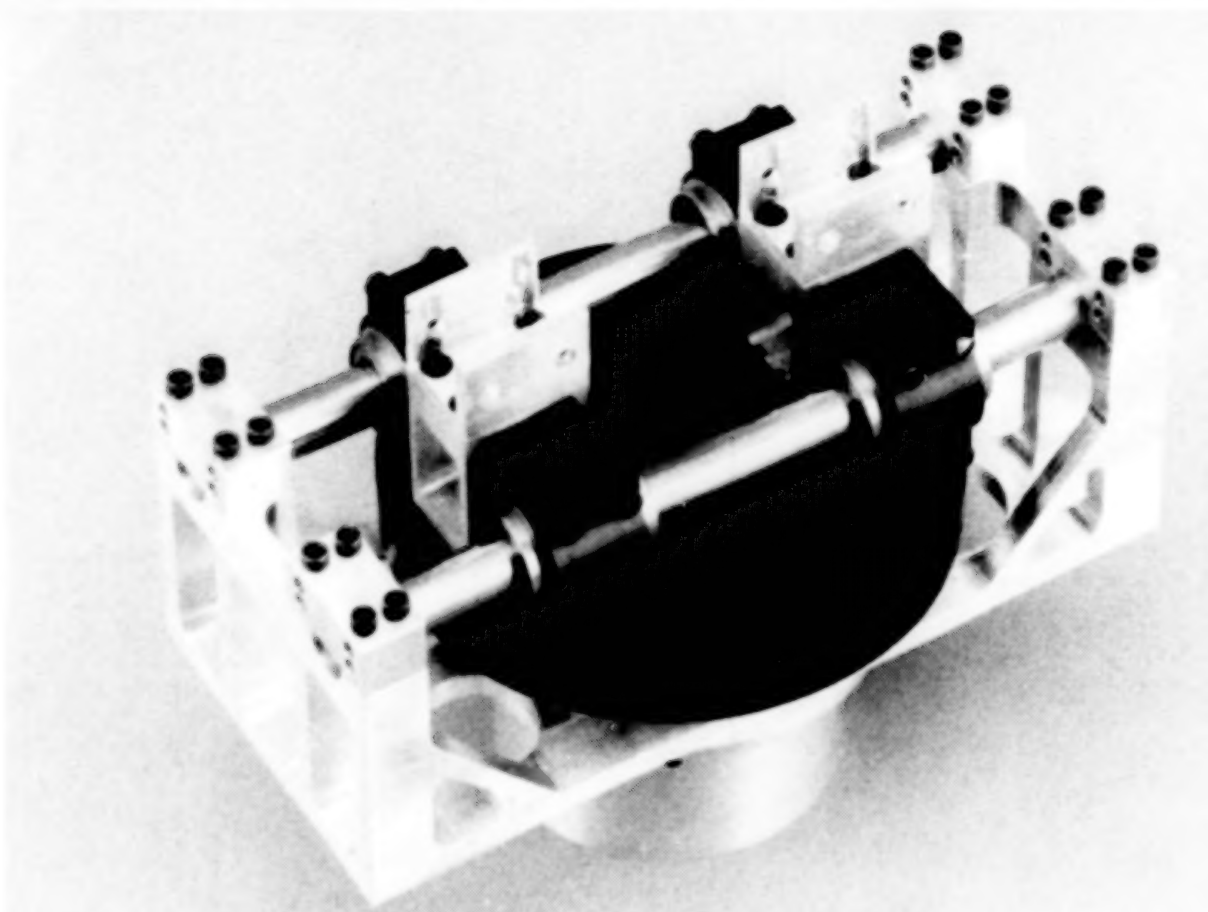
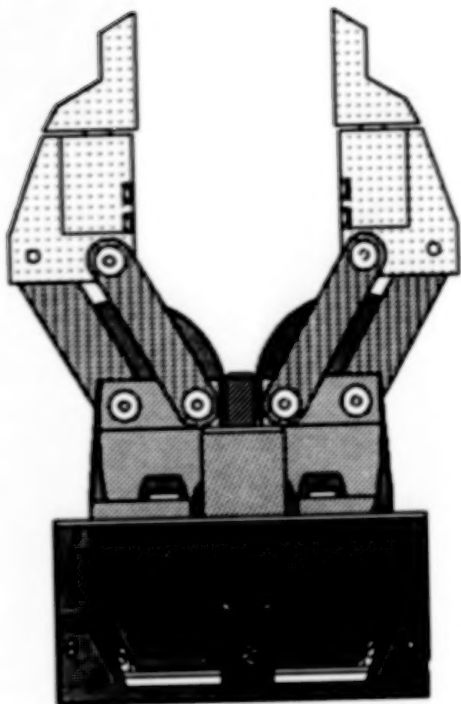
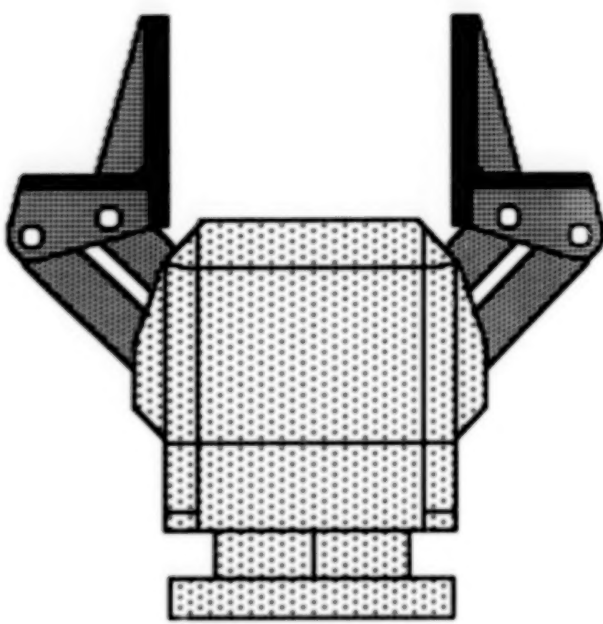


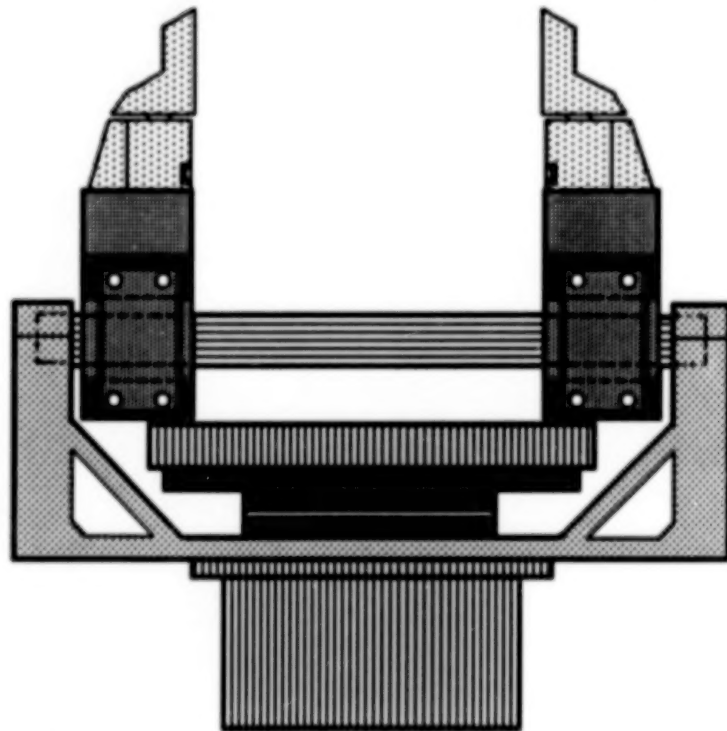
Figure 1. Double Lead Spiral Platen Parallel Jaw End Effector.



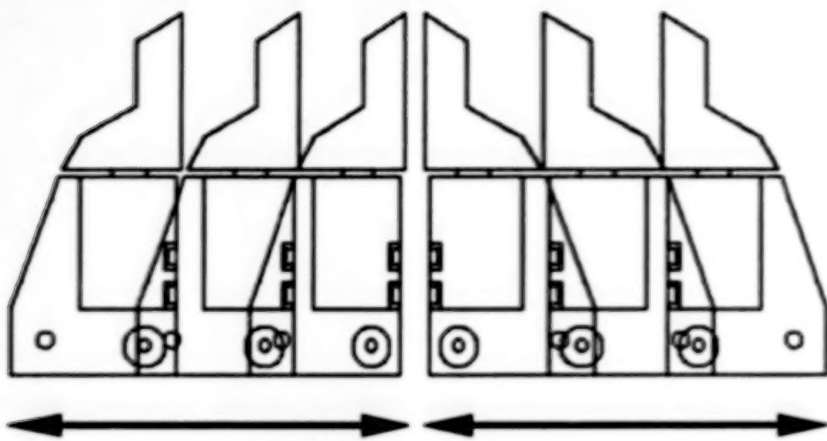
LP End Effector



TRI End Effector

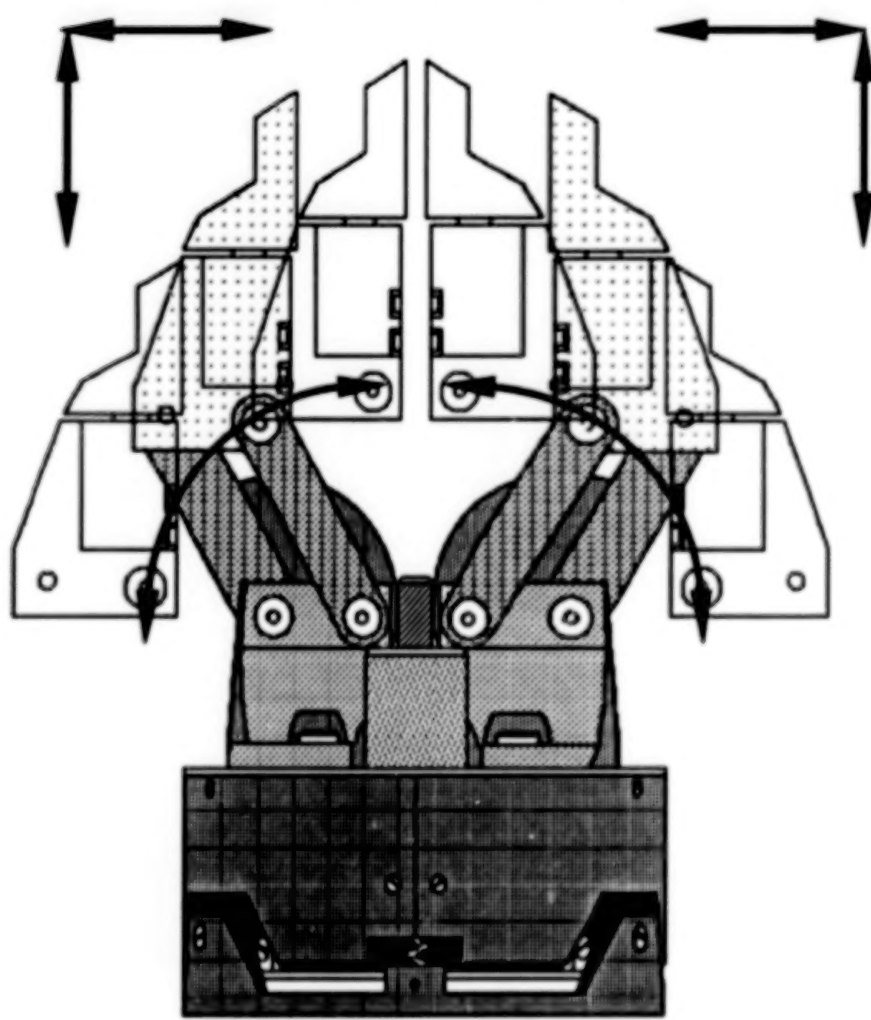


Double Lead Spiral Platen Parallel Jaw End Effector
Figure 2.

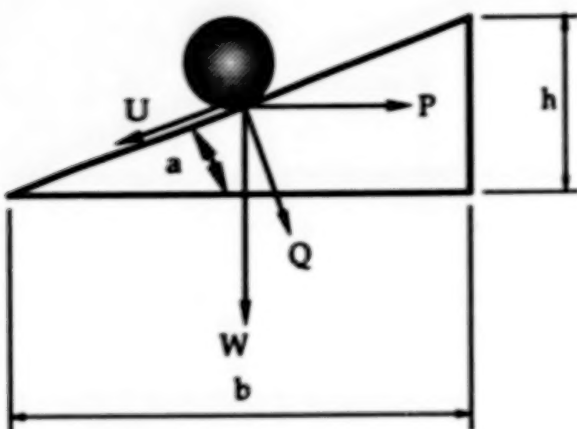


PARALLEL JAW MOTION

FOUR BAR MECHANISM MOTION. THE FINGERS REMAIN
PARALLEL AS THEY DESCRIBE AN ARC, MOVING
TRANVERSALLY IN THE X AND Y DIRECTION



LaRC Puma End Effector
Figure 3.



W = Weight (or Force), Gripping force for the end effector.
 P = Force Required to move W, the motor torque for the end effector.
 Q = The normal force on the inclined plane.
 U = Force of friction, $u \cdot W \cdot \cos(\alpha)$
 α = angle of incline
 b = run
 h = rise

Neglecting Friction:
 $P = W \cdot (h/b) = W \cdot \tan(\alpha)$
 $W = P \cdot (b/h) = P \cdot \cot(\alpha)$
 $Q = W/\cos(\alpha) = W \cdot \sec(\alpha)$

Figure 4. Inclined plane mechanics.

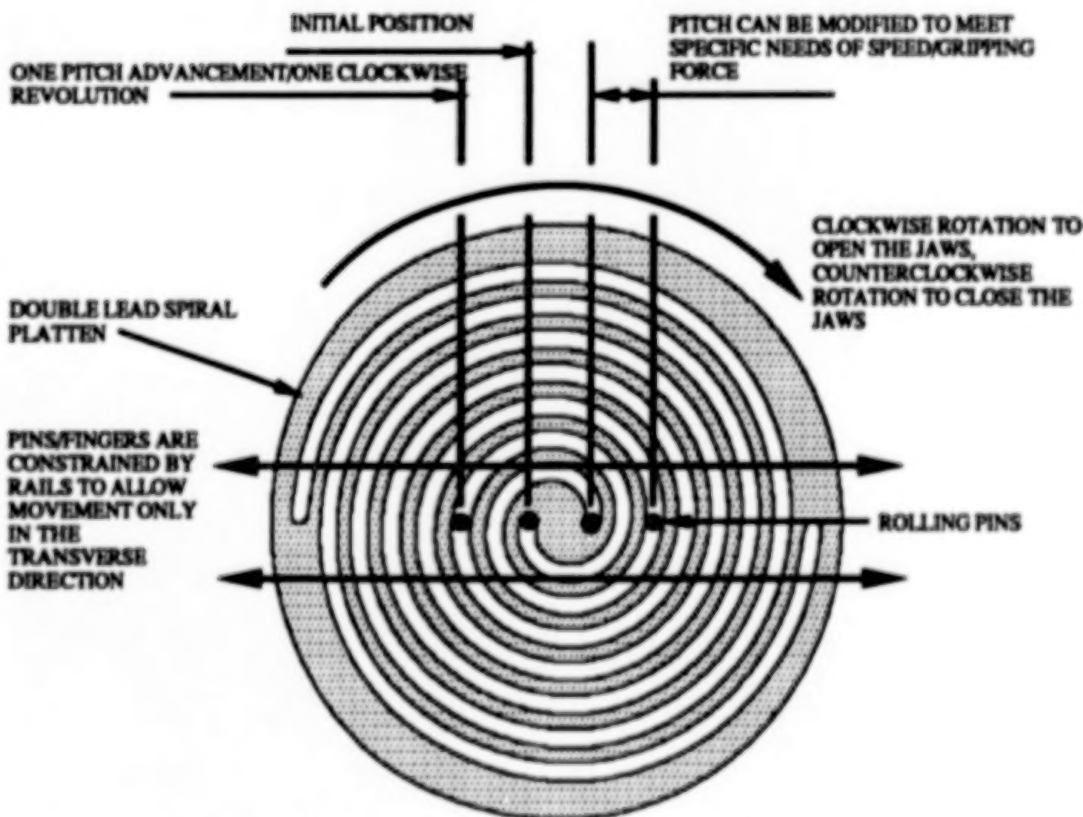


Figure 5. Inclined plane mechanics.

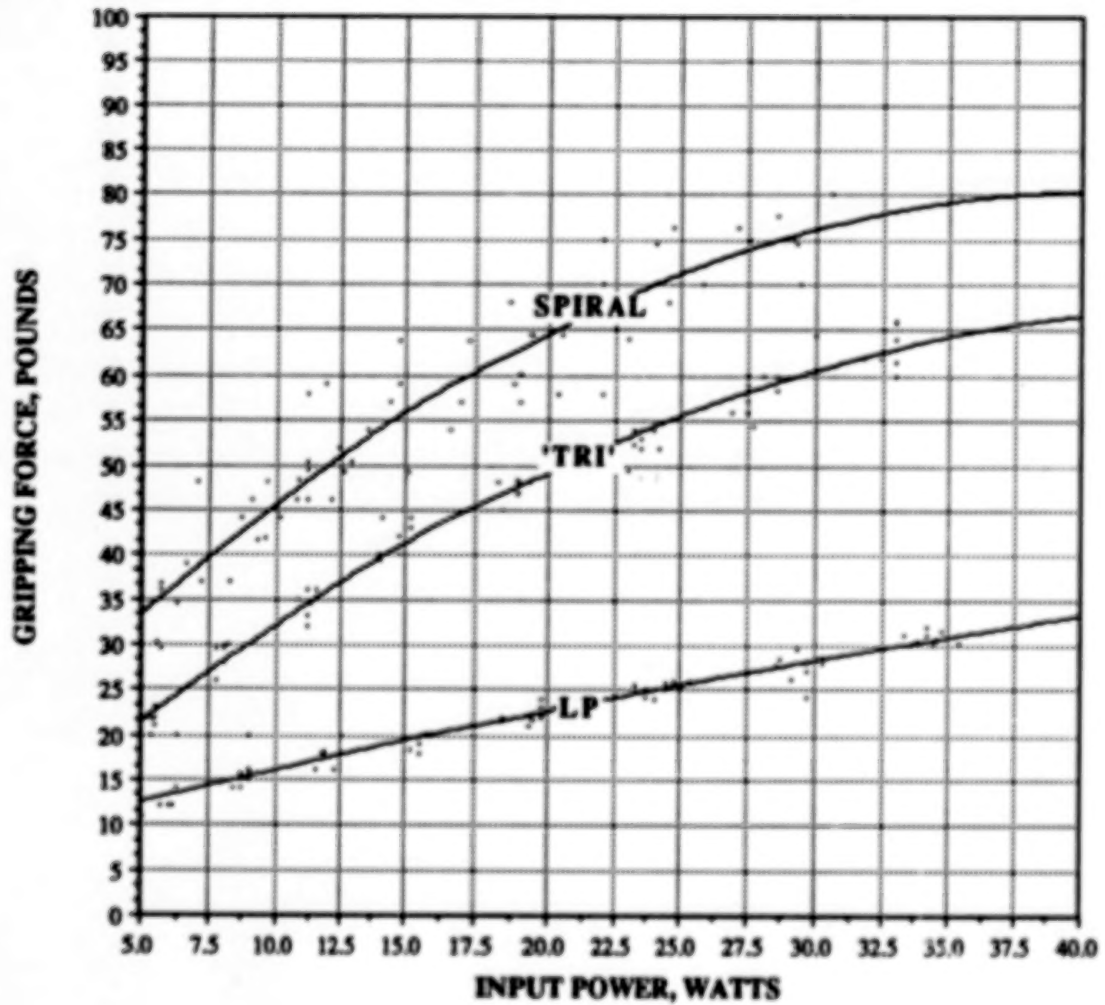


Figure 6. Gripping force versus power.

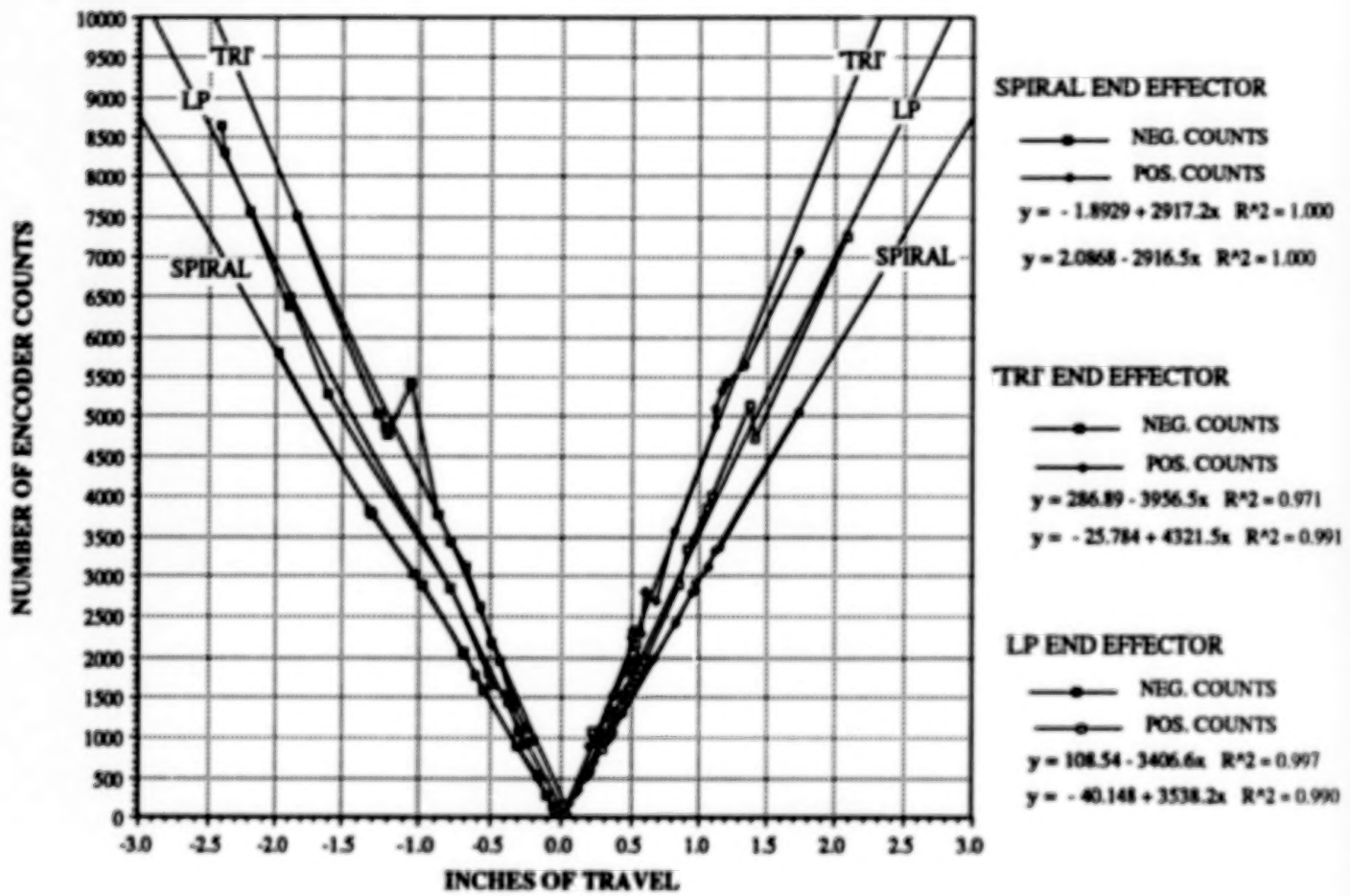


Figure 7. Linearity of jaw positioning.

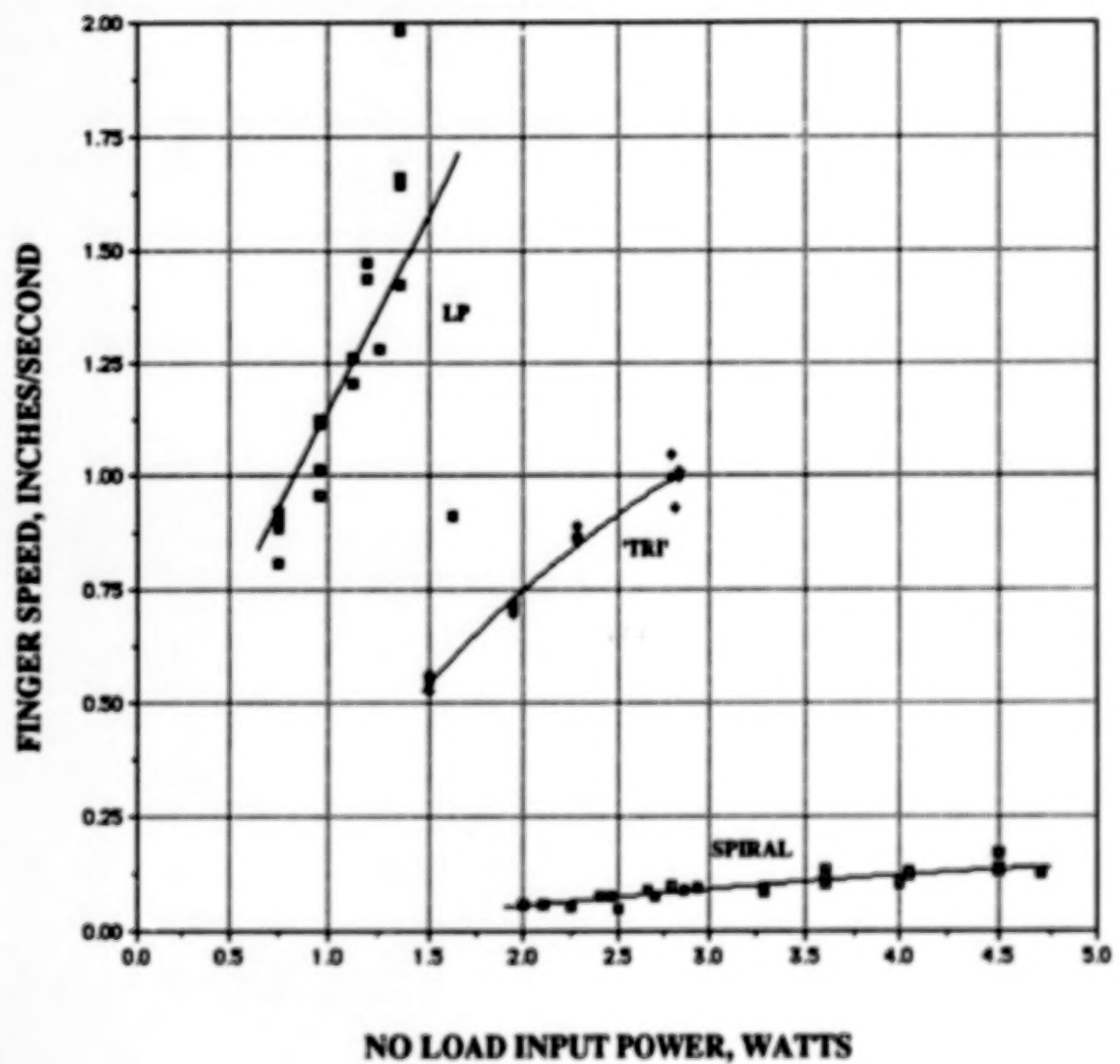


Figure 8. Finger speed versus input power.

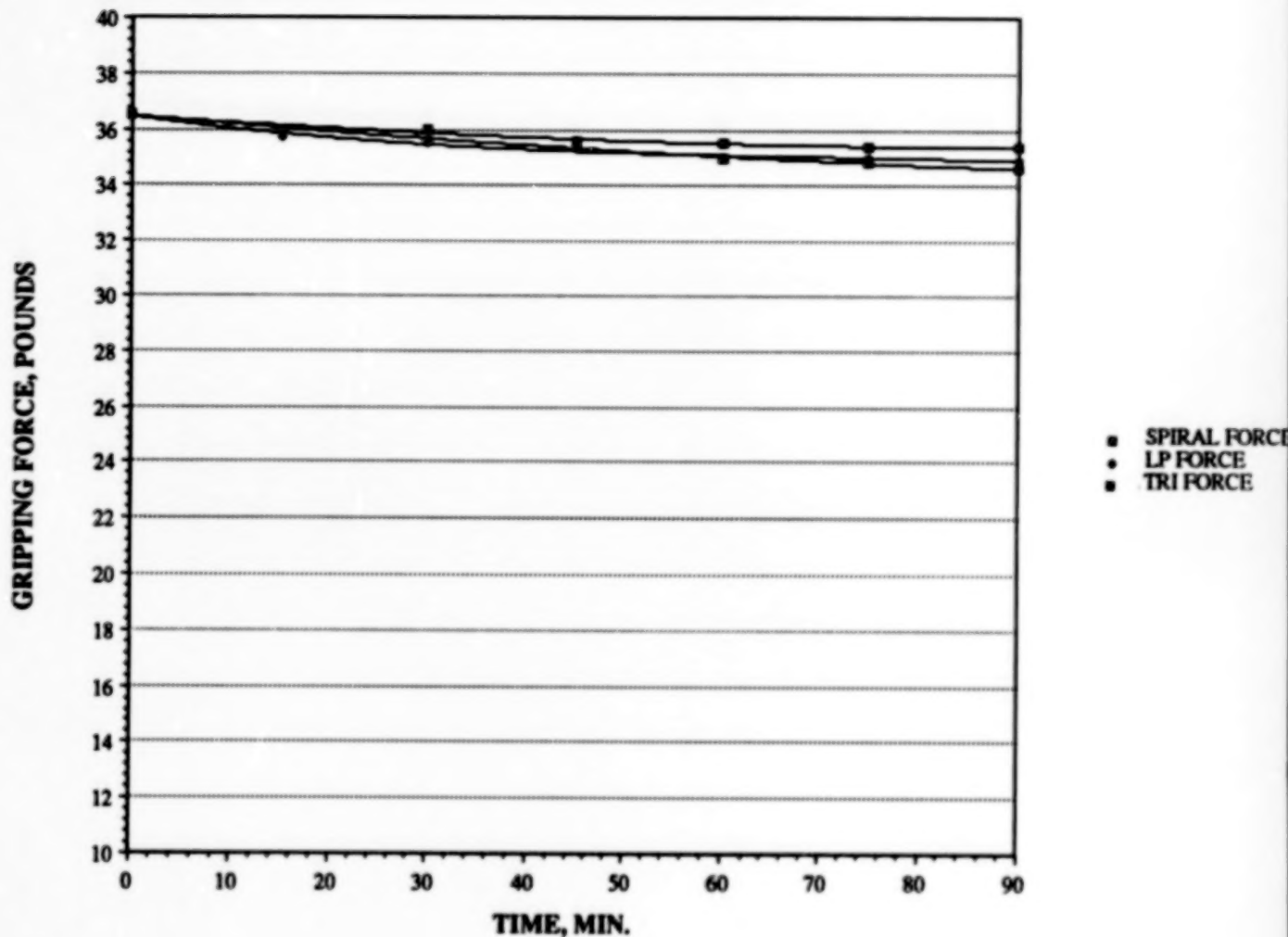


Figure 9. Gripping force relaxation.

TRACTION-DRIVE FORCE TRANSMISSION FOR TELEROBOTIC JOINTS*

D. M. Williams** and D. P. Kuban**

ABSTRACT

The U.S. Space Station Program is providing many technological developments to meet the increasing demands of designing such a facility. One of the key areas of research is that of telerobotics for space station assembly and maintenance. Initial implementation will be with teleoperated devices, but long-term plans call for autonomous robotics. One of the essential components for making this transition successful is the manipulator joint mechanism.

Historically, teleoperated manipulators and industrial robotics have had very different mechanisms for force transmission. This is because the design objectives are almost mutually exclusive. A teleoperator must have very low friction and inertia to minimize operator fatigue. Backlash and stiffness are of secondary concern. A robot, however, must have minimum backlash, and high stiffness for accurate and rapid positioning. A joint mechanism has yet to be developed that can optimize these divergent performance objectives.

A joint mechanism that approaches this optimal performance was developed for NASA Langley Research Center, Automation Technology Branch. It is a traction-drive differential that uses variable preload mechanisms. The differential provides compact design, with dexterous motion range and torque density similar to geared systems. The traction drive offers high stiffness and zero backlash for good robotic performance. The variable-loading mechanism (VLM) minimizes the drive-train friction for improved teleoperation. As a result, this combination provides a mechanism to allow advanced manipulation with either teleoperated control or autonomous robotic operation. This paper will address the design principles of both of these major components of the joint mechanism. Also, various surface modifications to these rollers were studied utilizing previous NASA Lewis Research Center experience. For the VLM, several designs were fabricated and tested to optimize operational performance. Test results from the test joints are included. At the time of this writing, final assembly is under way. Finally, the paper describes some of the limitations of this mechanism, as well as recommendations for further development of this technology.

*Research sponsored by NASA Langley Research Center under Interagency Agreement Number 40-1553-85 with Martin Marietta Energy Systems, Inc.

**Oak Ridge National Laboratory, Oak Ridge, Tennessee 37831-6353.

INTRODUCTION

The purpose of developing a telerobotic work package for space application is to increase astronaut and overall system safety, productivity, and flexibility. Astronaut safety is of increasing concern because of the number of potentially hazardous tasks, such as hydrazine fuel transfer, being planned for space execution. Astronaut risks increase as the demand for extra vehicular activity (EVA) time increases for work on large projects such as space station assembly, operation, and maintenance activities. A remote system would allow around-the-clock operation while the astronaut-operators remain safely inside the orbiter or space station. Finally, with a telerobotic-based dexterous remote-handling system, operations in the far future can be conducted at significant distances (such as geosynchronous orbit) from the orbiter or space station.

The basic criteria for this telerobotic work package are very straightforward. First, the telerobot must replace the dexterity of a suited astronaut, while allowing the operator to work remotely in a "shirt-sleeves" environment. In addition, the design must allow for the transition from near-term teleoperation to far-term autonomous robotic operation.

Traditionally, teleoperated manipulators have been designed primarily for low friction and inertia to minimize operator fatigue. Backlash and stiffness were of secondary concern. Robots, on the other hand, are designed with high stiffness and minimum backlash as a primary concern to accommodate accurate and rapid positioning. Friction and inertia are addressed secondarily, if at all. The design objectives of teleoperators and robots dictate mechanical approaches that are almost mutually exclusive. Attempts to merge these technologies into a "telerobot" have been strictly limited by these contradictory approaches. To accomplish this merger, a joint mechanism is needed that provides very low friction and inertia to accommodate teleoperator requirements and high stiffness and zero backlash to accommodate robotic requirements. A joint mechanism has yet to be developed that can optimize all of these requirements. However, a joint mechanism that approaches this optimal performance has been developed for NASA Langley, Automation Technology Branch called the Laboratory Telerobotic Manipulator (LTM). It consists of a traction drive differential that uses VLMs.

TRACTION-DRIVE JOINT MECHANISM FOR THE LTM

The LTM is a 7-degree-of-freedom (DOF) telerobot that employs replicated traction drive joint mechanisms as shoulder, elbow, and wrist joints (Fig. 1). Each joint mechanism provides pitch and yaw motions about orthogonal axes. Each joint is attached to the adjacent joints by means of only four fasteners to produce a modular mounting arrangement that allows the LTM arms to be easily assembled and disassembled. This modularity also allows the LTM arms to be easily reconfigured for changing requirements and permits maintenance on the arms by simple module replacement.

The LTM has load capacities to accommodate man-equivalent operation. Each LTM arm has a peak load capacity of 30 lb and a continuous load capacity of 20 lb. To accomplish this requirement effectively, the LTM arm was configured by joints having different torque capacities. The resulting torque requirement for each joint is 435 in.-lb for the wrist, 960 in.-lb for the elbow, and 1650 in.-lb for the shoulder. To reduce the fabrication and engineering cost, a large joint having a peak torque capacity of 1650 in.-lb is used at both shoulder and elbow positions. In an effort to optimize dexterity and minimize weight, a small joint having a peak torque capacity of 435 in.-lb is used as the wrist joint. An assembly of the small joint is illustrated in Figure 2. The large joint is simply an enlarged replica of the small joint and is illustrated in Figure 3. Both joint assemblies consist of a differential drive mechanism, two dc servomotors (Inertial Motors) with gearheads, two torque sensors, and two resolvers as shown in Figures 2 and 3. The speed-reduction ratio through the differential is $\sim 3\frac{1}{2}$ to 1. Special gearhead (Bayside Controls) with spring-loaded antibacklash gear trains were used. Commercially available (GSE) torque sensors have been modified and incorporated directly into the joint mechanism to produce a compact arrangement. Vernitron resolvers are located at each joint axis and are coupled directly to the axis of rotation. These resolvers and torque sensors provide the control system data indicating the joint's payload and position.

Cabling provisions have also been made to eliminate the use of external pigtails and connectors. A through-passage within the differential has been provided to accommodate the cabling bundle. This cabling bundle is also equipped with electrical connectors positioned at each mounting interface that engage and disengage automatically as each joint is attached and detached to the adjacent joint.

Permanent-magnet fail-safe brakes have recently become commercially available (Electroid). These brakes have been coaxially mounted to each drive motor and will safely stop each LTM arm during power failure and provide the capability of supporting maximum payloads for long periods without motor overheating. The operating principle of a permanent-magnet brake is similar to that of a standard spring-set brake in the sense that permanent magnets are used to generate a magnetic force that replaces the spring force of the spring-set-type brakes. When the coil of a permanent magnet brake is energized, it cancels this magnetic force, releasing the clamping force on the drive disc. The real advantage of these brakes is their high torque capacity per unit size and weight. These magnetic units are capable of supplying five times the torque-to-weight ratio as spring-set brakes.

The differential drive mechanism has two inputs and one output which rotate about orthogonal axes. Force transmission through the differential drive mechanism is accomplished by traction drives. Unlike force transfer through gear teeth that generate torsional oscillation as the load transfers between teeth, force transfer through traction is inherently smooth and steady, without backlash, and is also relatively stiff [1]. The elements of this traction differential drive can be seen in Figure 4. Two driving rollers provide input into the differential. A significant advantage in this setup is

that each driving roller is required to transmit only one-half of the total torque necessary to make a particular motion. These rollers drive two intermediate roller assemblies, which in turn drive the pitch/yaw roller about the pitch and yaw axes. The axis about which the pitch/yaw roller rotates depends on the direction of rotation of the driving rollers. The pitch/yaw roller is driven about the pitch axis when the driving rollers rotate in the opposite direction. When both driving rollers are rotated in the same direction, the pitch/yaw roller is driven about the yaw axis. Vernitron resolvers are located at each joint axis in an effort to maximize positioning accuracy. By locating these resolvers directly at each joint axis, any creep events that occur through the traction drive differential will not effect the positioning characteristics of the LTM.

The rolling surfaces of the differential are gold plated in an ion-plating process recommended by NASA Lewis Research Center [2]. This plating serves as a dry lubricant that prevents the rolling base materials from contacting. The ion-plating process was performed in a "TORUS 10 MAGNETRON" plating chamber. Each traction drive roller was sputter cleaned in the plating chamber before plating. This was accomplished by evacuating the chamber to 5×10^{-5} Torr, backfilling it with argon to 12×10^{-3} Torr and applying 2000 V negative potential to each roller for 10 min. After sputter cleaning, each roller was plated at a deposition rate of 10\AA per second for approximately 3 minutes until a total thickness of 2000\AA was reached.

VLMs have also been employed as an alternative to constant-loading mechanisms in an effort to improve the differentials back-driveability, mechanical efficiency, and fatigue life. Constant-loading mechanisms produce a constant normal load between the traction drive rollers. This constant normal load must be sized to ensure adequate traction at the joint's maximum torque capacity. The obvious disadvantage of this constant normal load is that the traction drive rollers and their supporting bearings are needlessly overloaded during periods of low torque transmission. This constant normal load not only generates extra bearing losses at low torque transmission but, more importantly, shortens the drive systems fatigue life [3]. To ensure adequate traction with minimum friction loss, VLMs were developed. These mechanisms produce varying normal loads between the traction rollers that are proportional to the transmitted torque [4]. Two VLMs have been incorporated into the traction drive differential. These VLMs are known as the input VLM and the output VLM.

The input VLM produces a varying normal load between the input roller and the intermediate roller assembly. This mechanism consists of an upper thrust cam, a lower thrust cam, a thrust bearing, two radial bearings, a thrust bearing retainer, and four ball bearing balls, referred to as cam balls as shown in Figure 5. This mechanism generates a thrust force proportional to the input torque. This thrust force is applied to the input roller and is counteracted by the thrust bearing and bearing retainer. The radial bearings provide stability to the upper thrust cam. The upper and lower thrust cams are equipped with tapered contours that are formed by helical grooves. These contours contain cam balls as illustrated in Figure 6. Each contour is formed

by two helical grooves, one cut on a right-hand helix and the other cut on a left-hand helix. These two helical grooves converge at a depth that is slightly less than that of the cam ball radius (0.031 in.). A free-body diagram of the upper thrust cam and lower thrust cam is shown in Figure 7. The input torque (T_i) is transmitted from the upper thrust cam to the lower thrust cam by a compressive force generated in each cam ball. This compressive force F is normal to the tangent helical groove and is the resultant force of a horizontal force F_T and a vertical force F_L . Force F_T is the tangential force required to transmit the input torque T_i . Force F_L is a varying thrust load that is counteracted by the thrust bearing and bearing retainer shown in Figure 5. This varying thrust load is applied to the input roller and produces a varying normal load between the input roller and intermediate roller assembly.

The output VLM produces a varying normal load between the intermediate roller assembly and the pitch/yaw roller. This mechanism is incorporated into the intermediate roller assembly as shown in Figure 6. It consists of the intermediate drive roller, eight cam balls, and an intermediate transversing roller. These rollers contain tapered contours that work in conjunction with the cam balls in the same manner as the upper and lower thrust cams of the input VLM. As torque is transmitted between the intermediate drive roller and intermediate transversing roller, a thrust force F_L is generated that produces the varying normal force F_N .

The operational performance of the LTM was verified through testing during its preliminary design. A photograph of the test stand used is shown by Figure 8. The test stand was originally designed to accommodate two different types of speed reducers; a power hinge reducer, which was seen to be economically unfeasible; and a harmonic drive reducer, which is now being used. The test-stand differential is very similar to the LTM small-joint differential. Similar bearings and traction drive rollers are employed in both cases. The test stand is equipped with an input VLM and an output constant-loading mechanism. This arrangement provides the capability to compare the two different types of loading devices. Some of the parameters tested were the starting torque, back-driveability, mechanical efficiency, and torque capacity. The test stand demonstrated that a traction drive differential equipped with VLMs will satisfactorily transmit its designed torque capacity with a mechanical efficiency of ~90 percent.

The starting torque of the test stand differential was measured for the pitch motion and yaw motion independently. The yaw motion involves only the input VLMs, while the pitch motion involves both the input VLMs and the output constant-loading mechanism. This allows comparison between VLMs and the constant-loading mechanism. To measure the starting torque of the pitch rotation, the yaw axis was fixed to the test stand base, and a torque wrench was chucked to one input shaft of the differential (this shaft is also the input shaft of one input VLM) while the other input shaft was free to rotate. Similarly, to measure the starting torque of the yaw rotation, the pitch axis was locked, and torque was applied to one input shaft. Starting torque for the yaw rotation ranged from 65 oz-in. to 105 oz-in., and rotation in the

counterclockwise direction averaged 10 oz-in. less than the clockwise direction. The starting torque for the pitch rotation ranged from 16.5 to 27.75 oz-in. with no significant difference in the direction of rotation. The starting torque for the yaw rotation is much higher due to the constant-loading mechanism which is not involved in the pitch rotation. Therefore, the VLMs accounts for 25 percent of the total starting torque while the constant-loading mechanism accounts for 75 percent.

The spring constant of the test stand input VLM was also measured. To measure this spring constant the pitch/yaw roller and intermediate roller were removed from the differential housing. Next, a rigid bar (6 in. x 1.5 in. x 0.5 in. aluminum) was clamped to the driving roller and wedged against the wrist housing to prevent rotation of this roller. A large C-clamp was tightened over the end of the driving roller and the differential housing to prevent axial motion of the roller shaft. To measure the angular rotation, a rigid aluminum bar (1.5 in. x 0.5 in.) was clamped to the input shaft of the VLM and a dial indicator was located 6 in. along this bar from the shaft axis. To load the mechanism, a torque wrench was chucked to the input shaft of the VLM. The applied torque was increased in 5 in.-lb increments, and three readings were recorded for each torque value. Data was taken for clockwise and counterclockwise rotations. The data was then plotted and linearized to determine the torsional spring constant of the mechanism. This spring constant was 1.3 in.-lb/min which is an order of magnitude smaller than the windup in the harmonic drive.

An important finding that was discovered from testing of the test stand was the inability of the input VLMs to satisfactorily produce loading and allow unloading between the driving roller and intermediate roller without modification to the differential. As the differential transmits a fluctuating torque, the input VLMs generate a thrust force that changes in magnitude. Compliance within the traction drive differential allows the drive roller to translate within the needle roller bearings as this thrust force (applied to the drive roller) changes in magnitude. A parasitic friction force is generated between the driving roller and needle roller bearing during this translation that counteracts loading in an increasing torque condition and unloading in a decreasing torque condition. The exact friction coefficient between the driving roller and needle roller bearings is unknown, making it impossible to calculate the exact value of this friction force. This friction force was originally estimated assuming a friction coefficient of 0.1. This estimate indicated that the driving roller would translate and satisfactorily produce loading and allow unloading between the driving roller and intermediate roller. It was discovered during testing that the friction coefficient was much higher than expected. This produced a higher friction force than calculated. During an increasing torque condition, the friction force counteracted loading to the extent that the driving roller would lose traction and slip. During a decreasing torque condition, the friction force counteracted unloading which caused the driving roller to remain loaded to the extent that it would hang. This hanging condition allowed the compression force generated in the cam balls of the input VLMs to diminish which caused lost motion between the upper and lower thrust cams of the input VLMs. To

correct this problem, a special linear ball bearing assembly was designed, fabricated, and installed between the driving roller and needle roller bearings as shown in Figure 5. The coefficient of friction between the drive roller and linear ball bearing assembly is much less than 0.1 which reduced the parasitic friction force and allowed satisfactory loading and unloading between the driving roller and intermediate roller.

Some of the limitations of LTM pitch/yaw joint that have been observed so far are compliance (wind-up experienced in the drive train) and backdriveability. Compliance is a result of deflection in the VLMs, traction drive rollers, and traction drive supporting bearings. Backdriveability is related to the rolling losses in the traction drive rollers and their supporting bearings. Both compliance and backdriveability are related to the initial preload of the traction drive rollers. Compliance can be decreased by increasing the initial preload, but unfortunately, the torque required to backdrive the LTM pitch/yaw joint is increased. At the time of this writing, final assembly of the LTM is underway and the exact values for compliance and backdriving torque are not known. The traction drive rollers of each LTM pitch/yaw joint have small preloads to accommodate low backdriving torque requirements and good teleoperator performance. Each joint can be backdriven by a torque that is less than 5 percent of its maximum torque capacity. Preliminary static load testing appears to indicate more compliance than expected at these small preloads. Compliance can be reduced in future designs by increasing the stiffness of the traction drive rollers' mounting arrangement and the VLMs. The mounting arrangement of the traction drive rollers can be improved by incorporating angular contact bearing assemblies directly into the pitch/yaw roller, intermediate roller assemblies, and their supporting "T" shaft. These traction drive rollers and their supporting "T" shaft could be equipped with mating grooves that contain bearing balls to create an angular contact bearing arrangement. This arrangement would allow the use of larger bearing balls than the commercial bearings that are presently used. Stiffness of the VLMs can be improved by increasing the number and size of the cam balls. Tapered rollers could also be used as an alternative to the spherical cam ball presently being used.

Future development of the LTM pitch/yaw joint should include thermal vacuum testing. Several concerns must be investigated such as galling of the traction drive rollers in a vacuum environment and effect of temperature change on the preload. Different plating materials and processes should be evaluated to determine their lubricating performance for the traction drive differential. Additional capabilities should be incorporated into the VLMs such as remotely adjustable and temperature compensating preloads.

CONCLUSIONS

A joint mechanism for a space telerobot was developed for NASA Langley Research Center. This joint mechanism incorporates a traction-drive differential that is equipped with variable preload mechanisms. It meets the requirements of both teleoperators and robots. Backlash is eliminated and high stiffness is provided that accommodates accurate and rapid positioning

needed in robots; and low friction and inertia is obtained to minimize operator fatigue needed in teleoperated manipulators. By meeting the requirements of teleoperated manipulators and robots, this joint mechanism is the first operational system to mechanically merge these two technologies into a "telerobot".

REFERENCES

1. Loewenthal, Stuart H., Rohn, Douglas A., and Steinmetz, Bruce M.: Applications of Traction Drives as Servomechanisms. Presented at the 19th Aerospace Mechanism Symposium.
2. Anderson, William, Steinmetz, Bruce M., and Rohn, Douglas A.: Evaluation of a High-Torque Backlash-Free Roller Actuator. Presented at the 20th Aerospace Mechanism Symposium.
3. Rothbart, ed. Mechanical Design and Systems Handbook - 1985, Loewenthal, Zaretsky, Traction Drives, Chapter 34, 1985.
4. Loewenthal, Stuart H., and Zaretsky, Erwin V.: Design of Traction Drives. NASA Reference Publication 1154, 1985.

**BLANK
PAGE**

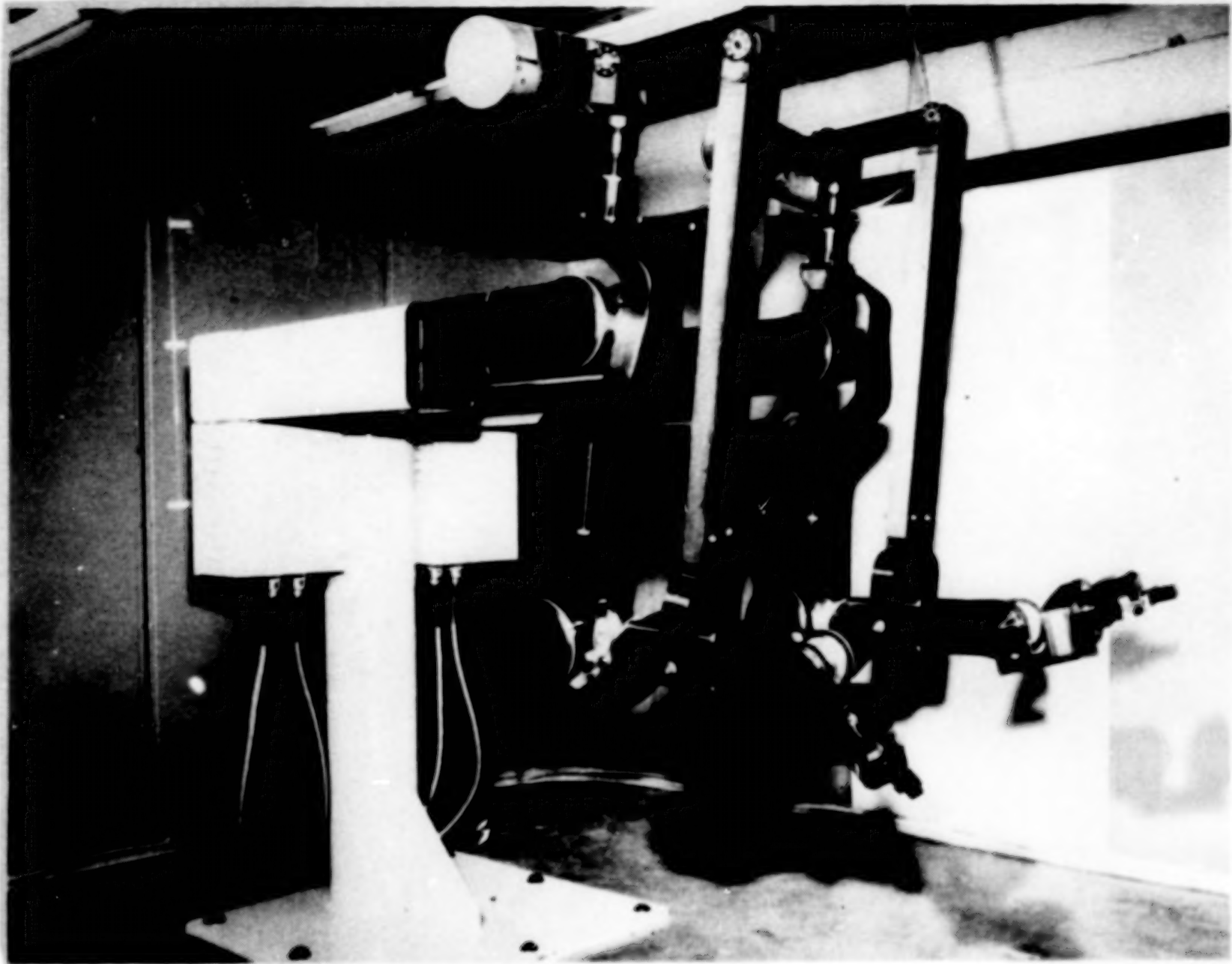


Figure 1. Laboratory Telerobotic Manipulator (LTM) slave.

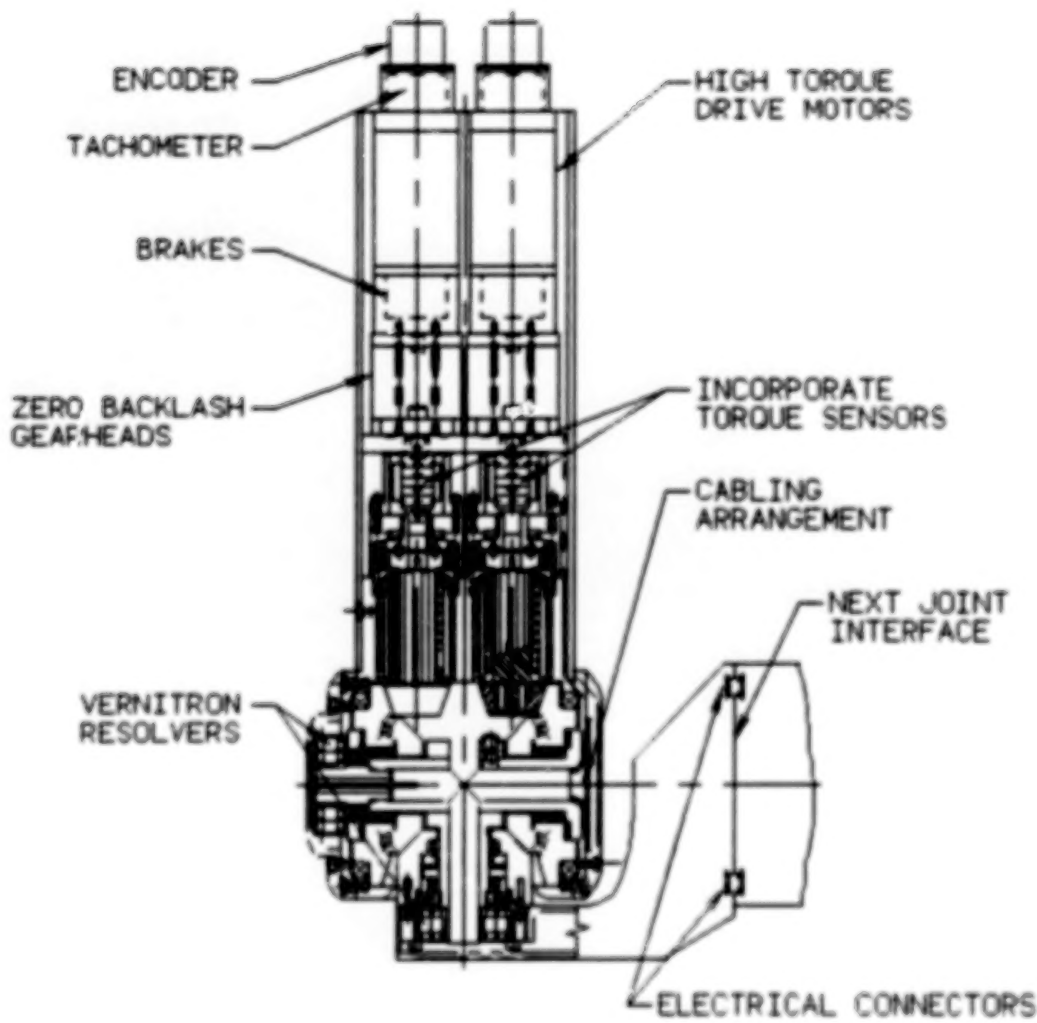


Figure 2. LTM small pitch/yaw joint assembly.

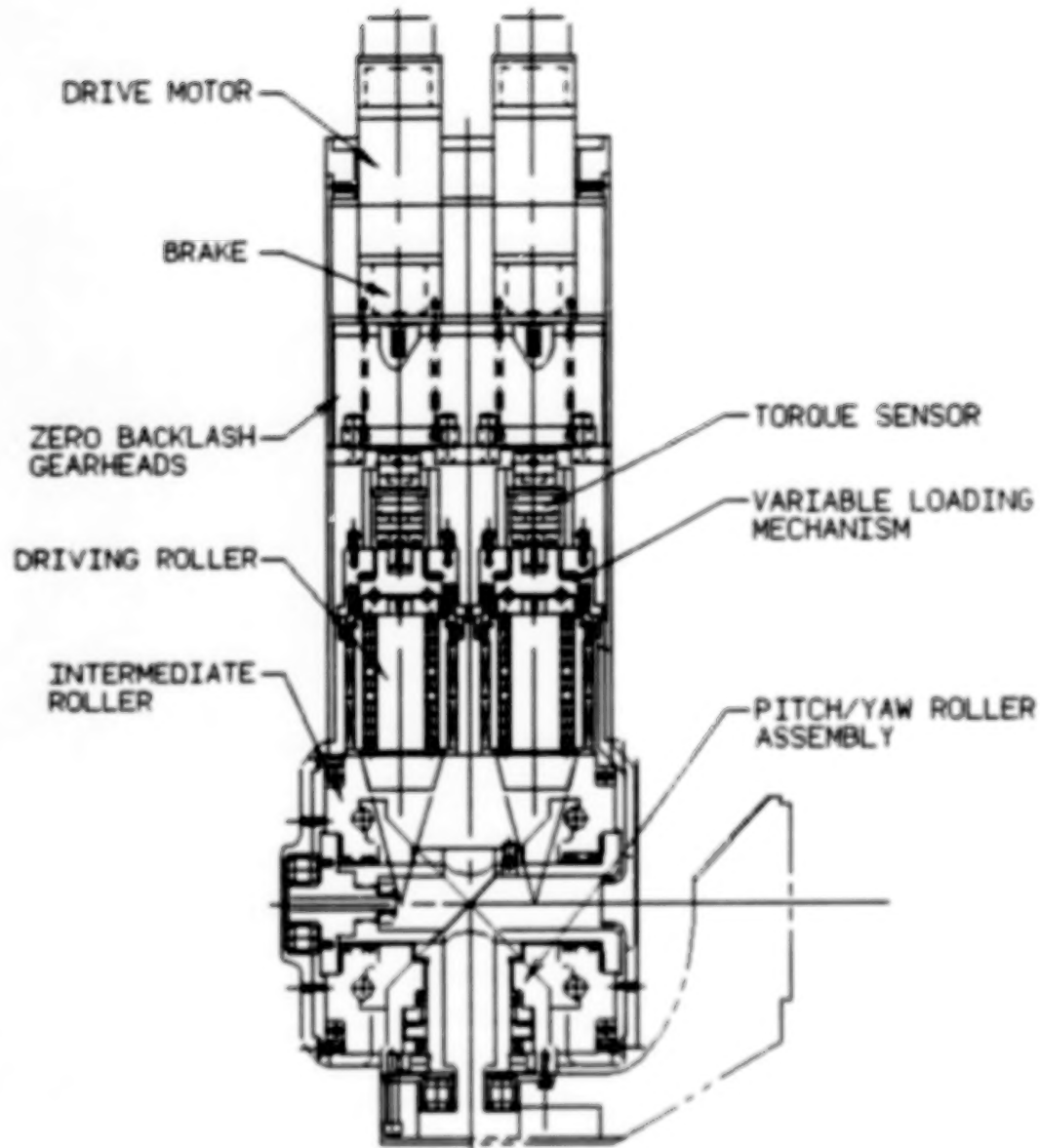


Figure 3. LTM large pitch/yaw joint assembly.

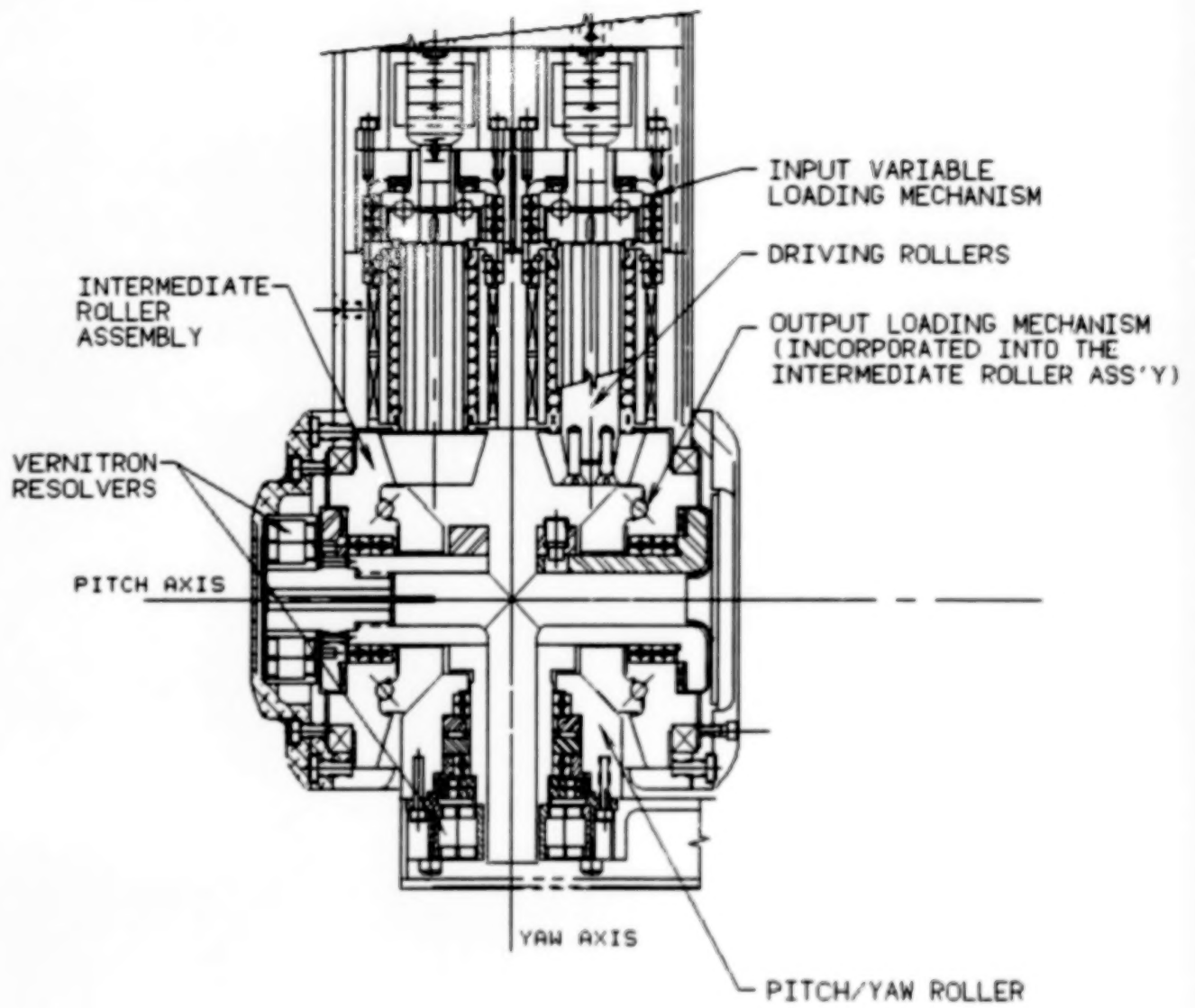


Figure 4. LTM traction drive differential.

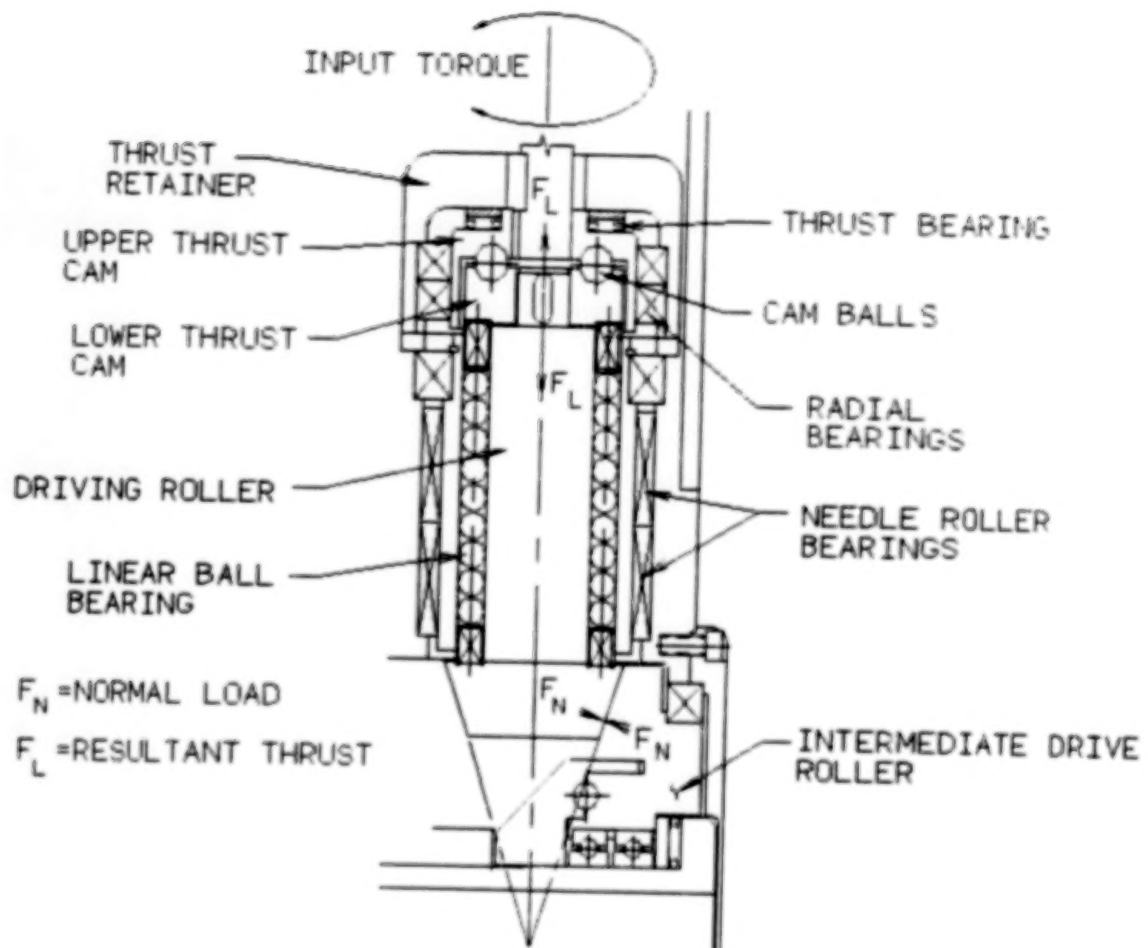


Figure 5. Input variable-loading mechanism.

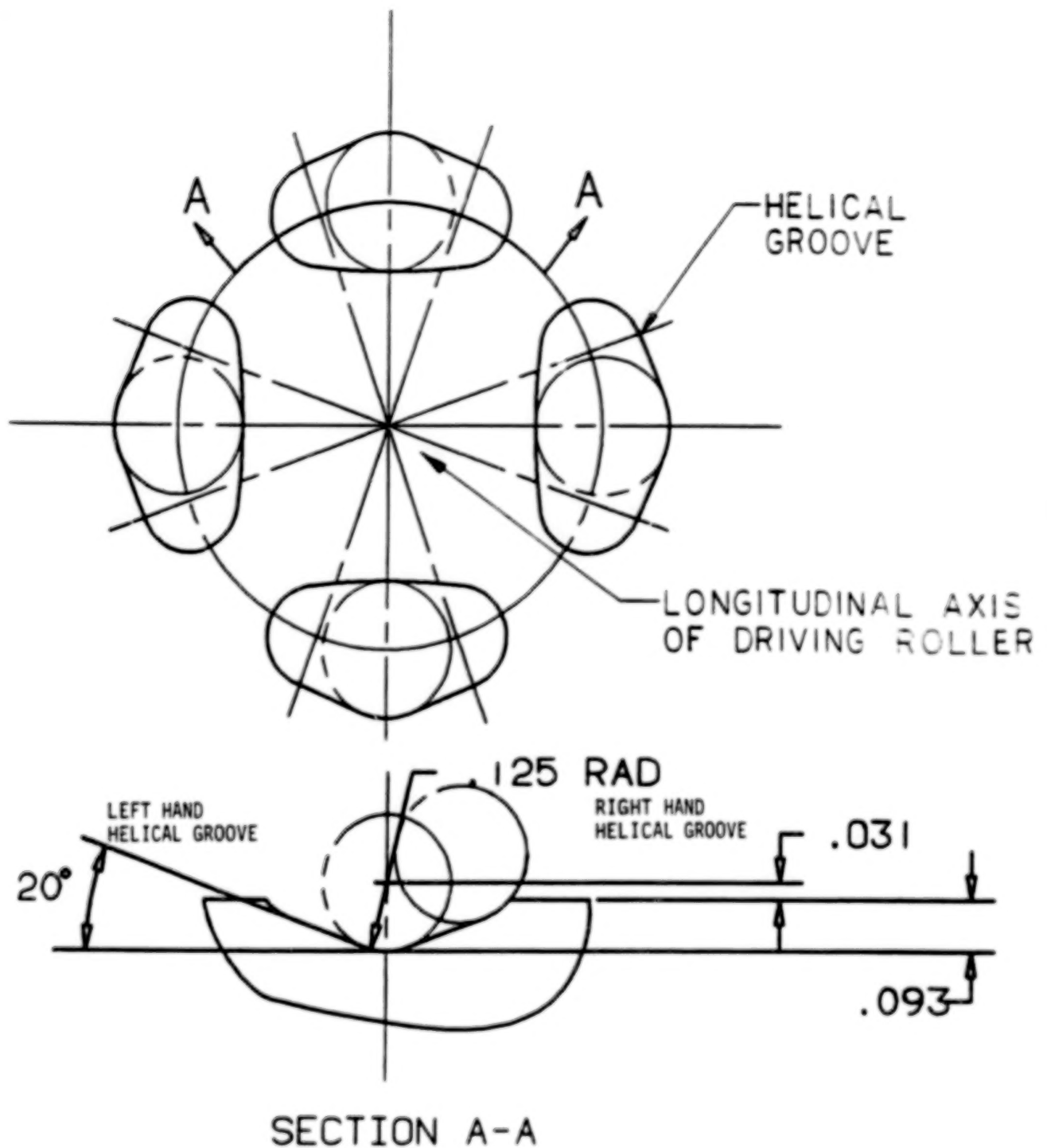


Figure 6. Thrust cam groove detail.

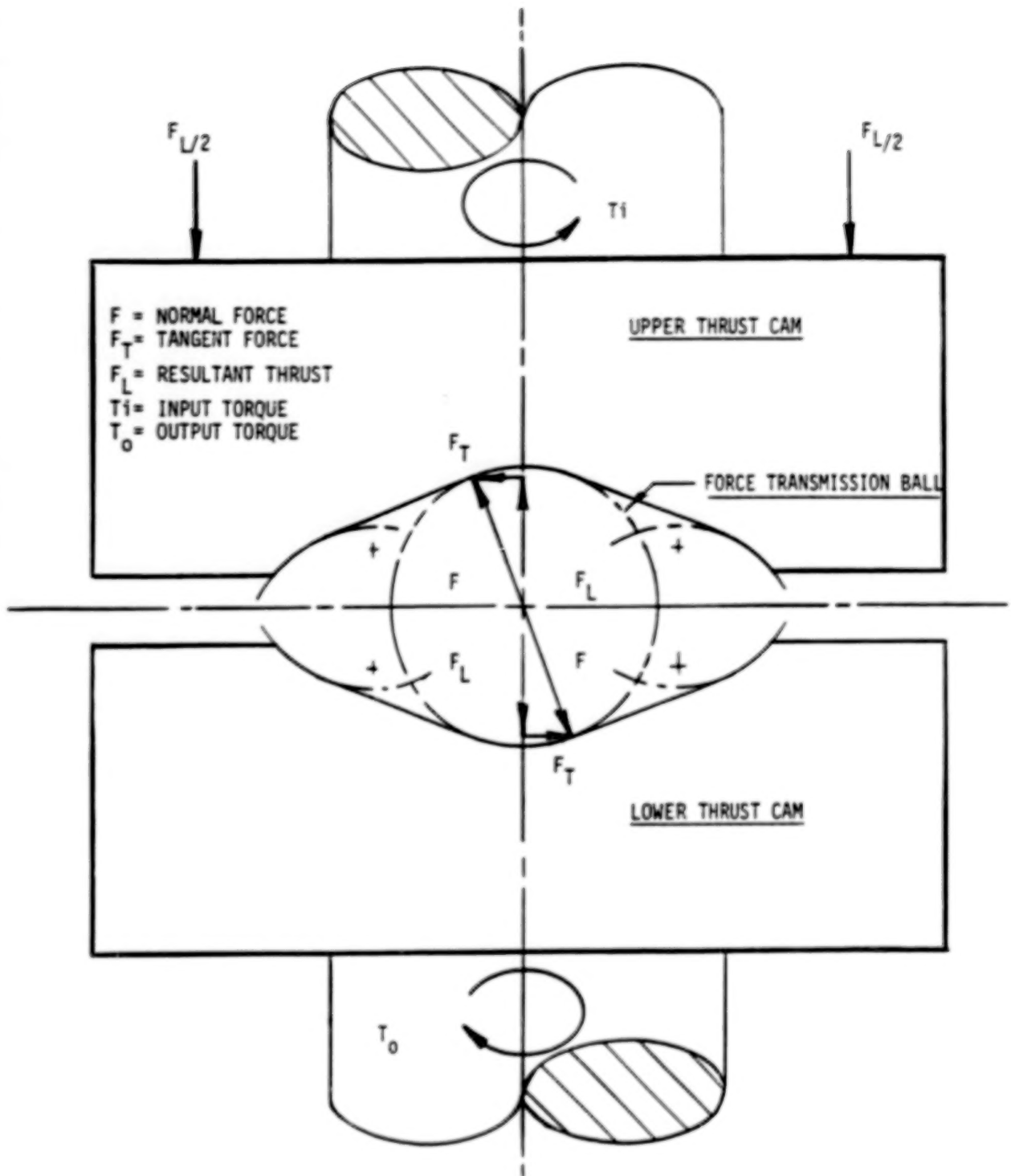
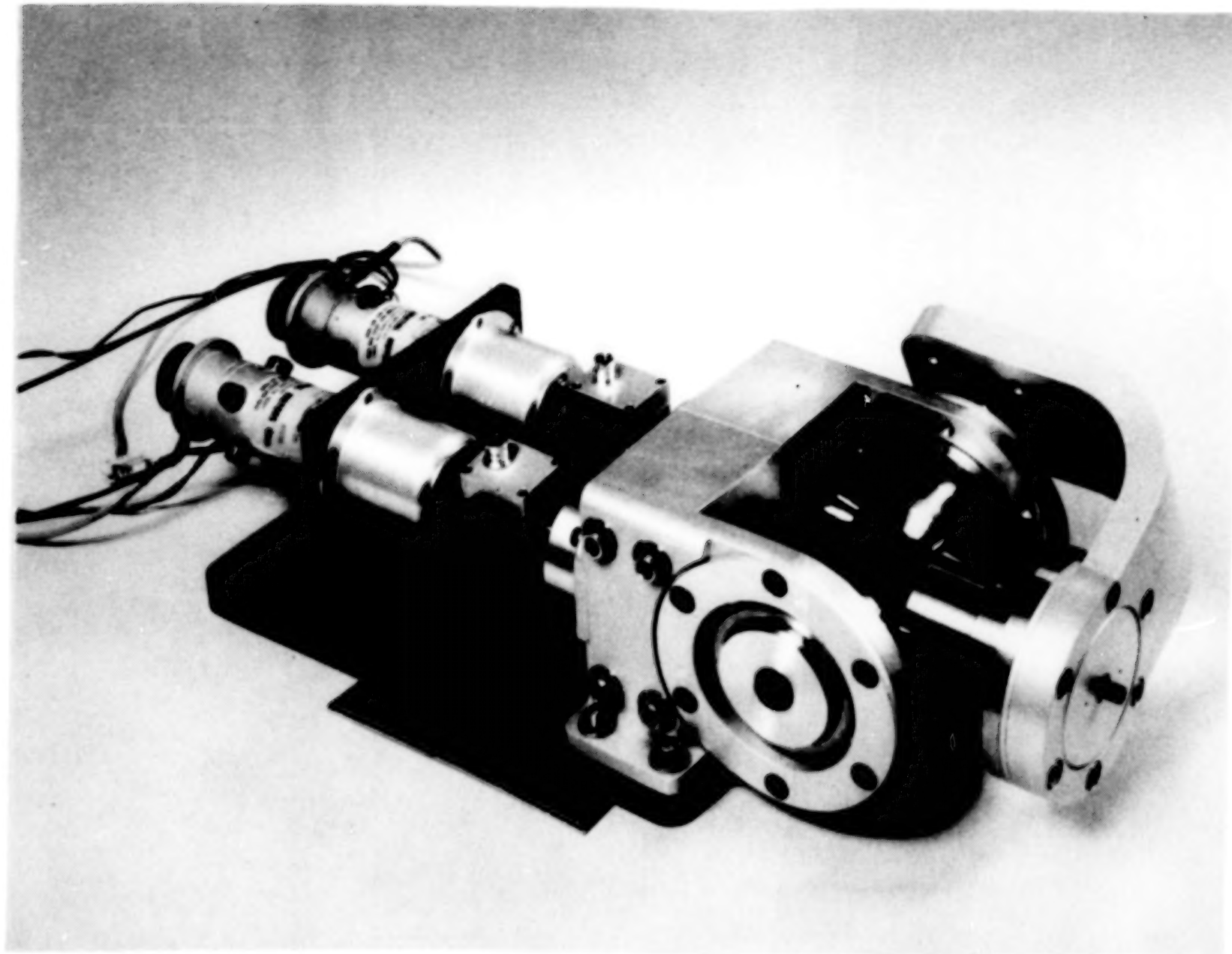


Figure 7. Free-body diagram of variable loading mechanism.



222

Figure 8. LTM test stand.

FLIGHT TELEROBOT MECHANISM DESIGN:
PROBLEMS AND CHALLENGES

John B. Dahlgren* and Edwin P. Kan**

Jet Propulsion Laboratory
Caltech Institute of Technology
Pasadena, CA 91101

ABSTRACT

This paper attempts to state some of the problems and challenges of designing flight telerobot mechanisms. Specific experiences are drawn from four different system developments at JPL, namely, the Force Reflecting Hand Controller, the Smart End Effector, the force-torque sensor, and a generic multi-degrees-of-freedom manipulator.

INTRODUCTION

An advanced telerobot system, which is the unification of teleoperation and robotics, is composed of many subsystems and assemblies. Some of these subsystems contain complex mechanisms, complete with sensors, electronics, and control processors. Many on-going research programs in the U.S. and internationally are directed toward the development of laboratory mechanisms and telerobot technology for terrestrial applications. Very few programs are addressing the development of flight telerobot mechanisms. In fact, the only flight manipulator now existing is the Space Shuttle Remote Manipulator System (RMS). Certainly, NASA's Flight Telerobot Servicer project [1,2] is the first major effort in developing a flight telerobot system in the U.S.

In parallel with and also in support of this Flight Telerobot Servicer project, the Jet Propulsion Laboratory (JPL) is developing a ground telerobot Demonstration System [3], which is a system-wide technology development, integration, and demonstration project. Because of the complexity of the total system, and in concert with the NASREM approach [4], the JPL Telerobot Demonstration System has a hierarchical architecture, as depicted in Figure 1.

The JPL architecture contains an Operator Control Station, a Reasoning and Planning Subsystem (also known as the Artificial Intelligence Planner), a Run-Time Control Subsystem, a Manipulator Control and Mechanization Subsystem, and a Sensing and Perception Subsystem. The Human Operator is not shown in this figure, but is implicit as the "commander" of the system, located at the Operator Control Station. Teleoperation elements are physically distributed

*Deputy Manager, Automated Systems Section.

**Member of Technical Staff.

among the Operator Control Station and the Manipulator Control and Mechanization Subsystem. Figure 1 also depicts the data flow in the two telerobot operational modes, namely teleoperation mode and supervised autonomous mode.

The telerobot mechanisms chosen for discussion in this paper are: (1) Force Reflecting Hand Controller (FRHC) - the input device used during teleoperation mode; (2) GSEE - the robot end effector used in both teleoperation and autonomous modes; (3) force-torque sensor - as part of the GSEE and as an individual sensor; and (4) a generic multi-DOF (degrees-of-freedom) manipulator - the telerobot output device. Specific experiences at JPL, resulting from ground telerobot system development and some flight system development, are summarized in this paper. Through this summary, the many challenges and design problems are exposed, which are common to future flight telerobot systems.

TELEROBOT MECHANISMS - COMPLEX INTEGRATED SYSTEMS

Flight telerobot mechanism design offers special problems and challenges. This is because of the relatively young state-of-the-art technology in telerobot mechanisms, let alone in flight telerobot systems.

Telerobot mechanisms are complex integrated systems. Because of the real-time processing requirements and normally immense data acquisition and dissemination, electronics are often distributed along and/or embedded within the mechanism. Distributed microprocessors are also often designed for optimum data processing and throughput, rather than centralized single-CPU processing. Thus, experience shows that mechanics, electronics, and controls are integrated design issues; hence, early top-down system design considerations are required.

Complex telerobot mechanisms are required in telerobot systems. A telerobot system is an extension of the human operator, designed so that even though the operator is remote from the worksite, the system provides all the necessary input and output devices/data/information to enable him to execute a task as if he were present at the task. This kind of proprioceptive and kinesthetic man-machine interface is said to provide "telepresence." One main attribute of telepresence is force sensing and feedback, which is particularly essential for the performance of dexterous task execution.

Indeed, a lot of research has been devoted to dexterous teleoperation and autonomous robotic operation with real-time sensory feedback and control. This paper addresses only a few elements in this area. The first subject of discussion, the FRHC, is an input device which is capable of force feedback, thus providing the operator with a kinesthetic sense of how the remote manipulator reacts to the environment and to the task object. The second subject of discussion, the GSEE, is a manipulator end effector which provides the capability of dexterous grasping of an object, and also provides sensing of the forces and torques experienced at the wrist of the manipulator. The third subject of discussion, the force-torque sensor, is the heart of this

force feedback and control. The last subject of discussion, a generic manipulator, is the executor of all telerobotic actions. By covering these four subjects, a large class of telerobot mechanisms will be dissected and analyzed.

FRHC - HAND CONTROLLER MECHANISM SYSTEM

The JPL FRHC (Fig. 2) is a general non-master-slave 6-DOF input device capable of backdriving itself [5,6]. It is a ground-based system designed primarily for research purposes as an input device for teleoperating a manipulator arm. By contrast, other 6-DOF non-master-slave input devices such as the Canadian Aerospace Electronics (CAE) trackball and the MSPC controllers, have normally limited travel envelopes, but are not capable of force reflection. Some newer designs at Martin Marietta and at Japan's Ministry of International Trade and Industry (MITI) have force feedback features and comparable travel envelopes as in the JPL FRHC. A comprehensive survey and qualitative evaluation of hand controllers can be found in Reference 7.

This FRHC has 6 DOF, each joint containing its own encoder and dc motor drive. Used as an input device, it provides a 6-DOF cartesian (position and orientation) input to a remote manipulator arm having 6 or more DOFs. As a matter of fact, the FRHC can also be used as a stand-alone robot manipulator device, providing 6-DOF actuation. However, the FRHC is primarily designed as an input device, and therefore is a robot with limited capability.

Two FRHCs, one right-handed and the other left-handed, have been integrated into the JPL/NASA Telerobot Demonstration System, shown in Figure 7. Here, the operator uses the FRHCs to control two robots, grappling and working with a mock-up satellite [8].

JPL is in the process of designing a flight force reflecting hand controller to be flown as part of the Robotic Technology Experiment (ROTEX) experiment in D-2 Spacelab of Federal Republic of Germany (FRG), now planned for 1991 [9]. In that experiment, the JPL flight hand controller (and electronics) will be used as one of the input devices to control a space robot arm developed by FRG. Force reflecting experiments will be conducted and analyzed, deriving guidelines for future design of flight force reflecting teleoperation and telerobot systems.

The following discussion will attempt to summarize certain existing design features, and then list some desirable future design features.

Requirements

High Control Bandwidth - If a telerobot system is to have high control bandwidth, both in its position and in its force control loop, the subsystems and mechanisms, including this FRHC, need to have high frequency response. It is well known that in a mechanical system, its natural frequency is directly proportional to the square root of its stiffness, and inversely proportional

to the square root of its inertia. Hence, the FRHC is desired to have high stiffness and low inertia.

Low Friction - Friction in the FRHC will distort the kinesthetic feedback to the operator, whether the FRHC is used to move the manipulator in free space or when the manipulator is in contact with a task object. The problem is compounded if the friction is not constant in the FRHC work envelope.

Low Effective Inertia - The FRHC needs to be designed so that the dynamics of the hand controller do not compromise the operator's kinesthetic sense of the manipulator motion.

Uniform Isotropic Effective Inertia - Uniform inertia in all directions is desired so as to minimize inertia's effects on operator motion. Experience has shown that if the FRHC has non-isotropic inertia, the FRHC will tend to move in the direction of the least inertia when the operator applies a force (motion) to it.

Design Options

As might be expected, some of the above requirements are conflicting. In the design of the FRHC, there are four major groups into which design options can be categorized:

Kinematics - The FRHC is required to input to the manipulator a 6-DOF position (3 translations and 3 rotations) with 6-DOF force/torque feedback. It is supposed to be a universal non-master-slave input device, i.e., it is not required to have the same link configuration as the remote manipulator. Thus, a multitude of FRHC joint configurations could be designed as in the case of manipulator arm designs. Link configuration could be cartesian, spherical, or articulated.

Structure - This is the main design factor affecting the natural frequency of the hand controller. The present FRHC design employs thin wall tubings as the main link members, in order to achieve high stiffness and low mass. Preloaded bearings are used to maximize joint stiffness, while compromising on friction.

Transmission - Transmission design affects joint stiffness, friction, mechanical advantage, efficiency, extent of backlash, and the placement of actuators. To date, the hand controllers developed at JPL, including this FRHC, all employ pre-tensioned cable/pulley transmissions for the reasons of high stiffness, low weight, low friction, zero backlash, minimal torque variation, and the ability to place the actuators away from the joints.

Actuators - From among the selections of pneumatic, hydraulic, and electric actuators, the FRHC was designed with conventional dc motors. Ripple torque effects, cogging torque effects, and brush frictions are the disadvantages of such a choice. With brushless dc motors, friction effects are minimized; however, electronics design becomes a bit more complex.

Future Design Considerations and Challenges

To date, the best FRHC system bandwidth achieved is estimated to be approximately 10 Hz. A prime objective of future work is to significantly improve this system characteristic. A bandwidth of 25 to 30 Hz is the goal of the flight FRHC presently under development for the ROTEX experiment [9].

Alternative FRHC designs need to be examined and comparatively evaluated. While the existing FRHC has a spherical coordinate design, two new designs are now being evaluated: a cartesian hand controller and an articulated (anthropomorphic) hand controller. Also, alternative designs in the transmission need to be examined. Their effects on stiffness and friction on the overall performance need to be investigated.

GSEE - SMART END EFFECTOR

The GSEE is a set of two smart end effectors developed at JPL for Goddard Space Flight Center. This GSEE [10] is designed to interface with the PUMA 762 robot arm. Its system design evolved from two earlier JPL smart end effector developments [11,12], one designed for the Orbital Maneuvering Vehicle and tested at Marshall Space Flight Center, and the second designed for the PUMA 560 robot at JPL.

Other development efforts in sensory control robot grippers are on-going in the industry (e.g., the Lord gripper and the Telerobotic Research Inc. gripper) and research centers. Much attention in recent years has also been given to multi-fingered hands. Notable for their brilliant but very complex designs, both in mechanism and in controls design, are the Salisbury (MIT/JPL) 3-finger hand the Jacobson (Utah) 4-finger hand. A thorough discussion on robot hands can be found in Reference 13. The GSEE is discussed here because its design is based on expected space applications.

The GSEE (Fig. 3) has all its electronics, microprocessor, and two sets of robotic sensors integrated at the end effector, thus minimizing the external interface to a RS-232 serial line for data, plus a power line. The two sets of sensors are a 6-DOF force-torque sensor and a set of two grip-force sensors. The former is familiarly known as the wrist force sensor, and the latter measures the grip force at the base of the fingers of the GSEE. Local electronics perform the conditioning of the data, analog-to-digital conversion, and multiplexing of the data. In addition, a communication process in the local processor performs the packaging and depackaging of the data, which is shipped over the RS-232 serial data line. Force-torque data and other engineering data is shipped to the external world, while commands and status requests are received by the GSEE. The local microprocessor performs the control computations for the closing, opening, and force control of the GSEE gripper; the control loop is closed at around 100 Hz.

Requirements

High Stiffness - The end effector must work in an end-to-end manipulator system, and in a tool and task environment where flexibility and compliance might be distributed, thus requiring active compliant advanced controls. In order not to add another complication to the control design, this end effector must have higher stiffness and mechanical bandwidth than the overall system.

Low Mass and Inertia - This requirement is necessary to minimize the dynamic effects on the control of the manipulator. For laboratory systems where payloads of the manipulator may be limited, extra mass and inertia from the end effector may degrade manipulator performance.

Force Control - For dexterous control during task execution, it is desirable to have control of the grasping force of the end effector. Current research is investigating compliant grasping with self-centering of fingers.

Design Options

Kinematics - Even with simple grippers, a number of kinematic arrangements is possible. The most popular design is the parallel jaw gripper which has low complexity, high grasp force to weight ratio, and ease of control. The GSEE utilizes a design in which both jaws are translated directly toward each other. The motion of grippers is linear, unlike a 4-bar linkage gripper that effectively has x-y motion when the gripper is closed or opened.

Structure - Design of the structure must be stiff but light, considering adequate thermal pathway or heatsink from the local electronics, especially the motor. Particularly during active clamping on an object, the motor will generate excessive heat and will cause failures if the heat is not properly dissipated. The heat sink design is critical for flight systems, which operate in the absence of an atmosphere.

Transmission - The transmission system selected depends heavily on the kinematics design. The transmission should have light weight, high stiffness, low friction, and should demonstrate little or no backlash. Low friction and little backlash are necessary for good position and force control. Past designs at JPL have used ball screws and rack-and-pinion drives for jaw actuation, using multi-stage gear reductions between the motor and the fingers.

Actuators - Direct current (dc) servomotors are most commonly used for grippers employing force control. To minimize heat generation, motors with high torque constants and low winding resistance are used. Torque output per unit mass should be high and motor friction should be low.

Future Design Considerations and Challenges

Performance of existing designs can be improved by further reducing friction levels present in the drive and actuation mechanisms. Placement of different sensors and real-time integration of the sensor information into local control loops will bring about more dexterous end effectors.

New end-effector finger design will expand the capability of the parallel jaw grippers. Self-centering fingers with quick release (quick change) mechanisms will further enhance the capability. Also, drastically different designs such as multi-DOF hands or multi-finger hands should be considered.

FORCE-TORQUE SENSOR

Since 1978, JPL has been developing wrist force-torque sensors that measure 6-DOF forces and torques. These sensors have been developed separately as well as being integrated with grippers for the performance of dexterous teleoperation. Experimental results using force-torque sensing for robot arm tele-manipulation, using the ground Shuttle RMS arm replica at Johnson Space Center and the ground OMV arm at MSFC have been reported [14,15].

A flight version of the same design has been under development for a planned Shuttle flight experiment in 1990. Figure 5 shows this flight sensor as compared to the ground sensor, Figure 4, which was developed for earlier feasibility experiments at JSC. Figure 6 is a schematic diagram for both sensors. Both sensors have the same goal specifications in terms of the range in payload force-torque sensing. The range is 880 N (200 lb) in forces and 270 N-m (200 ft-lb) in torques.

Casual comparison of Figures 4 and 5 reveals design differences between the two sensors, even though they are designed to the same operational force and torque range. In the following paragraphs, pertinent design changes necessary to move closer to a space-qualified sensor are discussed.

System and Flight Related Specifications

The flight sensor carries the following specifications:

- Launch dynamic g-loading in the Shuttle
- Launch configuration which has this sensor mounted at the end of the Shuttle RMS robot arm, with the Special Purpose End Effector (SPEE) mounted at the other end of the sensor; SPEE is the standard end effector of the Shuttle RMS arm.
- Flight safety considerations
- Flight electronics to be located in the Shuttle mid-aft-deck

- Power to in-situ (at sensor) electronics and data line limited to existing cable routed along the Shuttle RMS arm.

Because of the above specifications, major design changes had to be made to the ground sensor. The most major design change is due to the launch configuration and g-loading.

The flight sensor is now designed to the following specifications, as compared to goal specifications of 270 N-m (200 ft-lb) and 880 N (200 lb), with sensitivity at 0.27 N-m (0.2 ft-lb) and 0.88 N (0.2 lb):

<u>Launch Design Load</u>	<u>Operational Performance Parameters</u>	
	<u>Range</u>	<u>Sensitivity</u>
M_x 610 N-m (450 ft-lb)	680 N-m (500 ft-lb)	0.49 N-m (0.36 ft-lb)
M_y 2,400 N-m (1,760 ft-lb)	857 N-m (630 ft-lb)	0.86 N-m (0.62 ft-lb)
M_z 2,400 N-m (1,760 ft-lb)	857 N-m (630 ft-lb)	0.86 N-m (0.62 ft-lb)
F_x 47,100 N (10,560 lb)	16,700 N (3,764 lb)	16.5 N (3.7 lb)
F_y 7,250 N (1,625 lb)	3,980 N (892 lb)	4.0 N (0.9 lb)
F_z 7,250 N (1,625 lb)	3,980 N (892 lb)	4.0 N (0.9 lb)

where M_x , M_y , and M_z denote the x, y, and z torques, and F_x , F_y , and F_z denote the x, y, and z forces. Notice the sacrifice in the sensitivity of the operational ranges, because of the large range of forces and torques the sensor is now measuring.

Another noticeable difference in the flight sensor design is the need for temperature gradient compensation and absolute temperature compensation, because of the Shuttle space environment. Safety concerns also led to a number of actions: strength of the overload pin was increased; careful structural and fracture mechanics analyses were performed; finite-element model analyses were made to study the structural frequencies; and special placement of the strain gauges was designed, with selection of space qualified gauges and bonding compounds of the gauges.

In support of the calibration of the sensor, whose dynamic range was significantly increased over the ground sensor design, a special heavy duty calibration jig sitting on a stable base (like an optical bench) had to be developed. Previous crude methods of hanging weights to calibrate the ground version of 270 N-m/880 N (200 ft-lb/200 lb) sensor obviously would not work. On this jig, strain gauges were also instrumented, and these gauges in turn had to be calibrated.

System design also called for an analysis of the loading on the Shuttle RMS arm when loads up to the maximum range of the sensor are actually applied to the RMS.

A GENERIC MULTI-DOF MANIPULATOR

As mentioned in the Introduction, there is only one existing flight manipulator arm, namely the Space Shuttle RMS. The RMS has capabilities designed for large excursions and transports of large payloads (in space). Its requirements are far from being compatible with telerobot requirements where accurate, robust, and versatile motion of the manipulator is required. Control systems for dexterous manipulation also call for position-force control using rigid arms; such properties are absent in the RMS.

JPL has not developed a flight telerobot manipulator arm; its closest development is the flight FRHC (see earlier section of paper), which can be considered a flight manipulator. However, based on the experience with industrial robot arms, the latest research arms from Robot Research Inc., and the Laboratory Telerobot Manipulator (LTM) from Langley Research Center/Oakridge National Laboratory, certain observations can be drawn. They are provided in the following paragraphs.

Existing methods of specification for industrial robot arms are inadequate and likely unsuitable for specifying flight telerobot arms. Real-time processing and advanced controls using position-force control and adaptive control create heavy demands on dedicated processing and data communication that may be incompatible with current space station designs (of other platform). In consideration of the whole system, dynamic interaction of the robot arm with the robot task will create disturbance to the space station that may be outside its acceptable range.

The following lists present desirable features to be included or considered by the mechanism designer in the specification and design of future flight telerobot arms. This list is based on experience with certain industrial and experimental robot arms, exposure to system studies for the design of a flight telerobot system, and on the current design of the JPL ground Telerobot Demonstration System.

System and Flight Related Specifications

- Robot configuration and degrees of (redundant) freedom
- Robot speed, within the range of safety of flight operation and degree of dynamic interaction with the vehicle, where the robot arm is housed
- Robot effective inertia, with due consideration of payload augmented inertia; compatibility with flight system attitude control
- Dexterity required of robot arm manipulation versus size of robot
- Absolute accuracy, resolution, and calibration methodology; in consideration of the tasks required of the robot

- Data throughput from robot to supporting electronics/subsystems; compatibility with flight system data distribution design.

Mechanical, Electrical and Data Communication

- Structural flexibility versus desired dexterity of robot
- Direct drive, geared drive versus other power transmission schemes
- Trading between routing of many cables with distributed local electronics and intelligence
- Electrical data line versus optical fiber data line
- Data throughput rate
- Distributed processors (physical distribution) versus localized processing (which may still use distributed processors - distributed in data processing, not physical distribution).

Control and Real Time Processing

- Advanced control requires data cycle rates greater than 100 Hz; robotic computation requires a 10 MIPS machine
- Flexible robot arm control requires new concepts of sensors and control algorithms
- Flight system attitude compensation needs to be designed in coordination with robot arm control laws
- Position-force control of robot arms needs to be designed in coordination with flexible robot arm control.

User Interface

- For payload specialists to operate robot arms, simple robot arm macro commands are desired
- For telerobotic control where the operator interacts continuously with the robot arm and other controls, effective and efficient operator interface are desired.

CONCLUSIONS

Designing flight telerobot mechanisms requires a heritage and library of design rules that are only partially available. This paper has attempted to extrapolate some pragmatic issues and past experiences at JPL in ground telerobot systems and in flight telerobot mechanisms, and has condensed these experiences in a systematic fashion. These design problems will continue to

challenge designers, system architects, and managers until the telerobot technology further matures.

ACKNOWLEDGMENTS

This research was carried out at the Jet Propulsion Laboratory, California Institute of Technology, under contract with the National Aeronautics and Space Administration. The authors are also grateful to Mr. Edward Snow for his contribution to the sections on the FRHC and GSEE.

REFERENCES

1. Oberright, J.: Space Station Flight Telerobotics Servicer Program Overview. Proceedings of the First Workshop on Space Telerobotics, Pasadena, California, January 1987.
2. Andary, J., Hinkal, S., and Watzin, J.: Teleoperated and Robotic Manipulation on the Space Station with the Flight Telerobotic Servicer. Proceedings of the Second Space Operations Automation and Robotics Workshop, SOAR 88, Dayton, Ohio, July 1988.
3. Schenker, P.: Telerobot Program Objectives and Technology Outreach. Proceedings of the First Workshop on Space Telerobotics, Pasadena, California, January 1987, also JPL Publication 87-13, Vol. 1, July 1987, pp. 3-17.
4. Albus, J., McCain, H., and Lumia, R.: NASA/NBS Standard Reference Model for Telerobot Control System Architecture (NASREM). National Bureau of Standards, NBS Technical Note 1235, June 1987.
5. Bejczy, A., and Salisbury, K.: Controlling Remote Manipulators through Kinesthetic Coupling. Computers in Mechanical Engineering (CIME), Vol. 2, No. 1, July 1983.
6. McAfee, D.: Teleoperator Subsystem/Telerobot Demonstrator: FRHC Operation Manual. Jet Propulsion Laboratory, JPL Internal Report No. D-5172, January 1988.
7. Brooks, T., and Bejczy, A.: Hand Controllers for Teleoperation: A state-of-the-art technology survey and evaluation. Jet Propulsion Laboratory, Publication No. 85-11, March 1985.
8. Kan, E., and Austin, E.: The JPL Telerobot Teleoperation System. Proceedings of the 2nd Int. Symp. on Robotics and Manufacturing, Albuquerque, New Mexico, November 1988, pp. 577-586.
9. Hirzinger, G., and Bejczy, A.: ROTEX-TRIIFEX: A Joint FRG-USA Telerobotic Flight Experiment on the D-2 Spacelab Mission. Proceedings of the Second Workshop on Space Telerobotics, Pasadena, California, January 1989.

10. Killion, R., and Robinson, L.: The JPL OMV Smart Hand. Proceedings of the Goddard Space Flight Center Conference on Space Applications of Teleoperation and Artificial Intelligence, Greenbelt, Maryland, May 1987.
11. Bejczy, A., Kan, E., and Killion, R.: Integrated Multi-Sensor Control of Smart Robot Hand. Proceedings of the AIAA Conference on Automation and Control, Snowmass, Colorado, August 1985.
12. Fiorini, P.: Versatile Hand for Manipulator. IEEE Control Systems Magazine, September 1988.
13. Multiple papers in "Workshop on Robot Hands," Proceedings of the 1988 IEEE International Conference on Robotics and Automation, Philadelphia, Pennsylvania, April 1988.
14. Bejczy, A., Dotson, R., Brown, J., and Lewis, J.: Manual Control of Manipulator Forces and Torques Using Graphic Display. Proceedings of IEEE Int. Conf. on Cybernetics and Controls, Seattle, Washington, October 1982.
15. Hannaford, B.: Task Level Testing of the JPL-OMV Smart End Effector. Proceedings of the First Workshop on Space Telerobotics, Pasadena, California, January 1987, also JPL Publication No. 87-13, Vol. 2, July 1987, pp. 371-380.

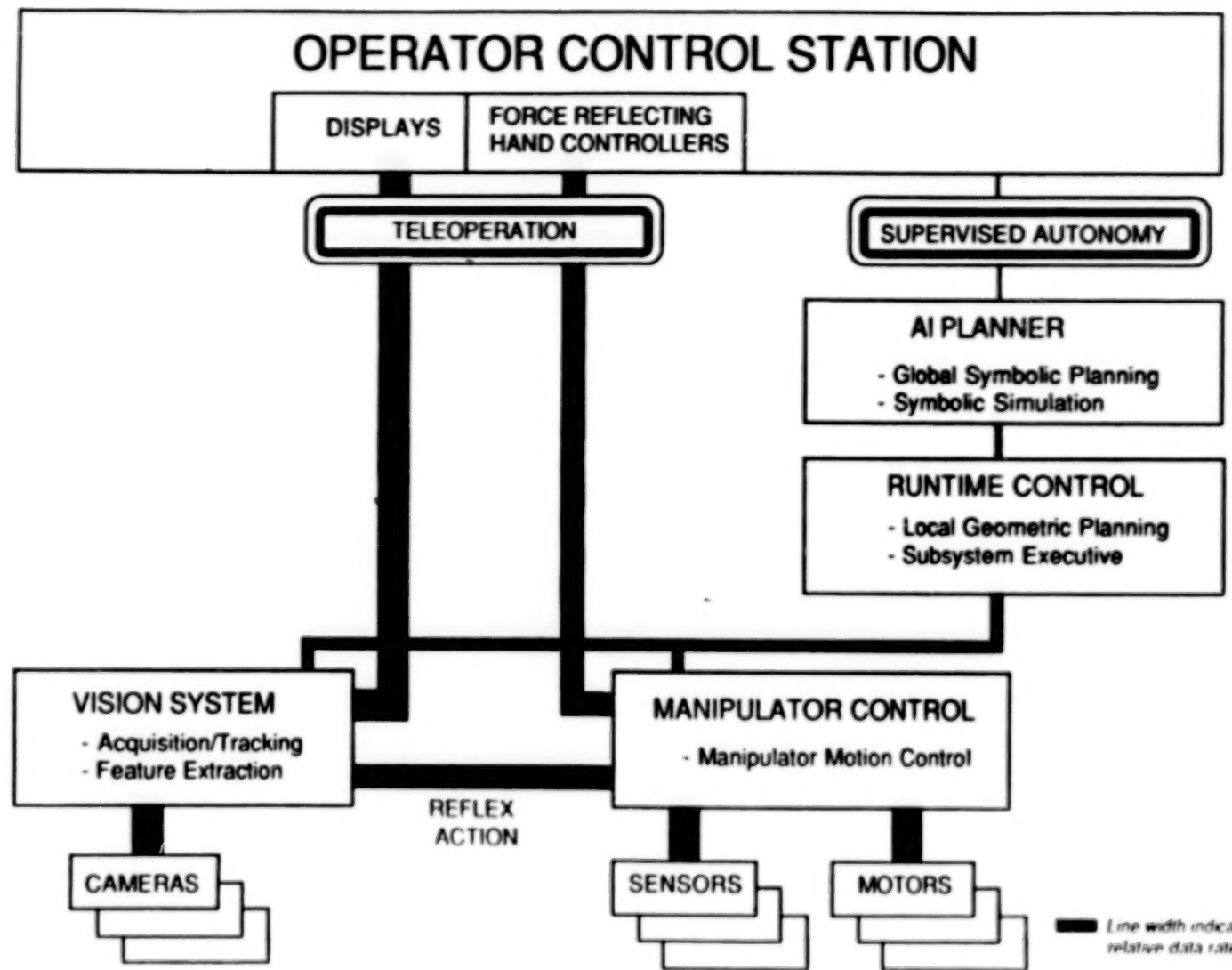


Figure 1. The JPL Telerobot Demonstration System Architecture.



Figure 2. The JPL Force Reflecting Hand Controller
(ground version).

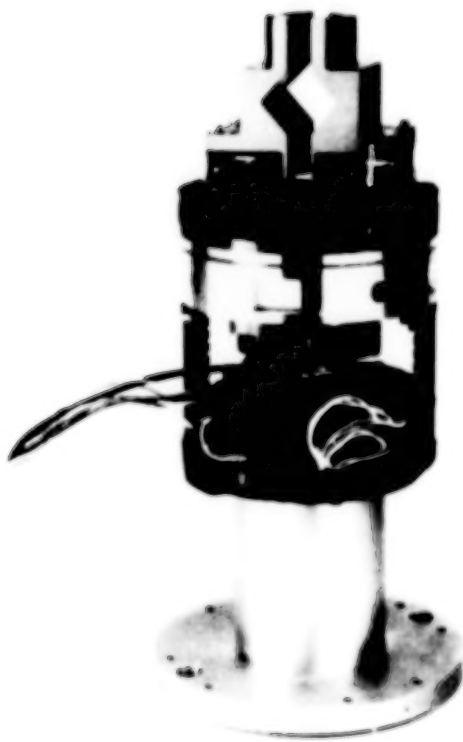


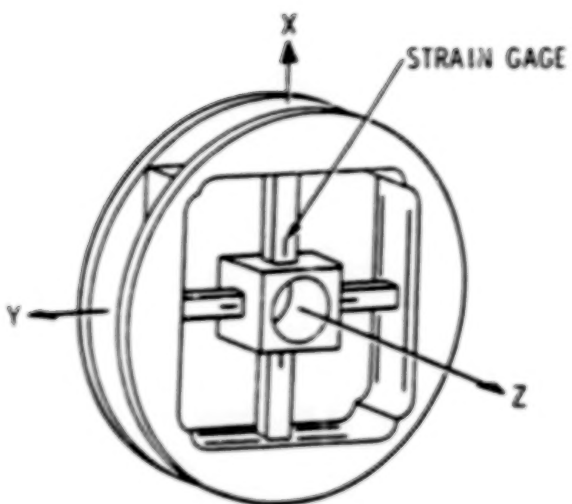
Figure 3. The Smart End Effector (GSEE for GSFC).



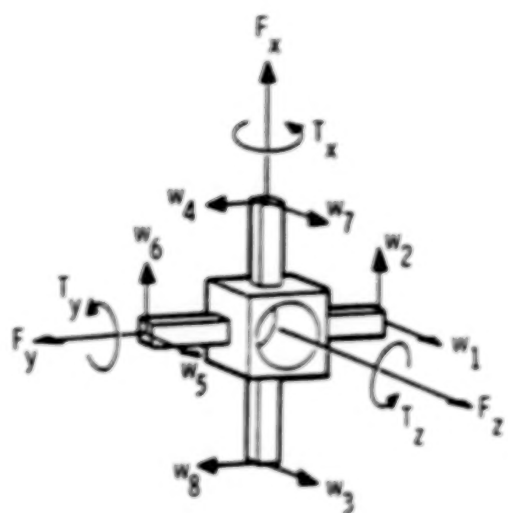
Figure 4. Force-torque sensor (ground version).



Figure 5. Force-torque sensor (flight version).

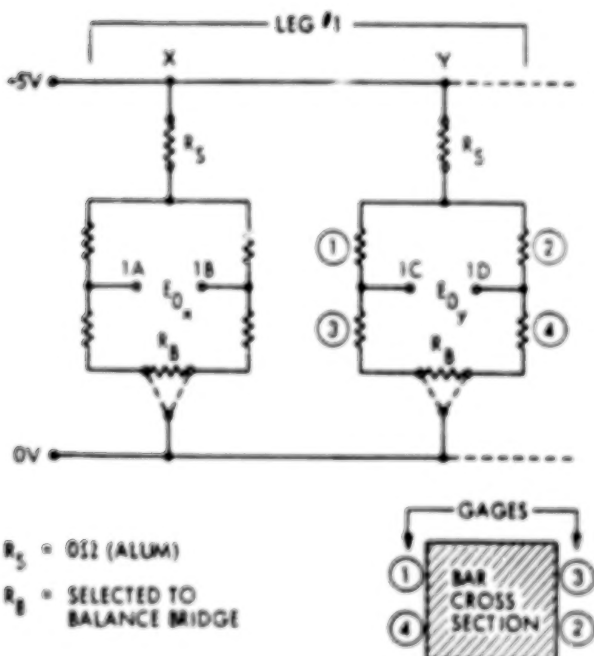


(a)



(b)

(c)



- (a) Placement of strain gauges on the cross beams.
- (b) Resolution of 6-DOF forces/torques into strain gauge strain components.
- (c) Circuit diagram for wiring strain gauges.

Figure 6. Schematics of the force-torque sensor.



Shown in figure: (a) a generic Operator Control Station with two FRHCs, (b) two manipulating robot arms with grippers, instrumented with force-torque sensors, (c) one vision robot arm, and (d) the task: grappling and working with a mock-up satellite.

Figure 7. The JPL/NASA Telerobot Demonstration System.

BLANK PAGE

240

A FAMILY OF BAPTA'S FOR GEO AND LEO APPLICATIONS

W. Auer*

ABSTRACT

The reliable function of a Solar Array Drive, a so-called Bearing And Power Transfer Assembly (BAPTA), is essential for the success of GEO and LEO missions. A failure of a BAPTA would not only jeopardize power supply but also orbit and attitude control.

For the German Communication Satellite DFS-Kopernikus, a BAPTA with some novel features was developed and qualified, including life testing. All flight models were delivered, together with an elaborate BAPTA Drive Electronics.

The modular design of this BAPTA offers a relatively easy adaptation to other specifications without losing the technological background and the experience gained.

INTRODUCTION

In the course of a proposal and selection process, TELDIX was awarded the contract for development and delivery of a BAPTA for the solar arrays of the German Communication Satellite DFS-Kopernikus in 1983. In the meantime, all flight models were delivered after an elaborate development and qualification period.

The following basic principles were used as guidelines for design and development:

1. Elimination of cage; devices; instead, damping of main resonances
2. Utilization of simple suspensions; the less parts, the better
3. Preference of drive systems which require no additional suspension; additionally, simple redundancy possibilities desirable.
4. Selection of drive principles that promise straightforward control; e.g., position drives instead of torque drives.
5. Combination of sensors and drive system; at least as a redundancy means.

*TELDIX GmbH, Heidelberg, Germany.

6. Definition of favorable mechanical/electronic interface; mechanical "muscles," electronic intelligence.
7. Preparation of modular concept to facilitate development, production and testing.
8. Selection of materials based not only on mass and strength but also on machinability, handling precautions, surface finish, etc.
9. Utilization lubrication schemes which work essentially independent of g-levels and under air pressure and vacuum; valid testing possibilities are necessary.
10. Optimization of reliability by avoiding single point failures and using passive redundancy switch-over.

In addition, the results achieved during the development and qualification of a BAPTA with rotary transformers instead of sliprings, gimbal arrangements and momentum wheels, were introduced in the design and development process. Likewise, the experience gained with power, control, and interface electronics assisted in this development.

All this was essential, already in the proposal phase, to provide the necessary background and confidence for a successful development. In the following, after a short description of the BAPTA and its functions, the BAPTA-Mechanism (BAPTA-M) is treated in some detail. Later, possible variations of the BAPTA-M are described, which can be relatively easily obtained due to the modular design.

GENERAL DESCRIPTION

The BAPTA for the DFS-Kopernikus consists of two BAPTA-Ms (Mechanisms) and two BAPTA-Es (Electronics). Each of the BAPTA-Es is capable of driving the two BAPTA-Ms; a solar panel is linked to each of the BAPTA-Ms.

The BAPTA-Ms incorporate two direct drive swashplate motors and two zero position sensors; one motor/sensor of each BAPTA-M is connected to the NORMAL BAPTA-E, the other to the REDUNDANT BAPTA-E. The non-energized motors are disengaged by spring force. Therefore, no switching or other means for a switch-over from normal to redundant operation is necessary.

The functions of the BAPTA can be explained by reference to Figure 1. There are two angular rates provided, with a capability to rotate in both directions.

The rotational speed is controlled by quartz oscillators in a normal speed ± 360 deg/day and a fast speed ± 360 deg/25 min. The normal speed can be adjusted in the range of $\pm 5 \times 10^{-4}$ to cope with possible drifts of the quartz frequency over mission time.

The actual position is defined by a zero pick-off plus step counting by an up-down counter.

The modes of operation are the following:

- o NORMAL: ± 360 deg/day, activated by TTC
- o INCREMENT: ± 360 deg/25 min, activated by TTC, angular incremental range ± 307 deg preselectable in 0.075 deg steps. After rotating through the preset angular increment transition to NORMAL operation with the stored rate commences.
- o SURVIVAL: 360 deg/25 min of selected NORMAL direction of rotation to zero position. Activated by AOCS; clearing is possible only via RESET (TTC).
- o HOLD: One coil each of the operating swashplate motors is permanently energized. Activated by ON or RESET (TTC) or HOLD (TTC) or automatically after reaching the zero position in the survival mode.

Redundancy is provided in the following way:

Normal: Power on/signals in/out to NORMAL BAPTA-E

Redundant: Power on/signals in/out to REDUNDANT BAPTA-E.

DESCRIPTION OF THE BAPTA-M

General

The modular design of the BAPTA-M comprises three main subassemblies which will now be described in some detail:

1. Bearing Unit
2. Drive Motors with Zero Position Sensors
3. Slipring Unit.

These assemblies allow for independent manufacture and testing prior to being assembled to obtain the BAPTA-M (Fig. 2).

The mechanical interface to the solar generator is the flange on one side of the shaft. The shaft also carries, via a tube-like part, the two diaphragms with the attached gear rotors on their circumference and the rotors of the zero pick-offs.

The sliring disk is mounted on the opposite end of the shaft. The connections are routed through the hollow shaft and, equipped with connectors, provide the electrical interface to the solar generator.

The flange plate which represents the mechanical interface to the satellite structure carries the bearing unit, the motor/sensor stators, and the brush assemblies of the sliring unit.

The BAPTA-M does not require any caging device.

Bearing Unit

The geometry of the bearing unit, including the ball bearing size, corresponds largely with the one employed in the well-known momentum wheels.

The parts are manufactured from a stainless steel having identical thermal expansion as the ball bearings. This is one essential prerequisite for employing a solid preload. Thus, no variations of the preload occur in the total temperature range.

In addition, by an appropriate selection of the distance between the two bearings, the contact angle and the conformity, there are only slight changes in the preload in the presence of temperature gradients.

The ball bearings, of the size 20 mm x 42 mm x 12 mm, consist of rings made of stainless steel, TiC-coated steel balls, and plastic retainers made from a composite containing MoS₂.

Although the TiC coating of the balls would be sufficient to avoid cold welding under vacuum conditions, for the required life of several thousand rotations, the raceways and the balls have been coated with MoS₂ by a plasma process.

In the presence of a central load, the bearing unit has a load carrying capacity of $>10^4$ N in all directions. The stiffness is >1 N/ μm and the tilting stiffness >10 Nm/mrad.

The nominal starting friction is on the order of 0.005 Nm.

Motors with Zero Position Sensors

The swashplate stepper motor consists of a bevel gear with 599/600 teeth, a diaphragm suspension, and 16 electromagnets mounted along the circumference of the motor stator. This special type of gear motor does not require an additional bearing suspension.

With none of the electromagnets energized, the gears are disengaged passively by the spring force of the diaphragm; the shaft of the BAPTA can be rotated freely. This is important in two ways. First, one can arrange two motors for full redundancy. Second, during vibration of the BAPTA-M while

integrated into a satellite, rotational vibration component loads are generated in the shaft which load an engaged gear.

A motor is set into operation by exciting one of the electromagnets, that is, stator and rotor of the gear become engaged. The holding torque on the order of 3 Nm, offers a stiffness on the order of 1 Nm/mrad.

Sequencing of the 16 electromagnets causes the toothed gear rings to roll-off on each other. After one electrical revolution (16 steps), an advancing of one step is accomplished. The rotation is transferred to the BAPTA-M shaft via the flexible diaphragm. The sense of the rotation depends on the sequencing being either clockwise or counterclockwise.

The stepping torque depends on the overlapping in time of the excitation of two successive coils. This is due to the necessary build-up of the magnetic field over time and the time needed to perform a step. An overlapping time of about 15 msec proved to be a good compromise, taking into account the stepping frequency capability. The stepping frequency capability is 40 Hz (for the lifetest, 33.3 Hz were employed). The nominal stepsize is 0.0375 deg (9600 steps/revolution).

The gears are dry running in vacuum. The surface of the gear is ion-nitrided to ensure the specified lifetime. The number of rotations of the motor is 600 times that of the shaft; for a 10-years mission with about 3650 revolutions of the BAPTA-M, the motor has to provide 2.2×10^6 revolutions.

Since the motor is a position drive and not a torque drive, very simple and clear dynamic and control conditions are obtained.

The opto-electronic zero-position sensor, combined with an up/down counter, determines the instantaneous BAPTA-M position. This sensor has a "window" width of about 12 steps; zero with one-step-accuracy is defined by the coincidence of sensor signal and exciting of one particular coil.

For reasons of redundancy, two sensors are provided.

Slipring Unit

The slipring unit, realized in a pancake configuration, offers a particularly compact design. This feature becomes more important from a satellite's design standpoint; the available distance between the outer envelope and the central tube of the satellite becomes smaller due to the trend to longer mission time (larger fuel tanks within the central tube). Therefore, the total length of a BAPTA-M is an important selection criterion.

The main drawback of this approach, compared with a cylindrical design, is the higher friction torque which is ≤ 1 Nm.

On its front and rear sides, the slipring disc is equipped with coin silver rings that are embedded in a fiber reinforced plastic material. This approach ensures the necessary strength and also a similar thermal expansion.

Four brush assemblies are foreseen, two each on both sides of the slipring disk. Each power ring is related to four brushes while the signal rings are contacted by two brushes each. This configuration ensures both low contact resistance/noise and high reliability.

The brushes are made of sintered silver/MoS₂. The sinter mixture is such that the content of MoS₂ is nearly zero at the side where the brushes are soldered to the springs. This provides an approximately constant contact pressure. The change of the MoS₂ content over the height of the brushes is important on the one side for low wear and friction, on the other side for achieving the necessary mechanical strength of the solder connection.

Main Data of the BAPTA-M (DFS)

The main data are given in the following form:

Mass	≤ 5.3 kg	
Diameter	225 mm	
Length	130 mm	
Rate of rotation	normal	± 15 deg/hr
	fast	± 14 deg/min approx.
Step width	0.0375 deg (2.25 min)	
Steps/revolution	9600	
Output torque	hold	> 3 Nm
	step	≥ 0.7 Nm
	friction	≤ 1 Nm
Zero position accuracy	1 step	
Power consumption	≤ 3.3 W	
Electrical transmission	2 x 22.5 A	
	8 x 4 A	
	3 x 1.3 A	
	12 x 0.25 A	
Loads, static (qualification)	200 Nm	
	or 88 Nm + 2000 N lateral force on interface	
	dynamic	20 Hz 0.013 g ² /Hz
	20 to 70 Hz	+ 6 dB
	70 to 100 Hz	0.2 g ² /Hz
	100 to 200 Hz	- 6 dB
	200 to 2000 Hz	0.05 g ² /Hz
Thermal vacuum	10.8 g RMS	
	- 40°C to +60°C	
	$\leq 10^{-5}$ mbar	
Life	≥ 10 years	
Reliability (2 BAPTA-M + 2 BAPTA-E) 0.985 (10 years)		
Power Consumption		
(2 BAPTA-M + 2 BAPTA-E)		≤ 16 W

LIFETEST

A thermal vacuum lifetest at about 10^{-5} mbar was performed, after passing the vibration qualification test.

An acceleration factor of 300 was chosen, leading to a step frequency of $1/9$ Hz \times 300 = 33.3 Hz. At this frequency, the BAPTA-M still comes to a complete stop after performing a step; only the pauses between steps, normally a little below 9 sec, are shortened.

The qualification factors were as follows:

Operation time	>1.5 (6000 revolutions)
Load torque	>3 (0.7 Nm)
Power over sliprings	>2 (currents > 1.5)
Temperature	>2 (-15° to +50°)
Temperature cycles	>3 (32)
Temperature gradient	very high ($\pm 25^{\circ}\text{C}/\text{h}$).

Figure 3 shows the test set-up.

The load torque was generated by a brushless dc motor (2).

The BAPTA-M (10) is mounted via a thermal insulation to the temperature controlled plate (4). This plate heats up or cools down the vertical plate shown in the figure which is in radiation contact to the circular plate (5). The circular plate is fixed to the solar generator flange. This arrangement was chosen to simulate the heating and cooling by the solar generator yokes as closely as possible.

Between the ball bearing unit rotor and stator, temperature differences of $\pm 20^{\circ}\text{C}$ (approximately) were measured.

All temperatures, currents, and voltage drops across the sliprings were recorded continuously. A daily check of the hold, step and friction torque was performed.

After the test performance, the evaluation of the BAPTA-M resulted in the following:

1. Bearing Unit: Practically no change of the friction torque, no wear whatsoever.
2. Motors: After 3.6×10^6 motor revolutions, equal to 57×10^6 steps, the surface of the gears showed a polishing wear only. The motors could have been operated for a much longer time.
3. Sliprings: A very small wear on the brushes has taken place; the slipring surfaces showed "optically visible" traces only.

EVOLUTION TO A BAPTA-FAMILY

Due to the modular design, a family of BAPTAs can be defined by modification and modified mounting of the subunits. Main possibilities are the following:

- o Configuration - The basic arrangement of the motor(s) and the slipring unit is interchangeable, leading to different configurations depending on results of trade-offs or specific customer needs.
- o Power and Signal Transfer - The slipring unit is adaptable to power and slipring transfer capacity requirements, for instance, by adding to the power transfer pancake slipring a small cylindrical slipring assembly.
- o Redundancy Provisions - The motor redundancy concept can be modified from two completely separate motors to one motor using redundant windings on the motor poles, or even the same windings, connected to two redundant electronics.
- o Angular Position Measurement - Pick-offs of different types, accuracies and redundancy levels can be implemented to fulfill specific requirements.
- o Interfaces - The mechanical interfaces to the solar generator and to the satellite structure can be modified within certain limits; the electrical interfaces are fully adaptable to customer needs.
- o Drive/Interface Electronics - The BAPTA-E is adaptable to the required modes of operation, power and signal interface requirements and to various redundancy concepts.

Together with the high resolution stepper motors, for all missions, GEO, LEO and highly excentrical orbits, the speed can be adapted. For the latter, an automatic control via sun sensors on the solar generators could be beneficial.

In Figure 4, an example of a BAPTA-M design is shown with double slipring discs, located at the solar generator side, and a stepper motor with redundant windings.

CONCLUSIONS

A modular BAPTA approach permits accommodation of practically all requirements.

First flight models were delivered after rigorous qualification in the course of the DFS-Kopernikus program.

The compact, lightweight, and rigid design led to a further application in the frame of the Chinese DFH-3 program.

REFERENCES

1. Boving, H. J., et al.: High Precision Coated Steel Balls. Proc. Bearing Conference 1987, Orlando, Florida.
2. Lansdown, A. R.: Molybdenum Disulphide Lubrication. ESA TRIB/7, 1979/1980.
3. Stevens, K. T., and Todd, M. J.: Thermal Conductance Across Ball Bearings in Vacuum. ESA Trib/1, 1980.
4. Auer, W., and Ruff, G.: A High Resolution Stepper Motor. Proc. First Europ. Sym. "Space Mechanisms and Tribology," 1983, Neuchâtel, Switzerland.
5. Stevens, K. T.: The Tribology of Gears for Satellite Applications. Proc. First European Sym. "Space Mechanisms and Tribology," 1983, Neuchâtel, Switzerland.
6. Anderson, J. C.: The Wear and Electrical Characteristics of Some Dry Lubricated Slip Ring/Brush Contacts. Proc. 2nd Sym. "Space Tribology Workshop," 1980, Risley, UK.
7. Parker, K. and Douglas, K.: Thermal-Vacuum Real-Life Test of a MSDS Solar-Array Drive Mechanism. ESA Trib/3, 1980.
8. Auer, W.: BAPTA with Rotary Transformer. Proc. 2nd Sym., "Photovoltaic Generators in Space, 1980, Heidelberg, Germany.

**BLANK
PAGE**

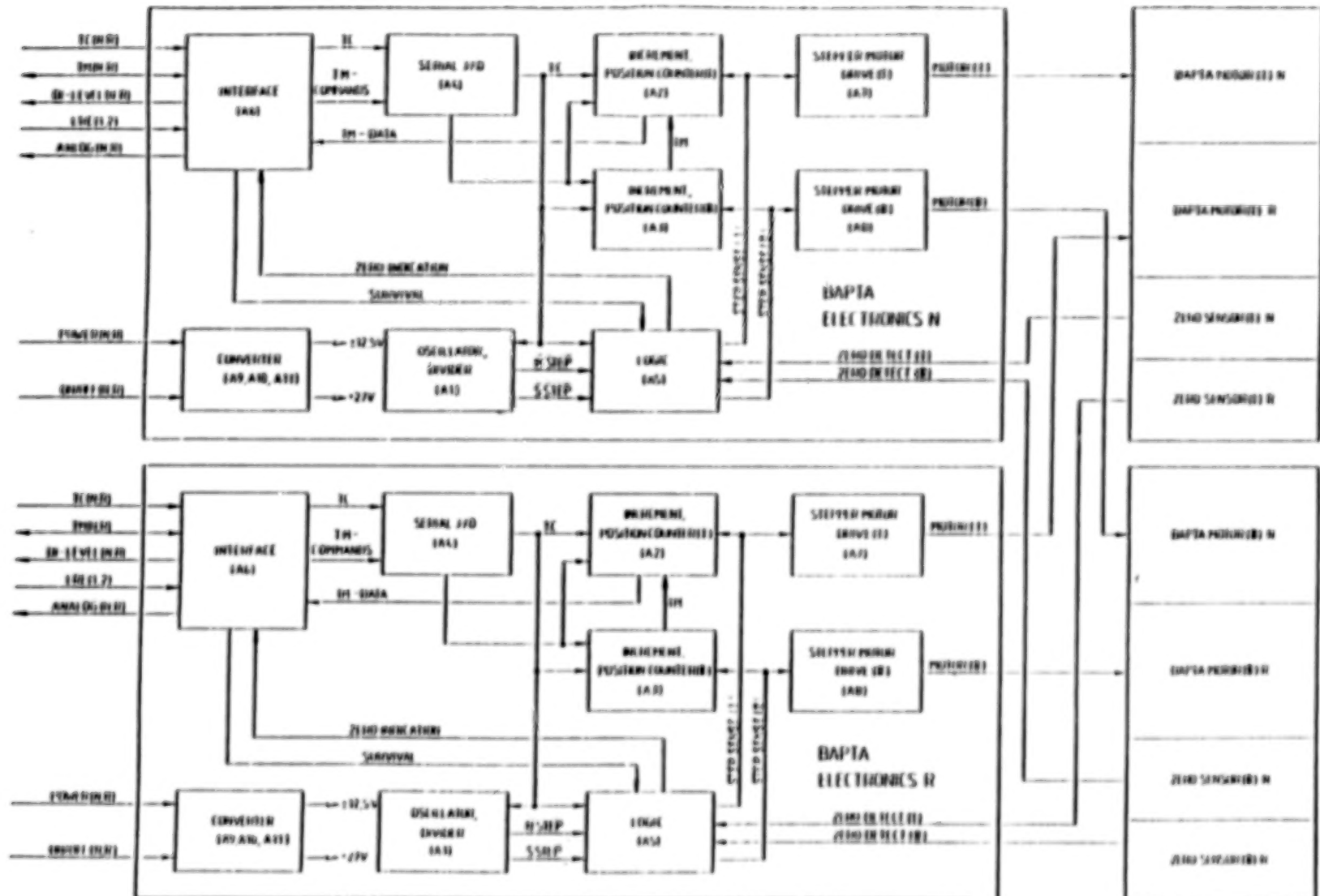


Figure 1. BAPTA block diagram.

۲۵۸

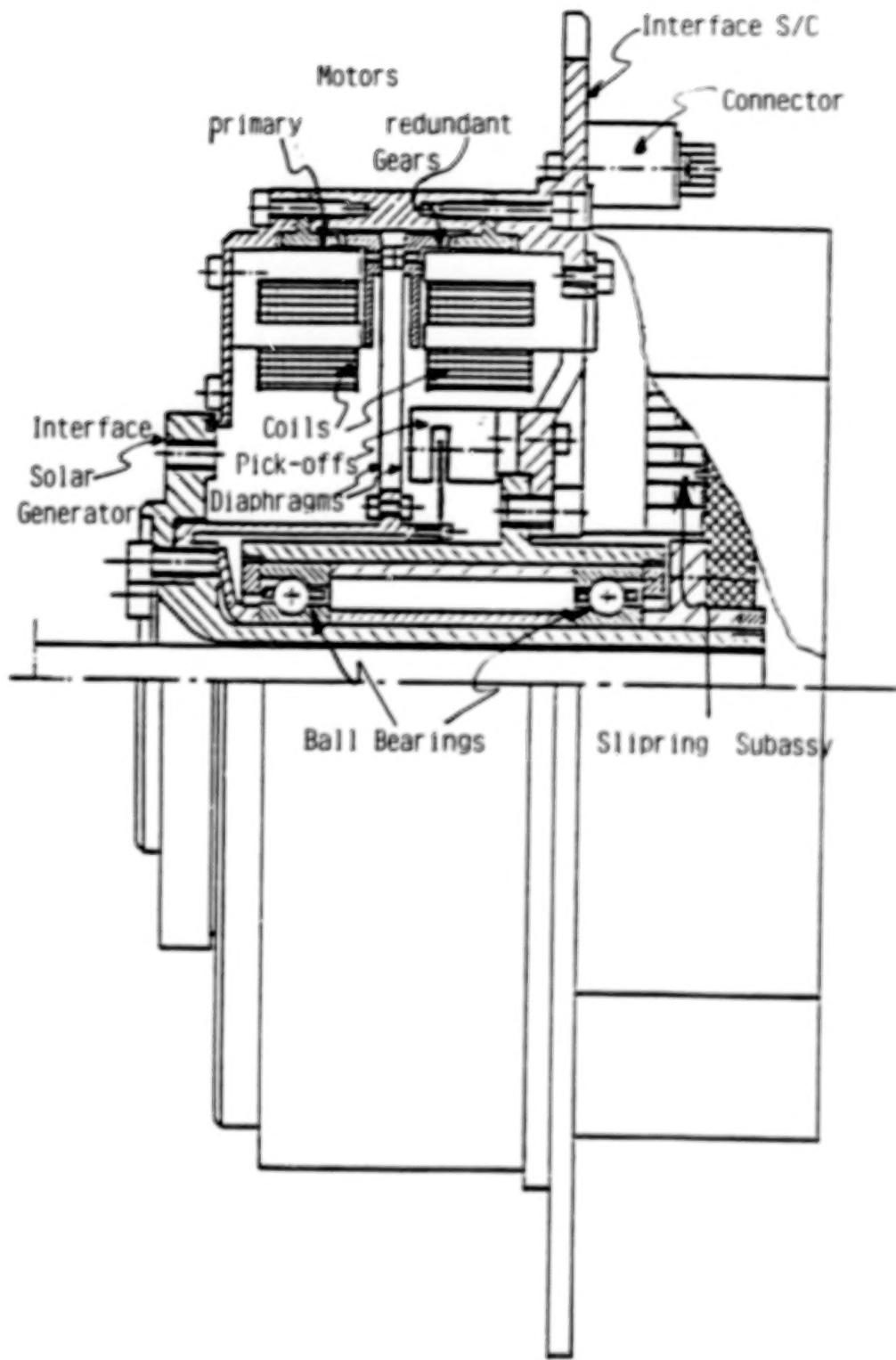
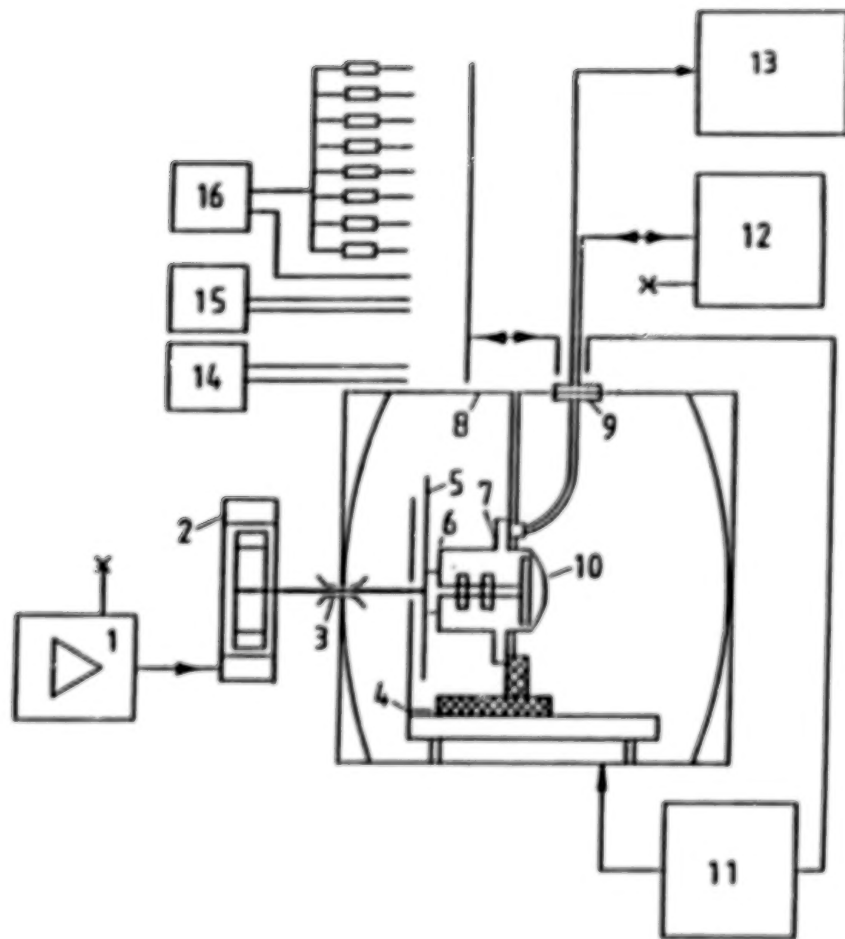


Figure 2. BAPTA-M/DFS.

**BLANK
PAGE**



1. Adjustable supply for torquer
2. Torquer
3. Rotational feed-through
4. Temp. sensor on black disk mounted to Cu-baseplate in the chamber
5. Temp. sensor on rotating black disk
6. Temp. sensor on SDA housing
7. Temp. sensor on SDA mounting flange
8. Temp. sensor for chamber
9. El. feed-throughs
10. SDA 1-0 under test
11. Temp. control unit
12. Motor drive
13. Recorder for temperatures
14. Current source 22.5 A
15. Current source 4 A
16. Current source 1.3 A

Figure 3. Lifetest on SDA.

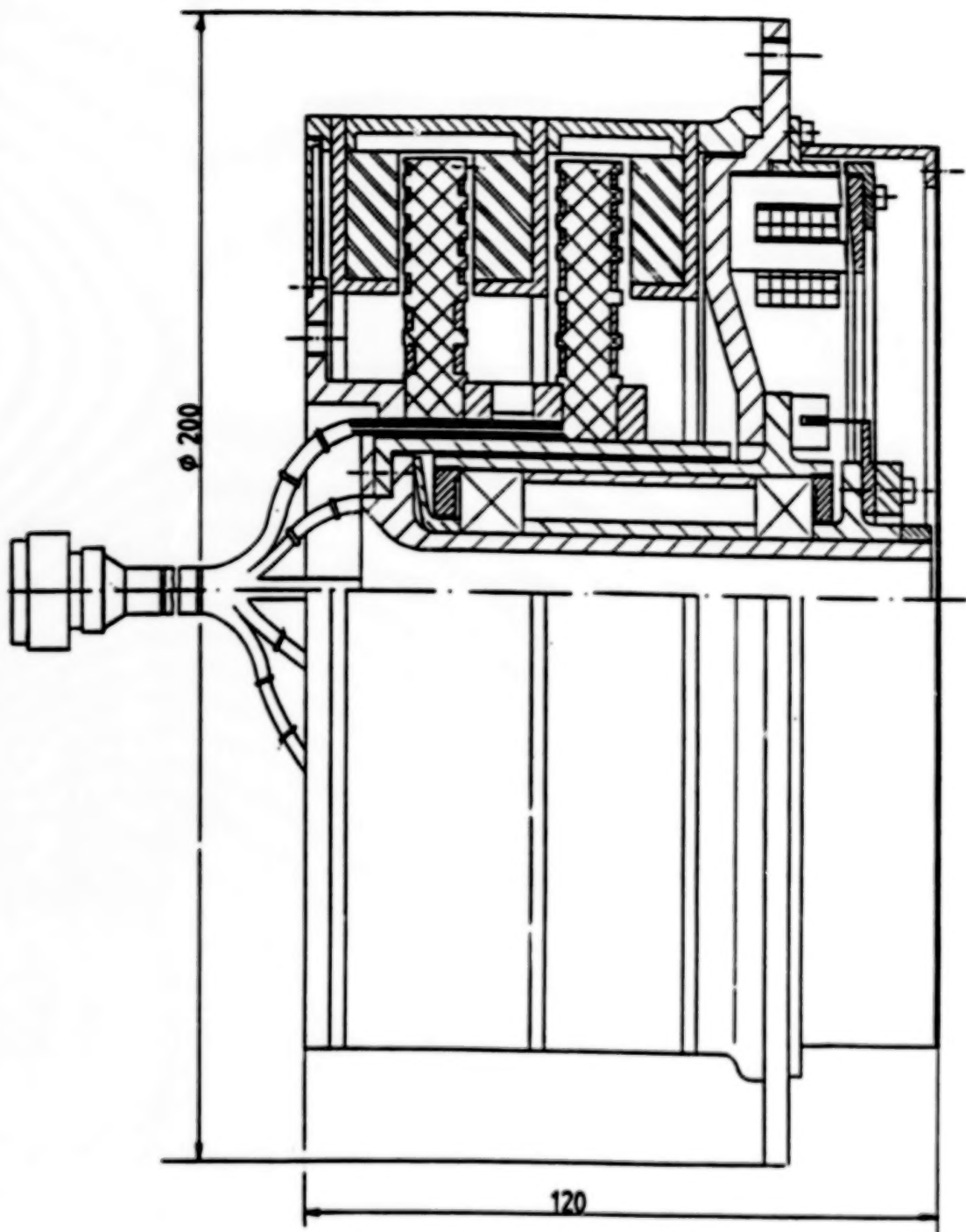


Figure 4. Example of a modified BAPTA-M.

BLANK PAGE

SIGNAL AND POWER ROLL RING TESTING UPDATE

Dennis W. Smith*

ABSTRACT

The roll ring was developed as a long-life, low-torque alternative to the slip ring. Roll rings showed significant advantages in two orders of magnitude lower torque, low debris generation, and transfer efficiencies well in excess of 99 percent (including high-power applications). Roll rings have also shown little sensitivity to storage and operating environments, minimizing handling problems and service requirements. A variation of the slip ring, the signal roll ring, was developed to achieve a low transfer-noise factor. Life tests of signal roll rings have accumulated 15 million revolutions with signal noise levels still below the requirements of other programs. Data on these life tests are presented, along with test results from the most recent signal roll ring design. The latest design operates at speeds of hundreds of rpm, with demonstrated life in the tens of millions of revolutions. Power roll rings were later developed, meeting the needs of large power transfers across a rotating joint (as in the space station application). Power roll rings have been tested by NASA Lewis to the equivalent of 200 years of space station operation and have carried currents of 200 A per circuit and 500 Vdc. In addition, alternating currents have been applied at frequencies of 20 kHz, with 440 V and 60 A current. Detailed results of these tests are presented, indicating that roll rings are ideal for low-noise requirement applications.

INTRODUCTION

The roll ring has been under development since mid-1970. Ryan Porter [1] presented a paper to the 19th Mechanisms Symposium entitled "A Rotating Electrical Transfer Device" in which he described the design and development of the roll ring concept in detail. Since the paper's publication, there has been considerable development and testing of both signal and power roll rings. This paper summarizes the life and performance test data for both signal and power roll rings after presenting a brief history of roll ring development, which is covered in more detail in Mr. Porter's paper.

ROLL RING DESIGN

A roll ring consists of one or more circular flexures captured by their own spring force in the annular space between two concentric conductors or contact rings. These inner and outer contact rings are rigidly mounted to the rotating and fixed sides, respectively, of the rotating axis.

*Honeywell Corporation, Satellite Systems Division, Phoenix, Arizona.

Three basic roll ring configurations are presently under development: a single flexure, 0- to 15-A configuration; a single flexure, 0- to 3-A, high-speed (200 rpm) configuration; and a 2- to 200-A, high power configuration. Figures 1 through 3 show photographs of each configuration.

The single flexure circuit, shown in Figure 1, is typical of over 400 circuits with a cumulative test history of approximately 900,000 circuit hours.

The high-speed, single flexure circuit (Fig. 2) is the most recent development. With inner and outer rings manufactured by plating onto plastic molded parts, 20-ring sets are contained in one pair of inner and outer rings. Up to six of these modules are designed to fit into a single housing that is 20.3 cm (8 in.) long and 7.6 cm (3 in.) in diameter. Besides its ability to operate at speeds of at least 260 rpm and fit into a small package, these single flexure circuits have incorporated a thicker nickel barrier under the gold outer plating on both rings and flexures and are expected to introduce less noise into the signal than in previous designs.

At present, four high-current designs have been fabricated and partially evaluated. Figure 3 is a plan view of one circuit in an 8-circuit module that was designed and fabricated with research funding. It has undergone extensive testing at NASA's Lewis Research Center.

Roll rings have several key advantages over other types of electrical transfer devices:

- o Extremely low drag torque
- o High transfer efficiencies in high-power configurations
- o Extremely low wear debris generation
- o Long life
- o Low weight for high-power applications.

DEVELOPMENT HISTORY

Signal

Initial development work on the roll ring concept was done on IR&D funding in 1975 for use in a vertical gyro gimbal. Three-amp signal roll rings were then developed for the Galileo program in the 1979 to 1980 time frame. This application had stringent noise requirements and necessitated the development of improved geometrics, plating matrices, cleaning procedures, and long-life flexure design. Other signal applications involving roll rings similar in size to the Galileo units advanced the state of the art through the early 1980s. The focus turned to power roll rings in the early 1980s and signal development was slowed until 1987 when a small, long life (107

revolutions), high-speed (100 rpm), 120-circuit roll ring unit was designed for Holloman AFB for use in a precision rate table.

Power

The multiflexure power roll ring was developed in mid-1980, primarily for space station application. Units of 4, 8, and 12 circuits have been delivered. Extensive testing has been performed at NASA Lewis on the 4- and 8-circuit modules.

SOME OBSTACLES OVERCOME

Flexure Fatigue

Early in the development of the 15-A flexure, a fatigue failure at 30×10^6 reverse bending cycles indicated that either the stress model or the allowable stress limit was incorrect. After the stress model was carefully scrutinized and exonerated, the material properties were investigated. It was empirically determined that the grain orientation for flexures (machined from rod stock) was nonoptimum for the direction of strain in operation. Published fatigue data were obtained from cantilevered strip stock or rotating beam testing, both of which stress the samples in a favorable axis along the grain. The difference in stress limits was nearly 20 percent. Figure 4 shows data for the rod, compared to published data. Once this lower stress limit was used, flexure fatigue problems disappeared.

Noise

The most difficult problem encountered in the development of the roll ring has been signal noise. The noise produced by a roll ring is different from that associated with a slip ring in that the signal is clean for most of the time with occasional resistance spikes. Figure 5 shows an example of noise from an ongoing life test originally begun for the Galileo program. While the noise spikes continue to be the principal concern of signal roll ring development, there has been considerable progress toward minimizing them and postponing their onset. Three areas in which significant noise reductions have been made are: (1) plating matrix development, (2) plating purity, and (3) surface cleaning.

Several different plating matrices have been evaluated on the contact rings and flexures in an effort to minimize electrical noise and wear. Most of these matrices consisted of a copper flash for adhesion, followed by either sulfamate or electroless nickel as a copper migration barrier and a hard underlayment of one of several types of gold outerplatings. The most recent surface analyses, performed using AUGER, indicated that a principal source of noise is from copper and lead oxides on the surface. One of the potential sources of these oxides is the migration through the plating matrix of active substrate metal. As a result, the thickness of the nickel layer was increased from a minimum of 2.5 microns (100 microinches) to a minimum of 5 microns (200 microinches). The type of nickel was also changed from sulfamate to

electroless to provide a denser barrier. The final gold layer is either a hard gold alloy, used particularly on the flexures and sometimes on the rings as well, or pure soft gold, often used on the rings to provide a relatively compliant track for the harder flexures. The gold-plated layers are typically about 125-microinches thick. If the hard gold alloy is used on both the flexure and ring, very little wear is evident; however, the contact resistance is somewhat increased. This outer gold layer is also a potential source of contaminating oxides, due to impurities in the plating itself. Extreme care is required in the plating process to minimize the potential for contaminants, particularly copper and lead, which are commonly present in plating equipment. Careful monitoring and scavenging of the plating baths are required to minimize contaminants, particularly when other specimens are plated in the same bath.

Once the plating is applied with great care and purity, contamination from outside sources must be avoided. Primary sources of outside contaminants include organic films, silicone and metallic oxides. Outside sources of metallic oxides include migration from nearby components, such as solder used to attach the lead wires. For that matter, the lead wires themselves provide a potential source of copper contamination. The location of solder lugs for the rings in the Holloman signal roll ring design reduces the potential for noise. These lugs were molded into the inner and outer rings. When the curvature of the raceway was subsequently machined into the ring, it also cut into the lug, therefore, when the raceways were plated, the lugs were part of the substrate. The result is that the soldering operation is separated from critical surfaces by the plastic ring.

A high correlation was found between the presence of silicones in the system and resultant electrical noise. Although the exact form of the nonconductive silicone-containing film was never identified, several sources of silicone contamination were eliminated from the test system. The primary source was silicon grease used to lubricate gearheads in the test fixture drive located in the vacuum chamber with the roll ring. Elimination of these silicone sources resulted in greatly improved electrical performance.

It is believed that, for a roll ring, the presence of an organic film does not cause electrical noise under most conditions. Indeed, the presence of a large quantity, as in an oil film, actually benefits the electrical performance for signal current levels. Although organics are by nature primarily nonconductive, their viscous properties permit a flexure with sufficient mechanical preload to make electrical contact, either by complete displacement of the film or by partial displacement to a thickness that will permit conduction by tunneling. However, there are exceptions. In the presence of large quantities of a viscous organic, experience has shown that currents exceeding 3 A may cause breakdown of the organic into less viscous insulators that will not permit efficient conduction. Also, viscous films result in hydroplaning of the contact at elevated rotational rates. The speed at which transition occurs is a function of both flexure preload and film viscosity. These results were compiled during testing of contacts intentionally lubricated with a variety of organic substances. While specific

organic compounds may be used for specific applications, stringent cleaning procedures have been developed to avoid surface contamination by unknown and unwanted compounds and particles.

Circuit Isolation

Particularly important in signal roll ring applications is the isolation of adjacent circuits. The latest isolation system, used on the Holloman signal roll ring unit, consists of 0.025-cm thick copper barriers located between each adjacent ring. The barriers are molded into the plastic, which electrically isolates them from the rings. All inner ring barriers are connected, as are all outer ring barriers. These may then be grounded to the housing, depending on the application. Circuit-to-circuit isolation is typically greater than 50 Db up to a frequency of 300 kHz, reducing to 33 Db at 1 MHz.

Multiple Flexure Design for High-Power Transfer

When the high-power transfer requirements for space station first became a goal for roll ring technology, the element limiting the design was the flexure. Single flexures were not capable of transferring the high-current loads (up to 200 A), and multiple flexures in the same circuit eventually caught up with each other, causing failures. The solution was a multiple flexure design in which the flexures are separated by rolling idlers. The design, shown in Figure 3, has idlers contacting two adjacent flexures and a rail that rotates with the inner ring. If the diameters of all of the elements are selected correctly, there will be theoretically, pure rolling at each of the contact locations. The idlers have a curvature along the axis where they contact the flexures, which causes them to self center on the flexures upon which they ride. This design has minimized sliding contacts and thus minimized friction and wear. The result is a mechanism that is capable of transferring 200 A per circuit with extremely high efficiency and ultra-low drag torque. (Refer to Figure 6 for test results.)

Corona Generation

One of the problems encountered during the development of the power roll ring was the generation of corona. This effect was first observed during high-voltage testing of the four-circuit test unit for NASA Lewis. Fortunately, the current level was low for these tests and no significant damage occurred. A significant redesign of the insulation system was then undertaken. Emphasis was placed on eliminating all line-of-sight between conductors of different electrical potential as well as providing adequate ventilation to prevent pockets of critical pressure. Corona will most readily form at voltages above 250 V with pressures of approximately 1 Torr. No further corona problems have been encountered.

CURRENT TESTING STATUS

Signal

Over the years, numerous tests have been conducted to determine the performance and life characteristics of various roll ring configurations, including variations in geometry, plating, lubrication, cleaning procedures, and environments. Many of these tests were short-term in nature and provided the results in a matter of days or weeks. Some of the units, composed of the most promising of the candidate parametric variations, were placed in life testing. The longest running of these, for signal configurations, began as six circuits of a Galileo roll ring assembly. These six circuits were unique in that they were lubricated with tricrysil phosphate (TCP). The pitch diameter of the roll ring circuits is 9.27 cm (3.65 in.) and the flexure diameter is 1.33 cm (0.525 in.). With insulation and housing, the module is 14.42 cm (5.68 in.) in diameter with a 4.45-cm (1.8-in.) hole through the center. Each circuit is 0.51 cm (0.20 in.) wide, and, with bearings and structure, the module is 15.2 cm (6.0 in.) long. Individual circuits are physically separate, as shown in Figure 1, and are, therefore, stackable. Using this design, units have been built with 1 to 20 circuits, and, by stacking modules of 20 circuits, virtually any number of circuits can be accommodated.

The life test, started in January of 1981, now has over 15 million revolutions on it. The operating speed was initially 3 rpm and, after nearly five years, was changed to 7 rpm, following a period in which the test had to be shut down. Figure 6 shows the change in signal noise as a function of time for each of the six circuits. It should be noted that the plotted data represent the highest resistance transient observed during the measurement period. The noise, as described previously, was the primary reason for running the test. Other performance and life issues have been satisfactorily demonstrated with short term tests, but the effects of long term running on the noise performance required a real time life test. The operating speed was not increased in an effort to accelerate the test because of the potential for elastohydrodynamic films developing between the rings and flexures.

Power

Since the power roll ring was initially developed with the space station in mind and because of their superior facilities, NASA Lewis has been responsible for most of the performance and life test results. Two test units were provided to NASA for testing: a 4-circuit (200 kW) unit and an 8-circuit (400 kW) unit. In addition to life testing with both dc and ac power, thermal equilibrium and corona testing were performed. The results are summarized here from the NASA report by David Renz [2].

Initial test showed the onset of corona to occur in the 450- to 625-V range. This was unacceptably low for a unit that is to operate at 500 V. The sources of corona formation were traced and corrected as discussed previously and the 4-circuit unit was retested. The onset voltage increased to the 800-

to 1180-V range and after six months of testing at 440 Vac to 20 kHz, the maximum onset voltage increased to 1650 V. This improvement is attributed to run-in and longer time in the vacuum; current designs minimize this conditioning time. These values are acceptable for most applications.

Three types of power transmission tests were performed on the power roll ring units: accelerated life, high-voltage, and high-current tests.

Accelerated life tests were performed on both the 4- and 8-circuit assemblies. Each was run at 5 rpm with a 100-A load. This speed is approximately 450 times the normal operating speed of the space station rotary joint (16 revolutions/day). Electrical transfer efficiencies were measured at intervals during the testing as a criteria of acceptability. The 8-circuit unit ran for an equivalent of 60 space station years with a minimum transfer efficiency of 99.987 percent. The 4-circuit unit ran for an equivalent space station life of 114 years with a minimum transfer efficiency of 99.966 percent. Table 1 shows the intermediate efficiency data.

An additional 3.3 equivalent space station years of operation were added to the 8-circuit unit during the six months of high-voltage testing at 500 Vdc and 10 A in a $<1.0 \times 10^{-4}$ Torr vacuum. No problems occurred during this test. The 4-circuit unit received corona suppression modifications following the accelerated life test and was then subjected to high-voltage/high-frequency testing at 440 Vac, 20 kHz, and 1.5 A in a $<1.0 \times 10^{-4}$ Torr vacuum. The test was run at 5 rpm for an equivalent of 22 years of space station operation after which the speed was reduced to the real time 16 revolutions per day in October 1987, where it is still running without problems.

High-power tests were conducted to determine the voltage drop across the 4-circuit unit. With 52.5 A, 420 Vac, 20 kHz, the measured voltage drop was 563 mV (0.0014 percent). Most of the voltage drop was reactive and would not contribute to heating the assembly. The inductance was calculated at 0.08 microHenry per circuit, using dc resistance (0.45 milliohm). AC resistance at 20 kHz would be substantially less. Since the cable inductance is 0.032 microHenry per meter, the roll ring is electrically equivalent to approximately one meter of cable.

FUTURE PLANS

Noise Reduction

Efforts to reduce the noise of signal roll rings are now focusing on the elimination of metallic oxides from the surfaces. Increasingly stringent demands for high-purity plating, improvements in migration barriers, and elimination of external contamination sources will continue to be pursued. Additionally, new substrate materials that do not contain easily oxidized metals will be investigated. While progress has been made on cleaning procedures, more potential lies in this area once the sources of metal oxides are minimized.

SUMMARY

A great deal of progress has been made in the development of the roll ring for power and signal transmission. Power roll rings are now fully capable of transferring hundreds of kilowatts of power, either ac or dc, for many years with minimum drag torque and extremely high efficiency. Signal roll rings are very suitable for all but the most noise sensitive applications, and research is continuing in an effort to achieve even lower noise levels.

REFERENCES

1. Porter, R. S.: A Rotating Electrical Transfer Device. 19th Aerospace Mechanisms Symposium, NASA, 1984.
2. Renz, D. D.: Multi-Hundred Kilowatt Roll Ring Assembly Evaluation Results. 23rd Intersociety Energy Conversion Engineering Conference, 1988.

TABLE 1. POWER TRANSFER EFFICIENCY DATA [2]

8-Circuit Roll Ring Assembly		4-Circuit Roll Ring Assembly	
Rolling, SS Years	Efficiency	Rolling, SS Years	Efficiency
20	99.995	20	99.977
40	99.987	40	99.970
60	99.987	60	99.975
-	-	80	99.974
-	-	100	99.966
-	-	114	99.966

NOTE: Lifetime (Rolling Station Years) and Average Efficiency
(500 V dc, 200 amp)

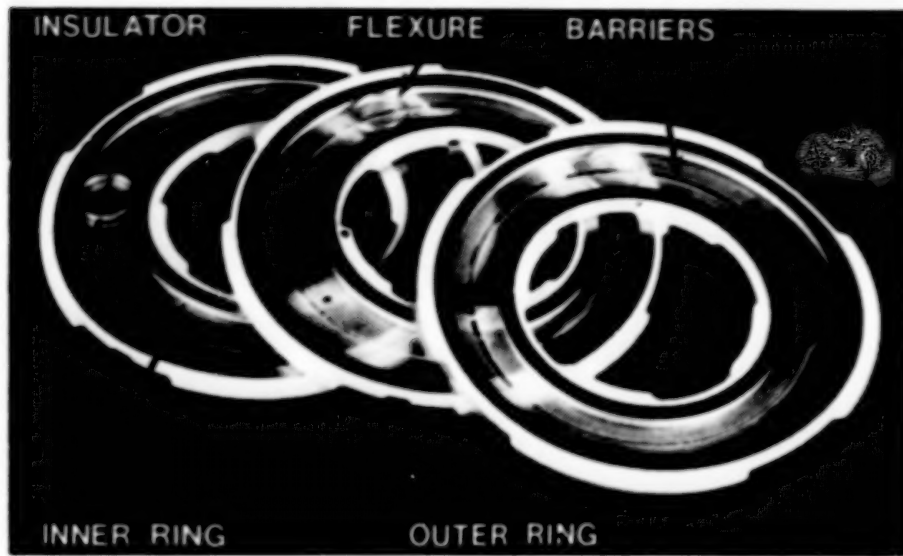


Figure 1. Single flexure roll ring circuits.

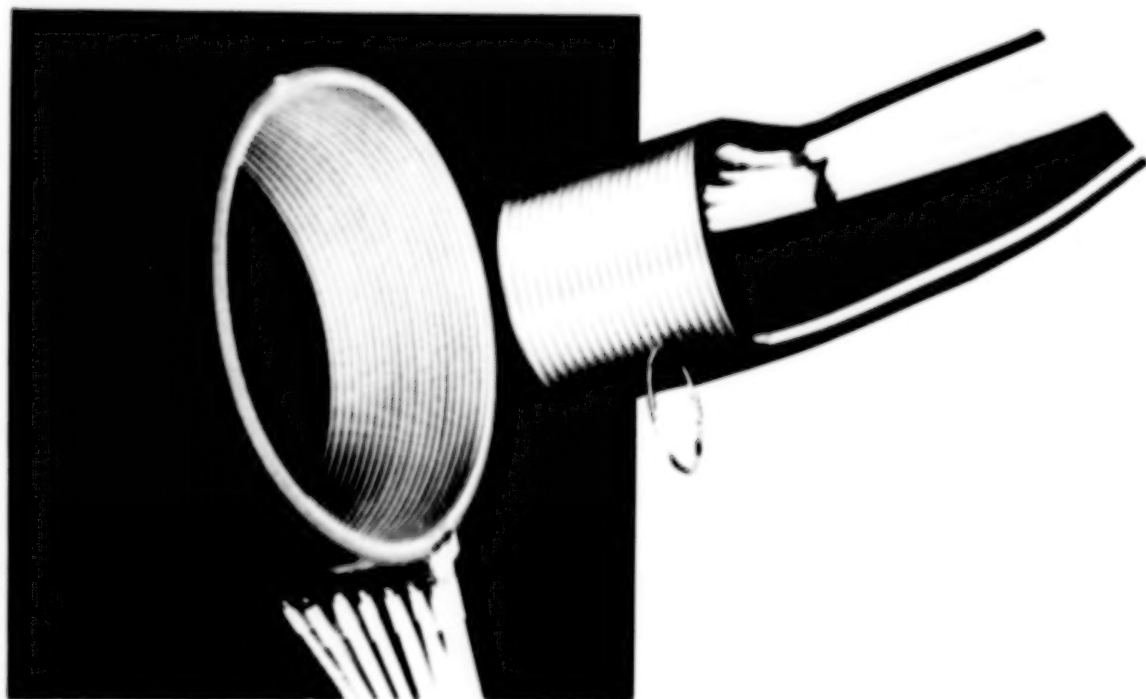


Figure 2. High-speed signal roll ring.

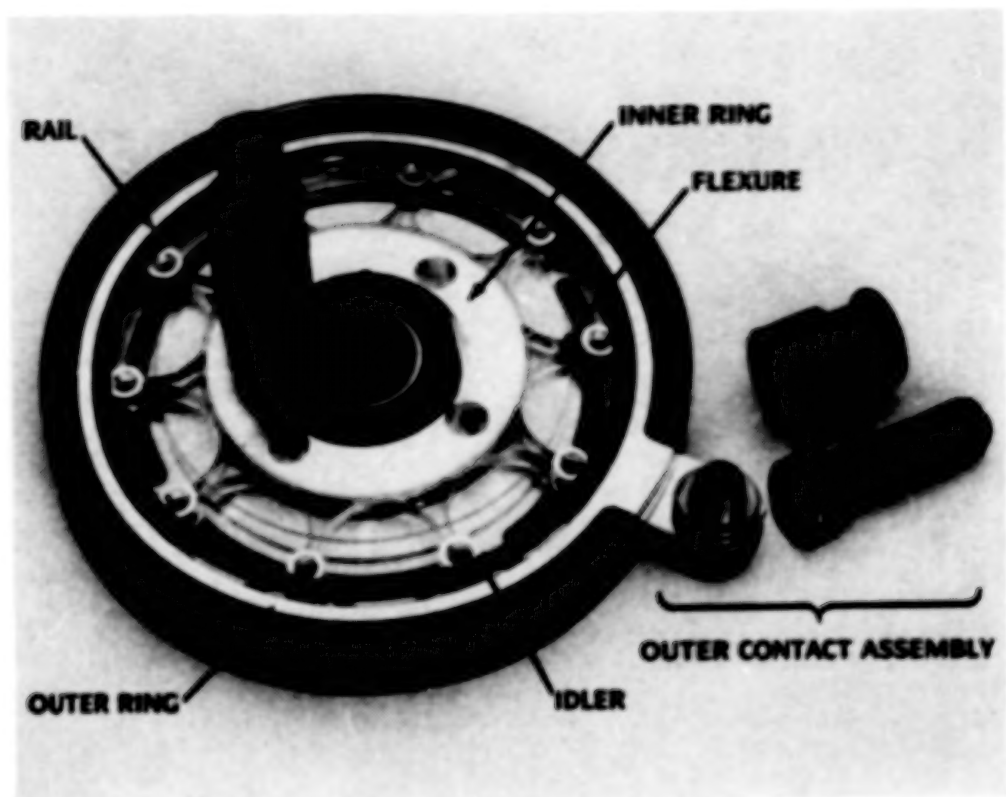


Figure 3. Multiflexure power roll ring.

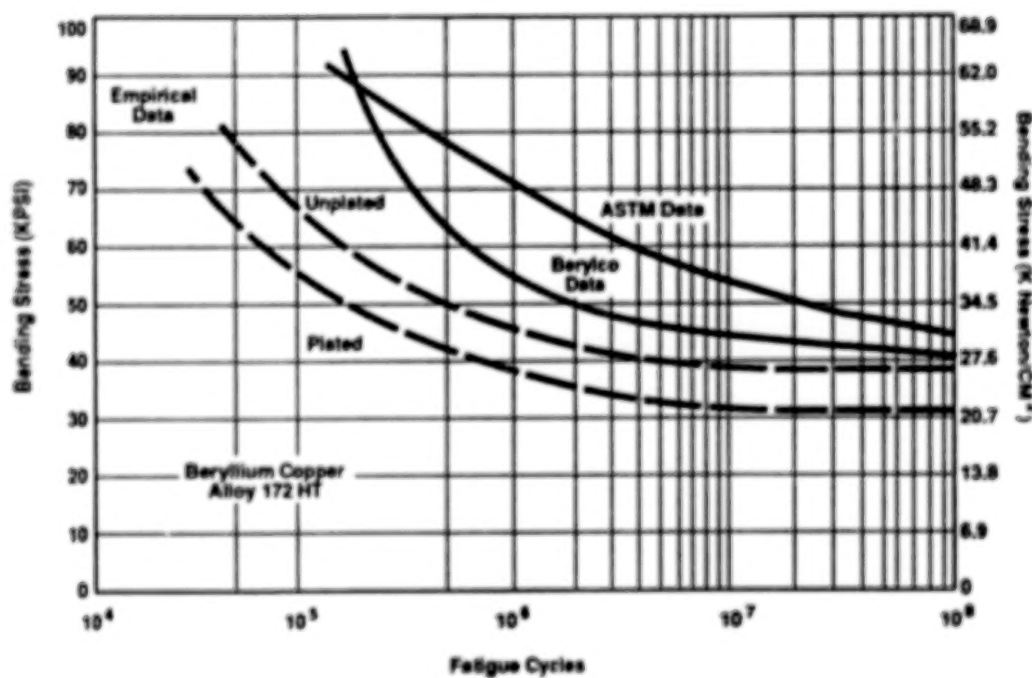


Figure 4. Fatigue characteristics of beryllium-copper alloy 172.

Typical Roll Ring Noise Trace
(After 14000 Revolutions)
GALILEO Life Test-Circuit 1

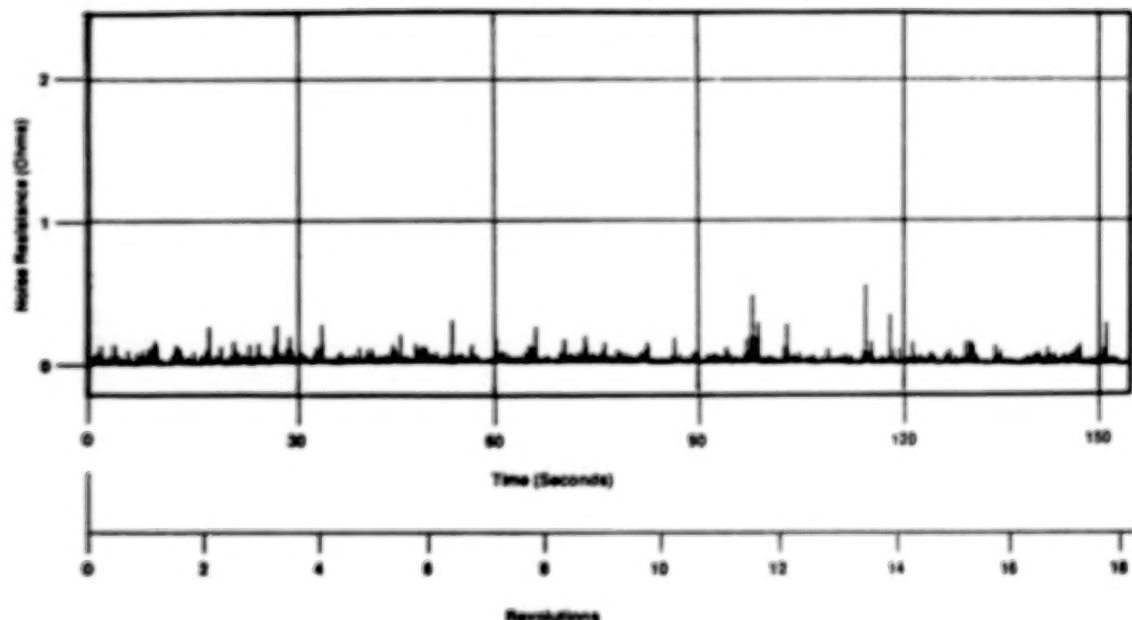


Figure 5. Signal roll ring noise characteristic.

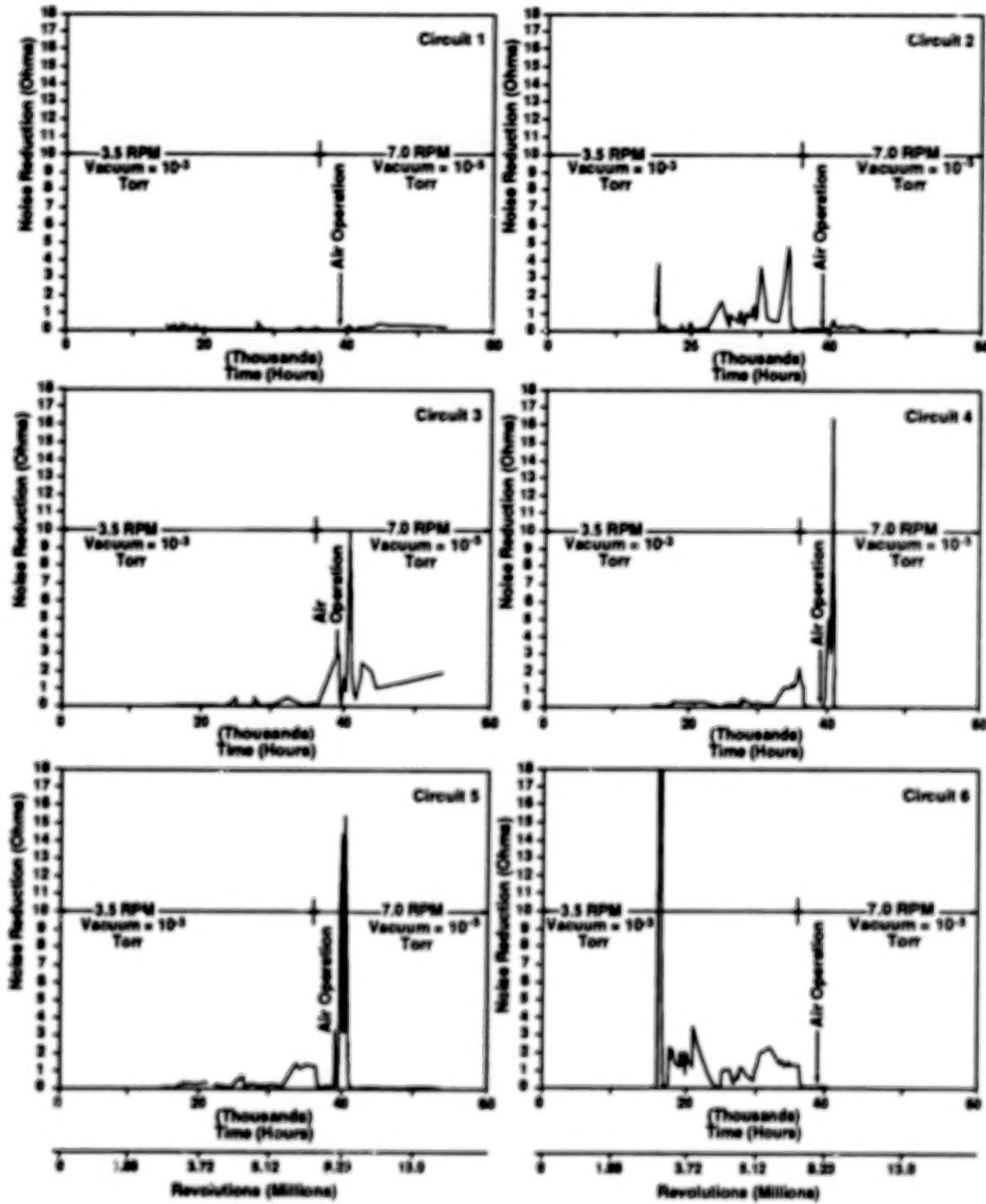


Figure 6. Six circuit LTU data.

DESIGN OF A 60 GHz BEAM WAVEGUIDE ANTENNA POSITIONER

Kenneth S. Emerick*

ABSTRACT

This paper presents a development model antenna positioner mechanism with an integral 60 GHz radio frequency (RF) beam waveguide. The system features a 2-ft diameter carbon-fiber reinforced epoxy antenna reflector and support structure, and a 2-degree-of-freedom (DOF) elevation over azimuth mechanism providing hemispherical field of view. The paper focuses on the constraints imposed on the mechanism by the RF subsystem and how they impacted the mechanical configuration. A description of the system hardware and performance characteristics will be presented. A discussion and comparison of alternative antenna mechanism configurations will also be given. The paper concludes with the presentation of experimental results, a summary, and conclusions.

BACKGROUND

The desire to have satellite communication links at frequencies of 60 GHz is driven by a number of factors. The high frequency reduces beamwidth, making the system more jam resistant. The system is less likely to cause interference with other systems operating in the vicinity. Finally, for a given antenna size, higher data rates can be supported, leading to a lighter, more compact design.

In a conventional RF system, an arrangement of waveguide tubing and rotary joints takes the RF energy from the feed to the transponder electronics, which are mounted on or near the spacecraft to provide them with a hospitable environment. However, using waveguide tubing at 60 GHz results in a loss of approximately 1 dB/ft. Each rotary joint adds an additional loss of approximately 1 dB. A 2-DOF elevation over azimuth antenna positioner with two rotary joints and one foot of waveguide would lose 50 percent of its RF signal strength in the waveguide system.

The system shown in Figure 1 is a method of transferring the RF energy to the transponder electronics in a more efficient manner. The RF energy transmitted by the feed is directed to the reflector by means of the beam waveguide assembly. The beam waveguide is a series of steerable RF mirrors which reflect and focus the beam as it crosses the axes of rotation. This allows the antenna feed and associated electronics to remain stationary while the reflector is tracking or acquiring a target. One of the mirrors (M_1) is a planer, while the other three are elliptically contoured in order to focus the

*Ford Aerospace Corporation, Palo Alto, California.

beam. The angle of incidence between the mirror and beam center is 45 deg, making the total angle through which the beam is reflected at each mirror equal to 90 deg. The beam waveguide has a projected loss of less than 0.5 dB. Our system has four mirrors arranged as shown in Figure 1. However, other configurations having different numbers of mirrors are possible.

SYSTEM REQUIREMENTS

The pointing error requirements are defined by the signal beamwidth, and assembly tolerances are defined by both the beamwidth and frequency. Ten percent of the beamwidth is allotted for the total antenna pointing error. This system, with a 0.2 deg beamwidth, has a total pointing error budget of 0.02 deg.

The acceptable assembly and alignment tolerances are related to the wavelength, similar to optical systems, and a total positional tolerance of $\lambda/20$ will ensure minimal losses. A 60 GHz signal has a wavelength of approximately 0.2 in., giving the system a positional tolerance of 0.010 in. This number represents the maximum true-position error that the RF centerline can deviate with respect to the focussing element optical centers, and is comprised of element manufacturing tolerances, element translational and rotational mounting errors, and system structural and thermal deflections. The location of the element in a plane perpendicular to the direction of wave propagation is crucial, as most elements are both non-planer and aspherical. As testing of the system occurred in a 1-g environment, with no offloading mechanism, structural deflections for all mechanism positions must also be within the pointing error and alignment tolerances.

The development model positioner mechanism provides hemispherical coverage with an elevation over azimuth configuration (see Fig. 2a). This configuration has a "gimbal lock," or mechanism singularity, located at the center of the mechanism pointing range, at the zenith location. The theoretical antenna tracking rates approach infinity as a target passes through this location. In practice, a circular "keyhole" region is defined by the target angular velocity, and maximum positioner angular velocity and acceleration. If the keyhole region is much smaller than the antenna beamwidth, very little signal degradation will occur. A computer program was written to analyze keyhole size as a function of the beamwidth, maximum gimbal velocities, and accelerations. The keyhole size for this system is 0.02 deg for a target moving at 1 deg/sec, and is much smaller than the beamwidth of 0.2 deg. An alternative antenna mechanism, with an X-Y configuration, would have two keyhole locations on the hemispherical field of view horizon (see Fig. 2b). This configuration may be preferable if very high tracking rates near the gimbal lock location are anticipated. The current configuration is applicable for most low-earth orbit and geostationary aircraft.

Stray RF reflections within the beam waveguide structure can also cause signal degradation. Any apertures or surfaces that may potentially reflect stray RF energy must be at a location where the RF intensity is at least 60 dB below the reference level. Unlike a typical optical system, the shape of the

beam edges cannot be accurately modelled using linear ray tracing techniques (see Fig. 3). When the beam diameter of a system approaches the wavelength, both the signal intensity across the wavefront and the diameter of the beamwaist as a function of propagation distance from a focussing element, can be represented by a gaussian function.

The beam intensity at an aperture or potentially reflective surface may be found and compared to the specification. Table 1 summarizes the system performance goals.

HARDWARE DESCRIPTION

Figure 4 shows the configuration selected for the beam waveguide mechanism. The main structure of the assembly is constructed using carbon-fiber reinforced graphite sandwich panels with an aluminum honeycomb core. Precision inserts are used to locate and align the critical RF components and the axes of rotation. The box shape of the structure makes it extremely rigid, while providing an unobstructed path for the RF energy. Note that there are no loss-producing apertures within the main structure, and only one aperture on the reflector which, as will be shown later, has an insignificant effect on system performance.

Figure 5 illustrates the layout of the positioner mechanism and the axes of rotation. Note that the elevation and azimuth axes have ± 90 deg and ± 180 deg, respectively, achieving a hemispherical field of view. Each axis is rotated by an assembly consisting of a drive actuator and position encoder. The signal path through the beam waveguide is illustrated, as is the location of the major waveguide components. Figure 6 is a photograph of the completed assembly with a reflector and sub-reflector mounted.

Alignment of the critical RF components was accomplished with precision tooling and careful measurement of the components themselves (see Fig. 7). Each component has a series of tooling balls with known locations with respect to the RF aspherical surface. No adjustments of the components were performed beyond the initial assembly.

The drive actuator selected for use in the development model is a Schaeffer Magnetics Type 5 rotary actuator. Flight models with small antennas will also use the Type 5. With larger antennas (such as a 4-m reflector), a Type 6 unit from the same manufacturer may be required. These actuators feature a permanent magnet stepper motor with a harmonic drive gear (cup type), resulting in a gearing system combining very small output step sizes with zero backlash (a characteristic of the cup-type harmonic drive). The actuator output shaft is supported by large-diameter angular contact duplex bearings, providing high load capacity and stiffness for the output shaft in radial, axial, and moment loading.

The Type 5 actuator consists of a 1.5-deg stepper motor with a 200:1 harmonic drive reduction. This production unit is modified to provide mounting locations for a Farrand Inductosyn rotary encoder. A shaft and

bearing set has also been provided to couple the encoder rotor to the output flange. Table 2 summarizes the actuator's operational characteristics. Figure 8 shows the actuator assembly.

Position encoding is provided by a Farrand Inductosyn, an inductively-coupled rotary-absolute position transducer. The device consists of a rotor and stator, with the relative position between the two providing a variation in inductance which is detected by the position readout electronics. The inductance variation is converted to a digital signal which can provide resolution up to 2^{19} bits per revolution. However, 2^{16} bits of resolution is adequate for this mechanism. The accuracy requirement is of a similar order. For the development model tests the electronics modules are non-redundant commercial quality units, as is the rotor and stator. However, upgrading the mechanical components to a flight status will require few if any design changes.

The stator is attached to the outside of the rear actuator housing. An angular contact bearing mounted in the back of the actuator provides support for the shaft that couples the Inductosyn rotor to the actuator output face. In this configuration, a gap of approximately 0.005 in. exists between the rotor and stator. An acceptable gap is maintained for all system conditions including vibration testing. The unit's diameter is slightly smaller than that of the actuator, with a total thickness of less than 0.5 in., allowing a very compact overall configuration. Note that the rotor has two pairs of cables protruding from its top surface, necessitating a rotary signal transfer assembly.

MATERIAL SELECTION AND ANALYSIS

Testing of the development model will occur in a 1-g environment, making analysis of the structural rigidity of the mechanism and comparison of the results with system alignment tolerances necessary. External loads to the mechanism will depend on the orientation of the 2-DOF mechanism. The deflection tolerances for the structure are driven by the requirement that the beam deflect less than 0.01 in. and 0.1 deg as it travels through the waveguide.

The finite element method was used to analyze the structure. The structural members of the positioner have been modeled with a combination of plate and brick elements to represent the composite sandwich. Brick elements represent the shear properties and compressive stiffness of the core, while remaining flexible in bending. Plate elements on either side of the core represent the composite faceskins. The actuators were modeled using stiffness matrix elements. The entire model contains 731 nodes and 956 elements.

The mechanism was analyzed for deflection under 1-g loading in three orthogonal directions to determine orientations of the mechanism which result in deflection maxima. After processing, a complete listing of nodal deflections is produced, which may be edited to show specific areas of interest. A sample deflection output for the reflector is shown in Table 3.

Stresses in the structure are typically under 10 psi, and the maximum deflections are well below system alignment tolerances.

Analyses of the gimbal structure were performed using a variety of materials. A composite sandwich structure with carbon-fiber reinforced graphite epoxy faceskins and an aluminum honeycomb core was selected on the basis of its high stiffness, low weight, and low thermal distortion. While not all of these properties are specifically required for testing the development model, the use of these materials will best simulate the flight hardware.

The faceskin material selected, Pitch 75, is an acceptable compromise of the above parameters, has adequate strength, and is a material with which Ford Aerospace Corporation has experience. A six-ply balanced weave was chosen for the faceskins of the structural members. This resulted in relatively isotropic material properties for the skin, which is required because the load orientation varies as the mechanism is moved. Aluminum honeycomb material with a cell size of 0.125 in. and a weight density of 2 lb/ft³ was chosen for the core. A summary of the properties of the faceskin material is shown in Table 4.

To reduce RF reflections from the gimbal structural components, a minimum clearance of 1 in. is maintained between the 4.75-in. diameter RF path and the mechanism. A computer program was written in 1987 to analyze the signal intensity of the beam at all locations along the signal path. Our analysis of the mechanism shows signal levels of less than -80 dB at surfaces which could potentially reflect RF energy, below the level needed to introduce significant losses into the system. In addition, efforts have been made to minimize the number of possible reflecting surfaces at locations along the waveguide. As a result, the signal path is completely enclosed at only one location for approximately 0.5 in. of travel. The RF energy at this point is -120 dB. No other apertures exist in the waveguide.

PERFORMANCE RESULTS

System testing consisted of measuring sum and difference patterns at several mechanism positions. Figure 9 summarizes the test results.

Theoretical performance is almost identical to the measured performance for the beam waveguide system. At the sum signal peak, only 0.2 dB difference between theoretical and measured signal amplitude was observed. The difference signal is also very sharply defined. The total system loss is less than 0.2 dB for the sum pattern, and 0.3 dB for the difference pattern.

SUMMARY/CONCLUSIONS

Design, analysis, fabrication, and testing of a two-axis positioner mechanism with an integral beam waveguide has been successfully completed.

Performance of the system successfully addresses the issue of low-loss high-frequency RF transmission systems in a compact, 2-DOF mechanism with a hemispherical field of view.

The mechanism is a development model, and while further work will be needed to space-qualify the system, all major components and materials are well suited for that environment. Additional work will be required to ascertain that the system will survive launch loads, and that thermal deformations do not significantly degrade RF performance.

The elevation-azimuth mechanism configuration is acceptable for most applications. However, keyholes or mechanism singularities may restrict performance when high tracking rates with a narrow beamwidth that pass near the zenith location are required. For these applications, a third DOF or an X-Y mechanism may be needed.

The stepper motors caused excitation of system resonances. Further investigation of this effect on signal integrity should be investigated. This undesirable excitation can be reduced by replacement of the stepper units with brushless dc motors. However, this will result in more complex servo electronics.

TABLE 1. SYSTEM PERFORMANCE GOALS

Mechanism configuration	Elevation/Azimuth
Field of view	Hemispherical
Frequency	60 GHz
RF transmission method	Beam Waveguide
Beamwidth	0.2 deg
Pointing accuracy	0.02 deg
Resolution	0.01 deg
"Waveguide" insertion loss	<0.5 dB
l-g deflection	<0.01 deg <0.005 in.

TABLE 2. TYPE 5 ACTUATOR PERFORMANCE SUMMARY

Step size	0.0075 deg
Torsional stiffness	15000 in.-lb/rad
Axial stiffness	415000 lb/in.
Moment stiffness	325000 in.-lb/rad
Nominal output torque	600 in.-lb
Power consumption	<15 W
Weight	4.7 lb maximum
Step rate	300 Hz maximum
Bearing lubrication	Brayco 601 grease

TABLE 3. ANALYSIS RESULTS SUMMARY

Load	Translations			Rotations		
	X (in.)	Y (in.)	Z (in.)	X (deg)	Y (deg)	Z (deg)
X	1.55E-03	-2.34E-09	1.36E-09	-4.90E-10	3.14E-05	2.43E-03
Y	-4.15E-09	6.04E-04	-1.54E-04	-1.89E-05	2.47E-10	-9.90E-09
Z	2.46E-09	-3.33E-05	1.83E-04	-9.51E-06	1.38E-10	7.80E-10

TABLE 4. MATERIAL MECHANICAL PROPERTIES

Material	Tensile Modulus (MSI)	Tensile Strength (MSI)	Flex Modulus (MSI)	Flex Strength (MSI)	Density lb./in. ³	CTE 10^{-6} in./in.*F
Pitch 75	16.0	34.8	14.5	42.0	0.06	-0.2

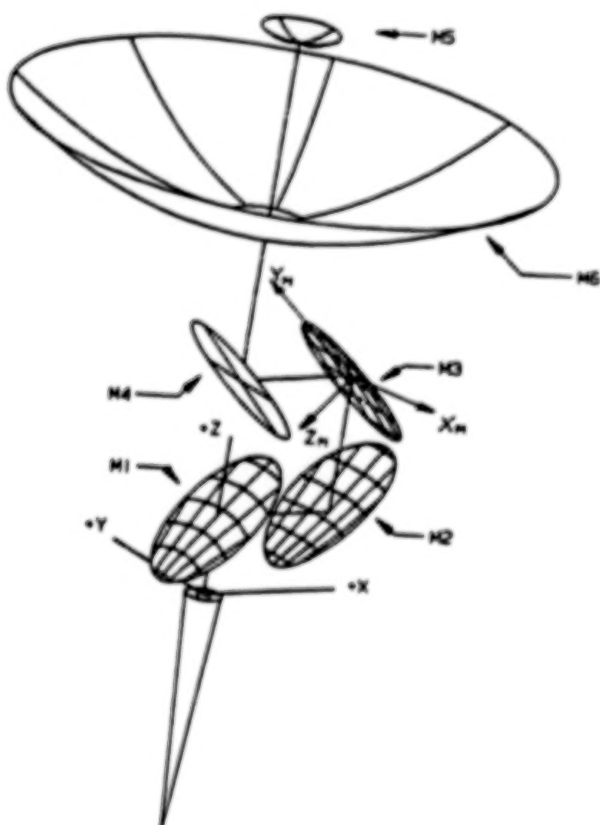


Figure 1. Beam waveguides provide a means of low-loss RF signal transfer.

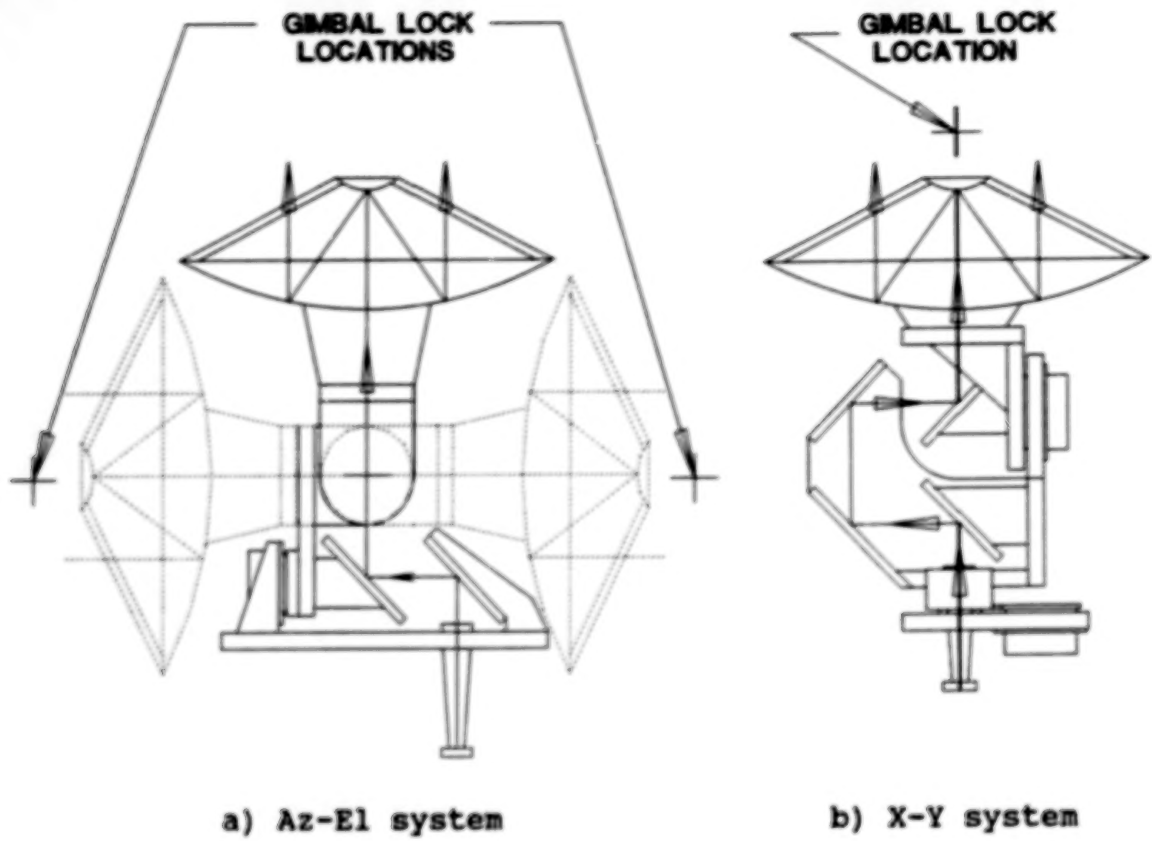


Figure 2. Gimbal lock locations depend on mechanism configuration.

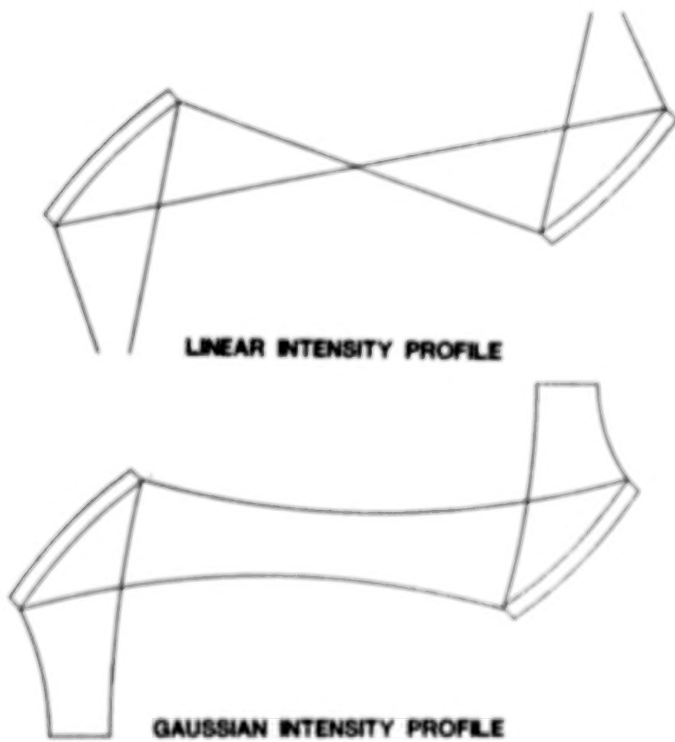


Figure 3. RF systems are best modelled assuming a gaussian intensity profile.

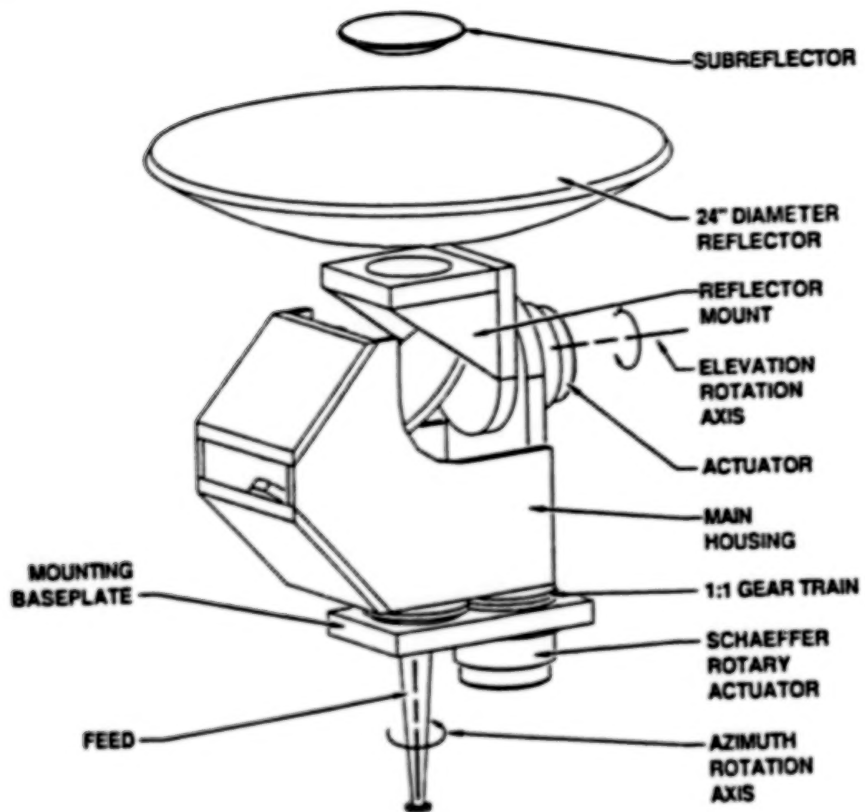


Figure 4. Beam waveguide housing, reflector, and subreflector.

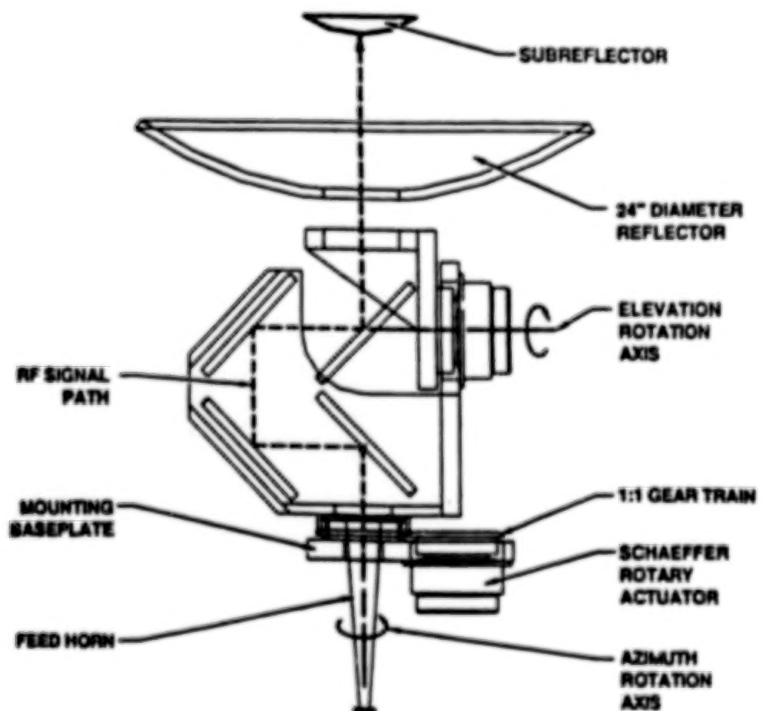


Figure 5. Mechanism cross section.



Figure 6. The beam waveguide is mounted to a range fixture for system tests.

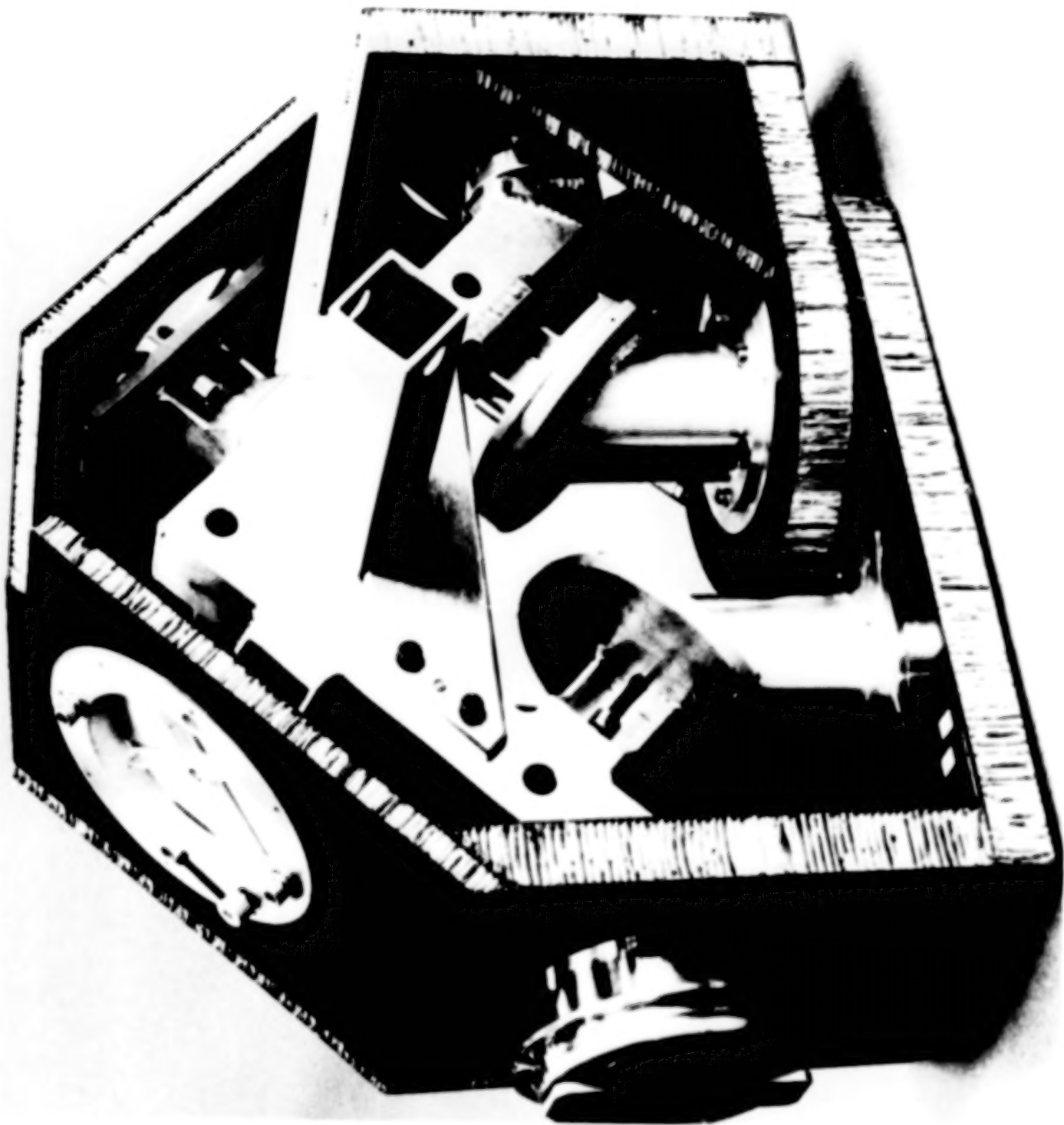


Figure 7. Precision tooling maintains system alignment during the assembly process.



Figure 8. The Schaeffer actuators are space-proven designs.

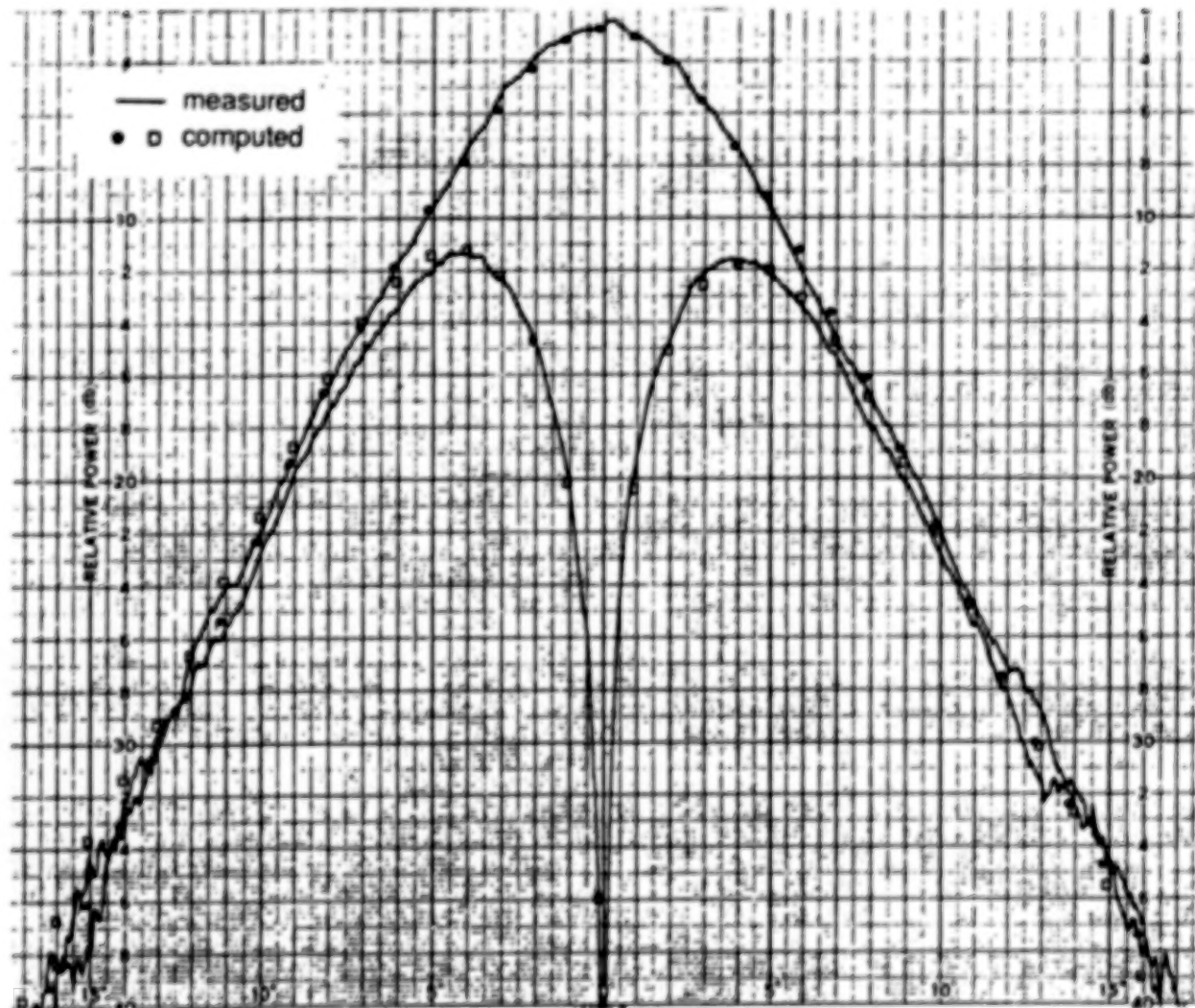


Figure 9. Test results correlate well with theoretical predictions.

AGE DISTRIBUTION AMONG NASA SCIENTISTS AND ENGINEERS

Michael L. Ciancone*

ABSTRACT

The loss of technical expertise through attrition in the technical workforce is a growing concern throughout NASA and the aerospace industry. A bimodal age distribution among scientists and engineers (S&Es) exacerbates the situation within NASA. This situation presents both challenges and opportunities to NASA managers as decisions are made that will shape the future of NASA.

This paper will document historical age-related information for S&Es within NASA in general, and at the NASA Lewis Research Center, Cleveland, Ohio, in particular, for 1968 through 1987. Recommendations are made to promote discussion and to establish the groundwork for action.

INTRODUCTION

The technical competence and reputation of an organization is based on the competence of the individuals who comprise the technical workforce. In this context, the technical workforce contains both supervisory and nonsupervisory scientists and engineers (S&Es). These individuals form the core of institutional technical memory which is the marketable commodity of an organization.

Imagine an organization in which all the technical personnel are replaced with inexperienced personnel. The organization would certainly suffer since the commodity they offer, technical experience, has been eliminated. Conversely, an organization that exhibits a uniform distribution of experience among its technical personnel is less likely to suffer significantly as a result of the loss of their most experienced personnel, since only slightly less experienced personnel would be waiting to fill the vacancies.

A bimodal age distribution, i.e., with two distinct peaks or modes, may preclude a smooth personnel transition. Experienced senior S&Es will be replaced with relatively inexperienced junior S&Es rather than with midlevel S&Es, since few are available. Age (i.e., length of NASA service) and experience are highly correlated characteristics among NASA S&Es, contributing to their low attrition rate. Because of this correlation, institutional technical expertise is a strong function of the age distribution among the technical workforce. A detailed discussion of factors that resulted in the age distributions presented is beyond the scope of this paper.

*NASA, Lewis Research Center, Cleveland, Ohio 44135.

Early in the U.S. civilian space program, after the formation of NASA in 1958, many S&Es were hired directly from the collegiate ranks. These inexperienced, but enthusiastic, graduates acquired valuable experience as they matured along with the Mercury, Gemini, and Apollo programs.

In the late 1960s, forces external to NASA (e.g., Congress, OMB, the national budget, and others) dictated a decrease in the size of the NASA workforce, and a corresponding decrease in the number of S&Es. Figures 1 and 2 show, however, that even as the size of the total NASA workforce and the S&E population decreased, the percentage of S&Es increased (from 43 percent in 1968 to 51 percent in 1987).

The issue of technology loss through attrition must be addressed now. If we assume that the S&Es hired in 1958 were recent college graduates with an average age of 22, then these employees will be eligible to retire under the existing Civil Service Retirement System in 1991, since they will have at least 30 years of service and will be 55 years of age. Valuable institutional technical knowledge and experience will be lost when these employees retire.

It may not be feasible to replenish the pool of experienced personnel by hiring from outside NASA if the bimodal age distribution among NASA S&Es is representative of the aerospace industry in general. The size of the available S&E manpower pool in the U.S. workforce cannot be stated with certainty, but it has been reported that upwards of 50 percent of those earning B.S. degrees in S&E-related fields transfer out of the S&E field [1,2].

DATA

The following information was obtained from raw data and summary reports prepared by the NASA Personnel Evaluation and Analysis Division for the years 1968 through 1987 [3]. S&Es are defined by the following NASA positions:

Support Engineering and Related Positions

This includes professional physical science, engineering, and mathematician positions in work situations not identified with aerospace technology.

Aerospace Technology (AST) Scientific and Engineering Positions

This includes professional scientific and engineering positions requiring AST qualifications, and professional positions engaged in aerospace research, development, operations, and related work, including the development and operation of specialized facilities, and supporting engineering.

Life Science Positions

This includes life science professional positions not requiring AST qualifications, and medical officers and other positions performing

professional work in psychology, the biological sciences, and professions which support the science of medicine such as nursing and medical technology.

Table 1 presents the historical NASA S&E age data for 1968 through 1987. The age data has been categorized in the following age groups: less than 25 years of age, 25 to 29 years, 30 to 34 years, 35 to 39 years, 40 to 44 years, 45 to 49 years, 50 to 54 years, 55 to 59 years, and 60 years of age or more.

Figure 3 illustrates that the NASA S&E population has been aging along with NASA. The peak age-group shifted from 30 to 34 years of age in 1968, to 40 to 44 years in 1978, and to 50 to 54 years in 1987. A smaller, secondary age-group peak (25 to 29 years) appears on the 1987 curve as a result of an influx of new employees, primarily recent graduates. The magnitude of the primary age-group peak decreases only slightly between 1968 to 1987, once again contributing to the relatively low attrition rate among NASA S&Es, during that time as the age distribution shifts from a skewed normal to a bimodal age distribution.

Figure 4 contains the same information shown in Figure 3, but with the number of S&Es in each age group shown as a percentage of the total number of NASA S&Es. Since 1968, 19 to 23 percent of the total S&E population has consistently been concentrated in the peak age group.

Figure 5 further illustrates the aging of the NASA S&E population. The percentage of S&Es in the 35 to 49 age group has steadily decreased since 1970, while the percentage of S&Es in the over-50 age group has steadily increased (although at a slightly lower rate of increase than the rate at which the percentage in the 30 to 49 age group decreased). In addition, the decreasing trend in the percentage of S&Es in the under-35 age group was reversed about 1980.

The NASA Lewis data represents a microcosm of NASA's S&E trends. Table 2 presents the historical NASA Lewis S&E data for 1968 through 1987, during which NASA Lewis S&Es constituted 10 to 13 percent of NASA's S&E workforce. Figures 6 to 8 present NASA Lewis S&E data, comparable to the NASA S&E data presented in Figures 3 to 5.

Figure 9 illustrates that NASA's aging trend stabilized about 1979, and was effectively reversed about 1984, primarily as a result of the infusion of S&E new-hires and the inevitable loss of senior S&Es. The average age of NASA S&Es increased at a rate of 0.65 years per year between 1968 and 1978. Among NASA Lewis S&Es, the rate was a comparable 0.68 years per year.

RECOMMENDATIONS

The following is a list of recommendations which, although not comprehensive, attempts to promote discussion and to establish the groundwork for action. It includes measures that are extensions of or variations on existing NASA initiatives.

Contractors/Consultants

Continue to use experienced S&E retirees through Support Service Contractors or as private consultants when comparable, but unavailable, S&Es are needed. This measure is particularly appealing when manpower funding (R&PM) is limited, but contracting funds (R&D) are available. Such an effort, however, should not detract from the development of an in-house technical workforce.

Technical Mentor Programs

Establish and formally implement technical mentor programs that pair technical new-hires with experienced S&Es. Variations exist within some NASA organizational elements. For example, the NASA Ames Research Center (ARC) has introduced a new training program known as the Interactive Development of Engineers, Administrators, and Scientists (IDEAS) program. This program was specifically designed to counter the loss of institutional knowledge and experience arising from a bimodal age distribution in their S&E workforce.

Documentation

Establish and promote a policy or policies that formally encourage or require documentation during the life of projects and programs. Valuable information is lost to NASA when adequate documentation does not occur until a program/project is either cancelled or completed. By then, it is often too late as personnel move on to other work or are not provided with the proper incentive to document their work. The feasibility of implementing such policy is enhanced by the existence of electronic storage media and telecommunications. As an example, the Space Station Technical and Management Information System (TMIS) is planned to serve as the knowledge base of information for the U.S. space station program, precluding the loss of key information resident in specific individuals.

Employee Development Programs

Continue to promote programs that provide junior and midlevel S&Es with development opportunities for greater technical and/or managerial experience. These S&Es are likely to increase the pool of manpower that will be available to fill the roles vacated by senior S&Es. An example is NASA's Professional Development Program (PDP). The PDP allows selected NASA professional personnel to participate in a one year developmental program at NASA Headquarters and/or at a different NASA Center. Such a program broadens the individual's technical and organizational experience.

Awareness Programs

Increase the dissemination of information on relevant issues through presentations and articles in technical and nontechnical forums, e.g., the Aerospace Mechanisms Symposium, employee newsletters, and technical journals.

Chief Engineer/Scientist Positions

Promote positions for Chief Engineers/Scientists who report directly to the midlevel (second- or third-level) manager. Such positions enable a greater number of individuals to benefit from the experience of senior, nonsupervisory S&Es.

Deputy Manager Positions

Establish and promote positions for deputies to first-level managers that allow junior S&Es to gain managerial experience on a probationary or rotating basis. These positions provide work experience while minimizing the risks associated with submerging an untrained individual in an unfamiliar role. Caution should be exercised to ensure that such positions do not generate an undesirable, and possibly unnecessary, level of bureaucracy.

Hire Experienced S&Es

Efforts should be continued to attract experienced S&Es. As mentioned previously, the size of the pool of available experienced S&Es is an open question. S&Es are in demand now, but many may have made career changes in the 1970s. These changes are a result of factors such as the lucrative offers being made to the MBA candidates with technical backgrounds, as well as the downturn in employment opportunities in the aerospace and energy-related fields. However, as with the use of experienced S&E retirees, such efforts should not detract from the development of the existing in-house technical workforce.

ACKNOWLEDGMENTS

Thanks to the staff of NASA Headquarters, Code NPB, Personnel Evaluation and Analysis Division, especially Stan Kask, Jr. and Dave Thompson, for their time and patience.

REFERENCES

1. "The Science and Engineering Talent Pool." Proceedings of the 1984 Joint Meeting of the Scientific Manpower Commission and the Engineering Manpower Commission, National Academy of Sciences, Washington, D.C., May 15, 1984.
2. "The Technological Marketplace - Supply and Demand for Scientists and Engineers." Scientific Manpower Commission, May 1985.
3. Personnel Management Information System (PMIS) Reports from NASA Headquarters Personnel Programs Division, Washington, D.C.

TABLE 1. AGE DISTRIBUTION AMONG NASA SCIENTISTS AND ENGINEERS

Year	Age range								Total	
	0-25	25-29	30-34	35-39	40-44	45-49	50-54	55-59		
1968	633	2168	2945	2767	2136	1874	815	347	166	13 851
1969	459	1946	2849	2829	2150	2097	900	406	203	13 839
1970	381	1718	2658	2914	2235	2167	1085	472	207	13 837
1971	286	1396	2435	2837	2243	2103	1248	477	202	13 227
1972	135	1109	2185	2746	2383	1950	1452	453	203	12 616
1973	89	801	2000	2594	2517	1900	1559	467	158	12 085
1974	108	606	1769	2524	2541	1888	1684	486	164	11 770
1975	153	521	1537	2408	2608	1962	1701	594	181	11 665
1976	186	468	1308	2264	2662	2050	1738	736	200	11 612
1977	167	456	1063	2072	2574	2314	1685	974	239	11 544
1978	176	503	874	1928	2528	2406	1683	1098	269	11 465
1979	199	503	728	1744	2475	2482	1671	1175	314	11 291
1980	349	598	725	1544	2379	2562	1733	977	333	11 200
1981	317	666	725	1343	2212	2551	1772	952	385	10 923
1982	328	710	660	1159	2060	2475	1927	966	461	10 746
1983	602	809	709	958	1940	2454	2049	1034	539	11 094
1984	557	909	706	842	1723	2379	2091	1074	598	10 879
1985	636	1168	781	837	1508	2269	2171	1137	637	11 144
1986	549	1375	887	862	1327	2120	2207	1183	637	11 147
1987	627	1612	1055	916	1229	2044	2206	1307	683	11 679

TABLE 2. AGE DISTRIBUTION AMONG NASA LEWIS SCIENTISTS AND ENGINEERS

Year	Age range								Total	
	0-24	25-29	30-34	35-39	40-44	45-49	50-54	55-59		
1968	56	271	340	355	301	296	118	53	22	1812
1969	35	233	321	342	294	326	138	57	32	1778
^a 1970	27	194	312	331	302	329	170	66	28	1757
1971	19	154	302	320	309	332	202	75	23	1736
1972	12	102	271	306	308	287	238	73	31	1628
1973	6	66	223	265	300	260	249	67	22	1458
1974	5	43	188	256	286	245	245	73	22	1363
1975	6	38	153	254	271	265	242	89	25	1343
1976	18	34	111	244	270	262	250	128	31	1348
1977	25	36	90	230	260	268	240	158	32	1339
1978	28	40	64	209	253	276	228	173	43	1314
1979	29	42	58	177	247	285	220	197	47	1302
1980	27	50	57	141	251	266	244	155	47	1238
1981	19	59	52	116	240	253	226	157	61	1183
1982	33	66	49	96	226	239	212	151	72	1144
1983	133	98	80	73	213	236	227	148	88	1296
1984	122	112	79	64	180	240	233	156	91	1277
1985	114	176	87	74	146	247	226	173	94	1337
1986	46	218	92	75	122	231	230	161	104	1279
1987	56	249	127	92	108	228	229	164	120	1373

^aFigures for 1970 were obtained through interpolation of the data from 1969 and 1971.

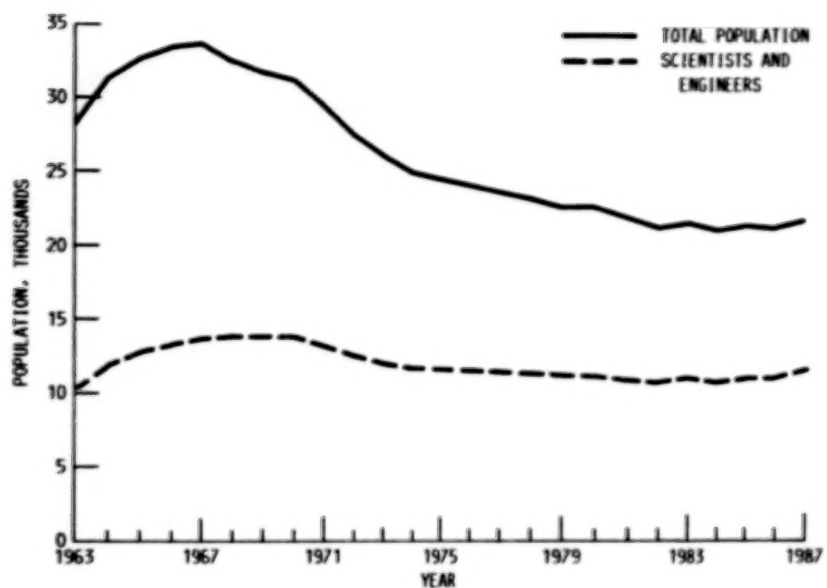


Figure 1. NASA Civil Service population.

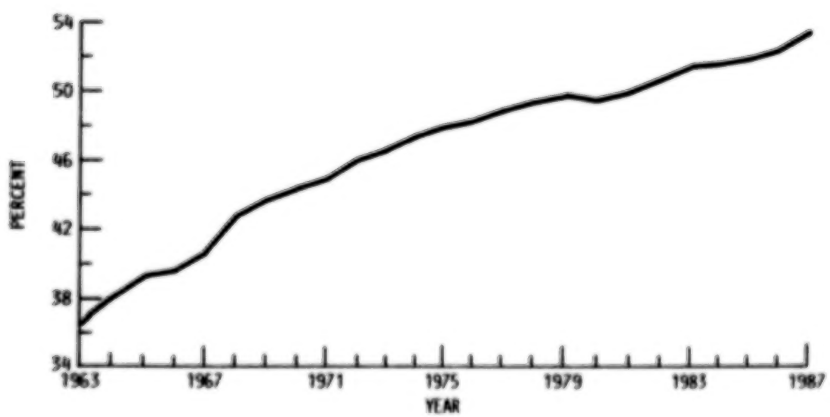


Figure 2. S&Es as a percent of the total NASA Civil Service population.

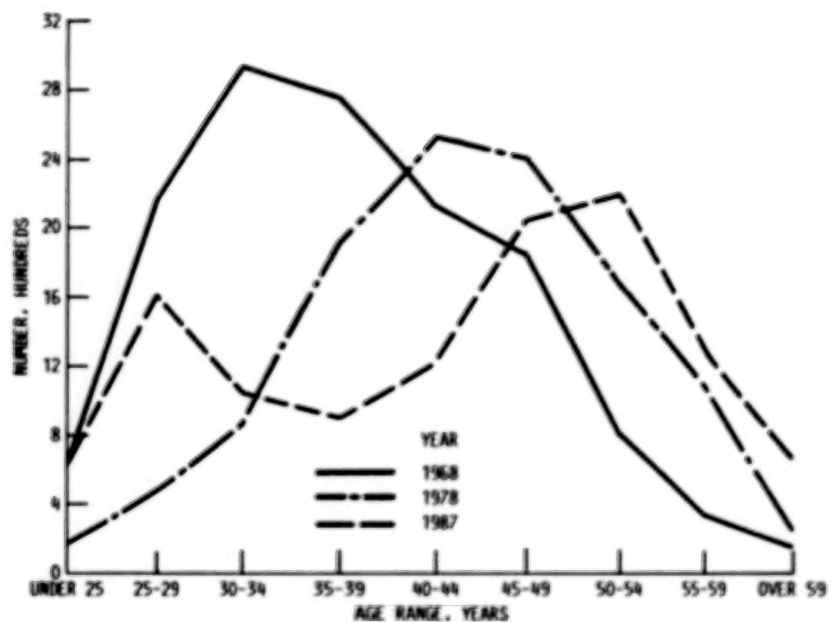


Figure 3. Age distribution among NASA S&Es (number).

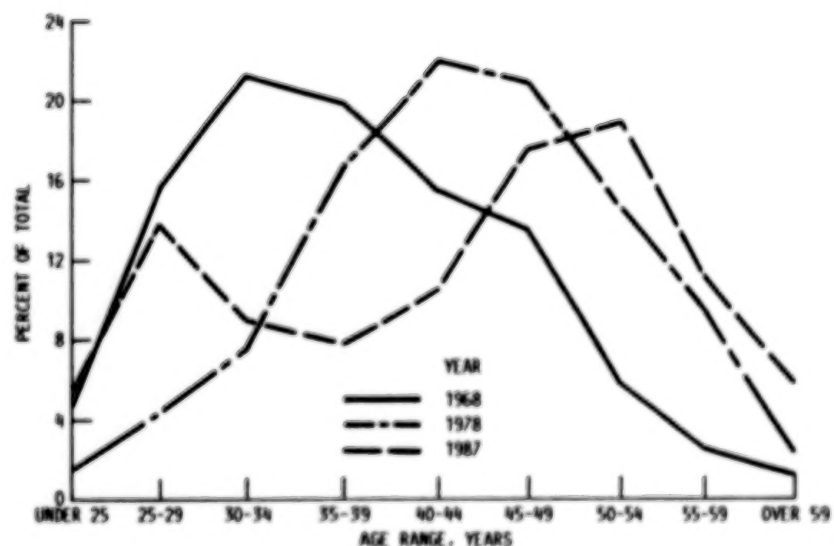


Figure 4. Age distribution among NASA S&Es (percent).

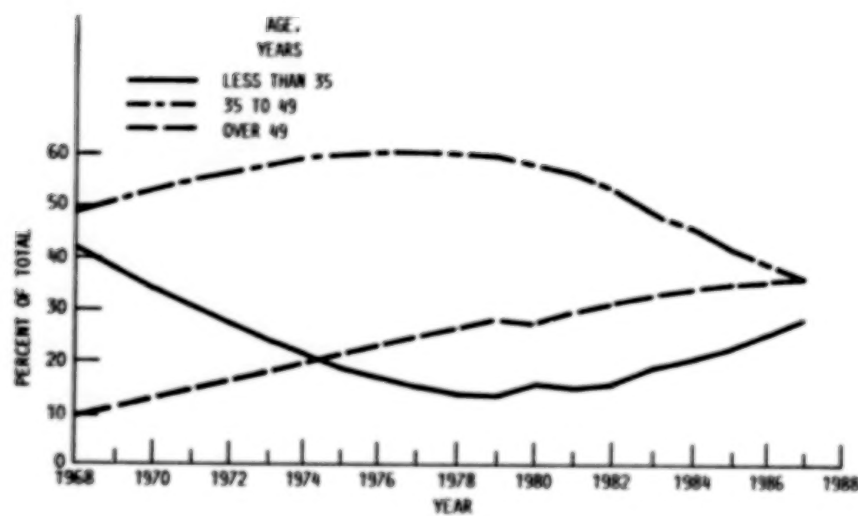


Figure 5. Percent of NASA S&Es in given age ranges.

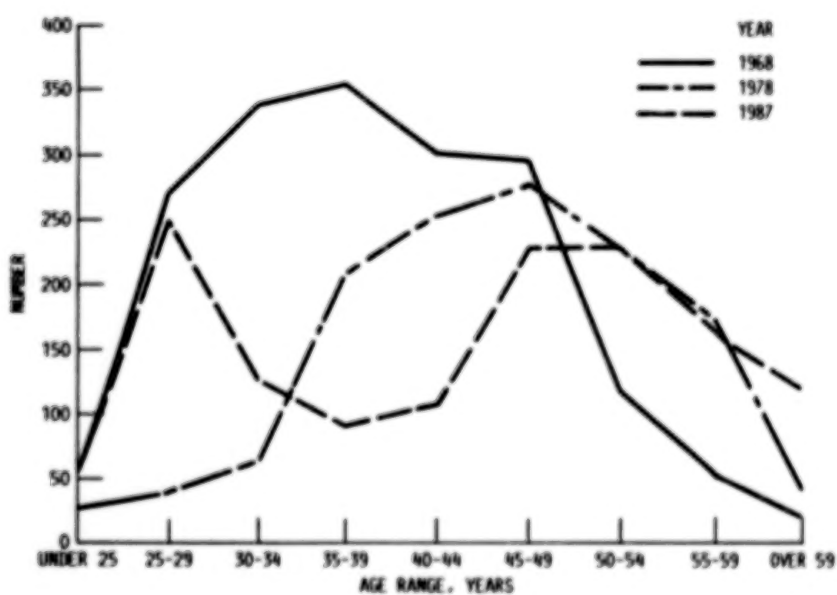


Figure 6. Age distribution among LeRC S&Es (number).

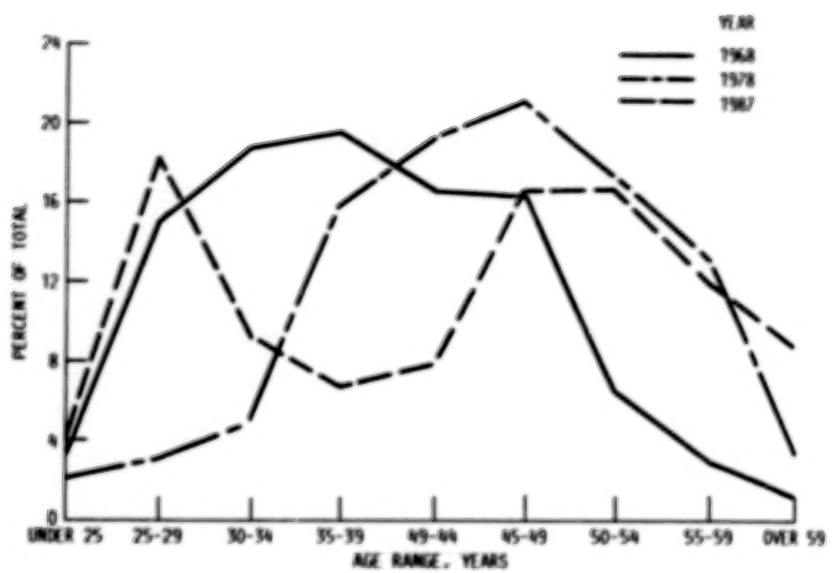


Figure 7. Age distribution among LeRC S&Es (percent).

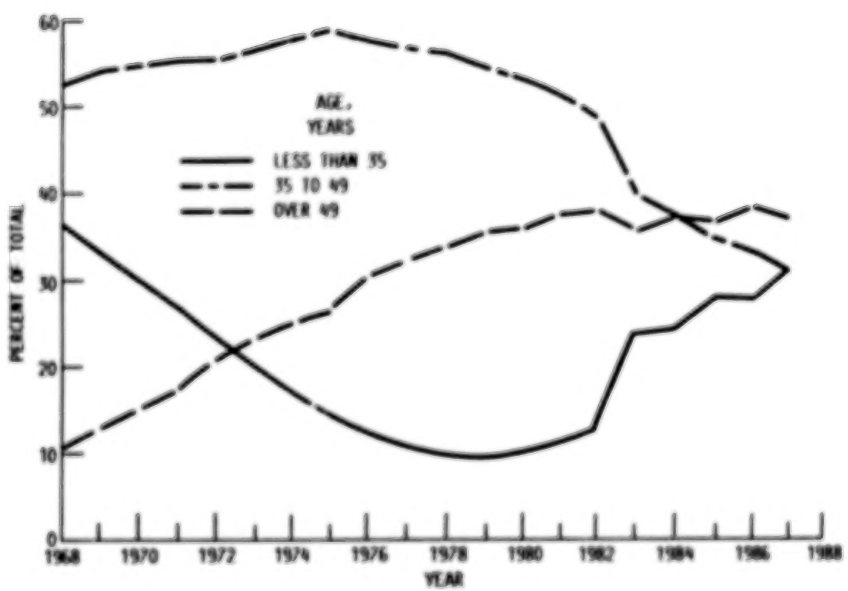


Figure 8. Percent of LeRC S&Es in given age ranges.

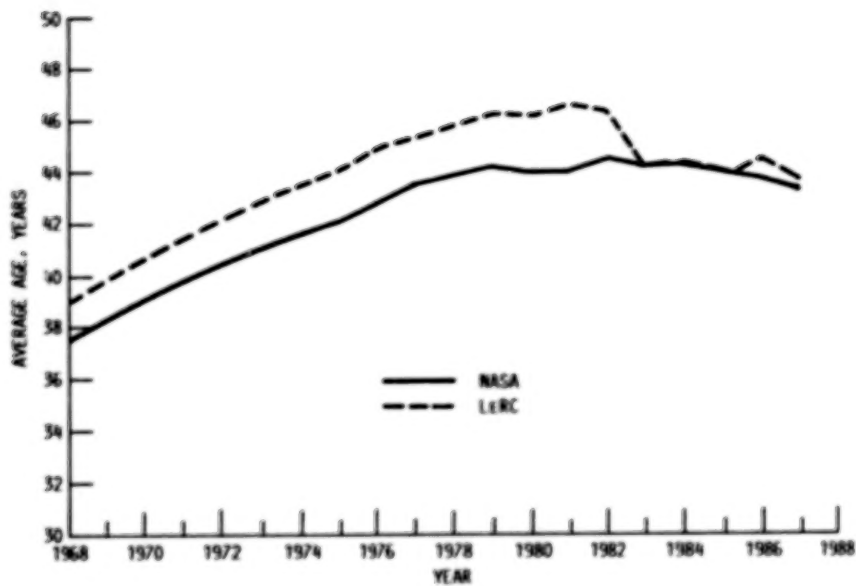


Figure 9. Average age of NASA and LeRC S&Es.

BLANK PAGE

PRACTICAL EXPERIENCES WITH WORM GEARING FOR SPACECRAFT
POWER TRANSMISSION APPLICATIONS

William Purdy* and William McCown**

ABSTRACT

Experiences of several organizations using worm gearing for spacecraft power transmission are discussed. Practical aspects and subtleties of using worm gearing in a space environment are covered. An overview of advanced considerations for design and operation is included. Knowledge gained from these applications is analyzed, and guidelines for usage are proposed.

INTRODUCTION

Worm gearing is often specified for spacecraft mechanisms because it offers moderate reduction ratios in a single gear stage with 90-deg shaft orientation, and because it is backdrive resistant. Worm gearing is one of the smallest, lightest gear-reduction methods available, and can also withstand high shock loads. With these advantages, worm gearing seems to be an obvious choice for spacecraft mechanisms.

Worm gearing, however, is not simple in nature. The same attributes that give worm gearing its unique features also act to its disadvantage. By transferring all power through a sliding interface, power transmission efficiency and predictability can be adversely effected by many factors, most of which act through increased sliding friction. Lubrication of this interface is the single most important part of any worm gear system.

Lubrication in the contact interface is sensitive to many design, operational, and environmental factors. The effects of tooth geometry, mounting, materials and finishes, lubrication, loads, rubbing speeds, temperatures, and vacuum, influence gearset output. With so many variables, no two worm system applications tend to be exactly alike. Drive efficiency can be difficult to predict, obtain, and maintain, and often requires a trial-and-error test process to produce acceptable levels.

Spacecraft worm gear systems have the additional challenges of working with compromised lubrication in extreme environments while being required to work at low to stall speeds. Worm gearing has a mixed history of success and failure in spacecraft mechanisms due to demands beyond those of industrial speed reducers. Stock gearing and speed reducers generally rely on copious lubrication, benign environment, non-critical weight, moderate loads and speeds, and maintenance availability. Most successful applications undergo

*Naval Research Laboratory, Washington, D.C.

**Rexnord Aerospace Mechanisms

interactive development to achieve adequate levels of performance. The purpose of this paper is to help spacecraft mechanism users and designers achieve the advantages inherent in worm gearing by investigating several practical experiences, and by showing the finer points of worm gearing technology.

OPERATIONAL BASICS OF WORM GEARING

Most texts do not describe the complex nature of the worm gear interaction. A review is beneficial before analyzing applications and recommending guidelines for spacecraft use. Single enveloping, 90-deg worm gear systems will be addressed.

The sliding motion between worm and gear forms lines of contact across the faces of the worm thread and gear teeth, as shown in Figure 1. These contact lines continually move and change shape through the engagement of a single thread and tooth. Individual points on these lines have both lateral and radial movement relative to the gear. Lateral movement effects rubbing speed while radial movement changes the shape and position of the contact line. The worm usually contacts the gear on several teeth simultaneously. The shape and movement, or gear action, of the contact lines is controlled by the pressure angle, lead angle, and other geometric constraints.

Lateral sliding works to deplete lubricant from the gear interface. This depletion process is modified by the orientation and shape of the contact line. When there is a substantial radial component of the line shape, a wedge of lubricant tends to be pushed ahead of the laterally advancing contact line.

Standard gears sets feature approach and recess gear action. Approach action occurs during early engagement between the worm and the gear as the line of contact moves from the tip area toward the root of the gear tooth. Recess action follows as the gear tooth recedes from engagement, and movement of the contact line reverses direction, heading back toward the tip of the tooth.

Forces and sliding characteristics can vary greatly between approach and recess phases. When coupled with lateral sliding and grease lubrication, gear action can act as a squeegee to remove lubricant from the face of the gear. This effect can be minimized by control of lubrication, contact stresses, contact forces and directions, gear action, contact line shape, rubbing speeds, and cycle duration.

The relationship between lead and pressure angles and efficiency is not obvious. Despite low angles describing a shallow wedge and increasing mechanical advantage, efficiency is reduced because sliding action increases, resulting in lubricant depletion. Increased lead and pressure angles can reduce this sliding, thus reducing lubrication degradation and increasing drive efficiency.

The coefficient of sliding friction in the thread/tooth interface is a large factor in the mechanical efficiency of a worm gear system. Efficiency prediction is difficult at best for worm gearing. Many efficiency equations are available which do not consider lubricant-starved conditions. Predictability and control of the efficiency mandates good lubrication of this sliding interface. Efficiencies should be verified by test, as worm gearing does not deliver precise outputs, especially for low speed and stall applications.

Adequate lubrication is usually the key to a successful worm gear system. Examination of the action between the tooth and thread shows the harsh environment in which a lubricant must succeed.

PRACTICAL EXAMPLES

A discussion of several different applications provides insight into the behavior of worm gearing in spacecraft mechanisms. Design, detail, and operating requirements for each system are presented in Table 1. Discussion of each example emphasizes operational characteristics, problems encountered and their causes, symptoms, and solutions. A comparison of the characteristics of each system shows the effects of design features and operating conditions on performance.

The following examples are presented:

1. Naval Research Laboratory (NRL)/Sundstrand; two similar worm gear systems in a single ballscrew actuator
2. NASA Goddard; double enveloping worm gear system in latch mechanism
3. Astro Aerospace; worm gear systems used for drive and braking of deployable masts
4. Rexnord Aerospace Mechanisms (RAM); worm gear set in latch drive.

NRL/SUNSTRAND WORM GEARING IN BALLSCREW ACTUATOR

Requirements and Design

Two similar worm gear systems were used to drive a ballscrew actuator built by Sundstrand Corporation in conjunction with the Naval Research Laboratory for a spacecraft application. The first gearset, referred to as the primary system, had an 86:2 ratio and consisted of a 20.2 mm (0.797 in.) diameter steel worm and beryllium copper gear. There were two of these type worm gear systems in the actuator called the primary and back-up drives. The second type of system, called the emergency system, was on a redundant drive for the first two systems. This gearset consisted of a two-start worm of the same design as the primary system, and a 58-tooth gear cut into a steel ballnut, called the emergency drive. The actuator was required to drive under

a constant load for 15 min, generate a sufficient stall load, then reverse its cycle. The emergency system had to drive against constant load for 30 min.

In addition to the requirements of Table 1, another requirement was that neither system could produce more than 580 in.-lb. This maximum output requirement severely limited the amount of torque margin that could be designed into the drive train.

Discussion

The two systems operated as designed in ambient air, ambient vacuum, and hot vacuum testing. All systems demonstrated an unexpected failure mode during cold vacuum qualification testing. The actuator would start a cycle working normally but would gradually slow down during the cycle, indicating increasing torque demand on the drive motor. The emergency and one of the primary systems would actually slow down to the point of stall under a constant load. After much investigative testing it was shown that the efficiency of the worm gearing was dropping over time. The worm gear system efficiency has to drop to approximately 12 percent for the primary drive to stall in these conditions and to 19 percent for the emergency system to stall. This is a very low efficiency as compared to the 40 percent efficiency the systems demonstrated in ambient tests and at the start of each cold vacuum cycle. Design calculations predicted efficiency to be between 47 and 62 percent.

This decay was severe in cold vacuum conditions, minimal in ambient vacuum conditions, and nonexistent in hot vacuum and ambient conditions. The severity of the decay varied for each system and for each drive direction of each system. The cause was shown to be lubrication depletion in the worm gearing. The decay, and therefore the lubrication problem, was not permanent. Whenever the actuator was retested in cold vacuum, it exhibited the same behavior of starting well and then decaying. This decay problem was eliminated by switching from Braycote 601 to Braycote 608 grease for the worm gear lubrication. This fix was demonstrated only on the emergency system, although it is expected to succeed on the primary systems also.

The decay phenomenon was attributed to a gradual wiping away of the grease, with the poor efficiency demonstrating a weakness in the boundary lubrication regime. The MoS₂ bonded dry-film lubricant applied to the gear teeth wore off the driving surfaces during run-in, and provided no lubrication during operation. The manner in which the 608 grease solved the problem is not fully understood, because it has two major differences from 601 grease. The 608 grease has MoS₂ added, which could be improving the boundary lubrication. The 608 grease also has much higher oil content, which could help the healing process of lubricant after it has been wiped away. It has not been determined whether the problem was solved by either one or both of these changes.

The decay was strongly affected by temperature and load. In cold vacuum, the actuator did not slow down under a moderate load (approximately 1/3 of the

maximum required load). However, the stall load generated at the end of this cycle was unacceptably low. Decay could not be detected during no-load, cold vacuum operation of the actuator and the stall load generated at the end of this cycle was normal. Decay in ambient vacuum was minimal to nonexistent, depending on the system tested.

An interesting discovery was the healing ability of the worm gear system lubrication. The primary systems would show normal efficiency when restarted after they had been turned off for a 20 min period after decaying to stall. A graph of the typical speed-versus-time characteristic in cold vacuum testing is shown in Figure 2. The figure covers two cycles showing the healing effect.

After disassembly and reassembly of the worm gear system, with no change to the grease other than slight smearing during disassembly, the actuator's performance was much improved, but only temporarily. After two cycles the performance had returned to its normal problems. This demonstrates a high sensitivity to lubrication in harsh operating conditions.

All of these symptoms show that worm gearing efficiency can be very sensitive to small factors when used in harsh conditions. Lubrication with Braycote 601 grease was found to be ineffective only in cold vacuum conditions, while Braycote 608 was always successful. The non-permanent decay observed was the significant symptom of worm gear problems in this application.

NASA-GODDARD CONE DRIVE SYSTEM

Requirements and Design

At the Goddard Space Flight Center, a 50:1 cone drive (double enveloping) worm gear system was used to drive an over center latch for a Shuttle payload capture mechanism. The worm gear drives for approximately 10 sec against a torque that increases to a peak at the 6 deg before center position. The worm is driven by a motor with a peak torque at stall of 27.5 Nm (250 in.-lb), and has a requirement to produce a minimum 339 Nm (3000 in.-lb) peak output at the gear. The system must operate from -70°C to +70°C in a vacuum environment.

The reduction ratio was changed from 50:2 to 50:1, after galling and poor efficiency were observed in cold vacuum testing of a development motor/worm gear system. The development system was lubricated with Braycote 601, which was changed to a mixture of 50 percent Braycote 802EP grease and 50 percent Braycote 815Z oil for the final system. The 802EP grease is different from the 601 in that it contains a molybdenum disulfide based compound, and it is based on a different oil than the 601, which is based on 815Z oil. The system was designed to operate properly with a worm gear efficiency of 40 percent.

Discussion

The final system operated as designed between -50°C and +70°C in thermal vacuum testing. Below -50°C, however, the worm gear efficiency was significantly lower, dropping as low as 21 percent at -70°C. Gear efficiencies in test were from 40 to 50 percent at ambient and hot vacuum conditions. With the system's ample torque margin, it barely passed its -70°C vacuum operation requirement. At this writing, the system has not yet been disassembled and examined for galling or other degradation.

Tests on the development system showed generally poor efficiency during operation below -10°C. The efficiency was anywhere from 5 to 50 percent lower than efficiencies measured at higher temperatures. The original system failed during these cold vacuum tests, having wiped bronze from the gear onto the worm. Data on torque versus speed at high and low temperatures showed that at low speed, high torque conditions, the efficiency was significantly lower and more inconsistent in the cold case. Data taken at low torque, higher speed conditions showed equal performance in hot or cold conditions.

Some important worm gear performance characteristics were demonstrated by this system. At extreme low temperature conditions, the worm gear efficiency dropped from normal efficiencies of 40 to 50 percent to 21 percent. The system was highly successful at temperatures above -50°C. As a result of development testing, the performance of the system was significantly improved by the switch to a wetter grease that contained MoS₂.

ASTRO WORM GEAR SYSTEM

Astro Aerospace has successfully used two worm gear systems as drives and governors in deployable masts. The worm gear systems are used as a drive to retract the mast and as a brake/governor when the mast deploys under its own spring energy. This paper will discuss the systems' characteristics only when used as a drive. Two systems used in this capacity are being examined. One system, detailed in Table 1, was a 30:1 ratio gear set with a 25.4 mm (1.000 in.) worm and 63.5 mm (2.500 in.) gear. The other system will not be discussed in detail. However, lubrication failed completely allowing massive gear tooth wear when a dry film lubricant was the sole lubricant. Following a switch to grease lubrication, the system was successful.

The first system mentioned had to produce an output torque of 4.8 Nm (42 in.-lb) for several minutes, after briefly producing a torque of 25 Nm (225 in.-lb). The system had to operate in vacuum at temperatures from -85°C to 70°C.

One of the most important aspects of this design is the grease lubrication and its application. A thin coat of Braycote 601 grease is used as the only lubricant for the worm gear set. The grease is applied before run-in, and then cleaned off, first using freon, and then toluene to remove freon residue after the run-in is finished. A thin film of grease is then applied in the final assembly.

This system performed successfully with no difficulties encountered. A critical factor in the success of this design is the ample torque margin of the drive motor at nominal loads. At nominal loads, the motors had greater than 6 to 1 torque margin, although there was only a 10 percent margin at peak output. It is important that the system succeeded at extremely cold temperatures as low as -85°C.

REXNORD AEROSPACE MECHANISMS WORM-GEAR DRIVEN LATCH SYSTEM

Requirements and Design

A worm gear system is used in a rollerscrew latch used to clamp a connector system together. The gearset features a 40:1 ratio consisting of a 15.9 mm (0.625 in.) diameter steel worm, and an aluminum-bronze gear of 63.5 mm (2.500 in.) diameter. This system undergoes minimal loads for latch extension and engagement, then is driven under power to stall as the screw and nut tighten.

This system operates in vacuum at ambient temperatures, with a peak torque output of 12 Nm (107 in.-lb) with a maximum input torque of 2.0 Nm (18 in.-lb) available. Output load variance using governed motor power was limited to 10 percent in a life cycle test of 20 full actuations. Sliding velocities run from as great as 1.52 m/sec (60 in./sec) down to stall, going from high to low extremes in as little as 3 sec. Design details are listed in Table 1. Braycote 601 grease is applied to lubricate this system. Tungsten disulfide dry film is applied and is worn away during break-in.

Discussion

The drive system demonstrated a load degradation after 10 full load cycles, decreasing steadily to a 60 percent level at 20 cycles. Gear lubrication was found to be at fault, as re-lubrication brought back initial loads. A wiper system was installed to force grease back onto the gear teeth, eliminating the load decay, and providing successful operation.

Stall conditions under peak loading aggravated the tendency of the worm to wipe grease from the gear teeth. A healing effect was evident, but produced output loads of only 80 percent at best from previous, well lubricated runs.

COMPARISON OF EXAMPLES

NOTE: The system(s) demonstrating a characteristic are referenced by number.

1. NRL/-Sundstrand
2. NASA Goddard
3. Astro
4. Rexnord

All worm gearing problems encountered by the examined systems were caused by inadequate lubrication. Three of the systems (1,3,4) showed that Braycote 601 would do a fine job of lubricating when it was present in the tooth interface. The NRL system worked at the start of each cycle, the Astro system always worked, and the Rexnord system worked well with the addition of a wiper to force grease into the teeth. A switch to wetter greases containing molydisulfide resulted in satisfactory lubrication in two examples (1,2).

In three instances (1,3,4), dry film lubricants were completely wiped off the worm and gear teeth. Two of the organizations (1,2) had problems only under cold, vacuum conditions. The symptoms of efficiency decaying over time, and healing of worm gear systems were observed on two of the examples cited (1,4), and also in one other system not discussed elsewhere in this paper.

In most cases, the mechanisms would have survived low efficiencies with motors having larger torque margins. Limitations on the output force often limited this option. The Goddard system benefitted from a motor and worm gear subsystem development test.

ADVANCED CONSIDERATIONS FOR WORM GEARING DESIGN

Beyond general guidelines (Table 2), worm gearing for spacecraft can benefit if additional aspects are considered. The optimization of gear interface lubrication is of primary importance to the function of the gearset. Secondary functions include techniques to augment this lubrication. The following areas of importance in worm gear design will be briefly discussed.

1. System Design
2. Lubrication
3. Actuation
4. Design, Analysis, and Geometry
5. Mounting
6. Materials and Finishes
7. Break-in and Development
8. Qualification Test and Flight.

Several of the topics to be presented require great expertise to implement. The authors do not possess this expertise and have therefore identified experts known to them in the field of the paper.

Systems Design

Before choosing worm gears for an application, their suitability must be assessed. Worm gearing does not lend itself well to precise outputs, low input power margins, very low speeds, redundant systems, high cycle life, and long duty cycles. Motor sizing should be able to accommodate low worm gear efficiencies, even as low as 10 percent. Component strength must accommodate high efficiencies, even as high as 95 percent. Worm gear systems can be very weight efficient, but if motor and component sizes must be oversized to accommodate uncertain efficiencies, the weight benefit quickly disappears. Development and good design are the keys to extracting all of the potential advantages of worm gearing.

Lubrication

The key element in worm gearing is interface lubrication. Most worm gearing failures reflect back to lubrication problems. The worm gear interface operates in boundary layer conditions. The choice of a lubrication scheme for worm gearing benefits greatly from development work.

Wet lubrication is almost always necessary for these harsh contacts, as dry film lubricants are typically worn away very quickly. The addition of moly-disulfide to the wet lubricant helps reduce friction in the boundary lubrication regimes present. Lubricant replenishment systems, such as wipers, are very helpful by replenishing the oil or grease scraped away by the rubbing contact. High oil content greases may be beneficial in cold operating environments. Tests are currently underway on lubricants specifically for spacecraft worm gearing by John Christian of Aerospace Lubricants, Inc., and Rick Scott of NASA-Goddard.

Actuation

Successful worm gearing becomes harder to attain when used in harsh duty cycles. Actuations should, if possible, be planned to overcome peak loads early in each cycle before lubrication has been worn down. High cycle life should be avoided, as well as long durations and very high and low rubbing speeds. Stalling at peak load should also be avoided, especially if it occurs in the same worm gear position on each cycle. This can lead to localized wear similar to a notching effect. Under repeated cycling, expect lubrication degradation to occur unless a relubrication system is employed.

Design, Analysis, and Geometry

Initial system design can be done with handbook formulas and catalog ratings if significant derating factors are used. This initial derating does not allow for reduced lubrication, but rather provides adequate envelope for later design changes.

Several approaches are used to design worm gearing for lubrication-critical applications. All of these use derating relative to terrestrial

applications. These factors are somewhat empirical relative to the gear geometry approach used. Three methods found include: (1) standard geometry with high derating factors, (2) optimized recess action geometry, and (3) optimized contact stress reduction.

Standard geometry worm gearsets can benefit from high derating factors if rubbing duration is low, speeds are kept moderate, and lubrication is present. Factors of 2.5 for peak torque loads and 10 for nominal torque loads relative to commercial ratings have worked for short-term applications. Empirical values must be developed in test to establish derating values suitable to individual applications. This is a "brute force" approach that does not critically address weight or lubricant degradation.

Recess action geometry is a method favored by a number of experts including Eliot Buckingham of Buckingham Associates. A computer program and texts are available which aid in altering worm and gear geometry to put the entire contact interface into recess action, where friction is reduced and contact lines do not reverse direction. Speed reducer data indicates this to be a valid approach, but no examples were found for review in this paper.

Contact stress reduction between worm and gear extends life and can aid lubricant survivability. This method is proposed by Henry Minaisian of Grant Gear Company. A computer program is available on a consulting basis which predicts contact stresses on the tooth face of the gear. Using iteration, contact stress is lowered by increasing the contact area of the worm and gear, lowering relative curvatures between teeth, and modifying approach and recess action. An example of the results of this analysis is shown in Figure 3. Again, no spacecraft applications of this technique were available for review.

Other programs and consulting services are available from Ken Gitchel of Universal Technical Systems and consultant Henry Ryffel, Gear Section editor for Machinery's Handbook.

Mounting

Worm, gear, shaft, bearing, and housing stiffness must be adequate to preserve proper interface contact under load. Any deflection in the system that moves the contact interface away from the previously established contact zone will drive contact stresses up and degrade lubrication. The mounting should be very accurate to maintain the geometry specified by design and manufacture. A means for adjusting the location of the contact region during assembly and break-in should be provided.

Materials

Materials choice can be very difficult. While steel worms and bronze gears are most common, stainless steel worms and gears have been used in space, as well as steel, beryllium copper, and aluminum gears. Testing and experience are important to evaluate a material's suitability to each application.

Most spacecraft worm systems use steel worms and bronze gears with a hardness differential of 50 to 80 Brinnell points, so that the gear will wear in to conform to the worm. All worms should be of fine finish, preferably polished, before break-in.

Gear materials can vary widely depending on their application. Bronze gears are chosen because their wear and failure characteristics are generally more gradual than that of other materials. As a result of extensive testing, Robert Campbell, of Mueller Brass Company, recommends the proprietary Dynalloy 603 manganese bronze in a forged and heat-treated condition. Cast tin and nickel-tin bronzes also exhibit good properties in test.

As of this writing no data has been found on worm gear materials for vacuum use. It is assumed that terrestrial data is somewhat applicable in that grease lubricants are used. Leaded and molybdenum disulfide-impregnated bronzes have been tried but were found to have gear wear rates under moderate loads.

Break-in and Development Test

Break-in is considered the final machining operation for a worm gearset. Break-in should be run with abundant lubrication, starting at low loads and gradually progressing to a flight-like scenario. Break-in should always be run in final component form. Debris generation will occur during this phase, and must be removed prior to use. Care must be used to clean and reassemble exactly as the gearset was broken in.

The gearset should be set up to produce an even wear pattern on the leaving side of the gear tooth. This pattern will gradually progress across the face of the gear to include the entering side.

Separate gearset testing will determine the ability of the worm gear system to transmit adequate power. This testing should be run informally to resolve any difficulties before the design has been finalized.

Flight and Use

Characteristics of the gearset should be well known at this time. Despite this, problems may yet occur. As with many other complex devices, worm gearing benefits from practical experience, empirical knowledge, and plenty of backup test data. Recognize that eventually worm gears will degrade to the level of failure, but with good technique that point should be well beyond the life of the spacecraft.

CONCLUSIONS

Several key points should be understood by everyone involved with a worm gear application in a spacecraft mechanism.

1. Worm gearing is not simple. Knowledge, experience, and testing is necessary for superior performance.
2. Lubrication is a key factor.
3. The requirements typical of spacecraft mechanisms are often difficult for worm gearing to meet.
4. Proper design is necessary for good performance.
5. Worm gearing benefits from and often necessitates development testing and tuning to achieve predictable advantages.

ACKNOWLEDGMENTS

The authors are deeply indebted to many individuals who generously donated their time, effort, knowledge, and insight to this project. We wish to thank the contributors of examples, without which this paper would have been impossible; Rick Scott, NASA Goddard; Peter Preiswerk and Keith Edwards, Astro Aerospace; Loren Pfeil and Duane Teske, Sundstrand. We also wish to thank the industry experts who educated us in the advanced considerations for worm gearing; Henry Minaisian, Grant Gear; Eliot Buckingham, Buckingham Associates; Henry Ryffel, gearing consultant; John Christian, Aerospace Lubricants; Richard Kelley, Bray Castrol; Bill Nygren, Martin Marietta; Robert Campbell, Mueller Brass; Ken Gitchel, Universal Technical Systems.

REFERENCES

1. Minaisian, H.: Worm-Gearing Contact Analysis Program. Grant Gear Co., Norwood, Massachusetts, December 1988.
2. Brown, J.: Computer Program Aids Worm-Gear Development. Power Transmission Design, August 1989, pp. 63-66.
3. Buckingham, Eliot: Taking Guesswork Out of Worm-Gear Design. Machine Design, March 20, 1975, pp. 82-86.
4. Buckingham, Earle: Analytical Mechanics of Gears. Buckingham Associates Inc., Vermont, 1988.
5. Buckingham, E., and Ryffel, H.: Design of Worm and Spiral Gears. Buckingham Associates Inc., Vermont, 1973.
6. Dudley, D. W. (Ed.): Gear Handbook. McGraw-Hill Book Co., New York, 1962.
7. Jones, F. D., Horton, H. L., et al.: Worm Gearing. Section 34 of Machinery's Handbook; Ed: P. B. Schubert, Industrial Press Inc., New York, 1975.

8. Pacholke, P. J., and Marshek, K. M.: Improved Worm Gear Performance with Colloidal Molybdenum Disulfide Containing Lubricants. A.S.L.E. Lubrication Engineering, August 1987, pp. 623-628.
9. Vest, C. E., Courtney, W. J., and Farrell, J. J.: Evaluation of Gear Materials For Space Applications. Proceedings of ASTL-ASME Lubrication Conference, Houston, Texas, October 1969, pp. 214-222.
10. Campbell, R. A.: Alloy Evaluation for Gear Applications, Summary Report RP2-1. Mueller Brass Co., Port Huron, Michigan, 1988.
11. Castleberry, G. A.: The Little Things Count In Designing For Contact Stresses. Machine Design, August 8, 1985, pp. 75-78.

**BLANK
PAGE**

TABLE I. SUMMARY OF DESIGN DETAILS AND REQUIREMENTS

DESIGN										REQUIREMENTS						
SYSTEM TITLE	PITCH DIAMETER OF TEETH	NUMBER OF TEETH	DIAMETER, PITCH	MATERIAL	SURFACE FINISH	SURFACE FINISH	LUBRICANTS	LEAD ANGLE	PRESSURE ANGLE	OUTPUT TORQUE	OUTPUT TORQUE	INPUT TORQUE	ROTATING SPEED (IN/SEC)	TEMP. CELSIUS ESTIMATE	DESIGN LOAD/HIGH EFFICIENCY	
"None"	"None"	In. (-1)	"None"	"None"	"None"	"None"	"Trade Name"	Degrees	Degrees	Peak	Normal	Peak	m/s	(IN/SEC)	(%)	
Gear	Gear		Gear	Gear	Gear	Gear		-Inches		No	No	No				
				(Rock- well)	(Micro-In.)	(Micro-In.)				(In-lb)	(In-lb)	(In-lb)				
		(In.)														
REL/SHLD-	"20.2"	"2"	24	"1000 STL"	"In. 60"	"0.0"	"Sandstrom	6	20	9.5 (84)	2.8 (25)	1.8 (16)	.16 Max	-25 / 65	40 - 50	
STRAND	61.5	56		1000 COPPER	In. 60	1.6	LC 300*			(full)	(full)				(6.3)	
PRIMARY	"(.797)" (.360)			per AMS 4650		"(32)" (32)	Dry File			(cycle)	(cycle)				0 Min	
							"Bray 601"								"15 minute cycle"	
REL/SHLD-	"20.2"	"2"	24	"1000 STL"	"In. 60"	"0.0"	"Sandstrom	6	20	28 (284)	2.8 (25)	5.1 (45)	.051 Max	-25 / 65	40 - 50	
STRAND	61.7	56		1000 STL	In. 60	0.8	LC 300*			(full)	(full)				(2.6)	
EMERGENCY	"(.797)" (.343)					"(32)" (32)	Dry File			(cycle)	(cycle)				0 Min	
							"Bray 601"								"30 minute cycle"	
							"Bray 601"									
ASTRO	"25.4" 63.5	"3"	12	"1025 C1117"	"In. 62"	"0.0(Psi)" Recessed	"Bray 601"	4-45°	14.5	25 (225)	4.8 (42)	28 (250)	.19 Max	-45 / 70		
				Perf. BRONZE						(Briefly at start)	(full)	start &		(7.5)		
															"30 minute cycle"	
SHIELD	"15.9" 63.5	"3"	16	"1045 STL"	"In. 59"	"0.4" In. 57	"Bimetallic"	5-43°	14.5	12 (107)	No-load	2.0 (18)	.41 Max	Ambient		
				BRONZE per	In. 57	0.8	W52			(start)	(8% of cycle)				(16)	
						"(32)" (32)	Dry File								0 Min	
							"Bray 601"								"15 minute cycle"	
							Wiper									
GEARBOX	"47.2"	"1"	8	"4150 STL"	"In. 60"	"0.0"	50% "Bray	3-45°	22.25	399	N/A - (3000)	28 (250)	.11 Max	± 70	40	
CONE DRIVE	161.0	56		CASE BRONZE	In. 35	1.6	6025P*								(4.5)	
						"(32)" (32)	50% "Bray									
							6152"								"10 Second cycle"	

304

TABLE 2. GENERAL GUIDELINES

A list of general guidelines is useful for the initial design. These guidelines apply to most worm gear systems and are taken from worm gear specific texts.

GUIDELINE	REASON
1. Make the hob as nearly identical to the worm as possible. Use slightly larger center distance for hobbing.	1. Optimize contact prior to break-in
2. Make face-width a maximum of 50 percent of worm diameter	2. Avoid high-contact load on outer edges of gear teeth
3. Avoid low pressure angles on low-tooth-count gears	3. Avoid under cutting
4. Total tooth count (worm + gear) should be a minimum of 40	4. Avoid geometric interference
5. Avoid low speeds and stall	5. Low speed promotes severe boundary lubrication
6. Grease lube may require special techniques to maintain performance	6. Oil film benefits from replenishment such as in oil bath
7. Use fine surface finishes	7. Improves lube and wear
8. Set the gearset up so that initial contact pattern is on the leaving side of the gear	8. Provide oil reservoir on the entering side. Pattern will grow to cover entire width over life
9. Break in gradually with light loads and abundant lubrication	9. Break-in greatly increases life

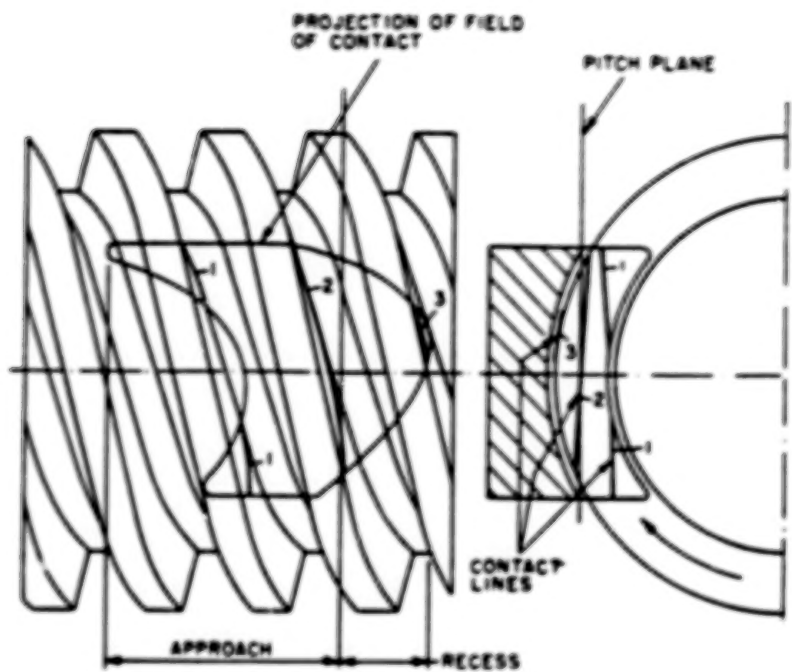


Figure 1. Tooth contact lines.

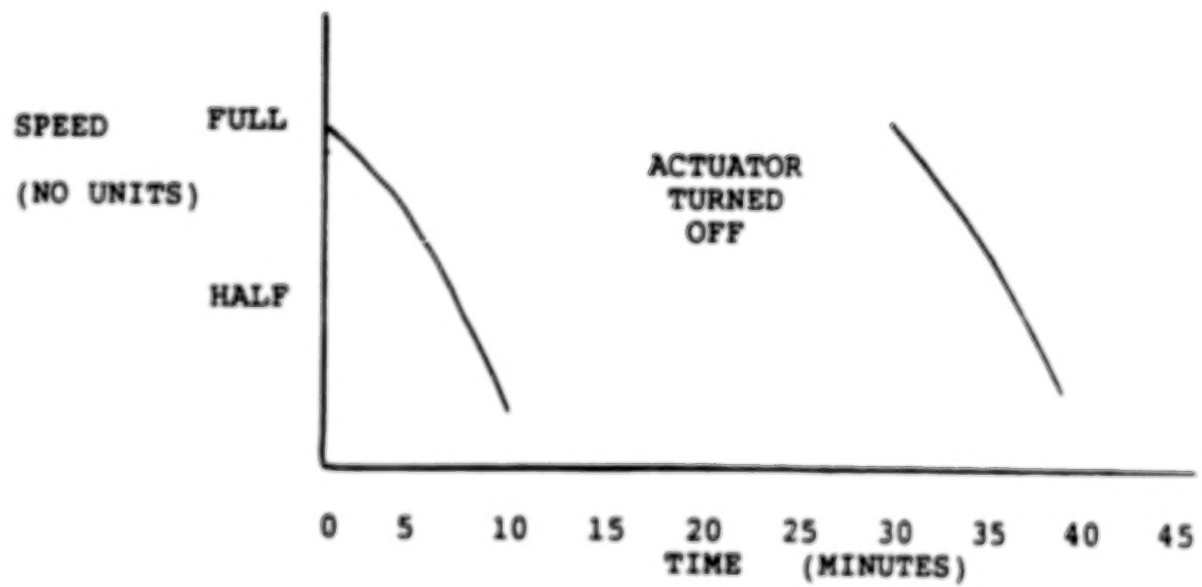


Figure 2. NRL actuation speed versus time.

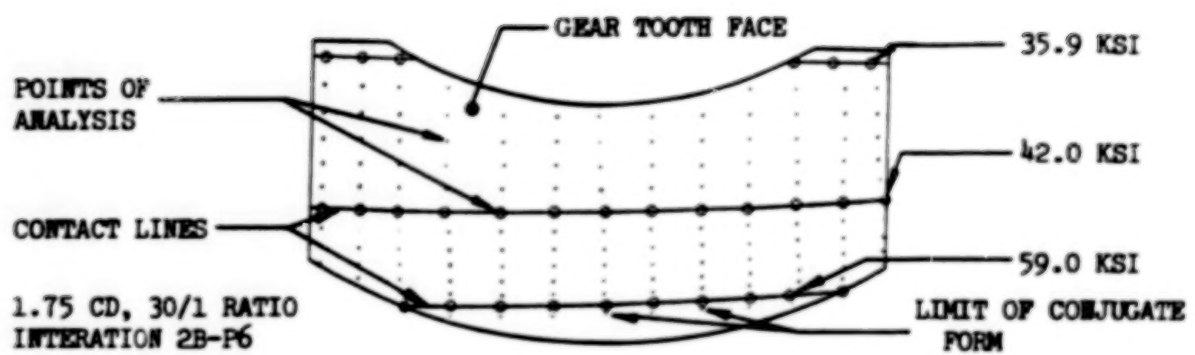


Figure 3. Contact stresses for ASTRO system.

RE AMY PAGE

208

A TWO-AXIS LASER BORESIGHT SYSTEM FOR A SHUTTLE EXPERIMENT

Joseph F. DeLorme*

ABSTRACT

A two-axis gimballed laser pointing mechanism is being developed for the Lidar In-space Technology Experiment (LITE) to be flown on the National Space Transportation System (NSTS) Space Shuttle in February 1993. This paper will describe the design requirements and goals, the configuration, analysis, and testing plans for this highly stable, high-resolution, high-energy laser pointing device.

INTRODUCTION AND BACKGROUND

There are two main objectives of LITE, the first being to evaluate a light detection and ranging (LIDAR) system's operation in space. The second objective is to obtain measurements of planetary boundary layer and cloud top heights, tropospheric and stratospheric aerosols, and atmospheric temperature and density using the LIDAR technique. LITE (see Fig. 1) consists of an Nd:YAG Laser Transmitter Module emitting a 10-Hz pulsed beam at three wavelengths (1064 nm, 532 nm, and 355 nm), a Telescope-Receiver, Instrument Electronics, and a Boresight System. All LITE components are mounted on an aluminum orthogrid platform structure that is carried on a standard Spacelab 3-m pallet.

As the transmitted laser pulses propagate through the atmosphere, a portion of the beam will be directly backscattered and collected by the Telescope-Receiver. The Telescope-Receiver consists of a 1-m telescope and an aft optics assembly containing the necessary lenses, filters, and detectors needed to measure the intensity of the backscattered pulses. The Boresight System turns the transmitted beam 90 deg toward Earth and maintains its colinearity with the Telescope-Receiver. The Boresight System (see Fig. 2) is a closed-loop control system that utilizes a quadrant photomultiplier detector located in the aft optics to monitor the position of the return beam. If the returning beam pulses are not colinear with the telescope axis, the quadrant detector generates positional error signals to the Boresight Electronics. The Electronics then command the Boresight Assembly to redirect the outgoing beam pulses to null the error signals and thus align the experiment. Figure 3 shows a computer-generated model of this Boresight Assembly, which is a two-axis laser pointing mechanism and is the subject of this paper.

*NASA Langley Research Center, Hampton, Virginia.

DESIGN REQUIREMENTS AND GOALS

The Boresight System is required to maintain colinearity between the transmitted laser beam and the Telescope-Receiver axis to within 50 microradians. This is accomplished through a closed-loop system that steers the outgoing beam. The system must be able to search for and lock in on a return signal anywhere within the telescope field of view. The system is activated only when it is desired to check or adjust the boresight and does not continuously adjust boresight setting during lidar operations; therefore, the system is required to maintain alignment in a passive, unpowered mode. The mechanism must have a dynamic adjustment range of ± 1.0 deg and must be able to efficiently redirect all three wavelengths of the Laser Transmitter Module 90 deg toward Earth. The mechanism must also have the capability of being driven back to its initial on-orbit position at any time during the mission.

Some additional design goals exist for the Boresight Assembly. One goal is a first mode vibrational natural frequency above 35 Hz to avoid the main launch excitation frequencies. The minimizing of thermal distortions that could affect pointing accuracy and stability and the protection of the reflecting surface from contamination are two other design goals.

CONFIGURATION DESCRIPTION

A cross-sectional layout of the Boresight Assembly is shown in Figure 4. It utilizes a stepping motor and harmonic drive gear reduction to produce a 1.543 arcsec per step angular positioning resolution in each axis. This translates to a 14.96 microradian pointing resolution of the beam, well within the 50 microradian requirement. The unit is constrained using mechanical limit stops to a maximum travel of ± 0.5 deg in each axis, which, due to the 90-deg deflection, translates to the required ± 1.0 -deg dynamic adjustment range of the outgoing beam. The two motors are space-flight qualified samarium-cobalt permanent magnet, brushless, stepping motors with integrally-mounted, high-capacity, spur gearheads that rotate 0.0857 deg/step. Each motor is connected to a harmonic drive gear reducer via a zero backlash flexible coupling, the design of which will be described later.

The harmonic drive consists of an elliptical wave generator inside an externally-toothed flexspline which is, in turn, mounted inside an internally-toothed circular spline with two more teeth than the flexspline. Figure 5 illustrates the operating principle of the harmonic drive. For every full rotation of the wave generator (driven by the stepping motor), the flexspline rotates by two teeth. Thus, for the 400-toothed flexspline used in this application, a 200:1 gear reduction is achieved. This converts the 0.0857 deg/step rotation of the stepping motor to a resulting 0.000429 deg/step or 1.54 arcsec/step output. Also, a preload is created by the elliptical wave generator which results in a purely radial engagement of the teeth of the flexspline and circular spline. This allows the harmonic drive to operate with essentially zero backlash. Reference 1 gives a much more detailed description of the functioning of the harmonic drive.

Flexural pivots are used in each axis instead of bearings due to the high rotational stiffness and small total angular travel required. The two 1-inch diameter cantilever-type flexural pivots need no lubrication; therefore, they are ideally suited to a space environment where bearing lubrication is often a problem. Each pivot acts as a torsional spring with a spring rate of 0.0864 kg-m/deg (120 in.-oz/deg). This requires 0.0432 kg-m (60 in.-oz) of motor torque to drive each pivot to its maximum desired deflection of 0.5 deg. Each stepping motor has a driving torque of 0.0173 kg-m (24 in.-oz) and an unpowered detent torque (due to the permanent magnet) of 0.0504 kg-m (70 in.-oz), which, with the 200:1 gear reduction of the harmonic drive, become 3.456 kg-m (4800 in.-oz) and 10.081 kg-m (14000 in.-oz) respectively. Thus, at the 0.5 deg maximum flexpivot displacement, the motor is loaded at 0.0864/3.456 or 1.25 percent of its rated maximum torque and 0.43 percent of its detent torque. The remaining 10.038 kg-m (13940 in.-oz) of detent torque causes the Boresight Assembly to be very rotationally stiff, thereby satisfying the requirement of being able to maintain alignment in a passive, unpowered condition. Reference 2 gives more detail on the functioning of the flexural pivot.

A modular incremental encoder is employed to measure the angular output position of each axis. An encoder is used, rather than a Rotary Variable Differential Transformer (RVDT) on the motor shaft or by the counting of motor steps, because it directly measures the actual rotation of the output shaft. It gives positive feedback that the system has responded to a given command and that the reflecting surface has been moved. It also eliminates the possibility of missed motor steps or other errors in shaft coupling between the motor and the actual output causing an incorrect angular position reading. The encoder enables the system to satisfy the requirement of being able to be driven back to its initial on-orbit position. The encoder operates by shining light through a transparent disk with lines scribed radially on it, into a detector. The disk is mounted to the output shaft of the harmonic drive and as it rotates, the lines pass through the light creating a square wave pattern at the detector which is converted by the encoder electronics into an angular position. The angular resolution is limited by the number of lines that can be scribed on the disk and the amount of signal interpolation that can be achieved by the electronics. The Boresight Assembly uses a 4500 line disk and 40x signal interpolation to give a 360 deg/(4500x40) or 0.002 deg resolution of the encoder. This is probably the best resolution that can be hoped for with the existing encoder technology and a four-inch diameter disk envelope.

A 70-mm right angle prism is used as the reflecting surface. It is preferred over a mirror since the total internal reflection of the prism is the most efficient way to transmit all three LITE wavelengths. It can transmit the 0.15 J/pulse at 355 nm, 0.40 J/pulse at 532 nm, and 0.20 J/pulse at 1064 nm emitted by the Laser Transmitter simultaneously, with over 99-percent efficiency. In contrast, a coated aluminum mirror can have an efficiency as low as 87 percent which can lead to localized heating of the mirror due to absorption. This could cause the mirror to warp and also potentially damage the reflective surface. The front and top faces of the prism will be canted by 2 deg to prevent any reflections off the prism faces

from going back into the Laser Transmitter and possibly quenching the laser rod.

The Boresight Assembly is enclosed by a housing (see Fig. 6) to protect the prism from contamination. The housing is connected to the Laser Transmitter Module via a bellows which provides a light-tight, contamination-proof seal, yet permits relative motion of the structures during the launch vibration environment. The laser beam pulses leave the housing through an optical window that has a motorized, movable cover to protect it from contamination. The center of the cover will be made of an optical material to allow the experiment to obtain some data in the event of a stuck cover. The housing will be covered with MultiLayer Insulation (MLI) thermal blankets to minimize the temperature variations that could affect pointing accuracy during LIDAR operations. This housing enables the system to achieve the second and third design goals of minimizing thermal distortions and preventing reflective surface contamination.

As mentioned previously, zero backlash flexcoupling is used to connect each motor shaft to each harmonic drive wave generator. The flexcoupling (see Fig. 8) is a hollow tube within a hollow tube that acts like an axially stiff bellows in that it will allow a small degree of shaft misalignment and radial runout, yet transmits torque with zero windup or backlash and axially locates the wave generator within the flexspline. This flexcoupling combines with the zero backlash harmonic drive and very low backlash stepping motor to maximize stepping accuracy and repeatability while eliminating any possible hysteresis effects. The flexcoupling is machined entirely from a block of 6061-T6 aluminum, and thus the existing inner tube dimensions are driven by current machining capabilities as well as the required axial and torque loading. The flexcoupling stiffness, expressed by the amount of radial runout allowed, R, and the corresponding load on the motor shaft, F, is a function of the tube geometry and material. There is a linear relationship between F and R, which, for the existing configuration is, $F = R \times 3308 \text{ N/cm}$. Thus, for an expected 0.000254 cm (0.0001") runout, the shaft load would be 0.840 N (0.189 lb), which is easily withstood by the motor.

ANALYSIS

A Finite Element Model (FEM) has been created (see Fig. 7) and used to determine system vibrational modes and natural frequencies, as well as stress loading and displacements during shuttle launch and landing load conditions. The vibration results (see Table 1) indicate a first mode natural frequency at 45.7 Hz and is a rocking motion of the upper housing on the lower output shaft. This satisfies the remaining design goal of having a first mode natural frequency greater than 35 Hz. The highest stresses (984.2 kg/cm^2 (14000 psi) occur in the lower output shaft and are well below the 2320 kg/cm^2 (33000 psi) cutoff for a positive margin of safety for the 7075-T73 aluminum shaft material. A detailed stress analysis of the Boresight Assembly has been conducted to confirm these results.

TESTING PLANS

The Boresight Assembly has been fabricated and is being assembled. Upon completion, the system will undergo tests to determine and verify the predicted resolution, accuracy, response time, and search and reset routines. The motor for the housing output window cover will also be functionally tested to verify its performance. A vibrational survey will then be conducted to verify the FEM predicted modes. A rotational stiffness test will be performed to verify the system's ability to passively maintain alignment. A thermal/vacuum test will be run to verify the system's ability to withstand the space environment. Following these tests, the unit will be integrated into the LITE instrument and undergo full-up instrument testing.

CONCLUSION

At this stage in the development of the LITE Boresight Assembly, it appears that all of the existing design requirements will be met and proposed design goals will be achieved. System testing will be utilized in combination with past, present, and future analyses to fully prove the design.

There are many possible future applications for this highly stable, high-resolution, high-energy laser pointing system including a possible follow-on to LITE called the Tropical Atmospheric Lidar Observing System (TALOS), an instrument that is proposed to be permanently mounted on the Space Station Freedom.

REFERENCES

1. Carlson, J. H.: Harmonic Drives for Servomechanisms. Machine Design, Penton/IPC, Inc., Cleveland, OH, January 10, 1985.
2. Seelig, F. A.: Effectively Using Flexural Pivots. ASME Publications, United Engineering Center, New York, NY, February, 1970.

Table 1. FEM predicted natural frequencies (lowest 4)

<u>Mode</u>	<u>Frequency</u>	<u>Mode Shape</u>
1	45.7 Hz	Torsion of lower shaft
2	66.6 Hz	Vertical motion of lower shaft
3	93.1 Hz	Vertical motion of upper shaft
4	113.3 Hz	Front-back motion of upper shaft

**BLANK
PAGE**

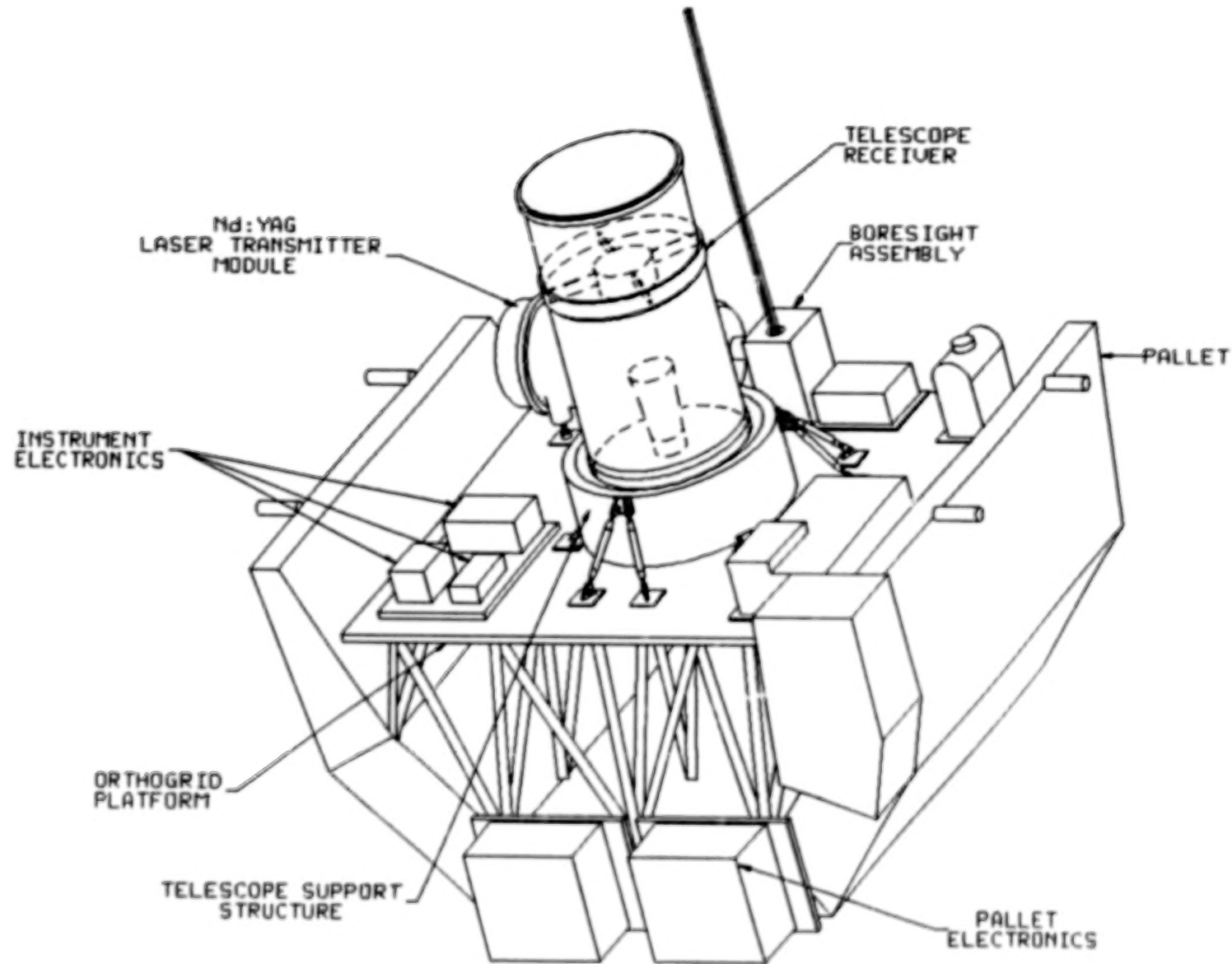


Figure 1. Lidar In-space Technology Experiment (LITE).

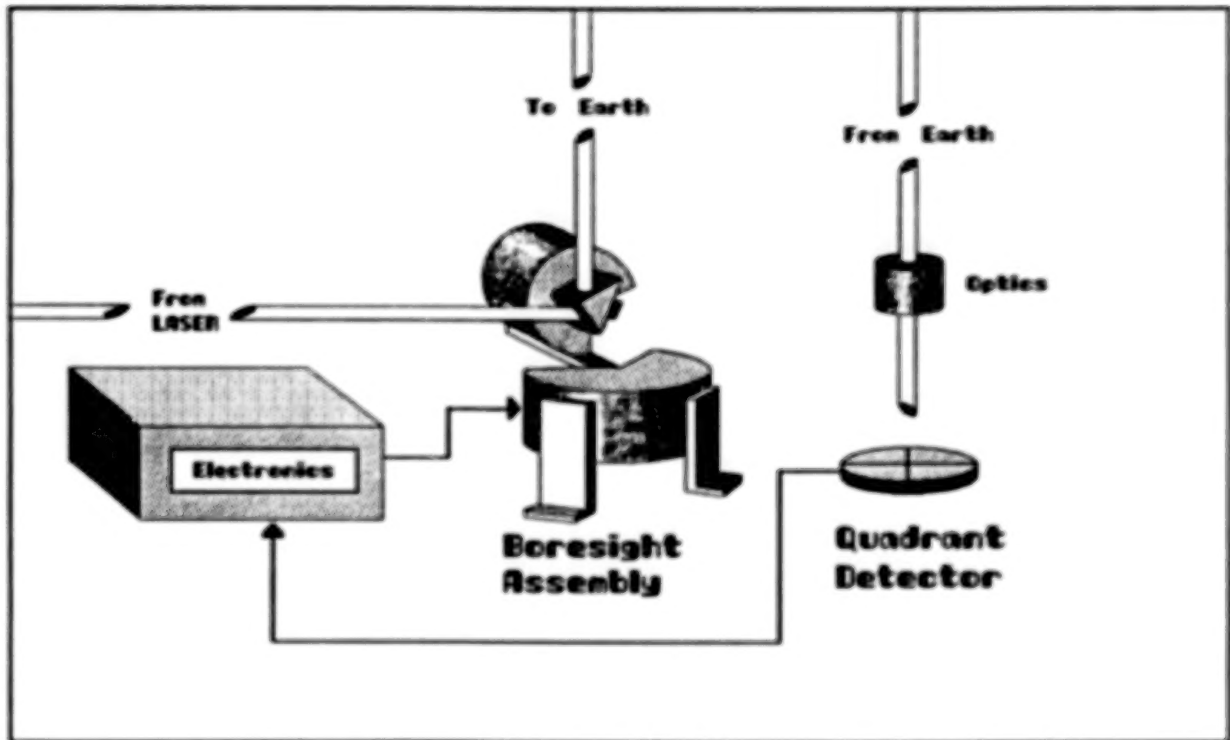


Figure 2. LITE boresight system.

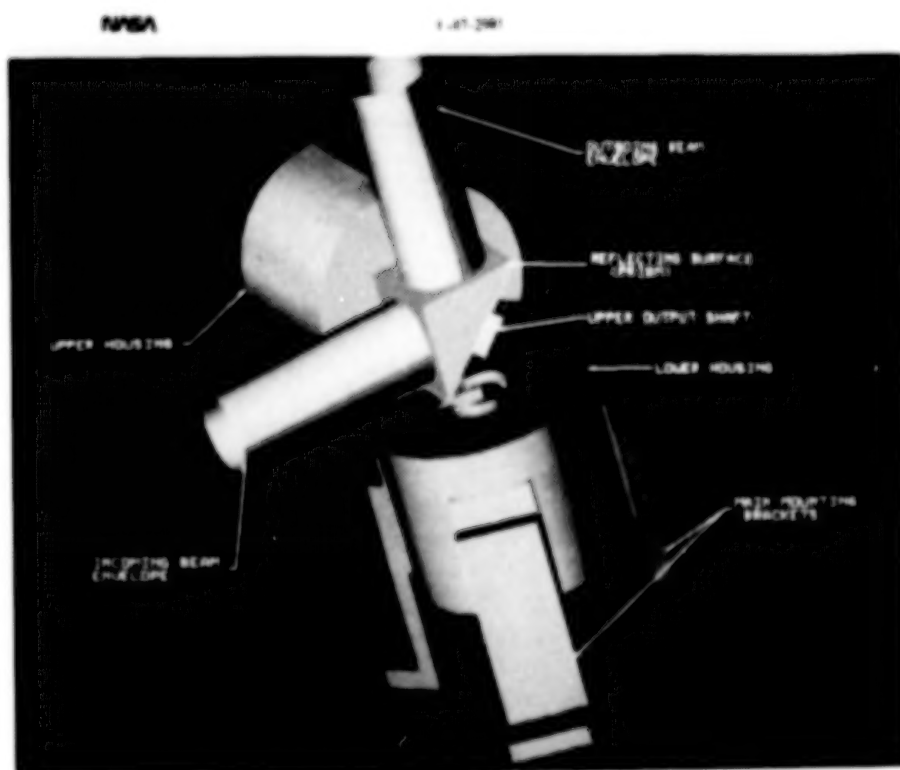


Figure 3. LITE boresight assembly model.

**BLANK
PAGE**

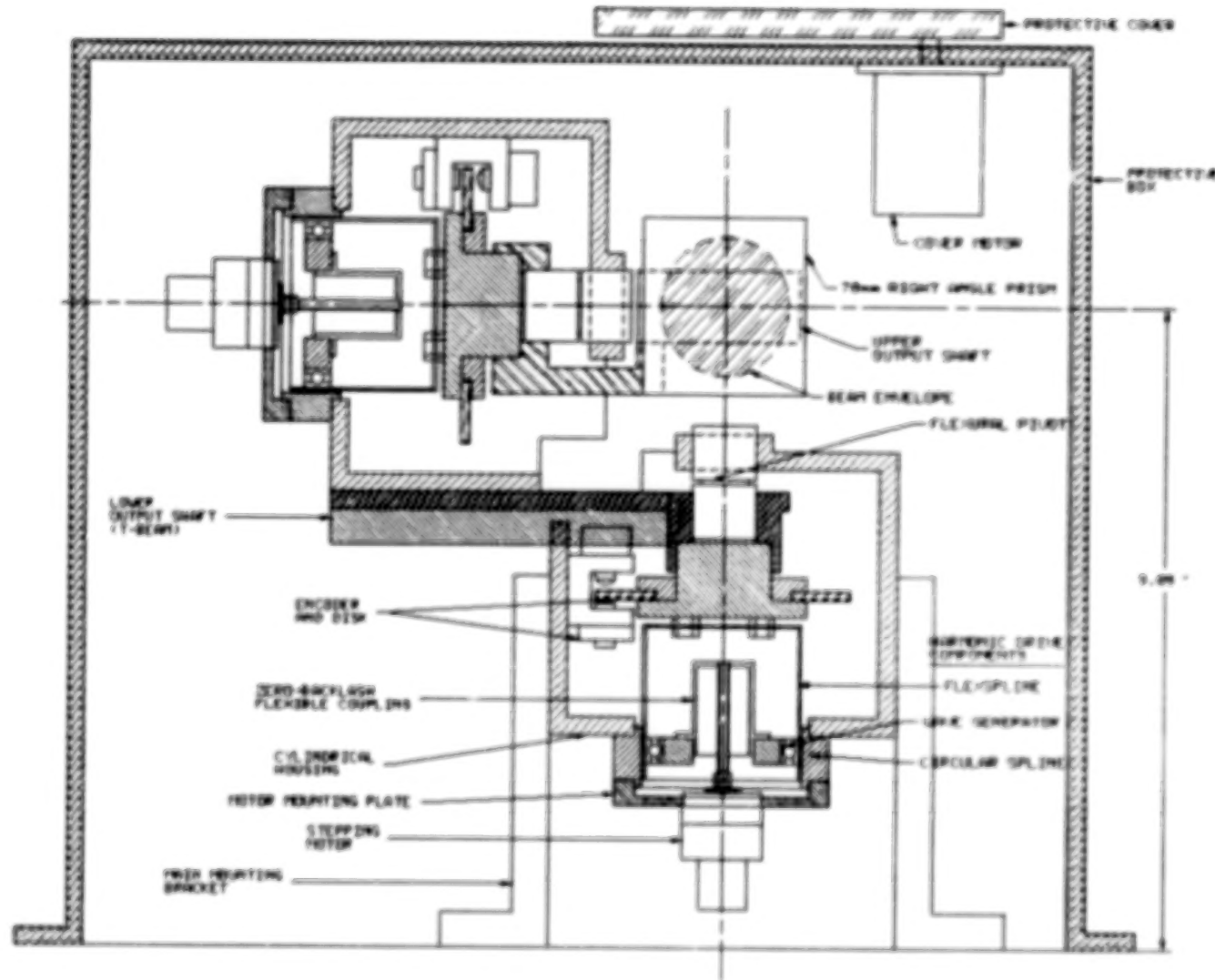


Figure 4. LITE boresight assembly cross-sectional layout.

**For every 180° rotation of the wave generator,
flexpline rotation lags by one tooth**

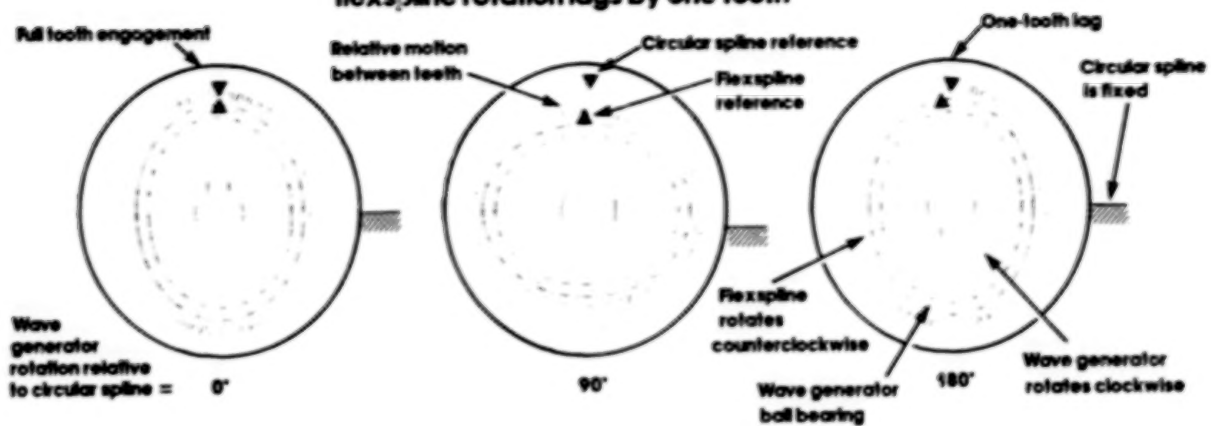


Figure 5. Harmonic drive operating principle.

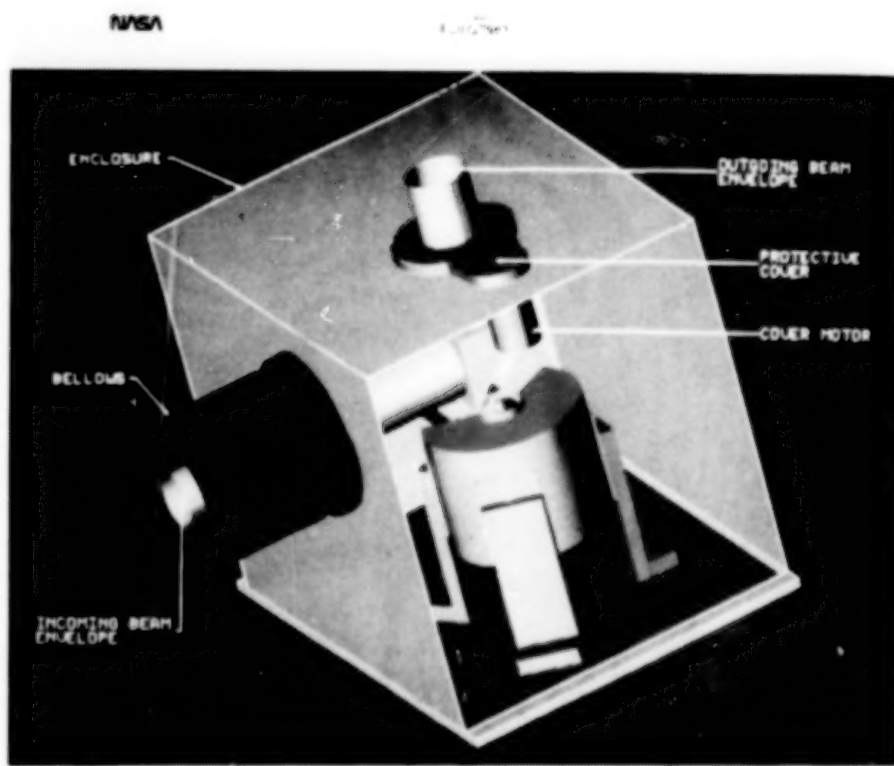


Figure 6. LITE boresight housing model.

**BLANK
PAGE**

318

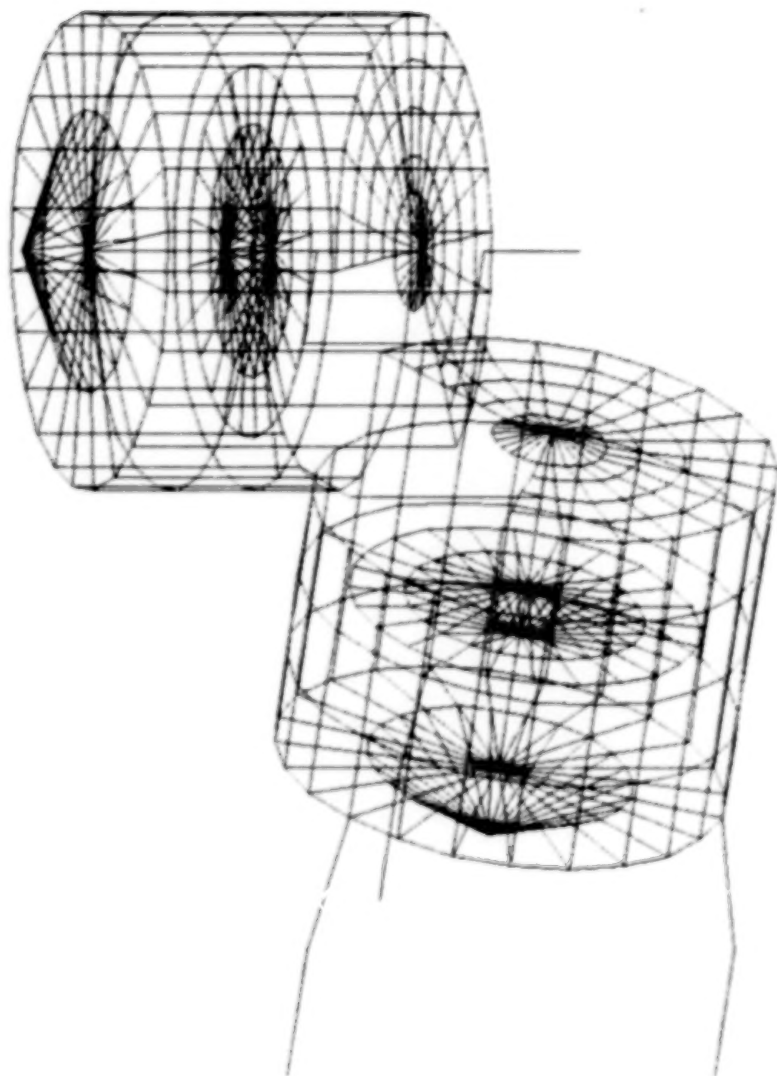


Figure 7. LITE boresight assembly
finite element model.

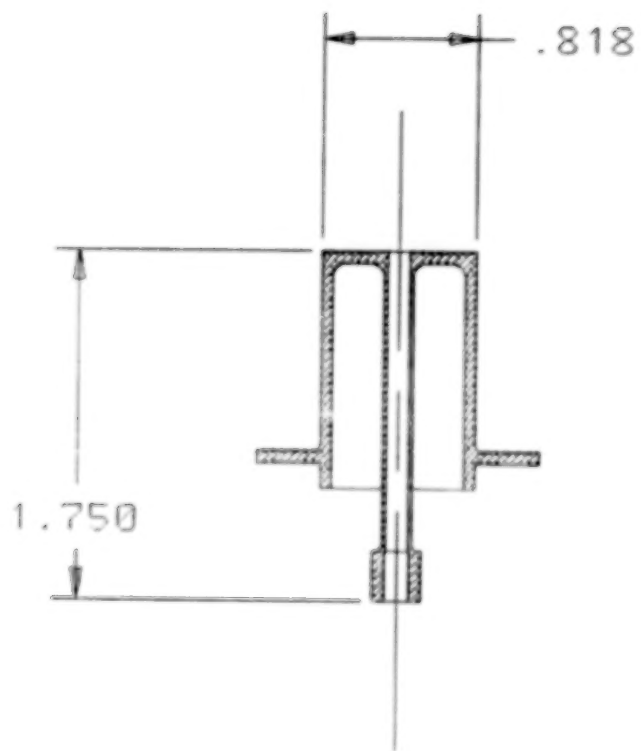


Figure 6. Flexcoupling cross-section.
318

THE IN-VACUO TORQUE PERFORMANCE OF DRY-LUBRICATED BALL BEARINGS
AT CRYOGENIC TEMPERATURES

S. G. Gould* and E. W. Roberts*

ABSTRACT

The performance of dry-lubricated, angular contact ball bearings in vacuum at a temperature of 20 K has been investigated, and is compared with the in-vacuo performance at room temperature. Bearings were lubricated using dry-lubrication techniques which have previously been established for space applications involving operation at or near room temperature. Comparative tests were undertaken using three lubricants, namely molybdenum disulphide, lead, and PTFE. It was observed that the mean bearing torque and torque noise of bearings lubricated with either PTFE or molybdenum disulphide increases with cryogenic cooling (down to 20 K). In contrast, bearings fitted with lead-containing cages (ball retainers) and lubricated with ion-plated lead films show no deterioration, in that torque levels remain unaffected on decreasing the temperature from 300 K to 20 K.

INTRODUCTION

The development of cryogenically cooled spacecraft mechanisms has created a requirement for efficient lubrication in vacuum at very low temperatures. Only solid lubrication is practicable under these conditions as oils and greases solidify at temperatures well above the cryogenic range, and the viscosities of cryogenic fluids are too low to generate sufficient load carrying capacity [1]. However, at present there exists a lack of basic tribological data upon which cryo-mechanism designers can base a reasoned choice of lubricant. Over the next few years, several space missions are planned which depend on instruments which require cryogenic cooling. These instruments include infrared detectors, superconducting devices, and a variety of "telescopes" - infrared, X-ray, gamma-ray, and high energy. Infrared detectors are of particular importance in both astronomy and Earth applications instruments. Future missions include the Infrared Space Observatory (ISO), the Far Infrared Space Telescope (FIRST), and the Upper Atmosphere Research Satellite (UARS).

Depending on their particular application, many low temperature devices contain moving mechanical parts in which pure sliding or rolling-with-sliding contacts occur (as in screw threads and ball bearings respectively). These components must be lubricated to ensure their proper operation. While it is known that molybdenum disulphide (MoS_2), lead, and polytetrafluoroethylene

*European Space Tribology Laboratory, UKAEA, Risley, Warrington, U.K.

(PTFE) are effective lubricants under vacuum at or near room temperature, their frictional properties in vacuo at very low temperatures have been little studied.

The research described in this report was carried out in order to assess the performance at cryogenic temperatures of the three main types of solid lubricant, with a view to applying them to cryogenically-cooled spacecraft instruments [2,3]. Mechanisms in these instruments typically operate under light loads at rotation rates on the order of 1 rpm per 10^4 rotations. This research is believed to be the first systematic investigation of the performance of lubricants for ball bearings operating in vacuum at temperatures below 20 K.

LUBRICANTS TESTED

There are three classes of solid lubricant: soft metals, lamellar solids, and polymers. The most commonly employed space lubricants of each of these classes are lead, MoS_2 , and PTFE respectively. Typical "torque bands" for 20 mm bore angular-contact ball bearings lubricated with each of these lubricants are shown in Figure 1 [4]. These values represent room temperature torque measurements made on bearing pairs, axially loaded to 40 N and rotated at speeds of up to 200 rpm in high vacuum. Torque values are presented in terms of bands because, in addition to the torque noise, the performance of similarly lubricated ball bearings is observed to vary from component to component.

Each of these lubricants has been tested in the same size bearings operating in vacuum at temperatures below 20 K. The methods used to apply each lubricant are now discussed individually.

PTFE (Duroid)

The PTFE lubricant film was applied by using a self-lubricating cage constructed from a PTFE/chopped glass-fiber/ MoS_2 composite (trade name Duroid). On rubbing against bearing surfaces, this cage produces, and replenishes, a thin "transfer film" of PTFE. Those surfaces which are not in direct contact with the cage are lubricated by means of film transfer via the balls. Thus, in the first instance the bearing is effectively unlubricated and a "run-in" is required before an effective transfer film can be established.

Lead

Lead films of approximately 0.5 microns thick were deposited onto the inner and outer raceways of test ball bearings by the technique of ion plating. The balls were not coated. Each bearing was fitted with a cage manufactured from lead-impregnated bronze, the lead within the cage serving to supplement the lead film lubricant applied to the raceways.

Figure 1 indicates that pairs of 20 mm ball bearings lubricated in this manner and subjected to an axial load of 40 N exhibit, on initial running in vacuum, torque levels of between 10 and 20×10^{-4} Nm. The torque increases to between 15 and 30×10^{-4} Nm during the running-in period and tends to remain at this level. At room temperature, such bearings have been operated for up to 10^9 revolutions in high vacuum without any serious degradation in torque behavior. The torque noise will typically be 10 to 15×10^{-4} Nm with periods of excessive noise during which peak torque values of up to 200×10^{-4} Nm are observed. The torque noise is caused by wear debris from the cage and it is common practice for bearings lubricated in this manner to be flushed with solvent following running-in to remove such debris.

Molybdenum Disulphide

Thin (1 micron) films of MoS₂ were deposited onto the inner and outer raceways of test ball bearings by the technique of magnetron sputtering. This technique leads to the formation of lubricant films which have exceptionally low friction when operated under high vacuum [5], though the actual value of friction coefficient is governed by a number of factors which include contact stress, sliding speed, vacuum pressure, and surface roughness [5,6,7].

The torque behavior and useful lifetime of ball bearings treated with sputtered MoS₂ are dependent on both the cage material and whether the balls as well as the raceways are coated with the lubricant film. It is observed that when only the raceways are lubricated, low torques and relatively short lifetimes are obtained. However, on coating both the balls and the raceways, an improvement in lifetime is gained at the expense of higher torque levels [5]. With regard to cage material, it is observed that bearings fitted with composite PTFE (Duroid) cages exhibit longer lifetimes than bearings fitted with either MoS₂-coated steel cages [5] or cages manufactured from a composite of MoS₂ and polyimide [8].

For the purposes of the present test program, MoS₂-coated bearings were used in conjunction with Duroid cages.

THE ESTL CRYOGENIC FACILITY

The cryogenic test facility consists of a cryostat which is cooled by a Philips PGH 107S Stirling cycle cryogenerator. The cryogenerator is a two-stage expansion engine which circulates helium gas at two quasi-independent stable temperatures - nominally 80 K and 20 K. Because of its attendant noise and vibration, it is installed outside the laboratory in which the cryostat is located. The cold helium gas is circulated between the cryogenerator and the cryostat by means of a vacuum insulated transfer line which contains four pipes - a "supply" and a "return" for each stage.

The cryostat consists of a high vacuum chamber 40 cm in diameter, which contains two thermally isolated copper "cryo-pots" (Fig. 2). These cryo-pots are concentrically mounted, with the inner suspended from the outer by means of three pieces of PTFE. The outer cryo-pot is supported within the vacuum

chamber by three stainless steel tubes which are welded to the wall of the vacuum chamber. Heat conduction along these tubes is reduced by including PTFE insulators in the supports. The inner cryo-pot, in which test rigs are housed, has an internal diameter of 250 mm and a depth of 225 mm. Access to the cryo-pots is by way of removable lids on both the vacuum chamber and cryo-pots.

The outer and inner cryo-pots are maintained by the cryogenerator at nominal temperatures of 80 K and 20 K respectively. Thermal contact to the individual cryo-pots is made by "peening" the appropriate supply pipe into the base of the appropriate cryo-pot. The cooling power of the "20 K" stage is 25 W below 19 K; the cooling power of the 80 K cryo-pot has not been measured.

THE EXPERIMENTAL APPARATUS

The Ball Bearing Test Apparatus

The ball bearing test apparatus is shown in position in the vacuum chamber in Figure 2. The apparatus is designed to test a pair of 20 mm bore angular contact bearings arranged in a face-to-face configuration. Details of the bearings are given in Table 1.

The apparatus consists of three main parts: the bearing housing, the drive shaft, and the torque transducer. The housing in which the bearings were located was clamped to the base of the 20 K cryo-pot and cooled conductively (Fig. 2). To minimize differential thermal expansion, both the bearing housing and the bearing mounting (located at the base of the drive shaft) were constructed from low-carbon mild steel. A 38 N preload was applied by means of a stainless steel "deadweight" which rested on the outer raceway of the top bearing. To improve the thermal contact between the preload mass and the cryo-pot, four pieces of copper braid were strapped between the bearing housing and the preload mass. The lower part of the drive shaft was cooled by thermal conduction along the bearing housing and through the bearings themselves.

To aid disassembly, the drive shaft consisted of two sections which were connected by a demountable universal coupling. To minimize thermal conduction down the shaft to the test bearings, the lower (cold) section of the shaft consisted of a glass-fiber-reinforced epoxy rod 6.35 mm in diameter. It was connected at its bottom end to the bearing mounting by means of a second universal coupling. The upper (warm) section consisted of a 6.35 mm diameter stainless steel tube, which was connected at its top end to the torque transducer by a third universal coupling. The shaft was driven by a motor located on top of the vacuum chamber via a ferrofluid rotary feedthrough.

One novel feature of the apparatus was the method used to measure the bearing torque; a torque transducer was mounted integrally with the drive shaft and rotated with the shaft. The transducer was conditioned electrically by means of a slip ring in conjunction with a vacuum feedthrough installed on-axis.

Two types of thermometry were used on the cryostat. The main thermometer was a cryogenic linear temperature sensor (CLTS) [9] which was mounted on the inner cryo-pot. In addition, carbon resistance thermometers were mounted in several locations, as shown in Figure 2. In particular, a carbon resistance thermometer was located at the base of the bearing drive shaft.

EXPERIMENTAL TECHNIQUE

Pairs of angular contact ball bearings were preloaded to 38 N by means of a deadweight, and run at a rotation rate of 100 rpm. The bearing torque and torque noise were measured by a torque transducer, as described above. The output of the torque transducer was recorded on a potentiometric chart recorder and measured by a programmable voltmeter.

Because the drive shaft consisted of two separate shafts which were connected by a demountable coupling, the shaft splayed out radially at rotation rates above 10 rpm and caused an increase in the torque noise. Because of this "run-out" of the drive shaft, all torque measurements described in this paper were made at a rotation rate of 0.44 rpm. It is believed that such measurements, made at reduced speed, are valid, as it is generally observed that the torque of dry-lubricated bearings is independent of rotation rate. During a measurement of torque, the bearings were rotated in both the clockwise and counterclockwise directions for five rotations, while the output of the transducer was sampled at 20 Hz by the voltmeter. Values of the mean and standard deviation of the two signals, as calculated by the voltmeter, were noted for each direction of rotation. The torque signal was also analyzed periodically on a spectrum analyzer to see if it contained a non-dc component. There was no appreciable signal at frequencies above 1 Hz.

A typical torque trace is shown in Figure 3. The mean torque and torque noise are also defined in Figure 3. It should be noted that the range-bars shown on the experimental data represent the total torque variation (that is, six standard deviations) rather than the experimental error; the experimental error is one third of these range-bars. In addition, some of the range-bars include "negative torques." This is due to the elasticity of the (epoxy) drive shaft, and does not originate from the test bearings. In practice, therefore, the range-bars overestimate the actual torque variation.

Each pair of bearings was run in vacuum at room temperature for one million revolutions; the bearing housing was then cooled to below 20 K and the bearings were run for a further two million revolutions. For both the PTFE and the lead, a second pair of bearings was then tested under the low temperature condition only, without an initial "run-in" at room temperature. A similar run for the MoS₂ is in progress.

RESULTS

PTFE (Duroid)

The torque profile of the Duroid-lubricated bearings at room temperature and at 18 K is shown in Figure 4. During the run-in, the mean torque increases from 1.2×10^{-3} Nm to a maximum of 3.3×10^{-3} Nm. It then decreased progressively to 5×10^{-4} Nm, and the bearings were fully run in after approximately 0.5 million rotations. (Note that this torque is exceptionally low for bearings lubricated in this manner, and is below the lowest levels expected from Figure 1.) The torque remained at this level for the remainder of the room temperature measurements. The torque noise after run-in was typically 5×10^{-4} Nm. (The torque noise is taken to be ± 3 standard deviations, hereafter referred to as "3-sigma".) On cooldown (at one million rotations), the torque immediately increased by a factor of approximately three. It remained at this level for the next 1.5 million rotations, at which time the bearings suffered a disturbance which considerably increased both the mean torque and the torque noise. During the final 0.5 million rotations, the mean torque was typically 2.5×10^{-3} Nm with a torque noise of 1.7×10^{-3} Nm. Both bearings were in very good condition at the end of the run; the raceways were covered with a transfer film, there was no visible pitting, and the cage wear was acceptable. However, on one of the bearings a relatively large piece of Duroid was in the process of being rolled into the running track. It is likely that this caused the disturbance in the torque profile.

The torque profile of Duroid-lubricated bearings operated at 17 K without being run in at room temperature is shown in Figure 5. In a similar manner to the room temperature results, the data contain a maximum which probably corresponds to a low temperature run-in. During this run-in, a larger number of rotations was required to lay down a transfer film, and the mean torque was high and noisy while the film was being transferred - typically 4×10^{-3} Nm with a 3-sigma noise of 2.5×10^{-3} Nm. However, after the run-in was achieved, the performance was the same as for the bearings which were run in at room temperature. At the end of the run, the condition of both bearings was consistent with that expected for equivalent bearings run in vacuum at room temperature; the raceways were covered with a transfer film, there was no visible pitting, and the cage wear was acceptable.

Lead

The torque profile of the lead-lubricated bearings at room temperature and at 18 K is shown in Figure 6. The torque performance of lead is much noisier than that of Duroid. However, both the mean torque and the torque noise do not change on cooldown, and the torque performance at 18 K remains the same as that at room temperature. At the end of the run, the condition of both bearings was consistent with that expected for equivalent bearings run in vacuum at room temperature; the raceways were covered with a lead/bronze film, there was no visible pitting, and the cage wear was acceptable.

The torque profile of lead-lubricated bearings operated at 17 K without a room temperature run-in is shown in Figure 7. These results are consistent with those described above, and might even indicate that a run-in at room temperature is detrimental since the torque noise observed here is lower. These bearings were also in good condition at the end of the run.

MoS₂/Duroid

The torque profile of the MoS₂/Duroid-lubricated bearings at room temperature and at 17 K is shown in Figure 8. The room temperature behavior was consistent with that expected from Figure 1, the mean torque being typically 4×10^{-4} Nm with a 3-sigma noise of 8×10^{-4} Nm. Immediately after cooldown, the torque was unchanged. However, after 7×10^4 "cold" rotations the mean torque had increased to 5.6×10^{-3} Nm and the noise had increased to 2.7×10^{-3} Nm. Thereafter, the torque profile was consistent with that obtained for Duroid-lubricated bearings which were not run-in prior to cooldown.

The post-run inspection of the bearings revealed that the MoS₂ film had been removed from the running tracks of both bearings. In addition, a PTFE transfer film had been established, and the condition of the bearings was consistent with that obtained for Duroid-lubricated bearings. It is therefore concluded that the MoS₂ film had poor endurance and ceased to contribute to the lubrication of the bearings after some 7×10^4 rotations. However, the very first "cold" measurement indicates that the lubricity of MoS₂ is unchanged at 17 K, so it should be possible to use MoS₂ films at cryogenic temperatures, provided that only a few thousand revolutions are required.

DISCUSSION

Duroid

Bearings lubricated by means of a PTFE-based, self-lubricating cage exhibited higher torque and torque noise during operation at cryogenic temperatures. We believe that this behavior can be attributed to the manner in which the shear strength of PTFE increases with decreasing temperature. While the shear strength of PTFE is not known to the authors, it is reported [10] that its value at 200 K is twice that at 300 K. As has been discussed elsewhere [11], the torque is expected to increase proportionately with shear strength. The observed increases in torque are therefore not unexpected.

Lead Film/Lead-Bronze Cage

Our observations on bearings lubricated by lead indicate that their torque behavior is the same as that at 300 K. Furthermore, the evidence indicates that a running-in period at room temperature may not be beneficial to subsequent operation at cryogenic temperatures.

The temperature independence of the torque and torque noise is unexpected, as the shear strength of lead increases by a factor of four on

cooling to 20 K [12]. At present we cannot explain these observations, but tentatively propose the following as possible causes:

- a) Frictional heat generated in the region of the contact area in which micro-slip occurs is sufficient to increase the local temperature of the lead to a level at which its shear strength is lower than expected.
- b) The temperature dependence of the shear strength of thin lead films may differ from that of bulk lead.
- c) Adsorption of gas molecules within the vacuum environment gives rise to the formation of surface monolayers whose presence at the interface reduce contact adhesion, thereby reducing friction.

Molybdenum Disulphide/Duroid

The torque behavior may be summarized as follows. On reducing the temperature from 300 K to 20 K, the torque and torque noise are initially unchanged. However, the torque gradually increases, and after approximately 7×10^4 revolutions, the torque behavior becomes characteristic of that of bearings lubricated solely by means of a Duroid cage. In addition, our evidence suggests that the MoS₂ film is worn away. We therefore conclude that the endurance of the sputtered MoS₂ films is reduced at a temperature of 20 K.

Our interpretation of this behavior is as follows. At room temperature, a very low torque is developed commensurate with the low friction afforded in vacuum by sputtered MoS₂. At 20 K the torque rises, indicating an increase in friction coefficient. This increase in friction could be due to the adsorption of water vapor which is present in the vacuum system, and indeed comprises the principal gaseous component therein. The effect of the adsorption of very small quantities of water on the lubricity of MoS₂ has been demonstrated previously in vacuum at room temperature [5,6], under which condition a much higher partial pressure of H₂O is required to maintain an adsorbed population. At cryogenic temperatures, water molecules once adsorbed remain adsorbed since their removal by thermal desorption is essentially precluded. In this contaminated state we would expect the friction to be increased and the film endurance to be severely reduced.

A further factor which might contribute to the removal of the MoS₂ film is differential thermal contraction between the steel substrate and the lubricant film. We are unable to calculate the magnitude of any mismatch due to differential contraction because the (average) coefficient of thermal expansivity is not known to us. Nevertheless, such effects will occur to some extent, resulting in stresses in the film which could lead to either the disintegration of the film or its detachment from the surface.

CONCLUSIONS

The following conclusions are drawn with regard to the in-vacuo torque behavior of dry-lubricated bearings:

1. While all the dry-lubricated bearings tested at 20 K survived 2 million revolutions, the best performance was obtained from bearings lubricated with thin lead films and fitted with a lead/bronze cage.
2. Bearings fitted with PTFE-composite cages showed increased torque and torque noise at 20 K. The torque performance of bearings lubricated in this manner was improved by running-in the bearings prior to cooldown.
3. Bearings lubricated with thin lead films and fitted with a lead/bronze cage showed no torque deterioration on reducing the temperature from 300 K to 20 K.
4. Bearings lubricated with sputtered MoS₂ and fitted with Duroid cages showed appreciable increases in torque and torque noise after limited operation at 20 K.

ACKNOWLEDGMENTS

The authors are pleased to acknowledge the following: The work described in this paper was financed by the European Space Agency by means of an ESTEC contract. J. A. Duvall of ESTL designed the ball-bearing test apparatus and the cryogenic facility. A. L. Garnham of ESTL conducted the post-test inspection of the bearings.

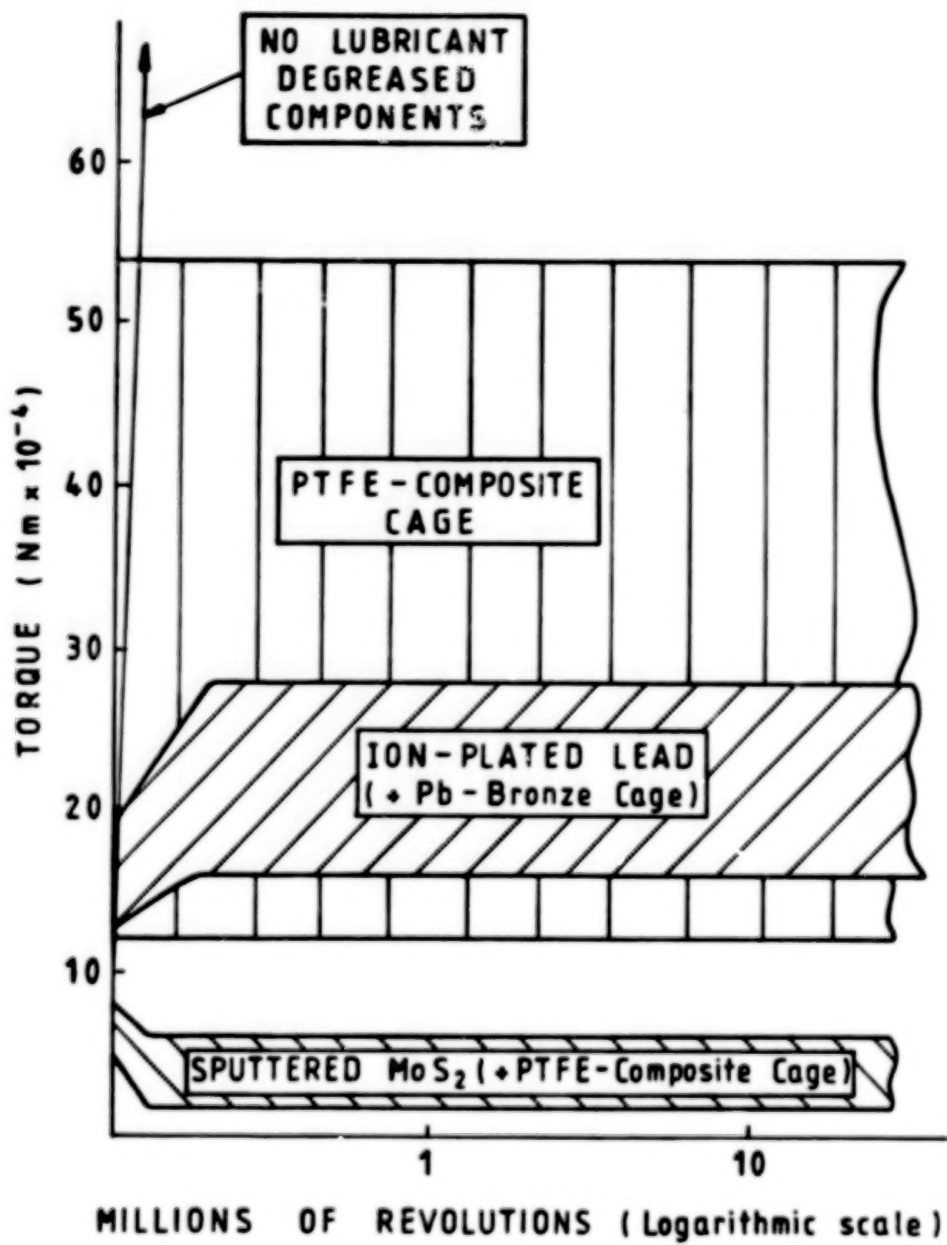
REFERENCES

1. Scibbe, H. W.: Bearings and Seals for Cryogenic Fluids. NASA TM X-52415, 1968.
2. Patrick, T. J., Sidey, R. C., and Towlson, W. A.: Cold Stepping Drive for the ISO/LWS. *Cryogenics*, Vol. 27, February 1987.
3. Kulzer, G., Lemke, D., Bauer, H., Bellemann, H., and Neumann, G.: Cryogenic Ratchet Wheel Drive for the ISOPHOT Experiment. *Cryogenics*, Vol. 27, February 1987.
4. Roberts, E. W.: Sputtered MoS₂: An Ultra-Low-Friction Lubricant For Space. ESTL Technical Bulletin No. 6, June 1986. Northern Research Laboratories, UKAEA, Risley, Warrington, Cheshire, UK.
5. Roberts, E. W.: The Lubricating Properties of Magnetron Sputtered MoS₂. ESA (ESTL) 76, October 1987.

6. Roberts, E. W., and Price, W. B.: The In-Vacuo, Tribological Properties of "High Rate" Sputtered MoS₂ Applied to Metal and Ceramic Substrates. MRS Symposium, Fall Meeting, Boston, November/December 1988.
7. Roberts, E. W.: The Tribology of Sputtered Molybdenum Disulphide Films. Proc. Inst. Mech. Eng., Tribology - Friction, Lubrication and Wear, Fifty Years On, Vol. 1, London, July 1987, pp. 503-510.
8. Buck, V.: The Performance of Unbonded MoS₂ for Space Applications. Proc. 2nd European Space Mechanisms and Tribology Symposium, Meersburg, ESA SP-231, October 1985.
9. Telinde, J. C.: Discovery, Development, and Use of a Cryogenic Linear Temperature Sensor. McDonnell Douglas Astronautics Company, Paper 10, 2C5, April 1970.
10. Minhas, P. S., and Petruccelli, F.: A New High Performance Fluoropolymer That Can be Readily Melt-Processed. Plastic Engineering, Vol. 33(3), March 1977, pp. 60-63.
11. Roberts, E. W., Gould, S. G., Duvall, J. A., and McDonald, P.: A Test Facility for the In-Vacuo Assessment of Dry Lubricants and Small Mechanisms at Cryogenic Temperatures. Proceedings of the 3rd European Space Mechanisms and Tribology Space Symposium, Madrid, Spain, 30 September - 2 October, 1987.
12. Simon, I., McMahon, H. O., and Bowen, R. J.: Dry Metallic Friction as a Function of Temperature Between 4.2K and 600K. J. Applied Physics, Vol. 22, No. 2, February 1951.

TABLE 1. DETAILS OF THE TEST BEARINGS.

Race and ball material	AISI 52100 steel (1 percent C, 1 percent CR)
Internal diameter	20 mm
External diameter	42 mm
Width	12 mm
No. of balls	10
Ball diameter	7.14 mm (9/32 in.)
Precision	ABEC 7
Conformity	1.14



(Bearing type : ED 20 : 40 N preload)

Figure 1. Mean torque bands from repeated tests of solid lubricated ball bearing pairs in vacuum.

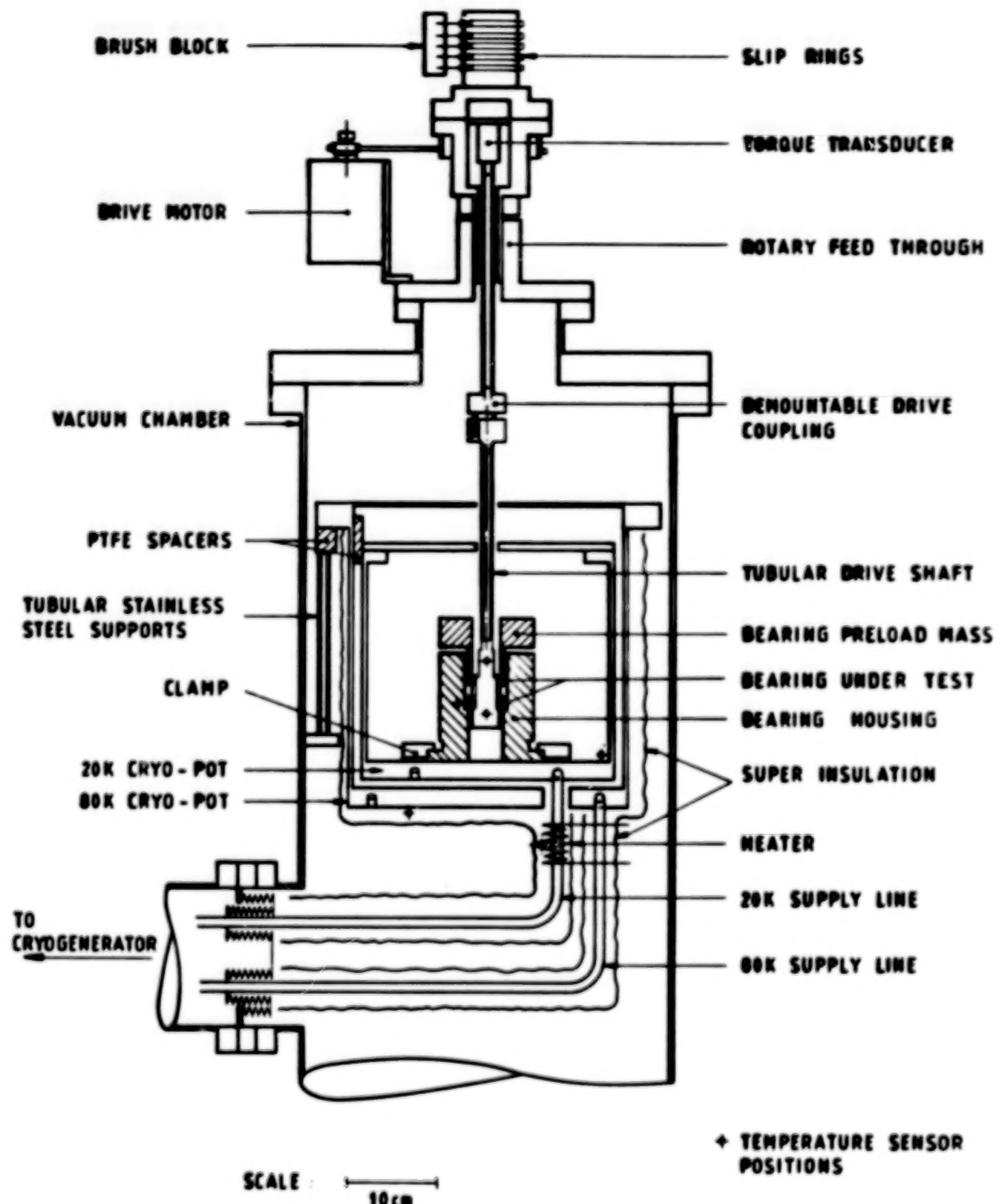


Figure 2. Schematic of the cryogenic vacuum chamber and ball bearing test apparatus.

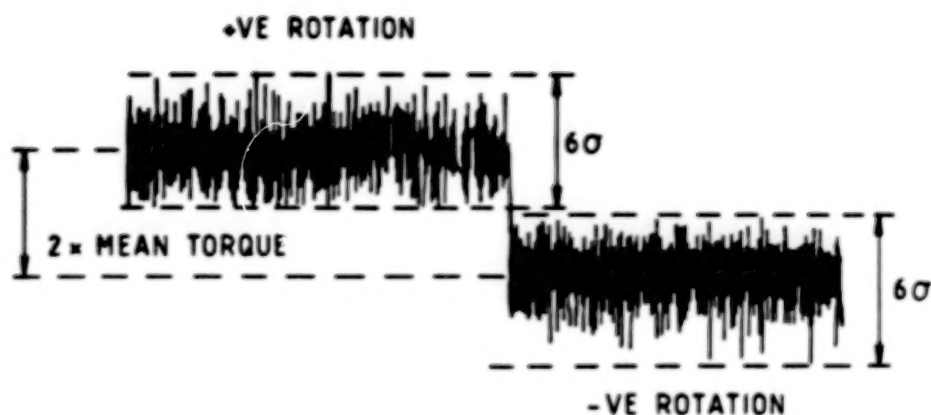


Figure 3. A typical torque trace, showing the definition of mean torque and torque noise (6σ).

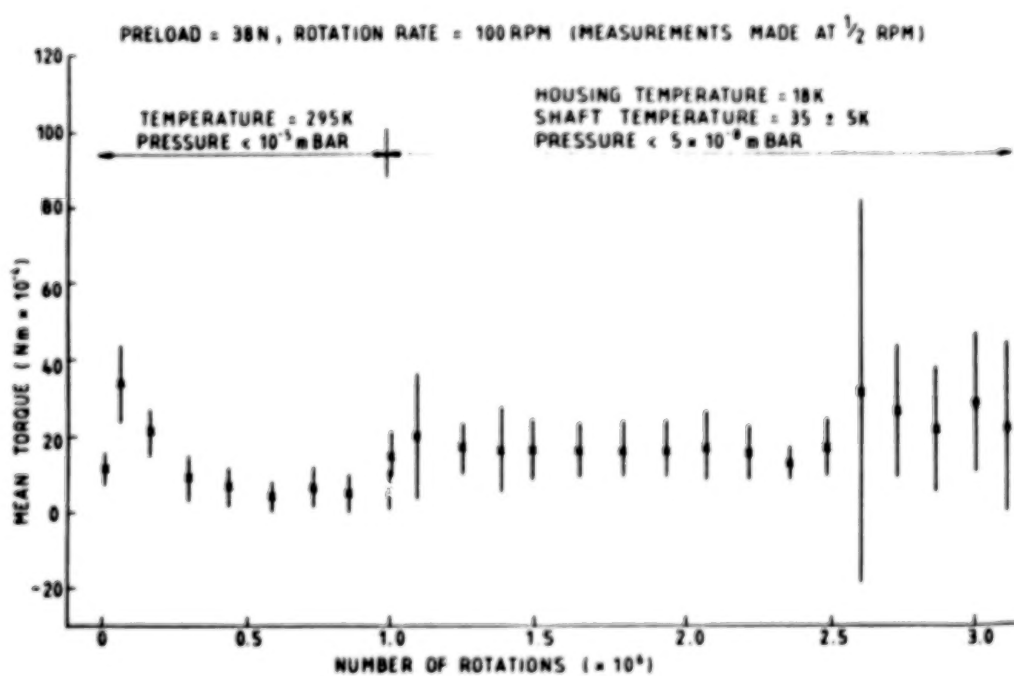


Figure 4. The torque profile of Duroid-lubricated bearings operating at 295 K and at 18 K.

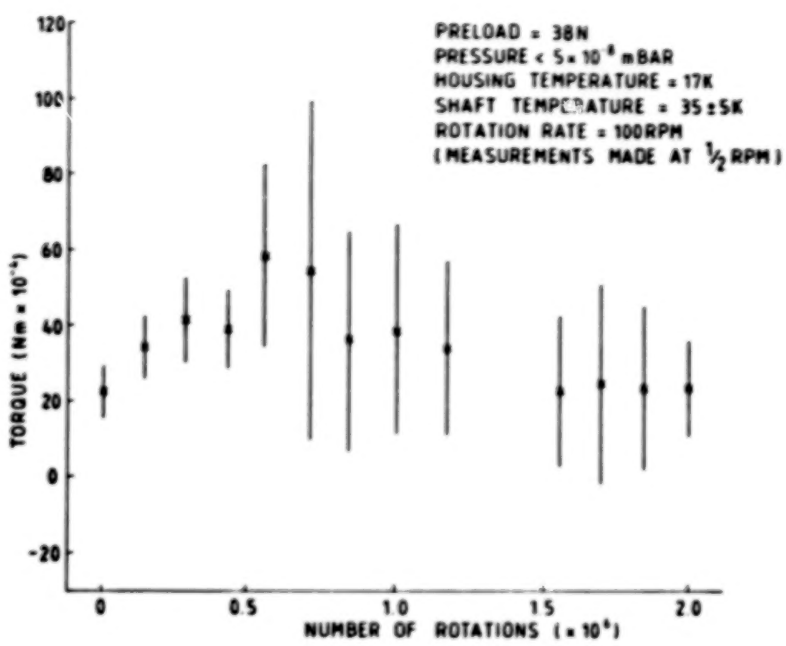


Figure 5. The torque profile of Duroid-lubricated bearings operating at 19 K.

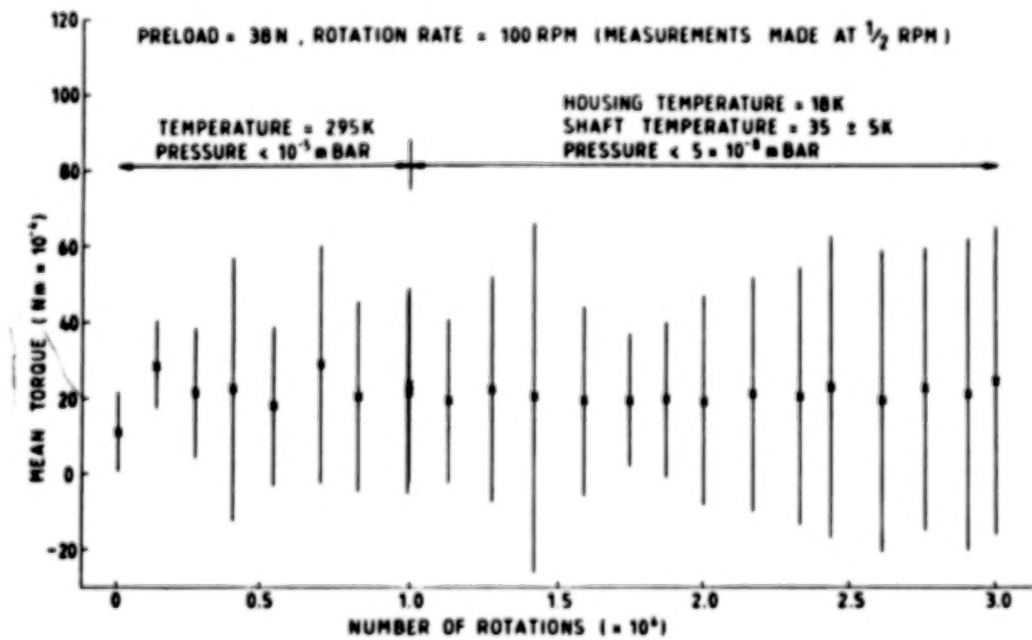


Figure 6. The torque profile of lead-lubricated bearings operating at 295 K and at 18 K.

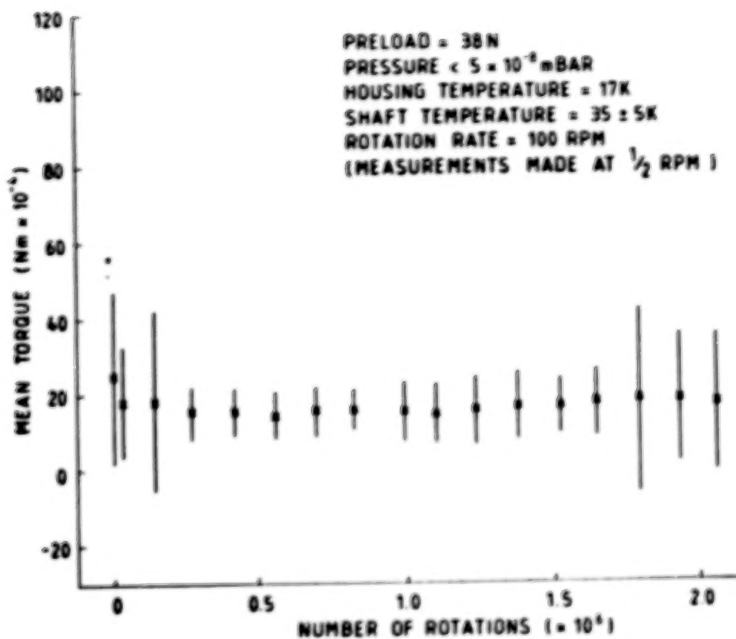


Figure 7. The torque profile of lead-lubricated bearings operating at 17 K.

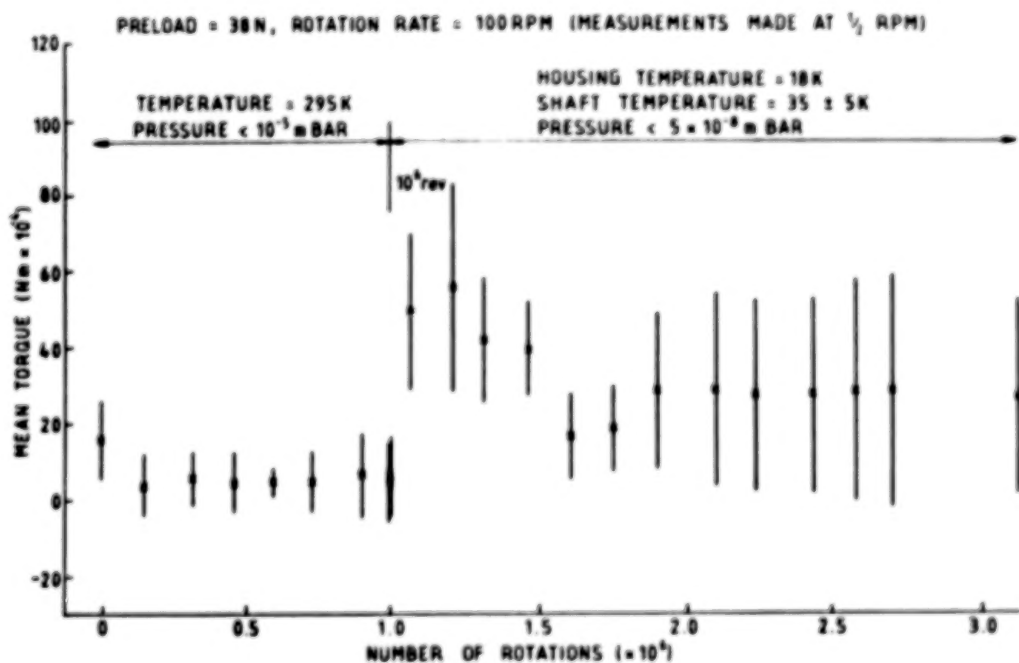


Figure 8. The torque profile of MoS₂/Duroid-lubricated bearings.

BLANK PAGE

334

APPENDIX

PANEL DISCUSSION SUMMARIES
22ND AEROSPACE MECHANISMS SYMPOSIUM
MAY 4 TO MAY 6, 1988
NASA-LANGLEY RESEARCH CENTER

As reported by Harvey H. Horiuchi, Jet Propulsion Laboratory,
California Institute of Technology, and
John F. Rogers, NASA-Langley Research Center

Based on the successful panel discussion held at the 20th and 21st Aerospace Mechanisms Symposia, the organizing committee selected three topics as outlined below for discussion at the 22nd Aerospace Mechanisms Symposium.

<u>Topics</u>	<u>Introduced by</u>
Training/Development of Mechanisms Engineers	John Stammreich
Reliability versus Redundancy versus Maintainability	Otto H. Fedor
Vacuum Tribology	Michael Todd

The discussion sessions were moderated by Mr. Ronald Mancini of the NASA-Ames Research Center. Each topic was introduced by a panelist who presented overview material and comments followed by stimulating discussion between the audience and members of the panel. Following each panelists' comments the other panelists and audience attendees were given the opportunity to respond, ask questions, and express their individual views and comments on the problems.

TRAINING/DEVELOPMENT OF MECHANISMS ENGINEERS
22nd AMS, May 5, 1988

Ronald Mancini opened the panel discussion by emphasizing the importance of an open interaction between the audience and the panel. He stated the objective of the panel discussion was to provide another forum for exchange of ideas and experiences with the emphasis on making the symposium a positive learning experience for all who attend. He then introduced the panel: John Stammreich, General Manager of Rexnord's Aerospace Mechanisms Division; Otto H. Fedor, recently retired from Lockheed Space Operations at Kennedy Space Center (KSC), and prior to this, retired from NASA-KSC where he served as Section Head for systems assurance on Apollo and Skylab programs; and Michael Todd, manager of European Space Tribology Laboratory, a founding member of the National Center for Tribology who played a key role in establishing the European Space Tribology Laboratory.

The first topic, entitled "Training/Development of Mechanisms Engineers," was introduced by John Stammreich. He indicated that as a follow-on to last year's discussion there were eight questions raised concerning this topic. Rather than trying to answer each question individually, he would try to address the issues common to all of the questions. One common theme dealt with how well young engineers understand the mechanism design process, and whether that process is still relevant today. He suggested that the mechanism design process has not changed, but that new tools are available to aid in accomplishing the tasks. One of the new design tools available today is computer-aided design, which is mainframe oriented and available with detail interactive analysis techniques. Another new tool is computer-aided drafting, which is the automation of the task requiring the largest amount of time in the design process. Also available are real-time computer simulations, modal analysis techniques, increased knowledge of material behavior, new hybrid materials, new fabrication and testing techniques, and easier access to these tools.

The next area of discussion dealt with the status of automation in mechanism design. Mr. Stammreich stated that the heavy usage of automated tools came from large companies. They were using the tools on big problems in hopes of a fast payback to offset the initial high cost of equipment and training. However, more recently the hardware price reduction and the simplicity of computer-aided design packages have led to quick acceptance by small companies and universities alike. Because of these rapid expansions in PC systems, larger companies have built compilers in order to communicate between the PC-based systems and the mainframe systems.

He also stated that he felt the low production quantities coupled with the high complexity of most aerospace mechanisms limited computer-aided manufacturing and simulations to just a few applications. He pointed out that along with the increased capabilities of these new tools there were some concerns which needed to be addressed. Early program management controls become more critical now because of the increased speed in the design process. Also, in the past there was typically time for one or two iterations of the design, while now there can be time for many more iterations. This tends to negate any savings resulting from the automation process. Additionally, he emphasized the need to closely check the output of the numerical techniques to ensure that the answers make sense.

Mr. Stammreich discussed the generation gap and the challenge that this presents in transferring technology from the experienced engineers to the younger engineers. He stated that some universities were stressing the need to learn the new tools over the ability to learn and analyze, and discussed the inherent problems associated with this. He emphasized the need for organizations to encourage greater vertical communication of goals and allow for feedback.

In closing, he stressed that the future of the mechanisms design will be an evolutionary refinement of the design process. New tools will constantly be evaluated and new requirements, such as design-to-cost, will be included in

the design process as they become relevant. He emphasized that the cost-plus environment was changing to fixed price. This will create added pressure on program managers to look for off-the-shelf mechanisms, which may not be the best solution. He also mentioned the challenge to young engineers in communication with more sophisticated manufacturing technologies, particularly with the theoretical emphasis at universities.

At this point the audience was invited to comment on this subject. The majority of the discussion centered around the computer-aided design/drafting (CAD) and the problems associated with implementing a CAD system into an engineering department. The primary concern dealt with the inability to effectively transfer data files between various systems. It was felt that this problem would have to be overcome in order for CAD to be fully implemented. Concerns were also raised about CAD software and its lack of sophistication in relation to advances in hardware.

Other issues centered around our educational system. The general feeling seemed to be that the universities were too theoretical in their training, and needed more emphasis on the practical hands-on type of training. A concern was also raised that there was no formal training for a mechanisms engineer - the closest being the mechanical engineering curriculum. Several speakers voiced the need for a more disciplined approach to providing the appropriate kinds of experience for young engineers. The panel expressed the idea that we need to individually accept responsibility for some of these problems, and suggested that we should make a more concerted effort to relate our needs to the universities. Also we should take a personal interest in helping the young engineers to bridge the gap between the theoretical and the practical.

RELIABILITY VERSUS REDUNDANCY VERSUS MAINTAINABILITY 22nd AMS, May 5, 1988

Panel speaker, Mr. Otto Fedor, discussed the issues of reliability, redundancy, and maintainability of the space and ground-based mechanisms based on his extensive work experience at NASA's KSC. He shared with the audience his experience with the Apollo and Skylab programs. The following is a synopsis of his presentation and the subsequent discussion with the audience.

Who is a reliability engineer? Reliability engineering requires a highly specialized engineer. He is a specialist in the field of design who supports the designer. He must understand the design requirement. If he does not understand it, he must not be afraid to ask questions. He must be obnoxious at times to get the information he needs. He gives a customer what the customer needs, not what the customer wants.

He must understand the operational environment of the mechanism in the early stage of the program. Then he must determine the criticality of components in their applications, and insist on testing of critical components. Identification of a timely test program is one of the critical functions, and is the responsibility of the reliability engineer.

What causes an unreliable product? From the reliability engineering point of view, major causes of mechanical unreliability due to uncontrollable (or less controllable) uncertainties include inability to predict actual working environment, deficient customer requirements, and incompatibility of requirements with state-of-the-art design. There are other uncertainties which are more controllable and can be minimized, such as human errors made by the designers, and errors made during manufacturing processes and in maintenance.

How can the reliability and maintainability be improved in a mechanism design process? Mr. Fedor pointed out the following issues: Simplicity is the key; make the design simple to operate and maintain. Look for a benign environment with less load and stress in which the mechanisms operate. Control component quality. Design for redundancy, but not duplications. Use a different method for a redundant unit. Detect and eliminate a progressive failure design, that is, a design in which one failure leads to another failure, and so on. Mr. Fedor stated that a fail safe mechanism design using redundancy does not take the place of a good reliable non-redundant design.

Symptoms of design fault and the degree of unreliability in mechanisms design can be detected in many ways by the reliability engineer. Watch for defects at engineering changes, at design and product acceptance decision points, at in-process check points, and in product receiving inspections. Watch for compliance with delivery schedule, deviation from life cycle cost projection, and scrap and rework cost. Watch for performance test results, audit findings, and material review board actions. All of these activities provide clues to the reliability of the product delivered to the customer.

Mr. Fedor discussed the decision-making process within a company. He stated that a company which is proud of its democratic process of design management, which is based on majority rule, may tend to reject a minority viewpoint, which may be a crucial factor in design.

He stated that the role of reliability engineering should be more emphasized. It should be noted that rules, regulations, and reports are not a substitute for sound engineering judgment. The reliability engineer must have the ability and sensitivity to coordinate and evaluate the engineering and management disciplines.

Do not surprise the management. Reliability engineers should maintain the communication link with the management. Reliance on a complex paper system should not obscure the need for the reliability engineer to identify the issues that truly require top management attention. Also, reliability, safety, and quality organizations should be visible to the engineering management decision process.

In summary, Mr. Fedor offered the following recommendations to the reliability and mechanisms engineers:

A system reliability program should be developed "up front" to identify reliability drivers and prioritize hardware for functional and component criticality. To accomplish this, it is important that early attention be given to reliability in the design process. The reliability program should be directed to provide a healthy, creative "work environment" for the mechanisms designer and reliability engineer. Also, it should create an environment that assures highly desirable features such as minimizing engineering changes, abiding by test protocols, and using proven hardware and techniques. Thorough environmental test programs should be conducted during the subsystem build sequence, not during the final system test. Like hardware, reliability must also be built into software development processes and they should not be allowed to be a cult. After each program, a lessons-learned final report should be written to assure that the next program builds on past experiences.

At this point the audience was invited to participate in the discussion. One member of the audience responded that in the area of bearing design, a higher margin of safety is built into the design, and redundancy is eliminated. Another member of the audience in the systems discipline mentioned that in the attitude control system a fourth reaction wheel (where three wheels are needed) is used as a spare on their spacecraft to facilitate an extended mission. He further commented that it is more difficult to provide redundancy in mechanisms than in electronics. Mr. Fedor commented that redundancy is "a piece of cake" in electronics. "Not so," said Mr Stammreich. "Sometimes redundancy in electronics can be very complex when one tries to achieve true redundancy."

It was mentioned that in a government contract, a simple redundancy is often emphasized. That is, redundancy should not degrade or jeopardize reliability. Mr. Fedor advised that when redundant mechanisms are employed, you should be certain that the system is really redundant.

The discussion moved on to the topic of developing capability to repair and service in space versus product reliability. Although space serviceability has been demonstrated (for example, by the Solar Max mission), it seemed that there would be many tradeoffs which need to be worked out, including those of spare parts cost and weight. How small should a part be to be advantageous for serviceability? Mr. Fedor responded that it is determined by its function.

Mr. Fedor re-emphasized the importance of testing in reliability. He said he was impressed by the thorough test program the Soviets had developed for their space program. "Put your money in testing," he stressed.

The discussion was very lively, intriguing, and informative thanks to Mr. Fedor, who shared his unique experience with the audience, and thanks to the audience who responded with their views and comments.

VACUUM TRIBOLOGY

22nd AMS, May 5, 1988

As reported by Donald Sevilla
Spacecraft Mechanisms Engineer
Jet Propulsion Laboratory, California Institute of Technology

Michael Todd of the European Space Tribology Laboratory introduced his subject by asking the philosophical question: Is the environment inside a spacecraft (typically 10^{-6} torr) tribologically hostile? Would unprotected sliding steel surfaces adhere to each other? He called this pressure a "soft vacuum," due to the presence of the water vapor and other outgassing products. Mr. Todd presented recent friction and wear test results of degreased 52100 steel against itself in air and vacuum. Surprisingly, the friction levels were comparable, and the wear of the surfaces in air were 70 times greater than in a "soft vacuum." However, when the tests were performed in a "hard vacuum" of the pressures to be expected when directly exposed to space (10^{-8} to 10^{-10} torr), there was a complete reversal of the wear results. In addition, considerably higher friction was present at 10^{-8} torr than in air. As is well known, "hard vacuum" is a tribologically difficult situation. He noted that "soft vacuum," while not tribologically benign, is somewhat "tribologically polite."

Mr. Todd presented the required characteristics of an ideal space lubricant. It should:

- Prevent counterface wear completely
- Not escape by evaporation or surface migration
- Not exhibit friction property changes with sliding speed
- Be indifferent to temperature changes
- Not create debris
- Exhibit radiation resistance.

He discussed various merits of wet lubricants and solid lubricants, asking if there was an optimum lubricant for space. The merits of two types of wet lubricants, perfluorides and mineral oils, are somewhat opposing. The perfluorides meet most of the required criteria, but not all. The ones with the lowest vapor provide poor elastodynamic lubrication, exhibiting breakdown by polymerization. The mineral oils are very good for elastodynamic lubrication, but have unacceptably high vapor pressures. He classified solid lubricants into three types: soft metals (such as lead), laminar solids (such as moly-disulfide), and polymers (such as PTFE). Soft metals are good in low to heavy stress, but are poor in air and have a finite life. Laminar solids are very good for low stress and light duty applications, exhibiting very

smooth torque characteristics. However, he stated, that they are not good in air with restricted life. Polymers exhibit similar characteristics in air and vacuum, but are useful for low contact stress and they break down readily under load. Again, as with the wet lubricant, Todd stated that no single solid lubricant appears to be an answer to all the requirements. He suggested that one practical solution appears to be the use of oils in conjunction with nitride surfaces such as silicon-nitride and titanium-nitride. Even with the lowest vapor pressure, lubricant polymerization is not a problem.

Todd concluded his segment by discussing areas for advances in the near future. The field of solid lubricants is ripe for development. He discussed recent work in synergy, using two different lubricants in conjunction to give better performance than each one alone. By example, he presented the technology of pre-sputtering moly-disulfide on a steel surface and using a moly-impregnated PTFE bearing material (Duroid). He stated that very favorable characteristics have resulted.

Another field that is ripe is surface modification through ion beam mixing and ion implantation. He called this technology "ion milling," showing great promise for improved solid lubricant performance.

The discussion was then turned to questions and comments from the audience. The first question posed was for an explanation for the beneficial synergy when moly-disulfide is used with PTFE. Todd answered that he only had a half-explanation: He stated that PTFE, if left to itself, will transfer from the (parent) surface in a "lumpy way", and this phenomenon will be speed- and temperature-dependent because PTFE is a viscoelastic material. The presence of the moly-disulfide seems to inhibit the transfer of the PTFE.

One comment from the audience was that chemical compatibility of the lubricant with the substrate was not discussed. A classic example mentioned was a PTFE-type lubricant that works well "statically," but as the surfaces are rubbed, very highly active iron and chrome particles are created, leading to the black polymer. This black polymer tends to drive the lubricant from the working surfaces. (Todd called it "autophobic.")

A member of the audience observed that tribology technology for space is a "sinusoidal learning curve" in which research and hardware errors are repeated in ten year cycles. The problem is education. He stated that in Europe they hope to set up a committee to set standards of quality, and recommend the direction that future work in space tribology will take. He also discussed the fact that while synergy was mainly mentioned with respect to moly-disulfide and PTFE, a trend being pursued in Europe was the use of a combination of solid and liquid lubricants in an attempt to combine the best properties of both.

A question posed was whether cold-sputtering moly-disulfide with gold would solve the problem of in-air performance of moly-disulfide. Todd discussed some work involving synergy in solid lubricant mixing. Additional comments from the audience presented varying results in this endeavor, where a

"general-use" lubricant was still not developed. However, it was stated that favorable results are being found with co-sputtering of metals with molydisulfide.

The last questioner asked whether it was sufficient to just develop seals and labyrinthths to keep mineral oils from migrating or evaporating away. One response was that while this is the lowest cost solution, it is not always possible to seal the bearing surfaces sufficiently.

ABBREVIATIONS AND ACRONYMS

A	Amps
Å	angstroms
ac	alternating current
ACS	Attitude Control Stabilization
ADP	Advanced Development Program
ALS	Advanced Launch Systems
AMS	Aerospace Mechanisms Symposium
ARC	Ames Research Center
ASCIE	Advanced Structures/Controls Integrated Experiment
AST	Aerospace Technology
BAPTA	Bearing and Power Transfer Assembly
BAPTA-E	Bearing and Power Transfer Assembly-Electronic
BAPTA-M	Bearing and Power Transfer Assembly-Mechanism
BBT	Balanced-Bridge Control Theory
BRM	Binary Rate Multiplier
C	Centigrade
CAD	Computer Aided Design/Drafting
CFRP	Carbon Fiber Reinforced Plastics
CLTS	Cryogenic Linear Temperature Sensor
cm	centimeter
CMG	Control Moment Gyroscope
CNSR	Comet Nucleus Sample Return
CRT	Cathode Ray Tube
CTM	Coilable Tube Mast

ABBREVIATIONS AND ACRONYMS (Continued)

dB	decibel
dc	direct current
deg	degree(s)
DGCMG	Double Gimbal Control Moment Gyroscope
dm	decimeter
DOF	Degree(s)-of-Freedom
DPA	Digital Position Actuator
DRB	Deployable Retrievable Boom
DTS	Deployable Truss Structure
EMF	Electromotive Force
EMI	Electromagnetic Interface
ERM	Extendable and Retractable Mast
ESA	European Space Agency
ESTEC	European Space Research and Technology Center
ESTL	European Space Tribology Laboratory
ESW	Energy Storage Wheel
EVA	Extra-Vehicular Activity
F	Fahrenheit
FEM	Finite Element Model
FIRST	Far Infrared Space Telescope
FORJ	Fiber Optics Rotary Joint
FRG	Federal Republic of Germany
FRHC	Force Reflecting Hand Controller
g	gram

ABBREVIATIONS AND ACRONYMS (Continued)

GHz	Gigahertz
GSD	Guidance Systems Division
HPM	Hemispherical Pointing Mechanism
HRM	Hold-down and Release Mechanism
HST	Hubble Space Telescope
Hz	Hertz
IDEAS	Interactive Development of Engineers, Administrators and Scientists
IGA	Inner Gimbal Assembly
IGEA	Inner Gimbal Electronics Assembly
in.	inch(es)
in.-lb	inch-pounds
in.-lb sec/rad	inch-pounds seconds per radian
ISO	Infrared Space Observatory
J	Joules
JPL	Jet Propulsion Laboratory
JSC	Johnson Space Center
K	Kelvin
kg	kilograms
kHz	KiloHertz
kpsi	thousand pounds per square inch
KSC	Kennedy Space Center
lb	pound(s)
lb-in.	pounds-inch
LDR	Large Deployable Reflector

ABBREVIATIONS AND ACRONYMS (Continued)

LeRC	Lewis Research Center
LIDAR	Light Detecting and Ranging
LITE	Lidar In-space Technology Experiment
LTM	Laboratory Telerobotic Manipulator
m	meters
mbar	millibars
MGIM	Micro-Gravity Isolation Mount
MHz	MegaHertz
MIPS	Million Instructions per Second
MITI	Ministry of International Trade and Industry
MIT	Massachusetts Institute of Technology
MLI	MultiLayer Insulation
mm	millimeter
mrad	milliradians
msec	milliseconds
MSFC	Marshall Space Flight Center
mW	milliwatt
N	Newton
NASA	National Aeronautics and Space Administration
NASTRAN	NAsa STRuctural ANalysis
Nm	Newton meter
N·m·sec	Newton meter second(s)
NRL	Naval Research Laboratory
NSTS	National Space Transportation System

ABBREVIATIONS AND ACRONYMS (Continued)

OGEA	Outer Gimbal Electronics Assembly
OMB	Office of Management and Budget
ORU	Orbital Replaceable Unit
oz-in.	ounce inch
PDP	Personal Development Program
PHA	Panel Hinge Assemblies
PMIS	Personnel Management Information Systems
psi	pounds per square inch
PTFE	polytetrafluoroethylene
PWM	Pulse Width Modulation
PZT	lead-zirconate-titanate
rad	radian(s)
rad/sec	radians per second
RAM	Rexnord Aerospace Mechanisms
R&D	Research and Development
REA	Rotor Electronics Assembly
RF	Radio Frequency
RMS	Remote Manipulator System
ROTEX	Robotic Technology Experiment
R&PM	Research and Program Management
rpm	revolutions per minute
RVDT	Rotary Variable Differential Transformer
SAR	Synthetic Aperture Radar
S&Es	Scientists and Engineers

ABBREVIATIONS AND ACRONYMS (Concluded)

sec	second(s)
SGCMG	Single Gimbal Control Moment Gyroscope
SPDS	Stabilized Payload Deployment System
SPEE	Special Purpose End Effector
SPIRAL	Double Lead Spiral Platen Parallel Jaw End Effector
STS	Space Transportation System
TALOS	Tropical Atmospheric LIDAR Observing System
TMA	Torquer Module Assembly
TMIS	Technical and Management Information System
2D	Two-dimensional
3D	Three-dimensional
TSS	Tethered Satellite System
UARS	Upper Atmosphere Research Satellite
UQS	Unique Signal
V	Volts
Vdc	Volts direct current
VLM	Variable-Loading Mechanism
W	Watts

1. REPORT NO. NASA CP-3032	2. GOVERNMENT ACCESSION NO.	3. RECIPIENT'S CATALOG NO.	
4. TITLE AND SUBTITLE 23rd Aerospace Mechanisms Symposium		5. REPORT DATE March 1989	
7. AUTHOR(S)		6. PERFORMING ORGANIZATION CODE	
9. PERFORMING ORGANIZATION NAME AND ADDRESS George C. Marshall Space Flight Center Marshall Space Flight Center, Alabama 35812		10. WORK UNIT NO. M-611	
12. SPONSORING AGENCY NAME AND ADDRESS National Aeronautics and Space Administration Washington, D.C. 20546		11. CONTRACT OR GRANT NO.	
		13. TYPE OF REPORT & PERIOD COVERED Conference Publication	
15. SUPPLEMENTARY NOTES California Institute of Technology, Pasadena, CA 91109. Lockheed Missiles and Space Company, Inc., Sunnyvale, CA 94088.		14. SPONSORING AGENCY CODE	
16. ABSTRACT <p>The proceedings of the 23rd Aerospace Mechanisms Symposium, which was held at the Marshall Space Flight Center, Huntsville, Alabama, on May 3 to 5, 1989, are reported. Technological areas covered include space lubrication, bearings, aerodynamic devices, spacecraft latches, deployment, positioning, and pointing. Devices for Space Station docking and manipulator and teleoperator mechanisms are also described.</p>			
17. KEY WORDS Docking devices Drive mechanisms Actuators Space lubricants Vibration isolation Teleoperation Stress corrosion		18. DISTRIBUTION STATEMENT Unclassified - Unlimited Subject Category 39	
19. SECURITY CLASSIF. (of this report) Unclassified	20. SECURITY CLASSIF. (of this page) Unclassified	21. NO. OF PAGES 356	22. PRICE A16

E N D

1-22-92